13th MULTINATIONAL CONGRESS ON MICROSCOPY

september 24-29, 2017
rovinj, croatia

BOOK OF ABSTRACTS

Ruđer Bošković Institute

Croatian Microscopy Society

13th Multinational Congress on Microscopy

September 24-29, 2017 in Rovinj, Croatia

BOOK OF ABSTRACTS

Editors

Andreja Gajović, Igor Weber, Goran Kovačević, Vida Čadež
Suzana Šegota, Petra Peharec Štefanić and Ana Vidoš

Publishers

Ruđer Bošković Institute and Croatian Microscopy Society

Ruđer Bošković Institute

Croatian Microscopy Society

13th Multinational Congress on Microscopy: BOOK OF ABSTRACTS

September 24-29, 2017 in Rovinj, Croatia

Editors: Andreja Gajović, Igor Weber, Goran Kovačević, Vida Čadež, Suzana Šegota, Petra Peharec Štefanić and Ana Vidoš

Publishers: Ruđer Bošković Institute and Croatian Microscopy Society

Zagreb 2017

ISBN 978-953-7941-19-2

Committees

CONFERENCE CHAIRS

Andreja Gajović, Division of Materials Physics, Ruđer Bošković Institute and Croatian Microscopy Society

Igor Weber, Division of Molecular Biology, Ruđer Bošković Institute and Croatian Microscopy Society

INTERNATIONAL ORGANIZING COMMITTEE

Gerd Leitinger, Institute of Cell Biology, Graz, Austria

Michael Stöger-Pollach, Technische Universität Wien, Austria

Jana Nebesarova, Institute of Parasitology, České Budejovice, Czechia

Sašo Šturm, Jožef Stefan Institute, Ljubljana, Slovenia

Rok Kostanjšek, University of Ljubljana, Slovenia

Katalin Solymosi, Eötvös Loránd University, Budapest, Hungary

Mihály Pósfai, University of Pannonia, Egyetem, Hungary

Falcieri Elisabetta, Università degli Studi di Urbino, Italy

Roberto Balboni, National Research Council, Rome, Italy

Dusan Chorvat, International Laser Centre, Bratislava, Slovakia

Serap Arbak, Acibadem University, Istanbul, Turkey

Mehmet Ali Gülgün, Sabanci University, Istanbul, Turkey

Nataša Nestorović, University of Belgrade, Serbia

Dragan Rajnović, University of Novi Sad, Serbia

Andreja Gajović, Ruđer Bošković Institute, Zagreb, Croatia

Igor Weber, Ruđer Bošković Institute, Zagreb, Croatia

LOCAL ORGANIZING COMMITTEE

Vida Čadež, Ruđer Bošković Institute, Zagreb, Croatia

Goran Kovačević, Department of Biology, Faculty of Science, University of Zagreb, Zagreb, Croatia

Suzana Šegota, Ruđer Bošković Institute, Zagreb, Croatia

Marko Kralj, Institute of Physics, Zagreb, Croatia

Petra Peharec Štefanić, Department of Biology, Faculty of Science, Zagreb, Croatia

Vesna Babić-Ivančić, Ruđer Bošković Institute, Zagreb, Croatia

Ognjen Milat, Institute of Physics, Zagreb, Croatia

Ana Vidoš, Marketing and Events Coordinator, Ruđer Bošković Institute, Zagreb, Croatia

The Multinational Congress on Microscopy 2017 has been designated an EMS Extension meeting by the European Microscopy Society.

13th Multinational Congress on Microscopy

September 24-29, 2017 in Rovinj, Croatia

CONTENTS

KEYNOTE LECTURE

From Micrometer to Sub-Angstroem Resolution – the Development of the Electron Microscope

Herald Rose (1)

(1) Ulm University, Albert-Einstein-Allee 11, 89081 Ulm, Germany

Electron microscopy is based on the fundamental discoveries made in 1924 by Louis de Broglie who postulated that a wave is attributed to each elementary particle and in 1926 by Hans Busch who showed that the magnetic field of a solenoid acts on electrons in the same way as a glass lens on the light rays. It had been these two fundamental discoveries which initiated Ernst Ruska to realize an electron microscope in 1931. Unfortunately, round electron lenses suffer from large unavoidable aberrations which limit the resolution of any electron microscope to about 100 wavelengths, as shown by Otto Scherzer in 1936. Fortunately, he found an ingenious way in 1947 to enable aberration correction by employing non-rotationally symmetric elements. However, all subsequent experiments to improve the resolution by means of various correctors failed because the resolution was limited by mechanical and electrical instabilities rather than by the defects of the electron lenses. Owing to these facts experiments on aberration were abandoned in the mid 1980th after a group of experts in the US had concluded that the successful realization of aberration correction was “unthinkable”. As a result, funding on aberration correction was stopped worldwide. Experimental work on aberration correction was resumed in 1992 within the context of the “Volkswagen Project” aimed to improve the resolution limit of a 200 kV transmission electron microscope (TEM) by eliminating the spherical aberration and the coma of the objective lens by means of a novel highly symmetric aplanatic hexapole corrector. In addition, an effective alignment procedure was developed which enables a precise and fast elimination of the spherical aberration and of all resolution-limiting parasitic aberrations originating from mechanical inaccuracies, magnetic in homogeneities, and misalignment. By means of these measures the resolution limit of a commercial 200kV TEM was reduced from 2.1Å (100λ) to 1.4Å in 1997. In the meantime this limit has been lowered further to about 0.5Å in the frame of the US TEAM project. In April 2016, the SALVE Project ended with spectacular success. Within the frame of this project, which aimed to obtain atomic resolution of radiation-sensitive objects at low voltages, the resolution limit has been reduced to 15λ giving sub-Å resolution down to 40kV. First promising results will be presented

EMS SPONSORED PLENARY LECTURES

Operando and multimodal studies of speciation and activity of Pt catalysts during the hydrogenation of ethylene

Eric A. Stach (1,2*), Yuanyuan Li (3), Deyu Liu (5) Shen Zhao (2,5) Jing Liu (3) Yao-Min Liu (5), Dmitri N. Zakharov (2), Qiyuan Wu (4), Alexander Orlov (4), Andrew A. Gewirth (5) Ralph G. Nuzzo (5), Anatoly I. Frenkel (3,4)

1) Department of Materials Science and Engineering, University of Pennsylvania, Philadelphia, PA 19104 *stach@seas.upenn.edu
2) Center for Functional Nanomaterials, Brookhaven National Laboratory, Upton, NY 11973
3) Department of Chemistry, Brookhaven National Laboratory, Upton, NY 11793
4) Department of Materials Science and Chemical Engineering, Stony Brook University, Stony Brook, NY 11794
5) Department of Chemistry, University of Illinois, Urbana, IL 61801

The creation of fuels and large volume chemicals (such as olefins) from crude oil feedstocks involves the hydrogenation of unsaturated hydrocarbons. These processes involve numerous catalytic reforming and hydrogenation/dehydrogenation processes, and are generally mediated by supported metal nanoparticle catalysts. These catalysts are generally chosen for their high activity, long term stability and the ease with which they can be regenerated and recovered. However, despite the extensive use of these materials, there are many questions that remain about how specific attributes of the structure and composition of the catalysts are affected by the gases with which they interact. Furthermore, it is critically important to understand how these structural changes affect selectivity, as well as how deactivation occurs because of the conversion process. In this work, we will describe how we use a multi-modal, *operando* experimental approach to understand the subtle changes that occur to both the atomic structure and the chemical state of palladium nanoparticle catalysts supported on SiO_2 during the hydrogenation of ethylene. The core of this approach is the use of a closed-cell microreactor (1) that allows sequential experimental investigation via scanning transmission electron microscopy (STEM), x-ray absorption spectroscopy (XAS) and microbeam infrared spectroscopy (μ-IR), and gas-chromotography/mass spectroscopy (GC-MS), with all measurements being made in the same *operando* reaction conditions (2,3). We will describe how this approach allows us to directly correlate the measurements in a robust fashion, leading to novel insights regarding several aspects of ethylene conversion. In specific, we will describe

how the specifics of reactive gas composition lead to interconversion of both hydride and carbide phases of the Pd clusters, which processes affect the stability of the particles against coarsening, the reversibility of structural and compositional transformations and the role that surface oligomers that form under hydrogen limited reactant conditions, leading to deactivation.

Acknowledgements:

The authors gratefully acknowledge support for this by the US Department of Energy, Office of Basic Energy Sciences under Grant No. DE-FG02-03ER15476. The development of the micro-cell was supported, in part, by an LDRD grant at Brookhaven National Laboratory. We acknowledge the facilities support provided at the Centre for Functional Nanomaterials, the National Synchrotron Light Source at the Brookhaven National Laboratory (US Department of Energy, Office of Basic Energy Sciences, Contract No. DE-SC0012704) and the Synchrotron Catalysis Consortium (US Department of Energy, Office of Basic Energy Sciences, Grant No. DE-SC0012335).

References:

1. Li, Y., D. Zakharov, S. Zhao, R. Tappero, U. Jung, A. Elsen, Ph Baumann, Ralph G. Nuzzo, E. A. Stach, and A. I. Frenkel. “Complex structural dynamics of nanocatalysts revealed in Operando conditions by correlated imaging and spectroscopy probes”, Nature Comm. 6, 7583, 2015.

2. Zhao, S., Li, Y., Stavitski, E., Tappero, R., Crowley, S., Castaldi, M.J., Zakharov, D.N., Nuzzo, R.G., Frenkel, A.I. and Stach, E.A., “Operando Characterization of Catalysts through use of a Portable Microreactor”, ChemCatChem, 7(22), pp.3683-3691, 2015

3. Zhao, S., Y. Li, D. Liu, J. Liu, Y.-M. Liu, D.N. Zakharov, Q. Wu, A. Orlov, A.A. Gewirth, E.A. Stach, R.G. Nuzzo, A.I. Frenkel, in review.

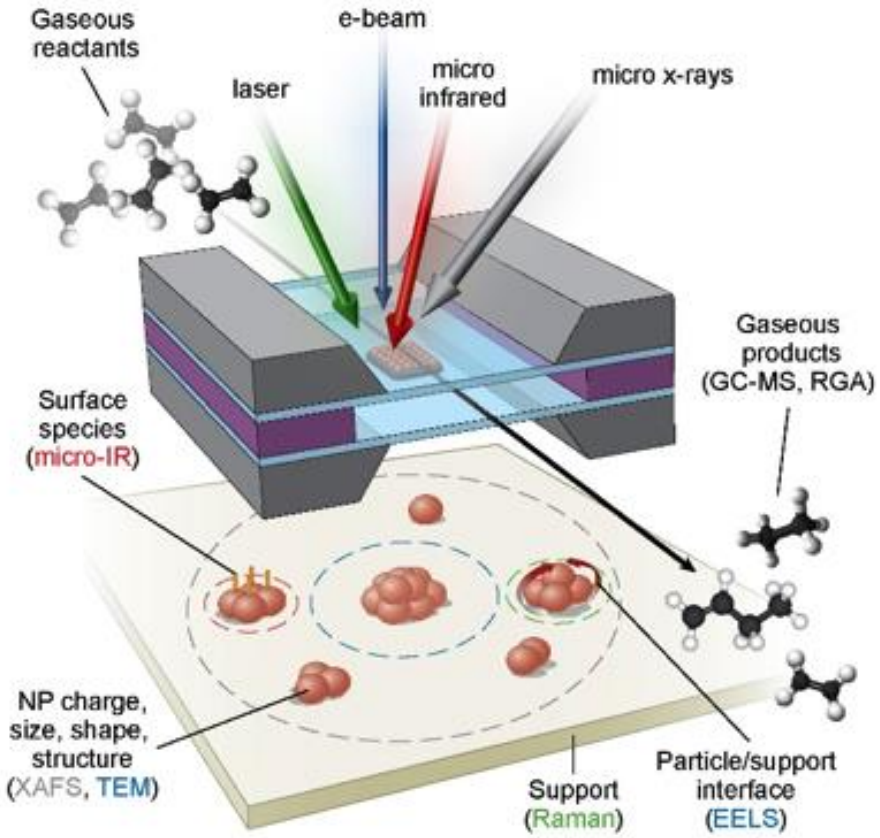

Figure 1. Schematic of the portable microreactor utilized for operando and multimodal studies which shows both the the probes that we have demonstrated and the information that we can obtain from each technqiues.

Coherent diffraction imaging in transmission electron microscopy for atomic resolution quantitative studies of the matter

Elvio Carlino (1), Liberato De Caro (2), Francisco Scattarella (3), Alessandro Colombo (4), Davide E. Galli (1)

1) Istituto di Microelettronica e Microsistemi, Consiglio Nazionale delle Ricerche (CNR-IMM) - Sezione di Lecce - Campus Universitario - Via per Monteroni, 73100 Lecce – Italy
2) Istituto di Cristallografia, Consiglio Nazionale delle Ricerche (IC -CNR), via Amendola 122/O Bari, 70125 Italy
3) Istituto Officina dei Materiali, Consiglio Nazionale delle Ricerche (IOM-TASC-CNR), Strada Statale 14 km 163.5, 34149 Trieste, Italy
4) Università degli Studi di Milano, via Giovanni Celoria 16, 20133 Milano, Italy

Keywords: TEM, Coherent diffraction imaging, quantitative atomic resolution, data reduction, phase retrieval algorithms

Coherent electron diffraction imaging (EDI) in the transmission electron microscope (TEM) is a method to image the sample atomic structure at a resolution not limited by the aberrations of the electron lenses[1]. The method can be applied to isolated nano-objects or to extended objects; in the latter case by using an approach named keyhole electron diffraction imaging (KEDI)[2], which is obtained by confining properly the illumination function on a nanosized area of an extended specimen. Possible future applications of EDI/KEDI are foreseen in the field of femtosecond and 3D imaging. EDI is theoretically based on the sampling theorem of Shannon and requires the acquisition of the diffraction pattern at least at the Nyquist's frequency[1]. The phase of the scattered waves is recovered by using iterative Fast Fourier Transform (FFT) algorithms that relates information available from the standard HRTEM to that available from the measured intensities in the diffraction experiment[2]. The electron diffractions for EDI requires an extensive data reduction before the application of phasing algorithms and the presence of eventual diffraction intensity artifacts, due to the experimental limitation related to the equipment and to the detector, complicate the application of EDI. In addition, the presence of strong dynamical effects in the electron diffractions can produce results not reliable[2] requiring the use of extremely thin TEM samples. Another subtle point is the phasing process, which is particularly demanding in the case of electron diffraction experiments. This is due to

the complex nature of the electron diffracted waves and to the size of the area to be reconstructed, which is very close to the size illuminated by the electron probe[3]. Here we show the results of our recent research in: -The treatment of the intensity artifacts in the experimental diffraction pattern;-The handling of the dynamical intensities as always present in the diffraction pattern of any standard good quality TEM specimen; -The developing of new phasing methods based on genetic algorithms capable of reconstructing the phase of the scattered waves starting from random phases and from an HRTEM image with a resolution four times worst with respect to the resolution achieved in the phase reconstructed image. In figure 1 an example of KEDI experiments on a specimen of $SrTiO_3$ in [001] zone axis is shown. The retrieved function is a structural image of the $SrTiO_3$ seen in the [001] zone axis and the intensity of the projected potential is in agreement with calculations within accuracy, in the worst case, of 14%. The methods developed for the quantification of EDI/KEDI experiments are not only methods to improve the resolution of TEM imaging experiments, but represent a set of tools to maximize the information that can be extracted from coupled HRTEM and electron diffraction experiments enabling high accuracy and spatial resolution in the quantitative study of the properties of the matter.

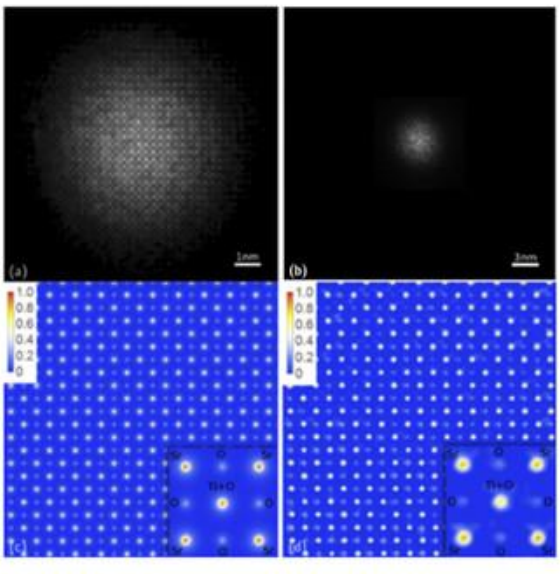

Figure 1. Results of phase reconstructed experimental KEDI data: (a) modulus of the retrieved scattering function extracted from the relevant experimental HRTEM image; (b) KEDI HRTEM image of $SrTiO_3$ in [100] zone axis; (c) simulation of the $SrTiO_3$ projected potential in [100] zone axis and (d) experimental projected potentials extracted from the phased map

References:

1. L. De Caro et al., Nature Nanotech., 5, (2010) 360–365.

2. L. De Caro et al., Acta Cryst. A, 68, (2012) 687–702.

3. A. Colombo et al., Sci. Rep., 7 (2017) 42236–42248

PLENARY LECTURES

HRTEM and HRSTEM Investigations of oxide thermoelectric materials

Miran Čeh (1), Sašo Šturm (2), Boštjan Jančar (3), Aleksander Rečnik (2), Nina Daneu (2), Goran Dražić (4), Marja Jerič (2), Mateja Košir (2), Matej Presečnik (2), Slavko Bernik (2), Cleva Ow-Yang (5), Mehmet A. Gülgün (5), Johannes de Boor (6)

1) Nanostructured Materials, Jožef Stefan Institute, Ljubljana, Slovenia, Center for Electron Microscopy, Jožef Stefan Institute, Jamova cesta 39, 1000 Ljubljana, Slovenia
2) Nanostructured Materials, Jožef Stefan Institute, Jamova cesta 39, 1000 Ljubljana, Slovenia
3) Advanced Materials, Jožef Stefan Institute, Jamova cesta 39, 1000 Ljubljana, Slovenia
4) National Institute of Chemistry, Hajdrihova ulica 19, 1000 Ljubljana, Slovenia
5) Sabanci University, Orta Mahalle, Üniversite Caddesi No:27 Tuzla, 34956 İstanbul, Turkey
6) German Aerospace Center, Cologne, Germany

Keywords: thermoelectrics, planar faults, modulated structures, HR (S)TEM

It is known that thermoelectric (TE) properties (i.e. figure of merit, ZT) of oxide-based TE materials can be improved by introducing planar faults and/or modulated structures into the matrix material which reduce thermal conductivity via enhanced phonon scattering. In order to tailor TE properties of materials, it is prerequisite to assess structural and chemical information of such nanostructures on atomic scale. In our work we used high-resolution electron microscopy techniques (HRTEM, HRSTEM) accompanied with spectroscopic techniques (EELS and EDS) to characterize the following planar faults and modulated structures in oxide based thermoelectric materials: Ruddlesden-Popper (RP) type planar faults (1) in CaO-doped $Sr(Ti,Nb)O_{3-\delta}$ (STNO), inversion boundaries (IB's) (2) in $ZnO_k(In_2O_3/Al_2O_3)$ and modulated structures in $Ca_3Co_4O_9$-Na_xCoO_{2+x} system (3). All results were obtained in a Jeol 2010F and in Jeol ARM-200CF with Cs probe corrector. TEM BF imaging of CaO-doped STNO showed regions with ordered RP faults and regions with a network of random RP planar faults. HAADF analysis of the perovskite matrix additionally showed that the Nb content on the Ti sites largely varied from app. X=0.05 to X=0.35 for the STNO compositions with 10 mol% of added CaO. Furthermore, the concentration of Ca at the RP faults was always higher as compared to the STNO matrix (Fig. 1). This was attributed to preferential incorporation of smaller Ca ions into the rock-salt-type structure of the RP faults. Within In_2O_3-doped ZnO grains pure In monolayers

parallel to the {0001} ZnO lattice planes were readily observed by the HAADF. These basal inversion boundaries (b-IB) separate domains with different orientation. On the other hand, the pyramidal IB's (p-IB) were much easier observed with ADF due to additional strain contrast caused by In incorporation in these IB's. When some fraction of In_2O_3 was replaced by Al_2O_3, the EDS spatial difference showed that Al is incorporated into the b-IB's as well as into p-IB's (Fig. 2a,b,c,d). The ADF of the $Ca_3Co_4O_9$-Na_xCoO_{2+x} layered cobaltate system revealed coherent intergrowth of two structural types within individual grains. The intergrowths are comprised of the Na_xCoO_2-type where the CoO_2 layers are separated by a layer of Na^+ ions and the $Ca_3Co_4O_9$-type in which the CoO_2 layers are separated by three-layer rock-salt-type structure consisting of one CoO and two CaO layers. The two structural types are intergrown through the octahedral CoO_2 layer (Fig. 2e,f,g). STEM further revealed that Ca incorporates between the CoO_2 layers of Na_xCoO_2 structural part of the grain, thus increasing complexity of interlayer space. Employing EELS we found that differences in local interlayer structure do not affect the oxidation state of Co within the CoO_2 octahedral layers. Finally, TE measurements of above investigated materials confirmed that the presence of planar faults and/or modulated structures increased the ZT value.

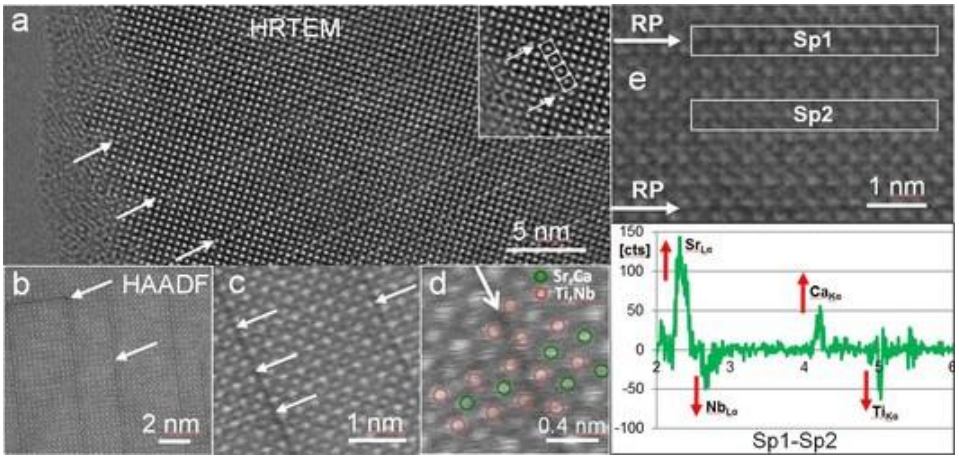

Figure 1. (a) HRTEM of RP faults in CaO-doped STNO. The inset marks four perovskite unit cells in between two RP faults. (b,c,d) HAADF STEM images RP faults that run along {001} perovskite planes. (e) Region of EDS analysis and spatial difference spectrum.

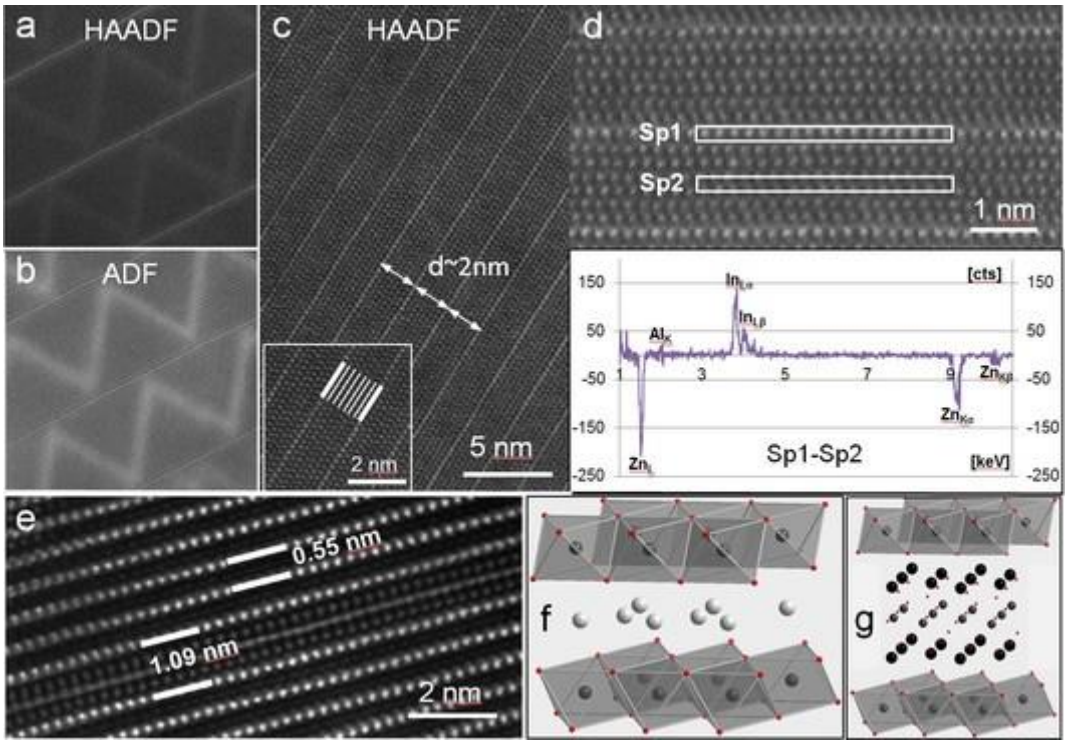

Figure 2. (a) HAADF STEM image of In-rich basal IB's. (b) ADF imaging revealing the pyramidal IB's. (c) Ordered IB's corresponding to $(ZnO)_5.In_2O_3$ phase. (d) Region of EDS analysis and spatial difference spectrum. (e) Intergrowth of $Ca_3Co_4O_9$-Na_xCoO_{2+x} layered cobaltates. (f) $NaxCoO_{2+x}$ structure and (g) $Ca_3Co_4O_9$ structure.

References:

1. S.N. Ruddlesden, P. Popper, Acta Crystallogr. 11 (1958) 54-55.
2. A. Rečnik et al., J. of the European Ceram. Soc. 27(4) (2007) 1999-2008.
3. D. Vengust et al., Chem. Mater. 25 (2013) 4791-4797.

Developments in cryo-electron tomography for *in situ* structural biology

Juergen M. Plitzko

Max Planck Institute of Biochemistry, Department of Molecular Structural Biology
82152 Martinsried, Germany

To chart the landscape of cellular territories at the molecular level, to directly observe molecules and macromolecular machines and to investigate their location, their neighbourhood, and their interaction partners, within the cellular context, thus *in situ* was and still is the grand vision of cellular tomography. Recent developments and breakthroughs in instrumentation encompassing novel direct electron detectors, phase plates, and micro-machining/preparation methods and their combined use for cryo-electron tomography (cryo-ET) are clearly the basis towards realising this vision. The word tomography derives from the old Greek tomos (τόμος) - to 'slice' or 'section', and graphō (γράφω), to 'write'. The 'write' part, thus the efficient detection of electrons accelerated to 300 keV, had been a real challenge for the past several decades. Most of the signal was lost on its way through the detector or just too scattered. Images from the "cameras of yesteryear" can be literally described as a look through frosted windows, when compared to the latest detector generation. Detecting electrons directly did enhance the vision enormously by a more than three-fold increase in signal transfer and the ability to discriminate every incoming electron. However, the 'slice' aspect is equally as important as the 'write' part. Electrons do not like a lot of material to interact with and the attainable resolution in cryo-ET is directly related to the sample thickness. Therefore, thin samples are mandatory for any high-resolution tomographic study. 'Slicing' in the 21st century, to obtain electron transparent lamellas, can be done gently and in a targeted fashion with the focused-ion-beam instrument. Originally designed for the quality control of silicon wafers and for troubleshooting erroneous wiring of their circuits, it was first explored for frozen-hydrated samples 10 years ago: A fine focused beam of ions ablating material of a cryo-specimen to make it transparent enough for cryo-ET, while at the same time keeping it frozen hydrated. That pilot study was the start of further exploration of this methodology for *in situ* structural biology. Perhaps it is too early to say that cryo-focused ion beam milling (cryo-FIB) is now the method of choice for obtaining 150-300 nm thin slices from a wide variety of cell types ranging from larger bacteria to neuronal primary cultures. However, the method is certainly gaining

momentum and in combination with direct detection and phase-plate assisted tomography, we are now able to explore the ‘wonders’ of the inner space of cells at molecular detail. But one has to be aware, only a tiny fraction of the cell’s volume is covered in such a ‘slice’. For a given mammalian cell, a FIB-ed lamella contains less than 0.1% of the whole cellular volume. Therefore, it is necessary to find ways of navigating and localising specific features and structures within this ‘huge’ (at least ‘huge’ from the electron microscopists point of view) cellular volume. This fact necessitates the introduction of correlative light and electron microscopy (CLEM) and at best in all three dimensions to guide the FIB milling and thus to allow us to capture unique and transient structures within these lamellas. Ongoing developments hold promise for targeting specific cellular structures, even within tissues and multicellular organisms. The fidelity with which macromolecules can now be visually identified in cryo-electron tomograms of FIB-ed lamellae is dependent on several factors. Foremost is assuredly the thickness of the sample, since resolution scales with the thickness, but the degree of molecular crowding has to be considered as well, since crowding can vary greatly from one cell type to another (e.g. yeast is denser than algae) and between different regions within a single cell (e.g. the nucleoplasm is denser than the cytoplasm). Together, a sample’s thickness and crowding will ultimately determine the level of detail that can be resolved by cryo-ET. This lecture will present recent work in the field of cryo-electron tomography and *in situ* structural biology and highlights technological developments, limitations and their opportunities. Furthermore, it will give a prospective towards obtaining structural insights from an *in situ* context, possibly at atomic resolution.

Electron tomography and multi-dimensional electron microscopy

Paul A. Midgley

Department of Materials Science and Metallurgy, University of Cambridge,
27 Charles Babbage Road, Cambridge, CB3 0FS, UK.

Since its introduction into materials science, STEM-based electron tomography has become an almost-routine method to examine the 3D structure of materials at the nanometre level. There have been significant advances in terms of optimal acquisition strategies (e.g. sub-sampling and in-painting) and reconstruction algorithms. The adoption of SIRT and more recently compressed sensing methods has led to greatly improved reconstruction fidelity by incorporating known (prior) information or comparable fidelity using greatly reduced data sets. Recently, with the introduction of more efficient spectrometers and cameras, and with a vast increase in computer power, analytical electron microscopy / tomography has yielded new quantitative nanoscale information about the crystallography, composition, chemistry and electric, magnetic and optical properties through the acquisition of 'multi-dimensional' data sets. This has been accomplished by combining different modes of electron microscopy, exploring real and reciprocal space, energy and time. I will discuss how this is best implemented, reviewing the state-of-the-art in multi-dimensional microscopy and look forward to how these techniques might be developed further for automated data collection and analysis.

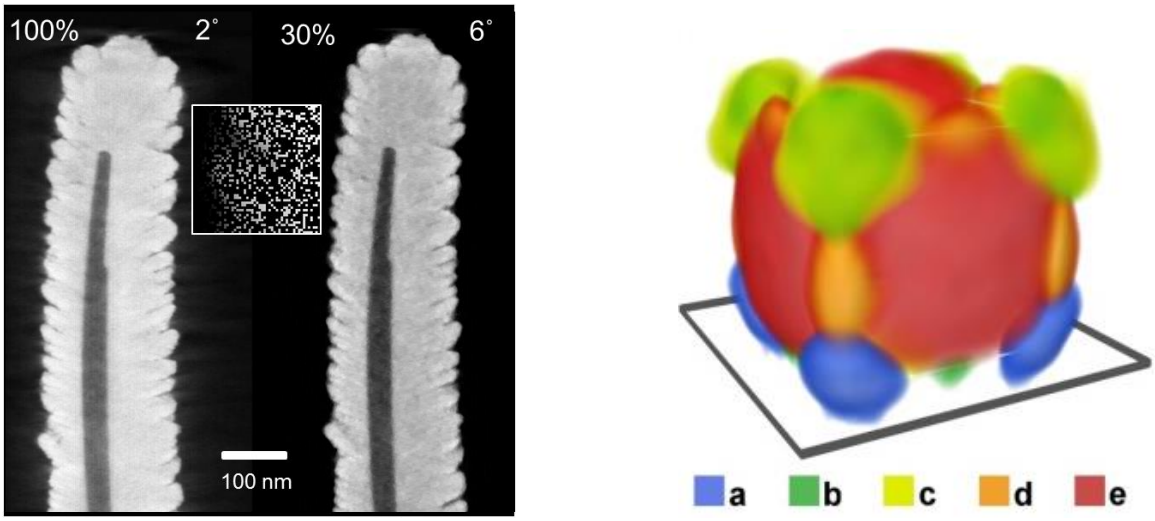

Figure 1. Left: Orthoslices from a reconstructed cobalt phthalocyanine (CoPc)/ZnO nanowire showing comparable fidelity after random sub-sampling (reduction of dose by a factor of 10) from Z. Saghi et al (2015) *Adv. Str. Chem. Imaging* 1:7. Right: Colour composite figure indicating five surface plasmon modes on a silver nanoparticle, 100nm in size; from O. Nicoletti et al., *Nature* 502 (2013) 80.

Nanoparticle interactions with human biological barriers

Eva Roblegg (1)

1) University of Graz, Institute of Pharmaceutical Sciences, Pharmaceutical technology and Biopharmacy

Keywords: drug delivery, nano-carrier, biological barrier, oral cavity, saliva

Due to scientific advances of the past decade the number of potent drug candidates in development has increased dramatically. However, new “designer-made” drug molecules are becoming increasingly complex, and as a consequence they are less soluble in aqueous media. Moreover, biological candidates, such as proteins and antibodies are prone to enzymatic degradation and are expected to be inactivated, when exposed to the harsh human physiological conditions. As a consequence, these substances are mainly administered via the parenteral route, which is associated with pain and anxiety, leading to poor patient compliance. To overcome these hurdles, innovative drug delivery systems, which are administered via alternative non-invasive uptake routes such as the mucosal tissues in the oral cavity are an interesting approach in this emerging field. Thereby, the use of nano carriers that embed, protect and transport a drug candidate to the site of action is being intensively researched. However, the rational design of such systems is still challenging, because of lack of understanding of the biological processes governing the main barriers that nanoparticles (NP) encounter during administration. This includes absorption of biomolecules on NP surfaces (i.e., formation of a biocorona), colloidal stability and mobility in saliva, cellular uptake mechanisms, interference with cellular components, and possible adverse effects considering distinct NP properties with respect to size and surface charge. To fill this knowledge gap, we studied the architecture, more specifically the pore size distribution of the human salivary network by the use of freeze fracture TEM. The fluid´s rheology inside of the pores was examined with optical tweezers and the agglomeration tendency, the protein binding capacity and the mobility of differently sized and surface-tuned NPs was investigated by dynamic light scattering and particle tracking analysis. Uptake studies and interference with cell organelles were performed with standardized in-vitro models and visualized by SEM (1). We showed that the salivary network facilitates the access of NPs to the underlying oral mucosa in general. However, the physico-chemical properties of the NPs were found to critically affect the impact of saliva on

colloidal stability and mobility: Compared with non-functionalized NPs, the mobility of positively and negatively charged NPs was significantly impaired in saliva, preventing diffusion through the salivary barrier and uptake into the oral epithelium. Moreover, NP immobilization was correlated with increased binding of mucoglycoproteins and agglomeration. Particle size critically affected cellular uptake. Compared to 25 and 50 nm NPs, 200 nm particles showed a higher uptake rate and penetrated into deeper regions of the epithelium. We found that this size-dependent uptake is attributed to the specialized structure of the epithelial surface membrane, which is covered with ridge-like–folds, also referred as microplicae. Thereby, uptake is driven by thermodynamic driving forces and interparticle repulsion, which are both reduced for smaller NP sizes (2). To sum up, the tuning of NP properties enables control of the rates of NPs elemination through swallowing versus NP cell entry in the oral cavity. These fundamental insights are expected not only to improve the rational design of therapeutic NPs for intraoral administration but also to enable the objective evaluation of the risks associated with engineered NPs taken up unintentionally through the mouth.

References:

1. Teubl et al., Eur J Pharm Biopharm. 84(2) (2013) 86-93.
2. Teubl et al., Small.9(3) (2013) 457-66.

Optical and electrical approaches in astrocyte physiology

Marko Kreft (1,2,3), Maja Potokar (1,2), Matjaž Stenovec (1,2), Marko Muhič (1), Tina Pangršič (1), Mateja Prebil (1), Jernej Jorgačevski (1,2), Nina Vardjan (1,2), Helena Chowdhury (1,2), Robert Zorec (1,2)

1) Laboratory of Neuroendocrinology-Molecular Cell Physiology, Institute of Pathophysiology, Faculty of Medicine, University of Ljubljana, Zaloska 4, 1000 Ljubljana, Slovenia
2) Celica Biomedical Center, Tehnološki park 24, 1000 Ljubljana, Slovenia
3) Department of Biology, Biotechnical Faculty, University of Ljubljana, Večna pot 111, 1000 Ljubljana, Slovenia

Astrocytes are increasingly viewed as crucial cells in supporting and integrating the brain function. An important process of communication between astrocytes and neurons is exocytotic release of gliotransmitters from astrocitic membrane-bound vesicles into the extracellular space. Patch-clamp membrane capacitance measurements were used to monitor changes in membrane area of a single astrocyte while the photolysis of caged calcium compounds by a UV flash was used to elicit steps in $[Ca^{2+}]_i$ to determine the exocytotic properties of astrocytes. Experiments show that astrocytes exhibit Ca^{2+}-dependent increases in membrane capacitance. Prior to fusing with the plasma membrane, membrane-bound vesicles are transported through the cytoplasm. Their trafficking and the consequent release of their content may be changed in altered physiological conditions, therefore affecting the physiological status of neurons. The results show that the delivery of vesicles to the plasma membrane for membrane merger involves an interaction with the cytoskeleton, in particular microtubules, actin and intermediary filaments. Astrocytes also play a significant role in the brain energy metabolism. Their anatomical position between blood vessels and neurons makes them an interface for effective glucose uptake from blood. Astrocytes contain glycogen, an energy buffer, which can bridge local short term energy requirements in the brain. Glycogen levels reflect a dynamic equilibrium between glycogen synthesis and glycogenolysis. Many factors that include hormones and neuropeptides, such as insulin likely modulate glycogen stores in astrocytes, but detailed mechanisms at the cellular level are sparse. We used a glucose nanosensor based on Förster resonance energy transfer to monitor cytosolic glucose concentration with high temporal resolution and a cytochemical approach to determine glycogen stores in single cells. Following the adrenaline or noradrenaline stimulation the availability of cytosolic glucose is increased promptly after stimulation. Insulin boosts the process of glycogen formation. This indicates, that astrocytic cytosolic glucose metabolism responds to neuronal activity in the time-domain of tens of seconds.

INSTRUMENTATION

I1: Tomography, 3D Imaging and Image Processing, Phase-Related Techniques (including holography, vortex beams, Bessel beams etc.)

INVITED LECTURES I1:

Tayloring the phase of electron probes for selective EELS experiments

Johan Verbeeck (1), Giulio Guzzinati (1), Armand Béché (1), Hugo Lourenço-Martins (2), Jerome Martin (3), Mathieu Kociak (4)

1) University of Antwerp, G.U.433, 2020 Antwerpen, Belgium

2) Université Paris-Sud 11, Orsay Département de Physique

3) Laboratoire de Nanotechnologie et d'Instrumentation Optique, Institut Charles Delaunay - UMR CNRS 6279, Université de Technologie de Troyes, 12 rue Marie Curie - CS 42060 - 10004 Troyes Cedex - France

4) Laboratoire de Physique des Solides, Université Paris Sud, Bât 510, 91405 Orsay, France

Keywords: EELS, adaptive optics, plasmon, inelastic scattering, phase plate

Electronic spectroscopies are important in the study of localised surface plasmon resonances (SPRs) of metallic nanostructures, allowing to detect and image the strong spatial variations in the electrical field of the induced resonances of a single nanostructure. These techniques do however present some drawbacks when compared to their optical counterparts. While optical spectroscopies can make use of polarisation to directionally probe the response of a nanoparticle, an electronic beam can't discriminate between energy-degenerate eigenmodes and is also blind to optical activity and dichroism. New developments (e.g. PINEM) have reduced this gap, without however eliminating the root of the problem: electron spectroscopies probe the intensity of the plasmon's field, but are blind to the dynamics of that field. Here we show how the electrical potential of a SPR inelastically couples to the in-plane phase modulation of the electron beam. We exploit this in a radically new approach based on the idea of controlling, through beam shaping methods (1), the wave function of the electronic probe. By fitting the probe to the plasmonic modes under investigation, it becomes possible to measure previously inaccessible properties. We theoretically describe this coupling, then design an experimental setup allowing to selectively detect localised plasmonic excitations that possess the same symmetry as the electron probe (2). Finally, we experimentally test this by

selectively detecting the dipolar mode of a nanorod with a two-lobed probe, which we successfully generate in a TEM by applying state of the art phase manipulation techniques. The above demonstrates the power of phase manipulation techniques and the topic will be cast in the broader perspective of generic phase manipulation and its potential for breakthrough advances in instrumentation and capabilities in the TEM.

Acknowledgements:

G.G. acknowledges funding from FWO project 42/FA070100/6088 ”Nieuwe eigenschappen in complexe oxides” and ERC starting grant 278510 VORTEX.

References:

1. G. Guzzinati et al., Ultramicroscopy 151 (2015) 85.

2. G. Guzzinati et al., Nature Communications 8 (2017) 14999.

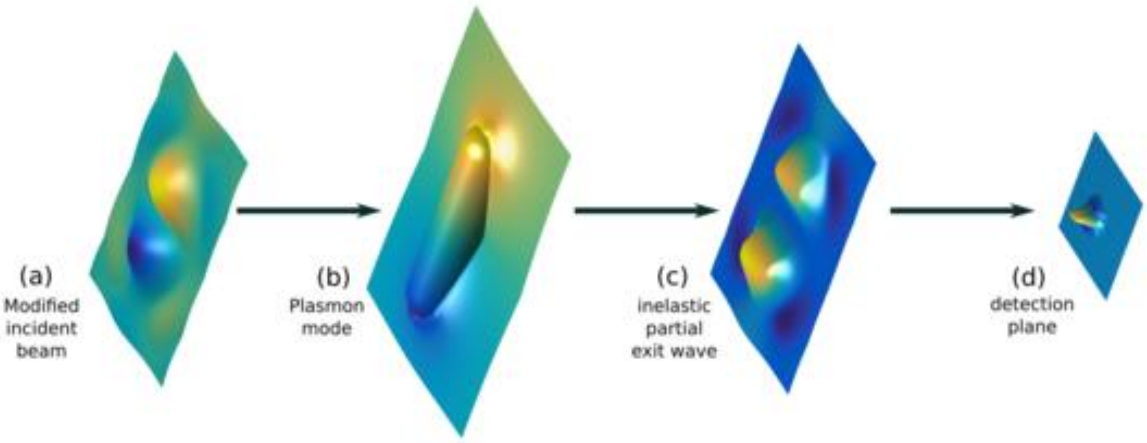

Figure 1. A schematic representation of the interaction described. A modified electron beam (a) interacts with the potential of a plasmon resonance (b). This interaction results in partial inelastic exit wave, whose form depends on both the incident beam, and plasmon potential (c). This information is then carried to the detection plane where a selection becomes possible (d).

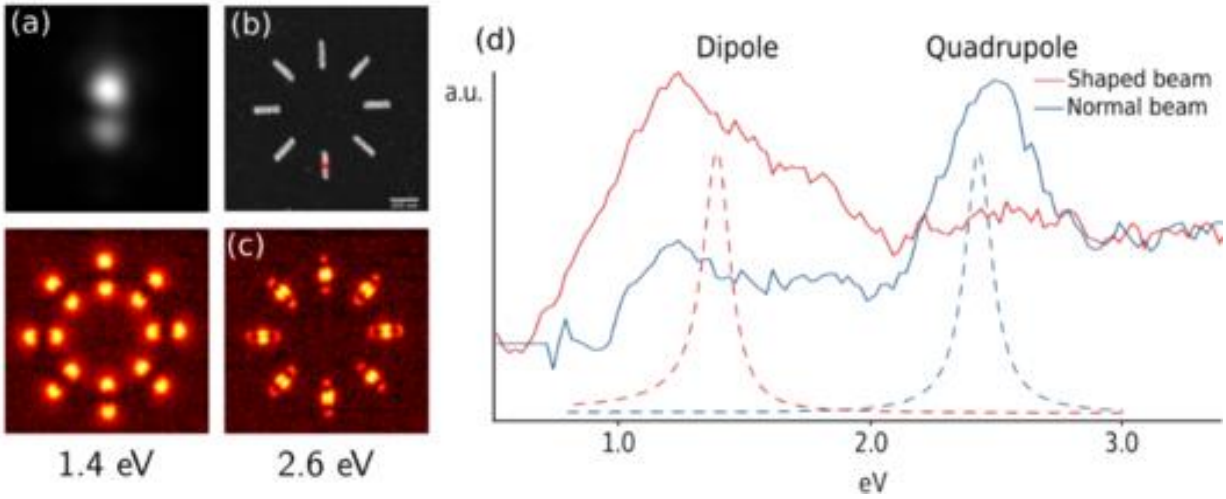

Figure 2. A modified electron beam with a 2-lobed profile (a) is used to selectively detect dipolar modes. Plasmonic nanorods (b) which show clear dipolar and quadrupolar modes (c) are probed with the modified beam (a) and a normal one, in the position marked with a red cross (b). The modes are individually detected as shown in (d), also compared with simulations (dashed line).

Holography with low-energy electrons: a tool for single molecule structural biology

Hans-Werner Fink (1)

1) University of Zurich, Winterthurerstr. 190, CH-8057 Zuerich, Switzerland

Keywords: Imaging single proteins, electron holography

While a remarkable amount of structural detail about proteins has been assembled from crystallography experiments, a strong desire to obtain such data from just a single molecule experiment is emerging. So far, none of all known and established mapping techniques using sufficient short wave-length radiation, be it X-rays or high energy electrons, allow looking at just one single biological molecule without destroying it shortly after the initiation of the observation process. Due to this unavoidable radiation damage problem, structural information can so far only be obtained by averaging over a large number of molecules. In contrast to this, coherent low energy electrons with deBroglie wavelengths in the Ångstrom regime allow imaging individual bio-molecules without detectable damage. The challenges to create a well-defined ensemble of low-energy electrons, capable of directly displaying interference effects without the need of electron lenses, will be discussed. Applications in view of imaging including holography and coherent diffraction with low-energy electrons will also be illustrated. Recent findings, obtained in collaboration between the Max-Planck Institute in Stuttgart and the University of Zurich, demonstrate that structural biology of single proteins has become possible by combining protein mass-spectrometry with low-energy electron holography (1).

References:

1. Jean-Nicolas Longchamp, Stephan Rauschenbach, Sabine Abb, Conrad Escher, Tatiana Latychevskaia, Klaus Kern, Hans-Werner Fink, PNAS (2017), vol. 114, no. 7

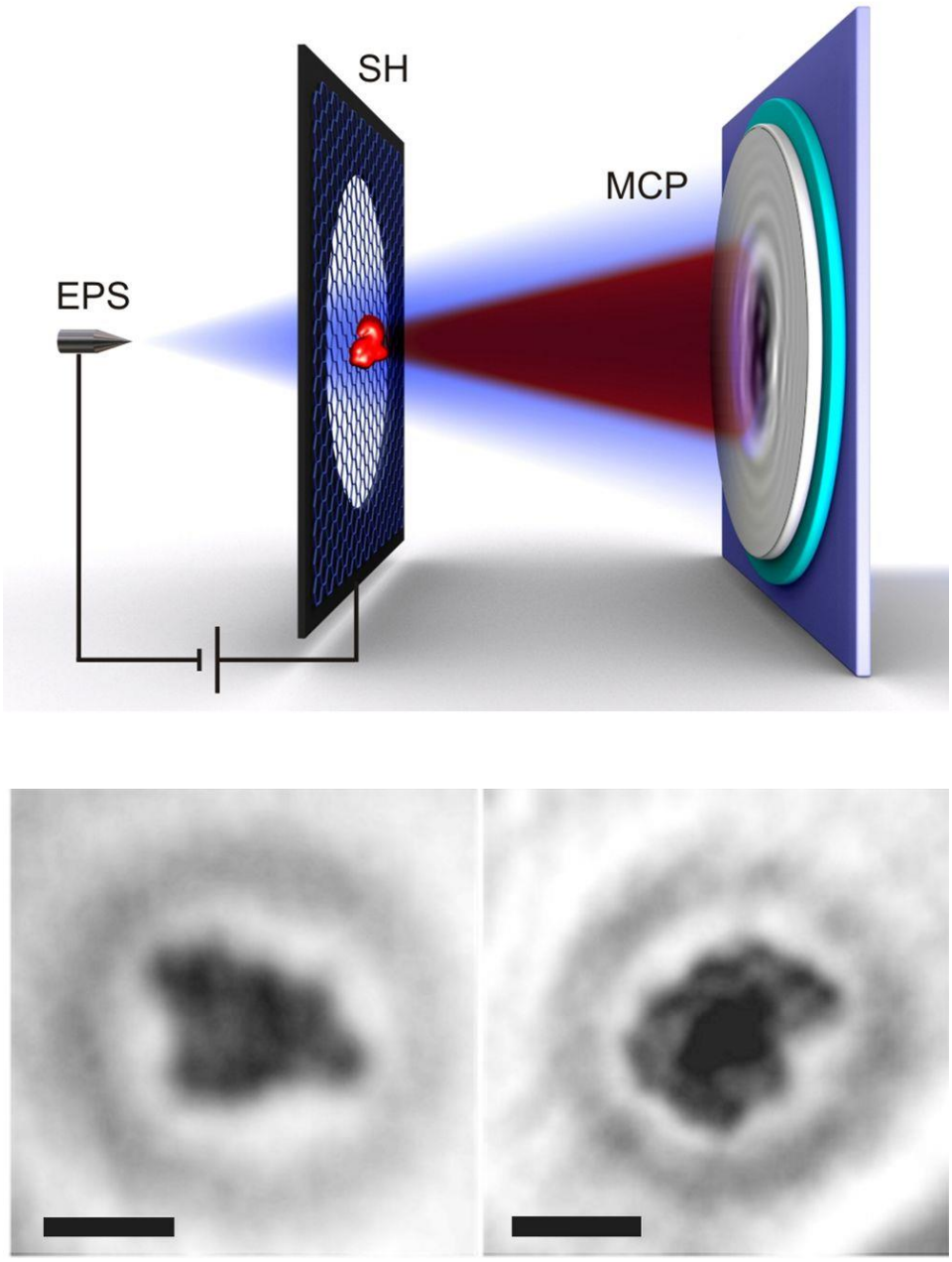

Figure 1. Top: Schematic setup for holography with low-energy electrons, featuring the coherent electron point source (EPS), free-standing graphene as sample holder (SH) and a multi-channel plate (MCP) for recording the holograms. Bottom: Two images of individual BSA proteins anchored on free-standing graphene. The scale bars correspond to 5nm.

ORAL PRESENTATIONS I1:

Surface plasmon tomography

Georg Haberfehlner (1), Anton Hörl (2), Franz P. Schmidt (3), Andreas Trügler (2), Ulrich Hohenester (2), Gerald Kothleitner (4)

1) Graz Centre for Electron Microscopy, Steyrergasse 17, 8010 Graz, Austria

2) Institute of Physics, University of Graz, Universitätsplatz 5, 8010 Graz, Austria

3) Institute for Electron Microscopy and Nanoanalysis, Graz University of Technology, Steyrergasse 17, 8010 Graz, Austria & Institute of Physics, University of Graz, Universitätsplatz 5, 8010 Graz, Austria

4) Institute for Electron Microscopy and Nanoanalysis, Graz University of Technology, Steyrergasse 17, 8010 Graz, Austria

Keywords: Surface plasmons, Electron tomography, Electron energy-loss spectroscopy, Photonic local density of states

Plasmonic modes in metal nanostructures induce field localization, strong coupling effects and high sensor sensitivity, properties that can be expressed by the photonic local density of states (LDOS). Coupling of metallic nanoparticles is recognized as a method for maximizing the photonic LDOS in the gap region between separate nanoparticles, but until recently no tool was available for the direct 3D nanoscale measurement of the photonic LDOS. However, to exploit the full potential of plasmonics, full 3D characterization and simulation taking into account the imperfections of real structures become mandatory. Here we present tomography-based approaches to understanding complex plasmonic nanoparticles created by electron beam lithography and to access local near-fields around nanoparticles and in gap regions. In our first approach the precise 3D geometry of a particle dimer fabricated by means of electron beam lithography was reconstructed through electron tomography. This full 3D morphological information was used as an input for simulations of energy-loss spectra and plasmon resonance maps (Figure 1). Here excellent agreement between measured EELS data and theory was found, bringing the comparison between EELS imaging and simulations to a

quantitative and correlative level (2). In our second approach we directly reconstruct particle plasmon fields from a tomographic tilt series of EELS spectrum images. While first approaches and demonstrations of plasmon field tomography were limited to very small particles – small enough to neglect retardation – we lift this limitation with our approach making plasmon field tomography generally applicable to nanoparticles of all sizes. Formulation EELS tomography as an inverse problem allows reconstructing the complete dyadic Green tensor for plasmonic particles, from which the photonic LDOS can be calculated. Using this approach, we are able to reconstruct the full 3D LDOS for different metallic nanoparticle geometries (Figure 2) and reveal the strong near-fields in the gap regions of nanoparticle dimers, both in lateral and vertical arrangements. This work overcomes the need for geometrical assumptions or symmetry restrictions of the sample in simulations and generalizes plasmon field tomography to particles of all sizes, paving the way for detailed investigations of realistic and complex plasmonic nanostructures.

Acknowledgements:

We thank Gernot Schaffernak, Andreas Hohenau and Joachim Krenn for access to and support with electron beam lithography and helpful discussion. This research has received funding from the European Union within the 7th Framework Program [FP7/2007-2013] under Grant Agreement no. 312483 (ESTEEM2). We acknowledge support by the Austrian Science Fund FWF under project P27299-N27, the SFB F49 NextLite, and NAWI Graz.

References:

1. G. Haberfehlner et al., Nano Lett. 15: 7726–7730 (2015)

2. A. Hörl, G. Haberfehlner et al., Nat. Commun., accepted (2017)

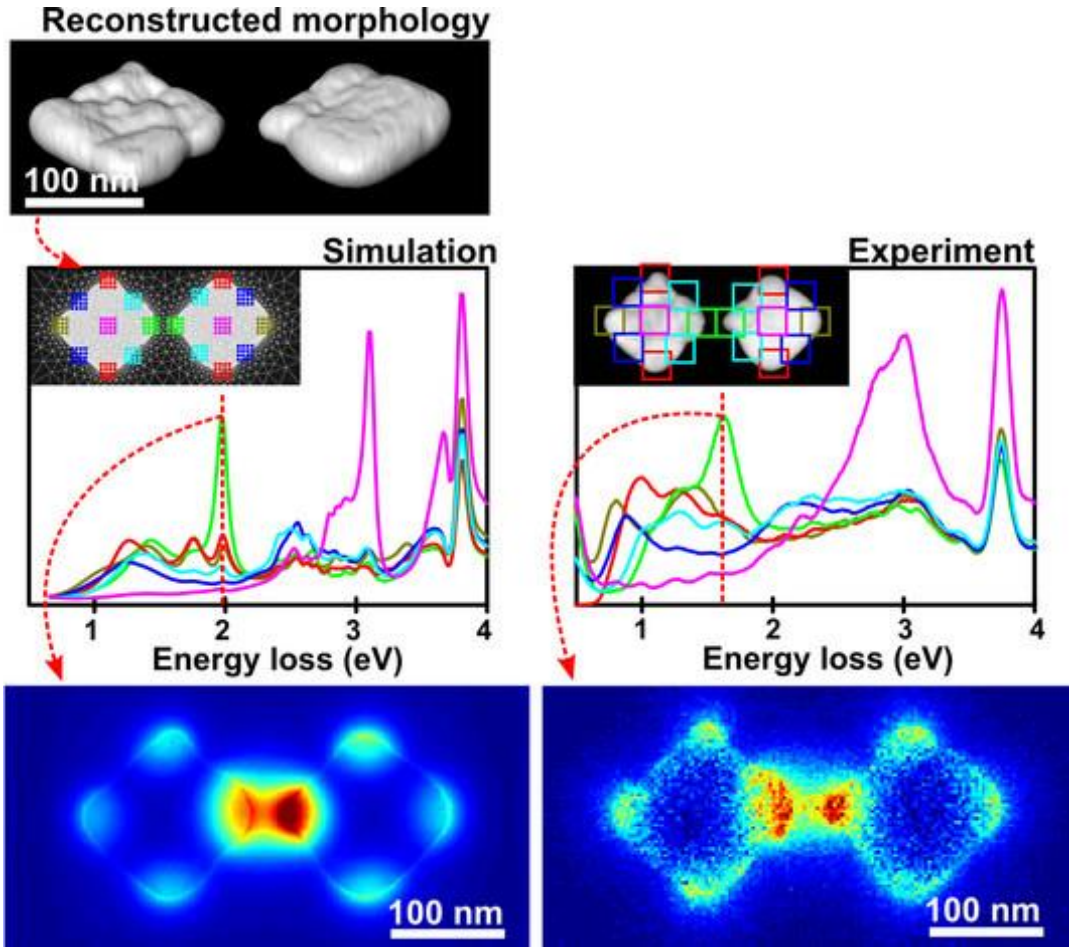

Figure 1. Tomographically reconstructed morphology of coupled nanocuboids and simulated and experimental EELS spectra and plasmon resonance maps. Simulations are based on the reconstructed 3D model of the nanocuboids. Colored locations in the inset indicate regions from which the spectra were extracted (1).

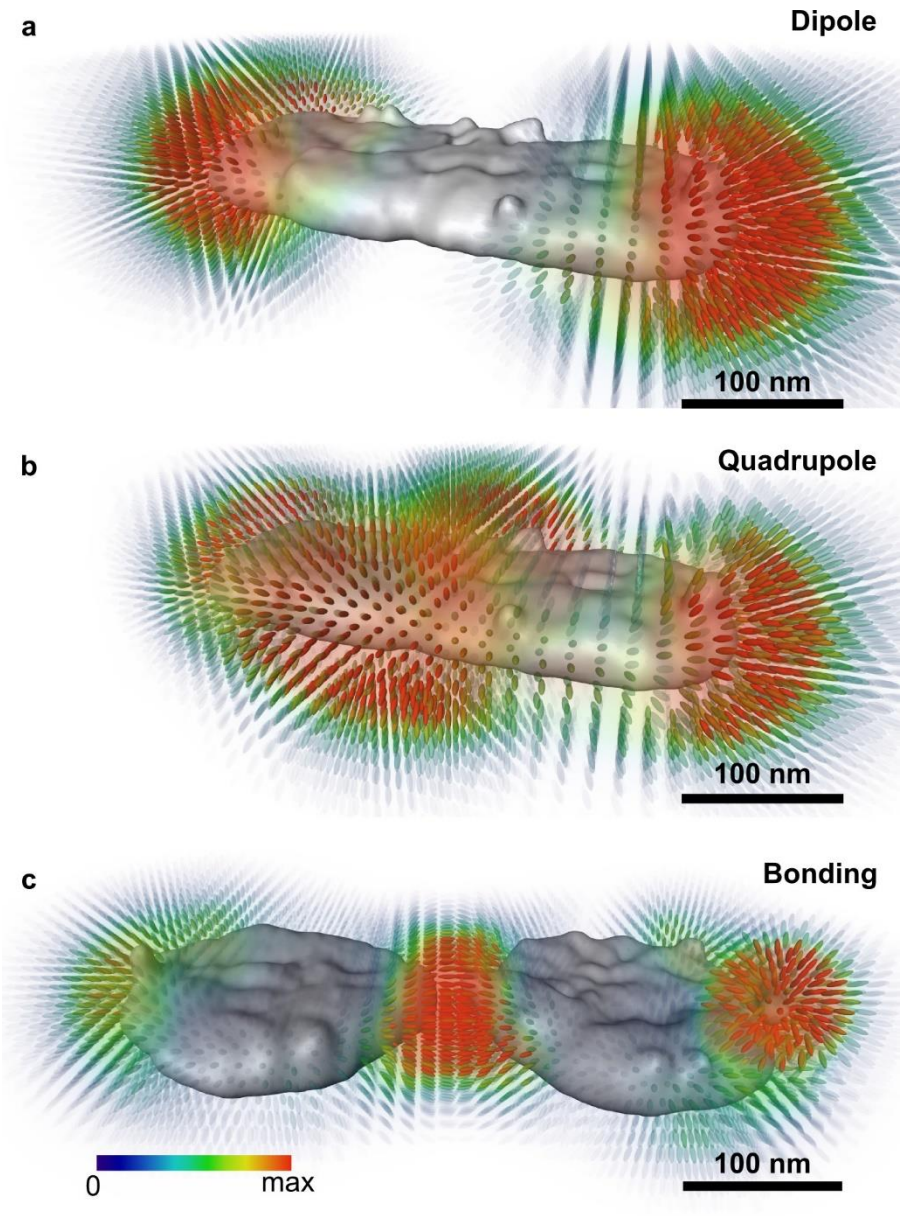

Figure 2. Photonic local density of states (LDOS) for a (a) dipolar and (b) quadrupolar mode on a silver nanocuboid and (c) bonding plasmon mode on coupled silver nanodisks reconstructed from tilt series of EELS spectrum images. The orientation of the markers indicates the direction along which the LDOS is maximal, the color represents the magnitude of the LDOS (2).

Electron phase modulation with topologically patterned electrostatic mirrors

Maurice A.R. Krielaart (1), Pieter Kruit (1), Navid Abedzadeh (2), Chung-Soo Kim (2), Richard G. Hobbs (2), Karl K. Berggren (2)

1) Department of Imaging Physics, Delft University of Technology, Lorentzweg 1, 2628CJ Delft, The Netherlands

2) Department of Electrical Engineering and Computer Science, Massachusetts Institute of Technology, 77 Massachusetts Ave., Cambridge, MA 02139

Keywords: Electron beam shaping, Phase manipulation, Electron mirror

Electron beam shaping involves the controlled manipulation of either amplitude or phase of the electron wave. A variety of methodologies exist for this purpose. For instance, Zernike phase plates are used for phase contrast microscopy (1) and other holographic reconstructed phase plates allow the creation of electron vortex beams (2). All these methods work in a transmission mode and although proven methods, these techniques do share common practical difficulties, being sensitive to local thickness variations, charging effects and inelastic scattering events (3). To circumvent these issues, we suggest a topologically patterned electrostatic mirror that is used to manipulate the relative phase of the incident electron wave. An electron mirror avoids the above-mentioned practical complications, as the electron reflects in front of the physical mirror structure, thus avoiding charging, surface roughness and undesired scattering effects. Using focused ion beam lithography, a grating-like structure is created with pitch and amplitude of (sub)micrometre order. This grating mirror is used in a proof of principle experiment (figure 1) where it is expected that phase modulation due to the mirror pattern will induce diffraction in the reflected beam. When this reflected beam is used to image a holey carbon sample (positioned inside the specimen chamber of a conventional SEM) the diffraction is expected to produce fringes near the edges of the holes inside the sample. The analysis of the grating effect is based initially on applying the WKB approximation along the electron trajectories in front of the mirror. Next, a more rigorous description of the pattern effect is obtained by solving the time-independent Schrodinger equation in the region just before the reflection point, where

the equipotential landscape is sinusoidal. These studies support the expectation that a patterned electrostatic mirror can be used as a diffractive element for electron microscopy. Future applications of patterned electrostatic mirrors include use as coherent beam splitter in the scheme of a quantum electron microscope (3) or correcting for chromatic and spherical aberrations.

References:

1. F. Zernike, Physica, 9 (1942), p. 686.

2. J. Verbeeck, H. Tian and P. Schattschneider, Nature 467 (2010).

3. P. Kruit, R.G. Hobbs, C-S. Kim, Y. Yang, V.R. Manfrinato, J. Hammer, S. Thomas, P. Weber, B. Klopfer, C. Kohstall, T. Juffmann, M.A. Kasevich, P. Hommelhoff, K.K. Berggren, Ultramicroscopy 164 (2016).

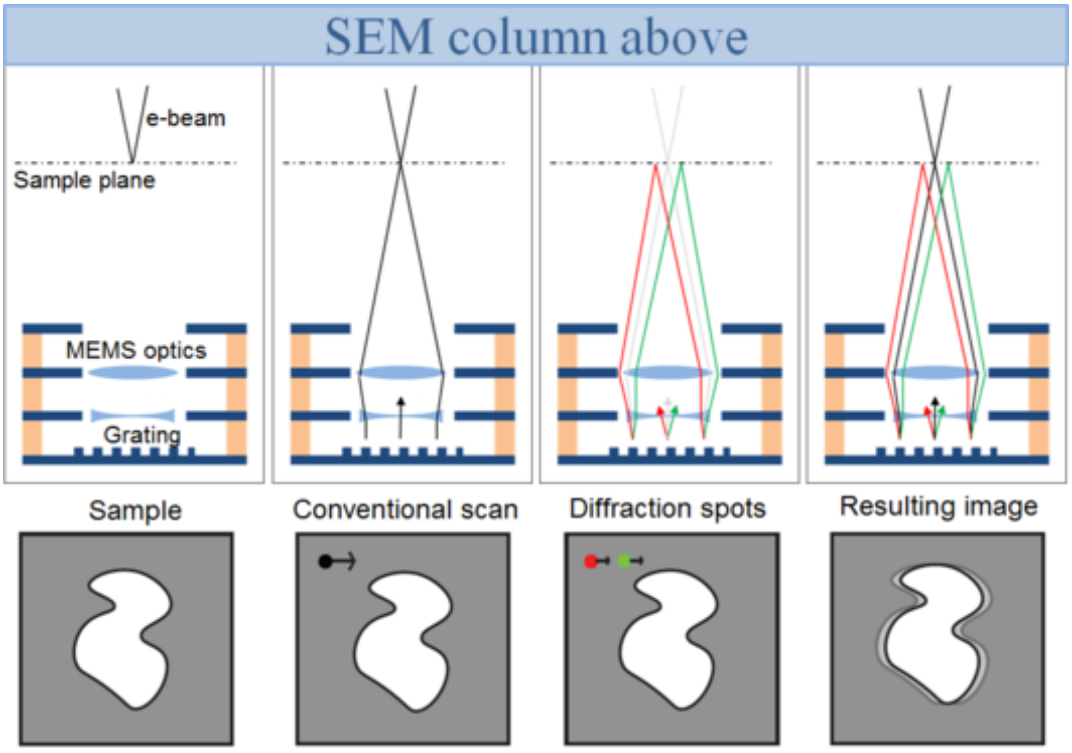

Figure 1. Image formation principle of the grating mirror. On hole-locations, the beam is collimated to the mirror plane below. The reflected (black) and diffracted (red, green) beams are focused back onto the sample, creating fringes around the edges.

Electron Vortices in Solids: From Crystalline to Amorphous Materials

Stefan Löffler (1), Stefan Sack (2), Thomas Schachinger (2)

1) Universitäre Service-Einrichtung für Transmissionselektronenmikroskopie (USTEM) Vienna University of Technology / E052, Wiedner Hauptstraße 8-10 / 052, A-1040 Wien, Austria

2) Vienna University of Technology, Wiedner Hauptstrasse 8 -10,1040 Wien, Austria

Keywords: vortices, propagation, orbital angular momentum, multislice

Electron vortex beams (EVBs) are fundamental solutions to the free-space Schrödinger equation in cylindrical coordinates. Their peculiar properties, such as their orbital angular momentum (OAM) and the associated magnetic moment, make them a very interesting novel tool for nanoanalysis. Actual and predicted applications include nanomanipulation, energy-loss magnetic chiral dichroism (EMCD) measurements, and spectroscopy with ultimate energy resolution. Here, we investigate how vortices behave in a non-isotropic environment such as inside a crystalline or amorphous sample. The breaking of the rotational symmetry leads to superpositions of and scattering between different vortex orders, thus leading to a broadening of the OAM distribution. In some cases, such as nanomanipulation, the associated exchange of OAM between the beam and the sample is vital. In other cases, such as EMCD, this is an artifact that can severely distort the outcome of measurements or even prohibit their analysis. To elucidate the influence of elastic scattering, we use the theoretical framework of the multislice formalism. With it, dynamic scattering effects can be described in a general manner and can also be compared to numerical simulations. For crystalline materials, it is well-known that depending on the experimental geometry, the average OAM can oscillate drastically throughout the sample, but can also be protected by channeling along atomic columns (1). In amorphous materials, we find that the average OAM remains approximately unaffected over a significant thickness range (see Figure 1). Here, an incident m=1 beam was used. Of more practical relevance than the average OAM is the intensity of the m=1 component itself. This is found to decrease due to scattering to other vortex orders, but the m=1 component still remains dominant for a large range of thicknesses. It is noteworthy that the specific behavior depends

on both the atomic weight of the scatterer and the size of the EVB. These results are also combined with inelastic simulations to calculate the (defocus-dependent) EMCD effect when using EVBs. Vortex-EMCD has the unique benefit over classical EMCD that the sample does not need to act as a beam splitter. Therefore, vortex-EMCD is directly applicable to amorphous materials. Hence, it is clear that understanding the scattering behavior of EVBs is not only required for analyzing experimental data, but also paves the way for the development and efficient use of novel, emerging techniques for nanoanalysis.

Acknowledgements:

The authors acknowledge financial support by the FWF (J3732-N27, I543-N20)

References:

1. S. Löffler et al., Acta. Cryst. A 68 (2012) 443.

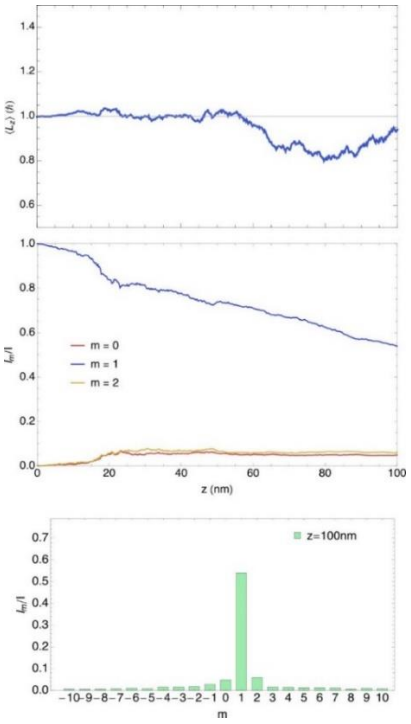

Figure 1. Thickness dependence of the average OAM (top) and the intensities of individual vortex components (middle), together with the intensity histogram at 100 nm (bottom) as simulated for amorphous Si with an incident m=1 EVB with 20 mrad convergence semi-angle.

Measuring band gaps of semiconductors by off-axis EELS with Bessel aperture

Svetlana Korneychuk (1), Giulio Guzzinati (1), Rajesh Ramaneti (2), Paulius Pobedinskas (2), Joff Derluyn (3), Ken Haenen (2), Johan Verbeeck (1)

1) Electron Microscopy for Material Science (EMAT), University of Antwerp, 2020 Antwerp, Belgium

2) Institute for Materials Research (IMO), Hasselt University, 3590 Diepenbeek, Belgium, IMOMEC, IMEC vzw, 3590, Diepenbeek, Belgium

3) EpiGaN NV, 3500, Hasselt, Belgium

Keywords: band gaps, bessel beams

The possibility to locally measure band gaps of materials in TEM appeared with the invention of the monocromator for electron energy loss spectroscopy (EELS). Despite this the technique hasn't become conventional for band gap measurements due to unwanted losses such as Cherenkov radiation emission which has an impact on low loss spectra and complicates the retrieval of the band gap signal1. Nevertheless, several approaches to measure the band gap were demonstrated 2,3. among which decreasing the acceleration voltage of the microscope and avoiding the retardation losses by off-axis acquisition. Based on previous experience in band gap measurement with EELS we attempt to improve this method in order to make it more feasible and accessible. In this work we demonstrate the off-axis acquisition technique highlighting its application for STEM mode. This method originates from the assumption that all undesirable losses take place in a certain narrow range of angles and can be avoided by measuring off-axis. Its effectiveness can be shown by simulations using the Kröger formula which allows to calculate the energy losses of fast electrons in thin foils with retardation starting from the dielectric properties. We minimize the impact of undesirable losses by selecting the retardation-free part of the outcoming signal using an annular (Bessel) aperture. The obtained band gap values are in good agreement with the conventional optical measurements, with a much improved spatial resolution.

Acknowledgements:

S.K. and J.V. acknowledge funding from the “Geconcentreerde Onderzoekacties” (GOA) project “Solarpaint” of the University of Antwerp. P.P. acknowledges Postdoctoral Fellowship of the Research Foundation Flanders (FWO).

References:

1. Erni R., Ultramicroscopy 160 (2016) 80-83.

2. Stöger-Pollach M. et al., Ultramicroscopy 173 (2017) 24–30.

3. Zhang L. et al., Phys. Rev. B 77 (2008), 195119.

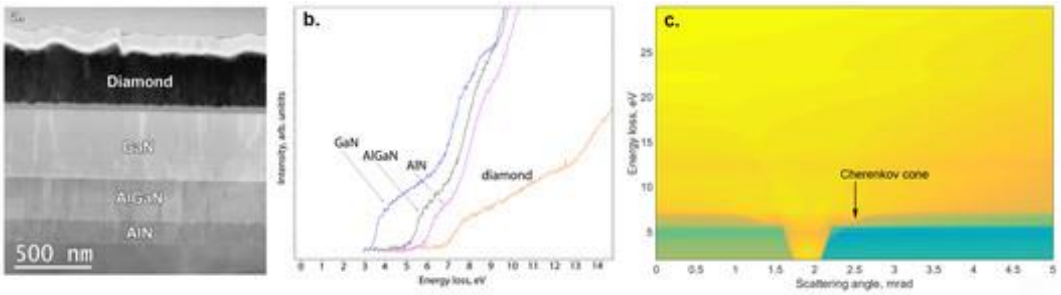

Figure 1. (a) ADF-STEM image of semiconductor heterostructure including diamond layer and (b) low loss EELS spectra demonstrating band gap onsets for every layer. (c) Simulation of low loss electron scattering for diamond at 60 kV for Bessel aperture and STEM mode based on Kröger formula.

POSTER PRESENTATIONS I1:

Electron tomography in the Scanning Electron Microscope for the investigation of biological and inorganic samples

Maurizio Donarelli (1), Matteo Ferroni (2), Vittorio Morandi (3), A. Migliori (3), Luca Ortolani (3), Luca Masini (3), ChandraKanth Reddy Chandraiahgari (4), Giovanni De Bellis (4), Maria Sabrina Sarto (4)

1) Department of Information Engineering, University of Brescia, Via Branze 38, 25123 Brescia (Italy)

2) Department of Information Engineering, University of Brescia, Via Branze 38, 25123 Brescia (Italy) & CNR-Microelectronic and Microsystems Institute, Via Gobetti 101, 40129 Bologna (Italy)

3) CNR-Microelectronic and Microsystems Institute, Via Gobetti 101, 40129 Bologna (Italy)

4) Department of Astronautics, Electrical and Energetics Engineering, Sapienza University of Rome, via Eudossiana 18, Rome 00184 (Italy) & Research Center for Nanotechnology Applied to Engineering of Sapienza (CNIS), SNNLab, Sapienza University of Rome, Piazzale Aldo Moro 5, 00185 Rome (Italy)

Keywords: STEM, tomography, compressed sensing

The recent advances in the fabrication of hybrid nanostructures for application in micro and nanoelectronics and the need to explore biological samples call for a three dimensional investigation of the constituents and their spatial disposition at nanometric resolution. For the purpose, Scanning-Transmission imaging in the SEM (STEM) is a already established implementation of the SEM platform, and when implemented with a rotating sample holder, it offers the capability of a tomographic reconstruction of the sample. In this paper, we report on the application of SEM tomography to a graphene-nanorods hybrid system and to a biological sample of dermal tissue. Graphene flakes have been fabricated by solvo-thermal exfoliation method and ZnO nanorods (NR) have been grown in-situ by aqueous hydrothermal method

(1). A graphene-NR hybrid system can be fabricated by dispersing the NR through the graphene flakes or promoting the nucleation of NR directly over graphene.

Samples, transparent to the electron beam, are prepared on a standard TEM grid and are mounted on a rotating sample holder. The in-house designed and fabricated detector, formed by four annular and concentric sections, is mounted on a separate support. The activation of specific sectors of the detector enables to obtain bright field (BF) or dark field (DF) images. The STEM signal, collected by the detector, is based on the intensity of the forward scattered electrons and the mass-thickness contrast should vary monotically when the sample is rotated in order to obtain images at different tilt angles. This requirement is fundamental for the tomographic reconstruction of the specimen from the STEM projection images taken at different tilt angles (2). A DF STEM image of the graphene ZnO hybrid system is reported in Figure 1, left. The brightest areas are related to the ZnO nanorods, which are heavier than the surrounding graphene flake, which is the bright area. The beam acceleration voltage was 27 KV. The DF projection images series has been recorded by tilting the sample between -60° and +50°, at 2° steps. After the alignment of the projection images with a cross correlation algorithm, the 56 projection images series has been reconstructed. The tomogram has been obtained by a standard retroprojection and followed by iterative refining. The resulting tomogram is reported in Figure 1, right. The aim of the 3D reconstruction is to achieve a tomogram without artifacts, allowing a quantitative description of the investigated sample. However, some ET limitations due to the geometry of the experimental setup, like a restricted angular range (“missing wedge”), hinder the achievement of this goal. Furthermore, in particular for biological samples, the electron beam exposure can damage the sample itself, so a limited number of projections can be recorded without damaging the specimen. Here we report the use of compressed sensing (CS) for the reconstruction of a human dermal tissue (3). The experimental setup is basically the same reported for the graphene-NR hybrid structure investigation. The sample has been tilted in order to obtain a series of projection images in DF STEM mode. The projection images have been aligned and nine of them are reported in Figure 2, top (the tilt angle is reported in each panel). The collagen bundle, which is the region of interest for the reconstruction, is reconstructed and refined by CS, and reported in Figure 2, bottom. The CS-reconstruction compares positively with the one obtained by ordered-subset simultaneous algebraic technique (OS-ART), implemented in popular reconstruction softwares (TomoJ). The OS-ART based reconstructions are strictly related with the number of projection images, with a loss of resolution with a decreasing number of projections. On the other hand, the CS refinement allows to reconstruct a tomogram from a

relatively low number of projections, without a significant loss of information. Therefore, it is a promising approach for the reconstruction of tomograms, limiting the artifacts due to the missing wedge and the low number of projection images. Furthermore, the CS reconstruction approach opens the possibility to perform ET on beam-sensitive samples and to reduce the acquisition times.

In conclusion, ET in SEM platform is a viable technique to perform 3D analysis and investigation of material science and biological samples. CS approach enables to reconstruct the specimens using a low number of projection images, limiting the artifacts due to the geometry of the ET setup, and reducing the acquisition times.

References:

1. C. R. Chandraiahgari et al., RSC Adv. 86 (2016) p. 83217.

2. M. Ferroni et al., J. Phys.: Conf. Ser. 644 (2015) 012012.

3. M. Ferroni et al., Scientific Reports 6 (2016) p. 33354.

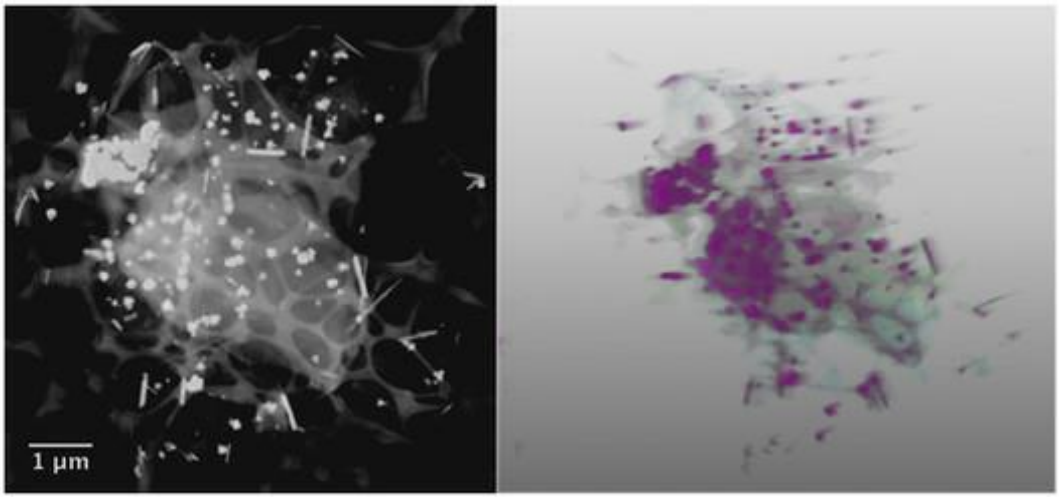

Figure 1. Left: STEM image of the graphene-NR in dark-field condition. Right: The reconstructed tomogram.

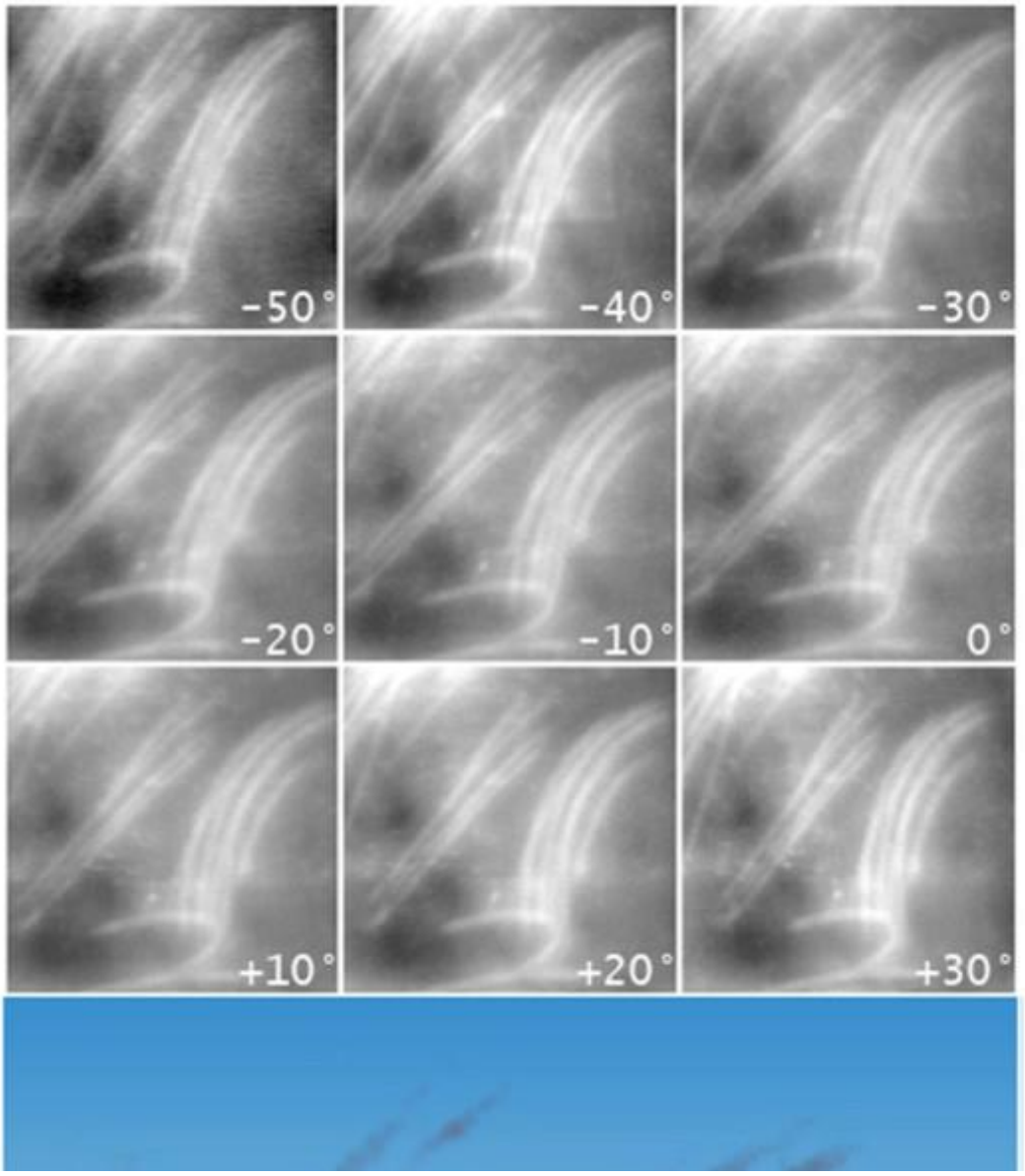

Figure 2: Top: DF STEM images of the collagene bundle. Bottom: CS based reconstruction of the sample.

Project „Pattern“ – an online tool for spatial analysis of immunolabeling in electron microscopy.

Dominik Pinkas (1), Vlada Philimonenko (1), Jiří Janáček (2), J. Novák (3), Marcel Jiřina (4), Pavel Hozák (4)

1) Institute of Molecular Genetics ASCR v.v.i., Microscopy Center, Electron Microscopy Core Facility, Vídeňská 1083, 142 20 Prague 4, Czech Republic

2) Institute of Molecular Genetics ASCR v.v.i., Department of Biology of the Cell Nucleus, Vídeňská 1083, 142 20 Prague 4, Czech Republic

3) Institute of Physiology ASCR v.v.i., Department of Biomathematics, Vídeňská 1083 142 20, Prague, Czech Republic

4) Czech Technical University in Prague, Faculty of Information technology, Department of Theoretical Computer Science, Prague, Czech Republic

Keywords: transmission electron microscopy, image analysis, immunolabeling, colocalization

In biological research, the term „colocalization“ is usually used in the context of fluorescence microscopy. However, the character of analyzed data such as signal leakage from different channels, signal originating from other focal planes and low resolution as well as subjective thresholding may lead to erroneous conclusions. On the other hand, immunolabeling in electron microscopy can be used to detect structures and molecules with much higher precision than even novel super-resolution techniques while sharing common principles with fluorescence immunolabeling. So far, the evaluation of such images was often subject to similar woes, lacking unbiased quantitative approach despite higher resolution provided by EM. We are developing an easy-to-use online tool for semi-automatic multi-stage analysis of immunolabeling on EM images spanning particle detection and classification, mathematical and statistical evaluation and visualization of results that builds on previous work of A. A. Philimonenko et al. (1) and C. Schofer et al. (2). Multiple types of common simultaneous labelling should be recognizable automatically, while custom particles of irregular shapes would have to be localized semi-manually. Spatial relations will be analyzable in 2-dimensional and 3-dimensional microscopic data and along linear structures such as membranes and

filaments. Clustering and colocalization of particles will be evaluated by pair correlation (Figure 1) and pair cross-correlation functions with results presented both numerically and graphically. Labelled structures will be visualized via mapping (Figure 2) and their spatial relations to other structures or particles will be further evaluated as shown by V. V. Philimonenko et al. (3). Statistical significance of detected patterns will be calculated and presented to the user without the need for deep insight into statistical analysis. This online tool will be provided by the Institute Molecular Genetics of Czech Academy of Science to the broad scientific community in open access mode within the Czech-BioImaging research infrastructure. The tool will emphasize understandability of the interface and results and will provide detailed explanations of all steps values and options. The platform will be modular and can be expanded with more capabilities in the future.

Acknowledgements:

This project is supported by MEYS CR (LM2015062), OPVVV (CZ.02.1.01/0.0/16_013/0001775), IMG grant (RVO: 68378050) and TACR (TE01020118) grants.

References:

1. Philimonenko, A. A., Janáček J. and Hozák P. "Statistical evaluation of colocalization patterns in immunogold labeling experiments." Journal of structural biology 132.3 (2000): 201-210.

2. Schöfer, C., Janáček, J., Weipoltshammer, K., Pourani, J., & Hozák, P. (2004). Mapping of cellular compartments based on ultrastructural immunogold labeling. Journal of structural biology, 147(2), 128-135.

3. Philimonenko, V. V., Philimonenko, A. A., Šloufová, I., Hrubý, M., Novotný, F., Halbhuber, Z., ... & Hozák, P. (2014). Simultaneous detection of multiple targets for ultrastructural immunocytochemistry. Histochemistry and cell biology, 141(3), 229-239.

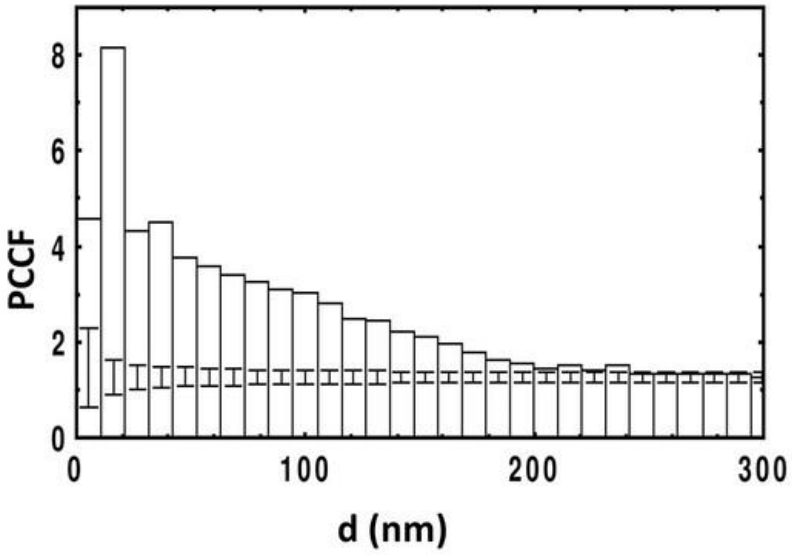

Figure 1. Pair corelation function representing clustering of DNA polymerase α. For distances in which the function value exceeds 1, density of particles is higher than that of random distribution. A. A. Philimonenko et al. (1).

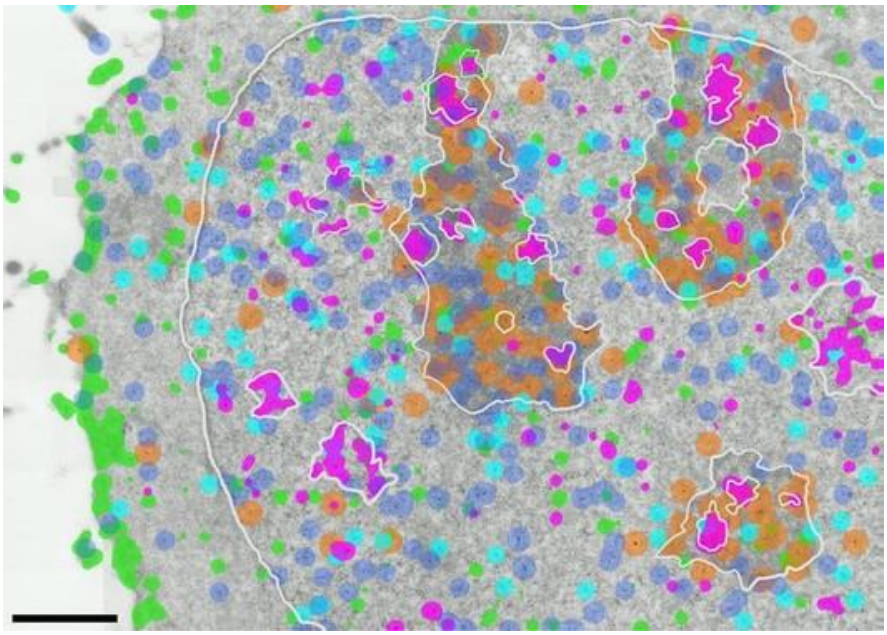

Figure 2 Example of graphic representation of mapping of five different immunolabeled antigens. Scale bar 1 μm. V. V. Philimonenko et al. (3).

Selective imaging of the Cu-sublattice in the complex Cu_2-xSe crystal structure

Ognjen Milat (1), Nazif Demoli (1)

1) Institute of Physics, Bijenicka 46, HR1000 Zagreb, Croatia

Keywords: electron diffraction, selective imaging

Imaging of crystal structure in high resolution electron microscopy (HREM) depends not only on observation parameters such as aperture, defocus, objective lens aberration, or the energy loss spectral window, but also on the crystal thickness and even more, on its crystallographic orientation. By computer control in variation of each of these parameters and image acquisition and processing, a new approaches to digital holographic electron microscopy can be envisaged. In the case of composite crystals such as the $Cu_{2-x}Se$ with two or more subsystems[(1)], these substructures can be selectively imaged and resolved by observing the projected structure of the same area of crystal along a number of crystallographic orientation(2). This method was termed “oblique zone imaging”(2) and applied here for the selective imaging of an exotic, and still disputed[(3)] arrangement of the Cu-atoms and vacancies in the Cu_{2-x}-layers of complex structure of the monoclinic room temperature (RT) $Cu_{2-x}Se$ phase(1,3). Regardless of its simple chemical formula, the RT-$Cu_{2-x}Se$ phase exhibits complex ordering in a kind of layered structure (1). This ordering mainly takes place within the Cu_{2-x}-layers via phase transition during cooling from the high temperature (HT) superionic phase (1,3). Namely, the superionic mobility in the HT-$Cu_{2-x}Se$ phase is supported by a disordered, “liquid-like sublattice” of Cu-cations within a rigid Se-sublattice usually termed “imobile cage”. At room temperature, the Se atom arrangement retains the symmetry of the slightly distorted HT-$Cu_{2-x}Se$ phase; a form of face centred cubic lattice slightly elongated along one of the [111] diagonal axis (1,3). This is revealed in electron diffraction patterns (EDPs), as well as in the HREM imaging, as represented in Figure1. In the basic sections of the reciprocal space, the weak superlattice spots are present together with the sublattice ones as it is shown for the EDPs in left panels of Figure 1(a,b). Along the “oblique” zone (with at least two indices different, and non equal zero), as in Figure 1(c), the separated superlattice weak spots fill one or more

additional rows between the basic spot rows. Such an “oblique” reciprocal section contains one or more rows of exclusively superlattice spots corresponding to resolvable spacing, while the rows of basic sublattice spots are at such a large reciprocal distance that the corresponding sublattice spacing is below the point resolution of the microscope, Figure 1(c). Along such an oblique zone the image reveals mainly the structural features due to the superlattice; the partial structure of the basic sublattice is unresolved in the background. This method is shown to be especially applicable to the HREM study of RT-$Cu_{2-x}Se$ lamellar structures built on Se-layers and Cu_{1-x}-layers in which the superlattice formation is due to Se-lattice elongation along one of the layer stacking directions accompanied by alternating displacements of subset of Cu-atoms (1,3). In such a case, imaging along principal zone axis, (perpendicular to the $[111]_c$ layer stacking direction), as in Figure 1(a,b), is heavily affected by the arrangement of bright and dark dots representing the average structure; a slight brightness variation, which becomes more prominent in thicker area reveals mainly the geometry of superlattice nodes in which the structural details have to be resolved by image simulation. In the other hand, imaging along the “oblique” zone axis, Figure1(c), reveals the main feature selectively of the RT-$Cu_{2-x}Se$ superstructure: the displacement of the Cu-atoms out of each Cu_{1-x}-layers along the $[111]_c$ and the perpendicular $<202>_c$ directions of the basic cubic lattice (1,3). Structure information obtained here by “oblique zone imaging” of the RT-$Cu_{2-x}Se$ composite crystal will be further approached in terms and methodology of electron tomography and digital holographic microscopy (4).Electron diffraction patterns of RT-$Cu_{2-x}Se$ along three crystallographic directions are presented in Figure 1. (left panels), with the corresponding structure projection images (right panels). Zone axis are labelled in the fcc notation of the Se-sublattice. Rows of spots which contain basic reflections are marked with arrows, while the arrowheads at the top indicate reciprocal rows that consist exclusively of the superlattice spots. Both types of spots are present in (a), as they are revealed in the right panel; no superlattice spots out of basic rows in (b) indicate the same lateral periodicity of both subsystems, while only the superlattice spots which are observed out of the central rows in (c), and consequently only the Cu-atoms with lateral spacing 0.23 nm is selectively imaged in the right panel; the Se-sublattice periodicity (0.08 nm) is out of the resolution range.

Acknowledgements:

This study is partially supported by Croatian Science Foundation (project: IP-2014-09-7515).

References:

1. Z. Vucic, O. Milat, V. Horvatic and Z. Ogorelec, Phys. Rev. B24 (1981), 5397.

2. S. Amelinckx, O. Milat and G. Van Tendeloo, Ultramicroscopy 51 (1993), 90.

3. S.L. White, P. Banerjee, P.K. Jain, Nature Com. (2017) 8:14514.

4. P.A. Midgley, R.E. Dunin-Borkowski, Nature Materials 8, 271 - 280 (2009).

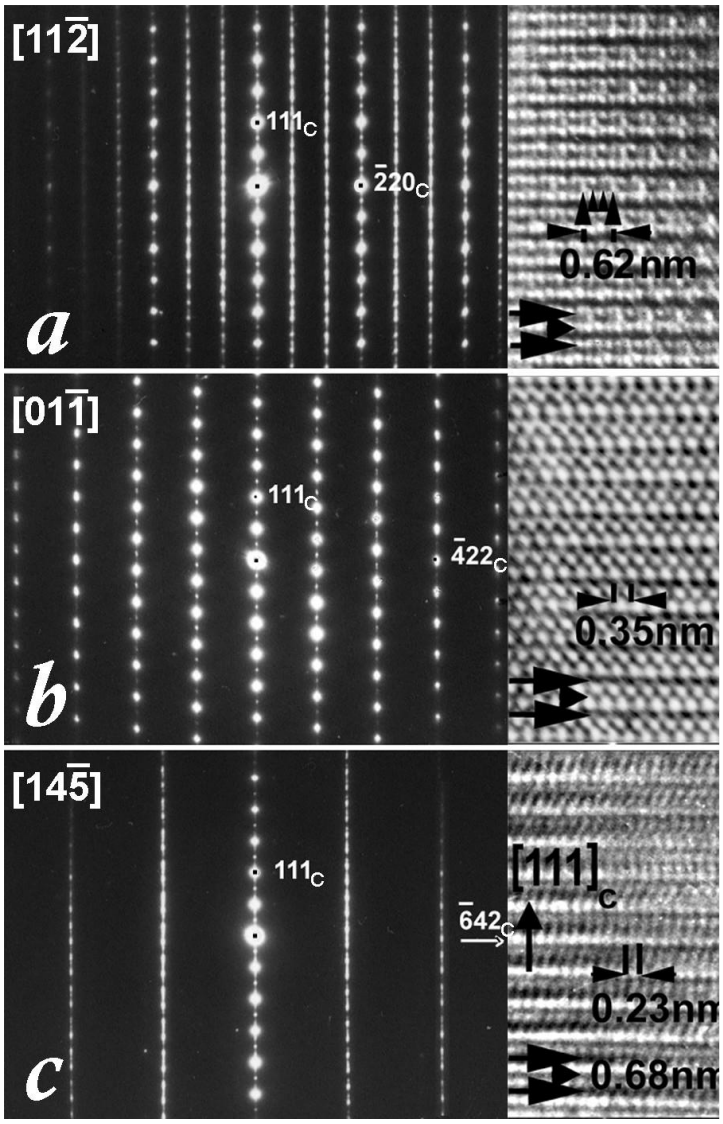

Figure 1. Electron diffraction patterns of RT-Cu2-xSe along three crystallographic directions (left panels) with the corresponding structure projection images (right panels). Zone axis are labelled in the fcc notation of the Se-sublattice.

Toward direct electron microscopy of nanomaterials in living systems

Domagoj Belić (1), Oihane Fragueiro (1), Dina Salah (2), Martin Volk (1), Mathias Brust (1)

1) University of Liverpool, Liverpool L69 3BX, United Kingdom

2) Ain Shams University, Khalifa El-Maamon St, 11566 Cairo, Egypt

Keywords: ESEM, Wet STEM, live cell imaging, gold nanorod

We use environmental scanning (transmission) electron microscopy in Wet STEM and ESEM mode to directly visualize the uptake of PEG-COOH or TAT-peptide functionalized Au nanorods into whole, as-cultured, fully hydrated mammalian stem cells, without any additional chemical or physical (pre)treatment. By carefully setting the experimental conditions within the environmental electron microscope, we examine nanorod-containing cells in near-native state, down to resolution of individual nanorods. We outline the pros and cons of these direct methods for straightforward imaging of nanomaterials in soft hydrated biological matrices, comparing them with the standard fixation-staining-sectioning protocol and more advanced cryo-EM and liquid-cell TEM approaches.

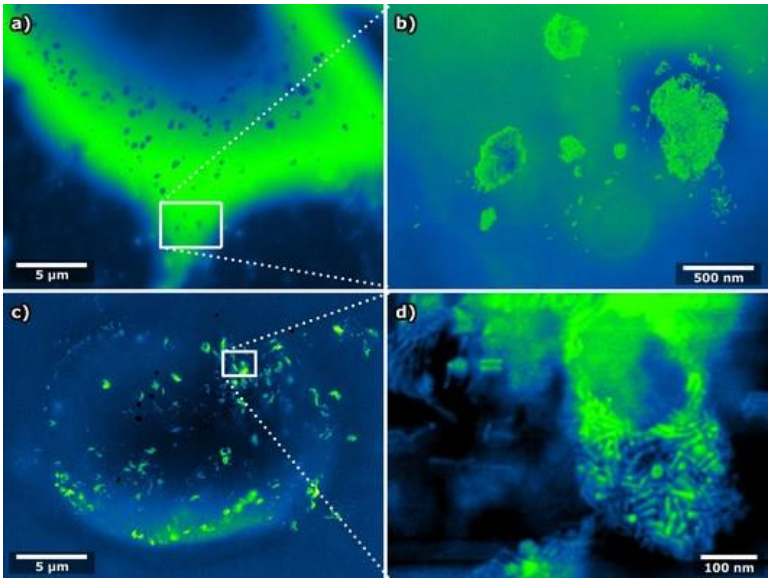

Figure 1. Wet STEM (a,b) and ESEM (c,d) images of uptake of TAT-peptide functionalized Au nanorods into a fully hydrated, as-cultured mammalian stem cell grown directly on a TEM grid (for Wet STEM) or glass slide (for ESEM).

A micro computed tomography quantitative study of tumor microvasculature changes after PhotoBioModulation therapy

Davide Porrelli (1), Simone Vodret (2), Katia Rupel (1), Luisa Zupin (1), Giulia Ottaviani (1), Jacopo Dus (1), Matteo Biasotto (1), Gianluca Turco (1), Serena Zacchigna (2)

1) Department of Medicine, Surgery and Health Sciences, University of Trieste, Trieste, Italy

2) Cardiovascular Biology Laboratory, International Centre for Genetic Engineering and Biotechnology (ICGEB), Trieste, Italy

Keywords: micro-computed tomography, tumor vascularization, PhotoBioModulation, cancer therapy,

We exploited micro computed tomography (µ-CT) to assess the effect of PhotoBioModulation (PBM) on the vascular network of tumors. Tumor tissues usually present altered vascularization, with a vessel diameter distribution different from normal tissues and vast necrotic regions. These abnormal vessels importantly limit an efficient delivery of chemotherapeutic drugs to cancer cells and vessel normalization is emerging as a novel, promising strategy to improve drug penetration into tumors and thus the efficacy of chemotherapy in various solid cancers (1). PBM is a form of light therapy that utilizes non-ionizing forms of light sources, including lasers, LEDs, and broadband light, in the visible and near infrared spectrum to impact on clinically relevant biological processes, including wound healing, bone remodeling and repair, pain control and the immune system (2). We have recently shown that PBM can be exploited to inhibit tumor progression and that this anti-cancer effect is associated to the appearance of more mature and regular tumor vessels, as assessed by histological analysis (3). Here, we wish to obtain further and more comprehensive insights on the structural modifications induced by PBM on experimental tumors in mice. Tumors were induced in C57BL/6 mice by dorsal sub-cutaneous injection of melanoma cell line (B16F10) and half of the mice were irradiated by the most effective PBM protocols able to inhibit tumor growth (3). Tumor-bearing mice were perfused with Microfil, a silicone injection compound used to fill and opacify microvascular spaces, thus providing x-ray contrast to the vascular network. From every animal, we harvested both the tumor mass and the kidneys, used as an intra-animal controls for µ-CT image acquisition. Images were used for three-dimensional

reconstruction and analysis using two different software, Amira and ImageJ, which allowed to define the border of the samples and to quantify the extent of both the vascular and avascular regions using the maximal sphere algorithm. This analysis provides a quantitative assessment of tissue vascularization, vessel diameter distribution and the volume of avascularized areas. We confirmed that the vascularization of tumor samples is very different from the one of normal tissues, exhibiting a broader distribution of vessel diameter and larger avascular spaces. Our preliminary data show that PBM is able to normalize the tumor vasculature, resulting in vessel diameter distribution more similar to healthy tissue and in a reduction of avascular, necrotic areas. These data support the feasibility of a μ-CT-based imaging approach to evaluate the structure of tumor-associated vascular networks and to evaluate the efficacy of anti-angiogenic therapies in animal models of cancer. In addition, the same approach could be used to evaluate the efficacy of pro-angiogenic therapies in inducing the formation of new blood vessels in ischemic tissues.

References:

1. R.K. Jain et al. 307 (2005) 5706-58.

2. V. Kathuria et al., Laser Ther. 24 (2015) 3-215.

3. G. Ottaviani et al., EBioMedicine 11 (2016) 165.

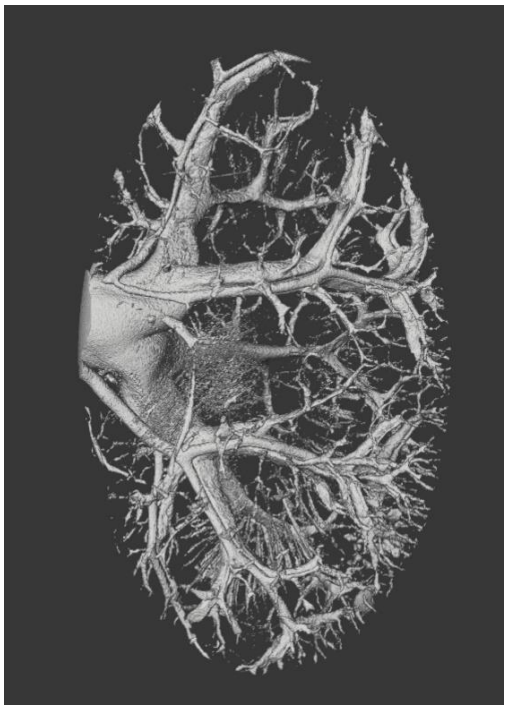

Figure 1. 3D rendering of the reconstruction of a kidney tomography. The microvasculature and the complete perfusion of the kidney by the Microfil, can be appreciated.

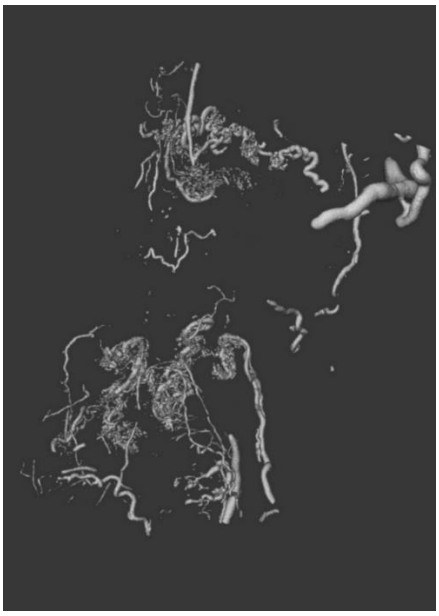

Figure 2. 3D rendering of the reconstruction of a tumor tomography. The tumor has not been treated with PBM therapy. Vast avascularized regions can be appreciated.

Optical Vortex Scanning Microscope - Imaging Procedures

Agnieszka Popiołek-Masajada (1), Jan Masajada (1)

1) Department of Optics and Photonics, Wroclaw University of Science and Technology, Wybrzeże Wyspiańskiego 27, 50370 Wrocław, Poland

Keywords: optical vortex, phase singularity, microscope

The optical vortex scanning microscope (OVSM) uses the focused vortex beam to scan a sample. The schematic view of our system is presented in Figure1: the laser beam (Gaussian beam) passes through the spiral phase plate (vortex lens) and is focused on the sample plane, where it interacts with the investigated object. The vortex lens introduces an optical vortex into the incoming laser beam. The sample plane is imaged into the CCD camera. The interferometer's reference arm enables detection of the interference fringes, from which the internal structure of the object beam can be recovered. The recorded interferograms are preceded using the carrier frequency technique which was described in paper (1). In this way the phase and amplitude distribution of the recorded image was reconstructed. The important part of the OVSM metrology procedures is the internal scanning method (ISM). ISM (2) is realized by moving the vortex lens perpendicularly to the direction of the incident laser beam. In this method the sample needs to be scanned just by an optical vortex, while the entire focused beam stays in a place. The intriguing properties of the ISM were discussed in the papers (2,3,4). It supports the precise method for finding the optimal position of the object plane. In the papers (5,6) the analytical model of the OVSM basic optical system was presented (Figure 1). The model was calculated with the Fresnel diffraction integral in scalar approximation. The model supported the first working image recovery procedures. In Figure (2) the image of the phase square reconstructed with the OVSM is shown. The ISM method can be also used for object characterization. In this presentation the following aspects of the OVSM will be discussed: The general idea of the imaging with a focused vortex beam; - Currently available topography reconstruction methods and its limitations. The exemplary images will be also shown; - possible applications both current and in the near features; -The most important problems to be solved for the OVSM development.

References:

1. J. Masajada, I. Augustyniak and A. Popiołek-Masajada, “Optical vortex dynamics induced by vortex lens shift – optical system error analysis,” J. Opt. 15, 044031 (2013).

2. I. Augustyniak, A. Popiołek-Masajada, J. Masajada, and S. Drobczyński, “New scanning technique for the optical vortex microscope,” Appl. Opt. 51(10), C117-C124 (2012). 3. A. Popiołek-Masajada, B. Sokolenko, I. Augustyniak, J. Masajada, A. Kohoroshun, and M. Bacia,” Optical vortex scanning in an aperture limited system,” Opt. Lasers in Eng. 55(), 105-112 (2014).

4. J. Masajada, I. Augustyniak and A. Popiołek-Masajada, “Optical vortex dynamics induced by vortex lens shift – optical system error analysis,” J. Opt. 15, 044031 (2013).

5. Ł. Plociniczak, A. Popiołek-Masajada, M. Szatkowski, and D. Wojnowski, “Transformation of the vortex beam in the optical vortex scanning microscope,” Opt. Las. Technol. 81, 127-136 (2016)

6. Ł. Plociniczak, A. Popiołek-Masajada, J. Masajada, and M. Szatkowski, “Analytical model of the optical vortex microscope,” Appl. Opt. 55(12), B20-B27 (2016).

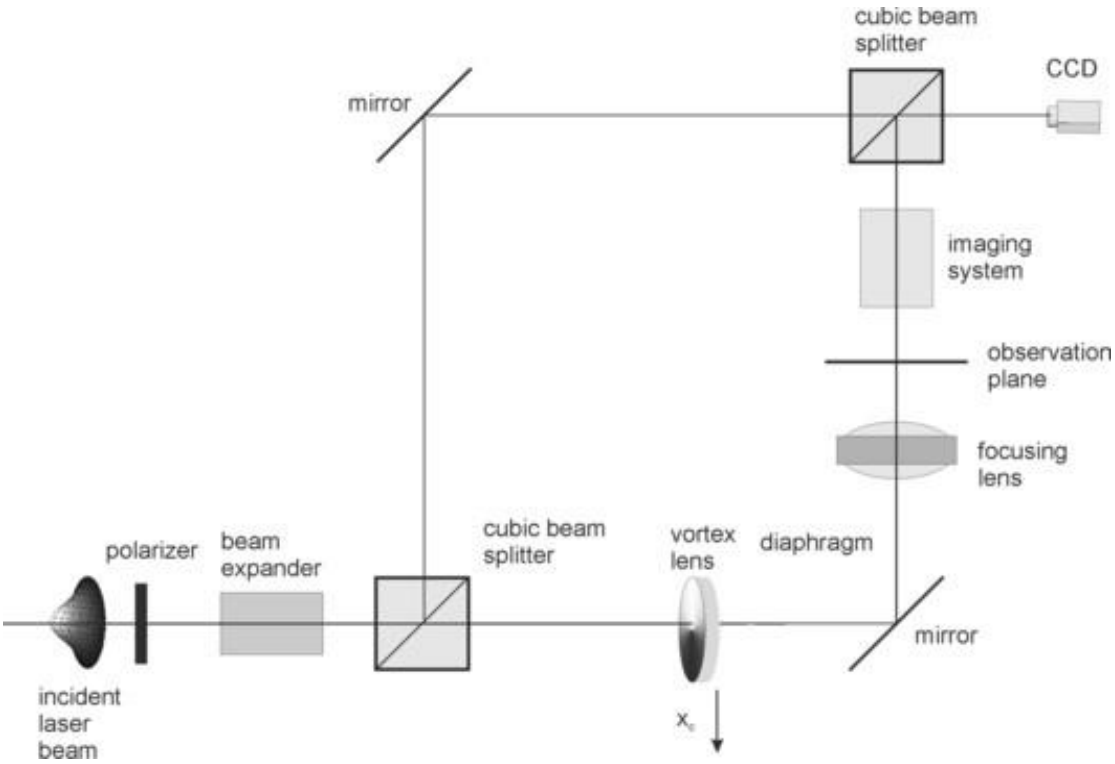

Figure 1. Optical scheme of the OVSM.

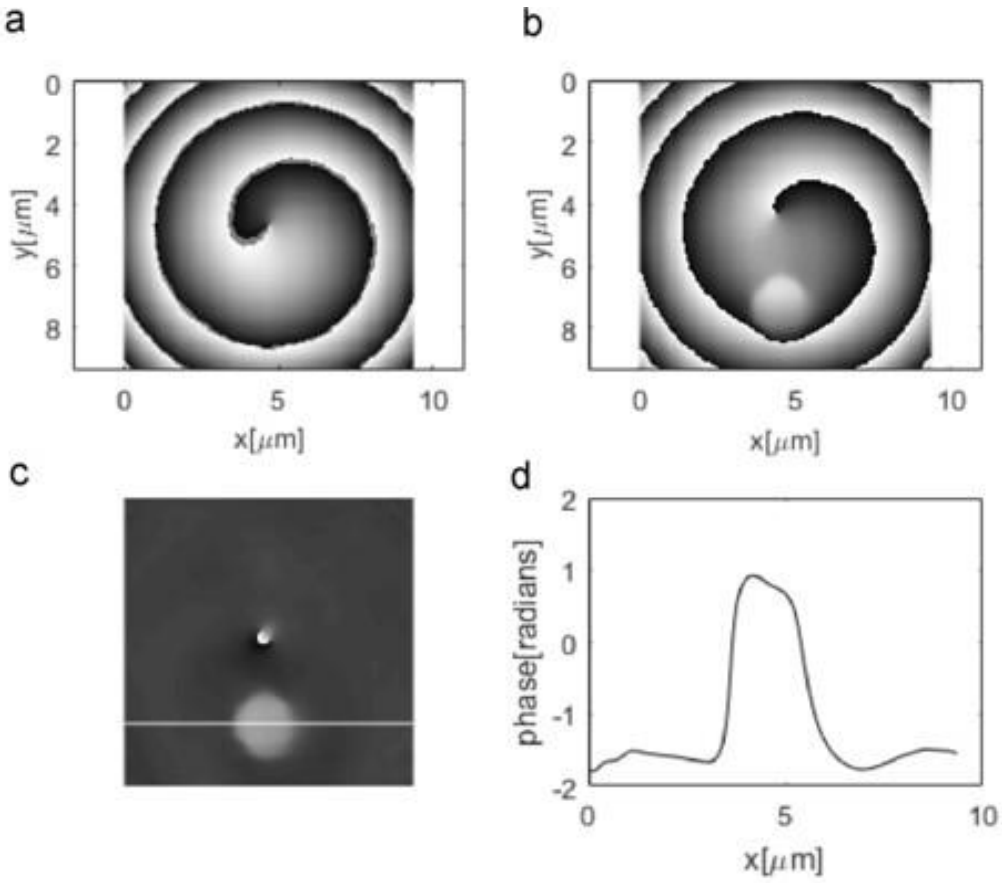

Figure 2. Recovering the image of the 1□mx1□m phase rectangle with OVSM. The figures are rescaled by system magnification (160x).

I2. *In situ* and Environmental Microscopy (including cryo-microscopy, heating, low-vacuum etc.)

INVITED LECTURES I2:

Vizualizing Catalysts in Action

Christian D. Damsgaard (1)

1) Center for Electron Nanoscopy, Technical University of Denmark, DK-2800 Kgs. Lyngby, Denmark and Department of Physics, Technical University of Denmark, DK-2800 Kgs. Lyngby, Denmark

Keywords: Catalysis, Environmental TEM, *in situ* characterization, methanol synthesis, soot oxidation

The rate of catalyzed chemical reactions is in general very dependent on the actual state and geometry of the catalysts surface. This state and geometry are very often dependent on the actual chemical environment the solid-state catalyst is exposed to. Electron microscopy in general and transmission electron microscopy (TEM) in particular gives unmatched detailed insight of the local chemical and structural state of the nanostructured catalysts. Adding the possibility of controlling the gaseous atmosphere around the studied sample at elevated temperature gives a unique way of watching catalysts in action. This work includes examples of how the Environmental TEM (ETEM) complements characterization of catalysts during catalyst formation and under reaction conditions. Ga-Pd alloys have recently been investigated for several catalytic reactions including hydrogenation of acetylene, steam reforming of methanol and methanol synthesis from CO_2/H_2(1). In this example, the focus is on the characterization of the $GaPd_2$ nanoparticles during catalyst formation, methanol synthesis and rapid ageing. ETEM investigations (electron diffraction patterns and images) show that nanoparticle size and dispersion are defined upon calcination with no significant changes observed after reduction and methanol synthesis. The Pd_2Ga phase is formed during reduction and the catalyst does not change phase during methanol synthesis and rapid ageing experiments. Figure 1 shows an ETEM image of a $GaPd_2$ NP along the [100] zone axis acquired at 550°C in 120 Pa H_2. These observations are supported by complimentary

characterization methods such as *in situ* XRD, *In situ* EXAFS, IL-TEM, and STEM-EDX. Soot particles in the exhaust from diesel vehicles are likely to cause lung cancer and to affect the climate both locally and globally. Soot particles are therefore typically removed from exhaust gases by filtration through a ceramic filter. However, increased fuel consumption due to filter regeneration demands development of soot oxidation catalysts that can lower the regeneration temperature. The heterogeneously catalyzed soot oxidation is a gas/solid/solid interaction; hence, the contact between soot and catalyst is very important for the catalytic activity. In this example, soot oxidation by a silver catalyst is monitored *in situ* in the ETEM by ramping the temperature in 300 Pa oxygen at identical rates as used in complementary temperature programmed oxidation experiments (2). Small Ag particles are observed to be highly mobile at an oxidation temperature of approx. 350˚C. The Ag particles travel throughout the soot partly oxidizing the carbon structures. A full oxidation of the soot is observed when the temperature reaches 700˚C. Snapshots of the *in situ* temperature programmed soot oxidation are shown in Figure 2. In conclusion, this work shows examples of how the ETEM is used in combination with other techniques to elucidate, study, and relate performance and local structure of catalysts.

References:

1. E. M. Fiordaliso, I. Sharafutdinov, H. W. P. Carvalho, J.-D. Grunwaldt, T. W. Hansen, I. Chorkendorff, J. B. Wagner, C. Damsgaard, ACS Catal. 5(2015), 5827–5836.

2. D. Gardini, J. M. Christensen, C. D. Damsgaard, A. D. Jensen, J. B. Wagner, Appl. Catal. B Environ. 183(2016), 28–36.

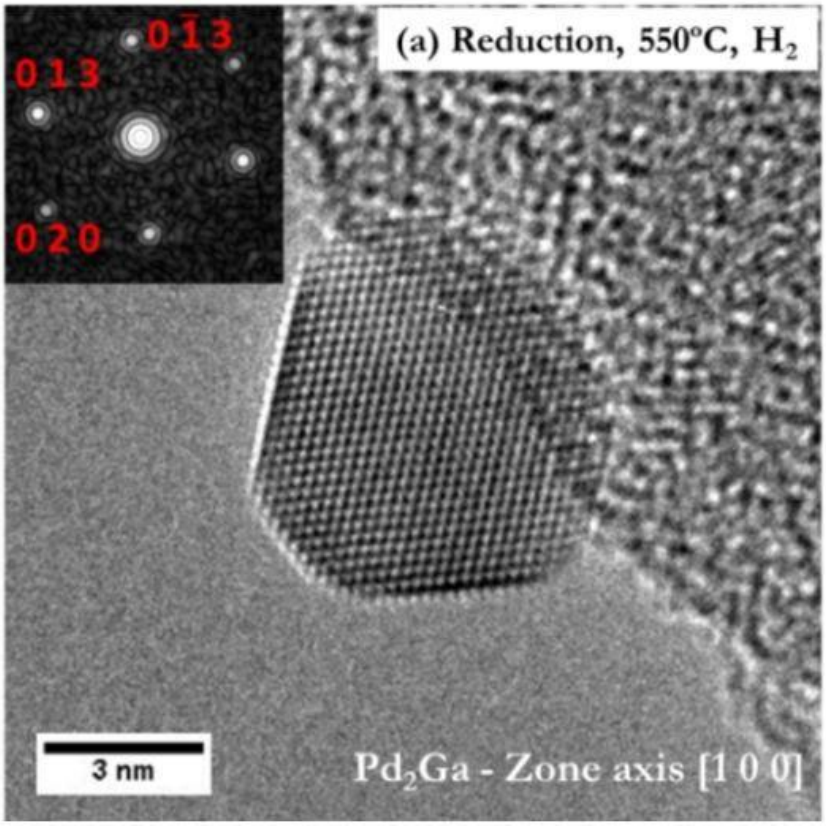

Figure 1. ETEM image of GaPd2 NP acquired at 550°C in 120 Pa H2(1).

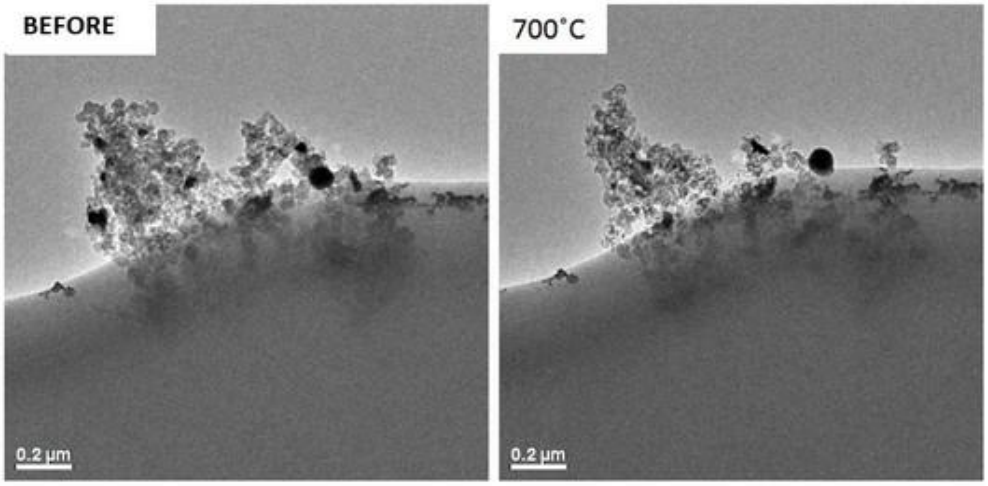

Figure 2. BF-TEM micrographs of *in situ* soot oxidation by a silver catalyst in the ETEM in tight contact condition. P(O2)=300 Pa(2).

In situ observation of nucleation processes in solution by TEM

Yuki Kimura (1)

1) Hokkaido University, Hokkaido University, Kita 8, Nishi 5, Kita-ku, Sapporo, Hokkaido, 060-0808 Japan

Keywords: Nucleation, nanoparticles, liquid cell, *in situ* observation, protein

How atoms or molecules (called growth units) coagulate, arrange and stabilize into a crystal from their mother phase (solution or vapor)? In the classical view, this crystallization process is simple; single growth unit attaches to a *n*-mer to be a (*n*+1)-mer, which process progresses sequentially from a formation of dimer by attachment of two growth units. This process, however, is not in one-way at the beginning of crystallization; growth unit detaches and comes back into a mother phase because of energetic disadvantage for creation of new surface. Increasing the surface energy makes a potential barrier and inhibits a nucleation, which is formation of a seed of its final crystal. Some amount of a driving force (supersaturation/supercoiling) is demanded for nucleation. If a seed of a crystal successfully overcome a potential barrier, the seed, called critical nucleus, grows continuously to its crystal in one-way. The size of the critical nucleus is determined depending on the strength of the driving force. Despite the simple picture, we cannot explain an actual nucleation process even in a considerably most simple case. For instance, it has been well known that nucleation rates obtained by classical nucleation theory are several orders of different from that obtained by experiments and by molecular dynamics simulation. The large difference implies existence of unknown nucleation pathways. To explain the actual nucleation process, several advanced nucleation pathways have been proposed; nucleation via metastable phase, which is able to nucleate at first and then transformed into a final stable crystal by dissolution and precipitation or solid-solid phase transition; nucleation of a crystal inside a pre-nucleated amorphous or dense-liquid particle; and aggregation of precursor particles. The non-classical pathway for nucleation is a hot topic in a field of crystal growth in recent years. Development of an innovative tool for transmission electron microscope (TEM), liquid cell, allows us to observe a nanoscale phenomenon in a water solution, and gives us a chance to find a direct evidence of

a nucleation pathway. The liquid cell also enables to observe hydrated organic materials under TEM (Figure 1). Here, we will report our resent results using a lysozyme protein (1), which has a very large size (~3 nm) and, therefore, has been used extensively for the study of crystallization. Nucleation rates of the lysozyme crystal in an experiment are also difficult to explain using a nucleation model and are ten orders smaller than that of theoretical estimation based on thermodynamics (2). Although two step nucleation process via dense liquid phase has been proposed as the nucleation mechanism (2), this process only works in limited experimental condition. Based on a direct observation of the nucleation phenomena in solution using a TEM, we approach to the actual pathway for nucleation of lysozyme and will tackle to the universality of the mechanisms.

References:

1. T. Yamazaki, Y. Kimura, et al., Proceedings of the National Academy of Sciences of the United States of America 114 (2017) 2154-2159.

2. P. G. Vekilov, Crystal Growth & Design, 10 (2010) 5007–5019.

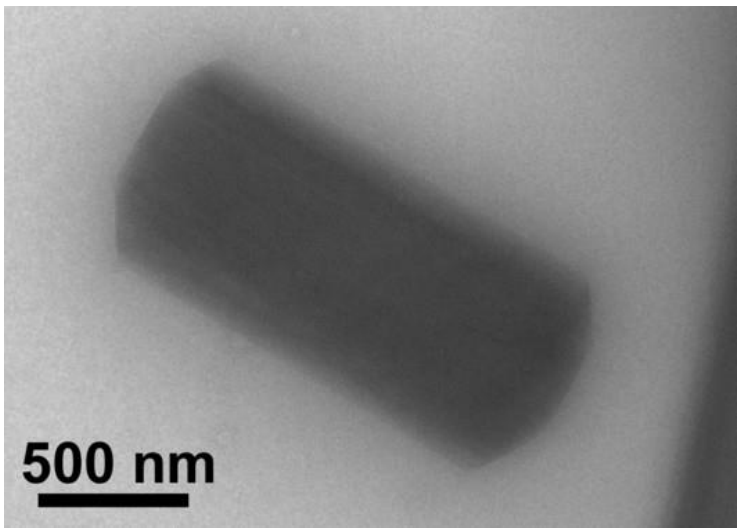

Figure 1. Typical TEM image of a lysozyme protein crystal observed in a water solution using a liquid cell with a spacer of 500 nm in thick. The TEM of Hitachi H-8100 with a tungsten filament was operated with an accelerating voltage of 200 keV.

ORAL PRESENTATIONS I2:

A combined in-operando approach for low-energy scanning transmission electron microscopy and grazing incident small angle X-ray scattering

Simone Dal Zilio (1), Marc Salleras (2), Lluis Balcells (3), Jaume Esteve (2), Allison P. Young (4), Chia-Kuang Tsung (4), Paolo Scardi (5), Benedetta Marmiroli (6), Heintz Amenitsch (6), Regina Ciancio (1)

1) CNR-IOM TASC, Area Science Park, Basovizza S.S. 14 Km 163.5, 34149 Trieste, Italy.

2) IMB-CNM (CSIC), Campus UAB, E-08193 Bellaterra, Spain

3) ICMAB-CSIC, Campus UAB, E-08193 Bellaterra, Spain

4) Boston College, Merkert Chemistry Center, Department of Chemistry, 2609 Beacon St., Chestnut Hill, Massachusetts 02467, USA

5) University of Trento, Department of Civil, Environmental & Mechanical Engineering, via Mesiano 77, Trento 38123, Italy

6) Institute of Inorganic Chemistry, Graz University of Technology, Stremayrgasse 9/IV, Graz, Austria and Austrian SAXS Beamline at ELETTRA,

Keywords: stem, in operando, saxs, multifunctional microreactor

The study of dynamic gas-solid interactions by probing the evolution of electronic, structural, and chemical properties of nanostructured materials under reaction conditions is a crucial issue to determine their structure-functionality relationships. A relevant example is represented by hetereogeneous catalysts whose properties change dramatically with respect to the environment. The common agreement is the need of different lengh scales information and, to this aim, the smart comobination of multiple acquisistion techniques. Much of effort has been made lately in designing new instruments and adapting existing ones to investigate catalysts under *operando* conditions. Another approach has been the use of micro- or nanoreactors that separate the high-pressure volume from the (ultra)high vacuum part via ultrathin walls of an

inert material. Very recently, microreactor cells have been developed to integrate the capabilities of ensemble-averaging synchrotron techniques with local probe ones as TEM to analyze the same catalytic process with different instruments (1,2). Despite the great power of this method, the extremely small probing size of TEMs restricts the application of a combined approach to a limited set of micro-focused synchrotron techniques. We propose here the development of a novel multifunctional microreactor for *operando* low voltage Scanning TEM in a SEM compatible with a broad range of synchrotron techniques. Low voltage STEM/SEM has indeed a series of advantages connected, in the first place, to the use of reduced electron energy (not more than 30kV). In addition, the high flexibility of the SEM chamber allows designing larger microreactors which can be adapted to many synchrotron techniques. The microreactor (sketch in Figure1) is a sealed chamber consisting of two facing SiN semi-transparent windows allowing transmission of both electrons and X-rays. It allows operation at atmospheric pressure, in presence of reactive gases and at elevated temperatures. The device is designed to be compatible with Grazing Incident Small Angle X-ray Scattering (GISAXS) and Wide-Angle X-ray Scattering (GIWAXS) where extended beam footprint (about 1x10 mm^2) and small penetration of the beam are involved due to the grazing incidence geometry. The entire fabrication protocol has been designed to ensure optimal electron transparency for STEM imaging and to preserve the mechanical resistance of the membranes for GISAXS experiments. We successfully demonstrated the feasibility of our approach by studying the stability, shape and size evolution of PVP-capped Pd nanocrystals under oxidation/reaction conditions. Information on size, morphology of the nanocrystals obtained at the nanoscale by STEM (Figure2a and 2b) have been coupled with that concerning their collective behaviour over extended areas such as size, aggregation and cristalline structure by GISAXS/GIWAXS (Figure2c and 3d), all in one portable microreactor and under identical reaction conditions.

References:

1. J.F. Creemer et al. Ultramicroscopy (2008), 108, 993– 998.

2. Shen Zhao et al.Chem. Cat. Chem. (2015), 7, 3683 – 3691.

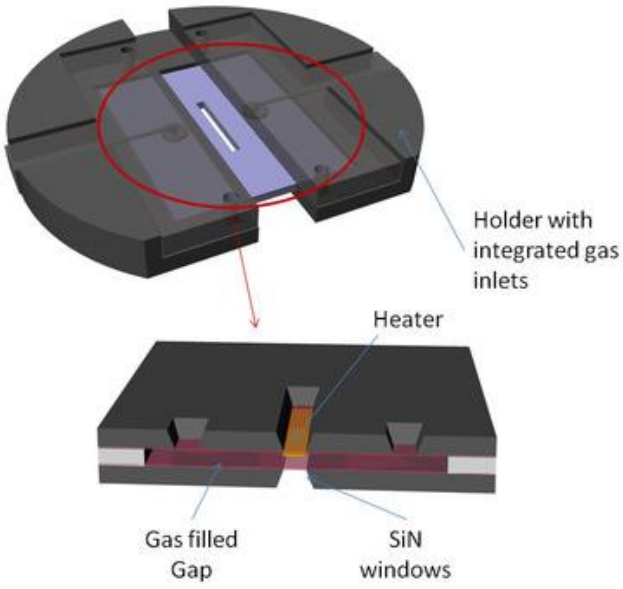

Figure 1. Sketch of the proposed reactor: (left) the holder, designed for STEM and SAXS measures, hosts the cell where the nanoparticles are inserted. Detail (right) of the SiN nitride windows chip with micrometric thinned windows.

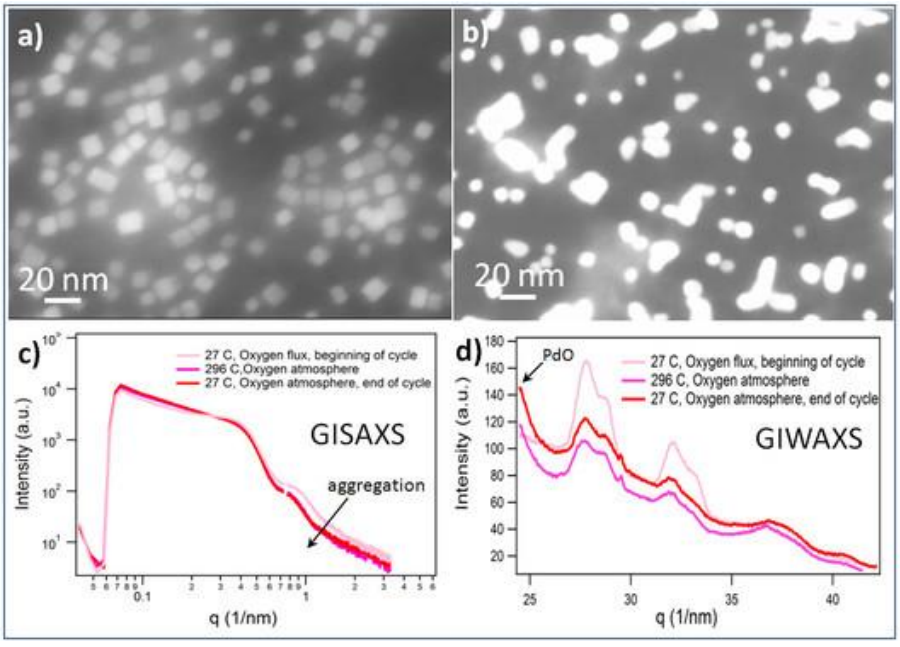

Figure 2. SAXS Intensity- scattering vector curves related to experimental cycle d in Figure5. For clarity, only few curves are reported: the initial one, the one after the end of the heating ramp under oxygen flow, and the one at the end of cooling ramp done in Oxygen rich atmosphere. (b) WAXS data for the same curves

Temperature Dependent Dynamics and Structure of Atomic Clusters in 3D by High Speed STEM

Trond Henninen (1), Marta D. Rossell (2), Rolf Erni (2)

1) EmpaElectron Microscopy Center, Empa, Swiss Federal Laboratories for Materials Science and Technology, CH-8600 Dübendorf, Switzerland

2) Electron Microscopy Center, Empa, Swiss Federal Laboratories for Materials Science and Technology, CH-8600 Dübendorf, Switzerland

Keywords: STEM, atomic cluster, *in situ* heating, 3D, high speed dynamics

The formation of solid matter is typically modelled by classical nucleation theory, assuming the solid forms a spherical nucleus. However, during the initial phase at sub-nm, non-spherical atomic clusters form with atomic structures deviating from bulk crystal. Thus understanding the dynamics of this regime requires considering individual atoms. Understanding this initial cluster formation, enables improved control of nanomaterial fabrication and potentially the creation of new materials. The aim of this work is to study the atomic dynamics of cluster formation, from single atoms of Pt combining to form clusters. Aberration corrected scanning transmission electron microscopy (STEM) has the resolution to directly image this system. However, STEM images are 2D projections, and 3D reconstruction must be done to recover the 3D geometry of the clusters. Using HAADF-STEM, the contrast is linearly proportional to the number of atoms stacked in a column (up to 10 atoms). This enables 3D reconstruction of these clusters through atom counting. The atomic dynamics of the clusters are affected by the e-beam, as have been studied for clusters of Ge and Si (1,2). However, to study cluster formation *in situ*, the effect of the e-beam should be minimized. By using a heating stage, the effect of the e-beam is evaluated, so instead thermal effects can dominate the system. Samples were made by sputtering Pt onto Protochips Fusion thermal chips, giving homogeneous coverage of single atoms of Pt and small clusters up to ~2 nm. STEM was done using a probe corrected FEI Titan Themis at 300 and 80 kV. Heating experiments were performed using a Protochips Fusion heating holder, from room temperature up to 500°C. Image series were recorded at ca 15, 35 and 75 fps. 3D reconstruction was done by atom counting, using Matlab code based on

StatSTEM (3). reliminary data shows the clusters at room temperature appeared amorphous below 2 nm in size, while quasi-molten crystalline above 2 nm. The amorphous clusters disassociated to single atoms over minutes due to the high energy e-beam, while the crystalline particles were more resistive, enduring imaging for more than an hour. Heating promotes crystallinity and clustering. At above 300°C single atoms were observed to combine, forming metastable (for minutes) amorphous clusters ranging from less than 10 atoms up to ~1 nm (ca 50 atoms). 1 nm clusters were also observed to turn quasi-molten at 350°C, with crystalline structures distinctly changing in every few 10s of frames. In contrast, amorphous clusters showed significant changes in structure for every frame. Atomic scale Ostwald ripening was observed when clusters came into contact, but also due to individual atoms crossing a gap between particles of up to a few nanometers (fig 1a). 3D reconstruction of particles and clusters showed that clusters form a flatter structure than the more spherical crystalline particles (Figure 2).

Acknowledgements:

We acknowledge funding from the European Research Council (ERC) under EU's Horizon 2020 program (grant agreement No. 681312).

References:

1. S. Bals, et al., Nat. Commun. 3:897, (2012).

2. J. Lee, et al., Nat. Commun. 4:1650, (2013).

3. A. De Backer et al., Ultramicroscopy 171, (2016).

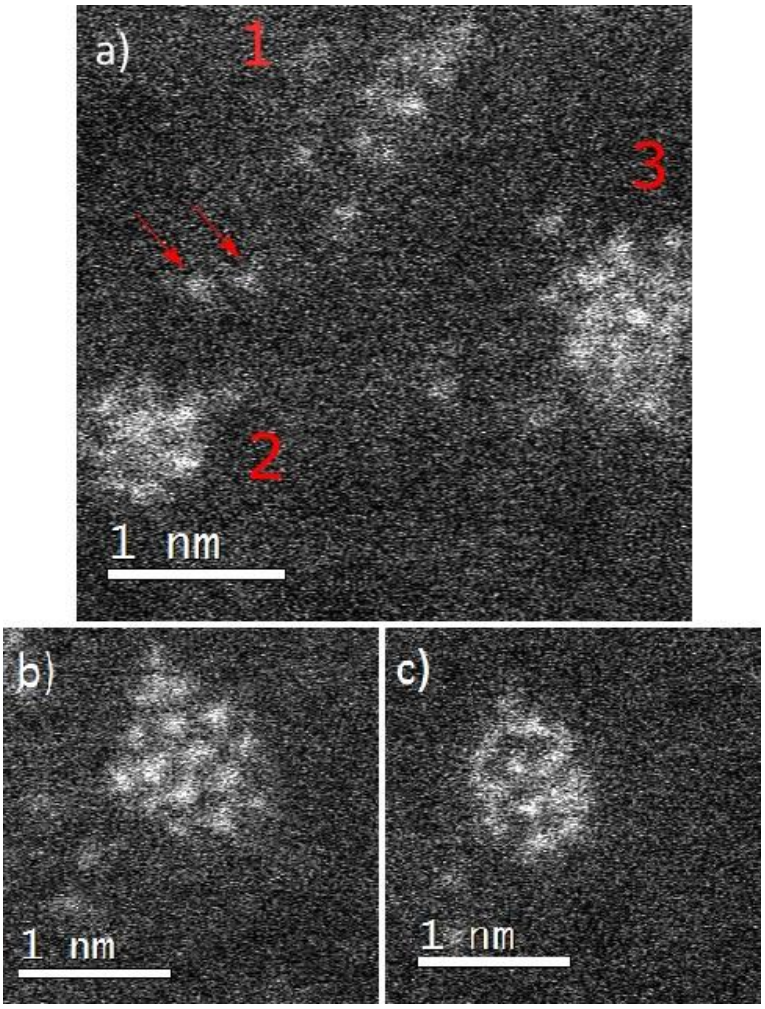

Figure 1. (a) Three clusters at 350°C. Marked atoms were moving from cluster 1 to 2. (b) Crystalline structure of cluster 3. (c) Structure of cluster 3 2.36 s later**.**

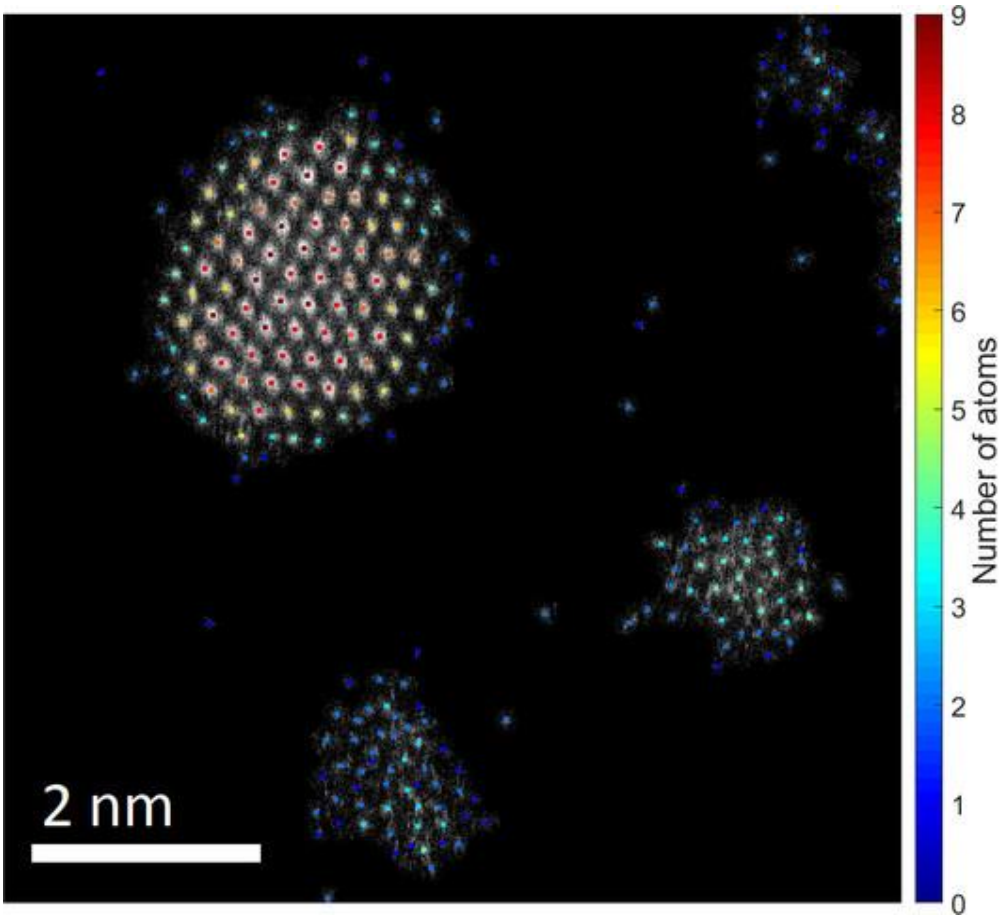

Figure 2. 3D reconstruction with atomic columns from 1 to 9 atoms, overlaid a noise-filtered HAADF-STEM image of a nanoparticle and three clusters.

In situ electrochemical deposition of Fe in a liquid TEM cell

Ulrike Wolff (1), Bojan Ambrožič (2), Janez Zavašnik (2), Kristina Žužek Rožman (2), Kornelius Nielsch (1), Sašo Šturm (2)

1) Leibniz Institute for Solid State and Materials Research Dresden, Helmholtzstraße 20, 01069 Dresden

2) Jožef Stefan Institute, Jamova cesta 39, 1000 Ljubljana, Slovenia

Keywords: electrodeposition, *in situ*, TEM

Materials science applications benefit from both the spatial resolution available with liquid cell electron microscopy and its temporal resolution, which allows reaction kinetics and mechanisms to be probed. Electrochemical processes provide an excellent example, with observations possible in a liquid cell that is filled with an electrolyte and also contains the three electrodes (1). Nucleation and growth of Ni (2), catalytic reactions, nanoparticle self-assembly at liquid interfaces (3) are just a few examples of the wide range of possibilities to use the liquid transmission electron microscopy (TEM) cell. We demonstrate the first stages of *in situ* electrochemical Fe deposition in a liquid TEM cell. The experiments were performed in a JEM-2100 (JEOL Ltd., Tokyo, Japan) microscope operating at 200 kV combined with the energy dispersive X-ray spectroscopy (EDXS). We used a Poseidon 510 TEM (Protochips Inc., Raleigh, NC, USA) holder combined with a Gamry Reference 600 potentiostat (Gamry Instruments, Warminster, PA, USA) for applying the electrochemical conditions (chronoamperometry). The microfluidic electrochemical cell consists of two chips with 50 nm amorphous silicon nitride windows where the smaller one has a spacer height of 50 nm, thus controlling the total thickness of the liquid layer between the two windows. The upper larger chip contains the glassy carbon working electrode and the Pt reference and counter electrodes. As electrolyte a Fe sulphate containing solution with a pH of 2 was used. Applying a potential of -1.2 V vs. Pt shows the electrodeposition of first, an amorphous Fe layer (diffraction pattern, Figure 1a) and b)), which then crystallizes to Fe-oxide (Figure 2a) and b)). The nucleation occurs instantaneously in dependence on the applied potential. The resulting deposition is discontinuous. During the time of electrodeposition the electron beam was blocked to minimize

the influence of the beam on the water radiolysis and radical chemistry. EELS measurements will clarify the nature of the amorphous and crystalline layers. Furthermore, growth mechanism will be determined.

Acknowledgements:

Fruitful discussion with K. Duschek and K. Leistner is gratefully acknowledged.

References:

1. N. De Jonge, F.M. Ross, Nature Nanotechnology 6, 695 (2011)

2. X. Chen, K.W. Noh, J.G. Wen, S.J. Dillon, Acta Materialia 60, 192 (2012)

3. L.L. Dai, R. Sharma, C.Y. Wu, Langmuir 21, 2641 (2005).

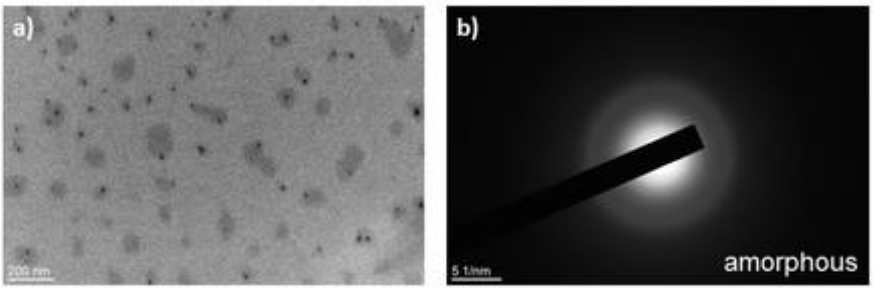

Figure 1. (a) + (b): TEM image and corresponding diffraction pattern of electrodeposited Fe after applying a potential of -1.2V/Pt.

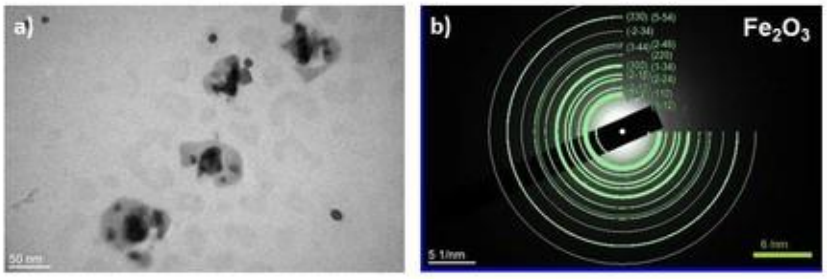

Figure 2. (a) + (b): Crystallization of Fe-oxide by longer deposition times (TEM image and corresponding diffraction pattern).

In situ tracking the structural and chemical evolution of nanostructured materials

Zaoli Zhang (1), Jinming Guo (1), Reinhard Pippan (1)

1) Erich Schmid institute of Materials Science, Austrian Academy of Sciences, Jahnstrasse 12 8700 Leoben, Austria

Keywords: *in situ* heating, nanostructured materials, EELS, STEM

Bulk nanostructured materials show extremely high strength compared to bulk materials, and have received unprecedented attention in material research also due to its potential applications in industry. Severe plastic deformation is an emerging and quite efficient route to generate nanocrystalline materials out of normally immiscible systems. However, the main issue on nanostructured materials is its thermal stability. In this contribution, the thermal stability of nanostructured materials will be explored at a very high-spatial resolution using modern spherical transmission electron microscopy (TEM) via simultaneous *in situ* imaging and spectroscopy analysis. CuCr (CuFe) nanostructured alloy was utilized for *in situ* monitoring the structural evolution and chemical composition changes simultaneously. A coarse-grained Cu-Cr composite material (43wt % Cr, 57wt % Cu, and corresponding to 48 at % Cr and 52 at% Cu, respectively) was deformed by high pressure torsion (HPT) at room temperature. The initial microstructure of the composite consists of a Cu matrix with Cr particles (volume fraction of about 50%, mean diameter of about 50 μm) produced by PLANSEE (Reutte, Austria). Disks with a diameter of ~8 mm and a thickness (*t*) of ~0.8 mm were HPT deformed for different numbers of turns *n* under a constant pressure of 6.25 GPa with a rotation speed of 0.2 rotations/minute. HPT disks which were deformed for 25 turns (equal strains = 400) were used for *in situ* annealing in TEM at 25°C, 212°C and 414°C after preparing TEM specimens from the edge of the disk, where the highest strain has occurred. A JEOL 2100F field emission microscope (200kV) equipped with an image-side Cs-corrector which possesses a 1.2 Å resolutions at 200 kV was used. The aberration coefficients were set to be sufficient small, i.e. C_S ~ - 15.0 μm. The HRTEM images were taken under a condition of slightly over-focus. The evolution of the structural and chemical composition in the nanostructured materials with

temperature was tracked in *real-time*. It demonstrates that the nanostructured materials are not only subjected to a structural change but also to obvious chemical composition fluctuations upon annealing. The destabilization process in the nanostructured materials starts at a quite low temperature. *Real-time* imaging and composition determination reveal the concentration changes with temperature, and allows further analyzing the dynamic behavior in nanocrystalline materials in details, i.e. deducing the instantaneous diffusion coefficients and excess vacancy concentration generated by severely deformation. The experiments demonstrated a direct approach to measure the excess vacancy concentration via measuring elemental profiles, except visualizing the morphology evolution. Essentially, the study uncovers the interplay between the thermal stability and chemical decomposition process of bulk nanostructured materials in *real-time*.

POSTER PRESENTATIONS I2:

Thermal vs. beam induced dynamics in the TEM: *in situ* experiments and simulation

Daniel Knez (1), Maximilian Lasserus (2), Martin Schnedlitz (2), Evelin Fisslthaler (1), Wolfgang Ernst (2), Ferdinand Hofer (1)

1) Institute for Electron Microscopy and Nanoanalysis, Graz University of Technology & Centre for Electron Microscopy, Steyrergasse 17, 8010 Graz, Austria

2) Institute for Experimental Physics, Graz University of Technology, Petersgasse 16, 8010 Graz, Austria

Keywords: electron beam damage simulations, *in situ*, atom dynamics, metallic clusters, interfaces

Knowledge about thermodynamic properties of metallic clusters, surfaces and interfaces is of paramount importance for a variety of applications, such as barrier layers in semiconductor devices, metallurgy or heterogeneous catalysis. Therefore, we perform *in situ* heating experiments via STEM, using clusters and metal/metal/semiconductor layer stacks. In principle, state-of-the-art STEM allows to gain elemental information on the atomic scale. However, the high electron energies and current densities that typically occur in such instruments often cause beam induced dynamic processes. This is true especially for systems with a high amount of low-coordinated and weakly bound atoms, such as clusters, surfaces and interfaces (1). For STEM experiments, we use a probe corrected FEI Titan^3 60-300 microscope. This microscope is equipped with a Super-X detector (EDXS) and a Gatan Quantum energy filter for EELS. *In situ* heating experiments are performed with a DENSsolutions Wildfire D6 holder, equipped with a heatable MEMS device. The nanoparticles used for our investigations were synthesized within superfluid helium nanodroplets, under ultra-high vacuum (UHV) conditions (2). This approach provides exceptional advantages over conventional methods, like sequential addition of a wide range of materials without the use of ligands and stabilizers. Thus, nanoparticles can be synthesised with any composition and

different structures (3), with extremely high purity. Figure 1a shows results of a heating experiment with a Cu/Ru/SiO2/Si layer stack. The Ru layer acts as a barrier to prevent Cu atoms to diffuse into the Si crystal. At a temperature of about 500°C the Ru barrier layer breaks and Cu particles can be observed diffusing randomly through crystalline Si, forming copper silicide on their paths. Figure 1b gives an example of a NiAu core-shell cluster supported by amorphous carbon. The cluster changes its morphology at elevated temperature and eventually forms an alloyed cluster. Observing this process live via STEM HAADF time-lapse series enables us to draw conclusions about diffusivity of Ni and Au on the nanoscale. The separation of beam induced sample changes from purely thermally driven processes is often challenging during *in situ* experiments. Hence, it is necessary to gain a deeper understanding of the observed processes, which we achieve by comparing experimental data with a theoretical description of beam-induced dynamics in metallic systems using molecular dynamics and Monte Carlo algorithms. We show that high purity metallic clusters are an ideal demo system to study such phenomena, in experiment and simulation. Figure 1c demonstrates electron beam induced sputtering on the example of an Ag cluster, which rapidly loses atoms under electron beam irradiation. We compare experimental STEM HAADF time-lapse series with corresponding simulation results obtained with our code.

Acknowledgements:

We kindly acknowledge financial support by the Federal Ministry of Science, Research and Economy with the project “Infrastrukturförderung 2015”, by the Austrian Research Promotion Agency (FFG) in the project 850220/859238.

References:

1. Egerton, R. F. Microsc Microanal 19 (2013) 479–486

2. A. Volk et al. J. Chem. Phys. 138 (2013) 214312

3. P. Thaler et al. Phys. Rev. B 90 (2014)

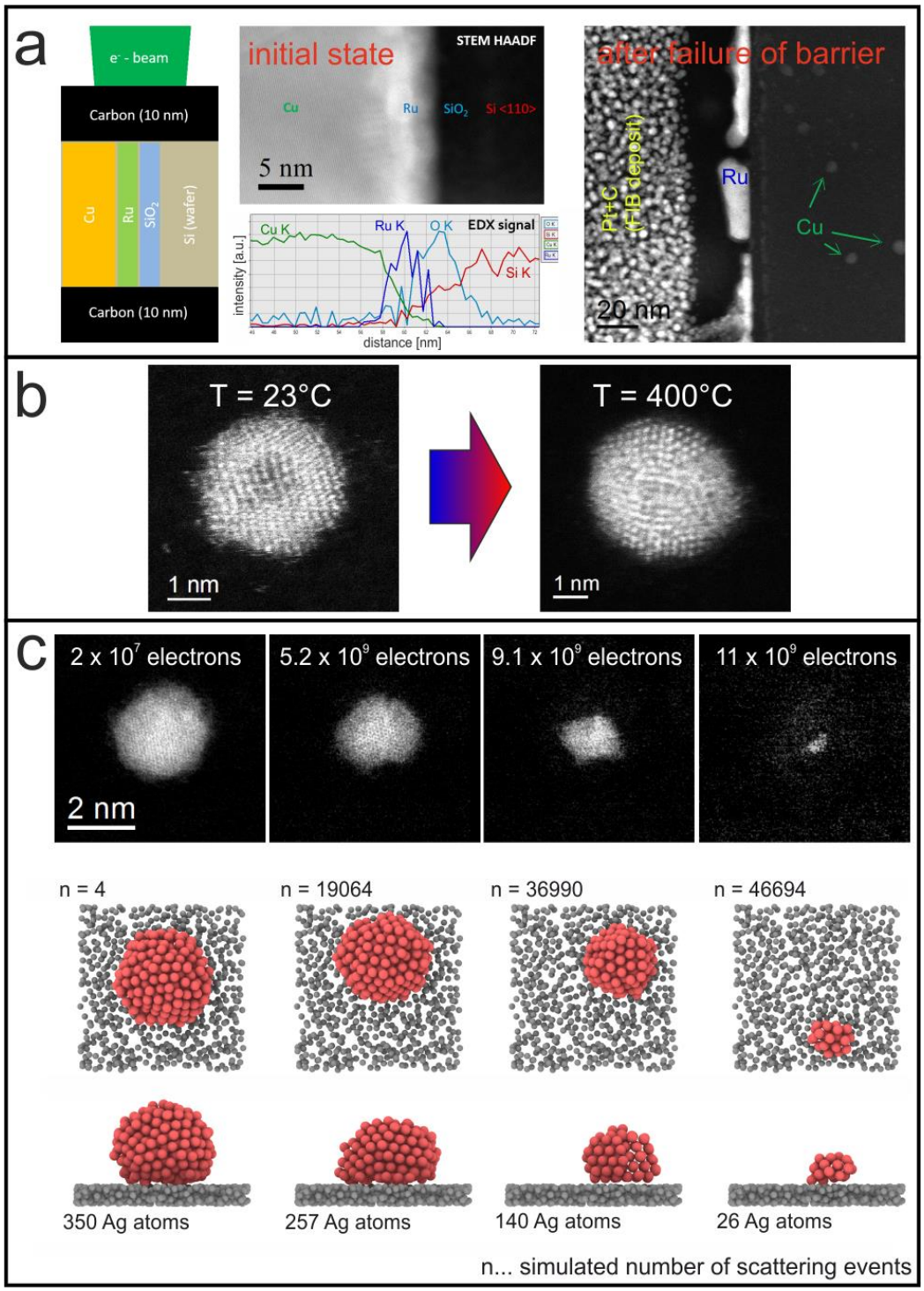

Figure 1. (a) Cu/Ru/SiO_2/Si layer stack before and after heating to 500°C. (b) Alloying of NiAu core-shell clusters during heating. (c) Electron beam (300 keV) induced sputtering of an Ag cluster: Experimental STEM HAADF image series compared with molecular dynamics simulations.

Precipitation mechanism and kinetics in the Al-Mn-Be-Cu alloy

Franc Zupanič (1), Tonica Bončina (1)

1) University of Maribor, Faculty of Mechanical Engineering, Smetanova ulica 17, 2000 Maribor Slovenia

Keywords: precipitation, Al-alloy, transmission electron microscopy, quasicrystal

The quasicrystal-strengthened Al-alloys have been attaining an increased attention because they can possess excellent combinations of strength and ductility (1). In some alloys, In Al-Mn-Be-Cu alloys the strength can be heightened by an appropriate heat treatment, even for 50 % in comparison with the as-cast state (2). In the rapidly solidified alloys, the strongest effect can be achieved by heat treatment because of extremely high precipitate density. Recently, *in situ* transmission electron microscopy (TEM) study have become an important tool for elucidating the mechanisms and kinetics of phase transformations. This method was also used for the study of precipitation kinetics and mechanisms within an Al-Mn-Be-Cu quasicrystal strengthened alloy at 300 °C (3). The FIB lamellas were examined using high-resolution TEM (HRTEM), energy-filtered TEM (EFTEM), scanning TEM (STEM), and energy-dispersive X-ray spectroscopy (EDXS) in FEI Titan 80-300. The initial condition of the alloy was an as-cast state after cooling by a moderate cooling rate. At 300 °C, icosahedral quasicrystalline precipitates formed within the Al-rich solid solution. On the other hand, the formation of Al_2Cu and T-phase was heterogeneous on the phases formed during solidification. In the presentation, several aspects regarding the nucleation and growth of different precipitates will be explained.

Acknowledgements:

This work was partly financed by the research programme P2—0120 (Slovenian Research Agency – ARRS). We appreciate the support of the European Research Infrastructure EUMINAfab, funded under the FP7 specific programme Capacities, Grant Agreement Number 226460), and its partner Karlsruhe Institute of Technology, especially to Dr. Di Wang for the excellent work on TEM.

References:

1. A. Inoue, H. Kimura, Current Opinion in Solid State and Materials Science 2, 305 (1997).

2. F. Zupanic, G. Lojen, L. Barba, T. Boncina, Mater. Charact. 70, 48 (2012).

3. T. Boncina, F. Zupanic, Archives of Metallurgy and Materials, 62 (2017) 5-9.

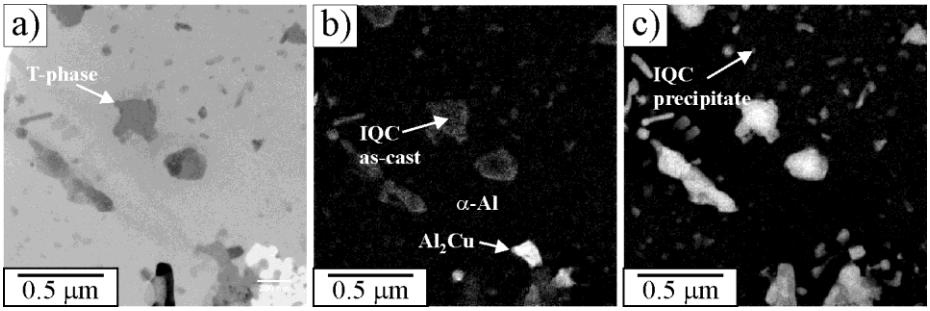

Figure 1. *In situ* treatment at 300°C for 60 and 150min. (a) TEM bright-field image, (b) EFTEM distributions of Cu, and (c) EFTEM distributions of Mn.

Structural dynamics of copper and platinum substrates during redox reactions studied by *in situ* SEM

Jing Cao (1), Mark Greiner (1), Adnan Hammud (1), Marc Willinger (1), Robert Schlögl (2)

1) Fritz-Haber-Institut der Max-Planck-Gesellschaft, Fritz-Haber-Institut der Max-Planck-Gesellschaft, Faradayweg 4-6, 14195 Berlin, Germany

2) Fritz Haber Institute of the Max Planck Society, Department of Inorganic Chemistry, Faradayweg 4-6, 14195 Berlin, Germany

Many efforts have been made in order to investigate catalyst under relevant working conditions. Indeed, the action of a chemical potential has to be considered when describing the state of a catalyst and recent studies have demonstrated that the catalyst surface evolves dynamically under reaction conditions (1,2). In order to complement *in situ* spectroscopic tools, such as near-ambient X-ray photoelectron spectroscopy (NAP-XPS), with visual information about the active surface structure, we have implemented *in situ* scanning electron microscopy (SEM) for the observation of dynamic processes at the µm to nm scale (3). By coupling *in situ* SEM with mass spectroscopy measurements we are able to relate structural dynamics at the surface of metal catalysts to changes in the gas phase composition. Under specific conditions, oscillatory behavior of the catalyzed chemical reactions was observed for the case of polycrystalline nickel, copper and platinum foils. Our on-going investigation of redox dynamics on the Cu surface has revealed several interesting phenomena. We find that three distinct phases coexist under hydrogen oxidation conditions, and over time the surface oscillates between these three phases, as shown in Figure 1. *In situ* NEXAFS (Figure 2) was performed on such samples in dynamic redox conditions. These measurements allowed to identify the coexisting phases as metallic copper and Cu_2O (as evident from the position of the Cu L3-edge), and has also revealed that an O-terminated Cu species is present (as evident from the O K-edge shoulder at ca. 530 eV) (4). Overall, it will be outlined how the implementation of complementary *in situ* SEM and NAP-XPS techniques can enrich our understanding of the dynamic behavior of active catalyst and how it complements spatially integrated spectroscopic data that is recorded under similar conditions.

References:

1. T. Lunkenbein et al., Angew. Chem. Int. Ed. 2015, 127, 15, 4627-4631.

2. S. Piccinin et al., Phys. Rev. Lett. 2010, 104, 035503.

3. Z. J. Wang et al., ACS Nano., 2015, 9, 1506-1519.

4. M. T. Greiner et al., Phys. Chem. Chem. Phys., 2015, 17, 25073.

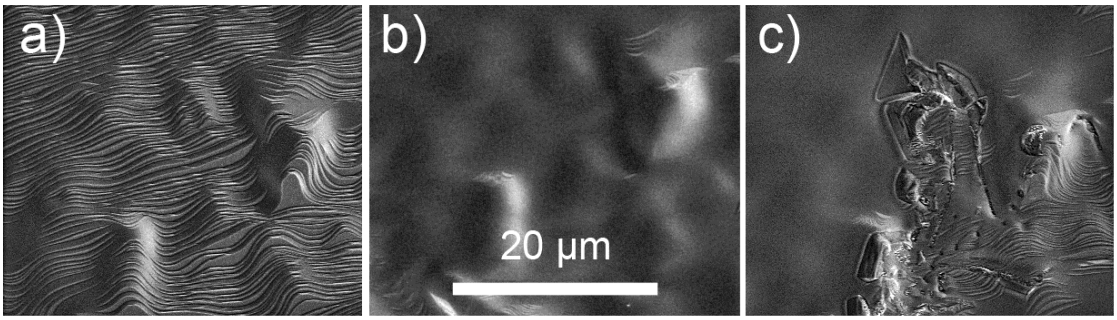

Figure 1. *In situ* ESEM images of a Cu surface during redox dynamics in H_2 + O_2 at 700°C. The regions shown in (a), (b) and (c) are of the same area, but at different time (t*, t*+506s, t*+724s).

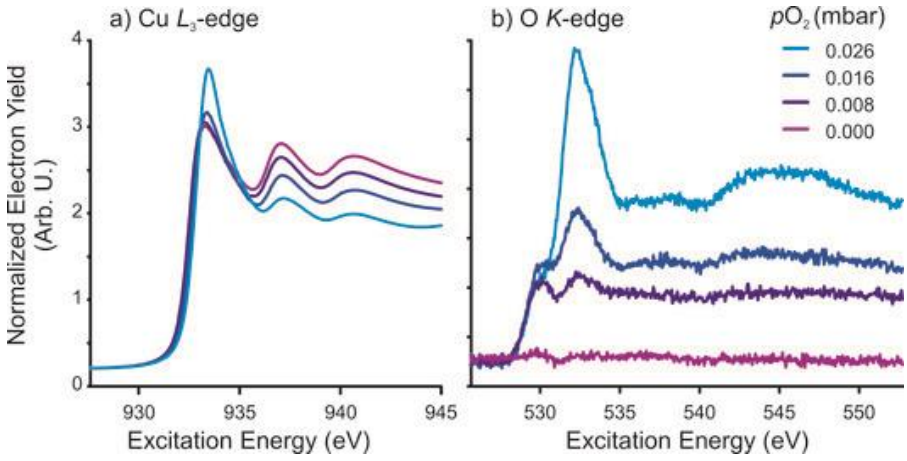

Figure 2. (a) Cu L3-edge and (b) O K-edge of Cu foil measured *in situ* in a mixture of H_2 and O_2 at 700°C.

In situ experiments in the ESEM – What can they tell us about the microstructure and behavior of polymeric microfiltration membranes?

Manfred Nachtnebel (1), Peter Poelt (2)

1) Graz Centre for Electron microscopy, Steyrerg. 17, 8010 Graz

2) Institute of Electron Microscopy and Nanoanalysis, NAWI Graz, Graz University of Technology, Steyrerg. 17, 8010 Graz

Keywords: microfiltration membranes, ESEM, *in situ*, 3D reconstruction

Asymmetrically layered flat sheet microfiltration membranes, consisting of a blend of polyethersulfone (PES) and polyvinylpyrrolidone (PVP), are widely used for wastewater purification. Apart from the microstructure of the membranes especially the content and distribution of PVP, which serves to increase the hydrophilicity of the membranes, are crucial parameters for their performance. Such membranes must be regularly cleaned and disinfected for long term usage to recover the loss of effectiveness caused by fouling. Typical cleaning agents used for this purpose are, amongst others, sodium hypochlorite (NaClO) and sodium hydroxide (NaOH). But the cleaning process itself can also cause membrane degradation. In the environmental scanning electron microscope (ESEM Quanta 600 FEG, FEI, Eindhoven, NL) the wetting and drying of cooled membranes can be carried out and the progress at the surfaces can be observed. Simultaneously the temperature changes at the surfaces of the membranes can be recorded. The correlation of both provides information about the microstructure of the membranes as well as the interaction of the membrane material with water (1, 2). Changes in the hydrophilicity of a membrane will cause a change both in the time necessary for the drying of the membranes and in the temperature characteristics (see Figure 1). Contrary to conventional test methods used for membrane characterization, these changes tell us to which layer the membrane degradation can be mainly attributed. Extensive investigations proved that all chemicals used for membrane cleaning also cause membrane damage. The main mechanism seems to be a loss of hydrophilicity directly at the membrane surface due to a decrease in the PVP concentration (2). The separation layer, which is the

main filtration layer, is less affected. This was corroborated by spatially resolved transmission IR-spectroscopy. A change in the membrane structure could not be observed. The temperature characteristics mentioned above provide only qualitative information about the membrane structure, but do not give quantitative values about the pore size, the pore length, the connectivity and other parameters. To get these parameters, a 3D reconstruction of the membrane structure is necessary. An ultramicrotome (3View® (Gatan, Pleasanton, CA) mounted in the specimen chamber of an ESEM was used for serial sectioning and imaging. Sectioning was possible at room temperature and without the need for staining, because the sulphur concentration in PES is high enough to provide sufficient contrast in the backscattered electron images. But whereas parameters like connectivity cannot be measured directly and thus confirm the calculations, this is possible for other even more important values like the trans-membrane flux (see Figure 2). Systematic modifications in the reconstructed models and recalculations of the relevant parameters might help in the design of new and more efficient membranes.

References:

1. H. Reingruber et al., J. Membr. Sci. 399-400 (2012) 86-94.
2. M. Nachtnebel et al., J. Membr. Sci 503 (2016) 81-89.
3. H. Reingruber et al., J. Membr. Sci 372 (2011) 66-74.

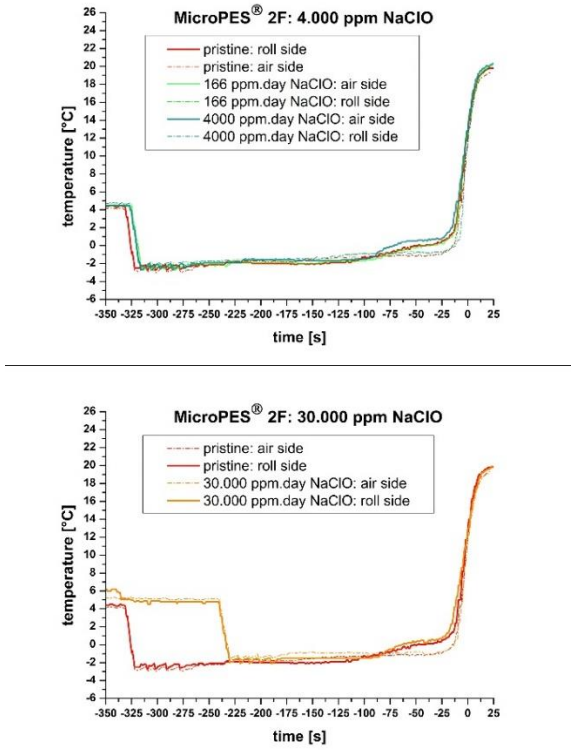

Figure 1. Temperature profiles of a flat sheet microfiltration membrane recorded at both surfaces after treatment with different doses of NaClO. The time axis was shifted and set to zero at the time the drying of the membrane was completed.

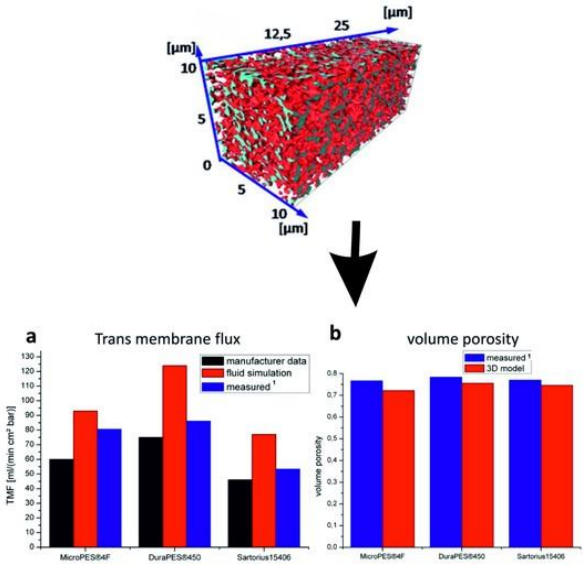

Figure 2. Calculation of the trans-membrane flux and the volume porosity for the membrane DuraPES®450 from a 3D reconstruction and comparison of the results with measured values and manufacturer data.

In situ EBSD Investigations of Al-Mg-Si-Alloy during heating

Stefan Mitsche (1), Jakob Grasserbau (1), Peter Pölt (1)

1) Institute of Electron Microscopy, NAWI Graz, Graz University of Technology, Steyrergasse 17, 8010 Graz, Austria

Keywords: *in situ* EBSD, Al-Mg-Si, recrystallization, texture

Heat-treatable aluminium alloys like the Al-Mg-Si alloy are of high interest in the automotive industry due to a combination of good formability, corrosion resistance, satisfactory strength and of course their light weight in comparison to steel. The texture of the Al sheets induced by the rolling process influences both the drawability of the Al alloys and the roping effect (1, 2). In order to minimize the roping effect a better understanding of the texture evolution during the heat treatment is essential. *In situ* EBSD analysis is a powerful technique to evaluate the change of the texture caused by a heat treatment. Our investigations were performed on rolled samples of Al-Mg-Si alloys. Due to the stored deformation energy caused by the rolling process static recrystallization can occur. With *in situ* EBSD measurements it is possible to determine the starting and the end point of the recrystallization in dependence on the temperature and holding time. Additionally, it is possible to establish a direct correlation between the texture of the deformed state and that of the recrystallized state of the sample. For the *in situ* EBSD investigations of the rolled Al-Si-Mg sheets a Zeiss Ultra 55 field emission scanning electron microscope equipped with a Kammrath&Weiss heating stage and the OIM System from EDAX was used. An inverse pole figure map is a colour coded map, where the colour is directly correlated to the orientation of the grains. Figure 1 shows the IPF maps of a rolled sample at 200°C (a) and at exactly the same area at 300°C (b). It is obvious that at a temperature of 200°C the sample is still fully deformed and there are no indications for recrystallization or recovery. However, after increasing the temperature to 300°C a fully recrystallized sample was obtained, as can be seen in Fig 1b. Comparing the orientations of both IPF maps it seems that the recrystallized grains show just those orientations which were already present at the deformed state of the sample. Additionally, the grain boundaries of the recrystallized grains seem to be distributed randomly, not connected to those of the deformed grains. This

recrystallization behaviour is completely different to that of e.g. the dynamic recrystallization of nickel base alloys (3). The correlation between the orientations of the deformed and recrystallized grains is confirmed by the inverse pole figures in Figure 2. The sample at 200°C (Figure 2a) shows a smeared distribution due to the high deformation of the grains but only in some preferred directions. The IPF of the recrystallized sample (Figure 2b) shows only clear points of the different grains, but it is obvious that these grains have only orientations in the same region were a smeared distribution of the orientation is present for the deformed sample. As a consequence, it can be concluded that the recrystallized grains show a “memory effect” concerning the orientation of the deformed grains.

References:

1. O. Engler et al., Materials Science and Engineering A336 (2002), 249–262.

2. J.J. Sidor et al., Acta Materialia 59 (2011), 5735–5748.

3. S. Mitsche et al., Journal of Microscopy 227 (3), 267-274.

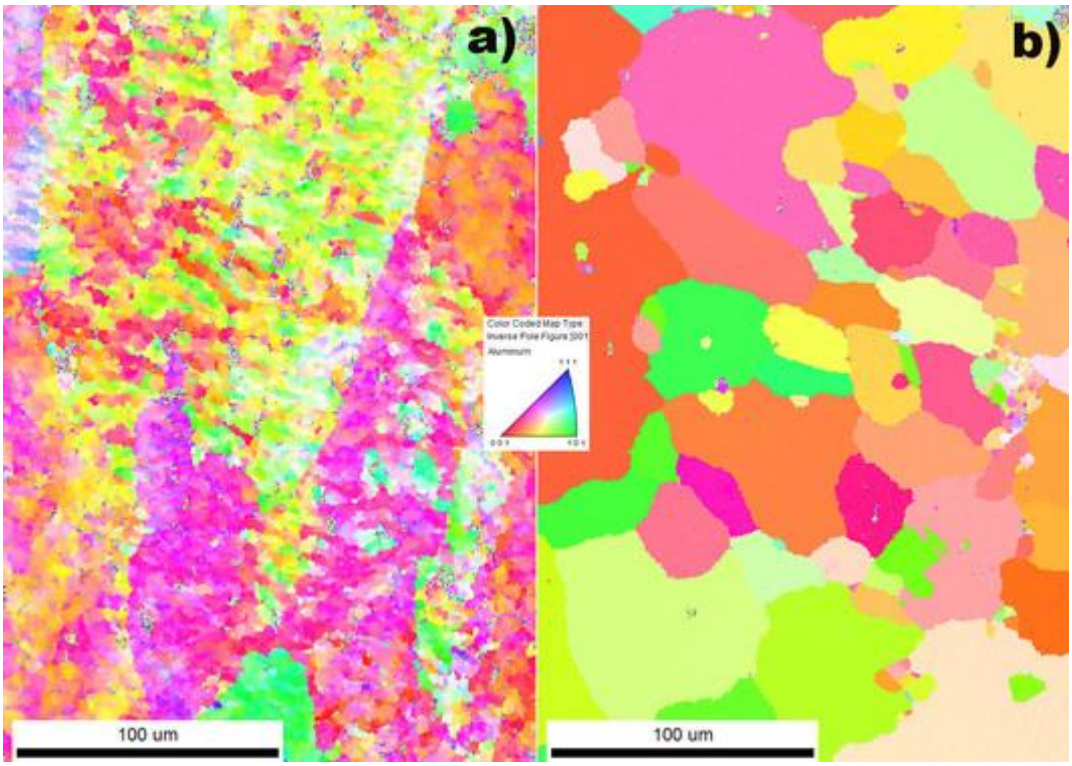

Figure 1. Inverse pole figure maps of a rolled Al-Si-Mg sample recorded at (a) 200°C and at the same area at b) 300°C.

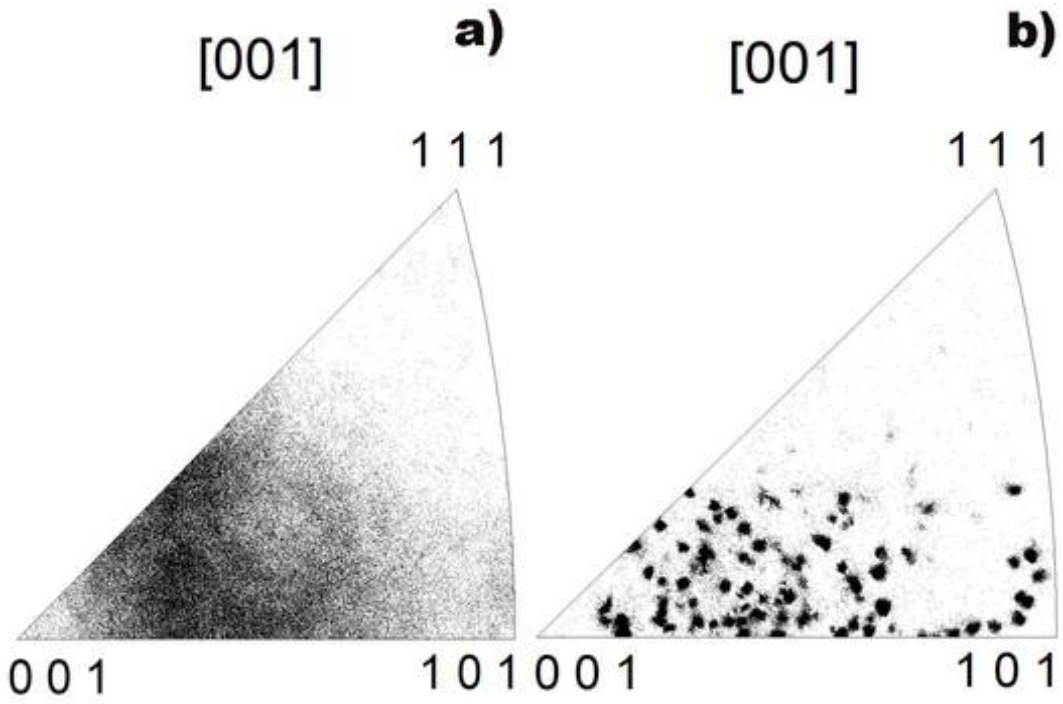

Figure 2. Inverse pole figure of a rolled Al-Si-Mg sample recorded at (a) 200°C and at the same position at (b) 300°C.

Nanoworld of acrobatic crystals – thermosalient effect (example of Scopolamine bromide)

Teodoro Klaser (1), Željko Skoko (1)

1) Department of Physics, Faculty of Science, University of Zagreb, Bijenička c. 32, HR-10000 Zagreb, Croatia

Keywords: Thermosalient effect, Scopolamine bromide, Phase transition

Imagine the surprise on one's face when, during the microscopic evaluation of the crystals' habits, these crystals start to literally jump and fly on the stage providing a vivid example of thermosalient effect. Thermosalient materials are the ones that during heating/cooling undergo an energetic phase transition which is so sudden and abrupt that the crystals are ballistically projected to heights of several hundred times larger than their own dimensions. Apart from providing visually extremely attractive phenomenon, these materials have a tremendous technological potential as the future self-actuation device (nanoswitches, thermal sensors, artificial muscles, etc.)[1]. Several exciting experimental studies on the origin of the thermosalient effect were published resulting in an astonishing wealth of information about the effect, but still we are far from the full understanding of the peculiarities and all the interplays and forces that govern this phenomenon. Here we present a systematic experimental study of the thermosalient effect in Scopolamine methyl bromide. As in most of the thermosalient systems, immense negative thermal expansion seems to be the most likely candidate for the driving force behind this phenomenon. This study presents combination of optical and electron microscopy, together with the x-ray diffraction measurements. Optical microscopy provides a direct insight into this visually extremely attractive phenomenon which is a manifestation of the macroscopic transformation of thermal energy into mechanical work. This analysis gives us a wealth of information about mechanical behaviour of thermosalient crystals – the macroscopic change of the crystal habit during the transformation, their trajectory, initial velocity and the dependence of the jumping height on the heating rate. On the other side, high resolution transmission electron microscopy gives us an insight into the fine details of the crystal structure and the stress field which is responsible for the thermosalient effect. These two microscopic

techniques, coupled with the *in situ* non-ambient x-ray powder diffraction measurements, enable us to fully elucidate the thermosalient phenomenon in this system.

References:

1. Skoko, Ž. et al., J. Am. Chem. Soc., 2010, 132 (40), pp 14191–14202

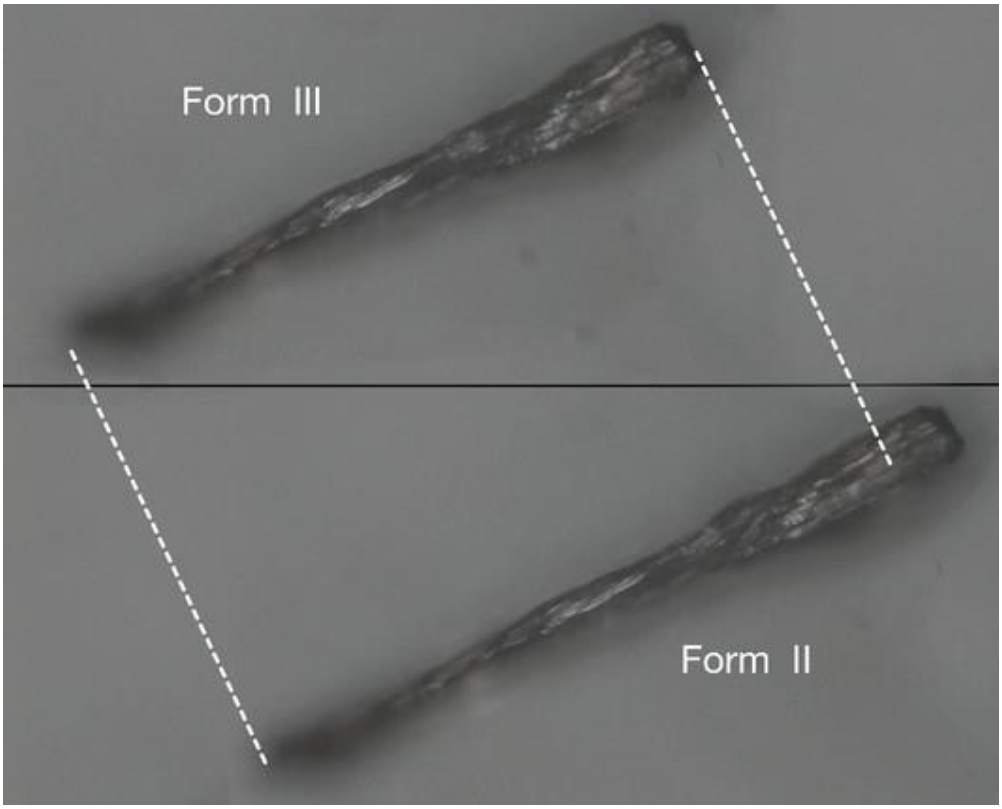

Figure 1. Change of the crystal's microscopic dimension during the thermosalient phase transition.

In vivo study of diatom assemblages using low temperature method for ESEM

Eva Tihlarikova (1), Vilem Neděla (1), Markéta Fránková (2)

1) Environmental Electron Microscopy Group, Institute of Scientific Instruments of the CAS, Brno, Czech Republic

2) Laboratory of Paleoecology, Institute of Botany of the CAS, Brno, Czech Republic

Keywords: ESEM, diatom, morphology, LTM

Diatoms are the most species-rich algal group represented by 12 000 described species and are recognized as powerful bio indicators and used for water quality monitoring (1). Diatom taxonomy is predominantly based on the morphology of ornate silicified cell wall called frustule composed of two overlapping parts (thecae). This frustule displays intricate patterns and designs unique to each species. For these studies conventional scanning electron microscopy (SEM) was and still is widely used. This method requires cleaning of diatom frustules in strong acids and peroxides followed by conductive coating. This aggressive procedure removes protoplast and damages delicate structures. Environmental scanning electron microscopy (ESEM) brings advantages of observation of fresh diatom material that are presence of whole intact diatom cells, not only empty diatom frustules, extracellular mucilaginous diatom secrets (e.g. pads, stalks, tubes) and whole diatom assemblages directly *in situ* together with other algal assemblages (e.g. cyanobacteria or green algae). However, in diatom research, ESEM is used mainly for elimination of conductive coating and observation of these organisms in their native wet state adhered directly on the host plant is not yet common (2). The ESEM observation of native aquatic samples is usually affected with radiation damage that can be lovered by the use of special methods like the Low Temperature Method (LTM) for the ESEM (3). Using the LTM for ESEM, we observed epiphytic diatom assemblages on a stem epidermis of common reed (*Phragmites australis)*. Samples were observed on the FEI Peltier stage. Epidermis was cut to 4 – 8 mm^2 segments and placed into a drop of 2 µl of water, to obtain better thermal contact between the sample and the Peltier stage. The observation conditions were adjusted according to (3): the air pressure was 250 Pa, sample temperature -20°C. All

experiments were performed on FEI ESEM QUANTA 650FEG and carried out under constant operating conditions (the beam energy 20 kV, probe current 35 pA, working distance 8.5 mm). Figures 1 A, B show a frustule of a common benthic species *Achnanthidium minutissimum* able to attach to the surface with a gelatinous stalk that is ornamented with lines of pores called striae that are radially oriented around pseudoraphe. Figure 1 C shows three individuals of the heteropolar genus *Gomphonema* attaching to the substrate with a mucilaginous stalk. Figure 1 D shows a common planktic centric diatom *Puncticulata balatonis* with well visible radial striae in distal part of the valve face and fultoportulae in proximal part of the valve face. The work shows high applicable potential of the LTM ESEM to observe aquatic plants and algae under conditions of reduced gas pressure and low relative humidity with higher resolution necessary for traditional diatom taxonomy as well as capability to observe susceptible structures like mucilaginous stalks that are destroyed during the preparation for SEM.

Acknowledgements:

This study was supported by the research grant of the Ministry of Education, Youth and Sports in frame of the research program COST CZ, grant nr. LD 14045, by the Institute of Botany CAS as a long-term research development project no. RVO 67985939 and the NPUI LO1417 and LO1212 together with the European Commission (ALISI No. CZ.1.05/2.1.00/01.0017).

References:

1. F. Rimet, Hydrobiologia 683 (2012), 1-24.

2. J John et al, Diatom Res. 7(2) (1992), 403-407.

3. V. Neděla et al, Microsc. Res. Tech. 78 (2015), 13-21.

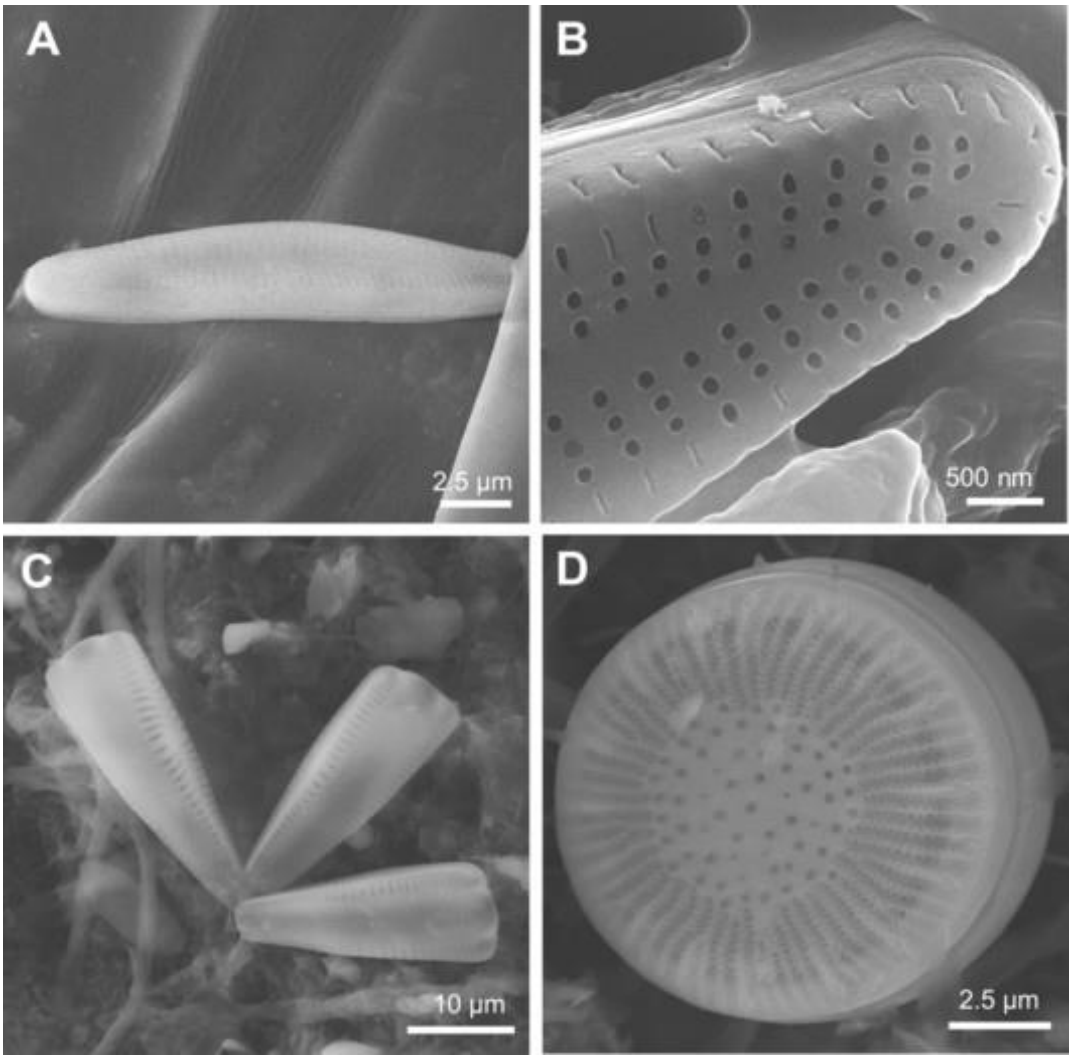

Figure 1. Fresh diatoms attached to the surface of reed. (A) Benthic pennate diatom *Achnanthidium minutissimum,* (B) detail of its valve end. (C) Gomphonema attached to the surface with a gelatinous stalk, (D) Planktic centric diatom *Puncticulata balatonis.*

I3. Correlative Microscopy and other Imaging Modalities (including AFM, STM etc.)

INVITED LECTURES I3:

Microscopic and spectroscopic characterization of epitaxial graphene and transition metal dichalcogenides

Marko Kralj (1)

1) Institute of Physics, Bijenička cesta 46, 10000, Zagreb, Croatia

Keywords: graphene, transition metal dichalcogenides, scanning tunneling microscopy, low energy electron microscopy, spectroscopy

The ability to control structure and uniformity of novel two-dimensional (2D) materials is greatly related to various promising applications arising from their electronic properties or mechanical strength. While linear bands in semimetallic graphene lead to record mobility, mono- and few-layer transition metal dichalcogenides (TMDs) attract increasing attention due to their intrinsic semiconducting and optoelectronic properties and corresponding advantages over graphene. In order to demonstrate possibilities of atomic-scale control of 2D materials, first a highlighted epitaxial system, graphene on iridium, has been characterized. It exhibits intrinsic properties matching that of a freestanding graphene but with added superperiodic potential (1). We use scanning tunneling microscopy (STM), low energy electron microscopy (LEEM) and electron spectroscopy to study a mechanism and effects of insertion/intercalation of atomic layers between graphene and iridium. Along with a pronounced charge transfer effects, a quasiparticle scattering of doped graphene is directly visualized in low-temperature STM, marking a pseudospin character of electrons in graphene (2). In the second part, we show how optical visibility of mono- and few-layer TMD samples on SiO2 covered silicon wafers at elevated temperatures was exploited to construct chemical vapor deposition system with optical access for real time microscopy that enables observation of TMDs during growth. This provides us a significant level of control of the growth process. After synthesis, the quality of grown MoS2 and WS2 samples is checked by the characterization of optical response, transport and in particular STM characterization of atomic-scale defects and their typical concentrations (3).

References:

1. I. Pletikosić, et al., Phys. Rev. Lett. 102 (2009) 056808.

2. M. Petrović, et al., Nat. Commun. 4 (2013) 2772, U.A. Schroeder et al., 2D Materials 4 (2017) 015013, D. Dombrowski, et al., Phys. Rev. Lett. 118 (2017) 116401.

3. D. Čapeta, et al., in preparation, I. Delač Marion, et al., in preparation.

Simultaneous STM/AFM imaging of oxide surfaces

Martin Setvin (1)

1) Institut für Angewandte Physik der Technische Universität Wien, 1040 Wien, Austria

Keywords: AFM, STM, oxides, TiO_2

Recent development in the field of noncontact atomic force microscopy (nc-AFM) has opened many new possibilities like submolecular resolution of organic molecules (1), measuring and switching the charge state of adsorbed species (2), or atomically-resolved chemical identification of surface atoms (3). The invention of the q-Plus sensor made the technique easy-to-implement into existing devices and thus accessible to a broad community of scientists. We focus on the possibilities and challenges of the combined q-Plus STM/AFM approach on oxide surfaces. Examples will be presented on surfaces of TiO_2 (rutile and anatase), In_2O_3, Fe_2O_3 hematite, and others. While traditional STM approach shows mainly electronic states localized at the cation sites, AFM offers the possibility of imaging the oxygen sublattice with superior resolution, thus provides complementary information to STM. Imaging of clean and hydroxylated oxide surfaces will be discussed, with emphasis of fundamental tip-surface interactions responsible for formation of the image contrast. AFM can provide information beyond simple imaging of surface atoms: It allows for instance the possibility of injecting or removing single electrons from adsorbed species. We use an example of O_2 adsorbed on anatase TiO_2 (101) surface to illustrating its impact on surface chemistry. Neutral O_2 is an inert species, while a negatively $(O_2)^-$ radical readily enters chemical reactions. We can switch between these two states at will, and directly image the resulting chemical change in the molecule.

References:

1. L. Gross, Nat. Chem. 3 (2011), 273.

2. L. Gross et al., Science 324 (2009), 1428.

3. Y. Sugimoto et al., Nature 446 (2007), 64.

Nanoscale thermal microscopy and spectroscopy of dissipation in quantum systems

Eli Zeldov

1) Department of Condensed Matter Physics, Weizmann Institute of Science, Rehovot 76100, Israel

Energy dissipation is a fundamental process governing the dynamics of physical systems. In condensed matter physics, in particular, scattering mechanisms, loss of quantum information, or breakdown of topological protection are deeply rooted in the intricate details of how and where the dissipation occurs. Despite its vital importance, direct imaging and microscopy of dissipation in quantum systems is currently impossible because the existing thermal imaging methods lack the necessary sensitivity and are unsuitable for low temperature operation. We developed a scanning nanoSQUID with sub 50 nm diameter that resides at the apex of a sharp pipette (1) that can act simultaneously as nanomagnetometer with single spin sensitivity and as nanothermometer providing cryogenic thermal imaging with four orders of magnitude improved thermal sensitivity of below 1 $\mu K/Hz^{1/2}$ (2). The non-contact non-invasive thermometry allows thermal imaging of minute energy dissipation down to the fundamental Landauer limit of 40 fW for continuous readout of a single qubit at 1 GHz at 4.2 K. In addition, by varying the potential between the SQUID-on-tip and the sample a nanoscale spectroscopic analysis of the dissipation process can be attained. These advances enable observation of changes in dissipation due to single electron charging of individual quantum dots in carbon nanotubes. Our thermal imaging study of hBN encapsulated graphene reveals a fascinating dissipation mechanism due to resonant localized states providing the first visualization of inelastic electron scattering from individual atomic defects, opening the door to direct imaging and spectroscopy of dissipation processes in quantum matter.

References:

1. Vasyukov et al., Nature Nanotech. 8, 639 (2013).

2. D. Halbertal, J. Cuppens, M. Ben Shalom, L. Embon, N. Shadmi, Y. Anahory, H. R. Naren, J. Sarkar, A. Uri, Y. Ronen, Y. Myasoedov, L. S. Levitov, E. Joselevich, A. K. Geim, and E. Zeldov, Nature 539, 407 (2016).

ORAL PRESENTATIONS I3:

Correlative multiscale tomography for additive manufacturing of biomedical components

Bartomiej Winiarski (1,2), Grzegorz Pyka (1), Dirk Laeveren (3) and Philip J. Withers (2)

1) Thermo Fisher Scientific (FEI Czech Republic s.r.o.), Vlastimila Pecha 12, Brno 627 00, Czech Republic

2) Henry Moseley X-ray Imaging Facility, School of Materials, University of Manchester, M13 9PL, U.K.

3) Thermo Fisher Scientific - Achtseweg Noord 5, Bldg 5651 GG, Eindhoven, The Netherlands

Correlative tomography (1) is a concept/workflow of spatial registration in two and three dimensions (2D and 3D) of many imaging modalities - light microscopy (LM), electron/ion microscopy (EM, IM), X-Ray tomography, 2D/3D EBSD (2), EDS, Raman, etc.) - that allows various types of information, and at different lenghscale (Figure 1A), to be collected for the same region of interest (ROI). In soft tissue biology, a 2D correlation of EM and LM s an invaluable tool to study the interactions of viruses with cells, and the ultrastructural changes induced in host cells by virus infection (3). While biological materials are generally characterized as having complex 3D hierarchical microstructures (4) giving rise to interesting combinations of anisotropic mechanical properties that, in many cases, surpass those of manmade materials. A better understanding of these hierarchical structures and engineering of biomedical materials and structures requires a multiscale correlative imaging approach, which brings together 3D multimodal information at each length scale (1) often aided with temporal (4D) imaging (5). Biocompatible titanium and its alloys are widely used in orthopaedic surgery for the replacement and stabilization of damaged bone tissue because of the high specific strength, low stiffness and high corrosion and fatigue resistance. Porous metal implants/scaffolds, additively manufactured (AM) by electron beam melting or selective laser melting (SLM), having an interconnected pore structure are of particular interest due to their potential ability to facilitate tissue ingrowth deep within the porous network and therefore present the possibility for reducing the stiffness mismatch between the load-bearing metal

implant and bone (6). Biomedical engineering uses computer-aided design models (CAD) and finite-element analysis (FEA) together with AM methods to design and reproduce scaffolds with controlled topology, porosity, pore shape and size, interconnectivity and mechanical properties. Nevertheless, AM processing conditions e.g. laser power, laser scanning speed, etc., and material impurities may have a significant impact on the scaffold morphology and mechanical performance leading to large deviations from the designed parameters (7). Thus in order to precisely tailor the morphology and mechanical performance of implants, the information about actual geometry and microstructural defects needs to be feed back to the CAD/FEA model. In this contribution we sketch the designing-manufacturing-testing feedback loop that uses correlative multiscale tomography workflow as an essential component for additive manufacturing of biomedical components. In this interactive design process by understanding the surface roughness we can optimize the biocompatibility and by helping optimize ALM process we can improve the mechanical properties. As a practical example, we study at different length scale and imaging modalities, morphology and microstructural features and imperfections of Ti-6Al-4V cellular orthopaedic scaffold produced by SLM from a CAD model. We use FEI HeliScan™ micro X-Ray Computed Tomography system and Helios™ Plasma FIB – SEM (PFIB-SEM) microscope to facilitate the correlative multiscale tomography workflow and close the designing-manufacturing-testing feedback loop (Figure 1B). The loop consists three major blocks: I) design and numerical modeling (for simple structures this can be abandoned as indicated by procedure step ‘g’ in Figure 1B); II) AM manufacturing and mechanical testing (for not load-bearing structures this can be abandoned as indicated by procedure step ‘h’ in Figure 1B); III) correlative multiscale tomography workflow. Here, a PFIB-SEM not only can facilitate number of 2D, 3D imaging modalities (EBSD, EDS, SEM see inset in Figure 2i) and residual stress mapping with micro-hole drilling (see inset in Figure 2h), but also is able to excise sub-millimeter size samples (Figure 2d and 2g) for further study and ROI correlation at smaller scale using micro XCT *(*as indicated by procedure step ‘i’ in Figure 1B), PFIB-SEM 3D imaging modalities, TEM or other techniques*.* The workflow and feedback loop is flexible and allows for: (a) smart information handling, e.g. feedback can be passed to different procedure steps (feedback loops ‘3’ and ‘7’ from XCT, and ‘4’ and ‘8’ from PFIB-SEM); (b) perform various procedure steps, e.g. temporal study (the procedure step ‘d’ and feedback loop ‘11’) with the feedback to CAD/FEA procedure step (loop ‘3’); (c) redesign material microstructure and surface topography (procedure ’h’ and/or ‘c,d’ and loop ‘7’). We demonstrated the feasibility of FEI HeliScan™ micro X-Ray CT system and Helios™ Plasma FIB – SEM microscope combo as an ideal research instruments for correlative multiscale tomography analyses of biomedical materials and structures. PFIB system allowed for site-

specific preparation and lift-out of massive sub-milometer blocks of material required for further 3D high resolution study. Presented designing-manufacturing-testing feedback loop has a potential for application in other bottom-up manufacturing methods.

References:

1. Burnett TL, McDonald, SA, Gholinia A, et al. Scientific Reports 4(2014): 4711.

2. Burnett TL, Kelley R, Winiarski, B, at al. Ultramicroscopy 161(2016): p. 119-129.

3. Bykov YS, at al. FEBS Letters, 590/13(2016): 1877-1895.

4. Fratzl P, Weinkamer R. Prog. Mater. Sci. 52(2007): 1263.

5. Bradley RS, and Withers PJ. MRS Bulletin 41(2016): 549.

6. Ryan G, at al. Biomaterials 27 (2006):2651–2670.

7. Taniguchi S, at al. Acta Biomaterialia 30 (2016) 345–356.

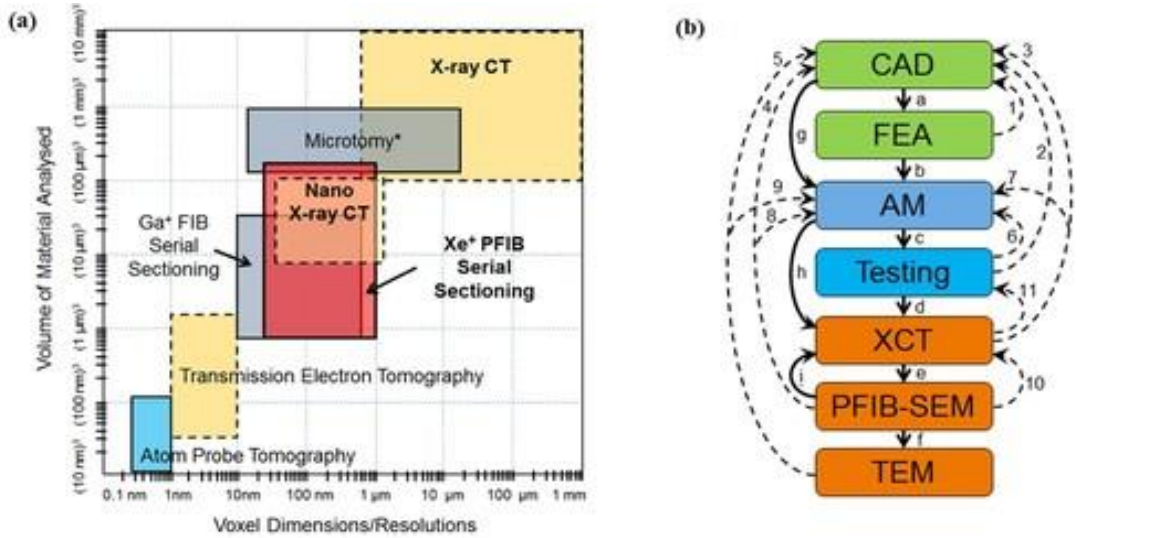

Figure 1. ***(a)*** *3D imaging methods for materials science (non-destructive methods represented by dashed lines; * – for soft materials only) [2]. Note: PFIB-SEM instrument creates a crucial link between imaging at sub-micrometer scale and sub-millimeter scale;* ***(b)*** *Shows correlative multiscale tomography for Biomedical Engineering Design, where indicate procedure steps (a-i) and dashed lines draws possible flow of feedback information (1-11). Note: PFIB-SEM in the correlative workflow is a multipurpose platform for sample preparation (micro- nano CT pillars, block for serial sectioning tomography, micro specimens for micro-mechanical testing, TEM lamellas), and for collection of various imaging modalities in 2D and 3D (SEM, EBSD, EDS, etc.)*

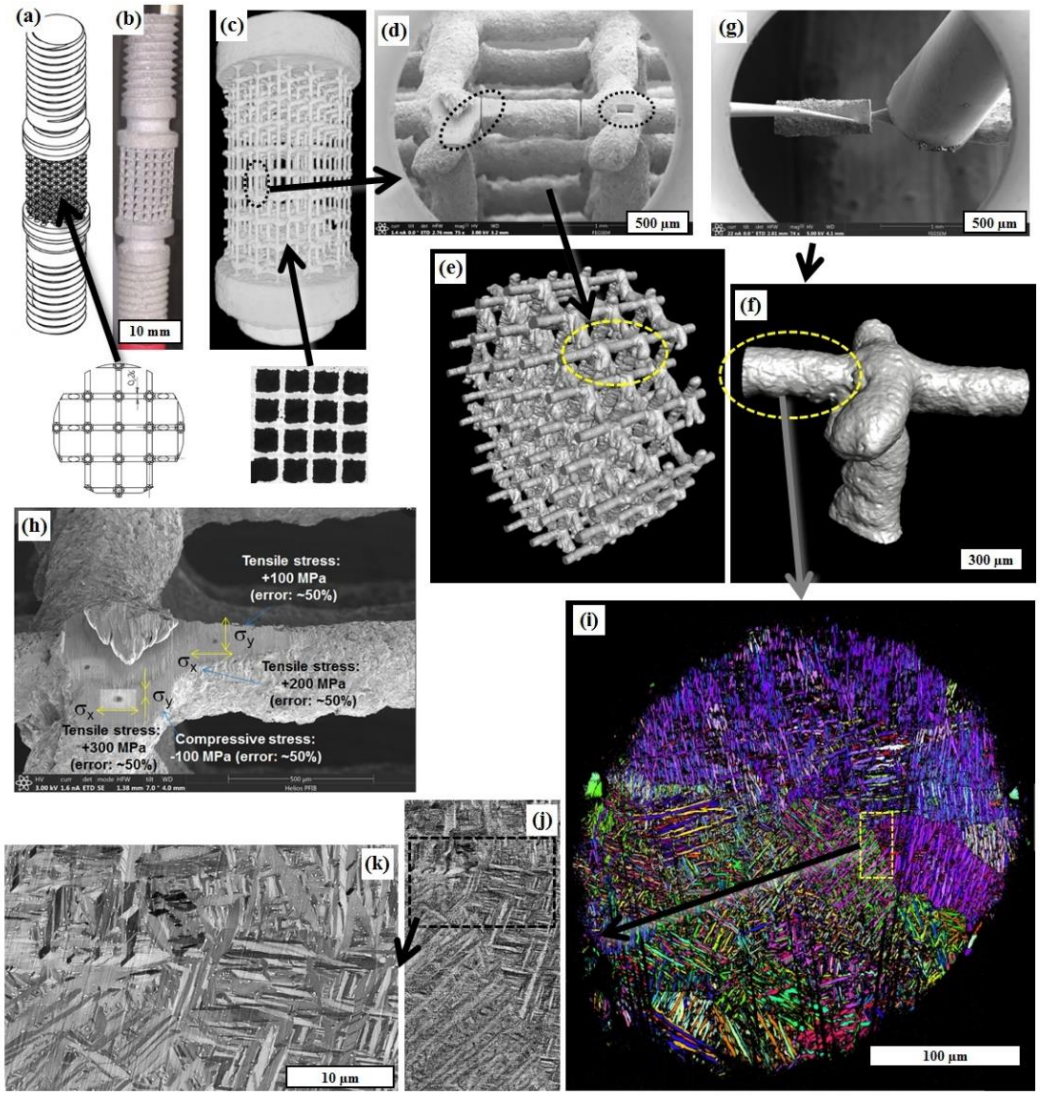

Figure 2. ***a)*** *CAD model of the scaffold with details of the scaffold (inset);* ***b)*** *optical image of SLM manufactured scaffold;* **c)** *3D reconstructed central section from XCT data with marked region for further study at smaller length scale; inset shows cross-section of XCT;* ***d)*** *ligament prepared for lift-out with EasyLift; dashed ovals mark regions where residual stresses were mapped with micro-hole drilling (left), and where cross-section was milled (right);* ***e)*** *surface details with indicated position of ligament;* ***f)*** *surface details of a junction;* ***g)*** *ligament positioned on a pin for high resolution XCT study;* ***h)*** *results of residual stress measurements using PFIB micro-hole drilling method (the position of measurements are presented in d and e); EBSD map (IPFX) of the whole cross-section of the ligament;* ***j-k)*** *SEM (CBS) image details of a microstructure of the joint indicated in j).*

Plasma FIB and microCT for Multi-scale 3D pore information in battery cathode material

Daniel Phifer (1), Herman Lemmens (1)

1) Thermo Fisher Scientific - Achtseweg Noord 5, Bldg 5651 GG, Eindhoven, The Netherlands

Keywords: plasma FIB, microCT, battery cathode, multi-scale

Many materials have features crossing several length scales which make it difficult to select the correct technique to fully characterize structure as it relates to properties and function. In developing instrumentation to image samples for 3D modeling, it would be interesting to know how well the overlap of the information can be and if there is a gap in available techniques that enables a “blind spot” at some length scale. As an example, the microstructure of battery electrodes has a significant impact on the transport properties and is hence key to understand ionic and electronic transport. This presentation is to investigate the relationship to the length scales in Ga and Xe based DualBeam (FIB-SEM) systems and compare this to data from microCT techniques employing helical scanning technology for energy storage materials. The 3D analysis of the composite electrode is typically a combination of microCT imaging and FIB-SEM imaging; where the microCT provides the representative volume and the FIB-SEM provides stochastical input to the fine structure in the microCT volume. In this way the lack of resolution of the microCT is offset by the higher resolution of the FIB-SEM; which itself has too small Field of View to be representative. In this paper we show how the Field of View limitation can be overcome by using a PlasmaFIB instead of a Ga-based FIBSEM system. The PlasmaFIB has much higher material removal rates and allows larger volumes to be imaged. Representative volumes of a Lithium ion battery anode and a Solix Oxide Fuel Cell are shown. Segmentation of the pore space is demonstrated to come to a pore network model from which transport properties over a representative volume can be calculated. Segmentation of the pore space is demonstrated to come to a pore network model from which transport properties over a representative volume can be calculated with a high degree of confidence.

POSTER PRESENTATIONS I3:

Scanning tunneling microscopy and spectroscopy of thin films of strontium ruthenates

Marion van Midden (1), Tjaša Parkelj (2), Jernej Mravlje (3), Rok Žitko (3), Matjaž Spreitzer (2), Erik Zupanič (1)

1) Condensed Matter Physics Department, Jožef Stefan Institute, Jamova 39, Ljubljana, Slovenia

2) Advanced Materials Department, Jožef Stefan Institute, Jamova 39, Ljubljana, Slovenia

3) Department of Theoretical Physics, Jožef Stefan Institute, Jamova 39, Ljubljana, Slovenia

Keywords: STM, STS, transition metal oxides, Ruthenates, strongly correlated materials

Due to strong coupling of charge, spin, lattice, and orbital degrees of freedom 4d- and 5d-transitional metal oxides exhibit a range of distinct electronic and magnetic properties. In the case of perovskite type transitional metal oxides these materials are also extremely sensitive to perturbations and can therefore be tuned via nonthermal parameters such as doping, pressure, and magnetic fields (1). We studied thin films of the Ruddlesden-Popper series of Strontium-Ruthenates $Sr_{n+1}RunO_{3n+1}$, which range from a spin-triplet superconductor (n = 1, Sr_2RuO_4), via a material with an electronic liquid-crystalline phase (n = 2, $Sr_3Ru_2O_7$) to the itinerant ferromagnet (n = 1, $SrRuO_3$) in bulk samples. The films were grown on different substrates using Pulsed Laser Deposition (PLD) (2). The pressure in the PLD vacuum system is below 10-9 mbar, which enables growth with a relatively small concentration of impurities. Controlling the substrate and film thickness, the electronic properties and strain in the material can be tuned, allowing us to explore a wide variety of phases. Growth was controlled *in situ* using Reflected High-Energy Electron Diffraction (RHEED). Using an ultra-high vacuum (UHV) suitcase the samples were transported to an UHV system equipped with Low-Energy Electron Diffraction and a Joule-Thompson Scanning Tunneling Microscope. Topography and spectroscopy measurements were perfomed on clean surfaces and in the vicinity of different defects. The obtained local density of states and information about the band structure obtained

from quasiparticle interference were compared with Angle Resolved Photoemission Spectroscopy measurements, focusing on discrepancies such as the zero bias anomaly.

References:

1. G. Cao and L. DeLong, Frontiers of 4d- and 5d- transitional metal oxides. 1st ed. New Jersey: World Scientific Publishing, 2013. (2) G. Koster et al, Structure, physical properties, and applications of SrRuO3 thin films Rev. Mod. Phys. 84, 253, (2012).

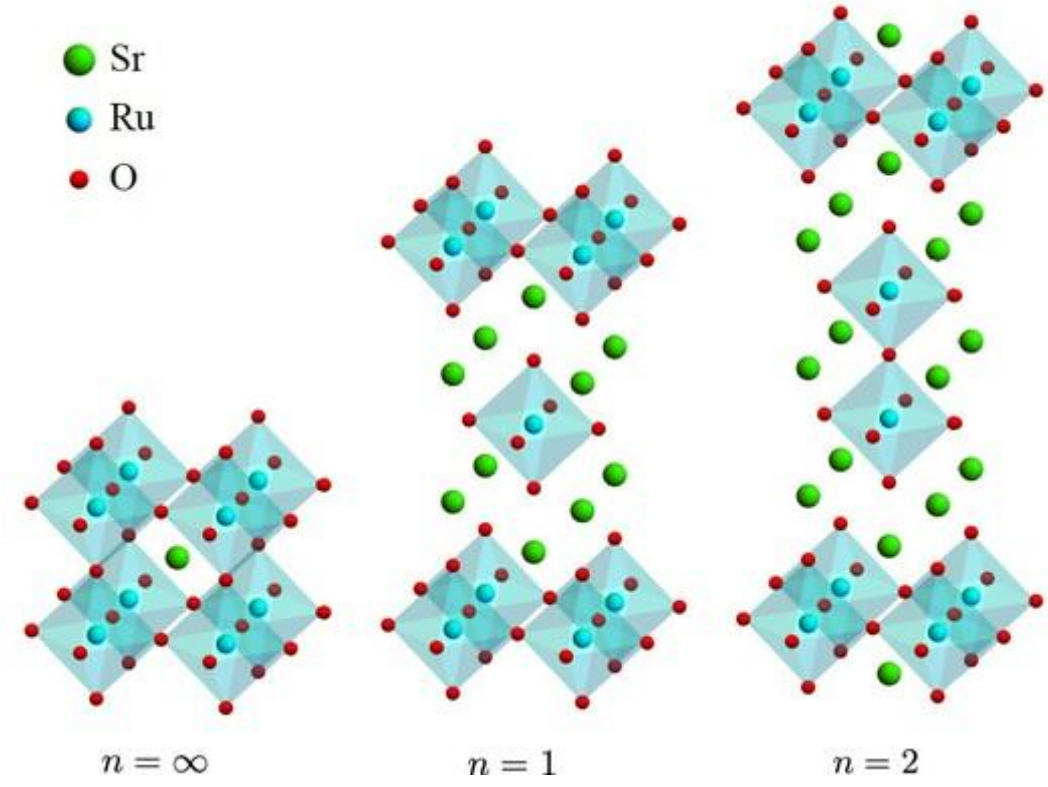

Figure 1. The unit cells of the Ruddlesden-Popper phase of (n = 1) $SrRuO_3$, (n = 1) Sr_2RuO_4, and (n = 2) $Sr_3Ru_2O_7$.

Preservation of the moss *Physcomitrella* patens for electron and light microscopy in correlation with element analysis

Margret Eckhard (1), Ingeborg Lang (1), Siegfried Reipert (1)

1) Core Facility Cell Imaging and Ultrastructure Research, Unversity of Vienna, Althanstraße 14 (UZA 1) A-1090 Vienna Austria

This study aims to establish a protocol for the best preservation method for electron energy loss spectroscopy (EELS). EELS is used to detect and quantify the amount of the heavy metal zinc in moss cells of Physcomitrella patens. This model organism is easy to cultivate and tolerant to heavy metals (1) but the preparation is very challenging due to its cell wall that is forming a really tight barrier. Therefore, a combination of various methods from light and electron microscopy is necessary to achieve this goal. At the electron microscopy level, I compare preparation protocols for chemical fixation and cryofixation using the Leica HPM 100 and the Leica AFS 2 with a new agitation module for accelerated freeze substitution (2). High-pressure freezing combined with rapid freeze substitution achieved the best preparation results so far. Chemical fixation protocols were tested light microscopically since they resulted in diverse reactions of gametophore and the protonema cells. An essential outcome is the precise adjustment of the chosen buffer.

References:

1. Sassmann, S. et al., Environmental and experimental botany 118 (2015) 12-20

2. Goldammer. H., et al., Protist, 167/4(2016) 369- 376

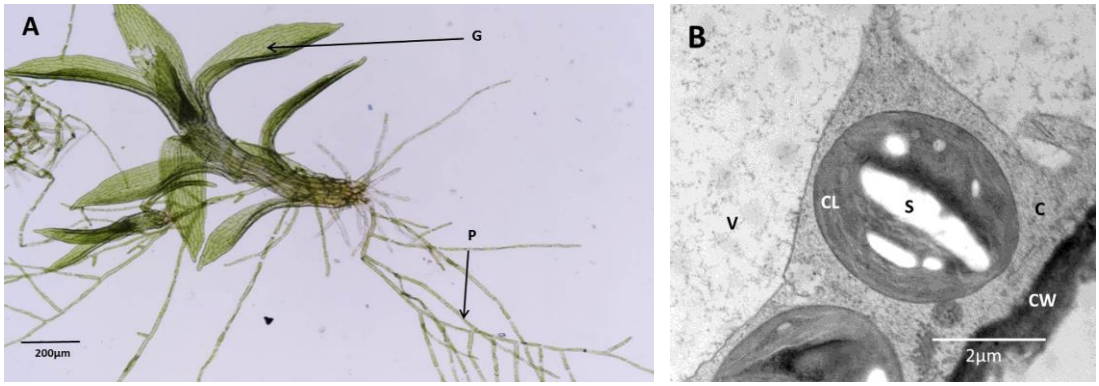

Figure 1. *Physcomitrella* patens. A: overview of gametophyte; B: gametophore leaf, cryofixed and freeze substituted. Gametophore (G), protonemata (P), vacuole (V), chloroplast (CL), starch (S), cytoplasm (C), cell wall (CW).

Localization of nanodiamonds inside cancer cells using cathodoluminescence imaging in the cryo-SEM

Nadezda Vaskovicova (1), Radim Skoupy (1), Kamila Hrubanova (1), Pavel Kulich (2), Jaroslav Turanek (2), Vladislav Krzyžánek (1)

1) Institute of Scientific Instruments, The Czech Academy of Sciences, v. v. i., Ústav přístrojové techniky AV ČR, v. v. i., Královopolská 147, 612 64 Brno, Czech Republic

2) Department of Chemistry and Toxicology, Veterinary Research Institute, v. v. i., Brno, Czech Republic, Hudcova 296/70, 621 00 Brno, Czech Republic

Keywords: cryo-SEM, cathodoluminescence, nanodiamonds, cancer cells, THP1 cells

Synthetic nanodiamonds, usually prepared with a method based on detonation, are carbon minerals with the size ranging between 5 and 200 nm. The detonation method is performed by an oxygen-deficient explosive mixture of TNT/RDX (trinitrotoluene / hexogene) that is allowed to detonate in a closed chamber. Nanodiamonds are neither biologically resorbable, nor degradable; however, certain biocompatible drugs may be present on their surface, functioning as cancer markers or a drug delivery system (1). The effect of cathodoluminescence (CL) present on nanodiamonds can be visualized with the use of an electron microscope (Figure 1). Consequently, they can be thoroughly localized within the cells (2) (Figure 2). In the course of our experiment, the Dulbeccoa's modified EAGles medium low glucose (Sigma Aldrich) was used to wash and store the nanodiamonds in, for they were needed to wash quickly in the PBS buffer before the application itself. THP1 cells were cultivated with nanodiamonds for 24 hours and frozen with a high pressure freezing method (HPF EM ICE, Leica Microsystems). Eventually, all the samples were fractured in the ACE600 device (Leica microsystems), and transferred to the SEM Magellan 400 (FEI) (high vacuum and low temperature necessary), using the shuttle VCT100 (Leica microsystems). Detection system MonoCL4 (Gatan) was used for the cathodoluminescence analysis. After the experiment had ended, all the samples were transferred to the ACE600 device again, where they were completely freeze-dried. Concentrated either in the ice bulk, or the multilayers (or both), individual cancer cells are visible and distinguishable in the cryo-SEM. It is problematic to localize the nanodiamonds clusters in the cryo-SEM directly, since there are phenomena such as irregular arrangement

of organelles, ice crystals, rests of cytoplasm and sample charging effects (Figure 2A). The cells can be visualized on the sample surface with the Cryo-SEM-CL imaging. The electron energy determines a generated CL signal of nanodiamonds from the deeper layers of specimen bulk (Figure 2B). “Bright spots” visible in the images of the cells are presumably the individual diamonds. If the sample is freeze dried, it is possible to investigate certain parts of the cells at higher magnification, and thus demonstrate the “bright spots” are in fact nanodiamonds clumps. The individual nanodiamonds of small sizes are rather difficult to observe due to cytoplasm rests. Groups of various-sized nanodiamonds can be imaged in a SEM, hence it is possible to determine their proportions required to finding the best nanodiamonds fraction for the drug delivery system. The Cryo-CL technique is a sufficient imaging method for nanodiamonds drug delivery system theory verification, and by combining both cryo-SEM and cryo-CL images, investigation of marked cancer cells or tissues can be performed.

Acknowledgements:

This study was supported by the Czech Science Foundation GA17 15451S and GBP503/12/G147, the Ministry of Education, Youth and Sports (LO1212 and CZ.02.1.01/0.0/0.0/15_003/0000495). We would like to thank A. Nowak (Leica Microsystems) for providing the HPF EM ICE.

References:

1. C.D. Gupta et al., Front Biosci (Schol Ed) 9 (2017), 62 70.

2. S. Nagarajan et al.: Nanoscale 8 (2016), 11588 11594.

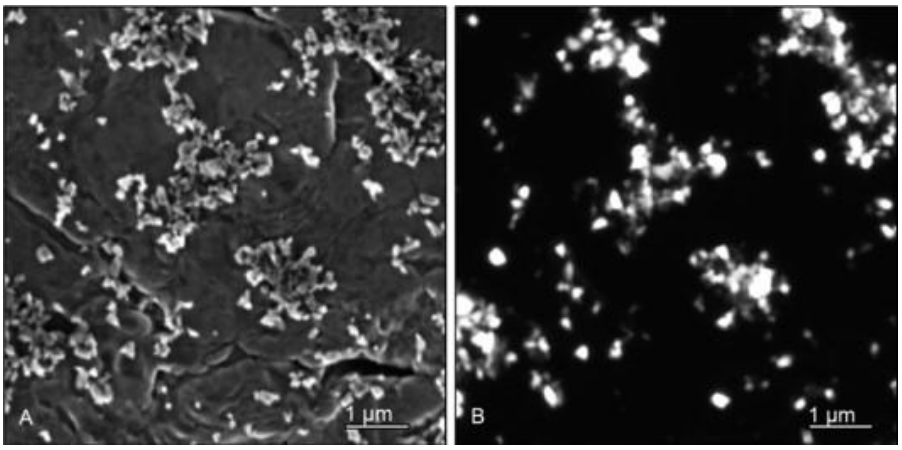

Figure 1. Nanodiamonds (size 100 nm) imaged with the use of (a) SE, (b) CL.

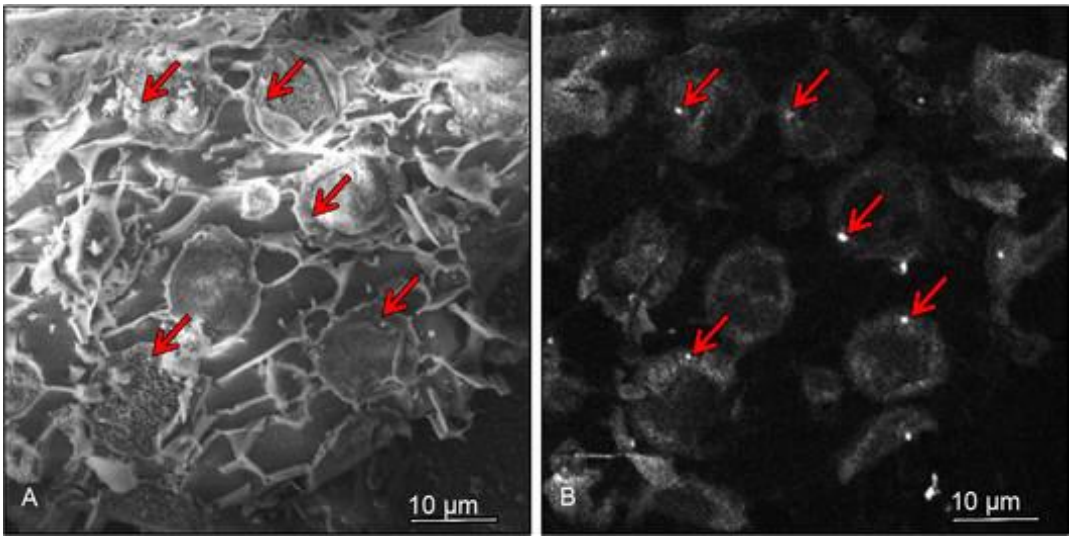

Figure 2. (a) Cryo-SEM-SE image, (b) Cryo-SEM-CL image of freeze-fractures that emerged within the cells. Nanodiamonds clusters marked with red arrows.

Ex vivo microangioCT and light microscopy: new correlative approach for the vasculature-focused studies

Ruslan Hlushchuk (1), David Haberthür (1), Laura Schaad (1), Roberto Gianni-Barrera (2), Andrea Banfi (2), Valentin Djonov (1)

1) Institute of Anatomy, University of Bern, Switzerland, Postfach 922, Baltzerstrasse 2, CH-3000 Bern 9

2) Department of Biomedicine, University Hospital Basel, Hebelstrasse 20, 4031 Basel, Switzerland

Keywords: microangioCT, microvasculature, light microscopy, correlative imaging, computed tomography

The cardiovascular diseases are the globally leading cause of death. Billions of cardiovascular patients would benefit from the effective angiomodulating treatments. The murine hind limb is a widely used model to study pro-angiogenic treatment strategies. Traditionally, the vasculature is evaluated based on histological sections, which lacks essential 3D information. A detailed vascular visualization and adequate quantification is essential for the proper assessment of novel angiomodulating strategies. To develop an ex vivo microangioCT-based imaging approach for the 3D visualization of the entire vasculature down to the capillary level and rapid estimation of the vascular volume and vessel size distribution. Moreover, it should be suitable for the successive correlative morphological analysis using light or transmission electron microscopy. A correlative imaging approach comprising two microCT scanning modalities followed by histology was introduced. After the perfusion with µAngiofil®, a novel polymerizing contrast agent, low- and high-resolution scans (Skyscan 1272; voxel side length: 2.58-0.66µm) of the entire vasculature were acquired. In a second step, samples were dehydrated and rescanned to delineate the muscle fiber architecture. Based on the microCT data, sites of interest were defined and samples further processed for correlative morphology (Figure 2). The solidified µAngiofil® remained in the vasculature and its autofluorescence allowed co-registering the histological sections with the corresponding microCT-stacks. The perfusion efficiency of µAngiofil® was validated based on lectin-stained histological sections: 98±0.5% of the total blood vessels were µAngiofil®-positive, whereas 93±2.6% were lectin-

positive. By applying this approach, we analyzed the angiogenesis induced by cell-based delivery of a controlled VEGF dose. VEGF increased vascular density by 426% predominantly by increasing the proportion of medium-sized vessels (20-40 µm). The introduced correlative and quantitative imaging approach is highly reproducible and allows a detailed 3D characterization of the vasculature and muscle tissue. Combined with histology, a broad range of complementary structural information can be generated.

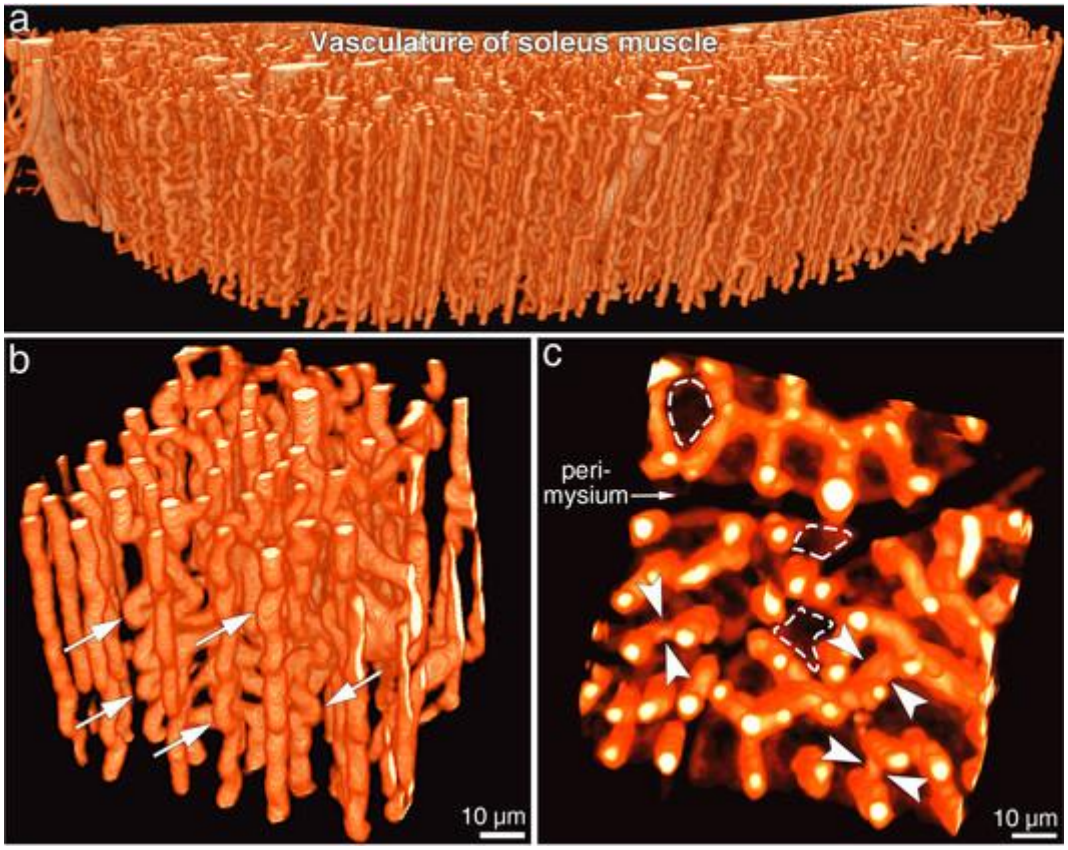

Figure 1. Microangio-CT of the vasculature of the sceletal muscle. Panel a: overview of the 500µm-thick slice of the murine soleus muscle. Panel b and c represent a subvolume of the volume in a: the capillaries with their connections and tortuosity are clearly and inambigously visualized (arrows, panel b). In panel c the perimysium as well as borders of the single muscle fiber cells can be easily recognized (dashed line).

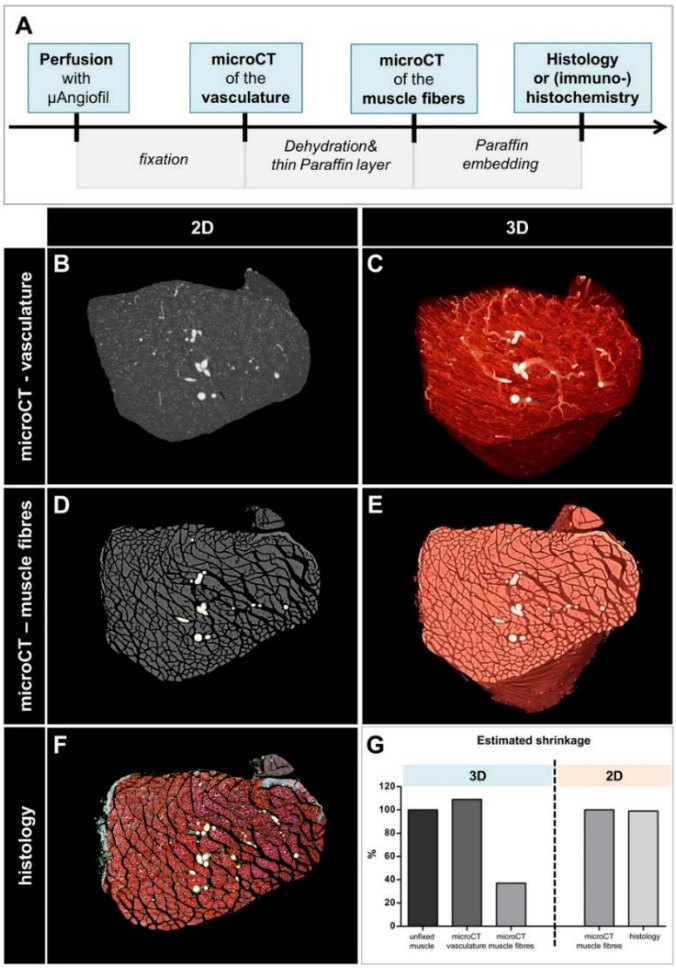

Figure 2. Correlative imaging approach to visualize the vasculature and fiber arrangement by microCT and histology. A Workflow. B, C Contrast-enhanced vasculature of plantaris muscle in 2D (B) and 3D (C). Voxel side length: 0.99 µm. C, D Muscle fibers of the same muscle in 2D (C) and 3D (D). Voxel side length: 1.39 µm. F Corresponding histological cross-section (Masson trichrome). G Estimated shrinkage between the different steps.

Acknowledgements:

The contrast agent has been developed in collaboration with FUMEDICA AG (Muri, Switzerland). The project was supported by the Swiss Federal Government (Grant Nr:14055.1 PFIW-IW).

References:

1. Schaad L, Hlushchuk R, Barré S, Gianni-Barrera R, Haberthür D, Banfi A, Djonov V. Correlative Imaging of the Murine Hind Limb Vasculature and Muscle Tissue by MicroCT and Light Microscopy. Scientific Reports.7:41842. (2017).

True tapping mode Scanning Near-Field Optical Microscopy with bent glass fiber-made probes

Anton Smirnov (1), Valeriy. M. Yasinskii (2), Dmitry. S. Filimonenko (2), Ekaterina Rostova (3), Giovanni Dietler (3), Serguei. K. Sekatskii (3)

1) Laboratoire de Physique de la Matière Vivante, Ecole Polytechnique Fédérale de Lausanne, BSP 410 (Cubotron UNIL), Rte de la Sorge, CH-1015 Lausanne, Switzerland

2) Institute of Physics, National Academy of Sciences of Belarus, Nezavisimosti ave 68, 220072 Minsk, Belarus

3) Laboratoire de Physique de la Matière Vivante, IPHYS, BSP-408, Ecole Polytechnique Fédérale de Lausanne, BSP 408 (Cubotron UNIL), Rte de la Sorge, CH-1015 Lausanne, Switzerland

Keywords: SNOM, tapping mode SNOM, bent fibers

Nowadays, sharpened glass fiber – made probes attached to a quartz tuning fork (TF) and exploiting the shear force–based feedback is by far the most popular in the field of Scanning Near-field Optical Microscopy. It was often discussed that the use of tapping mode feedback could be preferable and that such an approach can be realized e.g. using bent fiber probes. Here we report the following results in this direction. Detailed analysis of the vibration mode shows that an extreme caution is needed if one wants to realize truly tapping mode of the probe dithering: in case of using the 2nd resonance mode this occurs only for probes having a rather small (ca. 0.3 mm) bending radius and similarly small length of the part of the probe after the bend; otherwise, the shear force character of the dithering persists. Probes having these characteristics were prepared by irradiation of a tapered etched glass fiber with a CW CO2 laser resulted in their bending due to the effects caused by anisotropic heating. These probes were attached to the TF in double resonance conditions (TF working frequency coincides with that of the dithering of the free-standing part of the probe beam) which enables to achieve very large quality factor (4000 – 6000) of the TF + probe system. We also argue that to achieve a truly tapping character of dithering, short, not exceeding 3 mm, lengths of a free-standing part of bent fiber probe beam should be used also in the case of a usual probe gluing onto TF with non-resonant excitation.

I4. Light and Electron Optics, Super-Resolution Microscopy

INVITED LECTURES I4:

Reinke's crystal: the mystery still remains

Davor Ježek (1)

1) University of Zagreb, School of Medicine, Šalata 3, 10 000 Zagreb

Keywords: biocrystals, testis, crystal of Reinke, stereology, confocal microscopy

In humans, Reinke's crystals are found in Leydig cells but their nature and function are poorly understood. The aim of our study was to investigate the properties of Reinke's crystals in man with the normal morphology of the testis (control group) and infertile patients diagnosed with cryptorchidism. 20 biopsies from infertile patients and six biopsies from men with regular spermatogenesis (20-30 years.) were used. Sections of the testis tissue were stained with haematoxylin and eosin and a modified Masson's method. Specimens were observed by bright field, confocal and transmission electron microscopy (TEM). The number of Reinke's crystals in investigated groups was determined applying stereological methods. In both groups, Reinke's crystals were noted within the cytoplasm and nuclei of Leydig cells. Some "free" crystals were found within the interstitial space, outside Leydig cells. Confocal microscopy proved to be very useful in the assessment of the shape and 3D reconstruction of the crystal. TEM analysis confirmed a hexagonal form of the crystal, while crystallographic data on sections of 70-300 nm thickness provided a better insight into the organization of the crystal lattice. Stereological analysis revealed a significant increase in the number of crystals in cryptorchid testes when compared with controls. Increased number of crystals in cryptorchid specimens leads to the assumption that the prolonged exposure to higher (abdominal) temperature might stimulate enzymes involved in the synthesis of the proteins of the crystal. However, the exact molecular nature of the crystal lattice remains in both normal and cryptorchid testis obscure.

Acknowledgements:

This reasearch was supported by Ministry of Science, Research and Education, bilateral Croatian-Austrian grant.

References:

Kozina V, et al., Histochem. Cell Biol. 135 (2011) 215-28.

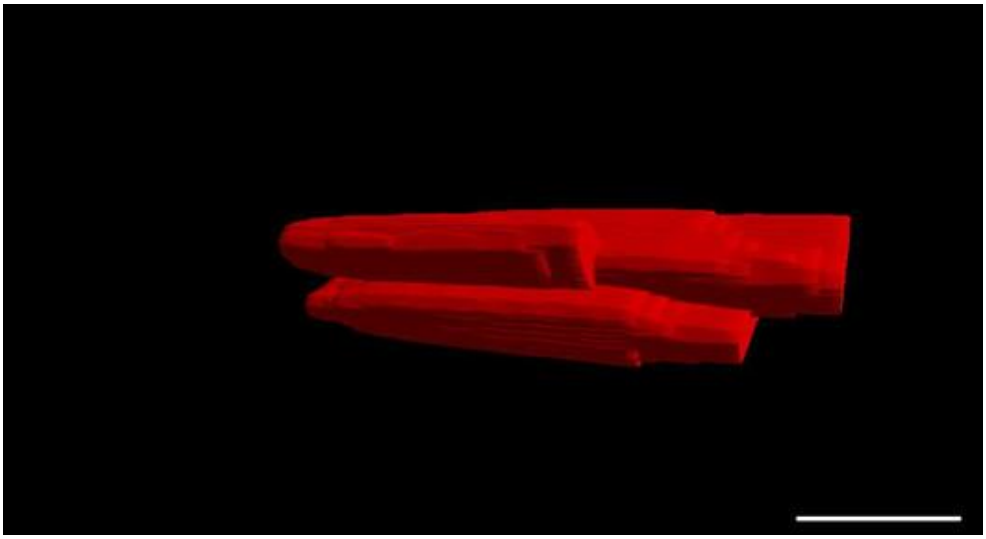

Figure 1. 3-D reconstruction of crystals of Reinke based on series of confocal microscopy images.

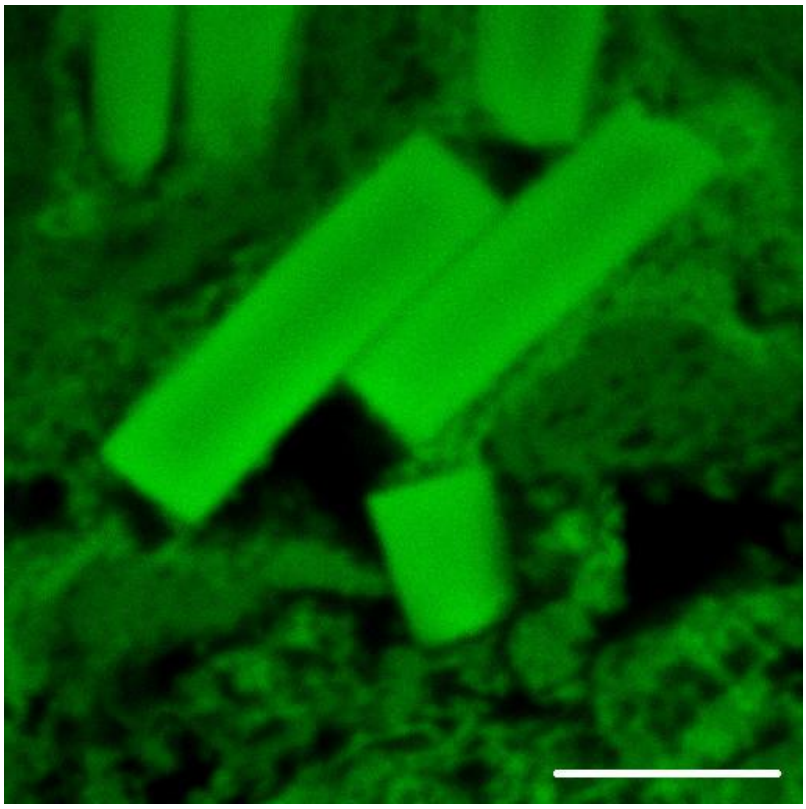

Figure 2. Abundant crystals of Reinke in a cryptorchid testis specimen.

Stimulated emission depletion (STED) nanoscopy of astrocytic vesicles

Jernej Jorgačevski (1), Marko Kreft (2), Robert Zorec (1)

1) Faculty of Medicine, University of Ljubljana, Vrazov trg 2, 1000 Ljubljana, Slovena

2) Biotechnical Faculty, University of Ljubljana, Jamnikarjeva ulica 101, 1000 Ljubljana, Slovenia

Keywords: STED, SIM, superresolution microscopy, astrocytes, vesicles

Fluorescence microscopy is one of the most powerful tools in the biological investigation of subcellular structures and dynamic processes, since it allows us measurements in live samples in real time. In the past decades far field fluorescence microscopy techniques have undergone extraordinary developments. The invention of super-resolution techniques has enabled fluorescence nanoscopy to achieve resolution well below the diffraction limit (~200 nm in the focal plane and ~600 nm along the optic axis). The first of the three general types of fluorescence-based super-resolution microscopies invented was stimulated emission depletion (STED) microscopy (1) (the other two types are structured illumination microscopy (SIM) and single-molecule switching (SMS)). In the first part of my presentation I will explain the basic concept of STED microscopy and present a two-color STED microscope, developed in the collaboration with colleagues from Laser Laboratorium Goettingen (Germany). In the second part of my talk I will illustrate the potential of STED microscopy on biological samples. Astrocytes are a sub-type of glial cells in the central nervous system that are now understood to play an active role in brain signaling. The intercellular communication of astrocytes with neurons and other non-neuronal cells involves the exchange of molecules by exocytotic and endocytotic processes. Studying the synaptic-like vesicles with diffraction-limited microscopies has proved to be challenging, since the diameters of these organelles are in the range of 30–50 nm (2). Here, I will compare astrocytic vesicle diameters, as measured by a diffraction-limited confocal microscopy and super-resolution microscopies STED and SIM (Figures 1 and 2).

Acknowledgements:

This work was supported by the Research Agency of Slovenia (Grant Numbers P3 0310, J3 4051, J3 4146, J3 7605 and J3 3632) together with CipKeBip.

References:

1. S.W. Hell et al. Opt. Lett., 19 (1994) 780–782.

2. A. Guček et al. Cell Mol. Life Sci., 73 (2016) 3719–3731.

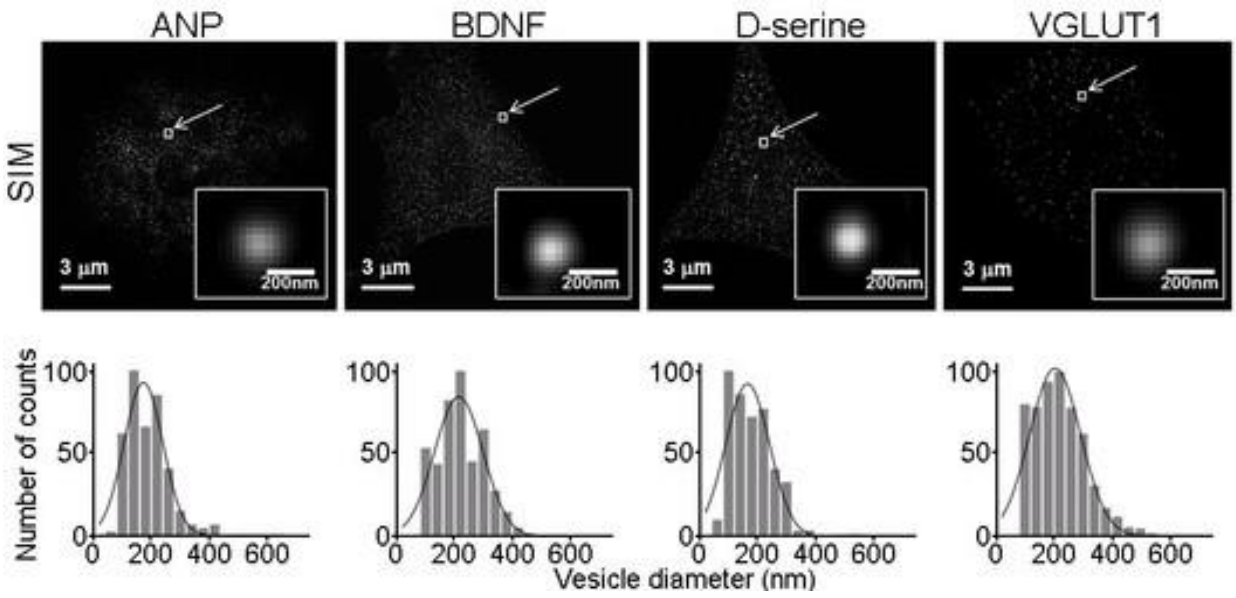

Figure 1. SIM images of vesicles containing peptides ANP and BDNF and amino acids D-serine and glutamate (immunostained with antibody against V-GLUT1). Histograms show distributions of vesicle diameters (in nm).

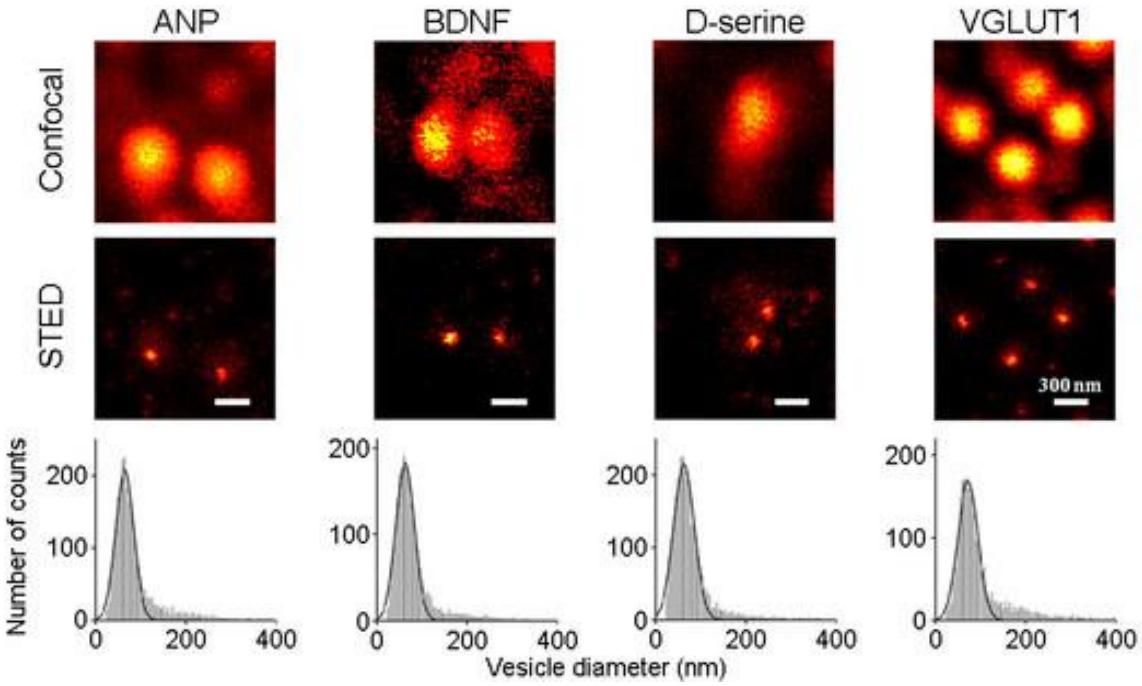

Figure 2. Confocal and STED images of vesicles containing peptides ANP and BDNF and amino acids D-serine and glutamate (immunostained with antibody against V-GLUT1). Histograms show distributions of STED-acquired vesicle diameters (in nm).

ORAL PRESENTATIONS I4:

Gaussian probes and highly efficient diffractive phase masks: new achievements in holographic electron beam shaping

Federico Venturi (1), Amir H. Tavabi (2), Gian Carlo Gazzadi (3), Roberto Balboni (4), Robert W. Boyd (5), Rafal E. Dunin-Borkowski (2), Ebrahim Karimi (6), Vincenzo Grillo (7), Stefano Frabboni (1)

1) (a) Dipartimento FIM Università di Modena e Reggio Emilia, Via G Campi 213/a, I-41125 Modena, Italy (b) CNR-Istituto Nanoscienze, Centro S3, Via G Campi 213/a, I-41125 Modena, Italy

2) Ernst Ruska-Centre for Microscopy and Spectroscopy with Electrons, Forschungszentrum Jülich, Jülich 52425, Germany

3) CNR-Istituto Nanoscienze, Centro S3, Via G Campi 213/a, I-41125 Modena, Italy

4) CNR-IMM Bologna, Via P. Gobetti 101, 40129 Bologna, Italy

5) (a) University of Ottawa, 25 Templeton St., Ottawa, Ontario, K1N 6N5 Canada (b) Institute of Optics, University of Rochester, Rochester, New York, 14627, USA

6) (a) Department of Physics, University of Ottawa, 25 Templeton St., Ottawa, Ontario, K1N 6N5 Canada (b) Department of Physics, Institute for Advanced Studies in Basic Sciences, 45137-66731 Zanjan, Iran

7) (a) CNR-Istituto Nanoscienze, Centro S3, Via G Campi 213/a, I-41125 Modena, Italy (b) CNR-IMEM Parco Area delle Scienze 37/A, I-43124 Parma, Italy

Keywords: Vortex beams, electron beam shaping, electron holography, Gaussian beams, astigmatic mode transformations

Since the introduction of holographic phase masks for the generation of electron vortex beams in 2011 (1), the field of holographic electron beam shaping has begun a constant and fruitful growth, as many different applications were proposed and implemented. In particular, phase holograms i.e. those that affect the beam's phase but are non-absorptive, open many interesting perspectives since they allow for 100% efficient diffraction gratings in the case of

blazed profiles, and a full control over the beam's transmitted amplitude and phase using a suitable encoding procedure (2). In this work, we fabricated phase holograms with focused ion beam on Si_3N_4 membranes following well-established procedures explained in (3). The holograms, when observed in a transmission electron microscope (TEM) in low-angle diffraction mode, generate the encoded wavefunction in the first diffraction order. We here show some newly generated probes and their characteristics. By carefully tuning the blazing peak-to-trough height difference, we fabricated a phase hologram encoding an L=1 vortex beam (Figure1a-b) with diffraction efficiency (I_{transm}/I_{1st}) of about 70% at the first diffraction order (Figure1c). Although theoretically it would be possible to reach 100% efficiency, there are many factors that worsen this value. For instance, inelastic scattering contributes to a diffuse intensity background, and fabrication defects like non-ideal peak sharpness and uneven blazing angle contribute to spread the intensity in all orders. Nonetheless, the efficiency value reached is still enough for the hologram to be employed in practical applications e.g. electromagnetic chiral dichroism experiments. By encoding both amplitude and phase of a wavefunction on a single hologram, we could produce different Gaussian probes, both low- and high-order. As an instance, we could generate a Gaussian beam (Figure2a) with flat phase wavefront. This flat phase wavefront is the main characteristic that differentiates holographically generated Gaussian beams from the usual ones obtained in a TEM by condensing the beam. Among high-order Gaussian beams, we could generate Laguerre-Gauss (LG_p^l) beams, controlling both the radial p and azimuthal l indexes. This allowed for the generation of an LG_0^{10} beam that is shape-invariant upon propagation (Figure2b), as peculiar of LG beams. Furthermore, by using TEM stigmator lenses in order to resemble a cylindrical lens, we could operate a mode transformation from LG_p^l to Hermite-Gauss (HG_m^n) beams, with index relation: $n=p$; $m=p+l$. In particular, we transformed an LG_0^{10} beam into an HG_{10}^0 beam (Figure2c). In this way, it is also possible to visually infer the orbital angular momentum (OAM) content of the former LG beam that, since n=0 and m=10, corresponds to l=10 i.e. an OAM value of 10ħ.

Acknowledgements:

S.F. and F.V. thank the University of Modena and Reggio Emilia for the grant FAR-2015-Project Title: Computer Generated Holograms for the realization and analysis of structured electron waves. F.V. thanks CNR for the grant STM-2016.

References:

1. J. Verbeeck, H. Tian, and P. Schattschneider, Nature 467, 301 (2010)

2. E. Bolduc, N. Bent, E. Santamato, E. Karimi, and R. W. Boyd, Optics Letters 38, 18 (2013)

3. V. Grillo, G. C. Gazzadi, E. Karimi, E. Mafakheri, R. W. Boyd, and S. Frabboni, Appl. Phys. Lett. 104, 043109 (2014)

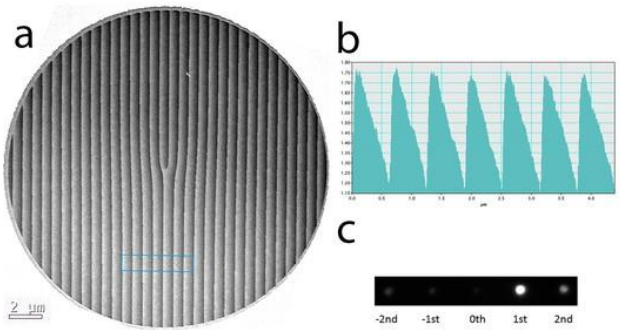

Figure 1. Highly efficient blazed phase mask. (a) Energy filtered TEM thickness map, (b) height profile in mean free paths from the blue area in (a), and (c) low-angle diffraction obtained from the phase mask showing high intensity at first diffraction order.

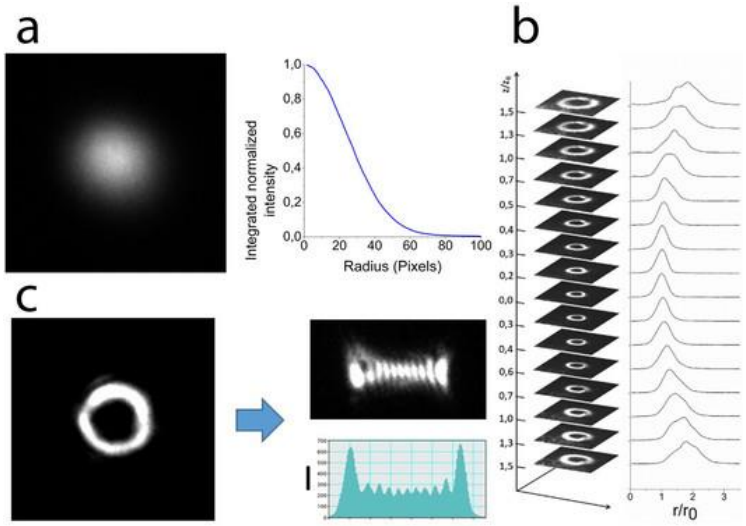

Figure 2. (a) Gaussian beam experimental intensity and radially integrated intensity profile, (b) LG(0,10) beam propagation shape invariance through focus over a range of 3 Rayleigh ranges, and (c) astigmatic mode transformation from LG(0,10) to HG(10,0) beam.

Sprague-Dawley rat (*Rattus norvegicus*) and European sea bass (*Dicentrarchus labrax*) as models for pathology of third stage *Anisakis* spp. larvae

Jerko Hrabar (1), Ivana Bočina (2), Ivana Bušelić (1), Anamarija Vrbatović (1), Željka Trumbić (1), Ivona Mladineo (1)

1) Institute of Oceanography and Fisheries, Šetalište Ivana Meštrovića 63, 21000, Split, Croatia

2) University of Split, Faculty of Science, Livanjska ul. 5, 21000, Split, Croatia

Consumption of raw or undercooked sea food infected with live third stage larvae (L3) of the nematode *Anisakis* spp. can lead to a zoonotic disease termed anisakiasis or anisakidosis. Although symptoms can vary greatly, in severe cases of disease perforation of gastric or intestinal wall, due to migration of the larva, occurs. Histopathologic changes in such cases typically exhibit severe eosinophilia and formation of eosinophilic granulomas as hallmarks of gastro-intestinal anisakiasis in humans. The aim of this study was to compare two host models experimentally infected with *Anisakis* larvae, namely Sprague-Dawley rat (*Rattus norvegicus*) as a model for human infection, and European sea bass (*Dicentrarchus labrax*) as a model paratenic host. Rats (n=15) and European sea bass (n=24) were each experimentally infected with 10 live third stage *Anisakis* larvae by oro-gastric intubation. At predefined time points, animals were euthanized with an overdose of anaesthetic, dissected and inspected for migrating larvae. Tissues with embedded migrating larva and lesions caused by its migration were sampled and routinely processed for classical histopathological analysis and transmission electron microscopy (TEM). In rats, larvae were mostly found penetrating gastric wall. Only rarely, larval migration through other tissues, i.e. intestinal wall, abdominal musculature or subcutaneous fat tissue, occurred. Histopathological analysis showed deep ulcerations of glandular epithelium in gastro-intestinal wall accompanied by tissue necrosis at the site of larval penetration. In *lamina propria mucosae* severe haemorrhages with extensive neutrophil and eosinophil infiltration were present. Affected muscles were infiltrated with neutrophils and eosinophils, some of which showed degranulation as revealed by TEM. Moreover, necrosis and structural disintegration of muscle fibres was observed. In European sea bass, *Anisakis* larvae were found penetrating either gastric or intestinal wall in a few

animals only, indicating successful expulsion of parasites by host's peristaltic. Larval migration through gastro-intestinal wall caused ulcerations and necrosis of glandular epithelium. *Lamina propria mucosae* was moderately infiltrated with mast cells that tended to accumulate around larvae themselves. Due to acute infection only, wounds caused by *larva migrans* healed rapidly and without proliferation of connective tissue. These findings demonstrate that rats, identical to humans as both being accidental and naïve hosts, exhibit strong innate immune response to an unknown pathogen, such as *Anisakis*. In contrast, fish as an evolutionary long-lasting paratenic host shows considerably milder immune response to *Anisakis* parasite together with rapid wound healing processes.

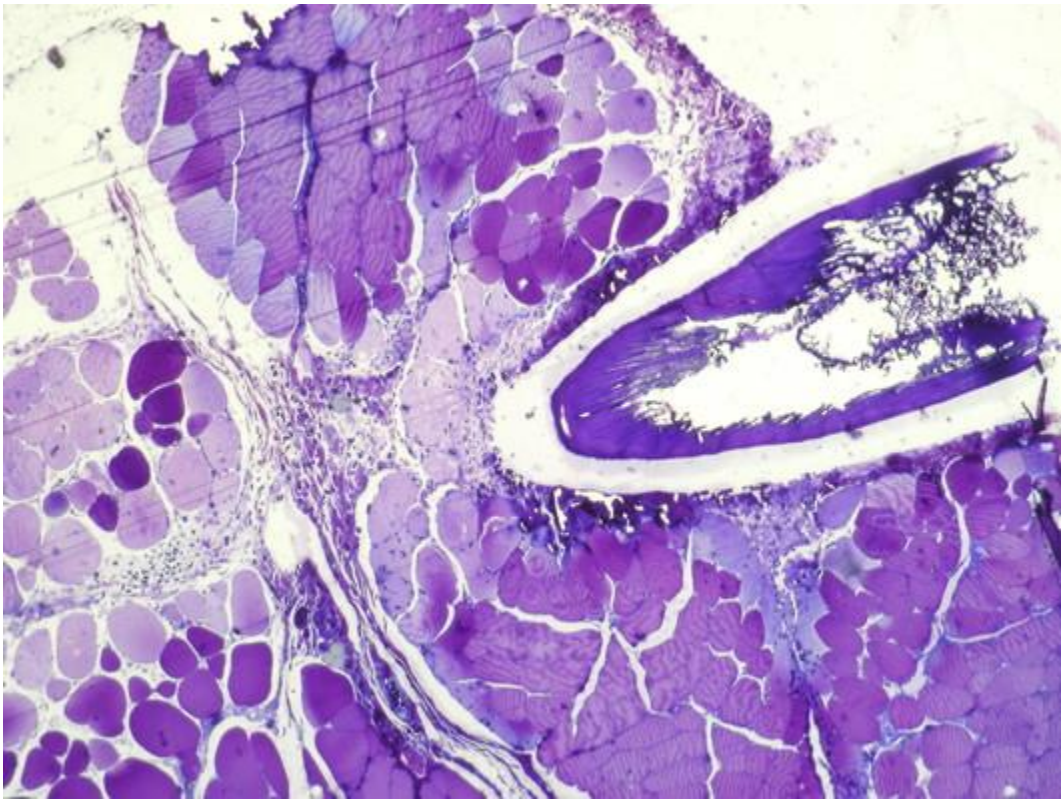

Figure 1. Semithin section of Anisakis spp. third stage larva (L3) migrating through abdominal musculature. Larval migration caused structural reorganization and necrosis of muscle fibres at the site of penetration, together with concentration of polymorphonuclear leukocytes around the larva. Extensive heamorrhage with polymorphonuclear leukocytes infiltration can be seen in perimysial connective tissue. 1% toluidine blue, 100x

POSTER PRESENTATIONS I4:

Colored micrographs significantly outperform grayscale ones in modern machine learning: Insights from a systematical analysis of lithium-ion battery micrographs using convolutional neural networks

Hermann Baumgartl (1), Ricardo Buettner (1), Timo Bernthaler (1), Ingo J. Timm (2), Andreas Jansche (1), Gerhard Schneider (1)

1) Aalen University, Beethovenstraße 1, 73430 Aalen, Germany

2) Trier University, Universitätsring 15, 54296 Trier, Germany

Keywords: machine learning, convolutional neural networks, colored micrographs, information content

While digital microscopy image analysis self-evidently shifted from grayscale to colored images years ago (1), it is still an open question if the information content of more efficient grayscale images is sufficient for powerful modern machine learning approaches. This question is an important one for practitioners since one-layer grayscale images can be stored and computed much more efficiently compared to multi-layer colored images. In addition – since a broad range of modern machine learning algorithms were built on the information content paradigm (such as Shannon's entropy in C5.0 or the Gini coefficient in Random Forests) – it is also very interesting from a theoretical point of view to know if colored images contain more relevant information content in comparison to grayscale images. To contribute to this question we systematically analyzed a series of greyscale versus colored material images from quality assessments of lithium-ion batteries. In this poster we report promising results from the Deep Convolutional Networks test series. Deep Convolutional Networks belong to the leading edge machine learning approaches that are working very well in image classification tasks [2, 3]. As a result, we found a significant increase in the classification accuracy of lithium-ion battery anode and cathode material quality, by using colored micrographs instead of monochrome ones. We showed that Convolutional Neural Networks are able to extract valuable information

from RGB channels, when compared to grayscale micrographs. We used a two layer Convolutional Neural Network architecture, trained to classify micrographs into “OK” and “Not-OK” classes (Figure 1). For training and testing purposes, we used 122 colored 128 times 128 pixel micrographs captured by a ZEISS Axio Imager.Z2 Vario microscope. We converted the colored images into grayscales using the ITU-R 601-2 luma transformation. In more detail: When using RGB colored micrographs, we found a 50% improvement of the area-under-the-curve measurement and a 14.2% increase in accuracy (Figure 2). Both values indicate a substantial gain in the information content of colored images.

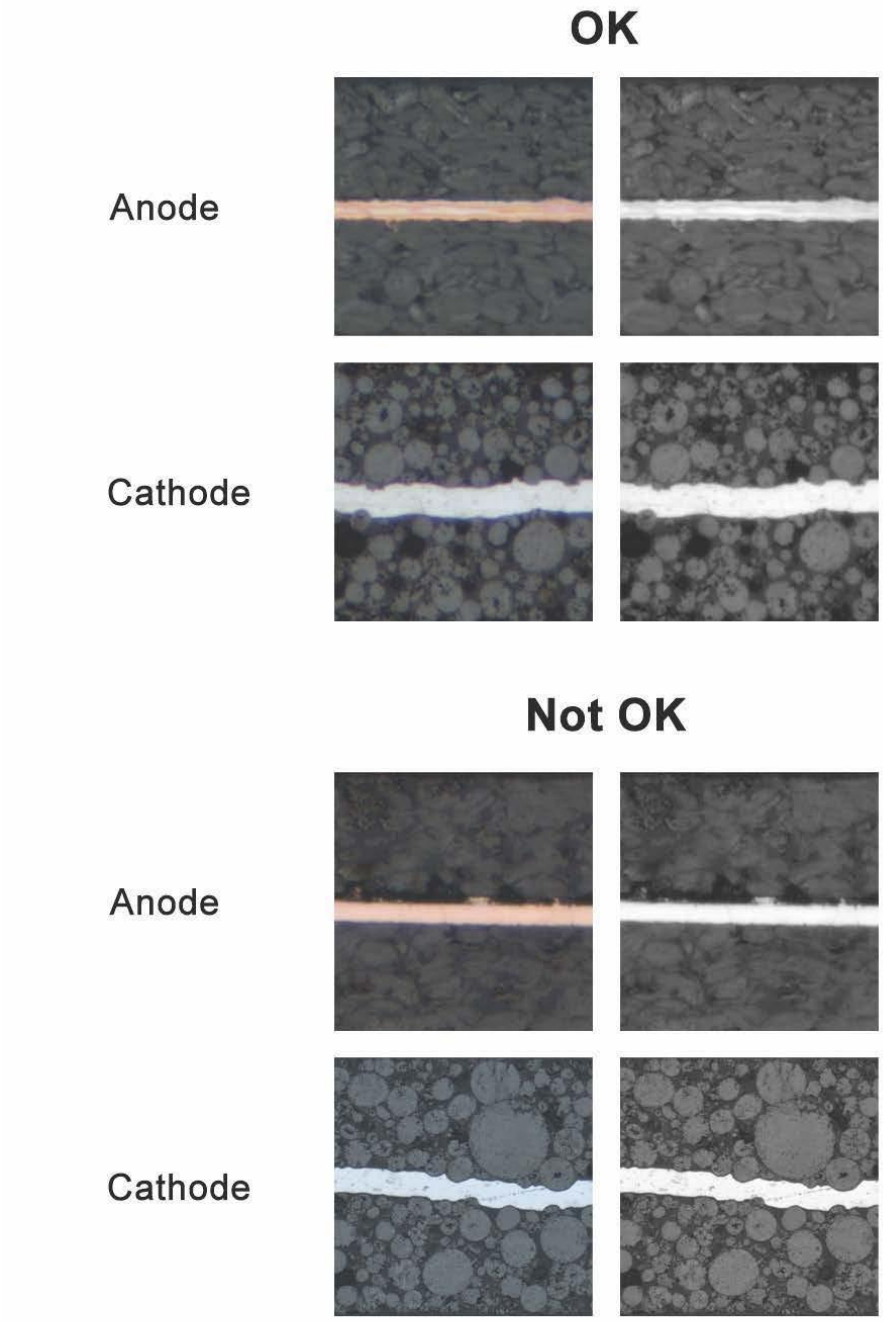

Figure 1. Examples of colored and non-colored micrographs from quality assessments

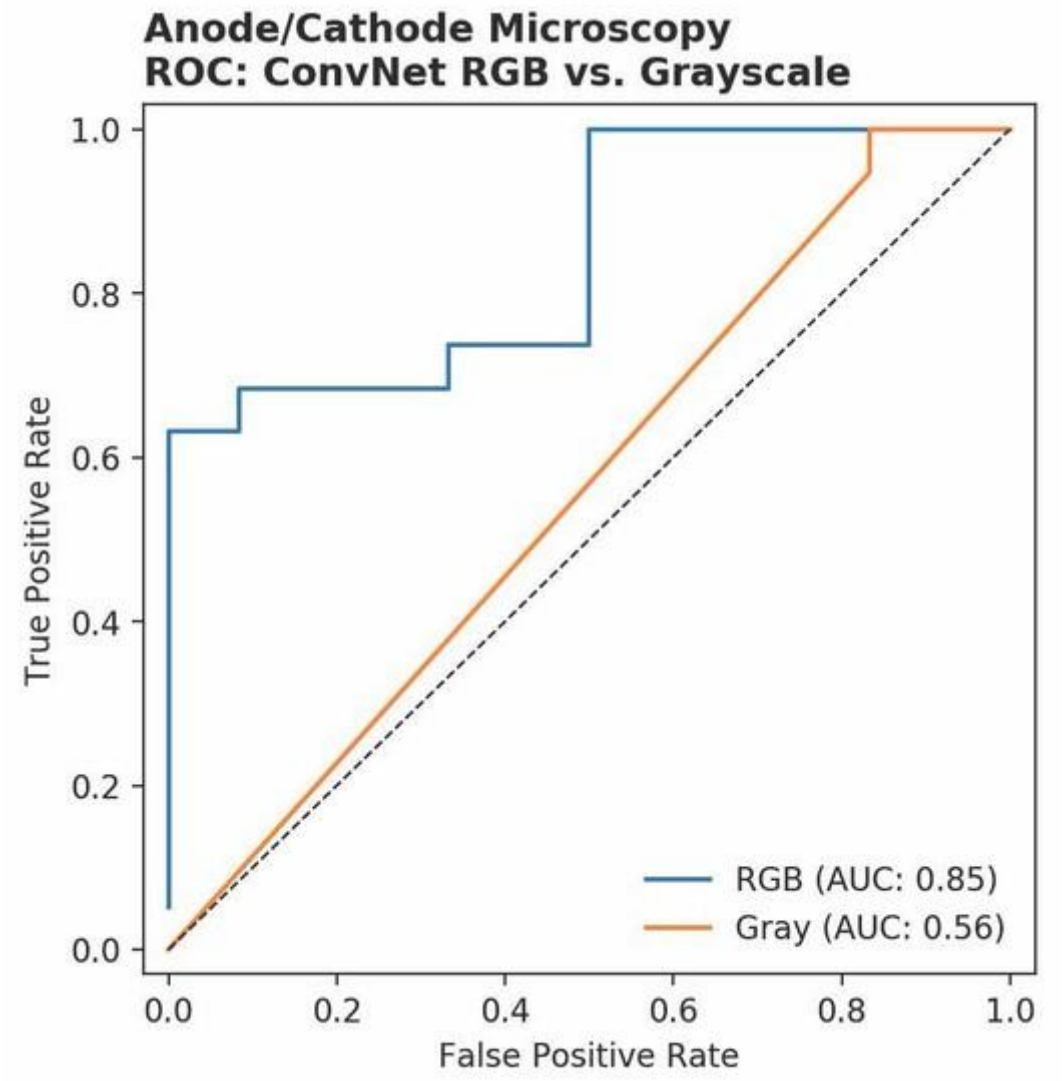

Figure 2. Performance indicators of trained convolutional network

References:

1. K.R. Castleman, Biol. Bull. 1994 (1998) 100-107.

2. N. Jones, Nature 505 (2014) 146-148. 3. Y. LeCun et al., Nature 521 (2015) 436-444.

I5. Specimen Preparation Techniques

INVITED LECTURES I5:

Effects of different sample preparation techniques of W-based composite for plasma-facing materials on electron microscopy characterization

Andreja Šestan (1), Matej Kocen (2), Janez Zavašnik (3), Petra Jenuš (4), Saša Novák (4), Miran Čeh (5)

1) Centre for electron microscopy and microanalysis, Jožef Stefan Institute, 1000 Ljubljana, Slovenija, Jožef Stefan Institute International Postgraduate School, 1000 Ljubljana, Slovenija

2) Department for nanostructured materials, Jožef Stefan Institute, 1000 Ljubljana, Slovenija,

3) Centre for electron microscopy and microanalysis, Jožef Stefan Institute, 1000 Ljubljana, Slovenija

4) Department for nanostructured materials, Jožef Stefan Institute, 1000 Ljubljana, Slovenija

5) Department for nanostructured materials, Jožef Stefan Institute, 1000 Ljubljana, Slovenija, Centre for electron microscopy and microanalysis, Jožef Stefan Institute, 1000 Ljubljana, Slovenija

Keywords: composites, sample preparation, electron microscopy, fusion

Sample preparation is the first and also the key step in every electron microscopy investigation which can potentially influence the correctness of the interpretation of obtained results due to possible present artefacts in the specimens resulting from the sample preparation procedures. Therefore, the key question is how to avoid, minimize or at least how to recognize the possible sample structural and chemical modifications due to different sample preparation techniques and how to take them into account when evaluating and interpreting the results. In present work we discuss and explain different sample preparation techniques that enable microstructural characterization of W_2C and WO_2 particle-reinforced W-matrix using various SEM and TEM analytical techniques. A combination of hard and brittle metal combined with ceramic-like particles, which is the case in our investigated material, is one of the most

demanding combinations for SEM and TEM sample preparation in the field of material science, since each of the components is subject to specific modifications during sample preparation (grinding, polishing, dimpling, ion-milling, etc). For example, for the most basic phase differentiation methods in SEM, i.e. BSE imaging, EBSD and EDS, we need flat samples with clean surfaces (1). Already due to the different etching rate of metal-ceramic composites, based on refractory metal matrix and refractory particles, sample preparation can be very challenging and demands careful planning of subsequent mechanical and ion polishing, combined with (non)selective chemical etching (2). W-based composites can be potentially used as plasma-facing materials in the fusion reactor. However, to further assess its suitability, systematic irradiation studies with deuterium, tritium, He-ions and neutrons need to be performed. Only then it can be justly evaluated whether these composites are suitable materials for fusion application (3). This is why the proper understanding of the pre-irradiation surface and near-surface structural modifications, caused by different sample preparation techniques, is of vital importance to properly distinguish between the changes developed during irradiation and preparation of the samples. The following preparations procedures were used for the preparation of W-based composites specimens for electron microscopy observations: Focused-ion beam (FIB), mechanical polishing and ion-milling. Our results for W-xW_2C composite (Figure 1) showed that FIB readily revealed the existence of a surface deformation layer with a thickness of approximately 2.5 μm, which is always present in mechanically prepared samples. The deformation layer was successfully removed by additional polishing with a mixture of OPS and H_2O_2. However, the final polishing using OPS and H_2O_2 can also etch away some of the oxide phases of interest in the matrix composites (Fig 2a). In the case of this, ion-milling procedure is preferential since also the existence of oxide phases could be retained (Figure 2b).

Acknowledgements:

This work has been carried out within the framework of the EUROfusion Consortium and has received funding from the European Union's Horizon 2020 research and innovation programme under grant agreement number 633053. The view is and opinions expressed herein do not necessarily reflect those of the European Commission.

References:

1. S.M., Mukhopadhyay, Sample Preparation for Microscopic and Spectroscopic Characterization of Solid Surfaces and Films, in Sample Preparation Techniques in Analytical Chemistry. 2003, John Wiley & Sons, Inc. p. 377-411.

2. E. Lassner, W.-D. Schubert, Tungsten-Properties, Chemistry, Technology of the Element, Alloys, and Chemical Compounds. 1999, Springer US, p.54.

3. G. Pintsuk, Reference Module in Materials Science and Materials Engineering, Comprehensive Nuclear Materials, ed. R. J. M. Konings, Elsevier: Oxford. p. 551-581 (2012).

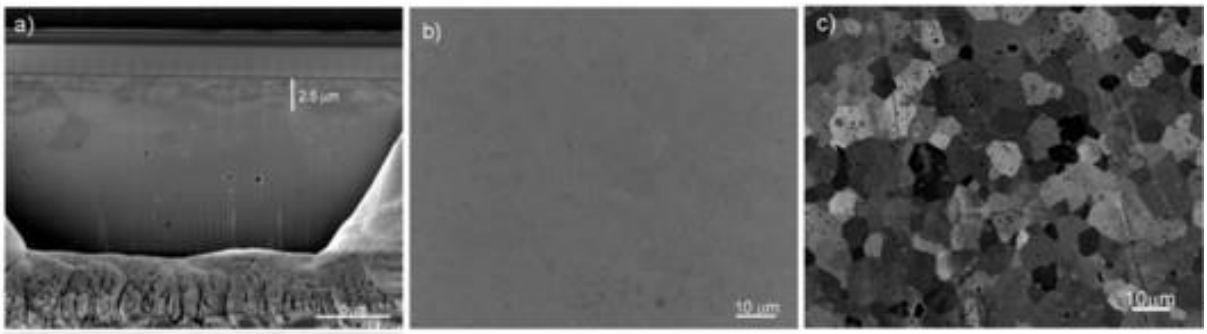

Figure 1. (a) Cross-section cut of W-xW2C sample using FIB (Ga+ ions) revealing the region with mechanically induced deformation app. 2.5 µm thick. (b) BSE image of W-xW2C after mechanical polishing. (c) Sample from (b) additionally polished with a mixture of OPS and H_2O_2 for 30 min.

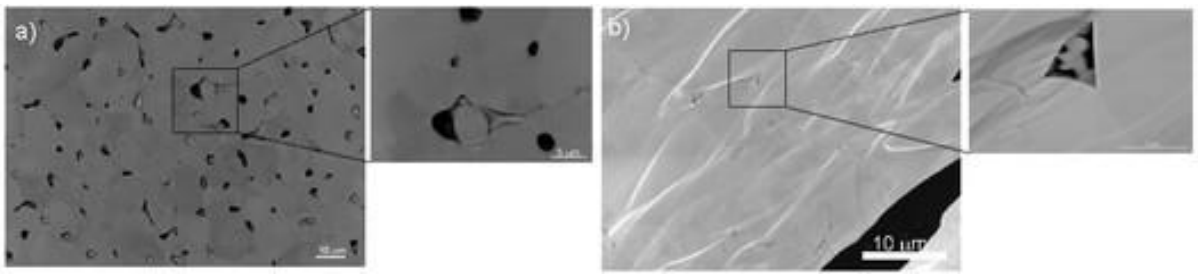

Figure 2. (a) BEI image of W-xWO2 after mechanical polishing and additional final polishing with a mixture of OPS and H_2O_2 for 15 min. (b) BEI image of W-xWO_2 after mechanical polishing and additional Ar+ ion-milling.

Overcoming the sample preparation hurdle for cryo-electron tomography

Miroslava Schaffer (1), Benjamin D. Engel (1), Stefan Pfeffer (1), Sahradha Albert (1), Stephan Kleindiek (2), Julia Mahamid (1), Philipp Stawski (1), Tim Laugks (1), Wolfgang Baumeister (1), Jürgen M. Plitzko (1)

1) Max Planck Institute of Biochemistry, Department of Molecular Structural Biology, Am Klopferspitz 18, 82152 Martinsried, Germany

2) Kleindiek Nanotechnik GmbH, Markwiesenstraße 55, 72770 Reutlingen, Germany

Keywords: Cryo-FIB, Cryo-ET

Sample preparation by cryo-focused ion beam (cryo-FIB) milling has been shown to be a key technique in advancing the capabilities of structural biology to investigate structures at high resolution directly within the native cellular environment [1-3]. The preparation of electron-transparent lamellas from vitreous frozen specimens enables the acquisition of previously inaccessible information by cryo-electron tomography (CET). These *in situ* studies of biological systems often reveal the molecular structures of specific conformational or assembly states, which are then mapped back into the cellular volume to gain a better understanding of biological processes. Recent developments in TEM imaging such as direct detection cameras and Volta phase plates help to further extend the possibilities of CET, but can only harness their full potential once the sample preparation workflow has been optimized to reproducibly yield thin, homogenous, fully vitrified and sufficiently conductive specimens. We can now routinely achieve this goal for plunge-frozen cells prepared directly on TEM grids. However, this standard preparation technique is not suitable for thicker specimens, such as large eukaryotic cells or tissue samples, which cannot be vitrified by plunge-freezing. We therefore have developed a new, complementary cryo-FIB preparation technique in which the volume of interest is completely extracted from frozen bulk material utilizing a novel cryo-gripper tool. The cryo-FIB lift-out routine has no strict sample size limitation and is thus applicable to high-pressure frozen specimens, which could also be first trimmed in a cryo-ultramicrotome to specific volumes of interest that were targeted by correlative light-microscopy. In this presentation, we will discuss the key aspects of both complementary cryo-FIB preparation

techniques and showcase recent *in situ* studies of membrane-bound macromolecules, such as photosynthetic complexes and ribosomes.

References:

(1) Schaffer et al., J Struct Biol. (2017) 197(2):73-82.

(2) Engel et al., eLife (2015) 4:e04889.

(3) Mahamid et al., Science (2016) 351(6276):969-72.

ORAL PRESENTATIONS I5:

Automatized freeze substitution under agitation: opportunities for studies of intracellular mesostructures

Siegfried Reipert (1), Elena Hollergschwandtner (1), Daniela Gruber (1), Helmuth Goldammer (1), Margret Eckhard (1), Josef Neumüller (2), Ulrich Kaindl (2), Michael Stöger-Pollach (3), Thomas Schwaha (4)

1) Core Facility Cell Imaging and Ultrastructure Research, Unversity of Vienna, Althanstraße 14 (UZA 1) A-1090 Vienna, Austria

2) Center of Anatomy and Cell Biology, Department for Cell and Developmental BiologyMedical University of Vienna, Waehringer Strasse 13, 1090 Vienna, Austria

3) University Service Center for TEM (USTEM), Vienna University of Technology, Wiedner Hauptstraße 8-10 / 052, A-1040 Vienna, Austria

4) Department of Integrative Zoology, University of Vienna, , Althanstraße 14 (UZA 1) A-1090 Vienna, Austria

Keywords: cellular inclusions, mesocrystals, confocal reflection microscopy, rapid freeze substitution, transmission electron microscopy

Cryopreparation based on high-pressure freezing and freeze substitution has been proven as superior for sample preservation if compared with chemical fixation and processing of cells and tissues at ambient temperature. Here, we address its potential for studies of paracrystalline cellular inclusions, with specific reference to our findings of novel intracellular mesostructures. Recently we applied our agitation module for accelerated automatized freeze substitution in a commercial freeze substitution unit to cryoimmobilized animal- and plant tissues for transmission electron microscopy (TEM). Besides other advantages, the initial tests indicated the usefulness of this technique for preservation of paracrystals in algal microbodies and polysaccharides in form of starch (1). We also generated data from oocytes of brine shrimp demonstrating that particular small, organelle-bound nanocrystals are preserved by this

method. Here we provide a clear example how high-pressure freezing in combination with rapid freeze substitution can prevent disintegration of crystal-like inclusions that are part of mesoscopic superstructures. If applied to epidermal cells of brine shrimp Artemia franciscana, we found novel, flake-like entities with electron-opaque and electron-lucent stripes (Figure 1a) in abundance both in the cytoplasm and nucleoplasm of these cells. Under conditions of chemical fixation and processing at room temperature the zebra-striped ´flakes´ disintegrated into individual crystal-like rhomboids (Figure 1b). These rhomboids resemble previous observations made in different context in other species, which have been interpreted as proteinaceous paracrystals. Confocal laser scanning microscopy of native tissues correlated with our data based on cryopreparation. Moreover, it revealed optical activity of the superstructured flakes and the full extent of their distribution in the tissue (Figure 1c). Electron tomography provided a 3D-impression of individual superstructures flakes and their edged interface with the cytoplasm, but selected area electron diffraction could not verify the status of crystallinity. We conclude that A. franciscana possess epidermal cells with crystal-like superstructured inclusions that resemble mesocrystals. Mesocrystals are known to self-assemble from inorganic crystalline components and biopolymers (2). However, energy dispersive X-ray spectroscopy detected no raise of inorganic elements potentially involved in crystallization, but an increase of nitrogen inside the inclusions. Accordingly, in the formation of mesostructures in Artemia tissue proteinaceous precursors seem to play the part of the inorganic ones. Our hypothesis is supported by TEM observations likely to be related to the process of self-assembly. Artemia, therefore, could serve as an excellent model for interdisciplinary studying of mesostructure formation *in vivo*. If correct, mesocrystals are more widespread and diverse than currently thought. Cryofixation in combination with rapid freeze substitution could possible bring more structures like those reported here to our attention, because of better preservation of both proteins and (poly) carbohydrates. The interest in this topic is explained by the fact that mesocrystals are subject of intense studies by biophysicist and material scientist because of their extraordinary physical properties (2).

Acknowledgements:

The FS agitation module is protected under Austrian patent number AT515423 and PCT applicationWO2015154118. We are grateful to Prof. G. van Stappen (Laboratory of Aquaculture & Artemia Reference Center, University of Gent) for providing Artemia cysts and to D. Abed-Navandi from the Haus des Meeres aquarium Vienna, for providing algae.

References:

1. H. Goldammer,et al., Protist 167 (2016), p. 369.

2. L. Bergström et al., Acc Chem Res 48 (2015), 1391.

3. This project is supported by the Austria Wirtschaftsservice (P1404894).

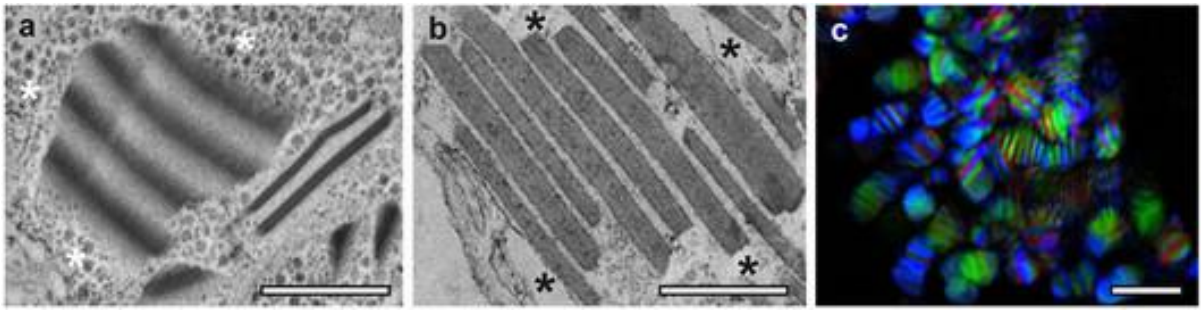

Figure 1. Mesostructured cellular inclusions in an epidermal cell layer of A. franciscana. Transmission electron microscopy: (a) Sample high-pressure frozen and rapidly freeze substituted. Note ´flakes´ with ´zebra striped´ patterns surrounded by cytoplasm filled with numerous glycogen rosettes (white asterisks). (b) Sample chemically fixed and processed at room temperature showing particular strong washing out of biological material (black asterisks). Confocal laser scanning microscopy: (c) Sample, not chemically fixed, displaying flake-like entities with striations resembling observations in the TEM. Bars in a and b, 1 µm. Bar in c, 5 µm.

A modified method to avoid loss of calcium mineral constituents during preparation of mineralized tissues for light and electron microscopy

Nada Žnidaršič (1), Polona Mrak (1), Jasna Štrus (1)

1) University of Ljubljana, Biotechnical Faculty, Department of Biology, Večna pot 111, Ljubljana, Slovenia

Keywords: calcification, dry sectioning, cuticle

Mineralized tissues are complex organic-inorganic hybrid materials produced by organisms and consist of minerals embedded in a hierarchically organized network of organic macromolecules. Crystalline and amorphous mineral forms are frequently present in close proximity and form defined functional regions of the tissue. Imaging of the mineralized biological tissues is demanding due to specific requirements for the preservation and visualization of chemically different constituents and due to sectioning difficulties. Preparation of biological samples for light and electron microscopy typically involves exposure of the tissue to aqueous solutions, that was reported to adversely affect the detection and analyses of early calcification in cell cultures (Studer et al., 2011). Calcification is an integrative part of the crustacean cuticle differentiation during development, in addition to organic matrix formation (Mrak et al., 2014). Thus, evaluation of the preparation procedures for calcified biological samples is an important issue in these studies. Here we report on comparative imaging of aldehyde fixed / resin embedded and methanol fixed / resin embedded crustacean cuticle samples, including the comparison of wet sectioning versus dry sectioning. Alizarin red S histochemical staining for calcified tissue localization was applied on semithin sections. A positive histochemical reaction was evident in the external part of the cuticle in the sections of aldehyde fixed samples, while the inner part of the cuticle was not stained. The whole transverse profile of the cuticle, comprising exo- and endocuticle, was stained only in certain sections of methanol fixed samples. As it is known that exocuticle in adult animals contains calcite, whereas the mineral phase in the inner cuticle layers (endocuticle) is amorphous (Hild et al., 2008), we consider that amorphous forms of calcium minerals were preserved and

stained in the thicker sections of methanol fixed cuticle. Therefore, methanol fixed samples were prepared for transmission electron microscopy imaging. Evaluation of the postembryonic cuticle ultrathin sections in TEM supports the view that wet sectioning resulted in the loss of mineral constituents, as abundant electron dense material was evidenced within the cuticular matrix in the dry ultrathin sections, corresponding in position to electron lucent regions in the wet ultrathin sections of the same sample. In conclusion, special precautions are necessary to avoid exposure of the samples to aqueous solutions in the studies of biomineralized tissues. Methanol fixation and dry-ultrathin sectioning was an advantageous additional approach in our studies of calcified cuticle architecture. This aspect is especially relevant when amorphous calcium mineral forms are likely present in the tissues, e.g. in imaging the *de novo* calcification of the matrix during embryonic / postembryonic development as well as in imaging calcified matrix renewal and repair.

References:

1. D. Studer et al., Cells Tissues Organs 194 (2011) 138-145.

2. P. Mrak et al., Arthropod Structure & Development 43 (2014) 423-439.

3. S. Hild et al., Journal of Structural Biology 163 (2008) 100-108.

Formaldehyde-induced membrane blebbing during fixation - a major risk for loosing cellular proteins.

Lukas Pastorek (1), Margrita Sobol (1), Tomas Venit (1), Pavel Hozák (2)

1) Institute of Molecular Genetics ASCR v.v.i., Department of Biology of the Cell Nucleus, Vídeňská 1083, 142 20, Prague 4, Czech Republic

2) Institute of Molecular Genetics ASCR v.v.i., Department of Biology of the Cell Nucleus & Microscopy Centre, Vídeňská 1083, 142 20, Prague 4, Czech Republic

Keywords: cell fixation, membrane blebbing, fixation artifacts, microscopy, histochemistry

The crucial step of the biological samples preparation is the fixation procedure. The effectiveness of the fixation process is assessed by the preservation of the cellular constituents and the suitability for further treatments (e.g. immunolabelling). Curiously, the detailed mechanisms of the cell fixation remain unclear. We focused on studying the fixation-induced cell blebbing and searching the methods to minimize this effect. Using different microscopy techniques, we quantitatively estimated the loss of cytoplasmic content during the blebs rupture. With time-lapse experiments, we found the crucial points in the blebs formation and rupture. Based on this, we tested a wide range of fixation mixtures applied during different time intervals to minimize the effect of blebbing. Taking into consideration various quantitative parameters, we determined the most optimal procedures to fix the cells. Finally, we discussed the possible mechanisms of the fixation-induced blebs formation and a requirement to choose the most appropriate fixation protocol for further experiments.

Acknowledgements:

We would like to thank for the financial support GACR (GA16-03346S, and GA15-08738S), TACR (TE01020118), HFSP (RGP0017/2013), project „BIOCEV – Biotechnology and Biomedicine Centre of the Academy of Sciences and Charles University“ (CZ.1.05/1.1.00/02.0109) from the European Regional Development Fund, IMG (RVO:68378050). The microscopy data presented in this paper were produced at the Microscopy Centre (Electron Microscopy Core Facilities), IMG ASCR, Prague, Czech Republic, supported by MEYS (LM2015062 Czech-BioImaging).

Advancement of broad and focused low energy ion milling procedures for the optimization of high resolution TEM samples

Martina Dienstleder (1), Evelin Fisslthaler (1), Christian Gspan (1), Gerald Kothleitner (2)

1) Graz Centre of Electron Microscopy, Steyrergasse 17, 8010 Graz, Austria

2) Institute for Electron Microscopy and Nanoanalysis, Graz University of Technology, Steyrergasse 17, 8010 Graz, Austria

Keywords: sample preparation, low voltage ion milling, transmission electron microscopy

Specimen preparation is the key to obtain representative insights into morphology, structure, chemistry and functionality of materials in a transmission electron microscope. Artefact generation during the sample preparation [1-2] is one of the limiting factors in order to perform high resolution transmission electron microscopy analysis. Mechanically or ion-induced artefacts are part of the preparation and should be kept as small as possible in order to be able to examine the samples in an as original state as possible. However, to exploit the full potential of high-end TEM instrumentation towards the sub-atomic scale, classical approaches and routine preparation protocols are no longer sufficient. The way to thin and consequently clean the samples as a post preparation step with low energy argon ions is a suitable way to remove some artefacts completely or reduce other artefacts to a minimum. We will present a couple of material science samples - both mechanically and PIPS™ or FIB prepared - which are cleaned and thinned in such a way and will show the assets and drawbacks of this post treatment with low voltage argon ions. Furthermore, a study to verify the NanoMill® equipment in terms of milling homogeneity as well as geometrical influences of the FIB prepared samples on the sample quality is presented with the intention to illustrate options to enhance this cleaning procedure.

References:

1. J. Ayache, et.al. “Sample preparation handbook for transmission electron microscopy” (Vol. 2), (2010)

2. L. Reimer „Elektronenmikroskopische Untersuchungs- und Präparationsmethoden“ (1967)
3. „We kindly acknowledge financial support by the Austrian Research Promotion Agency (FFG) (project 850220/859238).”

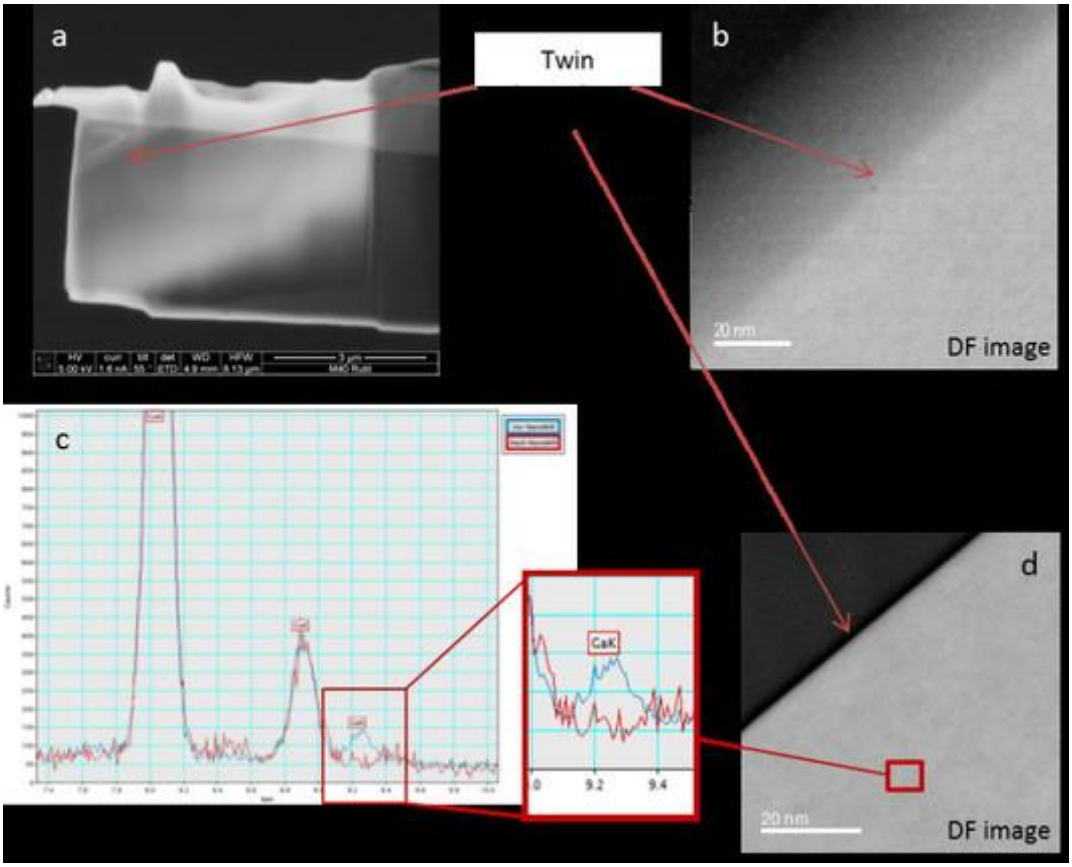

Figure 1. (a) FIB image of conventionally prepared TiO2 sample; (b) STEM DF image of twin boundary in a; (c) comparison of implantation of Ga by EDX measurements before and after low voltage argon ion thinning; (d) STEM DF image after low voltage argon ion thinning.

POSTER PRESENTATIONS I5:

Improving scanning capacitance microscopy by specimen preparation

Mao Nan Chang (1), Jhih Yang Chen (2), Chun Hsien Liu (1), Yung Han Chuang (1), Tsung Yu Chan (2), Chia Yi Wu (1), Yao Jen Lee (3)

1) Department of Physics, National Chung Hsing University, Taichung, 402, Taiwan

2) Institute of Nanoscience, National Chung Hsing University, Taichung, 402, Taiwan

3) National Nano Device Laboratories, NARL, Hsinchu, 300, Taiwan

Keywords: SCM, silicide, microwave, annealing, modulation

In scanning capacitance microscopy (SCM), contact electrodes including moving electrode, i.e., conductive probe, and back electrode, i.e., Ohmic contact at specimen, are essential components during imaging carrier concentrations.(1) It is well known that silver glue is a typically-used back electrode for SCM specimens. From conductive point of view, silver glue is hard to form good Ohmic contact with silicon, leading to a low modulation efficiency (ME) in SCM measurements. Since the ME value is a key indicator of the image contrast and signal to noise ratio, high ME values not only imply the SCM images with high signal intensity and high image contrast, but also guarantee the use of low modulation voltage. Low modulation voltage reduces the stray field effect and hence enhances the spatial resolution of SCM images. (2) The ME stability is also an important factor influencing quantitative analysis of SCM. A direct approach to high ME is reducing the contact impedance of SCM specimens. Therefore, it is necessary to improve the specimen preparation for SCM applications. In this work, we employed silver silicide to form the back electrode for the cross-sectional samples. Patterned n+ regions were formed on an n-type silicon substrate for demonstrating SCM image contrast. The silicidation processes were performed by microwave annealing for 80 seconds, which is a low thermal budget process. A PtSi conductive probe was used for acquiring the junction images. With ultraviolet treatment, a stable specimen surface was obtained. During the SCM

measurements, the modulation voltage is less than 300 mV. Experimental results revealed that using silver silicide as the back electrode we obtained 47.1%-63.1% improvements in the ME for n-type samples, as shown in figure 1(a). For p-type samples, we obtained more than 3 times of ME improvement. Using silver silicide electrode, the relative standard deviation (RSD) of the measured ME can be as low as 0.84% for n-type samples. For the specimen electrodes using silver glue, the RSD value was up to 8.07%. For p-type samples, the best RSD values for using silver silicide and silver glue electrodes are 4.41% and 46.09%, respectively. With the improved ME, figure 2 evidently shows that the silver silicide electrode provides a contrast improvement in the n+ region. In addition to the SCM image quality, the scanning capacitance spectroscopy benefitting by reducing contact impedance will also be discussed in this work.

References:

1. M.N. Chang et al., Appl. Phys. Lett. 84 (2004) 4705.

2. M.N. Chang et al., Appl. Phys. Lett. 101 (2012) 083503.

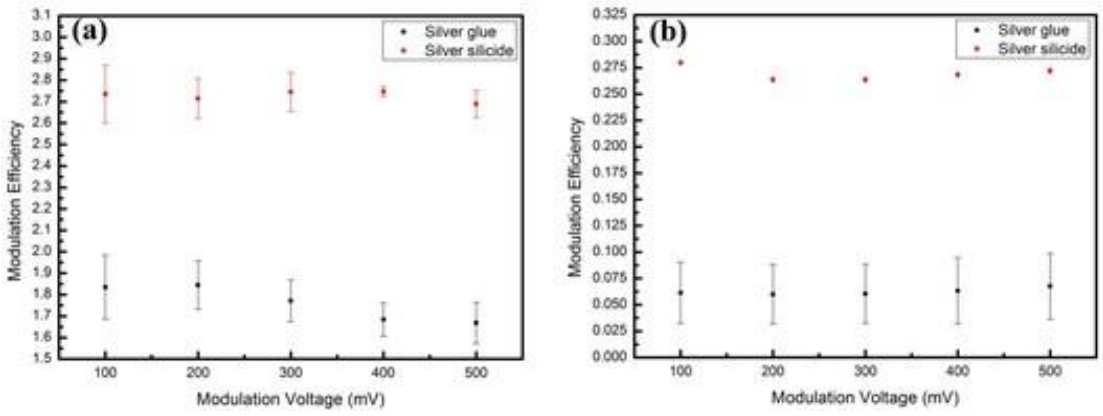

Figure 1. (a) and (b) respectively show the ME values for n- and p-type samples contacting with silver silicide and silver glue electrodes.

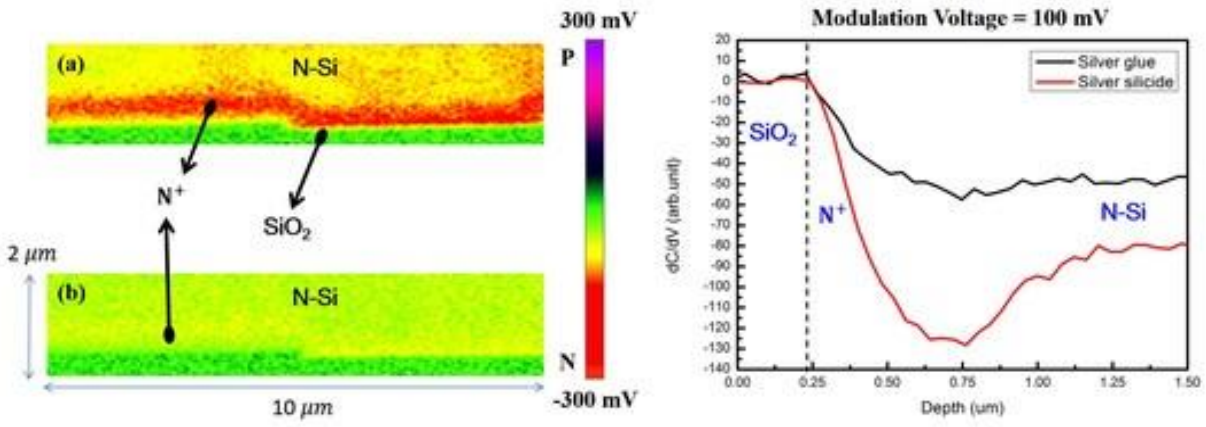

Figure 2. (a) and (b) show the SCM images by using silicide and silver glue electrodes, respectively. The sectional analysis reveals that clear non-monotonic behavior is obtained by using the silver silicide electrode.

Immunogold labelling of allergens at fine dust filter particles for SEM investigations

Manfred Nachtnebel (1), Tobias Achtsnit (1), Johannes Mertl (2), Gabi Ettenberger (2), Johannes Rattenberger (1)

1) Graz Centre for Electron Microscopy, Steyrergasse 17, 8010 Graz, Austria

2) OFI Technologie & Innovation GmbH, Brehmstraße 14a, 1110 Vienna, Austria

Keywords: SEM, immunogold electron microscopy, allergens, pollen, fine dust filter

In the last decades the number of people with allergies against at least one of the major allergens like birch, grass, ragweed pollen or domestic cat steady increases (1).There are various investigation methods available with which new insights were gained regarding the allergy potential, the concentration or position of specific allergens at various sample types. A more sophisticated method is immunogold electron microscopy, which enables to locate specific proteins who are responsible for an allergic reaction. Because of their high spatial accuracy and the used small gold particle size (approximately 10 – 40 nm), this method is typically applied for transmission electron microscope (TEM) investigation (2). The investigations presented were performed to obtain information about the presence of specific allergens at particles deposited at fine dust filters. Because of the sample size they have to be examined in a scanning electron microscope (SEM). Unfortunately, several examinations have shown that typical TEM labelling protocols are not directly transferable for SEM investigations. Therefore the immunogold labelling protocol had to be adopted to enable labelling at the samples under investigation. The main task was to achieve a high signal (gold particle concentration) at position where the allergen is present while the labelling of the background is sufficient low to enable a distinct differentiation. A protocol was found by an iterative sample preparation process, initially for the detection of the grass pollen allergen Phl p5. Here, among others, the appropriate primary antibody concentration had to be found. Monoclonal antibodies were used because of their highly specific binding to one protein. Additionally a fixation and blocking step were applied, to fix the proteins at its initial position on the one hand and to suppress a labelling of the background on the other hand. Subsequently, the protocol was

successfully tested at cryo-milled grass (as positive control) and birch (as negative control) pollen, see Img. 1. An initial test directly at the filter material had shown that the hygroscopic forces make it hardly possible to get rid of the unwanted background without losing the signal. A better result was gained by using carbon tape as substrate. Thus the particles have to be extracted from the filter material, by e.g. soaking them into the buffer solution and subsequently evaporate the solution at the carbon tape. For further improvement of the overall method, a better extraction method, which extracts a higher amount of particles, has to be found. Also further allergens should be labelled, but the developed protocol should easily be adaptable for other allergens by only changing the used primary antibody.

Acknowledgements:

The authors thank the Austrian Research Promotion Agency FFG (project 856321) for funding.

References:

1. N. Ghouri et al., J. R. Soc. Med 101 (2008) 466–472.9

2. T. M. Mayhew et al., Ann. o. Anat. – Anat. Anz. 191 (2009) 153-170.2

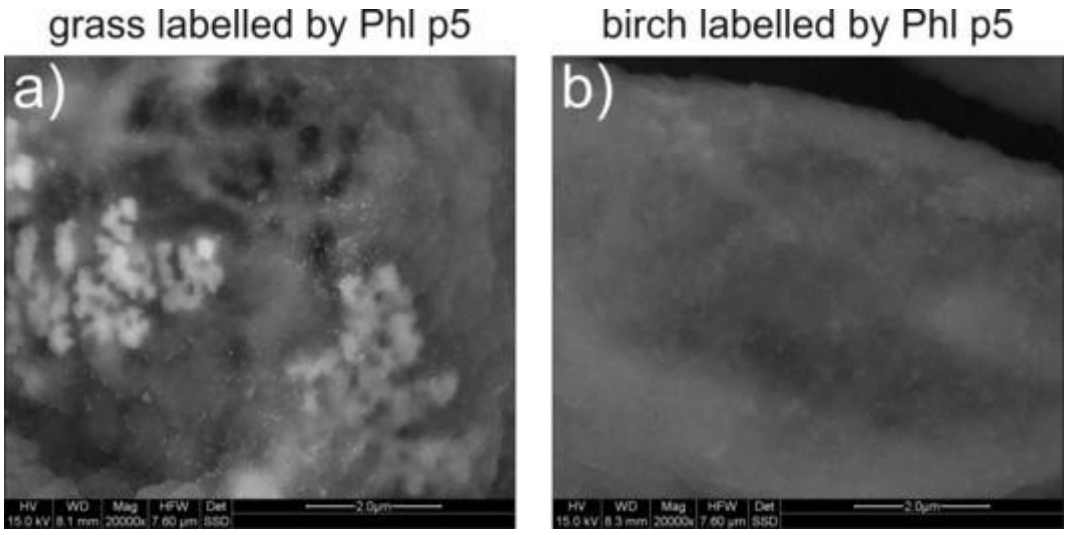

Figure 1. BSE images of immunogold labelling protocol test for the used Phl p5 antibody on cryo-milled grass pollen at a) (positive control) and same performed for birch pollen at b) (negative control). Bright white spots (used 20nm gold particles) marks allergy protein position.

Short freeze substitution under agitation: brevity is the soul of wit

Siegfried Reipert (1), Helmuth Goldammer (1)

1) Core Facility Cell Imaging and Ultrastructure Research, Unversity of Vienna, Althanstraße 14 (UZA 1) A-1090 Vienna, Austria

Keywords: rapid freeze substitution, agitation module, sample preparation, transmission electron microscopy

Freeze substitution (FS) is a well-established method for low-temperature dehydration and-fixation of instantly cryoimmobilized cells and tissues. It results in less extraction of biological material and, in consequence, improved sample preservation. Until recently FS had the reputation of being notoriously slow. In 2011, McDonald and Webb published a groundbreaking paper (1) demonstrating that sample agitation is essential to speed up the substitution process from days to a couple of hours. As a proof of concept they realized the agitation of their samples in a dry ice-filled bucket that was placed on a laboratory shaker. We found a straightforward way how to combine agitation of the samples in the substitution medium with the advantages of automatized FS (AFS), such as flexibility in programming, reproducibility and safety. We developed an agitation module for straightforward refitting in commercial FS units without interference with the electronics and construction of the AFS itself (2). In our initial publication we demonstrated the performance of a hand-made prototype for the AFS2 (LEICA Microsystems) on example of plunge- and high pressure frozen algae (3). Subsequently, we established the cost-effective ´on demand´ manufacturing of agitation modules based on 3D-printing. Besides testing in our own lab, we provided such agitation modules to other EM labs in Europe. Encouraged by positive feedback, we organized the manufacturing of agitations modules by a small start-up company, Cryomodultech e.U. (holder: H. Goldammer). The company offers agitation modules for both the AFS2 and its predecessor, AFS (1) (LEICA Microsystems), and it is prepared to find similar solutions for further FS units that are currently in use.

Acknowledgements:

This project is supported by the Austria Wirtschaftsservice (P1404894).

References:

1. KL McDonald KL, RI Webb.J. Microsc.243 (2011) 227-33.

2. Austrian patent number AT515423 and PCT applicationWO2015154118.

3. H Goldammer et al., Protist 167(2016) 369-76.

4. Reipert et al. 13th Multinational Congress on Microscopy, Sept. 2017, Rovinj, Croatia.

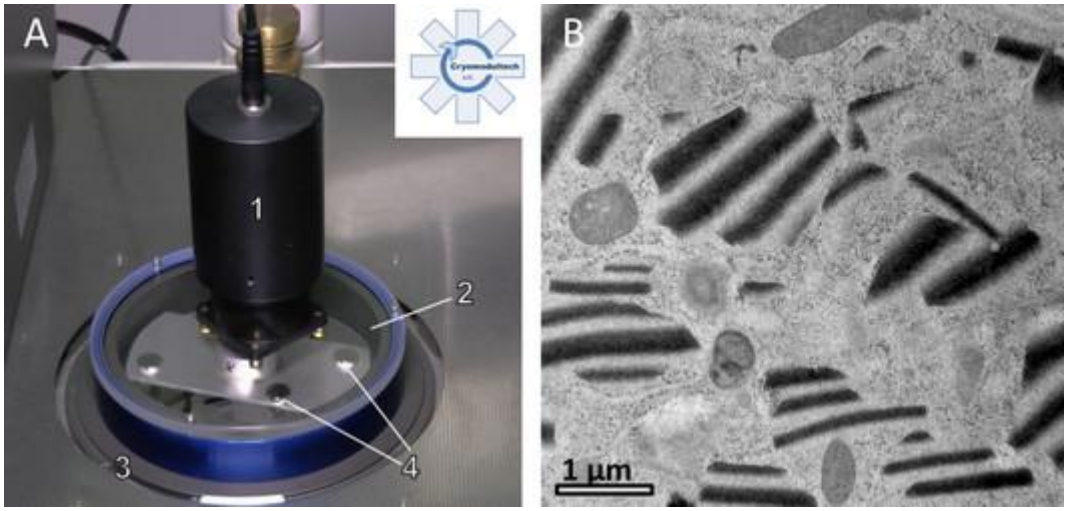

Figure 1. (A) Agitation module. The rotor, driven by a motor (1), runs between a Plexiglas lid (2) and the lid of the cryochamber (3). The agitation inside the chamber is induced by magnets (4). (B) Intracellular mesostructures preserved by FS under agitation (4).

I6. Advances in Instrumentation and Techniques (including aberration correction, low voltage SEM & TEM etc.)

INVITED LECTURES I6:

Universal pressure scanning electron microscopy (UPSEM) - electron microscopy up to atmospheric pressure

Johannes Rattenberger (1), Harald Fitzek (2), Tobias Achtsnit (1), Hartmuth Schroettner (3)

1) Graz Centre for Electron Microscopy (ZFE), Steyrergasse 17, 8010 Graz, Austria

2) Institute of Electron Microscopy and Nanoanalysis (FELMI), Graz University of Technology, Steyrergasse 17, 8010 Graz, Austria

3) Graz Centre for Electron Microscopy (ZFE)

4) Institute of Electron Microscopy and Nanoanalysis (FELMI) Graz University of Technology, Steyrergasse 17, 8010 Graz, Austria

Keywords: ESEM, Low Vacuum SEM, high pressure applications, wetting experiments

The imaging gas inside a Low Vacuum (up to a few hundred Pascal chamber pressure) or Environmental Scanning Electron Microscope (ESEM) (up to a few thousand Pascal chamber pressure) suppresses negative charging and prevents outgassing of the sample. With such a system electrically insulating, biological and even liquid samples as well as wetting experiments can be performed (1). The negative side effect of the imaging gas is the poor image quality. Electron scattering processes and an insufficient secondary electron detection system decrease the signal to noise ratio with increasing chamber pressure. As a result these experiments must be done at lowest possible pressure, high electron energies, long dwell times and large electron beam currents. However, recent publications on high pressure capabilities of state of the art microscopes have shown that they are working far away from physical limits and that there is plenty of room for improvements (2). The key to high image quality at high pressures is to reduce primary beam scattering as far as possible while maintaining ideal operation conditions for the secondary electron detector (3). In the FEI Quanta series ESEMs the gaseous environment in the sample chamber is separated by two Pressure Limiting Apertures (PLA) and a differential pumping system from the high vacuum

inside the electron column. Nevertheless, a lot of gas streams through the PLA upwards and a significant amount of electrons are lost for imaging before the beam is entering the sample chamber. Based on the insights of Monte Carlo and finite element simulations a new aperture holder was designed that significantly reduces primary beam scattering and increases image quality. In most of the state of the art ESEMs the secondary electron detector is a flat positively biased electrode positioned sideways or directly at the end of the pole piece. Secondary electrons are attracted and accelerated by the electric field of the detector and on their way through the gas collision ionization amplifies the signal. With increasing pressure the amplification efficiency decreases because secondary electrons do not gain enough energy between collisions to ionize the gas. However, nearby a needle detector with very small tip radius (R < 10 µm) the electric field is strong enough for amplification even at very high chamber pressure and by positioning the needle on the sample table it operates at ideal conditions regardless of pressure and working distance. A by-product of this design is that the conventional position of the backscatter electron detector (BSE) at the end of the column is no longer blocked by the SE detector. With this optimized high pressure design the limits of conventional ESEM technology can be crossed. Imaging at higher chamber pressures up to one atmosphere (see figure 1), investigations of living organisms (see figure 2) and much more are possible.

References:

1. Danilatos, G.D, Adv. Electron El. Phys. Vol. 71 (1988) 109-250

2. Danilatos G., Rattenberger J., Dracopoulos V., J. Microsc. Vol. 242 (2011) 166-180

3. Fitzek H., Schroettner H., Hofer F., Rattenberger J., J. Microsc. (2016) 85–91

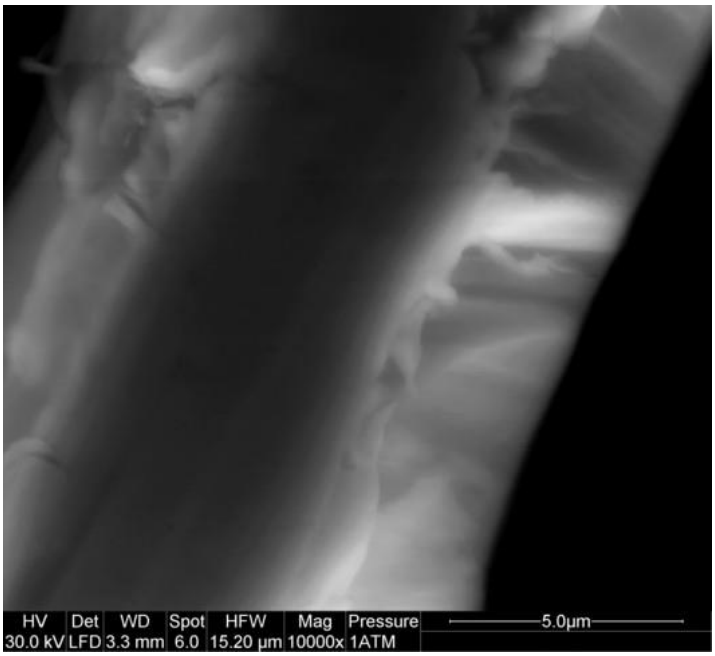

Figure 1. Copper wire (@ atmospheric pressure)

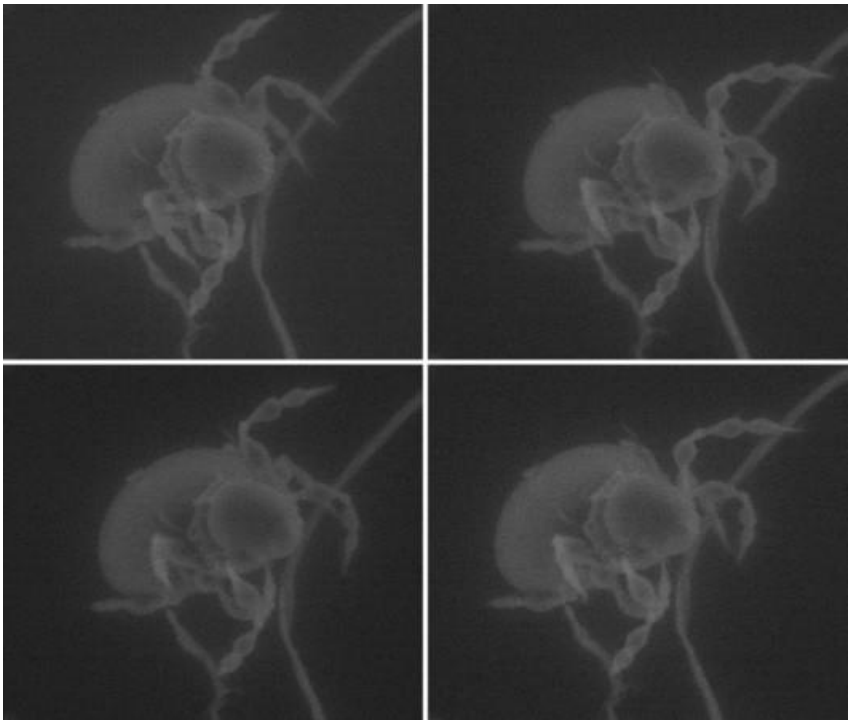

Figure 2. Images of a living mite

Towards atomic-scale studies of nucleation and growth of matter by *in situ* (scanning) transmission electron microscopy

Rolf Erni (1), Yucheng Zhang (1), Trond Henninen (1), Debora Keller (1)

1) Electron Microscopy Center, Empa – Swiss Federal Laboratories for Materials Science and Technology, 8600 Dübendorf, Switzerland

Keywords: fast STEM, atom dynamics, clusters, liquid cell

Solid matter is formed by the agglomeration of individual atoms, molecules or ions. This nucleation step triggers the subsequent growth process which eventually defines the macroscopic crystal, its morphology and properties. Proper understanding of both, the nucleation and the growth process, can provide crucial information on how the formation of solids can be controlled and modified, such that even thermodynamically unfavorable atomic structures could be synthesized with physical properties tailored to fulfill given tasks. Recently implemented *in situ* transmission electron microscopy methods have enabled to study such processes, even in environments which are close the ones used for (nano-)materials syntheses. We employ two approaches to study the onset and growth of crystalline matter formation. In the first approach we gently deposit individual Pt atoms on carbon membranes and study at high spatial and temporal resolutions how the atoms start to agglomerate and form clusters. The high temporal resolution, we achieve with an unconventional STEM approach, enables the study of atoms and cluster in almost real time, and at low electron doses. It is found that Pt atoms at room temperature stay largely unconnected and that only after a thermal excitation to above 300°C the atoms start to build rather stable cluster configurations which, however, deviate from the expected bulk structure. In the second approach, we employ the electron beam to induce reduction reactions of Ag- and Au-ions in liquid cell. It is found that the electron dose can be adjusted to favor either a facetted or a cauliflower-type of nano-particle morphology. Similar findings can be found in literature (see, e.g. (1)). Moreover, in the case of Pb-ions we observe that the growth mode is largely independent from the electron dose, but that when beam exposure is stopped, a change of particle morphology occurs “in the dark”. A key factor to understand these experiments is the

electron dose which essentially triggers nucleation and growth. Radiation chemistry is of outmost importance for such reactions in liquid cells. However, it is shown that at enhanced dose rates, which might be necessary for atomic-scale observations in liquid cells, a full understanding of the reaction process also needs to consider a substantial thermal effect, which is particularly due to elastic electron-atom interactions (2).

Acknowledgements:

This research is supported by the European Research Council (ERC) under EU's Horizon 2020 program (grant agreement No. 681312).

References:

1. T. J. Woehl et al., ACS Nano 6 (2012) 8599.

ORAL PRESENTATIONS I6:

Measuring the orbital angular momentum spectrum of an electron beam

Vincenzo Grillo (1), Amir H. Tavabi (2), Federico Venturi (3), Hugo Larocque (4), Roberto Balboni (5), Gian Carlo Gazzadi (6), Stefano Frabboni (7), Peng-Han Lu (2), Erfan Mafakheri (8), Frédéric Bouchard (4), Rafal E. Dunin-Borkowski (2), Robert W. Boyd (9), Martin P. J. Lavery (10), Miles J. Padgett (10), Ebrahim Karimi (11)

1) (a) CNR-Istituto Nanoscienze, Centro S3, Via G Campi 213/a, I-41125 Modena, Italy (b) CNR-IMEM Parco Area delle Scienze 37/A, I-43124 Parma, Italy

2) Ernst Ruska-Centre for Microscopy and Spectroscopy with Electrons, Forschungszentrum Jülich, Jülich 52425, Germany

3) (a) Dipartimento FIM Università di Modena e Reggio Emilia, Via G Campi 213/a, I-41125 Modena, Italy (b) CNR-Istituto Nanoscienze, Centro S3, Via G Campi 213/a, I-41125 Modena, Italy

4) Department of Physics, University of Ottawa, 25 Templeton St., Ottawa, Ontario, K1N 6N5 Canada

5) CNR-IMM Bologna, Via P. Gobetti 101, 40129 Bologna, Italy

6) CNR-Istituto Nanoscienze, Centro S3, Via G Campi 213/a, I-41125 Modena, Italy

7) (a) Dipartimento FIM Universita di Modena e Reggio Emilia, Via G Campi 213/a, I-41125 Modena, Italy (b) CNR-Istituto Nanoscienze, Centro S3, Via G Campi 213/a, I-41125 Modena, Italy

8) Dipartimento FIM Università di Modena e Reggio Emilia, Via G Campi 213/a, I-41125 Modena, Italy

9) (a) University of Ottawa, 25 Templeton St., Ottawa, Ontario, K1N 6N5 Canada (b) Institute of Optics, University of Rochester, Rochester, New York, 14627, USA

10) School of Physics and Astronomy, Glasgow University, Glasgow, G12 8QQ, Scotland, UK

11) (a) Department of Physics, University of Ottawa, 25 Templeton St., Ottawa, Ontario, K1N 6N5 Canada (b) Department of Physics, Institute for Advanced Studies in Basic Sciences, 45137-66731 Zanjan, Iran

Keywords: Orbital angular momentum, electron beam shaping, electron holography, OAM states sorting device, magnetic measurement

We here propose, design, and demonstrate the performance of a device capable of measuring the azimuthal wavefunction of an electron beam, i.e. its orbital angular momentum (OAM) content. Our device consists of two phase masks fabricated by focused ion beam (FIB) (1), shown in Figure1a, that are placed inside a transmission electron microscope (TEM) and used to analyse the beam. The two phase masks, also referred to as holograms, are named “Sorter” and “Corrector” and are positioned in sample and selected area diffraction aperture position respectively, as reported in Figure1b. The device analyses an arbitrary electron beam as follows: the first hologram (Sorter) performs a conformal mapping from log-polar to Cartesian coordinates, unwrapping the azimuthal phase variations due to OAM into intensity variations along one Cartesian coordinate. The second hologram (Corrector) corrects the phase distortions introduced by the Sorter, and is placed in its reciprocal plane. The result of this process is a spatial representation of the azimuthal phase components of the initial beam. There, the different positions along one Cartesian direction correspond to different OAM values, and the beam intensity at each position, integrated along the orthogonal direction, corresponds to the relative magnitude of the various $|c|^2$ coefficients of the decomposition in the OAM basis. We employed this device to sort pure and superposition OAM states of electrons that were generated by binary phase masks, ranging within OAM values of -10 and 10 as illustrated in Figure2a-d. This set of measurements served as a calibrating procedure for the device, setting up a correspondence between various spatial positions and different OAM values. This implementation, though similar to its light optical counterpart (2), can also unveil further information of materials by harnessing the interactions that are distinctive of electrically charged particles. In particular, we employed the device for the analysis of the OAM spectrum of electrons affected by a micron-scale cobalt magnetic dipole as in Figure2e. A magnetic dipole introduces a phase term proportional to its magnetic moment according to the equation $g(r,\varphi)=exp[i\chi(r)sin\varphi]$ where $\chi(r)=(e\mu_0 M)/(hr)$. With the sorting device, it has been possible to acquire the OAM spectrum and to recover the magnetic moment of this cobalt dipole, obtaining a good agreement with the estimated value. It is worth noticing that the result is obtained directly in the OAM space. Further developments of our device could aim to overcome the absorption due to the holograms, for instance by using structured electrostatic fields (3), and the use for atomic scale measurements or with scanning-TEM.

Acknowledgements:

V.G. acknowledges the support of the Alexander von Humboldt Foundation. We thank P. Pingue and F. Carillo for the access to the lithography facility of CNR. Nest in Pisa (Italy). S.F. and F.V. thanks the University of Modena and Reggio Emilia for the grant FAR-2015-Project Title: Computer Generated Holograms for the realization and analysis of structured electron waves. The research leading to these results has received funding from the European Research Council under the European Union's Seventh Framework Programme (FP7/2007-2013)/ ERC grant agreement number 320832. E.K. and A.S. acknowledges the support of the Canada Research Chairs (CRC) and Canada Foundation for Innovations (CFI) Programs.

References:

1. V. Grillo et al., Appl. Phys. Lett. 104, 043109 (2014).

2. G. C. Berkhout et al., Phys. Rev. Lett. 105, 153601 (2010).

3. B. J. McMorran et al., New J. Phys. 19 023053 (2017).

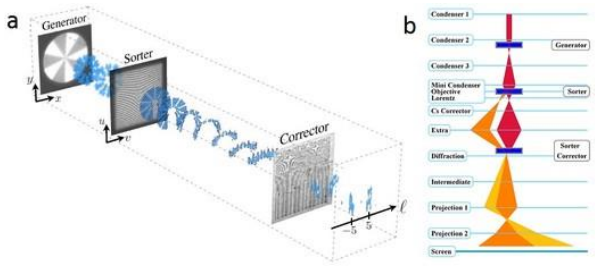

Figure 1. Experimental scheme of the OAM measuring device. (a) Sketch of the three phase masks, generator, sorter and corrector, and their effect on the beam; and (b) ray diagram and mask positioning inside the TEM.

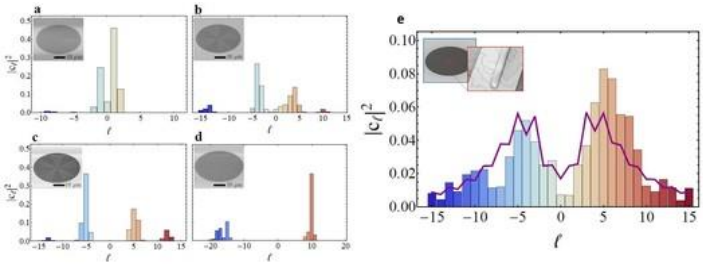

Figure 2. Generator masks and respective spectra measured with the sorter device of L=1 (a), L=±4 (b), L=±5 (c), L=10 (d) OAM, and cobalt dipole (e). The solid line in (e) refers to the theoretically calculated spectrum.

EELS experiments influenced by the CMR effect

Wolfgang Wallisch (1), Michael Stöger-Pollach (1), Stefan Löffler (1), Edvinas Navickas (1)

1) University Service Center for Transmission Electron Microscopy, Technische Universität Wien, Wiedner Hauptstraße 8-10, 1040 Wien, Austria

Keywords: CMR, VEELS, EMCD, band gap, low loss

For a wide range of applications, double perovskites are promising candidates due to their structural, physical and electronic properties. The La_2CoMnO_6 (LCM) composition exhibits a huge negative magnetoresistance (1), which is known as colossal magnetoresistance (CMR). The CMR effect is an interesting consequence of a metal-insulator transition, which describes the change of the resistance in the presence of a magnetic field. Transmission electron microscopes (TEMs) equipped with energy filters are powerful tools and their main advantage for probing band gaps is the high spatial resolution. It is primarily limited by the inelastic delocalization and the excitation of Čerenkov light (2). In the low energy part of the electron energy loss spectrometry (EELS) spectrum the optical properties and band gaps can be investigated by a technique called valence EELS (VEELS). An additional advantage of TEM is the opportunity to detect energy loss magnetic chiral dichroism (EMCD) with high spatial resolution and chemical sensitivity (3). In this study, the influence of the CMR effect on the EELS signal is shown. The change of the band structure in the low losses caused by the CMR effect and the magnetic behaviour of the material are measured. Different LCM thin film layers are investigated to ensure the reproducibility of our evaluation. The experimental results are confirmed by density functional theory (DFT) calculations. The preparation of the LCM thin films are done by pulsed laser deposition. The LCM layers are epitaxially grown on different substrates, $SrTiO_3$ and $LaAlO_3$. The cross section specimens for the TEM analysis are prepared by focused ion beam milling and the analytical TEM investigations are performed by using two TECNAI TEMs. In order to study the influence of the CMR effect, the magnetic field and the temperature are varied. The EMCD experiments are performed in the classical scheme to achieve a three-beam diffraction geometry. By considering the theoretical aspects, the experimental results are supported by DFT calculations using the WIEN2k code. In Figure 1A

the 40 keV and the 200 keV spectra are shown at a temperature of 85 K and a difference in the energy loss range of 1.5 eV to 4 eV is observed. An intensity variation caused by the CMR effect is detected by 40 keV VEELS spectra at different temperatures (Figure 1B). The chemical sensitivity of EMCD is shown in Figure 2. The EMCD effect can be observed at the Co L-edge (779 eV) in the 85 K experiment, whereas the same edge at room temperature (RT) exhibits no EMCD effect. The consequences of the CMR effect on the band gap are detected by observing the LCM oxide.

Acknowledgements:

The authors kindly acknowledge financial support by the Austrian Science Fund (FWF, F4501-N16 and F4509-N16).

References:

1. Mahato, R. N., et. al. (2010) Journal of Applied Physics, 107, 09D714.

2. Stöger-Pollach, M. (2010) Micron, 41, 577-584. (3) Ennen, I., et. al. (2012) Journal of Magnetism and Magnetic Materials, 324, 2723-2726.

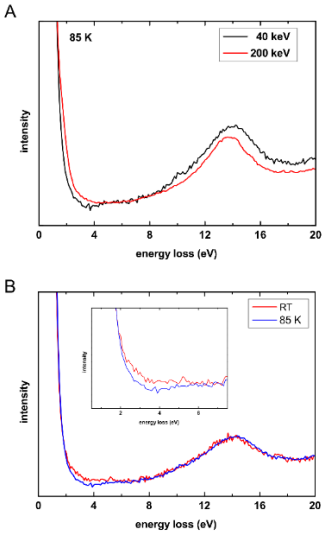

Figure 1. A) Unprocessed VEELS spectra recorded at 85 K using 40 keV and 200 keV. B) VEELS spectrum recorded at RT and 85 K using 40 keV. The insertion shows the difference between both spectra.

Superfast scintillators for SEM electron detectors

Petr Schauer (1), Ondřej Lalinský (1), Miroslav Kučera (2), Zuzana Lučeničová (2)

1) Institute of Scientific Instruments of the CAS, Královopolská 147, 612 64 Brno, Czech Republic

2) Charles University, Faculty of Mathematics and Physics, 121 16 Prague, Czech Republic

Keywords: Electron detector, Scintillator, Multicomponent garnet film, Liquid phase epitaxy, Cathodoluminescence

Scanning electron microscopes (SEM) require a high-quality electron detector. Such an electron detector must primarily be very fast to process a large number of imaging data in real time. For example, for the acquisition of a high-quality image in a scanning electron microscope (SEM) in real time, it is usually required to process each pixel in less than 100 ns without a loss of contrast (1). If the mentioned electron detectors are to be formed by scintillation detection systems, they must be equipped with very fast scintillators having a short decay time (decay to 1/*e* value, where *e* is the base of natural logarithms) and low afterglow even at a microsecond time range after an excitation cut-off. The scintillator with the long decay time causes an image blur and the scintillator with the high afterglow reduces image contrast in the SEM. In the scintillation electron detectors, Czochralski grown single-crystal scintillators such as YAG:Ce and YAP:Ce, whose cathodoluminescence (CL) properties have been thoroughly studied, are commonly used. A disadvantage of most of these single-crystal scintillators is their excessive scintillation decay time (even longer than 100 ns for the YAG:Ce) and especially their relatively high afterglow (even about 1 % at 1 μs after the excitation). Thus, new materials and new growth technology resulting in faster decay and substantially reduced afterglow were sought. To obtain new superfast scintillators the liquid phase epitaxy (LPE) technique has been used for the growth of various multicomponent garnets. Two of these multicomponent single crystalline epitaxial garnet films were selected and their CL properties are presented in this paper. (1) LuGAGG:Ce, i.e. $(LuGd)_3(GaAl)_5O_{12}$:Ce film and (2) LuGAGG:Ce,Mg, i.e. Mg^{2+} co-activated $(LuGd)_3(GaAl)_5O_{12}$:Ce film were prepared, measured and studied. The YAG:Ce and YAP:Ce single crystals were used as reference specimens. CL decay characteristics of all

mentioned scintillators, measured using the CL apparatus (2), are shown in Figure 1. CL emission spectra including CL intensities of the mentioned scintillators, together with PMT sensitivities, are shown in Figure 2. An important result is that the new multicomponent garnet films have the afterglow 1 to 2 orders lower than the standard single-crystal scintillators. The decay time as low as 28 ns and the afterglow of only 0.02 % at 1 μs after the excitation predetermines the LuGAGG:Ce,Mg film scintillators for extremely fast electron detectors in SEMs where a somewhat reduced intensity can be expendable. If the scintillator efficiency is to be preferred, the LuGAGG:Ce film with the same efficiency as YAG:Ce and still the excellent decay time of 61 ns and the afterglow of only 0.10 % at 1 μs after the excitation is a better choice. Regarding the scintillator-PMT matching, for the both film scintillators a photocathode S20 with a cheap glass window can be used, which is a great advantage compared to the YAP:Ce single crystals.

Acknowledgements:

This research was supported by the CSF (project, GA16-05631S and GA16-15569S), MEYS CR (project LO1212), and EC and MEYS CR (project CZ.1.05/2.1.00/01.0017).

References:

1. J. Bok, P. Schauer, Scanning, 36 (2014), 384-393.

2. P. Schauer, Nucl. Instrum. Methods B, 269 (2011), 2572-2577.

3. J. Bok, P. Schauer, Rev. Sci. Instrum., 82 (2011), 113109.

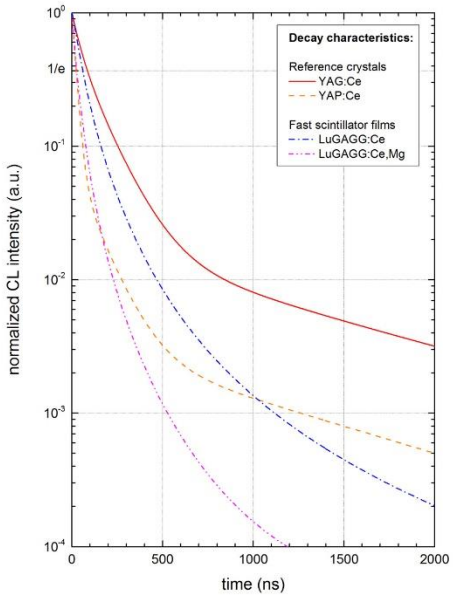

Figure 1. Cathodoluminescence decay characteristics of the LuGAGG:Ce and LuGAGG:Ce,Mg epitaxial film scintillators as well as of the YAG:Ce and YAP:Ce reference single crystal scintillators

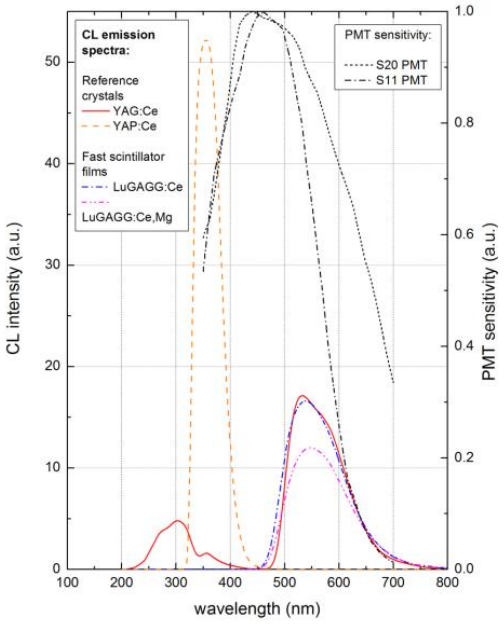

Figure 2. Cathodoluminescence emission spectra including the intensities of the LuGAGG:Ce and LuGAGG:Ce,Mg epitaxial film scintillators as well as of the YAG:Ce and YAP:Ce reference single crystal scintillators. PMT sensitivities are also plotted..

A Micro-combinatorial method for an efficient TEM study of binary films

György Sáfrán (1), Ildikó Cora (1), Zsolt Fogarassy (1), János Szívós (1), Miklós Fried (1), Peter Petrik (1), Tivadar Lohner (1), Miklós Serényin (1)

1) Centre for Energy Research, Intsitute for Technical Physics and Materials Science, H.A.S., Konkoly Thege M. út 29-33, H-1121 Budapest, Hungary

Keywords: micro combinatorial TEM, gradient films, all in one TEM grid

Phases of thin films may remarkably differ from those of bulk. Unlike to the comprehensive data files of Equilibrium Binary Phase Diagrams available for bulk, phase maps of thin binary layers are unrevealed, or incomplete! This is, mainly, due to the numerous metastable and instable phases feasible in thin films and the sophisticated techniques required for the analysis. For the systematic study of phases of such thin layers a micro-combinatorial method together with a device was developed and patented (1). It enables the deposition of a gradient sample onto a single TEM grid that is variable in its preparation parameters e.g. composition, background pressure, substrate temperature, amount of additives, etc. The main point is the deposition of binary samples with constantly evolving composition so that the transition region from 0 to 100% of one component i.e 100% to 0% of the other component is spread along a track of 1.5x1mm^2 in a single TEM grid (Figure 1). The actual composition at the area of interest can be measured by EDS (Figure2) or EELS, while the corresponding morphology and phases are studied by TEM and HRTEM imaging and electron diffraction methods, respectively. The method can be applied also for characterization of the samples by means of further analytical techniques e.g. Nanoindentation, AES and Ellipsometry. The effectivness is demonstrated by various (MnAl, SiGe) thin combinatorial samples. Obviously, the study of all possible phases of a binary system within a single TEM specimen is extremely efficient compared to the traditional “sample by sample” preparation and investigation. The remarkable save in the number of experiments, time and costs required for the investigations facilitates, remarkably, the search of binary phases and a reveal of composition-related properties of thin films.

References:

Hung. Patent No. P 15 00500 (2015).

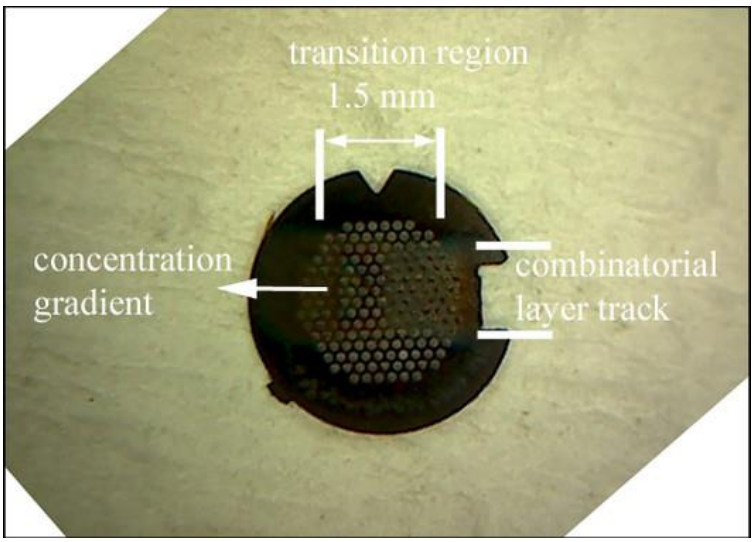

Figure 1. Mn-Al micro-combinatorial sample DC sputter-deposited on a TEM grid with a track of 1.5mm x 1mm for TEM characterization of all compositions in the 0-100% concentration range.

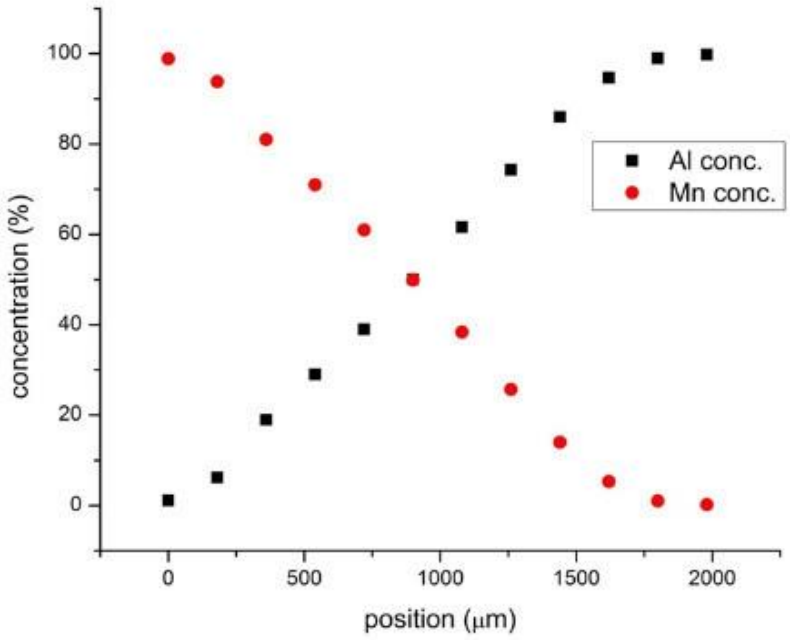

Figure 2. Concentration vs position curve of a Mn-Al micro-combinatorial sample measured in a TEM by EDS.

POSTER PRESENTATIONS I6:

Novel high vacuum heating for in situ experiments in FIB/SEM systems

Min Wu (1), Libor Novák (1), Petr Wandrol (1), Miroslav Kolíbal (2), Tomáš Vystavěl (1)

1) Thermo Fisher Scientific (FEI Czech Republic s.r.o.), Vlastimila Pecha 12, Brno 627 00, Czech Republic

2) CEITEC BUT, Brno University of Technology, Brno, Czech Republic, Antonínská 548/1, 601 90 Brno, Czech Republic

Keywords: novel *in situ* heating, EDS/EBSD, high vacuum, FIB/SEM

In situ heating experiments inside microscope chambers bear significant importance in investigating real-time dynamic behaviours of materials at elevated temperatures such as recrystallization, grain growth, and phase transformation. We present two new versatile *in situ* heating modules for FIB/SEM systems. These modules operate under high vacuum environment which brings significant advantages, such as achieving of optimal experiment cleanness, ultra-high SEM imaging and provide adaptable geometry for EBSD and EDS detection. A high vacuum heating stage designed for millimeter-sized samples can provide a heating rate up to 50°C per minute for temperatures up to 1000°C. The heating stage is fabricated using materials with negligible outgassing therefore can provide a high vacuum environment with chamber pressure in the order of 10^{-5} Pa. *In situ* SE/BSE imaging as well as EBSD and EDS signal collection can be obtained using standard detectors combined with dedicated heat shields. However, the EDS and EBSD acquisition is influenced by infrared radiation interference at temperatures above 600°C. This background can be reduced to minimum by employing a µHeater device. A novel µHeater based on microelectromechanical systems (MEMS) technology can achieve temperatures up to 1200°C at very high heating/cooling rates in the order of 10^4 degrees per second (1). This miniaturized heating chip is able to support nano-scale to sub-millimeter-sized samples (samples with dimensions in tens of µm are typically used). *In situ* observation of samples placed on the µHeater chip during

heating can be obtained using all types of detectors (2) including STEM, EBSD and EDS. The localised heating and small thermal mass capacity result in high uniformity of the heating area, high stability even during operations above 1000°C, site specification and minor sample displacement and drift stablilization, without introducing thermal radiation interference at elevated temperatures(1). Extraordinary image resolution can be attained at temperatures as high as 1200°C using the μHeater (see Figure1). *In situ* EDS maps collection above 1000°C has been achieved with standard EDS detector during heating of magnetite and hematite nanoparticles mixture, as shown in Figure2(a). Larger bulk-like samples with typical dimensions in the order of 10^2 μm can be first fabricated by FIB milling of the bulk, then *in situ* lifted out, welded on the μHeater chip and optionally the sample surface can be cleaned with low energy ions to enhance surface quality for diffraction studies. In Figure2(b) we present a sequential EBSD mapping of the grain evolution of a slightly deformed Ti6Al4V sample during *in situ* annealing at 1100°C on the micro-heating device in FEI DualBeam Helios G4 work station equipped with standard EBSD detector.

Acknowledgements:

The authors acknowledge funding from the Technology Agency of the Czech Republic, TE01020118.

References:

1. L. Mele et al., Microscopy Research and Technique 79 (2016), p.239.

2. L. Novák, J. Stárek, T. Vystavěl, L. Mele, Microsc. Microanal. 22 (Suppl. S3) (2016), p. 184.

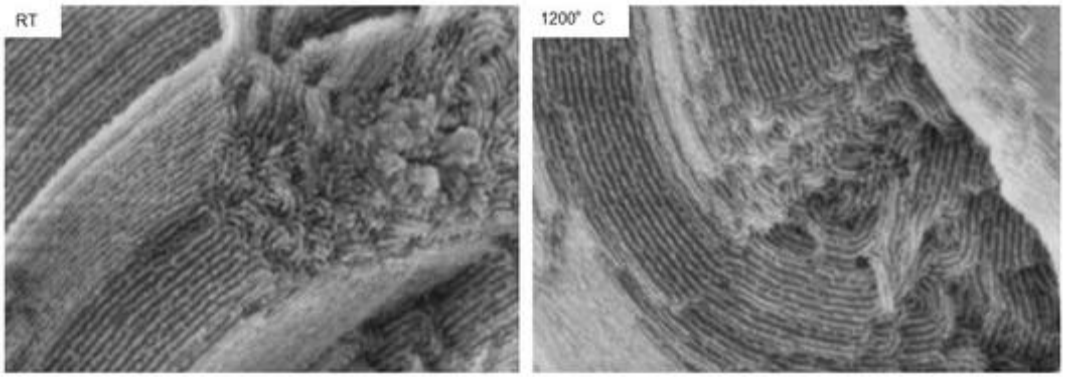

Figure1. SEM images of SBA15 nanoparticles on μHeater device at room temperature and at 1200°C. The horizontal field of view is 690nm.

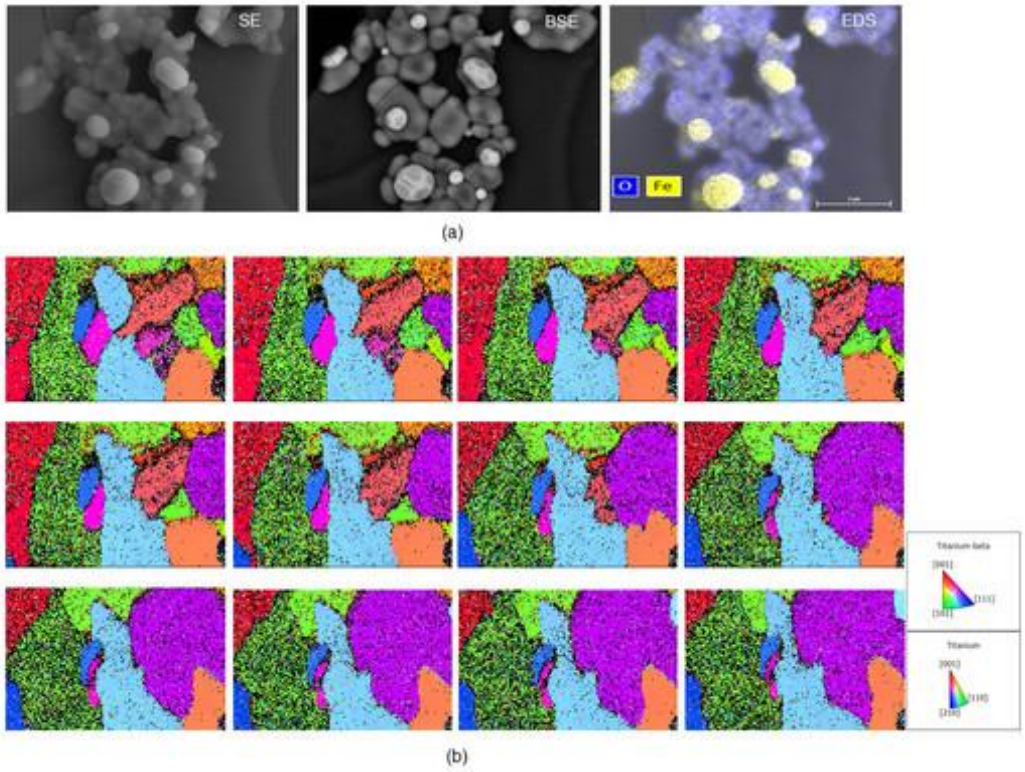

Figure 2. (a). Mixture of magnetite and hematite nanoparticles heated at 1030°C. Secondary electron image, backscattered electron image and EDS maps of iron and oxygen acquired simultaneously. The horizontal field of view is 8.1µm; (b). Sequence of 12 *in situ* EBSD IPFZ images of deformed Ti6Al4V alloys heated at 1100°C using the µHeater. The images were taken in 5 minutes intervals. The horizontal field of view is 20µm.

STEM modes in SEM – simulations and experiments

Ivo Konvalina (1), Aleš Paták (1), Filip Mika (1), Ilona Müllerová (1)

1) Institute of Scientific Instruments of the CAS, Královopolská 147, 612 64 Brno, Czech Republic

Keywords: STEM detector, trajectory simulations, cathode lens, collection efficiency

The semiconductor STEM detector in the Magellan 400 FEG SEM microscope (www.fei.com) is used to detect transmitted electrons (TE) and allows observing samples in four imaging modes (1). Two modes of objective lens, namely HR (high resolution) and UHR (ultra high resolution), differ by their resolution and by the presence or absence of a magnetic field around the sample. If the deceleration mode is chosen, cathode lens (CL) field is added, and two further microscope modes can be obtained. The aim of this work is to study the trajectories of the TEs in each mode with regard to their angular and energy distribution. The HR and HR + CL mode is without magnetic field around the sample, for that reason the electrons retain their angular information. In addition, the electrostatic field between the sample and the STEM detector collimates the electrons towards the optical axis. We can detect TEs emitted at a large polar angles with respect to the optical axis. On the other hand, for UHR and UHR + CL modes, the sample is placed in a strong magnetic field. The electrons under the influence of the magnetic field have spiral trajectories and can cross the optical axis plane several times during their path to the detector, thus angular information is not simply interpretable. The Figure shows the highly oriented pyrolytic graphite (HOPG) displayed in all four microscope modes. In order for the images to be comparable, the energy of the electrons incident on the sample is always 4 keV, we observe the same sample field of view and we do not change the setting of the detection parameters (contrast, brightness, etc.). In cathode lens mode, we have more signal in the final image. In the right part of the micrograph there is an illustration of trajectories of transmitted electrons with energy of 4 keV and 400 eV. TEs are emitted from the center of the sample, the polar angle varies from 0° to 90° in 10° increments. From the simulated trajectories we can determine acceptance diagrams of the STEM detector. We use EOD program (2) for magnetic and electrostatic field calculations and raytracing. If we consider the

measured transmissivity (T_M) of the sample in each mode, we see how it affects the final image. For HR and HR + CL the measured transmissivity is 7.5% and 43.3% respectively. For UHR and UHR + CL it is 13.8% and 28.2% respectively. The significant increase of the transmissivity in the modes with CL is due to the change in the intensity of the maximum image intensity; which is proportional to the beam current going through the hole in the sample. The simulation results show that for UHR and UHR + CL, the collection efficiency (CE) is 100%. CE of elastically transmitted electrons is for HR and HR + CL mode 52% and 61%, respectively.

References:

1. F. Mika et al., Microscopy and Microanalysis 21 (2015) 66-71.

2. J. Zlámal et al., Nucl. Instr. Meth. Phys. Res. A 645 (2011) 278-282.

3. The work is supported by the TA CR (TE01020118).

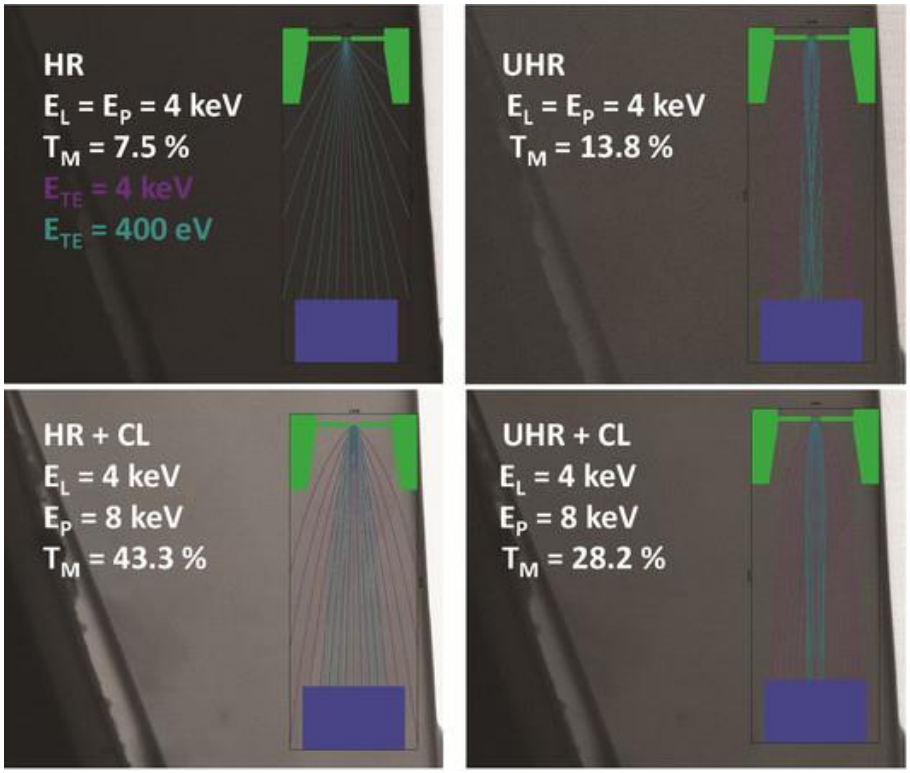

Figure 1. STEM images of HOPG taken by the STEM detector in four modes (EL – landing energy, EP – primary beam energy, TM – measured transmissivity). Trajectories of elastically TEs (ETE = 4 keV) and nonelastically TEs (ETE = 400 eV) are enclosed.

New approaches for reducing charging effects– TESCAN S8000

Michal Petrov (1), Samuel Záchej (1), Petr Sytař (1), Rostislav Váňa (1)

1) TESCAN Brno, s.r.o., Libušina tř. 1, Brno, Czech Republic

Keywords: charging artefacts, insulating samples, low energy

Sample charging is the cause of the most common artefacts that reduce image quality in scanning electron microscopy (SEM). This is especially true for non-conductive samples. Approaches used to suppress these artefacts are often time consuming or entail a trade off with respect to resolution. With TESCAN's new microscope – TESCAN S8000, comprising the innovative BrightBeam™ column, charging artefacts are suppressed by the design. This newly integrated technology is based on an electrostatic-magnetic lens, which filters away secondary electrons (SE) bearing the charging information from charge-free topographical back-scattered electrons (BSE). The resulting images are formed only from the topographic BSE signal, which does not include charging artifacts and is highly surface sensitive – see figure 1. Moreover, BrightBeam™ technology is built for operation at low energies, which also help to prevent charging of the sample. The low accelerating voltage also allows contrast variation and enhances surface detail sensitivity [1, 2]. Mitigation of charging artefacts on TESCAN S8000 is exceptionally effective and very easy to perform because it is a standard SEM operation in High Vacuum. Here we show how selecting the detected signal is important for imaging non-conductive biological samples. Apart from other biological and ceramic samples we took micrographs from different parts of a moth. In figure 1 a moth wing is displayed and the comparison of different signals is presented. Both images were taken simultaneously and charge mitigation with the preservation of topography is evident. The sample was imaged at 1kV in High Vacuum and without any coating. This is a clear demonstration of how TESCAN S8000 uses low-kV electron microscopy effectively for the high-efficiency SEM analyses of biological tissues, minerals, ceramics, composites, plastics and other non-conductive materials.

References:

I. Müllerová at al., Adv Imag Electron Phys 128 (2003), 128: 309–443. D.C. Joy at al., Micron (1996), 27.3: 247-263.

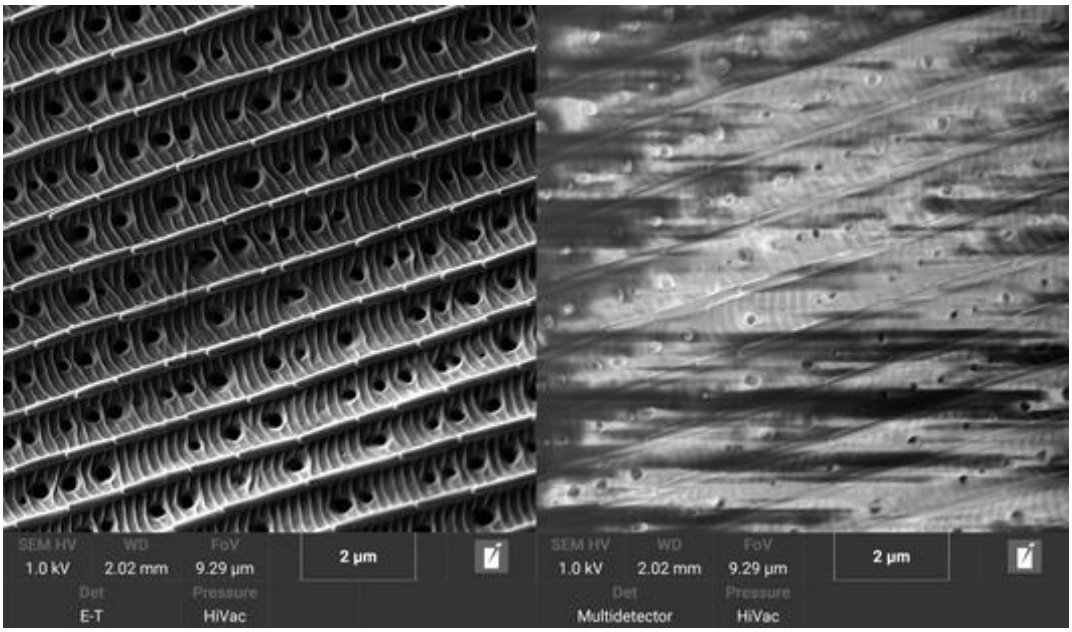

Figure 1: The comparison of micrographs of uncoated moth wing imaged by means of topographic BSEs (left) and SE signal (right).

Application of compressive sensing to multi-energy serial block-face SEM

Pavel Potocek (1), Milos Hovorka (2), Faysal Boughorbel (1), Tomas Janocko (2)

1) Thermo Fisher Scientific - Achtseweg Noord 5, Bldg 5651 GG, Eindhoven, The Netherlands
2) Thermo Fisher Scientific (FEI Czech Republic s.r.o.), Vlastimila Pecha 12, Brno 627 00, Czech Republic

Keywords: serial block-face scanning electron microscopy, virtual slicing, compressive sensing, radiation sensitivity, volume imaging

Serial Block-Face Scanning Electron Microscopy (SBEM) combines an *in situ* ultramicrotomy with electron microscopy to acquire large volumes of resin embedded specimens with a high resolution. Its potential has been recognized for tissue and cell biology, or in the observation of polymers, membranes, and metals. The technique relies on alternating the cutting of the specimen's surface, using a diamond knife, and electron signal detection to create a 3D image of a given specimen volume. A recent refinement of SBEM is using so-called virtual slicing, which is based on backscatter imaging at different electron beam energies, and enables the extension of z-resolution beyond physical cutting limits (1). In SBEM, the data acquisition step can be a time consuming process, depending on sample properties and the detection system. The cutting process and the reproducibly-achievable minimum slice thickness are, among other factors, constrained by the electron dose delivered by the primary electron beam. It is beneficial to further increase the data throughput, by decreasing the acquisition time, and also to reduce the electron dose to preserve the specimen integrity. One possible way is based on sparse data acquisition and processing strategies (2). We focused on the exploration of compressive sensing (CS) algorithms combined with appropriate sparse scanning schemes to improve the performance of the SBEM workflow. The full-frame image of the sample surface has been replaced by a sparse measurement matrix, obtained with an optimized scan strategy. The final image is reconstructed according to the CS principles. We present results from our comparison between standard full-frame acquisition and the CS approach to multi-energy SBEM. CS image quality and specimen radiation sensitivity have been investigated on stained mouse brain specimen embedded in resin.

Acknowledgements:

We would like to thank to TA CR, project TE01020118 for funding.

References:

1. Hovorka M. et al., The 16th European Microscopy Congress, Lyon, France.

2. Boughorbel F. et al., Microscopy and Microanalysis 2017, St. Louis, USA.

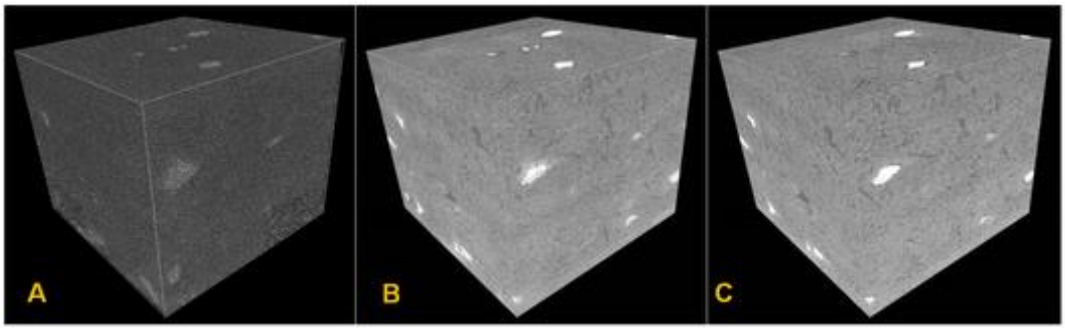

Figure 1. Comparison of standard full frame data acquisition and compressive sensing approach. (A) Large volume acquired with a sparsity of 20%; (B) CS reconstruction; (C) the full frame scanned volume of the same region. Data size: 100 µm x 100 µm x 80 µm.

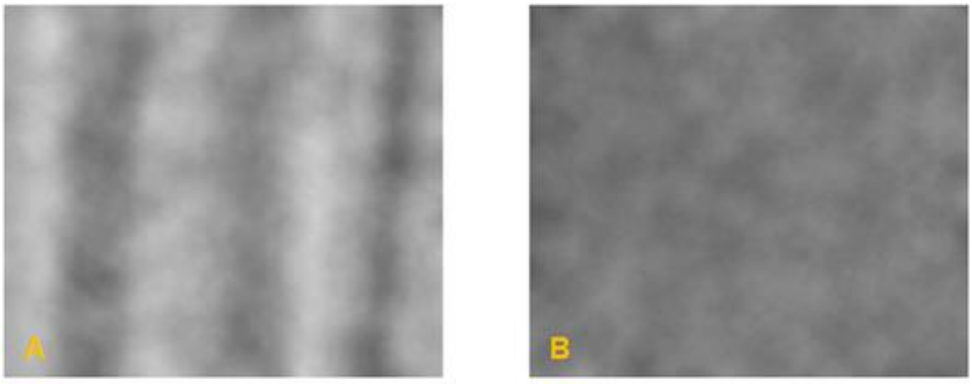

Figure 2. Radiation damage vs. cutting quality in overdosed condition. The images show height maps for the cut thickness of different regions of the same cut acquired by (A) full frame and (B) compressive sensing. The less variation the better cutting quality.

I7. Electron Spectroscopy, Diffraction and Analytical Microscopy

INVITED LECTURES I7:

Application of Concentric Electron Probe (CEP) method for accurate quantitative chemical analysis of interfaces on a sub-nanometer scale

Aleksander Rečnik (1), Thomas Walther (2) and Nina Daneu (1)

1) Jožef Stefan Institute, Jamova cesta 39, 1000 Ljubljana, Slovenia

2) Department for Nanostructured Materials, Jožef Stefan Institute, 1000 Ljubljana, Slovenia

3) Electronic and Electrical Engineering, University of Sheffield, Sheffield, United Kingdom

Keywords: TEM, quantitative analysis, 2D structures, quantum walls, interface chemistry

Understanding chemical and physical properties of interfaces in crystalline materials has always been the key issue in materials science. Due to the extremely low dimensionality of interfaces measuring their exact chemical composition remains to be a substantial analytical challenge. Together with phase and Z-contrast imaging at atomic resolution spectroscopic methods, *i.e.* energy-dispersive X-ray spectroscopy (EDS) or electron energy-loss spectroscopy (EELS), provide a valuable complementary information on the interface chemistry. One of the main drawbacks in quantification of EDS and EELS spectra is associated with determining the exact volume of analysis in transmission geometry. In most instances the fraction of analyzed interface within the volume of analysis is thus not precisely known leading to the erroneous interpretation of interface structure. Most common techniques for analyzing the interface composition are line profiling and spatial difference techniques. While the first is based on acquiring several spectra across the interface, spatial difference method relies on normalized difference between the spectrum acquired on the interface and the one recorded in bulk crystal close to that interface. Both techniques suffer from inaccurate estimation of the volume of analysis due to local thickness variations. To improve the accuracy and precision of quantitative analysis, we developed a new technique for measurement of chemical composition of interfaces at the atomic scale (1,2). The method is based on acquiring several EDS or/and EELS spectra with parallel electron probes placed directly on the analyzed interface. In order to eliminate the effect of sample thickness the probe is maintained concentric for all measurements, *i.e.* concentric electron probe (CEP) method. Using several examples

we will demonstrate that CEP method is approximately 10^2-times more precise and 10-times more accurate than spatial difference technique, allowing determination of down to ± 0.1 atoms/nm^2, depending on the type of the solute element that is measured in the interface plane. Because of its high precision we could extend the use of this method not only to accurately measure the amount of the trace element on the interface but also to determine complex solute distribution profiles in the interfacial region. Here we demonstrate implementation of CEP method on special interfaces such as twin, antiphase and inversion boundaries in sphalerite (ZnS), pyrite (FeS_2), spinel ($MgAl_2O_4$), bixbyite $(Mn,Fe)_2O_3$, zincite (ZnO) and rutile (TiO_2).

References

1. Rečnik A, Daneu N, Walther T, Mader W: *Structure and chemistry of basal-plane inversion boundaries in Sb_2O_3-doped ZnO*. J Am Ceram Soc **84** (2001) 2657-68.

2. Walther T, Daneu N, Rečnik A: *A new method to measure small amounts of solute atoms on planar defects and its application to IBs in ZnO*. Interface Science **12** (2004) 267-75.

3. Rečnik A, Zavašnik J, Jin L, Čobić A, Daneu N: *On the origin of 'iron-cross' twins of pyrite from Mt. Katarina, Slovenia*. Mineralogical Magazine **80** (2016) 937-948.

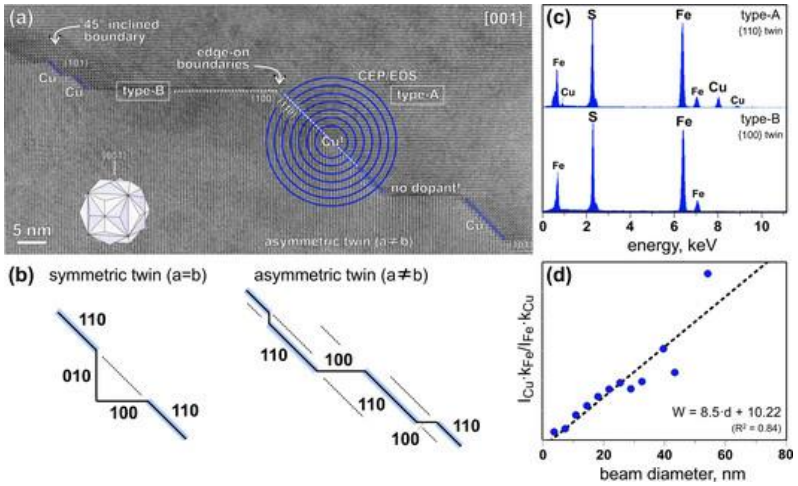

Figure 1. Application of CEP/EDS method on twin boundaries in pyrite (3). (a) TEM image of two types of twin boundaries in pyrite: type-A in {110} planes, and type-B in {100} planes. (b) Symmetric and asymmetric twin boundaries produced by linear combination of type-A and type-B twin boundaries. (c) EDS analysis of the twin boundaries. Only type-A twin boundaries are enriched with Cu, whereas type-B boundaries are pure. (d) Quantitative concentric electron probe EDS analysis (CEP/EDS) of type-A twin boundary; illustrated in.

PICO – application of chromatic aberration correction in materials science

Joachim Mayer (1,2), Juri Barthel (2), Lothar Houben (2), Maryam Beigmohamadi (1,2), Rafal E. Dunin-Borkowski (2) and Knut Urban (2)

1) Central Facility for Electron Microscopy, RWTH Aachen University, 52074 Aachen, Germany

2) Ernst Ruska-Centre for Microscopy and Spectroscopy with Electrons, Research Centre Juelich, 52425 Juelich, Germany

The invention of aberration correctors has revolutionized the development of TEM and STEM instrumentation. Only shortly after the development and installation of the first TEM with a corrector for the spherical aberration, commercial instruments with aberration correctors are now offered by all major manufacturers. In order to provide a platform for these novel developments and based on the experience with the first aberration corrected TEM, Research Centre Juelich and RWTH Aachen University have jointly founded the Ernst Ruska-Centre for Microscopy and Spectroscopy with Electrons (ER-C). At the Ernst Ruska-Centre we have recently installed the FEI Titan 60-300 PICO. PICO is a fourth-generation transmission electron microscope capable of obtaining high-resolution transmission electron microscopy images approaching 50 pm resolution in the C_C- and C_S-corrected mode at 300 keV. It is currently one of only two microscopes in the world capable of chromatic aberration correction (1,2). In the present contribution we will report on the initial results obtained with the PICO instrument (Figure 1a). In the PICO instrument, HRTEM images can be obtained with simultaneous correction of the spherical and the chromatic aberration. Furthermore, a spherical aberration corrector also exists in the illumination system for Cs-corrected STEM imaging. The blurring caused by the chromatic aberration C_c is proportional to the aperture angle θ, the energy spread ΔE and inversely proportional to the primary electron energy E. The benefits of chromatic aberration corrected imaging are thus particularly large for HRTEM imaging at low accelerating voltages and for energy filtered (EFTEM) imaging with large energy window width. In the present contribution we will focus on these two applications and will present results from our recent work (3), Figure 1b.

References:

1. H. Rose, Philos.Trans.R.Soc.A: Math.Phys.Eng.Sci. 367(2009)3809–3823.

2. M. Haider, P.Hartel, H.Müller, S.Uhlemann, J.Zach, Microsc.Microanal. 16(2010)393–408.

3. K. Urban, J. Mayer, J. Jinschek, M. J. Neish, N. R. Lugg, and L. J. Allen, PRL 110, 185507 (2013)

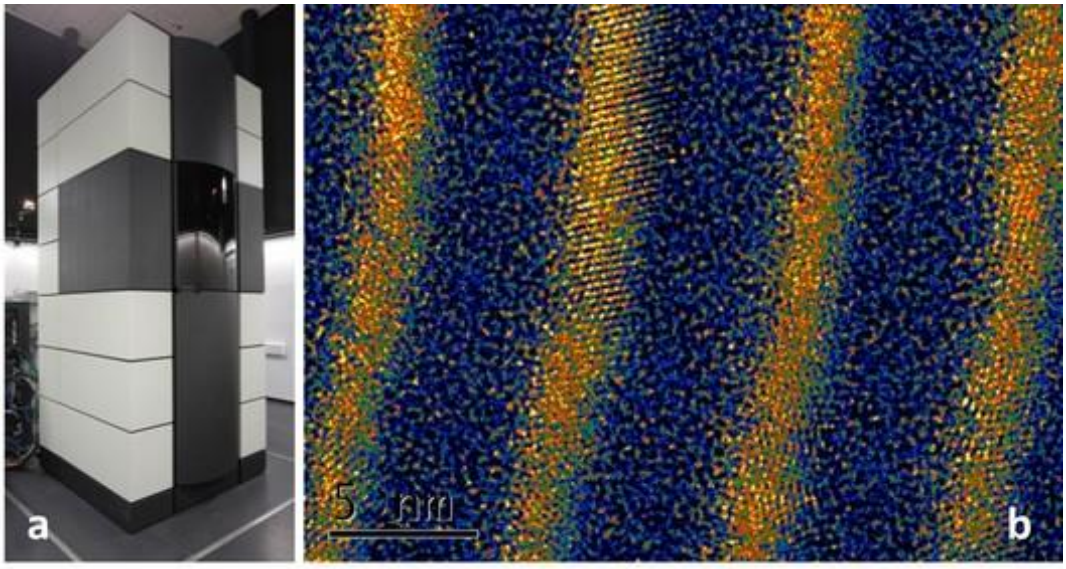

Figure 1. The PICO instrument and an EFTEM map of the Si distribution in a multi-quantum-well solar cell.

ORAL PRESENTATIONS I7:

Electron diffraction rietveld analysis of nanocrystals ensemble

Andrea Serafini (1), Francesca Tana (1), Luca Lutterotti (2), Silvia Gross (3), Luigi De Nardo (1), Stefano Gialanella (2)

1) Politecnico di Milano, Piazza Leonardo da Vinci, 32, 20133 Milano - Italy

2) University of Trento, via Calepina, 14 - I-38122 Trento, Italy

3) ICMATE-CNR, Università degli Studi di Padova

Keywords: Electron diffraction, Rietveld method, nanograins, size-strains, quantitative analysis

Transmission Electron Microscopy (TEM) is one of the most effective experimental technique for the analysis of nanostructured systems. TEM is commonly employed for the investigation of nanoparticles, allowing to characterize grain size and other microstructural features down to sub-nanometric scale. For this purpose, diffraction contrast imaging, based on bright field (BF) and dark field (DF) images, is particularly useful. However, if a strong overlap of the diffracted components does exist there might be some limitation. In particular, diffraction contrast may fail in the presence of agglomerated aggregates of nanoparticles, and multiphase nanocrystalline systems. An alternative method is proposed herewith, and relies on the attainment of the microstructural information directly from the Selected Area Electron Diffraction (SAED) patterns, following a procedure adopted with other diffraction methods, like XRD and neutron diffraction, using a full-pattern fitting approach (1,2), based on the Rietveld method. To test advantages, limitation and possible developments of the proposed approach two cases of study are presented herewith: 1) a two-phase nanostructured system composed by zinc sulfide (ZnS) and zinc oxide (ZnO) shown by Figure 1; 2) nanocrystalline powders of zirconia (ZrO_2) exhibiting the co-presence of the monoclinic and tetragonal polymorphs as shown in Figure 2. Both systems represent appropriate test samples for the proposed approach, since both exhibit homogenous electron diffraction rings without any graininess, which is a basic requirement to obtain reliable results. The conversion from two-dimensional to one-dimensional pattern, the correction of the electron diffraction pattern misalignment and

the determination of the instrumental broadening function were all performed using the MAUD software (3). The crystallite size and relevant shapes were successfully evaluated. The excellent results obtained in the microstructural characterization of the nanostructured multiphase samples demonstrate the capabilities of this approach, that may represent a fully quantitative method for the routine characterization of crystalline nanomaterials, even when a very limited amount of sample is available. This study also shows the possibility of attaining phase identification and quantification at a nanoscale level. Other advantages for electron diffraction acquisition are: fast data collection times: few seconds are necessary for the SAED pattern acquisition; possibility of combining the electron diffraction data not only with images but also with chemical compositions, obtained by Energy Dispersive X-ray Spectrometry (EDXS) and/or Electron Energy Loss Spectroscopy (EELS), that can be all integrated in a combined data analysis approach.

References:

1. A. Serafini et al., Powder Diffr. (2017) 1–6.

2. P. Boullay et al., Acta Crystallogr. Sect. A, Found. Adv. 70 (Pt 5), (2014) 448–456.

3. L. Lutterotti, Zeitschrift fur Krist. Suppl. 1 (26), (2007) 125–130.

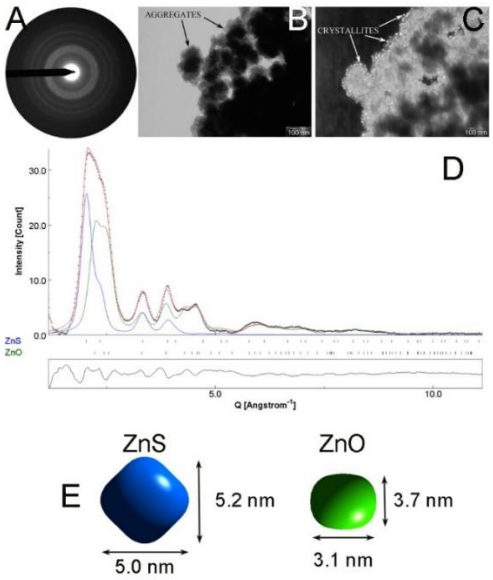

Figure 1. TEM characterization of ZnS/ZnO powders: A) SAED pattern; B) BF micrograph; C) DF micrograph; D) Rietveld analysis of 1-dimensional SAED intensity profile. E) extracted crystalline domains size and shape.

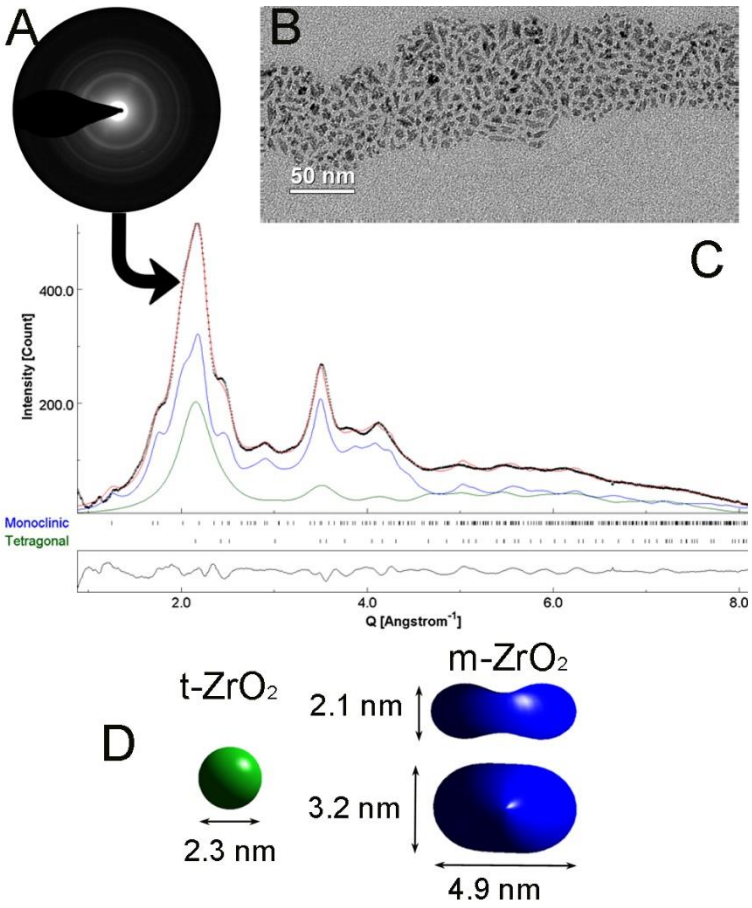

Figure 2. TEM characterization of ZrO2 powders: A) SAED pattern; B) BF micrograph; C) Rietveld analysis of 1-dimensional SAED intensity profile. Dot line: experimental profile; red line: calculated profile; D) extracted crystalline domains size and shape.

How sample holder geometries influence the quantification of X-ray spectra

Judith Lammer (1), Johanna Kraxner (1), Georg Haberfehlner (1), Gerald Kothleitner (2), Werner Grogger (2)

1) Graz Centre for Electron Microscopy, Steyrergasse 17, 8010 Graz, Austria.

2) Institute of Electron Microscopy and Nanoanalysis, Graz University of Technology, Steyrergasse 17, 8010 Graz, Austria

Keywords: EDX quantification, analytical STEM, Super-X, detector position, shadowing

Large area sensors and multi-detector systems have substantially improved X-ray spectrometry in (scanning) transmission electron microscopes in the last decade. Thanks to this increase in collection efficiency, even signals from single atoms have become detectable. Nevertheless, correct compositional analysis remains challenging and requires reliable parameters for ionization cross sections, the amount of absorption or for the shadowing effects from the sample holder [1, 2]. In this work, we focus on shadowing and show how different sample holders influence the quantification using a ChemiSTEM system (Super-X) on an FEI 60-300 Titan³ microscope. We compare the results of two FEI low background double tilt high visibility holders (an old and a new design, shown in Figure 1) and tomography holders. In order to do this, we determined the detector positions in the microscope chamber in terms of elevation angle and distance (3). For this purpose, we measured the X-ray intensities on each detector as a function of specimen tilt angle α and compared them to simulations, where we varied the detector positions such that deviations to the experimental data were minimal. For the simulations we generated realistic geometric models of the TEM holders by X-ray computed tomography (CT) and calculated shadow images for different detector positions in the 3D modelling program CINEMA 4D (by MAXON Computer GmbH). The sample used was an Au-Pd thin film deposited on a silicon nitride membrane grid. We noted that shadowing also depends on the X-ray energy (see Figure 2). Even at zero degree tilt, the detector illumination for the total of all four detectors did not always reach 100%, especially when it came to low X-ray energies. This is caused by the Beryllium specimen carrier inside the holder, which appears

fully transparent for high enough X-ray energies (e.g. Au-L), but partially blocks low-energy X-rays. Therefore, the amount of shadowing depends not only on tilt angles and specimen positions, but also on the X-ray energy, which can introduce significant errors upon quantification of both low- and high-energy X-ray lines. This method provides a means to determine accurately the positions of different X-ray detectors in a multi-detector system. The knowledge about the geometric arrangement of sample, sample holder and EDX detectors is paramount for a better understanding of the EDX system setup but also enables a post-experiment correction to quantitative results.

Acknowledgements:

We greatly acknowledge the help of Dr. Bernd Oberdorfer, Austrian Foundry Research Institute (ÖGI), Leoben, Austria for performing the X-ray tomography experiments. The authors also want to thank the Austrian Research Promotion Agency FFG (project 850220) for funding.

References:

1. T. J. A. Slater et al., Ultramicroscopy 162 (2016), 61–73.

2. W. Xu et al., Ultramicroscopy 164 (2016), 51–61.

3. J. Kraxner et al., Ultramicroscopy 172 (2017), 30–39.

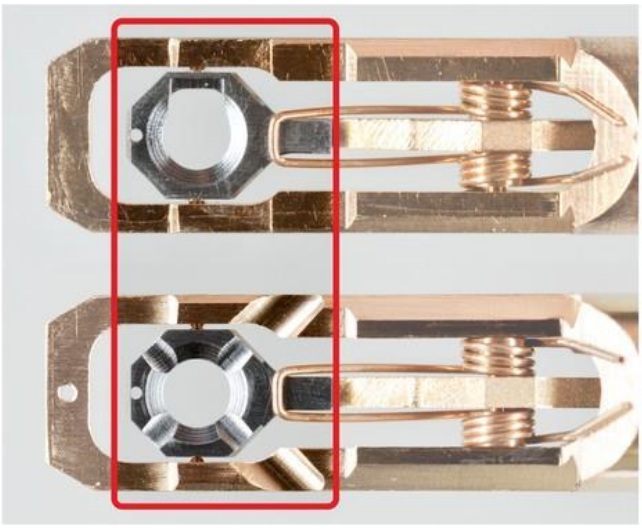

Figure 1. FEI low background double tilt high visibility holders: The old holder (top) and the newly designed holder (bottom) differ from each other in the shape of the beryllium and brass part (highlighted in red).

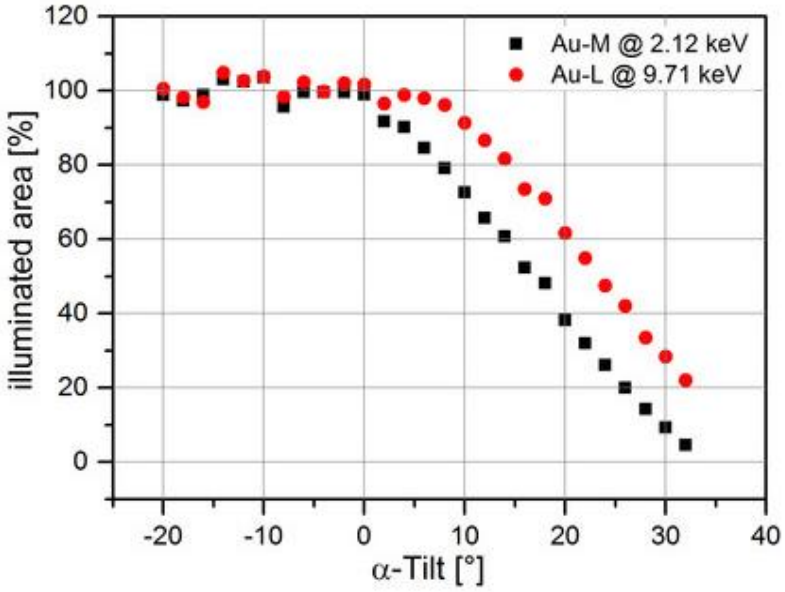

Figure 2.: Relative intensity values measured with detector Q4: The shift between the data points of a low-energy line (Au-M @ 2.12 keV) and a high-energy line (Au-L @ 9.71 keV) is caused by absorption within the Be specimen carrier.

Examination of strain evolution during micropillar compression with HR-EBSD

Szilvia Kalácska (1), Zoltán Dankházi (1), Dávid Ugi (1), Péter Dusán Ispánovity (1), István Groma (1)

1) Eötvös Loránd University (ELTE, Department of Materials Science, Pázmány Péter sétány 1/a., Budapest, Hungary

Keywords: micropillar compression, strain evolution, HR-EBSD

The understanding of the mechanisms occurring during plastic deformation of crystalline materials is in the focus of materials science research. In the last decade one of the remarkable results of plasticity was that plastic deformation of crystals becomes dramatically different when the sample size is reduced to the micron or submicron scale, compared to the behavior of bulk materials (1). This difference decisively influences today's industrial sectors with focus on miniaturization, as the size reduction effect is no longer negligible. Therefore the plastic behavior at the micrometer scale (in case of micropillars) is the main focus of the presented work. The aim of our research was to develop a focused ion beam (FIB) milling method to be able to produce micropillars in large numbers, which are also suitable for electron backscattered diffraction (EBSD) measurements. After the preparation phase of the copper single crystal sample, micropillars were formed on the surface, and then they were compressed to various deformation levels with a nanoindentation stage developed by the researchers at the Department of Materials Science, ELTE. After compression the pillars were cut in half with FIB and the resulting new surface was measured with high resolution EBSD (HR-EBSD). The HR-EBSD technique is capable of mapping the strain field in the deformed sample caused by the dislocations (2), therefore we can examine the strains' magnitude and distribution evolving in the material after plastic deformation. The micropillars made by the FIB preparation (Figure1.) were successfully compressed and measured by EBSD. The high resolution EBSD maps show interesting features when the different components of the strain tensor elements are plotted, and this presentation aims to introduce these findings. The experiments were conducted on differently oriented samples as well. The comparison of the results lead us to the

possibility to map and reconstruct strain states in 3 dimensions, which is a fairly new approach in the experimental research of microdeformations.

References:

1. C. A. Volkert and E. T. Lilleodden, Phil. Mag. 86 (2006) 5567. 2. Sz. Kalácska et al. Appl. Phys. Lett. 110 (2017), 091912.

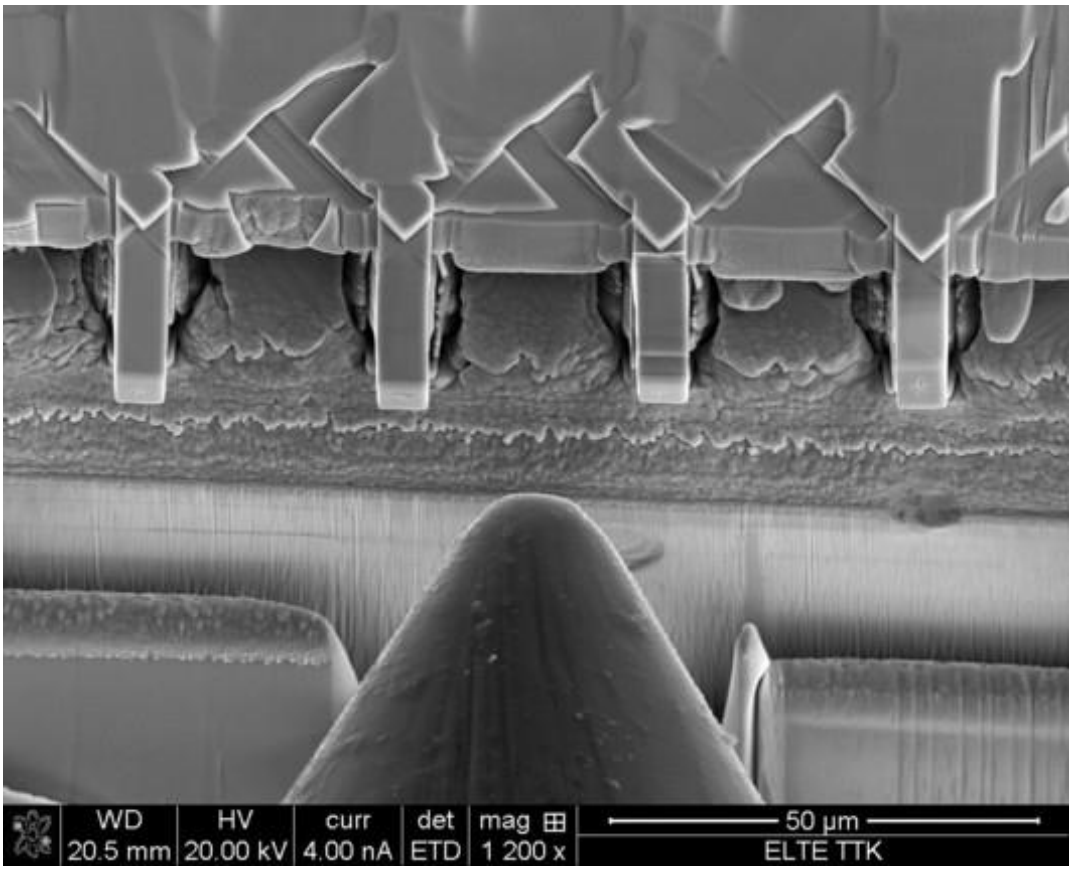

Figure 1. Secunder electron image of micropillars milled with focused ion beam (4 identical, each of them is 6 um x 6 um x 18 um), after compression with a nanoindentation tip.

Spectroscopic investigation of the electronic structure phase diagram of yttria-stabilized zirconia in an electron microscope

Thomas Götsch (1), Erminald Bertel (1), Alexander Menzel (1), Michael Stöger-Pollach (2), Simon Penner (1)

1) Institute of Physical Chemistry, University of Innsbruck, A-6020 Innsbruck, Austria

2) University Service Center for Transmission Electron Microscopy, Vienna University of Technology, A-1040 Vienna, Austria

Keywords: YSZ, electronic structure, EELS, Cerenkov radiation, crystallography

Yttria-stabilized zirconia (YSZ) is one of the most frequently used ionic conductors since the substitution of Zr^{4+} by Y^{3+} ions results in the formation of oxygen vacancies. These vacancies lead to a significant O^{2-} ion conductivity at elevated temperatures. Therefore, YSZ is employed as an electrolyte in devices like solid oxide fuel cells or chemical sensors. In this work, we investigate the influence of the Y_2O_3 concentration in the complex oxide on the crystallographic as well as the electronic properties. For this, we employed our self-built direct current ion beam sputter gun,(1) and deposited thin films with a nominal thickness of 25 nm for four different compositions, ranging from 3 mol% to 40 mol% Y_2O_3. These specimens were investigated using transmission electron microscopy as well as photoelectron spectroscopy to gain complementary information about their electronic structures. Usually, differentiating the tetragonal and cubic polymorphs of zirconium dioxide species is impossible with diffraction methods (both crystal structures yield the same diffraction patterns). The crystal class determination is nevertheless achievable by calculation of the unit cell height (i.e. the lattice parameter *c*), since this parameter is equivalent for both crystal structures (because the (002) spots in the diffraction patterns are identical). If this lattice parameter is subsequently plotted as a function of the yttria content, a distinct stagnation between 8 and 20 mol% Y_2O_3 can be observed (see Figure 1a). However, due to the significantly increased amount of Y^{3+}, which is the larger ion when compared to Zr^{4+}, the unit cell volume has to increase, which can only be explained by a phase transformation from tetragonal to cubic (i.e. a growth in the lateral dimensions). In later experiments, the phase transition could even be narrowed down to lie

between 8 mol% and 9.3 mol% Y_2O_3.(2) The same trend as a function of the yttrium oxide content is also observed for other parameters such as the direct band gaps, displayed in Figure 1b. These have been obtained by Valence EELS (VEELS),(3) for which the acceleration voltage is lowered to prevent Čerenkov losses from occluding the onset of the interband transitions, which corresponds to the band gap. Figure 1b reveals that the behavior of the band gaps is a mirrored version of that of the lattice parameter: when the yttria-concentration increases and the unit cell becomes larger, the band bap decreases, whereas it features a significant rise at the phase transition. A combination of core-loss EELS and UPS also gives rise to information about the O-vacancy related defect states within the band gap. Furthermore, it is shown that, using a cathodoluminescence spectrometer, the absorption of the emitted Čerenkov radiation inside the TEM can be used as a precise tool for the determination of the distance between the occupied and the unoccupied defect states (Čerenkov emission spectroscopy), as shown in Figure 2.

References:

1. T. Götsch et al., AIP Adv. 6 (2016) 025119.

2. T. Götsch et al., Appl. Surf. Sci. 402 (2017) 1–11.

3. M. Stöger-Pollach et al., Micron 37 (2006), 396–402.

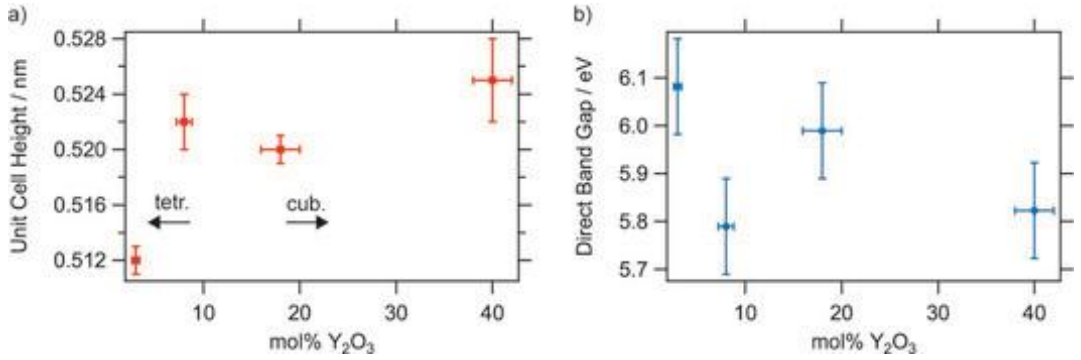

Figure 1. a) The unit cell height as a function of the yttria content reveals the phase transformation between the tetragonal and cubic polymorphs. b) The band gaps show the same behavior as the unit cell heights with a discontinuity at the phase transition.

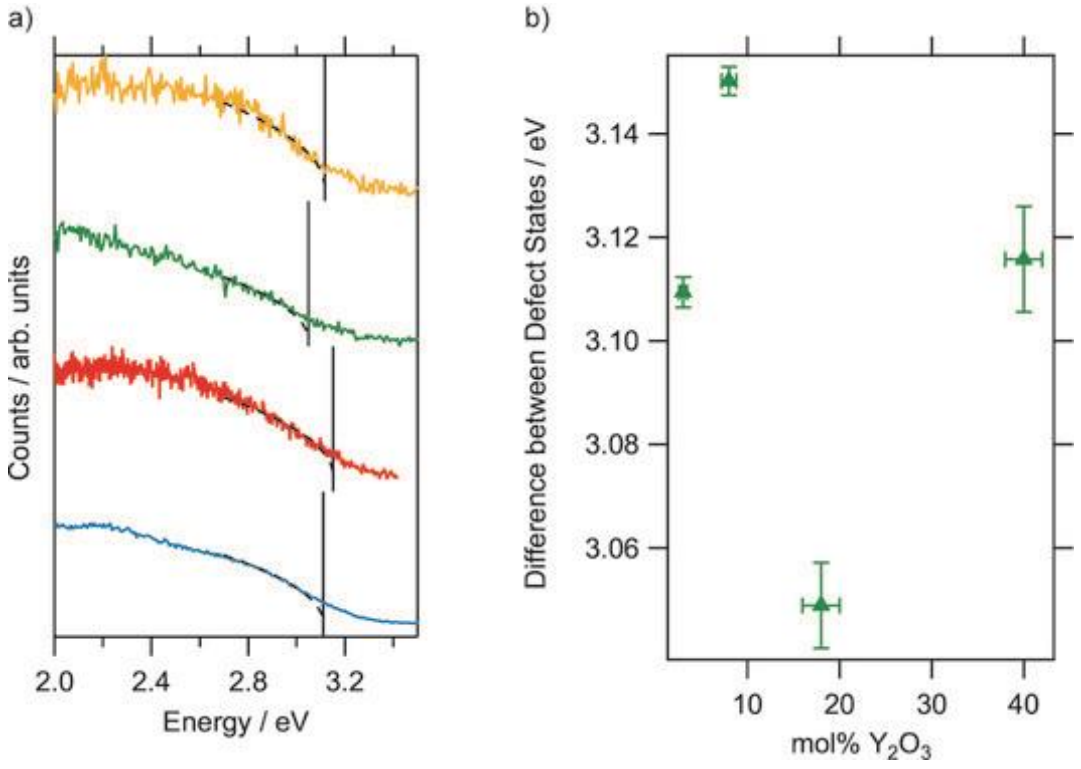

Figure 2. a) Cerenkov emission spectra, as measured using a cathodoluminescence spectrometer inside the TEM. b) The absorption edges yield information regarding the distance between the occupied and the unoccupied states within the band gap.

POSTER PRESENTATIONS I7:

Atomic-level strain response of amorphous TiAl thin film under tension measured by selected area electron diffraction

Christian Ebner (1), Rohit Sarkar (2), Jagannathan Rajagopalan (2), Christian Rentenberger (1)

1) University of Vienna, Physics of Nanostructured Materials, Boltzmanngasse 5, 1090 Vienna, Austria

2) Arizona State University, Department of Materials Science and Engineering, School for Engineering of Matter Transport and Energy, Tempe 85287, USA

Keywords: *in situ*, selected area diffraction, metallic glasses, strain mapping

Metallic glasses are a new class of materials with very distinct properties such as high yield stresses and large elastic limits. These properties make them promising materials for structural applications (1). Understanding the mechanisms of elastic and plastic deformation and modelling these on an atomic level is a challenge because of the lack of periodicity in these materials. This challenge needs to be tackled to fully take advantage of the materials properties. Especially, the local stress strain state and time dependent response in form of elastic, anelastic, viscoelastic and plastic deformations are of interest. In this study, *in situ* tensile tests with MEMS base thin films are performed (cf. Fig 1(a)). We present a selected area electron diffraction (SAED) based technique allowing the determination of the local atomic level elastic strain. The 2D strain tensor is contained within the experimental SAED patterns in form of elliptical distortions of the diffuse diffraction halo of amorphous alloys (cf. Fig 1(b)). Changes in the nearest neighbor distance distribution on an atomic level result in shifts of the radial intensity maxima positions. By accurately tracking these shifts from sector-wise calculated line profiles, the strain can be obtained in a semi-automated manner (2). This method is finally used to measure the following mechanical phenomena within the elastic regime of an amorphous TiAl thin film: (a) the elastic stress - strain response, allowing to calculate the Young's modulus and the Poisson's ratio, (b) uncopling the anelastic from the

elastic strain and (c) the viscoelastic strain response at fixed external stress over time. *In situ* tensile tests are performed using a Phillips CM200 TEM operating at 80 - 200kV. First, the principal strain e_1 (parallel) and e_2 (perpendicular to the loading direction) as a function of the external stress σ are measured for several stress levels with small increments. The Young's modulus is calculated from the slope of the stress -strain curve, the Poisson's number from the ratio of the obtained principal strains e_2/e_1. Anelastic contributions are decoupled by comparing the strain from the diffraction data with the external strain measured via strain gauges on the MEMS device. Also, the strain distribution at a high, fixed external stress is mapped over a larger specimen area (cf. Figure 2(a)). Finally, the specimens time response to loading and unloading to different levels of external stress (denoted as states 0 – 4 in Figure 2(b)) is measured. After each stress change a time series of SAED patterns with 2s resolution is acquired. Patterns are recorded for times up to 1h. The changes in principal strain Δe_1 with respect to the first pattern of the time series are shown in Figure 2(b). Fitting of these changes with a relaxation time model function gives a good fit only if two different relaxation times are used.

Acknowledgements:

C. E. and C. R. acknowledge financial support by the Austrian Science Fund FWF: [I1309]. R. S. and J. R. acknowledge funding from the National Science Foundation (NSF) grants CMMI 1400505 and DMR 1454109.

References:

1. A.L. Greer. Materials Today, 12 (2009) 1-2, 14-22.

2. C. Ebner et al., Ultramicroscopy, 165 (2016) 51-58.

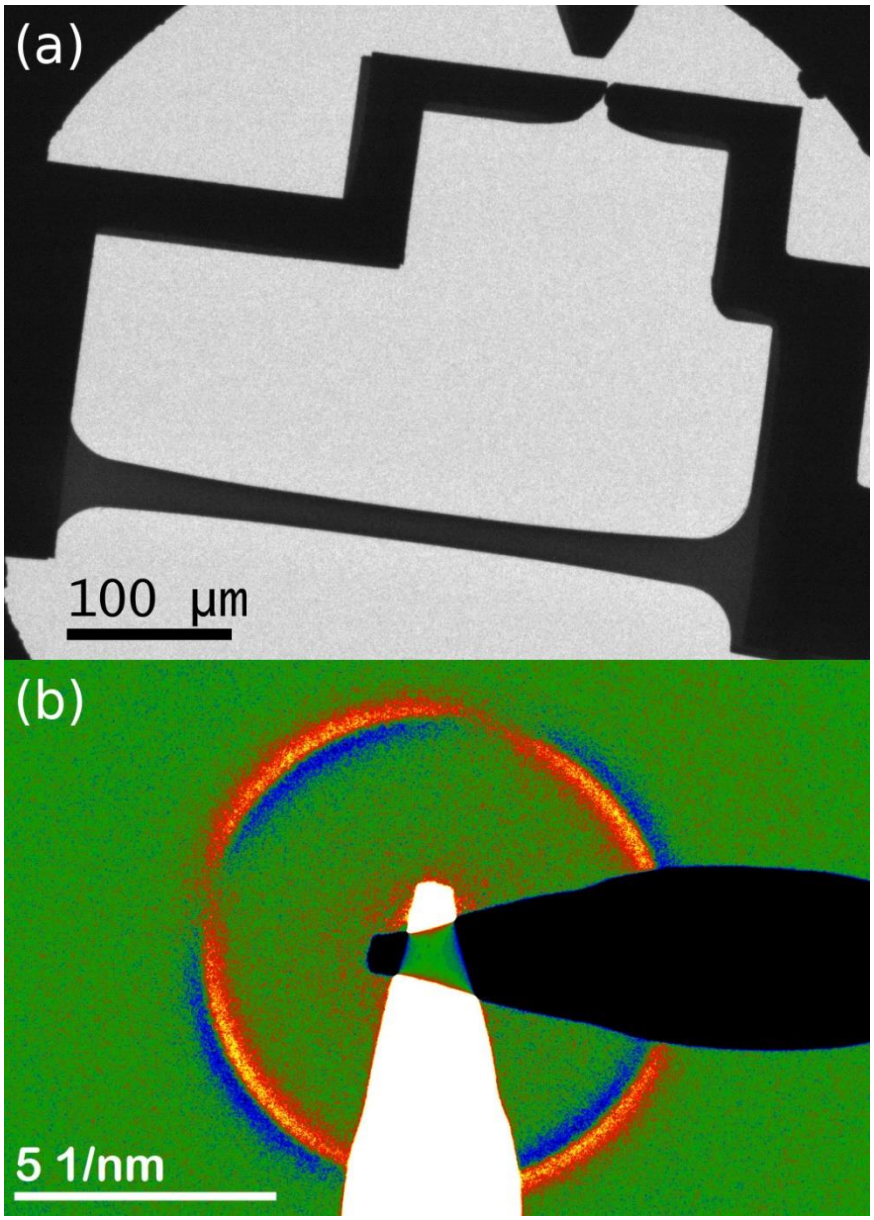

Figure 1. (a) Low magnification image of the amorphous TiAl thin film with the gauges to measure external stress and strain. (b) Color-coded difference image of a highly strained DP and its 90 degree rotated pattern.

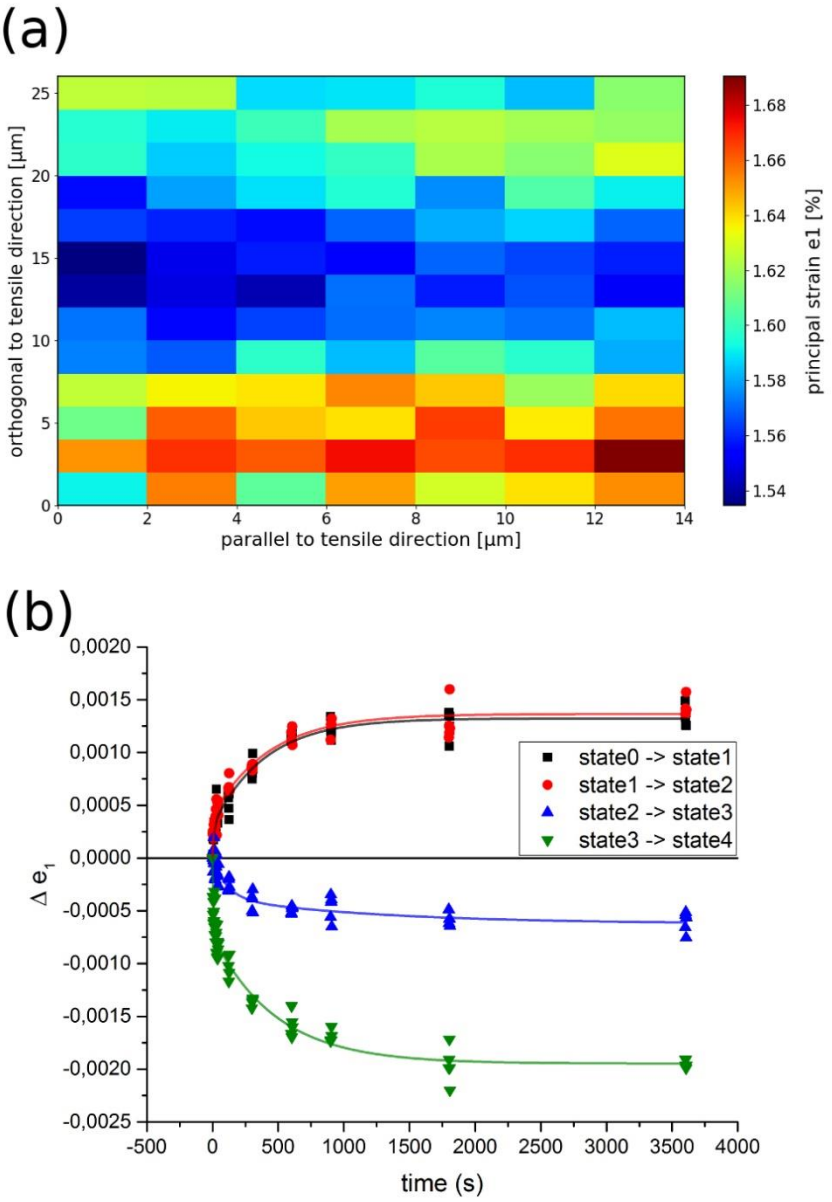

Figure 2. (a) Principle strain mapping at fixed stress over the width of the specimen shows variation caused by slight thickness fluctuations. (b) Time dependent strain evolutions and their fits according to a relaxation model.

Electron beam induced radiation explored by CL and EELS

Michael Stöger-Pollach (1), Lukáš Kachtik (2), Bernhard Miesenberger (3), Philipp Retzl (3)

1) University Service Center for Transmission Electron Microscopy, Technische Universität Wien, Wiedner Hauptstraße 8-10, 1040 Wien, Austria

2) Brno university of technology, Antonínská 548/1, 601 90 Brno, Czech Republic

3) University Service Center for Transmission Electron Microscopy, Technische Universität Wien, Wiedner Hauptstraße 8-10, 1040 Wien, Austria

Keywords: EELS, CL, Cerenkov radiation, transition radiation

When the electron beam passes through the specimen in a transmission electron microscope (TEM), several photon emission mechanisms are activated. The most common are the excitation if X-rays being detected within energy or wave length dispersive X-ray spectroscopy (EDX or WDX) and the excitation of IR-VIS-UV light detected by cathodoluminescence. The latter is generated if a valence electron was excited into the conduction band and recombines with its hole in the valence band or of a radiative surface mode of a non-periodic nanostructure is excited. Additionally Cerenkov radiation and transition radiation are generated by the swift electron. The emission probability per incoming electron for transition radiation (TR) is measured by employing electron energy losses spectrometry (EELS) and cathodoluminescence (CL) in a transmission electron microscope (TEM) using beam energies varying from 20 – 200 keV. We further demonstrate that TR is excited only at the sample surfaces, because the emitted intensity and the respective energy loss are independent of the sample thickness. As specimen we use an aluminium single crystal, because TR is known to be strongest on metals. For studying Cerenkov radiation we record CL spectra of a crystalline MgO specimen. Due to its low refractive index the Cerenkov limit can be determined to be approximately 90 keV (1). CL spectra were recorded using a GATAN VULCAN system, corrected for the spectrometer response and integrated over the whole visible range. Using EELS we explored the angular behaviour of the transition radiation losses (TRLs) and verified the emission probability by observing the corresponding inelastic contributions in the EELS spectrum. Summing up it is the first time that within a TEM transition radiation of aluminium

was studied by means of EELS and CL. We proved experimentally that the angular dispersion of the TRLs is within the light cone, that TR is emitted from the surfaces only, and we determined the photon emission probability with respect to the beam energy. Due to the fact, that the probability for the emission of TR is very low, even for aluminium, it is even smaller in the case of semiconductors, where low loss EELS is used for determining the local dielectric behaviour.

References:

1. M. Stöger-Pollach, Micron 39 (2008) 1092-1110.

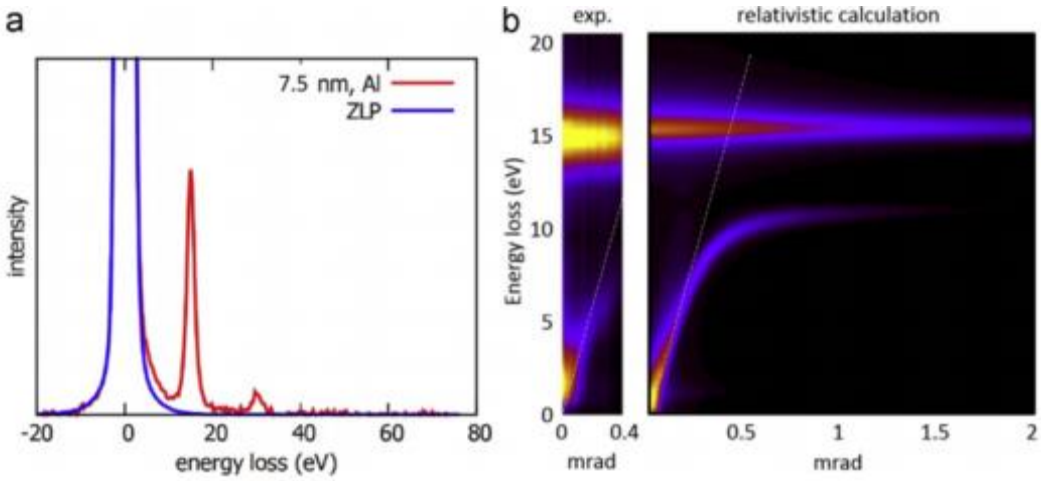

Figure 1. Left: VEELS spectrum of a 7.5 nm thin Al foil and the ZLP recorded in vacuum. Right: Comparison of the AR-VEELS experiment and the simulation being convolved with the spectral and angular resolution of the experiment.

Thickness and orientation dependence of the average HAADF STEM normalized intensity: a comparison with Monte Carlo and Multislice simulations.

Andrea Parisini (1), Stefano Frabboni (2), Gian Carlo Gazzadi (3), Aldo Armigliato (1), Rodolfo Rosa (1)

1) CNR-IMM, Sezione di Bologna, via P. Gobetti 101, 40129 Bologna, Italy

2) Dipartimento di Fisica, Università di Modena e Reggio Emilia, via G. Campi 213/A, 41100 Modena, Italy

3) CNR-Istituto di Nanoscienze-S3, via G. Campi 213/A, 41100 Modena, Italy

Keywords: STEM, HAADF, quantitative intensity measurement, QSTEM, Monte Carlo simulation

In the last years, much attention has been paid to the quantitative measurement of the HAADF STEM intensity wherefrom thickness and/or sample composition values may be obtained. The use of averaged values of this quantity allowing a useful filtering of unwanted signals, led to the determination of doping profiles in ultra shallow junctions in Si at subnanometer resolution (1). In general, there are still some open issues concerning the origin of the contrast in HAADF STEM images that mainly regard the dependence of the intensity on sample thickness and orientation. One of these issue concerns the suggestion (2) that for thin specimen, out of an axial sample orientation, elastic scattering is enhanced at the expense of thermal diffuse scattering. In this work, we focus on two main problems: i) we test this suggestion by seeking its maximum thickness limit and ii) we investigate the precise sample orientation conditions leading to maximize the Z-contrast contribution. The former problem is studied by a comparison of the experimentally determined average normalized intensity depth profiles with those obtained by Monte Carlo simulations. In MC simulations, scattering events are completely independent so that elastic scattering is temperature independent. Moreover, as in these simulations each single electron trajectory is followed, the HAADF detector response may be easily introduced. The second problem is faced by a comparison with Multislice simulations in which full account of sample orientation and thermal diffuse scattering is taken (3). We do this

on a wedged FIB lamella consisting of crystalline 4H-SiC and amorphous SiO_2 having average Z values that differ by no more than 7%. In Figure 1, a head-on SEM view of the lamella, the relative orientation of sample and electron beam, the HAADF detector response and finally an edge-on STEM image of the sample, are reported. In Figure 2, our main results are summarized. In the case of SiO_2 (Figure 2 b), irrespective of the given orientation conditions the different experimental depth profiles superpose in agreement with MC simulations, this contrast with the crystalline 4H-SiC (Figure 2 a) where the experimental profiles appear to slightly depend on the sample orientation. This dependence is investigated by Multislice simulations in different planar channeling sample orientations (Figure 2 c) revealing the presence of secondary intensity maxima. Thus, even out of axial channeling condition the precise sample orientation has to be taken into account when using the average intensity in quantitative works. Finally, in Figure 2 d we show that just outside planar channeling conditions the average intensity mass thickness profiles of the two material almost coincide. The residual difference is in keeping with the expected difference in Z-contrast contribution, this small average Z difference is thus revealed. Applications to the composition profiles determination in C-O-Si ternary films by X-ray EDS are in progress.

References:

1. A. Parisini et al., Appl. Phys. Lett. 92 (2008) 261907.

2. J. Liu and J. M. Cowley, Ultramicroscopy 37 (1991) 50.

3. C. T. Koch, Ph.D. Thesis, Arizona State University, (2002).

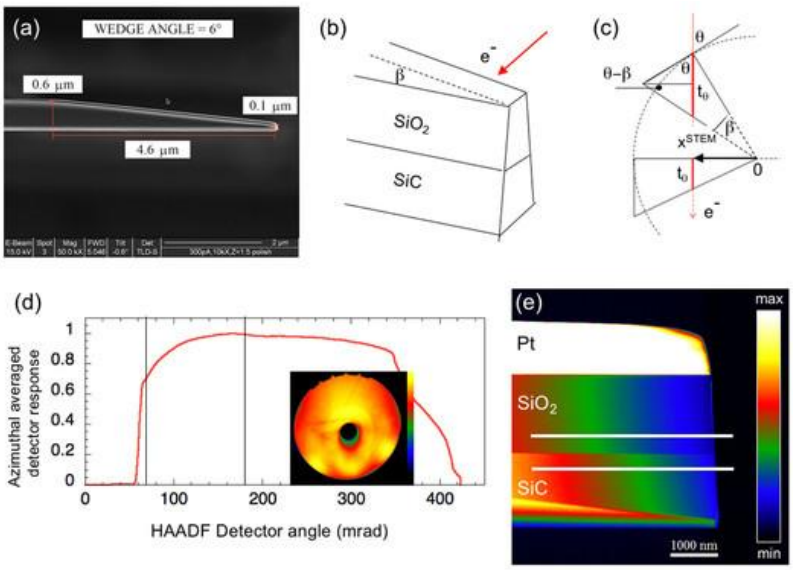

Figure 1. (a) Head-on SEM view of the wedged FIB lamella; (b, c) relative orientation of sample and electron beam; (d) HAADF detector response and image (inset); (e) edge-on STEM image of the sample with segments marking line profile directions.

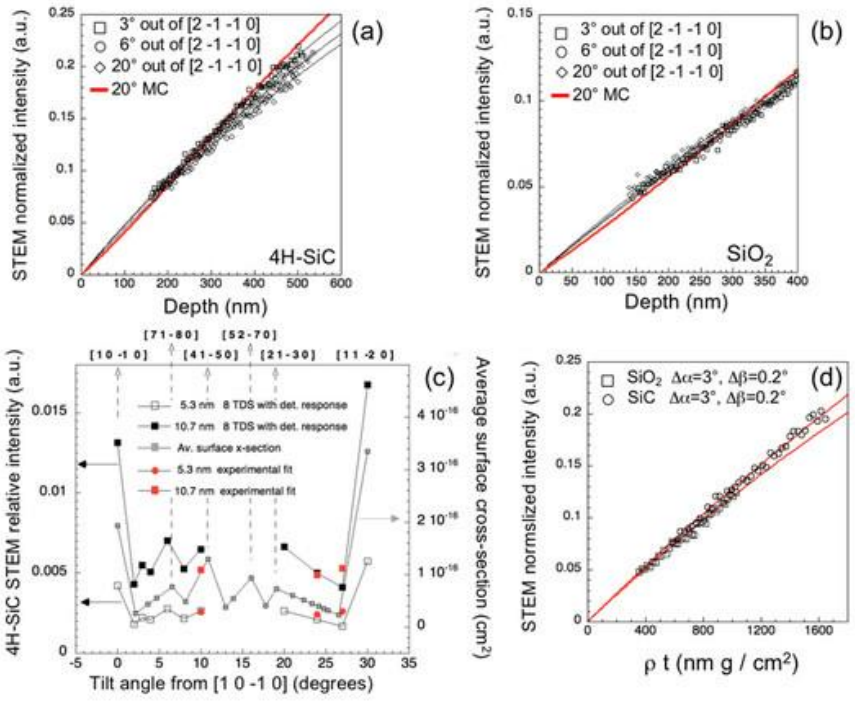

Figure 2. (a,b) Experimental averaged normalized intensity depth profiles and MC simulations; (c) Multislice relative intensities vs tilt angle, extrapolated data from experimental fits are also reported; (d) experimental intensity mass thickness profiles.

LIFE SCIENCES

L1. Live Cell Imaging and Intracellular Dynamics

INVITED LECTURES L1:

Imaging neurotransmitter receptor dynamics in the brain at the nanoscale

Juan A. Varela (1), Laurent Groc (2)

1) University of Cambridge, Department of Chemistry, Lensfield Road, Cambridge, CB2 1EW, United Kingdom

2) Interdisciplinary Institute for Neuroscience, Centre Broca Nouvelle-Aquitaine, CNRS 5297, University of Bordeaux, 146 rue Léo Saignat, 33076 Bordeaux Cedex, France

Keywords: single-molecule tracking, neurotransmitter receptors, brain extracellular space, quantum dots, carbon nanotubes

Single-molecule detection and tracking techniques have become powerful tools to study the dynamics of biological events, surpassing the molecular ensemble averages obtained with conventional microscopy. These techniques have significantly contributed to developments in the field of neuroscience, as the synapse is organized at the nanoscale. Furthermore, the extracellular space of the brain (which occupies ~20% of its volume) is also structured at the nanoscale, and until now, its high-resolution characterisation has been restricted to electron microscopy imaging. While organic fluorophores can be used for single-molecule imaging in cultured cells, thick tissue experiments require much brighter probes. In high background noise environments such as the brain, nanoparticles offer great potential for high-resolution imaging due to their brightness and small size. It is critically important to be able to develop and adapt imaging techniques in such a way that they can be used to unravel molecular information with minimal bias from the sample preparation. I will present our recent work where for the first time we succeeded tracking single-molecules in rodent acute brain slices (1). I will also discuss how single-molecule diffusion studies compare across different brain preparations (2). I will describe as well how we can use carbon nanotubes to study the extracellular space of the brain at the nanoscale (3).

References:

1. Varela JA, JP Dupuis, L Etchepare, A Espana, L Cognet, and L Groc. 2016. Targeting neurotransmitter receptors with nanoparticles *in vivo* allows single-molecule tracking in acute brain slices. Nature Communications, 7: 10947 (2016).

2. Varela JA*, JS Ferreira*, JP Dupuis*, P Durand, D Bouchet, and L Groc. Single nanoparticle tracking of N-methyl-D-aspartate receptors in cultured and intact brain tissue. Neurophotonics, 3: 41808 (2016).

3. Godin AG*, JA Varela*, Z Gao*, N Danné, JP Dupuis, B Lounis, L Groc, and L Cognet. 2017. Single-nanotube tracking reveals the nanoscale organization of the extracellular space in the live brain. Nature Nanotechnology, 12, 238–243 (2017).

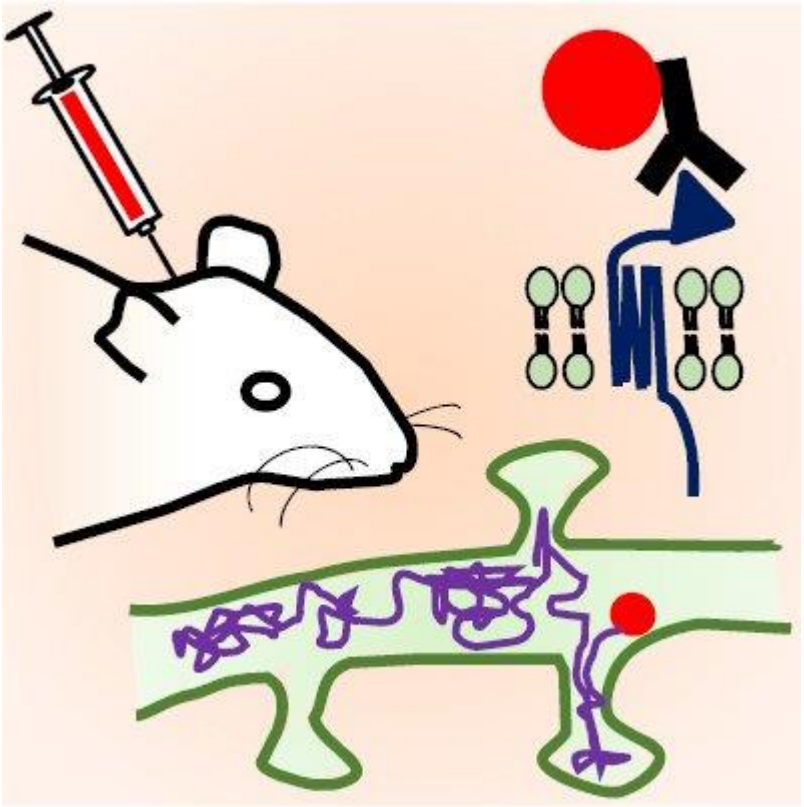

Figure 1. Single-molecule tracking techniques have been developed and used in cultured systems in neuroscience for the past 10 years. I will show how we can adapt techniques to target single molecules *in vivo* and image in acute brain slices.

Dynamics of the Golgi apparatus during dis- and reorganizations, visualized by 3D-electron tomography

Margit Pavelka (1)

1) Center for Anatomy and Cell Biology, Medical University of Vienna, Schwarzspanierstraße 17, 1090 Vienna, Austria

Keywords: Golgi apparatus, endocytosis, intracellular dynamics, 2-deoxy-D-glucose

The Golgi apparatus rapidly reorganizes its subcompartments in response to intra- and extracellular influences. A dynamic crossroads is formed consisting of stacks of flat cisternae in a polarized organization that is traversed by flows of membranes and contents in diverse directions, including anterograde traffic in the biosynthetic systems, retrograde traffic in endocytic pathways and flow via multiple recycling routes (1, 2). This high flexibly of the Golgi apparatus is assumed to be crucial for fulfilling its tasks in the cellular transport systems. In the first part of my talk, I will show our results on the dynamics of the Golgi apparatus connected with endocytic flow after internalization of peroxidase-labelled wheat germ agglutinin (WGA); the second part of the talk focuses on the Golgi stack dis- and reorganizations in response to metabolic stress induced by treatment with the glucose-analogue 2-deoxy-D-glucose (2DG), which reversibly lowers the cellular ATP-levels. All results shown here are obtained from experiments with human HepG2 hepatoblastoma cells either fixed chemically or cryo-immobilized by high pressure-freezing; WGA was visualized by oxidation of diaminobenzidine; the 3D-analyses were performed with the aid of electron tomography using a Tecnai-20 electron microscope (FEI Company) at 200 kV. The figure shows a summary of characteristic changes of the Golgi stack structure in connection with WGA-endocytosis and induced by treatment with 2DG and after its removal. The route to and into the Golgi apparatus is one of the main endocytosis pathways of WGA and is a complex process connected with extensive membrane dynamics. Initial accumulations of vesicular endocytic compartments at the *trans*-Golgi side after 5-10 min of endocytosis are followed by new formations of extended endocytic *trans*-Golgi networks after 10-30 min, which again decrease concomitantly with uptake of WGA into cisternae of the stacks after 30-60 min. By using 2DG, successive steps of Golgi stack

dis- and reorganizations can be followed. The 3D-analyses show that intra-stack networks occur within 10 min after onset of 2DG-treatment, which coincides with a rapid drop-down of the cellular ATP-levels. With ongoing treatment, regularly organized Golgi stacks disappear and are replaced by tubulo-reticular Golgi bodies. The early occurring bodies are rather loosely arranged; at later times, compact glomerular Golgi bodies with densely packed membranes dominate. After removal of 2DG, the cellular ATP again increases coinciding with a re-formation of regular stacks of cisternae. Initial mini-stacks are built in close spatial relationship to glomerular parts of densely packed Golgi bodies. Both the results of the endocytosis studies and the 2DG-experiments show the high flexibility and dynamics of the Golgi stack architectures in response to changed cellular functions and altered environmental conditions.

Acknowledgements:

I would like to express my cordial thanks to all my colleagues and co-workers, in particular to Adolf Ellinger, Josef Neumüller, Carmen Ranftler, Monika Vetterlein, Claudia Meisslitzer-Ruppitsch, Beatrix Mallinger, Regina Wegscheider, Ivanna Fedorenko, Ulrich Kaindl, Thomas Nardelli and Peter Auinger.

References:

1. F. Perez and D.J. Stephens Eds. Methods in Cell Biology Vol 118, Methods for analysis of Golgi complex function. Elsevier Academic Press Inc. San Diego (2013).

2. C. Ranftler et al. Histochem. Cell Biol. 147 (2017) 415-438.

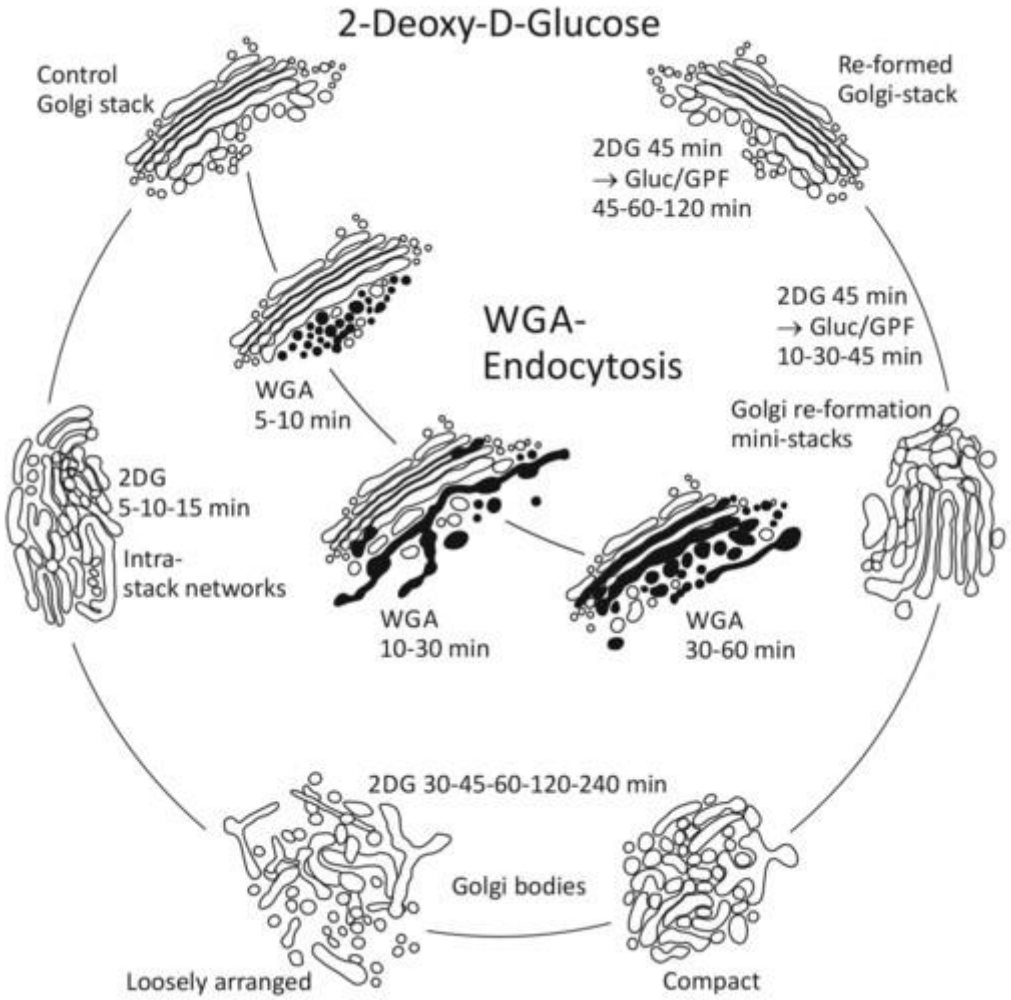

Figure 1. Summary of the Golgi stack reorganizations in human HepG2 hepatoblastoma cells in connection with endocytosis of wheat germ agglutinin and in response to treatment with the non-metabolizable glucose-analogue 2-deoxy-D-glucose and after removal of the agent.

ORAL PRESENTATIONS L1:

Ras proteins regulate actin assembly at endocytic structures via Diaphanous-related formin G

Alexander Junemann (1), Vedrana Filić (2), Moritz Winterhoff (1), Benjamin Nordholz (1), Christof Litschko (1), Helena Schwellenbach (1), Till Stephan (1), Igor Weber (2), Jan Faix (1)

1) Institute for Biophysical Chemistry, Hannover Medical School, OE 4350,Carl-Neuberg-Str. 1, D-30625 Hannover, Germany

2) Division of Molecular Biology, Ruđer Bošković Institute, Bijenička cesta 54, HR-10000 Zagreb, Croatia

Keywords: formin, Arp2/3 complex, macropinocytosis, phagocytosis, Ras

Formins and Arp2/3 complex are major actin assembly factors in eukaryotic cells. While Arp2/3 complex induces branching of the existing filaments, thus creating a dense actin meshwork at the cell's leading edge, formins promote nucleation and elongation of linear actin filaments, mostly in filopodia, stress fibers and cytokinetic rings (1). Formins are defined by the presence of a highly conserved C-terminal formin homology 2 (FH2) domain preceded by an FH1 domain, which are necessary and sufficient to nucleate actin polymerisation and elongate filaments (2). Diaphanous-related formins (DRFs) constitute a conserved subfamily in which core FH1 and FH2 domains are flanked by regulatory domains: a GTPase binding domain (GBD), a Diaphanous-inhibitory domain (DID) and a dimerization domain (DD) at the N terminus, and a C-terminal Diaphanous-autoregulatory domain (DAD). DRFs are autoinhibited through interaction between DID and DAD and binding of a Rho GTPase to GBD releases this inhibition. We have characterized formin G (ForG) from the professional phagocyte Dictyostelium discoideum as a Diaphanous-related formin that fully conforms to the canonical domain organization of DRFs, and described its role in large-scale endocytosis (3). Biochemical assays identified ForG as a rather week actin nucleator that efficiently elongates actin filaments. Live cell imaging demonstrated that ForG was enriched at the plasma

membrane during the formation and maturation of macropinocytic cups. Analysis of phagocytosis also revealed localization to nascent phagocytic cups and ForG remained associated with the membrane over the entire course of engulfment and internalization of yeast particle (Figure 1). Real-time assays of the nutrient uptake showed markedly decreased fluid-phase uptake of TRITC-dextran and phagocytosis of TRITC-labeled yeast particles in forG null cells compared with control cells. Interestingly, yeast-two-hybrid (Y2H) assay failed to identify any interaction of ForG with Rho family GTPases, although DRFs have been previously shown to act exclusively as effectors of Rho GTPases (1). Strikingly, another Y2H screen and bimolecular fluorescence complementation (BiFC) *in vivo* identified specifically activated forms of RasB and RasG, but not their dominant negative variants, as ForG interactors (Figure 2). The role of RasG in macropinocytosis has already been well established. To assess the role of RasB in this process, we have created rasB null cells and tested their nutrient uptake. The uptake of large particles was substantially impaired in rasB deficient cells, while pinocytosis rates were only slightly diminished. Taken together, these data demonstrate the significance of ForG for actin assembly in endocytic structures, with RasB being mainly responsible for its regulation during phagocytosis of large particles, and RasG being the main regulator of ForG in macropinocytosis.

Acknowledgements:

This work was supported by Deutsche Forschungsgemeinschaft Grants FA 330/6-2 and FA 330/10-1 (to J.F.). V.F. was supported by the FP7-REGPOT-2012-2013-1 Grant Agreement 316289–InnoMol.

References:

1. Pollard TD, Annu. Rev. Biophys. Biomol. Struct. 2007, 36:451–477.

2. Faix J and Grosse R, Dev. Cell 2006, 10:693–706.

3. Junemann A et al., Proc. Natl. Acad. Sci. U. S. A. 2016, 113:E7464–E7473.

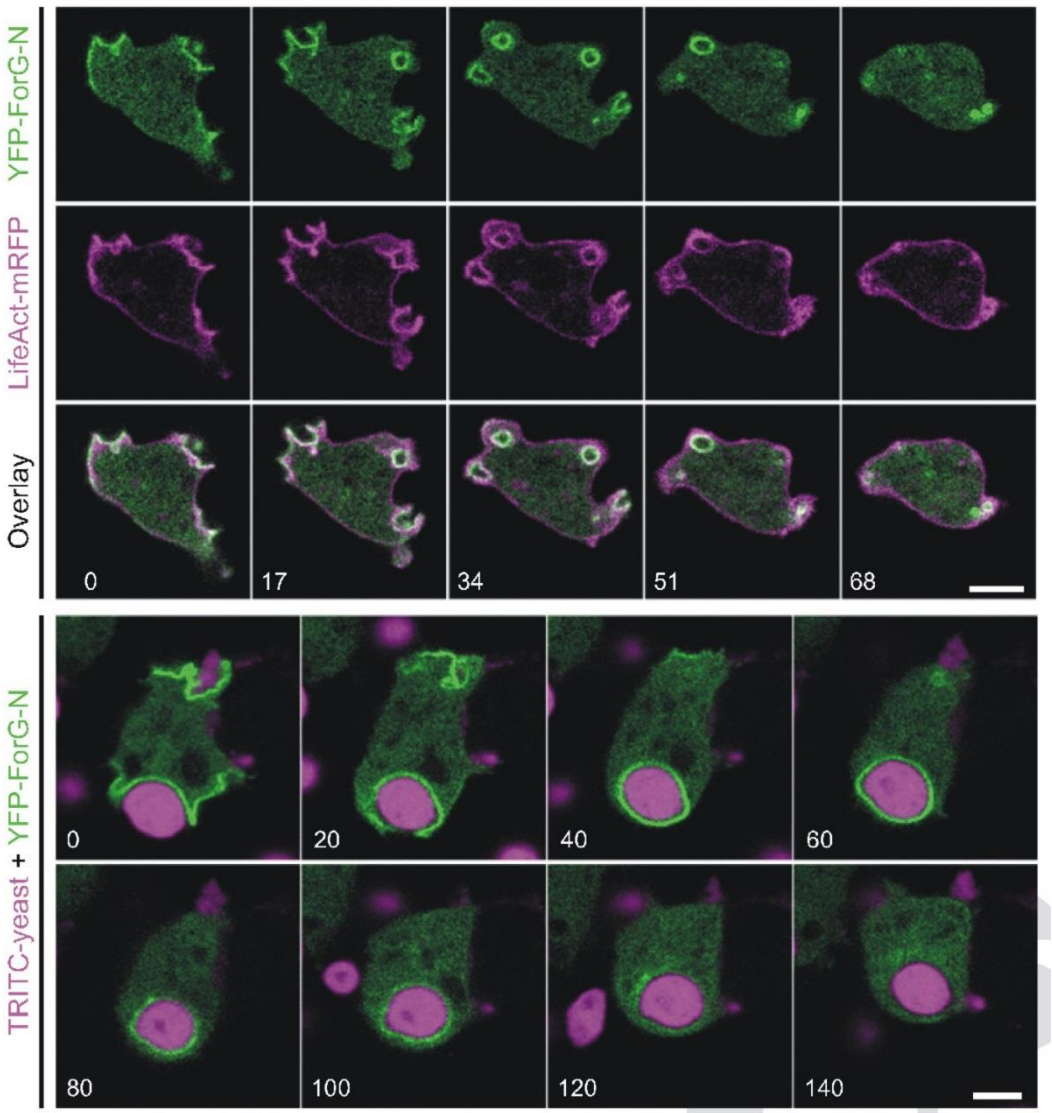

Figure 1. ForG localizes to endocytic structures during macropinocytosis (upper panel) and phagocytosis (lower panel). Time is given in seconds. (Junemann et al., 2016)

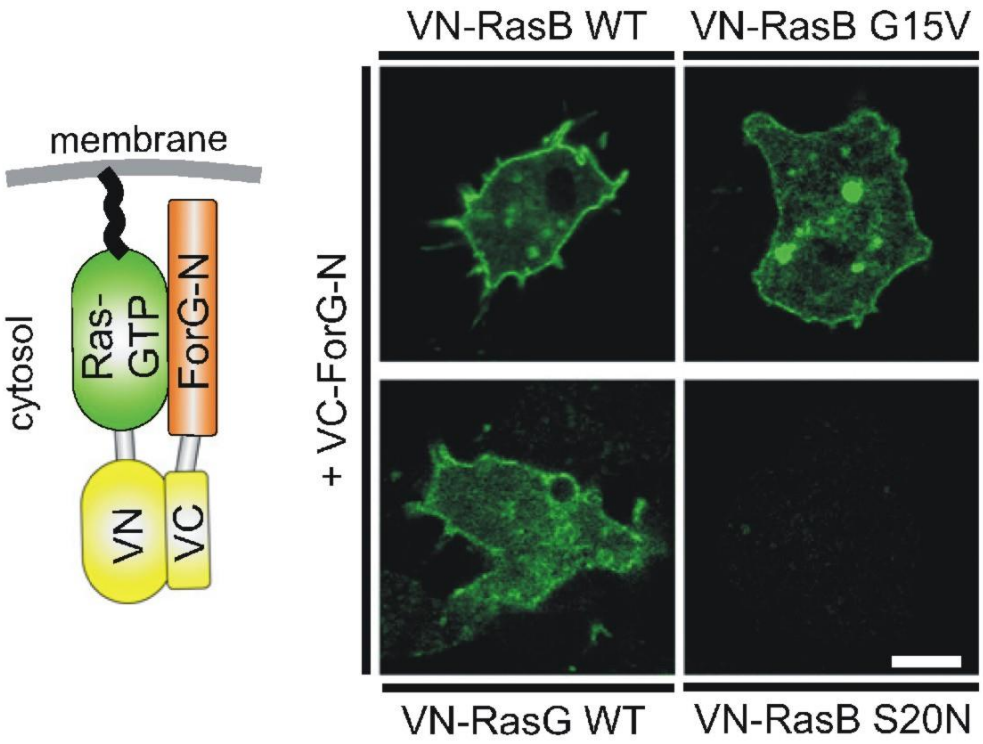

Figure 2. ForG interacts with active Ras *in vivo*. (Left panel) Scheme of the BiFC strategy. VC and VN, Venus C-terminal and N-terminal fragment. (Right panel) ForG interacted with active or WT forms of RasB and RasG. (Junemann et al., 2016)

Effect of intracytoplasmic morphologically selected sperm injection (IMSI) imaging system on intracytoplasmic sperm injection outcomes

Seda Karabulut (1), İlknur Keskin (2), Ö. Aksünger (3)

1) Medipol University, International School of Medicine, Department of Histology and Embryology, REMER, İstanbul, Turkey

2) Medipol University, School of Medicine, Department of Histology and Embryology, REMER, İstanbul, Turkey

3) Memorial Antalya Hospital IVF Unit, Antalya, Turkey

Keywords: sperm, ICSI, IMSI

Introduction: Intracytoplasmic sperm injection is an assisted reproductive technique used for treating infertility in male and female origin. In male factor infertility ICSI is used in cases of poor sperm quality (oligo/astheno/teratozoospermia) and morphology of spermatozoa used for injection is directly related to fertilization and pregnancy rates. ICSI is performed by selecting motile spermatozoa with normal morphology and motility under a magnification of ×400 which is hard to distinguish morphologically healty sperm. But, subtle morphological defects of the sperm cell are also related to low fertilization rates and poor clinical outcome. A new method, the intracytoplasmic morphologically selected sperm injection (IMSI) is introduced for choosing ultrastructurally normal motile sperm using high-power differential interference contrast optics. This high magnification (X 10,160) allowed the identification of spermatozoa and its organelles in a detailed manner. The aim of the present study is to evaluate the efficacy of IMSI in infertile patients undergoing ICSI. Material method: A total of 49 cycles performed between January 2016 and June 2016 at Memorial Antalya Hospital IVF Unit (Antalya, Turkey) were included in the study where IMSI is used in 21cycles and not used in 28 cycles. The patients were randomly selected for IMSI procedure. Cycles that testicular sperm is used were not included in the study. The causes for infertility among the patients were similar in the IMSI and no-IMSI groups. The motile sperm with normal ultrastructural feature were selected by using using high-power differential interference contrast optics (MSOME) and used in IMSI procedure. The ICSI

outcome parameters (fertilization, embryo quality and pregnancy rates) were compared between two groups in which IMSI is used or not. Results: Although the age of the women and mature oocyte numbers were similar in the IMSI and the no-IMSI group (34.7 and 34.8 resp.) ($p>0.05$), the fertilization rates were significantly higher in the IMSI group (70% and 59% resp.) ($p<0.05$). The mean number of embryos transferred were similar (1.4) in both groups but top quality embryo rate of transferred embryos were significantly higher in the IMSI group (81% and 71,5% resp.) ($p<0.05$). The pregnancy rates were higher in the IMSI group although the difference were not significant (60% and 53% resp.). Conclusion: In conclusion, the IMSI procedure not only significantly improves fertilization and embryo quality but also presents a tendency to increase pregnancy rates as compared with the no-IMSI group in a non-selected group of patients representing the effect of sperm ultrastructural consequences on the outcome of ICSI parameters. These data justify the clinical application of IMSI during infertility treatment. More studies, in which variables are controlled and with more cycles are needed to verify the data.

References:

1. Palermo G, Joris H, Devroey P, Van Steirteghem AC. Pregnancies after intracytoplasmic injection of single spermatozoon into an oocyte. Lancet. (1992)340: 17–18.

2. De Vos A, Van de Velde H, Joris H, Verheyen G, Devroey P, Van Steirteghem A. Influence of individual sperm morphology on fertilization, embryo morphology, and pregnancy outcome of intracytoplasmic sperm injection. Fertil Steril. (2003)79:42–48. 3.

3. Bartoov B, Berkovitz A, Eltes F, Kogosowski A, Menezo Y, Barak Y. Real-time fine morphology of motile human sperm cells is associated with IVF-ICSI outcome. J Androl. (2002)23:1–8. 4.

Imaging via multimode optical fiber: calibration by internal reference

Petr Jákl (1), Johanna Traegaardh (1), Jan Ježek (1), Martin Šiler (1), Pavel Zemánek (1), Tomáš Čižmár (2)

1) Institute of Scientific Instruments of the CAS, v. v. i., Královopolská 147, 61264 Brno, Czech Republic

2) Ewing Building, School of Engineering, Physics & Mathematics, University of Dundee, Dundee, DD1 4HN, Scotland, UK

Keywords: multimode optical fiber, imaging, beam shaping

Various biomedical problems suffer from a lack of a fast and reliable imaging technique that enables *in vivo* imaging deep in the tissue. The issue that obscures deep tissue imaging is the random light scattering. Several imaging techniques deal with these problems from different angels, such as optical coherence tomography, light sheet microscopy or structured light illumination. In the clinical studies rigid or flexible endoscopes are often used for imaging deep in the bodies of animals or in human patients. The flexible endoscopes are formed by a bundle of hundreds single mode optical fibers closely packed in a matrix. Each optical fiber then serves as a "pixel" of the output image. However, the endoscopes are rather bulky devices that cannot be further miniaturized because of evanescent light leaking between optical fibers. This causes cross-talks that ultimately scramble the whole image. On the contrary to single mode optical fibers multimode fibers (MMF) could in principle transfer the whole image at once. Until recently it was considered that imaging by the optical fiber is not possible due to the randomization of transferred light, see Figure 1a. However, it was shown (1) that by properly designing input light pattern the very well defined focal point might be created and placed in 3D in different positions with respect to the MMF facet, see Figure 1b. In principle, such point can be scanned and used for imaging in the tissue anywhere the optical fiber is placed. Further on, even the light sheet, Bessel beams, optical vortices might be created using the same approach (2). In order to achieve such imaging properties of the MMF has to be well known in an advance. These are described by the transmission matrix (TM) that relates the input and output light structure. The elements of TM have to be found by the calibration procedure that employs

interference of the light propagating through the MMF with a reference beam. It was even shown that the TM can be diagonalized, i.e. there exist propagation invariant modes that image the input fiber facet to the output one and, further, that the the transmission matrix changes due to the fiber deformations might be analytically predicted (3). The above mentioned studies used a complex optical setup that employed an external reference arm. In this contribution we show that this complexity is unnecessary and that the transmission matrix can be obtained using light transmitted by the MMF fiber only.

Acknowledgements:

This work was supported by EC (CZ.02.1.01/0.0/0.0/15_003/0000476), Scottish Universities Physics Alliance (SUPA – PaLS initiative) and its infrastructure by the MEYS Czech Republic (LO1212), CAS (RVO:68081731) and EC (CZ.1.05/2.1.00/01.0017).

References:

1. T Cizmar & K Dholakia, Nature Communications 3 1027 (2012).

2. M Ploeschner et al., Scientific Reports 5 (2015).

3. M Ploeschner et al., Nature Photonics 9(8) 529-535 (2015).

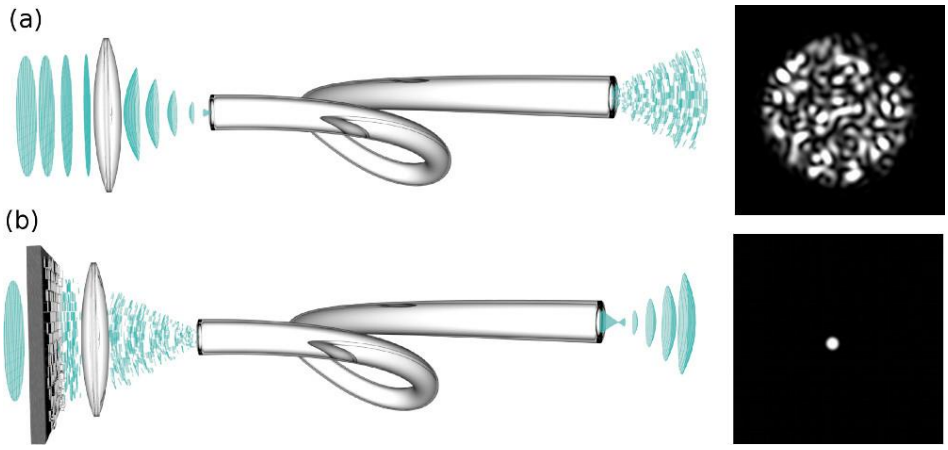

Figure 1. (a) Light passing through the MMF creates a speckled patten upon leaving the output fiber facet. (b) Properly designed and shaped (by spatial light modulator) input light creates a single focused spot close to the output fiber facet.

Biosensor based real-time single cell monitoring using microfluidics that generate spatial and temporal dynamic stimulation

Jiyoung Song (1), Hyunryul Ryu (2), Minhwan Chung (1), Youngtaek Kim (1), Sungsik Lee (3), Olivier Pertz (4), Noo Li Jeon (1)

1) Department of Mechanical and Aerospace Engineering, Seoul National University, Korea

2) Institute of advanced machinery and design, MIT, Boston, USA

3) Department of biochemistry, ETH Zurich, Switzerland

4) Department of biomedicine, University of Bern, Switzerland

Keywords: biosensor, microfluidics, dynamic stimulation, real time imaging, single cell analysis

Recent trends in dynamic response at single cell level have led to a number of new techniques to study cell biology. Above all, recent advances in time-lapse imaging techniques and fluorescent marker has made real-time cell monitoring wide-spread. Microfluidic devices with time-lapse imaging techniques allow us to study cellular response under the dynamic stimulation at a cellular level. Despite the number of publications that explore the generation of dynamic stimulation, the proposed microfluidic devices are limited in simultaneous variables. Thus, the main feature of our microfluidic device is its capability of generating various multiple profiles of diffusible chemicals such as GFs, hormones, and drugs in a single device without any modifications. Moreover, a computer controlled pressure pump allows us to generate multiple profiles in sequence. Consequently, we can generate pulsatile stimulation at a desired concentration, with persistent ramp up and down in concentration, and dynamic manipulation of baseline, slope, and direction of the gradient. In contrast, EKAR2G1 is a versatile biosensor to monitor ERK kinetics. By combining our microfluidic device and EKAR2G1 transfected HEK293 B5 cells, we can successfully monitor ERK kinetics under spatial and temporal dynamic stimulations. In particular, ramp-down profiles in concentration is unable to perform in conventional petri-dish based approach. In this aspect, we hope our microfluidic device will become an essential toolkit to elucidate unidentified regions in cell biology.

Acknowledgements:

This research was supported by the International Research & Development Program of the National Research Foundation of Korea (NRF) funded by the Ministry of Education, Science and Technology(MEST) of Korea (Grant No.NRF-2015K1A3A1A14021299) .

References:

1. Fritz, R. D., Letzelter, M., Reimann, A., Martin, K., Fusco, L., Ritsma, L., . . . van Rheenen, Sci. Signal. 6(2013) rs12.

2. Ryu, H., Chung, M., Dobrzyński, M., Fey, D., Blum, Y., Lee, S. S., . . . Pertz, O. Molecular systems biology 11 (2015) 838.

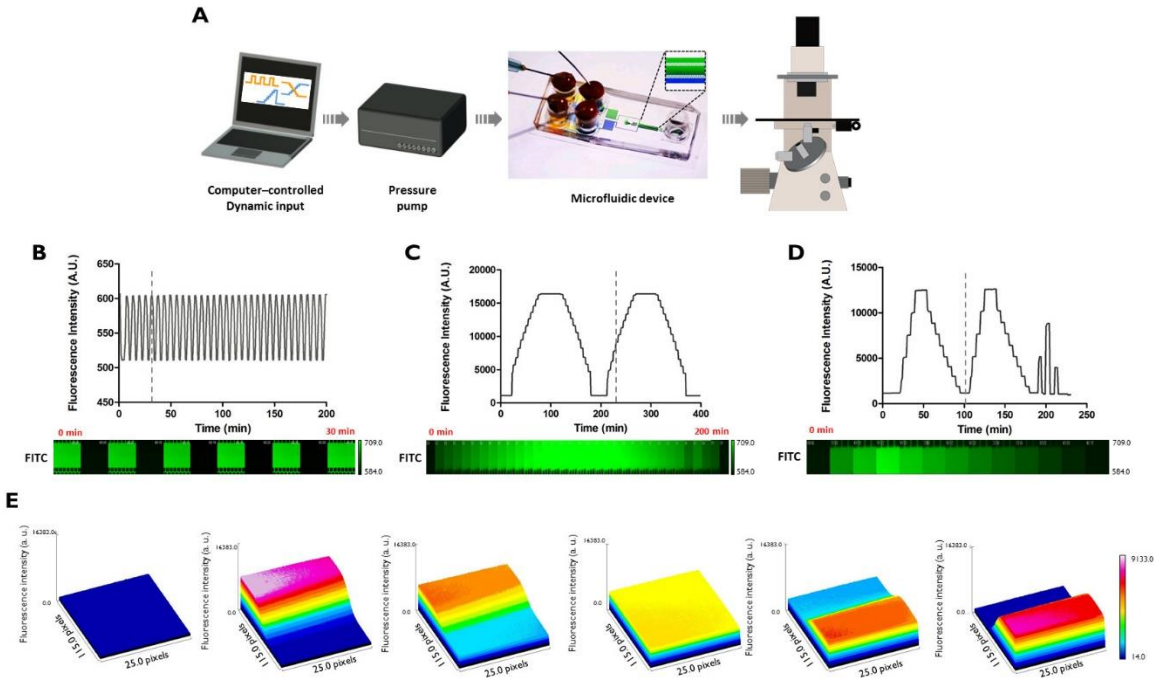

Figure 1. Microfluidic platform to generate spatial and temporal dynamic stimulations. (A) schematic of entire system. (B) pulsatile stimulation. (C) ramp-like changes in concentration. (D) combination of ramp-like stimulation and pulsatile stimulation at various concentrations. (E) dynamically changing gradient in baseline, slope, and direction.

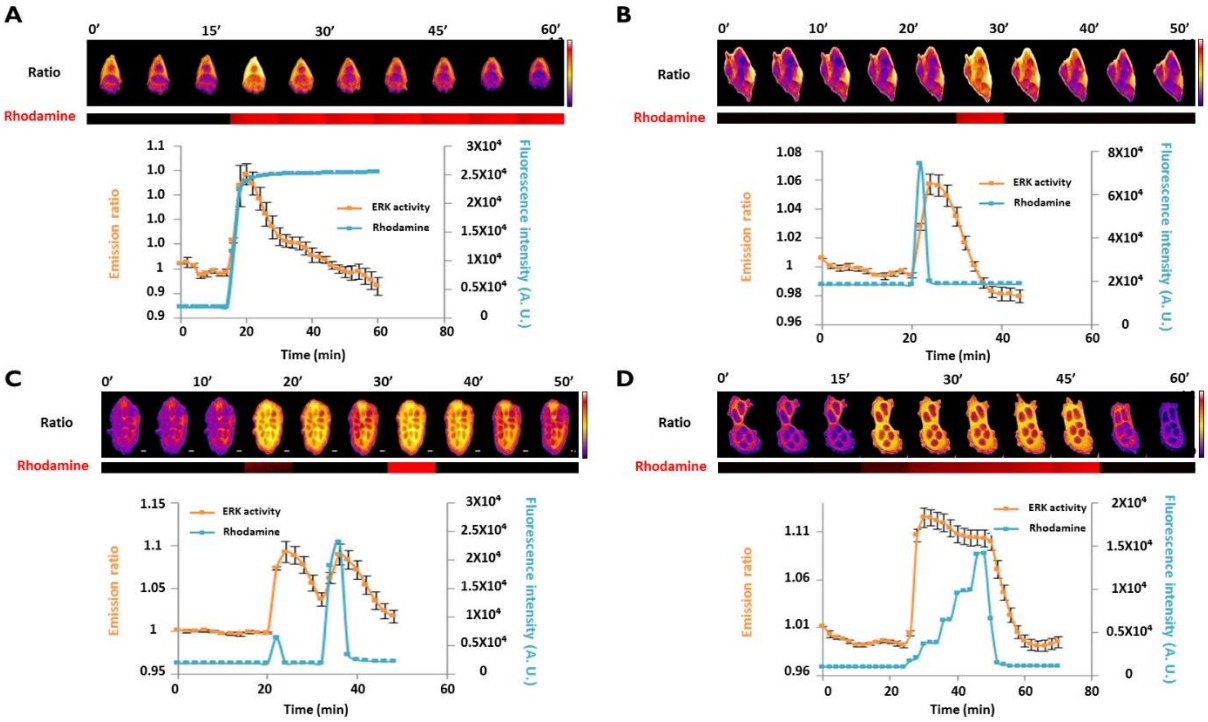

Figure 2. Monitoring of ERK kinetics under the dynamic stimulation. HEK 293 B5 cells were transfected with EKAR2G1 biosensor for monitoring of ERK activation. The cells were exposed to various profiles of EGF stimulations. (A) Sustained (B) single pulse (C) double pulse with different concentrations (D) ramp-like stimulation.

POSTER PRESENTATIONS L1:

The role of exercise in tenocyte activation at myotendinous junction level

Debora Burini (1), Pietro Gobbi (1), Elisabetta Falcieri (1), Davide Curzi (1)

1) Department of Biomolecular Sciences, University of Urbino Carlo Bo, Via Aurelio Saffi, 2, 61029 Urbino, Italy

Keywords: myotendinous junction, tenocyte, exercise, muscle atrophy, muscle strength

Myotendinous junction (MTJ) is the anatomical interface between muscle and tendon, with the key role to transfer the contractile strength (*Figure* 1A). The plasticity of MTJ has been demonstrated in different physiological conditions. In particular, in previous works we revealed the MTJ ability to reduce or to increase its complexity and the contact surface between tissues, in relationship to muscle atrophy and exercise protocols, respectively (1, 2). The molecular mechanisms and the different stages of these morpho-functional adaptations are still unknown, but, by means of transmission electron microscopy (TEM) observations, an interesting high presence of tenocytes close to the MTJ has been revealed (*Figure* 1B). At high magnification, these tenocytes display an increased amount of rough endoplasmic reticulum in the exercised group, compared to sedentary one (*Figure* 1C-D). The exercise ability to increase tenocytes rough endoplasmic reticulum amount has already been demonstrated and correlated to the production of collagen fibers and extracellular matrix components (3). Morphological observations of tenocyte behavior close to MTJ reveal their activation following a resistive exercise protocol, suggesting a key role of the cells in the modulation of MTJ morphology and plasticity.

References:

1. Curzi D. et al., Eur. J. Histochem. (2013) 57:247-54.

2. Curzi D. et al., Histol. Histopathol. (2014), 30:465-72.

3. Salamanna F. et al., Connect. Tissue Res. (2014), 56:35-43.

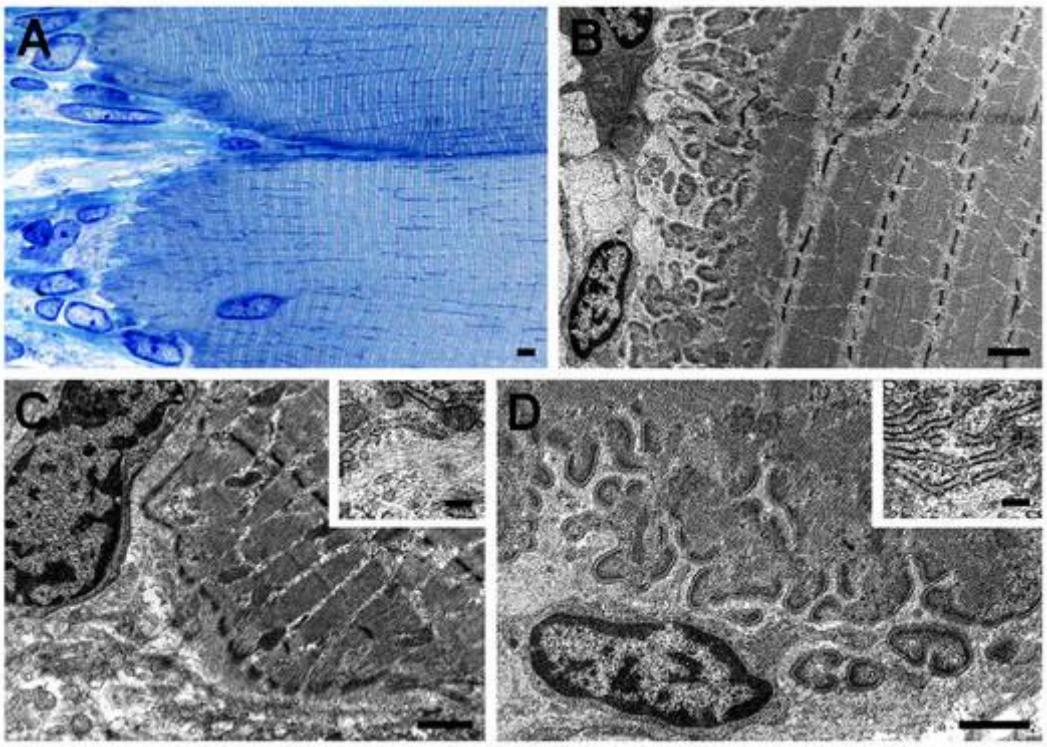

Figure 1. MTJ semithin section (A) and MTJ after TEM observation (B-D). Bars: (A-D)=1 μm; insert (C-D)=0,2 μm.

Cell damage induced by asbestos-like fibers

Michela Battistelli (1), Sara Salucci (1), Michele Mattioli (2), Michela Cangiotti (2), Matteo Giordani (2), Maria Francesca Ottaviani (2), Elisabetta Falcieri (1)

1) Department of Biomolecular Sciences, Urbino University, Via Aurelio Saffi, 2, 61029 Urbino, Italy

2) Department of Pure and Applied Sciences, Urbino University, Via Aurelio Saffi, 2, 61029 Urbino, Italy

Keywords: asbestos-like fibers, U937 human cell line, transmission electron microscopy, toxicity, mineral fibers

The presence, in nature, of asbestos-like fibers, highly toxic and potentially cancerogenic for human healthy, is well known (1). Inhalation of the fibrous form of some zeolites, has been shown to cause effects similar to those observed with mineral fibers classified as ‘‘asbestos,’’ including malignant mesothelioma, a disease typically associated with occupational and environmental exposures to asbestos (2). In this work different fibers of zeolite erionite (termed MD8 and GF1, demonstrated carcinogenic), offretite (termed BV12, suspected carcinogenic) and scolecite (termed SC1, poorly carcinogenic) were investigated (3), with particular regard to their possible interactions with U937 cell, a human hemopoietic cell line. Chemical and morpho-functional analyses have been carried out, both to characterize fiber structure and cell response. Cells showed the ability to internalize all the minerals, as observed after TEM analyses. With zeolite and erionite exposure time increasing, a diffuse cell damage with features of apoptotic and necrotic death could be evidenced (4). All fibers are able to induce a cell shape change which appears, at reverted microscope, more evident when increasing the exposure time (data not shown). The ultrastructural analyses reveal the capacity of cells to internalize these compounds (*Figure* 1). Erionite (A, B, C) and offretite (D) fibers enter the cells, even if their size is large. All fibers, showing an electron-dense aspect, can be detected both in the cytoplasm (▶) and in the nucleus (→) (A, B, C, D). All zeolites induce a diffuse cytoplasmic vacuolization (A, inset). A significant damage can be revealed after 24h of fiber administration, with an initial, potentially apoptotic, chromatin margination and nuclear pore translocation (*) (C and C, inset). Features of necrotic cell death, in particular after erionite

incubation and that with offretite (D), which appear those with greatest toxicity, are also present. Scolecite fibers, according to literature data (3), present poor interactions with the model membranes (E, F, G). Trypan Blue assay shows that all zeolites reduce cell viability, in particular after 24h of incubation (data not shown). These findings suggest that all asbestiform-like fibers enter U937 human cells and that, with a certain variability, they can be considered potentially toxic for cell culture *in vitro.*

References:

1. Mattioli et al. (2016) J Hazard Mater. 306:140-8.

2. Van Gosen et al. (2013) Environ Geochem Health. 35(4):419-30.

3. Cangiotti et al. (2017) J Toxicol Environ Health A. Feb 22:1-17.

4. Salucci et al. (2014) Int J Mol Sci. 17;15(4):6625-40.

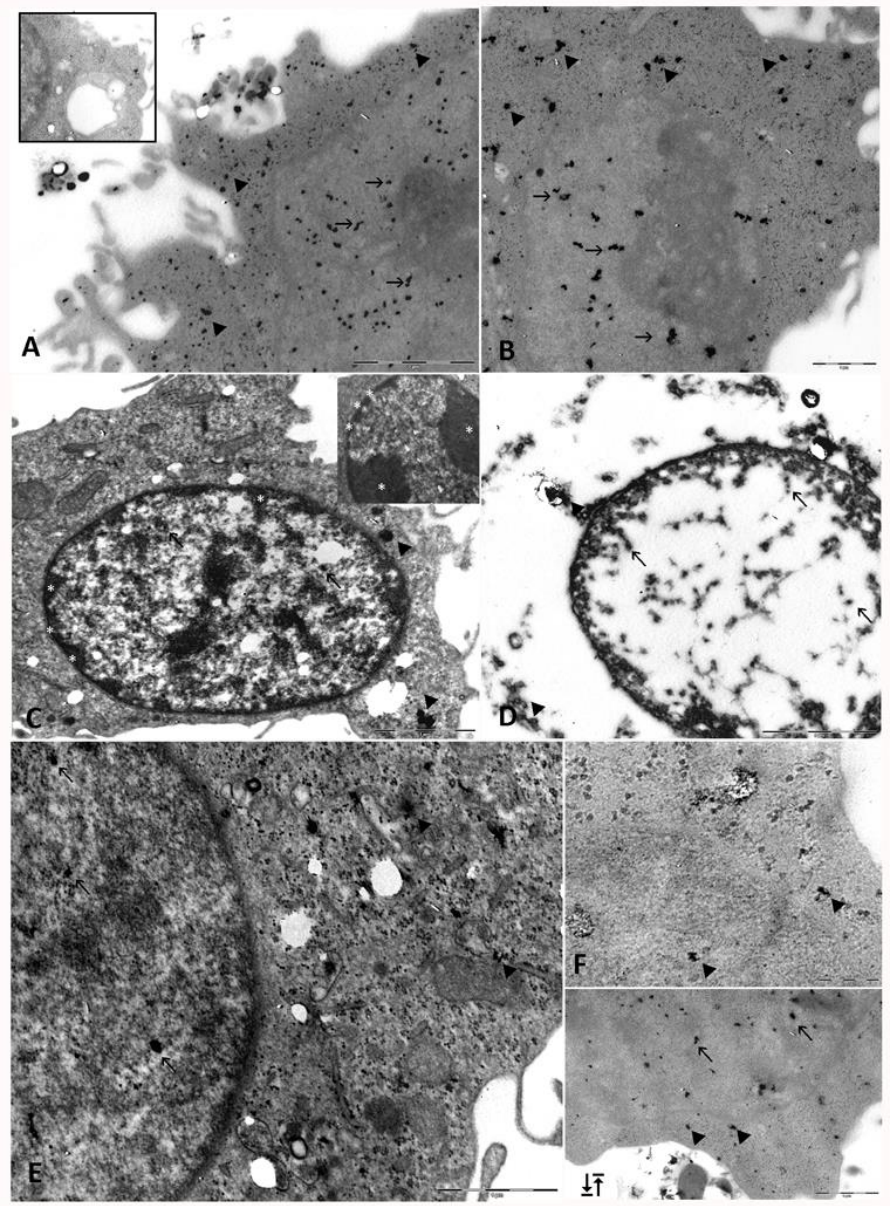

Figure 1. Unstained TEM sections of erionite (termed MD8 and GF1, demonstrated carcinogenic) (A), (B), (C), offretite (termed BV12, suspected carcinogenic) (D) and scolecite fibers (termed SC1, poorly carcinogenic) (E), (F), (G), internalized by U937 cell line. (B), (C), (E), Bar 1 μm; (A), (D), Bar 2 μm; (F). Bar 200 nm.

Ex vivo investigation of hemoglobin distribution in erythrocytes using two photon excitation microscopy: insight from an animal erythrocyte

Ana Z. Stančić (1), Ivana T. Drvenica (1,2), Svetlana Jovanić (3), Katarina Bukara (2,4), Vesna Lj. Ilić (1), Mihajlo D. Rabasović (3), Dejan V. Pantelić (3), Brana M. Jelenković (3), Branko M. Bugarski (2), Aleksandar J. Krmpot (3)

1) Institute for Medical Research, University of Belgrade, Dr Subotića 4, 11 129 Belgrade, Serbia

2) Department of Chemical Engineering, Faculty of Technology and Metallurgy, University of Belgrade, Karnegijeva 4, 11 000 Belgrade, Serbia

3) Institute of Physics Belgrade, University of Belgrade, Pregrevica 118, 11 080 Belgrade, Serbia

4) Department Pharmaceutics, University of Antwerp, Universiteitsplein 1, 2610 Antwerp, Belgium

Keywords: erythrocytes, two photon excitation microscopy

Introduction: Nonlinear laser scanning microscopy (NLSM) with its three modalities, two-photon excited fluorescence (TPEF), second and third harmonic generation (SHG/THG) is advanced optical technique mostly used in biomedicine for label free imaging (1). Hemoglobin, the main intracellular component of erythrocytes, emits strong Soret fluorescence with the peak at 438 nm upon two-photon excitation by femtosecond pulses in red and near infrared region (600-750 nm) (2, 3). Such optical properties of hemoglobin opened the possibility to use TPEF microscopy as a tool for label-free imaging of erythrocytes, even *in vivo* (4). Objective: Despite wide applicability of erythrocytes in diagnostic tests, and distribution of hemoglobin within erythrocytes as a marker of their functional status under physiological or pathological conditions [5], data on spatial distribution of hemoglobin at the single cell level are scarce. Materials & methods: Based on findings reported by Zheng and co-workers (2) we have utilized TPEF microscopy to map the spatial distribution of hemoglobin in porcine erythrocytes *ex vivo*. Porcine erythrocytes were used as extremely susceptible cells to stress and thus represent a good model system to study influence of stress factors (heat, humidity, malnutrition,

infections…) on erythrocyte morphology and hemoglobin distribution. The custom made experimental set up for NLSM utilized the train of the femtosecond pulses from Ti:Sapphire laser (Coherent, Mira 900-F) at 730nm. The repetition rate was 76MHz, and pulse duration was 160fs. Results: Two different morphological types of porcine erythrocytes, normocytes and echinocytes, are collected during mild autumn or extremely hot summer respectively (*Figure* 1a and 1c). Besides, erythrocytes having intermediate morphology i.e. having some characteristics of both abovementioned morphological extremes were also found (*Figure* 1b). Pseudo coloring in figures corresponds to the TPEF signal intensity and no further processing of image was performed. The results demonstrate that the resolution of the TPEF microscopy is good enough for the analysis of erythrocytes at single cell level. The distribution of hemoglobin in erythrocytes followed the cells' shape, where erythrocytes with altered morphology (*Figure* 1b and 1c) demonstrated significant accumulation of hemoglobin in cells' protrusions. Conclusion: Changes in erythrocytes morphology and hemoglobin distribution may influence erythrocytes' oxygen transport function. Erythrocytes monitoring might be of significance in analysis of their functional status in physiological condition, as well in numerous hematological and non-hematological disorders accompanied with erythrocyte morphology changes. Result of this studyeven though obtainedon animal cell model only, confirmed strong potential of TPEF for such application in human and veterinary medicine and basic biomedical research.

References:

1. Masters, B. R .& So, P. T. C. (2008) "Handbook of Biomedical Nonlinear Optical Microscopy", Oxford University Press.

2. W. Zheng, et al., "Two-photon excited hemoglobin fluorescence," Biomed Opt Express 2: 71-79. (2010) [doi:10.1364/BOE.2.000071].

3. G. O. Clay, C. B. Chaffer, and D. Kleinfeld, "Large two-photon absorptivity of hemoglobin in the infrared range of 780-880 nm," J ChemPhys. 126:025102. (2007) [doi:http://dx.doi.org/10.1063/1.2404678].

4. D. Li, et al., "Time-resolved detection enables standard two-photon fluorescence microscopy for

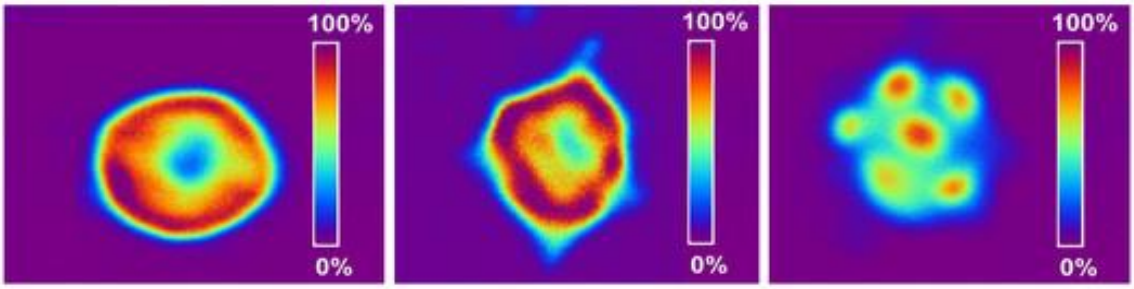

Figure 1. Representative raw TPEF image of (a) porcine erythrocytes with “normal” biconcave, (b) intermediate and (c) echinocytic morphology.TPEF signal is presented in pseudocolor.

CLEM and FIB for studing organisation of Golgi apparatus in urothelium

Samo Hudoklin (1), Tanja Korpar (1), Caroline Kizilyaprak (2), Bruno Humbel (2), Rok Romih (1)

1) Institute of Cell Biology, Faculty of Medicine, Vrazov trg 2,1000 Ljubljana, Slovenia

2) Electron Microscopy Facility, Faculty of Biology and Medicine, University of Lausanne, 1015 Lausanne, Switzerland

Keywords: urothelium, Golgi apparatus, GRASP55

Correlative light and electron microscopy (CLEM) and 3D reconstructions using dual beam microscopes with focused ion beam (FIB) can provide new insights into the structure-function of cell organelles. In differentiated superficial urothelial (umbrella) cells, Golgi apparatus (GA) plays a central role in the biogenesis of urothelial plaques, which are transported to the apical cell surface where they provide functional blood-urine permeability barrier of the urinary bladder (1). We used CLEM and FIB methods to correlate large-scale GA distribution in umbrella cells with its ultrastructure and spatial organization in order to get new insights into the function of GA in the urothelium. For CLEM, urinary bladders of 6-8 weeks old male C57B6 mice were fixed with 4% FA in 0.1M phosphate buffer, pre-incubated in 5% goat serum + 0.1% saponin in PBS and immunolabelled with anti-GORASP55 rabbit polyclonal antibody (Proteintech). GORASP55 antibody labels Golgi reassembly stacking protein of 55 kDa (GRASP55), which is medial- to trans-GA cisternae associated membrane protein involved in the stacking of GA cisternae and required for the GA ribbon formation (2, 3). Samples were then incubated with FluoroNanogold goat anti-rabbit IgG antibodies conjugated with AlexaFluor488 and 1.4 nm colloidal gold (Nanoprobes). For light microscopy, urothelial sheets were mounted in Vectashield with DAPI and observed from the apical surface with AxioImager.Z1 microsocope with ApoTome upgrade (Zeiss). For TEM, samples were silver enhanced, post fixed with 0.1% OsO_4, dehydrated and embedded in Epon. Ultrathin sections were observed with Philips CM100 TEM. For FIB, samples were cryo-fixed with CPC device (Leica), freeze-substituted in AFS (Leica) with 2 % OsO_4 in acetone, and embedded in Epon.

Epon block was trimmed with ultra-microtome UC6 (Leica) and FIB-sectioned with dual beam Helios NanoLab 650 microsocope (FEI). GRASP55 immunostaining showed continuous network distributed throughout the cytoplasm of umbrella cells (Figure 1). This is in-line with studies proposing that GA is involved in the formation of urothelial plaques, in their polarised sorting and transport toward the apical plasma membrane of umbrella cells (4). Gold particles were located between GA cisternae, confirming GRASP55 role in GA stacking in urothelial cells. Three-dimensional reconstruction of the GA in serial sections produced by FIB (Figure 2), further demonstrated lateral connections between individual GA stacks, which might form functionally connected GA network in the cell. In conclusion, we have successfully applied CLEM and FIB microscopy methods to reveal unique GA complexity in higly differentiated urothelial umbrella cells. Correlated results support the idea of special role of GA in the urothelial barrier function.

References:

1. S. Hudoklin et al., PLoS One 7 (2012) e32935.

2. C. Rabouille et al., Front. Cell Dev. Biol. 4 (2016) 1.

3. J. Shorter et al., EMBO J. 18 (1999) 4949-60.

4. S. Hudoklin et al., Cell Tissue Res. 336 (2009) 453-63.

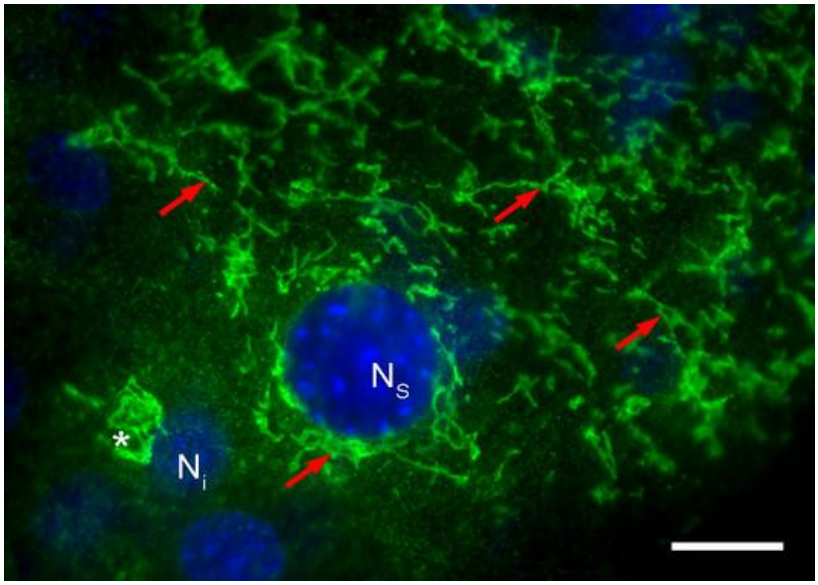

Figure 1. Distribution of GRASP55 in mouse urothelium. In the intermediate cells, GRASP55 (green fluorescence) is located in the perinuclear region (asterisk), while in the superficial cells, it is distributed throughout the cytoplasm (arrows). Ni – nucleus of intermediate cell, Ns – nucleus of superficial cell. Bar: 10 μm.

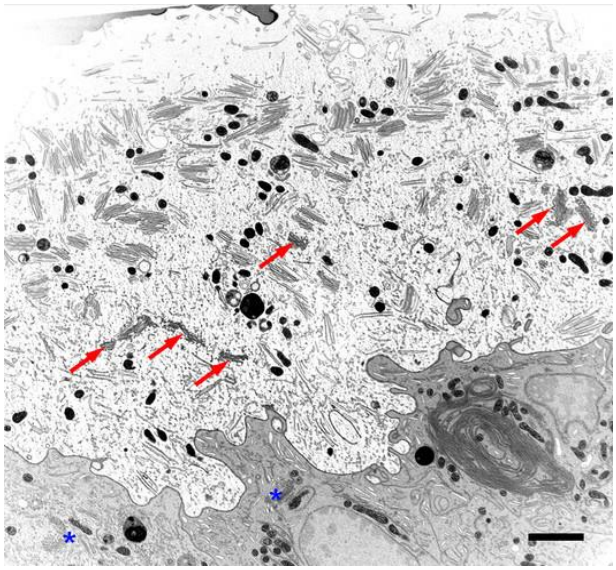

Figure 2. Serial section of mouse urothelium made by FIB. On individual FIB section (no. 856 out of 1056 sections is shown) multiple GA stacks (arrows) are seen in the umbrella cell. Simple GA stacks (asterisks) are seen in intermediate urothelial cells. Bar: 1 μm.

Custodiol versus blood cardioplegia; comparision of myocardial tissue effects in adult cardiac surgery

Ünal Aydın (1), Onur Şen (1), Ersin Kadiroğullaarı (1), Süheyla Gonca (2), Ünal Uslu (3), Alev Cumbul (4), Burak Orhan (1), Korhan Erkanlı (1)

1) Department of Cardiovascular Surgery, İstanbul Mehmet Akif Ersoy Thoracic and Cardiovascular Surgery Training Hospital, Istanbul, Turkey

2) Department of Histology and Embryology, Kocaeli University Faculty of Medicine, Kocaeli, Turkey

3) Private Practise, İstanbul, Turkey

4) Department of Histology and Embryology, Yeditepe University Faculty of Medicine, Istanbul, Turkey

Aim: Cardioplegic arrest is one of the most common myocardial protection strategies. During heart surgeries worldwide, substantially as a method of providing cardiac arrest 'Blood cardioplegia' is used. In some centers in long-awaited procedures, cardiac arrest is achieved using 'Custodiol' solution. In our study, during aortic clambing between Blood cardioplegia and Custodiol groups of patients, we plan to investigate whether there is a difference in cell level of the two methods determined by immunohistochemistry. Material and Methods: Ethics committee approval was received for this study. Our study carried out at Mehmet Akif Ersoy Thoracic and Cardiovascular Surgery Training Rsearch Hospital consisted of 24 cases of patients. The study was planned as two groups (Group I: Custodiol (C), Group II: Blood cardioplegia (BC) and each group contained 12 cases. Deoggraphic datas and risk factors were analyzed and both groups were similar to each others. Cardioplegia was performed via antegrad in both groups and complete cardiac arrest was achieved. Before declamping atrial tissue sample was taken and kept in formalin until histopathological evaluation. Immunohistochemistry was performed (Formalin/PFA-fixed paraffin embedded sections) using an avidin-biotin-peroxidase method. (Zymed, San Francisco, CA). Paraffin embedded sections of 5-µm thickness were stained using a modified terminal deoxynucleotidyl transferase dUTP nick end labeling (TUNEL) technique. The muscle cells from these sections were examined under a Leica DM 4000B microscope with Stereo Investigator version 11.0-image analysis

program. Result: According to immunohistochemistry, in the Blood cardioplegia group, moderate Bcl-2 staining (+++) was seen. In Custodiol group, severe Bcl-2 staining (++++) was seen. Apoptosis positive cells significantly attenuated Blood cardioplegia group as compared to Custodiol group (Figure 1). Conclusion: In this study, anti-apoptotic Bcl-2 molecule was well better preserved in the atrial tissue with the Custodiol group and Blood cardioplegia group, and especially important increased in Custodiol group. Because of the protective myocardial effect of Custodiol solution may result from anti-apoptotic response of tissue via Bcl-2 molecule. Our data suggest that Custodiol may interfere with the apoptotic mechanisms, which are involved in Blood cardioplegia induced cell death. The results of the available evidence suggest that single dose Custodiol solution well-preserved myocardial protection when compared to conventional cardioplegia. Large randomized trials are required to determine the efficacy of Custodiol for both myocardial protection in cardiac surgery and myocardial preservation in cardiac transplant.

References:

1. Misao J, Hayakawa Y, Ohno M, Kato S, Fujiwara T, Fujiwara H. Expression of bcl-2 protein, an inhibitor of apoptosis, and Bax, an accelerator of apoptosis, in ventricular myocytes of human hearts with myocardial infarction. Circulation. 1996 Oct 1;94(7):1506-12.

2. Viana FF, Shi WY, Hayward PA, Larobina ME, Liskaser F, Matalanis G. Custodiol versus blood cardioplegia in complex cardiac operations: an Australian experience. Eur J Cardiothorac Surg. 2013 Mar;43(3):526-31.

3. Karakoyun B, Uslu U, Ercan F, Aydın MS, Yüksel M, Öğünç AV, et al. The effect of phosphodiesterase-5 inhibition by sildenafil citrate on inflammation and apoptosis in rat experimental colitis. Life Sci 2011; 89: 402-7.

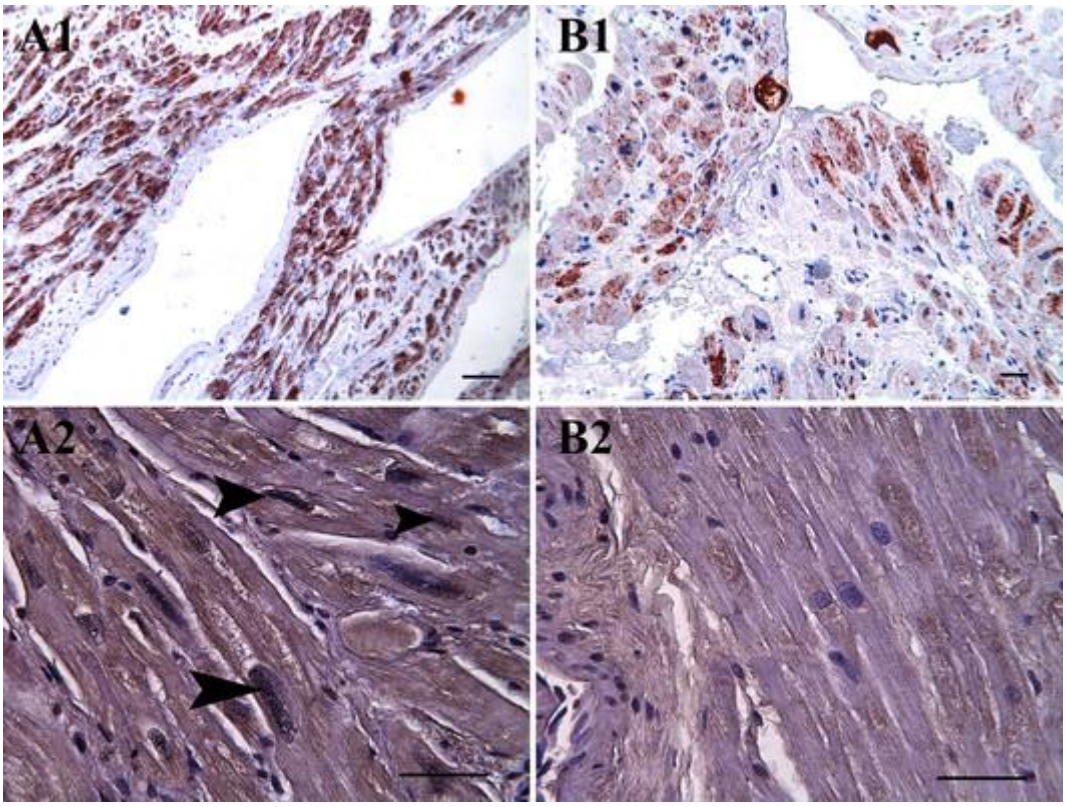

Figure 1. Bcl-2 immunoexpression in the atrial section of Custodiol group is showed (A1). Strong Bcl-2 immunoreactivity is presented in myocardiocyte (++++). Bcl-2 immunostaining in the atrial section of Control (Blood Cardioplegia) group is showed (B1). Moderate Bcl-2 immunoreactivitiy is presented in myocardiocytes (+++). Scale bars represent 200 μm and 150 μm respectively (A1-B1). TUNEL positive cells were increased in Blood Cardioplegia group. Photomicrographs demonstrate TUNEL staining of sections taken from myocardium (A2-B2). Groups: A1; Custodiol treated, A2; Control (Blood Cardioplegia), B1; Control (Blood Cardioplegia), B2; Custodiol treated. Apoptotic cardiac muscle cell (TUNEL positive cell) is demonstrated with arrowhead in A2. Scale bar represents 50 μm (A2-B2).

NDPK A and NDPK B – subcellular dynamics and interactions

Martina Radić (1), Marko Šoštar (2), Helena Ćetković (2), Igor Weber (2), Neda Slade (1), Maja Herak Bosnar (1)

1) Ruđer Bošković Institute, Division of Molecular Medicine, Bijenička cesta 54, HR-10000 Zagreb, Croatia

2) Ruđer Bošković Institute, Division of Molecular Biology, Bijenička cesta 54, HR-10000 Zagreb, Croatia

Keywords: NDPK A, NDPK B, live cell imaging, FRET/FLIM technique

The Nme gene/protein family was named after the first member identified, Nm23-H1/Nme1, which is responsible for metastasis suppression in many tumor types. The Nme1/NDPKA and Nme2/NDPKB are two units of a well-known enzyme nucleoside-diphosphate kinase (NDPK), which transfers the terminal phosphate form (d)NTPs to (d)NDPs and is, therefore, responsible for the maintenance of the cellular nucleotide pool. Besides this housekeeping role, the Nme/NDPK A and B proteins have been assigned several additional biochemical functions such as the His-protein kinase and the scaffold function. There has also been evidence that they may function as transcriptional factors and as exonucleases. The two subunits can assemble into enzymatically active hexamers in all possible combinations (A6, A5B…..B6). Our hypothesis is that the isoenzyme assembly, with potentially distinct roles of the two subunits, differs between specific cellular physiological processes and locations. To be able to determine the potential diverse functions of the A and B subunits, as well as their spatially specific assembly, we subcloned their cDNAs into pEGFP and pmCherry fluorescent reporter vectors, and transfected human tumor cells in culture. By using live cell imaging techniques, we monitored their cellular dynamics with and without induction of DNA damage. Further, we investigated localization of the interaction between subunits by FRET/FLIM technique. Our preliminary results suggest that the assembly of heterohexamers is generally favorable compared to homohexamers. Additional experiments are needed to determine possible spatial specificity of these interactions.

Novel colchicine-BODIPY conjugates for phototherapy

Vladimíra Pavlíčková (1), Silvie Rimpelová (1), Michal Jurášek (2), Ivana Křížová (3), Pavel B. Drašar (2), Tomáš Ruml (1)

1) Department of Biochemistry and Microbiology, University of Chemistry and Technology Prague, Technická 3, 166 28, Prague 6, Czech Republic

2) Department of Chemistry of Natural Compounds, University of Chemistry and Technology Prague, Technická 3, 166 28, Prague 6, Czech Republic

3) Department of Biotechnology, University of Chemistry and Technology Prague, Technická 3, 166 28, Prague 6, Czech Republic

Keywords: colchicine, BODIPY, phototherapy

Colchicine is a plant alkaloid well-known as an inhibitor of microtubule polymerization by binding to tubulin. Destabilization of microtubules leads to cell cycle arrest in the G2/M phase followed by apoptosis. A broader use of colchicine in the clinical practice has been limited by its high systemic toxicity. However, recent findings have opened new possibilities for colchicine application at very low concentrations, e.g. in cancer treatment. Photosensitizers based on BODIPY, especially iodo-BODIPYs, have been lately proven to be very potent for photodynamic therapy (PDT). PDT is one of the approaches for treatment of cancer as well as other severe diseases. PDT principle is based on an application of a photosensitive compound (PS) which is activated by light in presence of molecular oxygen. Then, PSs generate toxic, highly reactive O_2 species, which results in cell death. In this work, we have designed, synthesized and assessed biological properties of novel colchicine-BODIPY and colchicine-iodo-BODIPY conjugates aimed at PDT applications. We found that these conjugates localized efficiently in living cells of four human cell lines after 3 h. The intracellular localization was verified using live-cell fluorescence microscopy and cell organelle-specific fluorescent markers (MitoTracker, ER-Tracker, LysoTracker). The conjugates localized in the endoplasmic reticulum of MCF-7 and PC-3 cells. Further, we determined cyto- and phototoxicity of the conjugates as well as of pure colchicine and pure BODIPY/iodo-BODIPY in a panel of human cell lines. Either of the conjugates did not exhibit significant toxicity (without illumination) in

cancer cell lines LNCaP, PC-3, U-2 OS, HeLa, MiaPaCa-2, and MCF-7 up to 1 μM concentration. A iodo-BODIPY conjugate was very potent in terms of phototoxicity upon illumination with the light of 450–800 nm (the light dose of 4 $J \cdot cm^2$). Cancer cell treatment with this conjugate resulted in a 50% decrease in cell proliferation already at 5 nM concentration for HeLa cells and 10 nM for U-2 OS and PC-3 cells. Next, we will examine further biological properties of the conjugates, since we are convinced that they are very promising for application in photodynamic therapy and could be an effective tool for multimodal therapy, which utilizes two active compounds with a different mechanism of action.

Acknowledgements:

Support from Specific university research (MSMT No 20-SVV/2017) and by JIGA 2017 UCT grant.

Nucleoside-diphosphate kinase Nme6 in humans and sponges

Helena Ćetković (1), Martina Radić (1), Lucija Ačkar (1), Maja Herak Bosnar (1)

1) Ruđer Bošković Institute, Bijenička cesta 54, HR-10000 Zagreb, Croatia

Keywords: Nme6, Nm23-H6, NDPK

Nucleoside-diphosphate kinases (Nme/Nm23/NDPK) constitute a family of evolutionary conserved enzymes involved in many crucial biological processes. Despite of intensive studies in the last two decades, their biochemical functions have not yet been fully elucidated. The family consists of ten members divided in two groups. Group I, which encompasses Nme1-Nme4, has been extensively studied, especially Nme1 in the context of metastasis formation and Nme2 which appears to be involved in cardiac diseases. The Group I members in humans are generally highly homologous among themselves and in comparison to their orthologues in other Metazoans. They all possess the NDP kinase activity in their hexameric form. The Group II members display a lower level of mutual homology and apparently do not possess the NDP kinase activity. Their multimeric structure has not yet been revealed. The Group II members emerged very early in the evolutionary history, especially the Nme5, Nme6 and Nme7 and, therefore, considered to be involved in crucial biological processes. Building upon our previous work on the human and sponge Nme family proteins, the aim of this study is resolving the structure, as well as biochemical and biological functions of the human Nme6 and its changes during evolution. For this purpose we have been analyzing in parallel the human and the sponge nme6 homologs. Sponges are regarded to be living fossils, and it is widely accepted that their genome and proteome structure did not change much in the last 500 million years. Therefore, they have probably preserved the genome and proteome structure of the common ancestor of all Metazoans. Subcellular localization studies using confocal scanning microscopy reviled that the human Nme6 colocalizes mainly with mitochondria, while the sponge variant colocalizes with early, late and recycling endosomes of human tumor cells although it has a putative mitochondrial signaling sequence. The sponge Nme6 protein does not possess the NDPK activity. Bioinformatical analyses of the intron and promoter regions also reviled significant differences between the two nme6 homologs. Our results suggest that nme6

gene/protein changed significantly during evolution probably along with its biochemical and biological function. This, however, needs to be confirmed by future experiments.

Acknowledgements:

This work has been supported in part by Croatian Science Foundation under the project IP-2016-06-4021.

Injection molded microfluidic device for providing dynamic stimuli

Youngtaek Kim (1), Jiyoung Song (1), Youngguen Lee (1), Noo Li Jeon (2)

1) 1 Department of Mechanical and Aerospace Engineering, Seoul National University, Korea

2) 1 Department of Mechanical and Aerospace Engineering, Seoul National University, Korea 2 Institute of advanced machinery and design, Seoul National University, Korea

Keywords: microfluidic, single cell analysis, injection molding, live cell imaging, dynamic stimulation

As time-lapse imaging techniques has been evolved, as research for the response of cells by dynamic stimuli has been emerged. It can overturn the results of previous studies that are derived from static stimuli and obtain heterogeneous results for cells, not average value. The research is enabled by microfluidic devices, and generally. polydimethylsiloxane (PDMS) have been used to replicate the micro channel from the silicon master. However, the manufacturing process using PDMS is time-consuming, expensive and complicate to fabricate. In order to overcome limitations, we proposed a plastic microfluidic device through injection molding. By increasing width, height and gap between channels and simplifying a shape, we manufacture an injection molded device. Using fluorescein isothiocyanate (FITC) and phosphate buffer saline (PBS), we verified that the device was activated when diverse stimuli were provided. We also observed the extracellular signal-regulated kinase(ERK) response of pc12 cell for pulsatile stimulation.

References:

1. Fritz, R. D., Letzelter, M., Reimann, A., Martin, K., Fusco, L., Ritsma, L., . . . van Rheenen, J. (2013). A versatile toolkit to produce sensitive FRET biosensors to visualize signaling in time and space. Sci. Signal., 6(285), rs12-rs12.

2. Ryu, H., Chung, M., Dobrzyński, M., Fey, D., Blum, Y., Lee, S. S., . . . Pertz, O. (2015). Frequency modulation of ERK activation dynamics rewires cell fate. Molecular systems biology, 11(11), 838.

3) Levine, J. H., Lin, Y., & Elowitz, M. B. (2013). Functional roles of pulsing in genetic circuits. Science, 342(6163), 1193-1200.

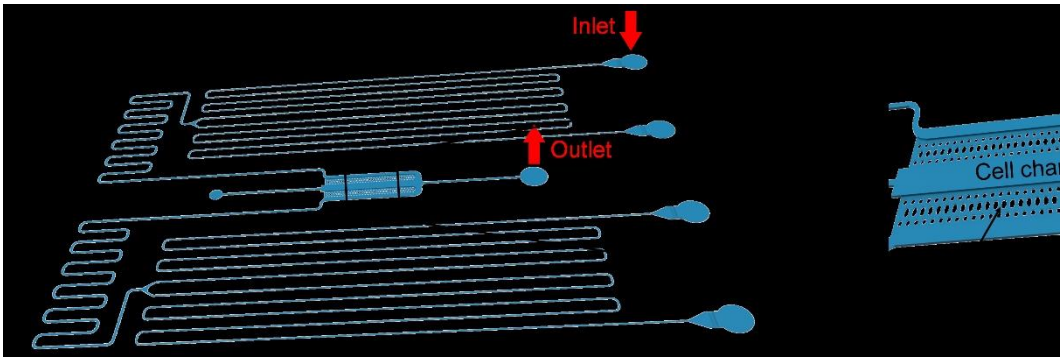

Figure 1. Device design.

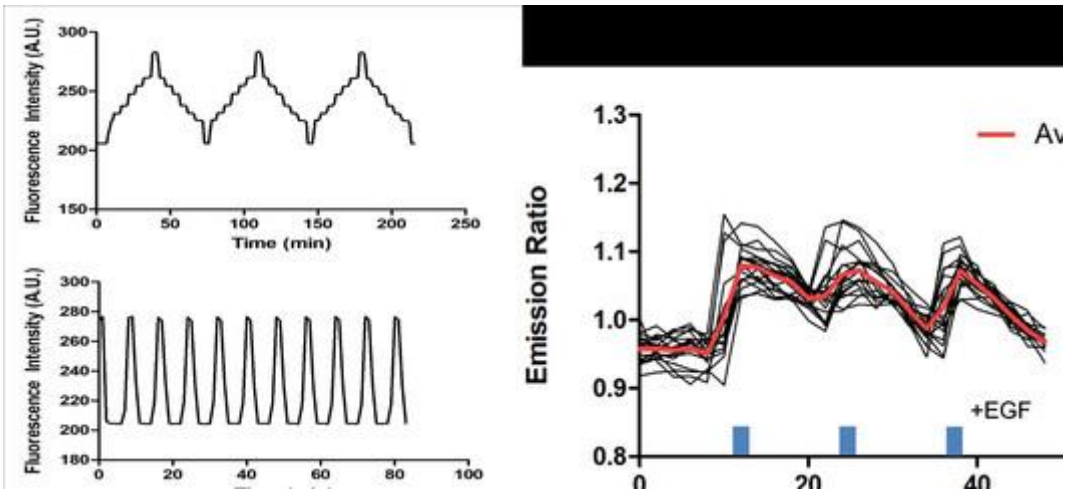

Figure 2. Left) Using PBS Solution and FITC-dextran, we verified that device can be applied for generating ramping and pulsatile stimulation profiles. Pneumatic pressure pump was used to control fluid flow. Right) Starvation medium and starvation medium containing growth factor (100ng/ml EGF) were provided to pc12 cell as pulsatile stimulation for 20 minutes and 3 minutes each. Persistent ERK response was showed as GF was applied to pulse-type.

L2. High-Resolution Microscopy in Biological Sciences

INVITED LECTURES L2:

Combining light sheet microscopy and optical projection tomography to visualize protein dynamics

Matthias Rieckher (1), Athanasios Zacharopoulos (2), Stylianos Psycharakis (2), Udo Birk (3), Nektarios Tavernarakis (4), Jorge Ripoll (5), Giannis Zacharakis (2)

1) Cologne Cluster of Excellence in Cellular Stress Responses in Aging-Associated Diseases (CECAD) Institute for Genome Stability in Ageing and Disease, 50931 Cologne, Germany

2) Foundation for Research and Technology-Hellas Institute of Electronic Structure and Laser, 71110 Heraklion, Greece

3) Institute of Molecular Biology GmbH, 55128 Mainz, Germany

4) University of Crete Department of Basic Sciences, Herklion, Greece, and Foundation for Research and Technology-Hellas Institute of Molecular Biology and Biotechnology, N. Plastira, 70013 Heraklion, Greece

5) Universidad Carlos III de Madrid Department of Bioengineering and Aerospace Engineering, Dr. Esquerdo 46, 28007 Madrid, Spain

Keywords: Light Sheet Microscopy, Optical Projection Tomography, FRAP, *C. elegans* ageing, 3D tumor spheroids

3 dimensional (3D) visualization of the localization and distribution of proteins within cells and whole animals is an essential tool to decipher the molecular mechanisms that underlie biological phenomena, such as development, tissue integrity and organismal ageing. The two novel imaging technologies Light Sheet Microscopy (LSM) and Optical Projection Tomography (OPT) have emerged as exceptionally suitable for rapid *in vivo* imaging of a wide range and size of specimen from the mesoscopic to the sub-micron scale. We present a customized system that combines LSM and OPT for rapid 3D imaging: The LSM is designed for high penetration depth, causes low photo-toxicity and allows for rapid image acquisition when using fluorescently labeled specimens, enabling extended time-lapse *in vivo* experiments. OPT removes the requirement for optical sectioning of specimens, which is required in conventional

confocal microscopy, and acquires high resolution fluorescence, as well as absorption imaging of whole samples. We use the SPIM and OPT modalities to image biomarkers of ageing, which are fluorescently tagged proteins that correlate with organismal lifespan, at different time points of ageing *Caenorhabditis elegans* individuals. To directly quantify the dynamics of de novo protein synthesis and protein distribution we implement fluorescent recovery after photobleaching (FRAP) into our imaging system. In a parallel project, we determine the growth dynamics of 3D spheroid tumor models in a longitudinal study. OPT and SPIM data are combined to merge absorption-derived anatomic information with images of fluorescently labelled proteins. We establish novel reconstruction algorithms to improve the reconstruction speed and the resolution of 3D images. Our versatile setup achieves recording of highly robust datasets when imaging dynamic developmental processes and animal ageing *in vivo*. Further, it permits monitoring of spatio-temporal gene expression and anatomical alterations with single-cell resolution and is easily modified to image a wide range of biological systems.

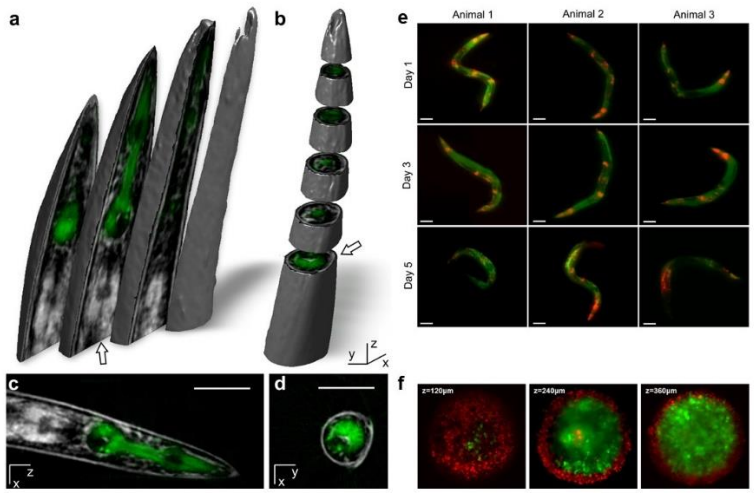

Figure 1. Various 3D images obtained with our combined LSM and OPT modalities. (a, b) 3D visualizations via OPT of anterior body anatomy of *C. elegans*. Three transversal and five coronal sections are shown in (a) and (b), respectively. The 3D view of absorption-derived data and fluorescent information allows detailed visualization and analysis protein localization, down to single cell. (c, d) Two-dimensional, single slices in transversal and coronal planes, respectively, are shown (indicated by white arrows in (a) and (b) respectively). Size bar indicates 50 µm. (e) LSM imaging of protein dynamics in a longitudinal ageing study in 3 single C. elegans individuals grown at 25°C at day 1, 3 and 5. The animals co-express two fluorescently tagged biomarkers of ageing. Size bars are 100 µm. (f) LSM-derived 3D visualization of a growing tumor spheroid with fluorescence-labelled cells.

In vitro handling of oocyte for fertility preservation. Recent ultrastructural acquisitions

Guido Macchiarelli (1), Giuseppe Familiari (2), Stefania A. Nottola (2)

1) University of L'Aquila, Via Giovanni di Vincenzo, 16/B, 67100 L'Aquila, Italy

2) La Sapienza, University of Rome, Piazzale Aldo Moro 5, 00185, Rome, Italy

Keywords: oocyte, ART, ultrastructure, human

Assisted reproduction technology (ART) success depends on the oocyte quality. *In vitro* handling of female gamete, and ART procedure itself, may alter the morphodynamics of oocyte organelles during maturation and thus may prejudice oocyte competence for fertilization. Electron microscopy significantly supports phase contrast microscopy, clinical, epidemiological and bimolecular data, for validation of ART procedures, such as *in vitro* fertilization, cryopreservation and *in vitro* maturation (Nottola et al 2007; Bianchi et al 2014; Coticchio et al 2016). In this study, we analyzed the ultrastructural features of the oocyte subjected to ART procedures, in order to understand whether *in vitro* handling of human oocytes might impair morphological integrity. The ultimate goal is providing a contribution to the realization of less aggressive protocols that may improve ART viability. We analyzed donated human oocytes, obtained during ART cycles after the informed consent of the patients. Our study demonstrated the presence of significant changes, occurring as the consequence of the application of certain ART protocols such as *in vitro* maturation and cryopreservation. In particular, ART derived oocytes showed vacuoles, alteration in the distribution of cortical granules, hardening of the zona pellucida and changes of mitochondria-vesicle complexes. These changes deserves of special consideration because may be related to ART failures and impairment of early embryo development, as well.

References:

1. Nottola SA et al. Hum Reprod. (2007) 22:1123-33.

2. Bianchi V et al. Reprod Biol Endocrinol. (2014) 12:110.

3. Coticchio G et al. Mol Human Rep (2016) 22: 110-118.

ORAL PRESENTATIONS L2:

Ultrastructural analysis of umbilical cord derived MSCs at undifferentiated stage and during osteogenic and adipogenic differentiation

Serbay Ozkan (1), Basak Işildar (1), Mahmut Öncül (2), Zafer Baslar (3), Semih Kaleli (2), Meral Koyutürk (1)

1) Department of Histology and Embryology, Cerrahpasa Medical Faculty, Istanbul University, Turkey

2) Department of Obstetrics and Gynecology, Cerrahpasa Medical Faculty, Istanbul University, Turkey

3) Division of Hematology, Department of Internal Medicine, Cerrahpasa Medical Faculty, Istanbul University, Turkey

Keywords: Mesencymal Stem Cells, Umbilical Cord, differentiation, Transmission Electron Microscopy

Mesenchymal stem cells (MSCs) are considered as an important tool for regenerative medicine and experimental treatment. MSCs are defined as multipotent stem-like cells which are able to differentiate into the cells derived from three germ layers. At this point, unveiling the ultrastructural changes during the differentiation might help to understand the nature of the process and to develop novel therapeutic approaches. In this research, firstly, isolation and characterization of MSCs from sub-amniotic (SAA), intervascular (IVA) and perivascular areas (PVA) of umbilical cord (UC) by utilizing two different methods -enzymatic and tissue explant- were performed to determine the most favorable region of UC, and technique. Consequently, it was aimed to examine the ultrastructural morphologies of the MSCs at undifferentiated status and during osteogenic and adipogenic differentiations. MSCs were isolated from different regions of human UCs (hUC) by enzymatic and tissue explant method. Characterization of the hUC-MSCs groups were done on the bases of morphologic, immunologic and growth kinetic analyses. Osteogenic and adipogenic differentiation were assessed by alkaline phosphatase

and osmium tetroxide black staining, respectively. In addition, ultrastructural morphologies of the MSCs at the end of the 1st and 3rd week of differentiation were also evaluated by transmission electron microscopy. Microscopic analysis showed that the hUC-MSCs generally have active fibroblast like (stellate) cell morphologies with euchromatic nucleus, distinct nucleolus, dilated rough endoplasmic reticulum, autophagic vesicles, filopodia and microvilli-like projections. Among the groups, there was no clear difference in growth kinetics and morphologies. Flow cytometric analysis showed that CD44 and CD90 MSC markers were highly expressed, while CD34 and CD45 hematopoietic stem cells markers were expressed at low degree. Because our preliminary results showed that there was no conspicuous superiority among the hUC-MSCs groups, for further differentiation analysis, MSCs were isolated from whole UC which was preferred for requiring less time and effort with respect to regional approach by applying tissue explant method which was favored for its less probability of damaging the cell membrane compared to the enzymatic one. At the 1st and 3rd week of osteogenic and adipogenic differentiation, ultrastructural analysis showed an increase in autolysosome/autophagosome ratio in comparison with the undifferentiated status. Increase in mitochondrial content was also detected at the 1st week of adipogenic differentiation. Consequently, ultrastructural changes including increased mitochondria number and autolysosome/autophagosome ratio during the adipogenic and osteogenic differentiation could be attributed to the switch in energy metabolism of the MSCs.

Microscopic evaluation of the enamel surface after debonding procedures: an ex-vivo study using scanning electron microscopy (SEM)

Sara Bernardi (1), Maria Adelaide Continenza (1), Guido Macchiarelli (1)

1) Department of Life, Health and Environmental Sciences, University of L'Aquila, Italy

Keywords: dental debonding, Scanning Electron Microscopy (SEM), enamel surface

The orthodontic bracket placement on the dental surface includes the modification of the enamel tissue to improve the adhesive bonding between the composite resin and the bracket-itself. The final stage of the orthodontic therapy, after the bracket removal, is the debonding procedure. Debonding procedure can be defined as the complete residual adhesive removal. This stage should lead to a complete polished enamel in order to prevent the plaque accumulation and future enamel injures. Aim of this study is to evaluate and compare on two groups of extracted teeth by use of Scanning Electron Microscopy (SEM) the enamel surface after the bracket removal and the enamel polishing with four different techniques. The teeth were extracted at the Dental Clinic of University of L'Aquila for periodontal reasons and donated for research with the patients consent. On one teeth group (group A) the enamel polishing techniques was performed with the aid of a magnifying loop. On the other group (group B) the polishing was performed with naked eyes. The four techniques used included the use of (1) Multiblade burr/soft-polisher tip Komet, 2) Multiblade burr/Blade, (3) Disks Sof-lex and (4) enhance/pogo. The teeth were stored in PBS solution and prepared according the protocol of D'Attilio et al.[1] (Angle Orthodonics 2005). The images were analyzed by the Image J software and qualitative and quantitative considerations referring to Adhesive Index Residual and Enamel Damage Index were made. From the qualitative and quantitative images analyses the most conservative technique resulted to be the tungsten carbide bur followed by the final polishing using the soft-polisher tip for composites. In group A, the percentage of the residual adhesive resulted 8% and the damages on the enamel surface showed to be 7%. In group B the percentage of the residual adhesive resulted 35% and the damages on the enamel surface showed to be 15%. From the above considerations, it can be concluded the use of a

magnification system aids in significant way during the debonding procedures for the enamel surfaces' preservation.

References:

1. M. D'Attilio et al., Angle Orthod. 3 (2005) 410-5.

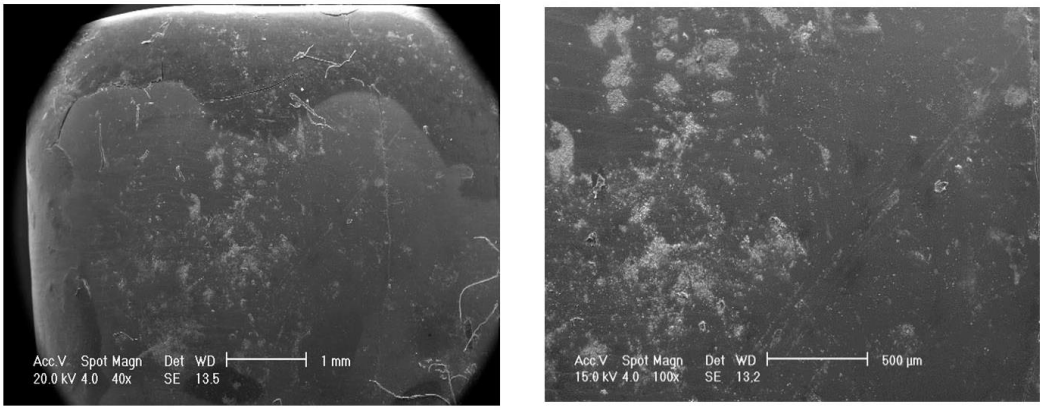

Figure 1. Representative Scanning Electron Microscopy photographs of the 1A sample.

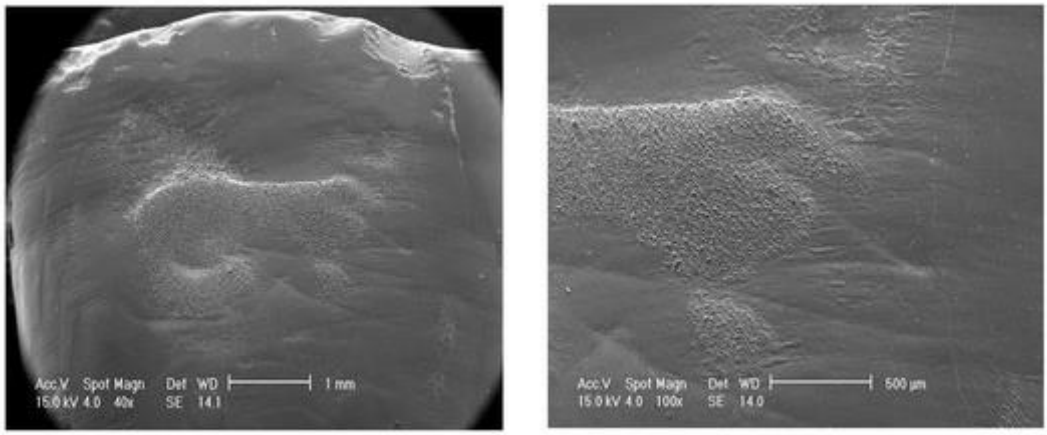

Figure 2. Representative Scanning Electron Microscopy photographs of the 1B sample.

Super resolution, multiphoton and light sheet microscopy for evaluation of two-dimensional and three-dimensional implantation models

Sercin Karahuseyinoglu (1,6), Gizem Nur Sahin (2), Kubra Sari (3), Nida Karahan (3), Ali Cihan Taskin (4), Ahmet Kocabay (4), Deniz Yucel (5)

1) Department of Histology & Embryology, Koc University School of Medicine, Rumelifeneri Kampusu, Maden Mah, 34450, Sariyer/Istanbul, Turkey

2) Cellular and Molecular Medicine PhD rpogram, Graduate School of Health Sciences, Rumelifeneri Kampusu, Maden Mah, 34450, Sariyer/Istanbul, Turkey

3) Reproductive Biology MS program, Graduate School of Health Sciences, Rumelifeneri Kampusu, Maden Mah, 34450, Sariyer/Istanbul, Turkey

4) Animal Facility Center, Koc University College of Sciences Rumelifeneri Kampusu, Maden Mah, 34450, Sariyer/Istanbul, Turkey

5) Department of Histology & Embryology, Acibadem University School of Medicine, Kayısdagi Cad,No:32, 34752, Atasehir/ Istanbul, Turkey

6) Koc University Research Center for Translational Medicine- KUTTAM , Rumelifeneri Kampusu, Maden Mah, 34450, Sariyer/Istanbul, Turkey

Keywords: implantation, culture, 2D, 3D, STED, DLS

Introduction & objectives: Implantation is a very complex biological event that involves the crosstalk between endometrium and blastocyst (1). Implantation failure is a common event that can be as frequent as 40-60% even with assisted reproductive technologies (2). Since the event takes place in a well-organized 3D environment, the *in vitro* mimicking of implantation process is very difficult to organize. The aim of this study involves construction of 2D and 3D culture models and compare the effects of the composed model via use of high-end microscopes as using light sheet, STED and multiphoton technology. Materials and methods: (A) Isolation of epithelial and stromal cells of mouse. The mouse uterus was divided into small pieces and enzymatic lysis was performed. Epithelial cells and stromal cells were cultured separately (Figure 1); (B) Infection of epithelial and stromal cells. Epithelial cells were marked

green with GFP virus. Stroma cells were marked red by FMC virus; (C) Preparation of the polymeric carriers (foams and films). A P(L-D,L)LA (70:30) solution in 1,4-dioxane was prepared by mixing for 24 hours. Polymeric carriers were coated by collagen before use. Polymeric carriers were imaged under a SEM (Zeiss); (D) Formation of 2D and 3D endometrial co-culture. i) Epithelial and stromal cells were mixed and 2-dimensional co-culture was formed on the films; ii) The 3D foam was covered with epithelial and stromal cells; iii) 3D co-cultures by use of jelly extracellular matrix (Matrigel). Blastocysts were placed on 2D and 3D co-cultures and cultured for 48 and 72 hours; (E) Evaluation of implantation parameters. Immunofluorescence staining was performed for LIF(leukemia inhibitory factor), MMP9 (matrix metalloproteinase), E-cadherin and progesterone receptors were measured as implantation parameters (Figure 2). Samples were observed under conventional confocal microscope (Zeiss and Leica) as well as a digital lightsheet set-up (Leica DLS) and multiphoton equipped confocal microsope to evaluate the depth of penetration. Surface modifications were revealed by a super-resolution set-up equipped with STED technology (Leica STED 3x). Samples for prepared in matrigel for DLS and sectioned for STED (3). Results: The parameters were designated as functional parameters (LIF, progesterone receptors) and invasion parameters (E-cadherin, MMP9). The results implicated that, three dimensional cultures with matrigel and foam were more effective in terms of both functional and invasive parameters to support implantation related mechanisms. Conclusion: It was concluded that 3D cultures can be used for implantation experiments.

Acknowledgements:

This research is supprted by KU Seed Fund 00023. The authors gratefully acknowledge use of the services and facilities of the Koç University Research Center for Translational Medicine (KUTTAM), equally funded by the Republic of Turkey Ministry of Development Research Infrastructure Support Program. Findings, opinions or points of view expressed on this article do not necessarily represent the official position or policies of the Ministry of Development.

References:

1. Wang et al. Roadmap to embryo implantation: clues from mouse models. Nat. Rev. Genet. (2006)7(3), 185–199.

2. Timeva et al. Recurrent Implantation Failure: The Role of the Endometrium. J Reprod Infertil. (2014)15(4):173-183.

3. Fendl et al. STED Imaging in Drosophila Brain Slices.Methods Mol Biol. (2017) 1563:143-150.

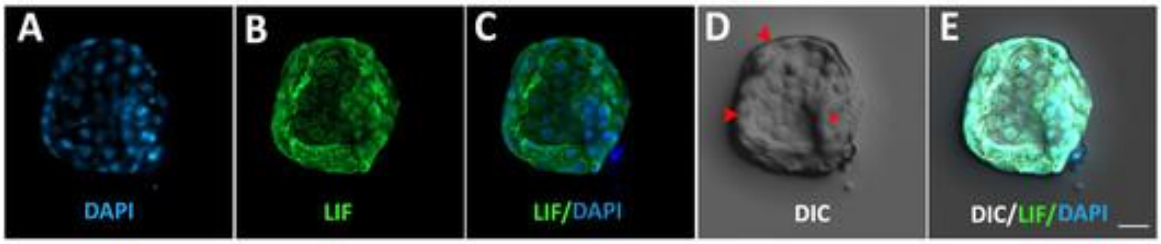

Figure 1. The visualization of a 4AA blastocyst. The sample is stained for LIF at hour 72. Blastocysts are 3D structures, so mounting was designed to be higher not to compress the blastocyst. Red arrowheads: trophoectodermal cells, asterisk: inner cell mass. Bar=20 μm.

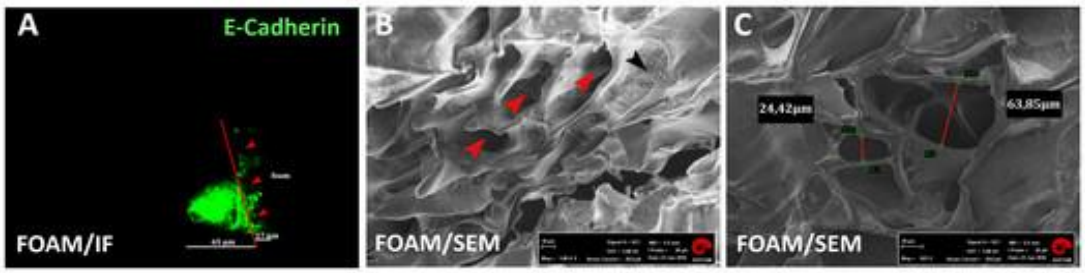

Figure 2. 3D co-cultture with Foam. Blastocyst is in interaction with foam in the inner area (A, foam side). Foam has pores (red arrowheads) of different size (B), (C). The foam is coated with collagen (black arrowheads).

High resolution visualisation of iron deposits in the human brain in health and disease

Mariella Sele (1), Christoph Birkl (2), Stefan Ropele (2), Johannes Haybäck (3), Walter Gössler (4), Gerd Leitinger (1)

1) Medical University of Graz, Institute of Cell Biology, Histology and Embryology, Harrachgasse 21, 8010 Graz, Austria

2) Medical University of Graz, Division of General Neurology, Auenbruggerplatz 22, 8036 Graz, Austria

3) Medical University of Graz, Institute of Pathology, Auenbruggerplatz 25, 8036 Graz, Austria

4) University of Graz, Institute of Chemistry, Universitätsplatz 1, 8010 Graz, Austria

Keywords: iron, ferritin, human brain, HPF, EFTEM

Iron is an important element in the human body not only as part of haemoglobin in erythrocytes but also in the neuronal tissue. It is known to be involved in the synthesis and degeneration of neurotransmitters like dopamine (1), and in the syntheses of myelin sheaths. During aging, from birth until the fourth decade of life, in various areas of the brain iron starts to accumulate (2). However, iron overload may induce oxidative stress to the nerve cell and also make it more susceptible to toxins and inflammatory processes (1). Iron has also been associated with many inflammatory and neurodegenerative diseases like Alzheimer's disease (AD) or multiple sclerosis (3, 4). Chelators for metals have been suggested for treatment of iron overload, but detailed studies about the iron accumulation and its subcellular distribution are necessary before realising such novel treatment ideas (5). Most of the iron in the human and mammalian brain (6, 7) was found in oligodendrocytes but it was also found in neurons and microglia. Because little is known about the mechanism of iron accumulation in the human brain we aim to elucidate the distribution of the stored iron in brain samples of deceased humans. With a comprehensive approach we aim to combine findings from quantitative magnetic resonance imaging, mass spectrometry, analytical electron microscopy, and immunochemical tests of samples taken from six different areas of the brain. Due to ethical and logistical reasons, there

is a considerable time delay from the time of death until the sample can be fixed, especially in comparison to freshly fixed animal brain samples. The autolytic processes partially dismantle the ultrastructure, hence an effective fixation of the samples, especially of the myelin sheaths is very important. As Cryo fixation has been shown to give a truer representation of the neuronal ultrastructure, especially of glial cells (8), we are using high pressure freezing (HPF), followed by freeze substitution and resin embedding, to conserve the ultrastructure as well as possible. We use electron microscope with energy filtered transmission electron microscopy (EFTEM) and Energy-dispersive X-ray spectroscopy (EDX) to localise iron in the brain. Preliminary results confirm that the cellular and subcellular distribution of iron differs between areas with high and low iron content in human brain samples. The basal ganglia which consist of the globus pallidus (205 ± 32 ppm Iron) and the putamen (153 ± 29 ppm Iron) is the brain area in which the most iron was found (9). In these areas were are able to show clusters of iron-loaded particles within oligodendrocytes. The particle size corresponds to the size of the cores of brain ferritin, confirming the notion that ferritin is the main iron storage protein in brain cells.

Acknowledgements:
We kindly acknowledge financial support by the Austrian Science Fund (FWF):[P-29370B27].

References:

1. Zecca L., et al. Nature Reviews Neuroscience 5 (2004) 863-873.

2. Hallgren, B. & Sourander P. Journal of Neurochemistry 3 (1958) 41-51.

3. Smith, M., Harris P., Pauly, S., Sayre, L., & Perry G. PANS 94 (1997) 9866-9868.

4. Khalil, M., Teunissen, C. & Langkammer, C. Mult. Scler. Int. 6 (2011).

5. Bush, A. I. Neuriobiol. Aging 12 (2002) 1031-1038.

6. Connor J, & Menzies S Journal of the Neurological Sciences 134 (1999) 33-44.

7. Merugo, R., et al. Arch. Histol. Cytol., 71 (2008) 205-222.

8. Korogod N., Petersen C. and Knott G. (2015) eLife.

9. Langkammer C., et al. Radiology 257 (2010) 455-462.

POSTER PRESENTATIONS L2:

Melatonin ameliorates mitochondrial status in leptin-deficient mice heart

Alessandra Stacchiotti (1), Gaia Favero (1), Lorena Giugno (1), Igor Golic (2), Marija Aleksic (2), Aleksandra Korac (2), Rita Rezzani (1)

1) Anatomy and Physiopathology Division, Department of Clinical and Experimental Sciences, University of Brescia, Viale Europa 11, 25123, Brescia, Italy

2) Center for Electron Microscopy, Faculty of Biology, University of Belgrade, Studentski trg 16, 11000 Belgrade, Serbia

Keywords: leptin-deficient mice, melatonin, heart, mitochondria, TEM

Question: Leptin-deficient obese mice (ob/ob) developing hyperphagy, abnormal body weight and diabetes represent an interesting translational model to study obesity *in vivo* (1). Melatonin (N-acetyl-5-methoxytryptamine), the pleiotropic product of the pineal gland with strong antioxidant properties, has been successfully tested against the metabolic syndrome and diabetes (2). We previously demonstrated a beneficial role of melatonin against renal and hepatic mitochondria alterations (3). So considering that cardiomyocytes are particularly rich in mitochondria and that data on melatonin in ob/ob mice are still lacking, we performed the present microscopic study to focus on ultrastructural feature and distribution of mitochondria in heart of ob/ob mice fed a regular rodent chow but supplemented or not with melatonin in drinking water at 100 mg/kg/day for 8 weeks. Methods: We described and measured diameter and distribution of subsarcolemmal and intermyofibrillar mitochondria in different groups. Moreover, by Alizarin red staining we observed calcium deposition and, by immunostaining, localized mitochondrial markers like mitofusin 2 and autophagic and oxidative markers like p62/SQSTM1 (sequestosome 1) and 4HNE (4-hydroxynonenal). Results: No statistically significant differences were detected in C57BL6 mice (lean) receiving or not melatonin, so we referred to these last as lean group. By contrast, in ob/ob mice a dramatic change in mitochondria cristae and size (mainly as mega-mitochondria) were described in both

subsarcolemmal and intermyofibrillar sites (Figure 1a). Melatonin supply partially restores cristae organization and mitochondria-sarcoplasmic reticulum association (Figure 1b). Hypoxic status and altered calcium signal associated to leptin-deficiency were attenuated by melatonin supplementation in the diet. Mitofusin 2 expression almost disappeared in ob/ob mice but lipid peroxidation and abnormal autophagic flux were greatly sustained as indicated by strong 4HNE and p62 reactions. In contrast, after dietary melatonin integration, mitofusin 2, a crucial regulator of sarcoplasmic reticulum/mitochondria coupling in the heart, is overexpressed, associated to sustained autophagic flux (Figure 2). Finally, melatonin hampers mitochondrial membrane oxidation and accelerated autophagy as documented by reduced 4HNE and p62/SQSTM1 signals. Conclusions: Taken together our results suggest that in this animal model, melatonin may act as useful adjuvant treatment in obesity, particularly able to sustain cardiac mitochondrial membranes health, clearly visualized by transmission electron microscopy and corroborated by light microscopy. However further biochemical and functional analysis are required to validate the therapeutic role of melatonin in the obese heart.

References:

1. Wang B et al., Curr Diabetes Rev 10 (2014) 131-145.

2. Paradies S et al., J Pineal Res 48 (2010) 297-310.

3. Stacchiotti A et al., Formatex Microscopy Book Series 7 (2017) 208-215.

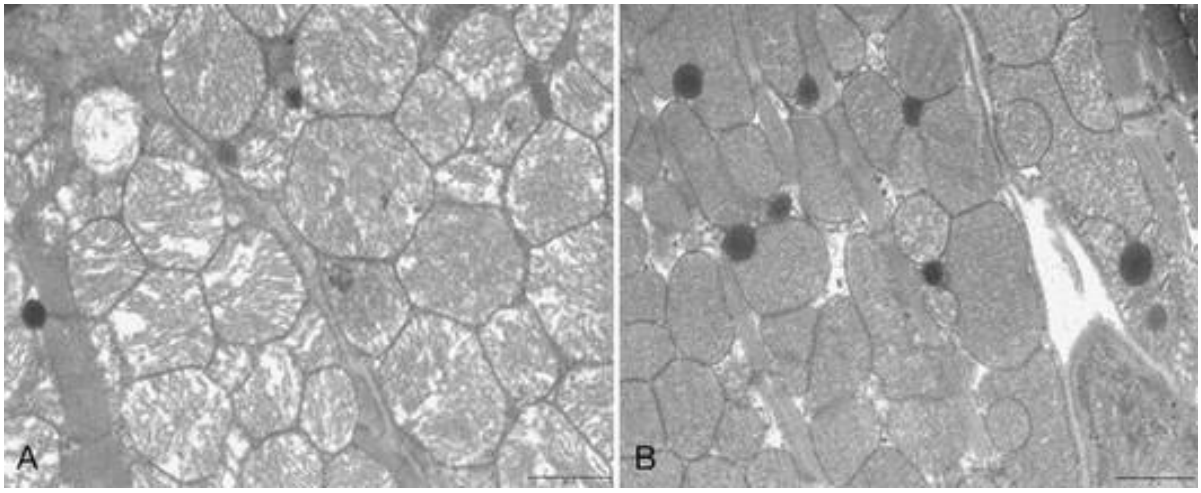

Figure 1. TEM showing mitochondria in leptin-deficient heart mice drinking or not melatonin (MEL) at 100 mg/kg/day for 8 weeks. (A) Leptin-deficient obese (ob/ob) mice, (B) ob/ob plus melatonin. Original magnification: 13000x.

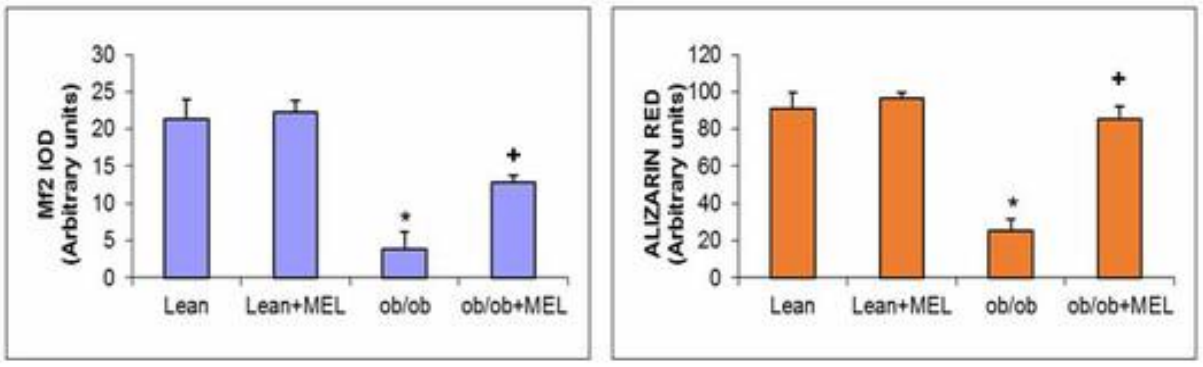

Figure 2. Quantitation of mitofusin 2 immunostaining and Alizarin Red calcium deposition in the heart. Significantly reduced in ob/ob and restored after MEL supply (* p≤ 0.05 significant vs lean/lean plus MEL/ob/ob plus MEL; + p≤ 0.05 vs ob/ob mice).

Reconstructing the auditory region of *Palorchestes azael* using micro computed tomography

Eva Papp (1), Alannah Pearson (1), Michael Curry (2), Julien Louys (1), Gilbert Price (3), Ken Aplin (1), Stephen Wroe (2)

1) The Australian National University, Australia

2) University of New England, Australia

3) The University of Queensland, Australia

Keywords: *Palorchestes azael*, micro CT, auditory region, Lake George NSW, extinct megafauna

Palorchestes azael (Owen, 1873) was an enigmatic, large palorchestid which has been variably reconstructed as a giant kangaroo, marsupial “tapir” and more recently as a unique browsing quadruped with a prehensile lip. *P. azael* was the last surviving member of Palorchestidae and became extinct in the late Pleistocene; well preserved fossils of this marsupial family are rare. The discovery of a fragmented partial *Palorchestes* skull in a limestone crevice near Lake George in South East NSW, Australia, provided a first ever opportunity to reconstruct high resolution 3D models of the auditory region. Due to the process of fossilisation, mineralised soil content adhering to the bone surface made reconstruction a challenging task. Using Micro Computed Tomography (µCT), we were able to reveal the fine-detail of the inner auditory region by digitally separating the rock matrix from the bone. We scanned the fossil using a GE Phoenix v|tome|x X-ray micro-computed tomography scanner, and reconstructed the volume using datos|x and VGStudio Max. Segmentation and 3D model generation was performed using ImageJ and Materialize Mimics.

Acknowledgements:

Funding from the Australian Research Council LP120200626 grant is acknowledged.

References:

1. John A. Cunningham, Imran A. Rahman, Stephan Lautenschlager, Emily J. Rayfield, Philip C.J. Donoghue (2014): Virtual Paleontology. Trends in Ecology and Evolution Vol. 29. No 6.

2. B.S. Mackness, (2008). Reconstructing Palorchestes (Marsupialia: Palorchestidae) - from Giant Kangaroo to Marsupial 'Tapir'. Proceedings of the Linnean Society of New South Wales 130, 21-36.

3. Xijun Ni, John J. Flynn, and André R. Wyss (2012): Imaging the inner ear in fossil mammals: High-resolution CT scanning and 3-D virtual reconstructions. Palaeontologia Electronica Vol. 15, Issue 2;18A, 10p; palaeo-electronica.org/content/2012-issue-2-articles/251-mammal-inner-ear.

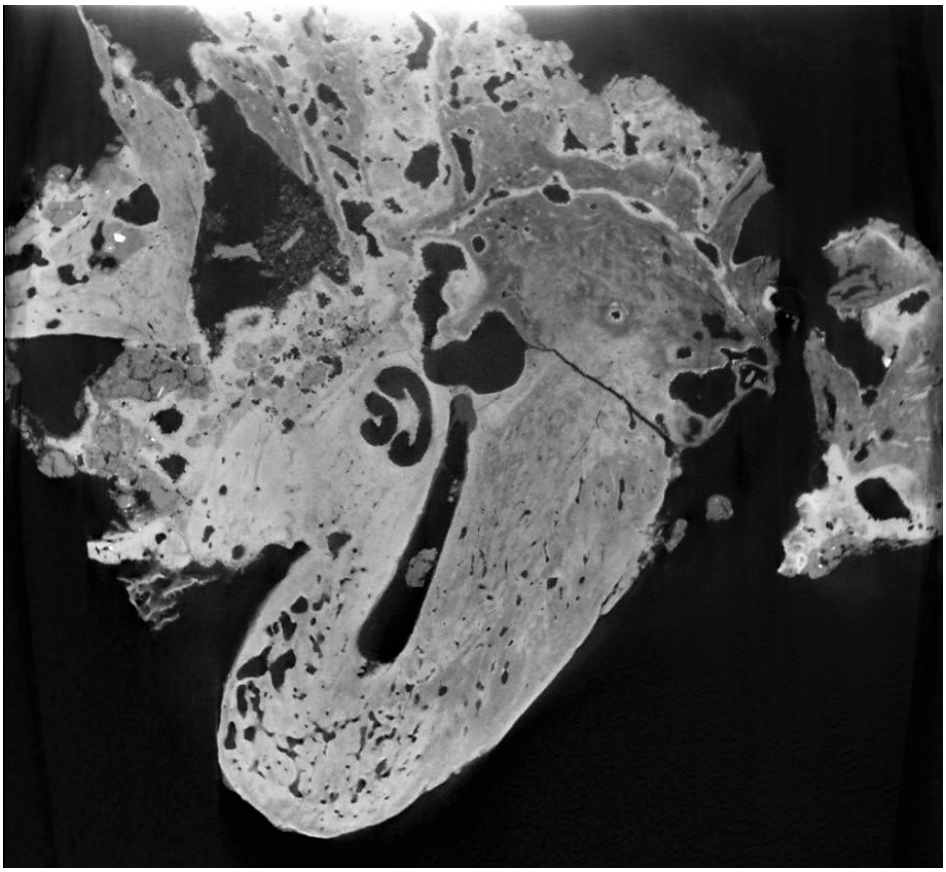

Figure 1. A segment of the micro-CT scan with two of the semicircular canals, a partial area of the cochlea and the tympanic cavity leading toward the external auditory meatus.

Figure 2. *Palorchestes azael*. Artwork by Peter Trusler 2016. Reproduced with permission from the artist.

Microscopy Centre: Electron Microscopy Core Facility

Vlada Philimonenko (1, 2), Zuzana Lubovská (1), Dominik Pinkas (1), Pavel Hozák (1, 2)

1) Institute of Molecular Genetics ASCR v.v.i., Microscopy Center, Electron Microscopy Core Facility, Prague, Czech Republic

2) Institute of Molecular Genetics ASCR v.v.i., Department of Biology of the Cell Nucleus, Prague, Czech Republic

Keywords: transmission electron microscopy, sample preparation, core facility, open access, Czech-BioImaging, Euro-BioImaging

The Electron Microscopy Core Facility provides expertise and cutting edge equipment for a broad range of biological sample preparation and ultrastructural imaging techniques. The core facility deals with various biological samples: human and animal cell cultures, plant and animal tissues, worms, microorganisms, lipid micelles. The sample preparation techniques include routine chemical fixation and resin embedding, cryofixation using high-pressure freezing technique, freeze-substitution, plunge-freezing, cryosectioning, and immunolabeling, including simultaneous detection of multiple targets by our self-developed methods. High-pressure freezing machine, two automatic freeze-substitution machines, cryo-ultramicrotomes, Vitrobot for automated plunge-freezing, as well as additional wet lab equipment are available. The core facility is equipped with two transmission electron microscopes (TEM) – a standard instrument for routine observation and an advanced 200 kV instrument providing the possibility of high-resolution TEM, 3D electron tomography, cryo-electron microscopy and electron energy-loss (EELS) analysis. The team has a long expertise in the development and optimization of sample preparation techniques for electron microscopy. We have optimized the cryofixation of cultured cells and sample processing after cryofixation, developed a completely new system for simultaneous immunolabeling of five molecular targets, a special technique for combination of 3D pre-embedding immunolabeling and 2D on-section immunolabeling to provide more possibilities for spatial analysis of biological processes. We have also implemented quick freezing freeze-fracture replica immunolabeling to the study of inner nuclear structure and developed algorithms for statistical evaluation of immunogold labeling. Currently, we also collaborate with the companies developing instrumentation for electron microscopy to

contribute in development of sample preparation for various modes of microscopic analysis. We collaborate with visiting scientists from the Czech Republic, Austria, Croatia, France, Japan, and Switzerland. The projects deal with a broad range of biological objects and questions, e.g. mechanisms of bacterial infection, nanoparticles uptake by mammalian cells, mechanisms of apoptosis induction and involvement of mitochondria, cell adhesion structures, study of lipid micelles structure, mechanism of heavy metals uptake by plant and human cells, study of mitochondrial structures in protists. The Electron Microscopy Core Facility associated to the IMG Microscopy Centre is part of the IMG Czech-BioImaging node and Prague Euro-BioImaging node. We provide open access to our technologies and expertise.

Acknowledgements:

The core facility is supported by MEYS CR (LM2015062), OPVVV (CZ.02.1.01/0.0/16_013/0001775), IMG grant (RVO: 68378050).

Figure 1. Sample preparation lab of the core facility.

Selenium induces accumulation of lipid droplets in antral follicles of porcine ovaries

Jelena Danilovic Lukovic (1), Anita Lazarevic (2), Maja Bogdanovic (2), Desislava Abadjieva (3), Milena Atanasova (3), Gennadiy Boryaev (4), Elena Kistanova (3), Aleksandra Korac (2)

1) State University of Novi Pazar, Department of Biomedical Sciences, Vuka Karadžića bb, 36300 Novi Pazar, Serbia

2) University of Belgrade, Center for Electron Microscopy, Faculty of Biology, Studentski trg 16, 11000 Belgrade, Serbia

3) Institute of Biology and Immunology of Reproduction, Bulgarian Academy of Sciences, 73 Tzarigradsko shose, 1113 Sofia, Bulgaria

4) Penza State Agricultural Academy, Ботаническая 30, Penza, 440026, Russia

Keywords: porcine oocyte, antral follicles, ultrastructure, lipid droplets

The selenium (Se) is an essential microelement included in diet for reproductive swine female. It is known that Se has an important role in antioxidative defense and maintenance of ovarian tissue in pathological conditions (1) though the information how it could be involved in healthy reproduction of female is limited. The present work is aimed to study the effect of injective application of organic compound selenopyran on ultrastructure of antral follicles of the porcine's ovary. The experiment was conducted with 18 gilts of Danube white breed, ages between 120 - 228 days, divided into two groups each consisting of 9 animals. The animals received equal basal diets without selenium additives (Se content was 15 mg per kg of forage). The experimental gilts (Se-treated) were injected intramuscularly with oil solution of selenopyran (9-phenyl-symmetrical octahydroselenoxanthene) once per month (0.1 mg Se/kg live weight). After euthanasia of animals, tissue from one ovary of each animal was fixed in 4% glutaraldehyde, post-fixed in 1% osmium tetroxide, routinely dehydrated and embedded in Durcupan. Semi-thin sections were stained with Toluidine blue and used to select areas of interest. Ultra-thin sections of selected areas were mounted on copper grids and examined on a Philips CM12 transmission electron microscope. This preliminary study indicates the presence of numerous lipid droplets (LD) (2), as roundish dark structures with electron-lucent

streaks, uniformly distributed and densely packed in the antral follicles oocyte's cytoplasm in the ovaries of Se-treated group (*Figure*1). These structures, containing the dark precipitate which was not detected in cytoplasm or other organelles, were placed in the close vicinity of mitochondria and numerous vacuoles. In contrast, these structures in control group appeared quite different, electron-lucent, various in size and randomly distributed in cytoplasm. These results indicate that Se-treatment induce the heterogeneity in size, distribution and lipid composition of LD in the antral follicle oocytes. In the light of the impact of Se-treatment on the serum lipid content (3), our ongoing research should further clarify the impact of potential lipid profile alteration in ovaries on process of oogenesis and folliculogenesis.

References:

1. M. Jamilian et al., Clin. Enocrinol. 82 (2015) 885-891.

2. R. C. Silva et al., Theriogenology. 76 (2011) 1647-1657.

3. J. T. da Rocha et al., J. Pharm. Pharmacol. 63 (2011) 663-669.

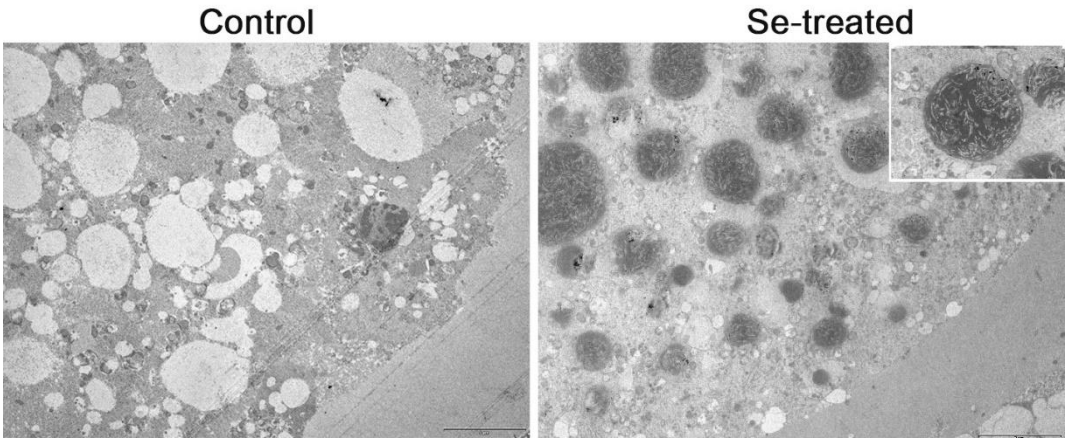

Figure 1. Ultrastructure of control and Se-treated porcine antral follicle oocyte's. Notice the great amount of lipid droplets in the cytoplasm of the Se-treated group. Magnification x3000, inset x13000x.

Hypothyroidism remodels mitochondrial population in rat brown adipocytes: ultrastructural & stereological study

Marija Aleksic (1), Igor Golic (1), Milica Markelic (1), Aleksandra Jankovic (2), Sava Masovic (2), Bato Korac (2), Aleksandra Korac (1)

1) Center for Electron Microscopy, University of Belgrade-Faculty of Biology, Studentski trg 16, 11000 Belgrade, Republic of Serbia

2) University of Belgrade-Institute for Biological Research „Sinisa Stankovic“, Bulevar Despota Stefana 142, 11060 Belgrade, Republic of Serbia

Keywords: thyroid hormones, mitochondria, brown adipocytes

Uncoupling oxidative phosphorylation in the mitochondria of brown adipose tissue (BAT) is a basis of non-shivering thermogenesis. This is accomplished via uncoupling protein-1 (UCP1), which renders the inner membrane of the mitochondria permeable to protons (1). Thyroid hormones (TH) plays an important role in modulating this process trought both, direct and indirect effect. It is well known that UCP1 transcription is positive regulated by thyroid response element (TRE) (2). Also, they regulate mitochondrial gene expression by increasing steady state mitochondrial mRNA levels, respiration, enzyme activity and protein synthesis and by increasing mitochondrial metabolism via TH receptor α2 (TRα2) (3). The aim of this study was to analyze ultrastructural alterations of brown adipocytes mitochondria induced by hypothyroidism using antithyroid drug methimazole. Two month old male Wistar rats were fed with standard pelleted food *ad libitum*. The rats were divided into four groups. Three groups were treated with 0.04% methimazole (MMI) in drinking water for 7, 15, 21 days respectively; untreated animals in the fourth group served as a control. The interscapular portion of BAT was isolated and fixed in glutaraldehyde in phosphate buffer, postfixed in osmium tetroxide, routinely dehydrated and embedded in araldite. Ultrathin sections were mounted on copper grids and examined on CM12 transmission electron microscope. Semithin sections were routinely stained by toluidine blue, and observed using a Leica DMLB microscope. Our results showed that, in comparison to control, induced hypothyroidism led to an increase in relative mitochondrial number, especially in the group treated with MMI for 15 days. Compared to the control, the mean mitochondrial diameter was increased in the group treated with MMI for 7

days, and then decreased with treatment duration. Also, the amount of damaged mitochondria (*Figure* 1), along with a lysosomes numbers was increased during the treatment. Hence, our results suggest that the lack of thyroid hormones can cause a mitochondrial dysfunction and consequently disruption of energy homeostasis in rat brown adipocytes.

Acknowledgements:

This work was supported by Serbian Ministry of Education, Science and Technological Development, Grant #173055.

References:

1. A Lombardi et al., Plos. One. 10(2) (2015) e0116498.

2. A Vaitkus et al., Int. J. Mol. Sci. 16(7) (2015) 16158-16175.

3. D Bassett et al., Mol. Cell. Endocrinol. 213(1) (2003) 1-11.

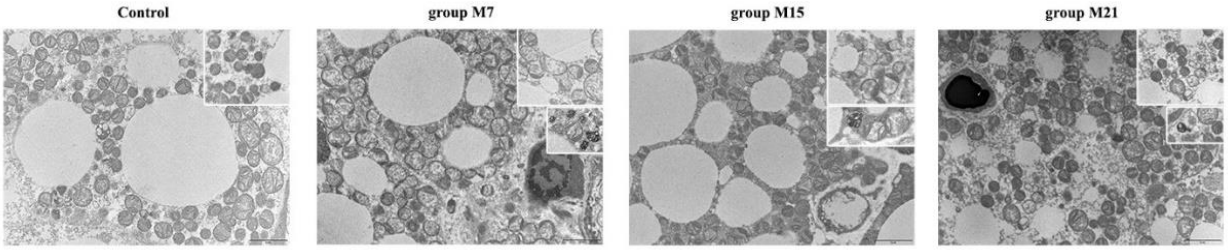

Figure 1. Ultrastructure of brown adipocyte. Methimazole-induced hypothyroidism damages mitochondria during the treatment, and increases the number of lysosomes. Magnification 6300x, insets 10000x.

Insulin-induced appearance of bi-hormonal (glucagon+insulin+) cells in rat pancreatic islets: immunofluorescnet and immunogold studies

Mila Pajevic (1), Marija Aleksic (2), Igor Golic (2), Milica Markelic (2), Aleksandra Jankovic (3), Vesna Otasevic (3), Ana Stančić (3), Bato Korac (3), Aleksandra Korac (2)

1) Clinical Center of Serbia, Department of Histopathology Belgrade, Belgrade, Serbia

2) Center for Electron Microscopy, University of Belgrade-Faculty of Biology, Belgrade, Serbia

3) University of Belgrade-Institute for Biological Research „Sinisa Stankovic“, 142 Bulevar despota Stefana, Belgrade, Serbia

Keywords: pancreatic islets, insulin, glucagon

Newly discovered cellular endocrine plasticity among cells of Langerhans islet may provide the way of their regeneration and treatment of diabetes. Also at the same time it may contribute to islet pathogenesis in diabetes by decreasing beta cell mass and increasing numbers of alpha cells, thereby promoting both hypoinsulinaemia and glucagon excess. Although co-expression of insulin and glucagon in islet cells is documented *in vivo* and *ex vivo*, so far there are no data regarding endocrine plasticity of rat pancreatic islet cells after sustained insulin secretion induced by insulin treatment. The aim of this study was to analyze the effect of insulin treatment on insulin and glucagon polypeptideco-expression in the pancreatic islets, using immunofluorescent and immunogold methods. Two month old male Wistar rats were fed with standard pelleted food *ad libitum*. The rats were divided into six groups. Four groups were treated with a low (0.4 IU/kg) or high (4 IU/kg) dose of insulin (Mixtard® 30, NovoNordisk, Denmark) intraperitoneally once a day, for one (acute) or three days (chronic). The last two groups served as a control and received a 0.9% saline intraperitoneal injection (1 ml/kg) for one or three days. The pancreas was isolated and routinely processed for paraffin or araldite embedding. We used immunofluorescent and immunogold staining with primary antibodies against insulin and glucagon to observe their localization in islet cells. In the group treated with chronic high-dose of insulin we observed the co-presence and specific localization of insulin

and glucagon granules in the same islet cell. These bi-hormonal cells (glucagon+ insulin+) are localized at the periphery of the islets, on the boundary between the α- and β-cells.The insulin granules are localized closer to islets core, while glucagon granules to α-cells. Our results suggest that chronic high-dose insulin treatment leads to co-expression of both hormones, gucagon and insulin in the same cell, with polarity in their localization. The question of possible β- to α-cells transdifferentiation in this conditions was raised.

Acknowledgements:

This study was supported by Serbian Ministry of Education, Science and Technological Development, grant #173055.

L3. Structure and Imaging of Biomolecule

INVITED LECTURES L3:

Varying label density to probe membrane protein nanoclusters in STORM/PALM

Florian Baumgart (1), Andreas Arnold (1), Gerhard J. Schütz (1)

1) TU Wien, Karlsplatz 13, A-1040, Vienna, Austria

Keywords: superresolution microscopy, plasma membrane, single molecule biophysics, immunological synapse

Superresolution microscopy has facilitated the investigation of cellular structures at length scales far below the optical diffraction limit. When applied to the plasma membrane, the presence of a variety of protein nanoclusters was revealed, which lead to speculations whether nanoclustering was a general feature of plasma membrane proteins. Particularly in T lymphocytes, clustering of signaling proteins has been proposed to represent a fundamental mechanism for cell activation. Recently, however, doubts were raised whether imaging artifacts inherent to PALM/STORM might have influenced or even caused the observation of some of those protein clusters. To approach these concerns, we developed a method to robustly discriminate clustered from random distributions of molecules detected with single molecule localization microscopy-based techniques like PALM and STORM (1).The approach is based on deliberate variations of the labeling density of the samples and quantitative cluster analysis. Our method circumvents the problem of clustering artifacts generated by the blinking statistics of the fluorophores used. It can be readily applied to PALM and STORM experiments where either overexpressed proteins are present over a broad range of expression levels or antibody concentrations are titrated to achieve different degrees of labeling. In my talk I will present the application of this technique to a variety of proteins expressed at the T cell plasma membrane.

Acknowledgements:

This research was supported by the Austrian Science Fund (FWF) and by the Austrian Research Promotion Agency (FFG).

References:

1. F. Baumgart et al., Nat. Meth. 13 (2016) 661-664 2.

Imaging therapeutic efficacy of toxin releasing stem cells in recurrent brain tumor

Nihal Karakas (1)

1) İstanbul Medipol University, School of Medicine, Department of Medical Biology, Regenerative and Restorative Medicine Research Center (REMER), Kavacık Mah. Ekinciler Cad. No.19 Kavacık Kavşağı-Beykoz 34810 İstanbul, Turkey

Keywords: bioluminescence imaging, stem cells, targeted toxin, brain tumor

Glioblastoma multiform (GBM), is the most common, agressive and malignant form of brain tumors in adults. Current treatment implementations for GBM include surgical debulking with adjuvant chemotherapy and radiotherapy. Nevertheless, these treatment methods remain insufficient due to the recurrence of tumor, cytotoxicity on healthy brain tissue and blood-brain barrier characteristics. Stem cells have been shown as they have the ability to migrate primary tumor sites and microinvasive tumor deposits in mice bearing brain tumors. Therefore, a new GBM treatment approach has been developed including stem cells as delivery vehicles of therapeutic proteins migrating towards tumor foci. Among therapeutic proteins, targeted toxins are one of the most promising candidates for the treatment of many cancers including GBM. On the other hand, Phase-III clinical trials with targeted toxins were failed due to short half life, systemic toxicity and insufficient tissue penetration. There is therefore an urgent need to safely and continuously deliver targeted toxins to overcome side effects and maximize therapeutic efficacy. In this study, two cytotoxins involving Pseudomonas Exotoxin (PE) and targeting either epidermal growth factor receptor (ENb-PE) or interleukin-13 receptor alpha-2 (IL13-PE) were engineered using lentiviral vectors to treat recurrent GBMs by stem cell delivery of targeted toxins. Our results showed that human neural stem cells (hNSC) secreting targeted toxins have significant therapeutic effect on both GBM cell lines and patient derived GBM cells via inhibition of protein synthesis as a result of toxin action. Protein synthesis kinetics and regression in GBM tumor mass upon therapeutic stem cell delivery was monitored by bioluminescence imaging tools that is based on luciferase signal records. Thus, therapeutic

stem cells increased long-term survival of mice. In conclusion, our findings serve pre-clinical data for the use of stem cells secreting targeted toxins to further adopt them into clinical applications of GBM treatment.

References:

1. Stuckey D.W. et al, Stem Cells. (2015) 33(2):589-600.

ORAL PRESENTATIONS L3:

Ultrastructural examination of the effects of piezoelectric and strontium methods on oocyte activation

Sıla Özlem Öztürk (1), Tuğba Kotil (2), Evrim Ünsal (1), Canan Hürdağ (1)

1) Istanbul Science University, Medicine Faculty, Department of Histology and Embriyology, Gayrettepe, İstanbul, Turkey

2) İstanbul University, İstanbul Faculty of Medicine, Department of Histology and Embriyology, Çapa, İstanbul, Turkey

Keywords: oocyte activation, strontium, piezo electric, ultrastructure

Oocyte activation is a process characterized by ultrastructural changes occurs in ooplasma like changes in organelle distrubution, exocytosis of cortical granules, disappearances of some organelle distribution patterns. Activation triggered with temporary increase of intracellular Ca^{+2} concentrations. If this doesn't occur, activation process arrests and causes infertility (1). Some methods are identified to increase intracellular Ca^{+2} concentrations in women who have activation problems. Strontium simulates the calcium oscillation and fertilization. It stimulates calcium oscillation from intracellular-storage and causes oocyte activation (2). In piezoelectric methods, an electric shock given to cell with 'electro cell manipulator' equipment after microinjection and consequently oocyte activation occurs (3). The aim of our study is to compare ultrastructure of the oocytes the group of treated with strontium and piezoelectric methods and non-treated oocyte control group with transmission electron microscope. Oocytes were obtained from the patients between the ages of 22-55 with the approval form. The waste oocytes were taken from the center after ICSI without fertilization from the Gen-Art Tube Baby, Women's Health and Reproductive Biotechnology Center. In all groups failure of fertilization were evident with intact cortical granules, large smooth endoplasmic reticulum (SER) vesicles and SER aggregates of tubules were seen in the ooplasm with lack of cytoplasmic halo. In the control group mitochondria with clear cristae and all other organelles showed intact morphology (Figure 1a-b). In the piezoelectric group, dilated SER cisternae were detected in

the cortical area, ruptures in the SER membranes and lamellary accumulations were seen in the SER vesicles. Mitochondria degeneration with cristae loss and intense matrix were detected. Autophagic vacuoles with ctoplasmic remnants were seen in the ooplasma (Figure 1c-e). Dilated SER aggregates of tubules and SER cisternia with lamellary bodies were distributed through the ooplasm. Degenerated mitochondria with loss of cristae and vacuole formation were detected. Some mitochondria showed intense matrix. Phagophore formation and autophagic vacuoles were also detected in the oocytes of Strontium group (Figure 1f-h). Cytoplasmic halo occurs after oocyte activation via movement of organelles from cortex to center of the oocyte. Large SER vesicles and SER aggregates of tubules were dissapeared after activation (1). In our findings these changes were not detected in all groups as an evidence of oocyte activation failure. Also degenerative changes like loss of mitochondria cristae, dilated SER vesicles, ruptured SER membranes, lamellary body formations and autophagic vacuoles were seen in the oocytes of piezoelectric and strontium groups. These findings suggested that clinical use of these methods must be evaluated in this regard, and further studies are required to address the issue.

References:

1. M. El Shafie et al., New York: The Parthenon Publishing Group (2000).

2. R.Tomashov-Matar et al., Reproduction (2005) 130 467-474.

3. V. Baltacı et al., Fertility and Sterility (2010) 94 900-904.

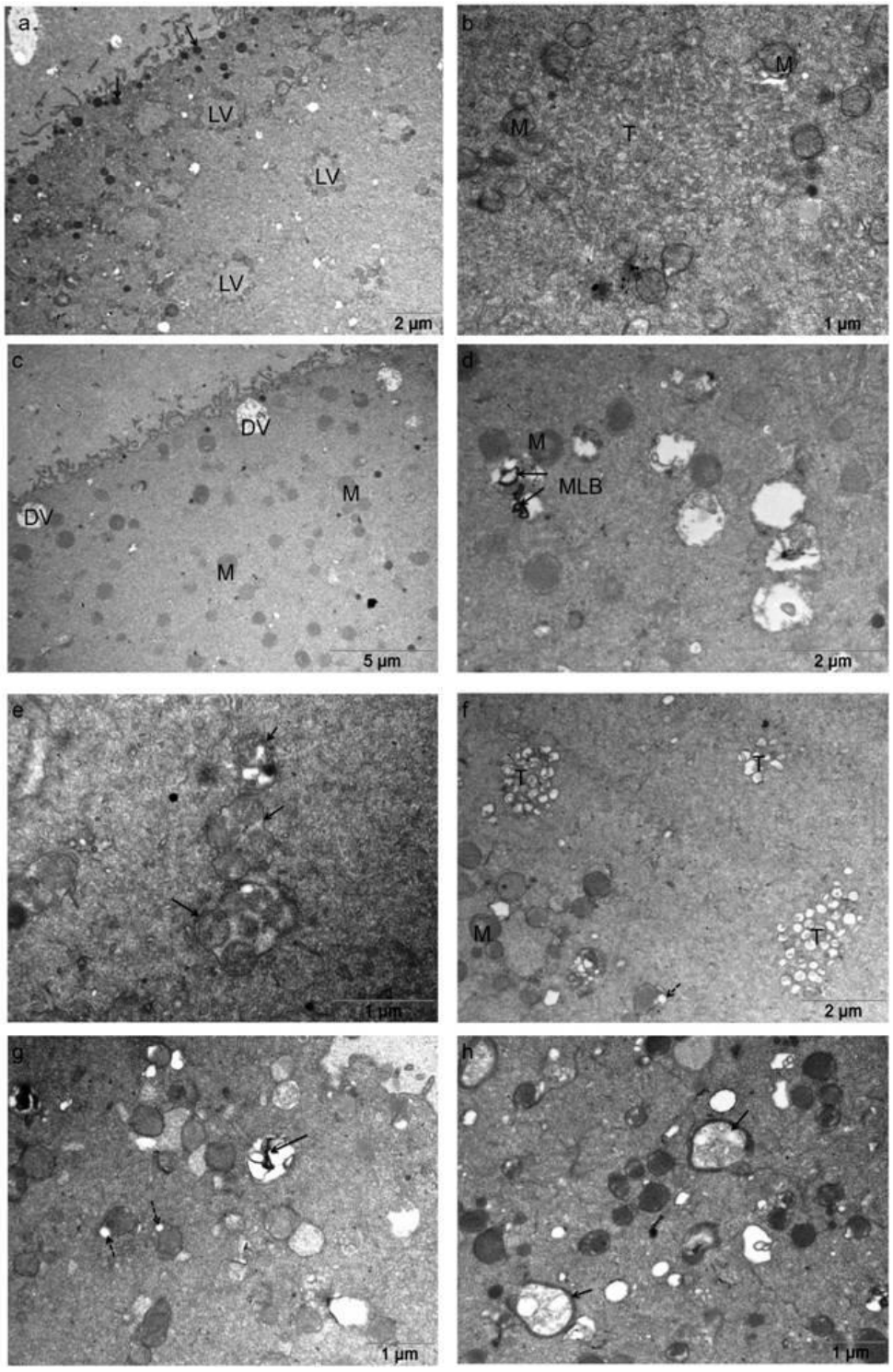

Figure 1. (a-b) Control, (c-e) Piezo, (f-h) Strontium groups. (a) cortical granules (arrows), large SERv(LV); (b) SER aggregates; (c) dilated SER vesicles (DV); (d) multilamellary bodies (MLB); (e) autophagic vacuoles (arrows); (f) dilated tubules (T); (g) MLB (arrows) and loss of cristae (dashed arrows); (h) phagophore (arrows).

Healing effect of p-coumaric acid on ethanol induced gastric damage

Meltem Kolgazi (1), Edanur Arsoy (2), Gulsen Oztosun (2), Muge Yalcin (2), Simge Oral (2), Neslisah Z. Unan (2), Sumeyye Cilingir (1), Merve Açıkel Elmas (3), Nilsu Atay (3), Serap Arbak (3)

1) Acibadem University, School of Medicine, Department of Physiology, Istanbul, Turkey

2) Acibadem University, School of Medicine, Second Year Medical Student, Istanbul, Turkey

3) Acibadem University, School of Medicine, Department of Histology and Embryology, Istanbul, Turkey

Keywords: ulcer, p-coumaric acid, anti-oxidant,rat

Introduction: P-coumaric acid is a phenolic acid that is found in a variety of edible plants, vinegar, wine, and barley grain. Recently, antioxidant, anti-cancer, antimicrobial, antivirus an anti-inflammatory effect of p-coumaric acid has been reported. Peptic ulcer formation depends on the impairments in the mucosal defensive system. Ethanol solubilizes the protective mucus and increases the concentration of hydrochloric acid and pepsin, causing the damage in the membrane and lead to ulceration. Aim: In this study we aim to investigate the anti-ulcer effects of p-coumaric acid in ethanol induced ulcer model. Methods: Following 24-h starvation, Sprague-Dawley rats (300-400g) were divided into 4 groups. Rats were given 75% ethanol (ulcer group) or saline (control group and p-coumaric acid group) by oral gavage. One hour before ethanol administration, rats were treated with either tween-80 (ulcer and control groups) or p-coumaric acid (250 mg/kg suspended in tween-80) (p-coumaric acid group and ulcer + p-coumaric acid groups) per oral. One hour after ulcer induction, all rats were euthanized and their stomach samples were collected for macroscopic examination, microscopic scoring and biochemical analysis. Stomach samples were analyzed for tissue-associated myeloperoxidase (MPO) activity as the indicator of neutrophil infiltration, malondialdehyde (MDA) which is the end-product of lipid peroxidation and endogen anti-oxidant glutathione (GSH) levels. Tissue samples were also examined microscopically under light microscopy. For histopathological evaluation, paraffin sections were stained with haematoxylin & eosin and scored according to

epithelial desquamation, mucosal hemorrhage, glandular damage and eosinophilic infiltration. ANOVA test were used for statistical analysis. Values of $p<0.05$ was regarded as significant. Results: Ulcer induction increased macroscopic ($p<0.001$) and microscopic damage scores ($p<0.001$), gastric MDA levels ($p<0.001$) and MPO ($p<0.01$) activity with concomitant decreases in gastric GSH ($p<0.05$) content. On the other hand, p-coumaric acid treatment reduced microscopic ($p<0.001$) and macroscopic damage scores ($p<0.05$), MDA levels ($p<0.01$) and MPO activity ($p<0.01$), while gastric GSH and were replenished ($p<0.05$). In ulcer group, there was severe damage of surface epithelium and glandular epithelium with hemorrhagic regions and desquamatic cells. Coumaric acid group had slight degeneration of gastric epithelium and moderate inflammatory cell infiltration, while ulcer + p-coumaric acid group the treatment group had minor damage at surface epithelium and gastric glands. Conclusion: It is concluded that p-coumaric acid ameliorates the inflammation in a rat model of ethanol-induced ulcer as confirmed by macroscopic and microscopic examination, along with biochemical assays.

Marine sponge alkaloid and its chemical derivatives as potential anticancer drugs

Sara Salucci (1), Sabrina Burattini (1), Francesca Buontempo (2), Ester Orsini (2), Lucia Furiassi (1), Michele Mari (1), Simone Lucarini (1), Alberto Maria Martelli (2), Elisabetta Falcieri (1)

1) Department of Biomolecular Sciences, Carlo Bo Urbino University, Ca' le Suore 2 street , 61029, Urbino, Italy

2) Department of Biomedical and Neuromotor Sciences, University of Bologna, Irnerio 48 street, 40126 Bologna, Italy

Keywords: U937, apoptosis, mitochondria alterations, TUNEL, Bcl-2 protein involvement

Apoptosis, the most well-characterized form of cell death, has critical roles in development and diseases, including cancer. It can be triggered by a variety of physiological and pathological stimuli and it is routed through two main pathways, the extrinsic and the intrinsic one (1). Marine organisms such as corals, sponges and tunicates produce active molecules which could represent a valid starting point for new drug development processes. The aim of this study is to highlight the action of new molecules, potential apoptotic inducers, extracted from marine sponge. Among the various structural classes, the attention has been focused on marine bisindole alkaloids which have shown significant cytotoxicity, antineoplastic and antimicrobical activity in different cell models (2). Here, for the first time, the effect of 2,2-di(6-bromo-3-indolyl) ethylamine and its chemical derivatives have been evaluated in a U937 tumor cell line (3). Ultrastructural (TEM) and confocal (CLMS) observations reveal apoptotic death in treated-samples, absent in control cells, which present preserved nuclei, negative TUNEL staining and viable mitochondria (*Figure* 1a, b, f). Chromatin condensation, micronuclei (*Figure* 1c) and *in situ* DNA cleavage (*Figure* 1d, e), can be detected. Moreover, mitochondrial alterations, characterized by cardiolipin peroxidation (*Figure* 1g) and loss of mitochondrial membrane potential, appear. Western blotting analyses show that 2,2-di(6-bromo-3-indolyl) ethylamine induce cell death following the caspase dependent pathways and involving the pro-apoptotic Bcl-2 proteins (*Figure* 1h). These findings display the potential role of sponge alkaloids as anticancer drugs in U937 cells *in vitro*. Their action is able to modulate

Bcl-2 protein, enhancing pro-apoptotic factor expression in detriment to cell survival proteins and for this aspect, they represent promising candidates for cancer therapies.

References:

1. S. Salucci et al., Eur. J. Histochem. 59 (2015) 2539.

2. S. Mantenuto et al., Eur. J. Org. Chem. 19 (2016) 3193–3199.

3. S. Salucci et al., Int. J. Med. Food 2017 in press.

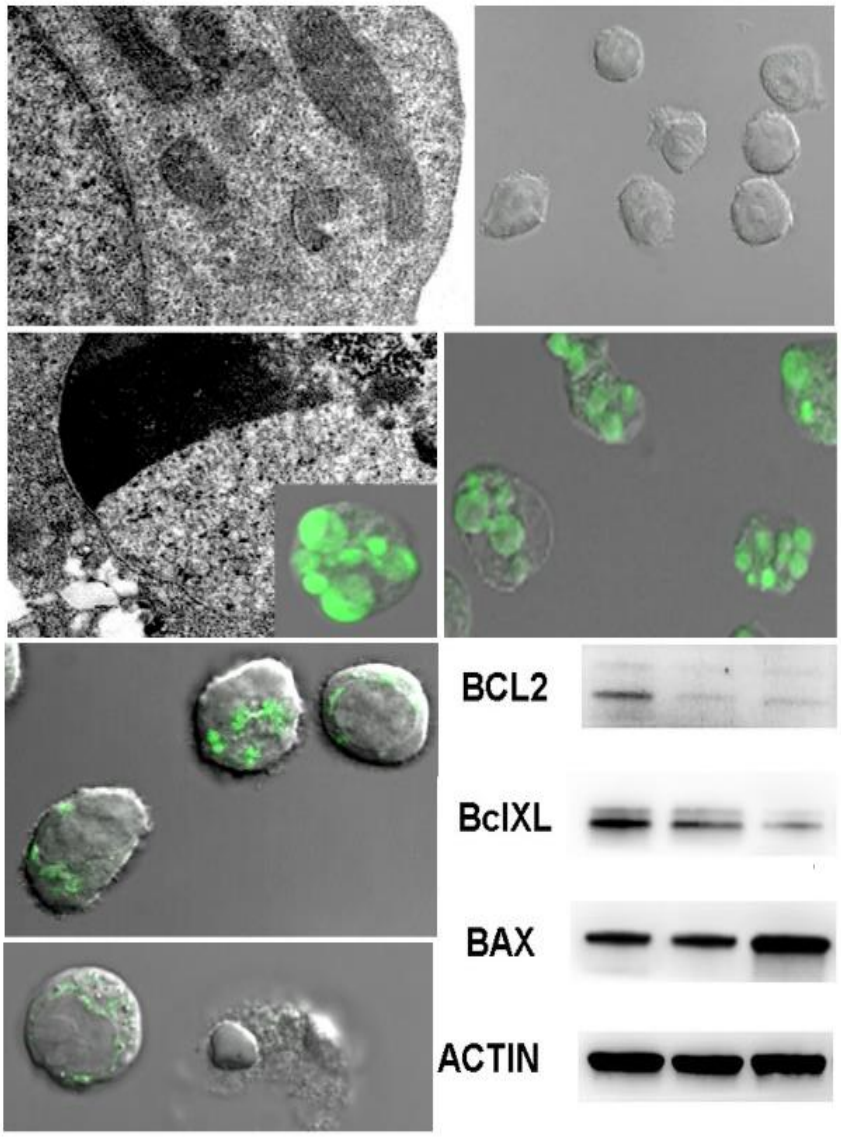

Figure 1. U937 control (a, b, f) and treated (c, d, e, g) cells after TEM observations (a, c) and after TUNEL reaction (b, d, e) or NAO staining (f, g) at CLSM. Western blotting of sponge alkaloid at different concentrations can be observed (h). Bars: 1μm for a and c; 2 μm for d; 5μm for b, e-g.

Comparison of the expression and localization of $FoxO_3$ in normal term and gestational diabetic placentas

Leyla Sati (1), Nilay Kuscu (1), Gizem Gamze Tas (1), Bikem Soygur (1), Ciler Celik-Ozenci (1)

1) Department of Histology and Embryology, Akdeniz University School of Medicine, Antalya, Turkey

Keywords: human placenta, gestational diabetes, FoxO3, immunohistochemistry, western blot

Forkhead box O (FoxO) proteins are a family of signaling molecules that act as nuclear transcription factors that mediate key functions in diverse pathways including cell metabolism, proliferation, differentiation, oxidative stress and cell survival in mammals (1). As a result, genetic mutations in FoxO genes or altered expression of FoxO proteins are associated with diseases such as diabetes. However, the regulation and interaction of these molecules in human are not well known. It was previously shown that FoxO1 involves in the establishment of maternal-fetal circulatory interaction and morphogenesis of normal and pathological placentas including preeclampsia and fetal growth restriction (2). In addition, the presence of FoxO3 and FoxO4 is implicated in normal human placenta suggesting both proteins might contribute to apoptosis and/or cell cycle regulation associated with fetal membrane rupture (3). In line with previous studies, we wonder whether the expression and localization of FoxO3 alters in gestational diabetic placentas that increased oxidative stress is seen in pregnancies in association with increased trophoblast apoptosis and deportation and altered placental vascular reactivity. Therefore, in the present study we aimed to investigate the localization and expression of FoxO3 in normal term and gestational diabetic placentas. Immunohistochemistry and Western Blot methods were performed to localize and determine FoxO3 protein in normal term (n=4) and gestational diabetic placentas (n=5). FoxO3 immunoreaction was observed in stromal cells and some endothelial cells in normal term placentas (Figure 1a, c). There was also weak nuclear FoxO3 immunostaining in some trophoblastic cells. In diabetic placentas, FoxO3 localization was similar with normal placentas; however, stronger nuclear FoxO3 immunoreaction was noted in diabetic samples compared to normal term placentas (Figure

1b, d). No staining was present in the negative controls for FoxO3 in all placenta samples. Western Blot analysis showed an increased expression in diabetic placentas compared to normal term placentas. Since it is known that activation of FoxO impairs glucose metabolism, it is important to investigate the expression of these proteins in placentas of gestational diabetes mellitus women. Here, we demonstrate that the expression of FOXO3 alters in human gestational placenta at protein level. However, further functional studies are needed to make a precise conclusion whether this protein is crucial in the placental pathogenesis of gestational diabetes mellitus.

References:

1. Ho, K.K. et al., Oncogene. 27 (2008) 2300-11.

2. Ferdous, A. et al., Proc Natl Acad Sci U S A. 108 (2011) 16307-12.

3. Lappas, M. et al., Placenta. 31 (2010) 1043-50.

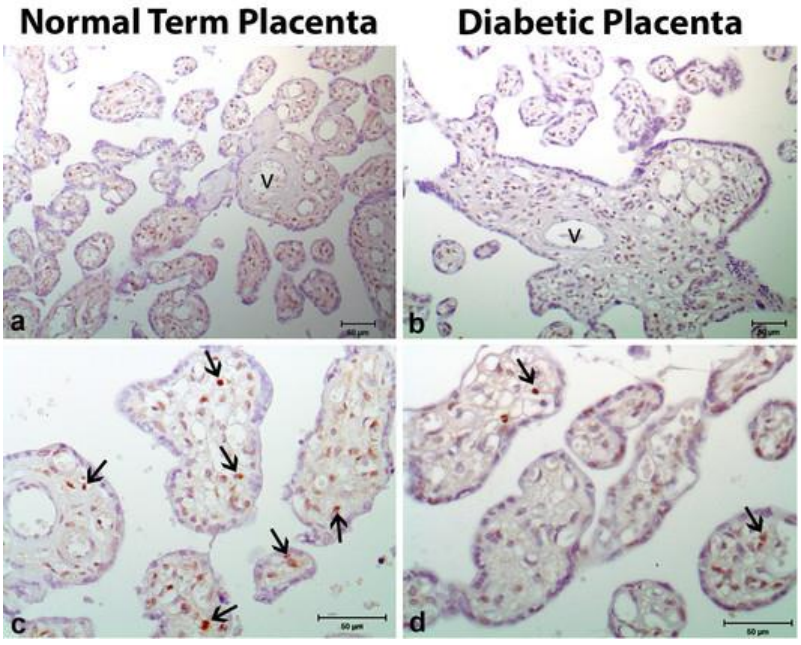

Figure 1. The immunolocalization of FoxO3 in normal term and diabetic placentas. FoxO3 immunostaining was observed predominantly in stromal cells (arrows) and also the endothelium of some vessels (V) both in normal term (a, c) and diabetic placentas (b, d).

POSTER PRESENTATIONS L3:

Modular architecture of Photosystem I-Light Harvesting antenna complex from eustigmatophyte alga, Nannochloropsis oceanica

Zdenko Gardian (1), David Bina (1), Radek Litvin (1)

1) Faculty of Science, University of South Bohemia, Branisovska 1760, 370 05 Ceske Budejovice, Czech Republic, Biology Centre CAS, Branisovska 31, 370 05 Ceske Budejovice, Czech Republic

Keywords: photosynthetic supercomplexes, heterokonta algae

Stramenopile (Heterokonta) algae are a diverse group of eukaryotes with different photosynthetic supercomplexes from those of green algae and land plants. Their chloroplasts are of secondary endosymbiotic origin, originating likely from an engulfed red alga. *Nannochloropsis oceanica* (Eustigmatophyta, Stramenopila) utilizes light-harvesting complexes of multiple classes: Lhcr-type proteins (related to red algae LHCI), Lhcv (VCP) proteins (violaxanthin-containing Lhcs related to Lhcf/FCP proteins of diatoms), Lhcx proteins (related to Lhcx/LhcSR of diatoms and green algae), and Lhc proteins related to Red-CLH of *Chromera velia*. The integral-membrane Lhcr-type light-harvesting antenna was found in association with Photosystem I *(Litvin et al., 2016)*. The precise arrangement of stramenopile PSI antenna is not known, but it can be assumed to have similar architecture as red algae − one or more sickle-shaped arrays attached to monomeric PSI core (Gardian et al., 2007). In this work we studied Photosystem I particles from *N. oceanica* by biochemical and electron microscopy methods, to reveal association of light harvesting system to Photosystem I. *N. oceanica* is shown to be a useful model for studying of stramenopile Photosystem I.

Acknowledgements:

The work was supported from European Regional Development Fund-Project "Mechanisms and dynamics of macromolecular complexes: from single molecules to cells" (No. CZ.02.1.01/0.0/0.0/15_003/0000441).

References:

1. R. Litvin et al., Photosynth Res, 130 (2016) 137-150.

2. Z. Gardian et al., Biochem Biophys Acta, 1767 (2007) 725–731.

Putative effect of exercise on liver in high-fat diet-fed rats

Merve Açıkel Elmas (1), Nilsu Atay (1), Özlem Bingöl Özakpınar (2), Meltem Kolgazi (3), Göksel Şener (4), Feriha Ercan (5), Serap Arbak (1)

1) Acıbadem University School of Medicine, Department of Histology and Embryology, Kerem Aydınlar kampüsü Kayısdagı Cad. İcerenkoy Atasehir İstanbul, 34752 Turkey

2) Marmara University Faculty of Pharmacy, Department of Biochemistry, Hastaneler cad. Haydarpasa İstanbul, 34567 Turkey

3) Acıbadem University School of Medicine, Department of Physiology, Kerem Aydınlar Kampüsü kayısdagı Cad. İcerenkoy Atasehir İstanbul, 34752 Turkey

4) Marmara University Faculty of Pharmacy, Department of Pharmacology, Basibuyuk Maltepe 34587 İstanbul, Turkey

5) Marmara University School of Medicine, Department of Histology and Embryology, Basibuyuk MaltepeİstanbuI, 34587 Turkey

Keywords: liver, microscopy, high-fat diet, exercise

Introduction: World Health Organization (WHO) is defined the obesity as hyperplasia and hypertrophy of adipose tissue that presents a risk to health. Obesity is increasing in western countries and which is the one of major epidemic problems in these countries. In particular, the increase in the consumption of high fat content is one of the most important factors for the spread of obesity in these countries. Obesity, diabetes and metabolic syndrome are important risk factors that cause the pathogenesis of non-alcohol-related liver disease, cirrhosis and hepatocellular carcinoma. Material and methods: Sprague Dawley male rats fed either standard chow (STD group; 6% fat) or high fat diet (HFD group; 45% fat) for 18 weeks and half of these animals were trained by daily swimming sessions (1h per day, 5 days/week) the last 6 weeks (STD+EXC group and HFD+EXC group respectively). After 18 weeks, the animals were sacrified under anesthesia, then blood and liver tissue were collected and prepared for light, transmission electron microscopical (TEM) and biochemical evaluations. Paraffin sections were stained with Haematoxylin–Eosin (H&E) and Masson's trichrome for light microscopical examination. All sections were evaluated for histopathological scoring to

determine the liver damage. Hepatic degeneration, sinusoidal dilatation, vasocongestion and leukocyte infiltration were scored using a scale ranging from 0 to 3 (0: none, 1: mild, 2: moderate, and 3: severe) for each criterion. The total score was 12. For biochemical examinations, malondialdehyde (MDA), glutathione (GSH) levels were measured. All data were analyzed statistically. Results: Normal morphology of liver tissue was observed in STD and STD+EXC group. Light and transmission electron microscopical evaluation of the STD revealed a regular liver parenchyme with intact hepatocytes and sinusoids. STD+EXC and HFD+EXC groups presented slight hepatocyte degeneration. Severe sinusoidal congestion and hemorrhage, degenerated hepatocytes with perinuclear vacuolization and leukocytic infiltration in portal triads were observed in HFD group. Biochemical results were consistent with the histopathological results. Conclusion: This study revealed that swimming training for 6 weeks could only a slight reducing effect on the hepatic parenchymal damage caused by HFD. Effect of daily swimming sessions could be considered as a source of stress and therefore would not be able to sufficiently reverse the hepatic damage due to high fat diet.

References:

1. Evangelista, F.S., et al., Physical training improves body weight and energy balance but does not protect against hepatic steatosis in obese mice. Int J Clin Exp Med, 2015. 8(7): p. 10911-9.

2. Schultz, A., et al., Swimming training beneficial effects in a mice model of nonalcoholic fatty liver disease. Exp Toxicol Pathol, 2012. 64(4): p. 273-82.

3. Sener, G., et al., Estrogen protects the liver and intestines against sepsis-induced injury in rats. J Surg Res, 2005. 128(1): p. 70-8.

Isolation of the chondrocytes and chondroprogenitor/stem cell from human articular cartilage, comparison of the chondrogenic capacity of these two cell lines

O. Ozbey (1), N. Acar (1), F. Tepekoy Ozcelik (1), A. M. Ozenci (1), S. Koksoy (1), I. Ustunel (1)

1) Akdeniz University, Antalya, Turkey

Keywords: CD90, Stro-1, CD105, CD166, Human Articular Cartilage

Articular cartilage has a very limited capacity for self repair. Recent studies have shown that articular cartilage contains a population of progenitor cells. We aimed to isolate and culture the chondrocytes and progenitor/stem cells from adult human femoral distal articular cartilage, and investigate the expression of stem cell markers and differentiation capacities. In our study, chondrocytes were isolated from adult human articular cartilage biopsies with pronase/collagenase digestion. Full-depth chondrocytes were cultured in different culture plates and single cell suspension were seeded on the fibronectin coated petri dishes for isolation of colony cells. Following seeding of chondrocytes, colony cells were selected and seeded on a different culture dish. Briefly, the parameters of this study were; determining the expression of stem cell markers such as CD90, STRO-1, CD105, C166 with flow cytometry and immunofluorescence techniques, induction of chondrocytes and colony cell lines to chondrogenesis, adipogenesis and osteogenesis. Our findings can be summarized as; expression levels were similar between chondrocyte and colony culture cell lines. Our immunofluorescence studies showed that, expressions of all markers were observed in two cell lines, and expression intensity of colony culture cell line was higher than chondrocyte culture cell line after a long-term culture period. On cell differentiation assay results, while chondrocyte culture cell lines were more efficient in the process of chondrogenesis, colony cells were effective in the process of adipogenesis and osteogenesis. In conclusion, according to the results of this study we can say that, there are progenitor/stem cells within the adult articular cartilage which are capable of mesenchymal stem cells (MSC) properties. Moreover, following the long-term culture period, chondrocytes may gain similar features with colony cells.

References:

1. C.W. Archer et al., Birth Defects Res C Embryo Today (2003) 69(2): p. 144-55.

2. G.P. Dowthwaite et al., J Cell Sci. (2004) 29;117(Pt 6):889-97.

The investigation of potential protective effects of tetrandrine against reproductive damage induced by Aroclor 1254 in male rats

Feride Karahan Özdemir (1), Aslı Taşlıdere (2), İlkay Teyyareci Özdemir (1), Fatma Nur Karakuş (1), Osman Çiftçi (3)

1) İstanbul University, İstanbul Faculty of Medicine, Histology and Embryology Department, Turkey

2) İnönü University, Medical Faculty, Histology and Embryology Department, Turkey

3) İnönü University, Medical Faculty, Pharmacology Department, Turkey

Keywords: Aroclor1254, testis, tetrandrine, rat, TEM

AR1254 which is one of the polychlorinatedbiphenyl compounds have immune system suppressive, endocrine disruptive, neurotoxic, carcinogenic and teratogenic effects. Tetrandrine (TET), a bisbenzylisoquinoline alkaloid, has anti-inflammatory, anti-cancer, immunosuppressive and cytoprotective effects. This study was planned to investigate of potential protective effects of TET againts reproductive damage induced by AR1254 in male rats. In our study 28 Sprauge-Dawley rats were used. Rat were randomized into 4 groups: Group 1: Control (corn oil; 1 ml/kg/day orally) Group 2: Ar1254 (2 mg/kg/day intraperitoneally) Group 3: AR1254+TET (2 mg/kg/day intraperitoneally and 30 mg/kg/day orally) Group 4:TET (30 mg/kg/day orally). At the end of the study testis tissue samples were taken from rats. These samples investigated under light and electron microscopy. For light microscopic examination the samples were processed by routine tissue techniques and embedded in paraffin. Tissue samples were cut in 5-µm-thick sections , mounted on slides, stained with Hematoxylin-Eosin (H-E) and examined under a Leica DFC280 light microscope by Leica Qwin and Image Analysis System. For electron microscopic examination the tissue were fixed in glutaraldehyde and postfixed in osmium tetroxide, and embedded in araldite. Sections with a thicknes of 60 nm were taken from the blocks with ultramicrotome (Leica EM UC7) and were examined with TEM (JEOL, JEM-1011) by contrasting with uranyl acetate and lead citrate. In control and TET groups, testis showed a normal histological appearance with TEM and H&E procedure. In AR1254 group, testis tissue showed some histological alterations such as:

Sertoli cells and leydig cells with vesiculated cytoplasm, and much smaller nuclei, Leydig cells showing nuclear shape abnormalities and cytoplasmic disorganization, degeneration and congestion in tunica albuginea layer, congestion, oedema and vacuolisation in interstitial area, reduction in germ line cells in seminiferous tubules, squamotion in lumen, arrested spermatocytes in different stages of division were observed. These fındings were significantly decreased in AR1254+TET group. In biochemical analysis, AR1254 lead to a significant increase in TBARS levels and significant decrease in GSH, SOD, GPxand CAT levels in testis tissue compared with other groups. Besides, in the AR1254+TET group there was an attenuated increased in TBARS levels and an increase in GSH, SOD, GPx and CAT activities. As a result of TET have protective effects againts the reproductive damage which created with AR1254.

References:

1. A. A. et al. , Basic Clin Pharmacol Toxicol 2010 Jun; 106, 6: 479-89.

2. Z. J. et al. , J Ethnopharmacol 2014, 151: 729-32.

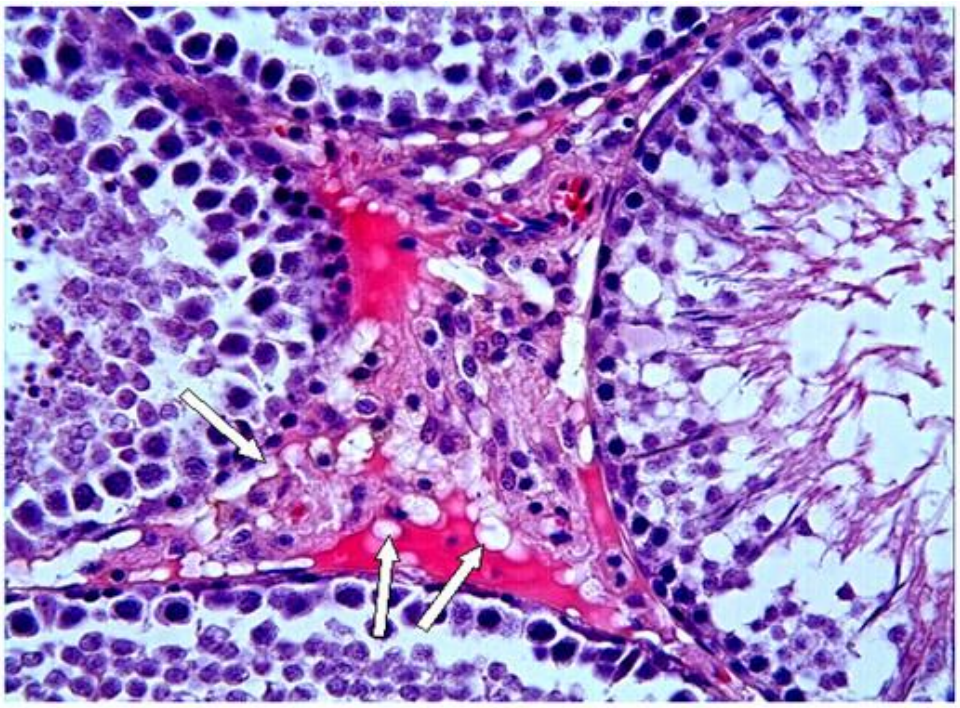

Figure 1. Vacualization (arrows) is observed in AR 1254 treated rat testis tissue. (h-e; X40)

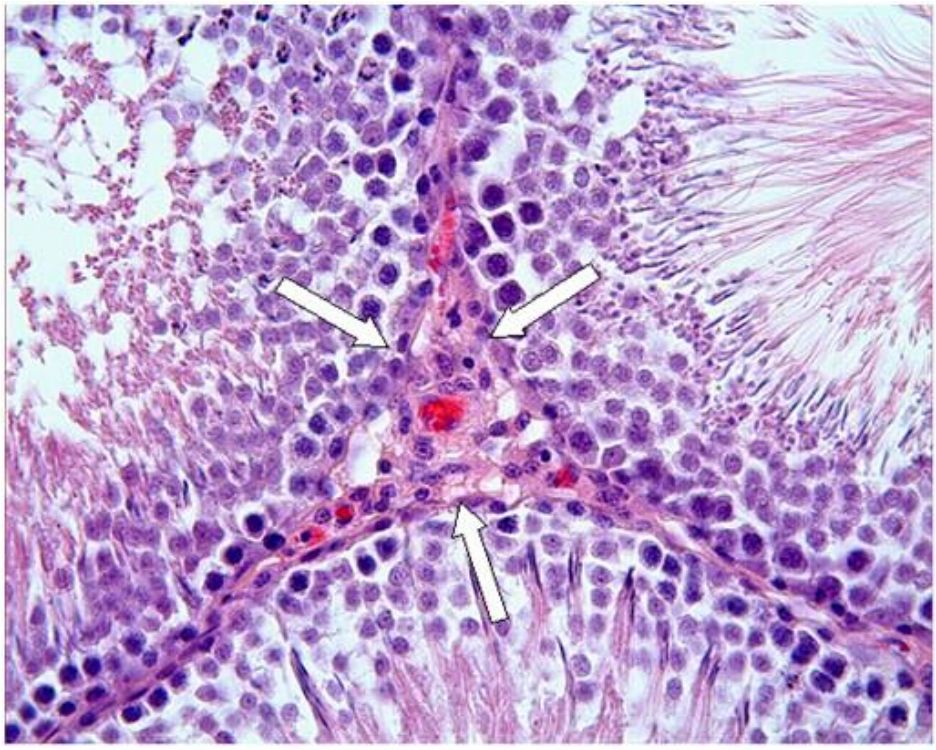

Figure 2. Decreased vacualization (arrows) is observed in AR 1254 + TET treated rat testis tissue. (h-e; X40)

Investigation of the protective effects of tetrandrine in Aroclor1254 exposed liver tissue

Feride Karahan Özdemir (1), İlkay Teyyareci Özdemir (1), A. Erdoğan (1), Asli Taşlıdere (2), Osman Çiftçi (3)

1) İstanbul University, İstanbul Faculty of Medicine, Histology and Embryology Department, Turkey

2) İnönü University, Medical Faculty, Histology and Embryology Department, Turkey

3) İnönü University, Medical Faculty, Pharmacology Department, Turkey

Keywords: Aroclor1254, tetrandrine, liver, electron microscopy

Aroclor1254 (AR1254) which is one of the polychlorinated biphenyl compounds have immune system suppressive, neurotoxic, endocrine disruptive, carcinogenic and teratogenic effects. Tetrandrine (TET), a bisbenzylisoquinoline alkaloid, has anti-inflammatory, anti-carcinogenic, immunosuppressive and cytoprotective effects. In this study we aimed to investigate the protective effects of TET against AR1254-induced hepatotoxicity in rats. 28 Sprague-Dawley rats were randomized to 4 groups and treated for 30 days: Group I vehicle (corn oil; 1 mL/kg/day orally); Group II TET (30 mg/kg/day orally); Group III AR1254 (2 mg/kg/day intraperitoneally); Group IV TET+AR1254 (TET (30 mg/kg/day orally) and AR1254 (2 mg/kg/day intraperitoneally)). At the end of the study, livers were excised and investigated by light microscopy and transmission electron microscopy (TEM). For light microscopic examination, liver samples were fixed with formaldehyde and embedded in paraffin. 5µm thick sections of tissues were cut, stained with Hematoxylin-Eosin (H-E) and examined under light microscope (Olympus BX61). To examinate with TEM, samples were fixed with gluteraldehyde and embedded in epon. 60 nm thick sections of tissues were cut and examined with TEM (JEOL, JEM-1011). In control group, livers showed normal histological appearance with normal hepatic acinar architecture. In TET group, there was no evidence of hepatic abnormality. In AR1254 group, livers showed a visible increase of lymphocyte infiltration at the portal tracts as compared to that of controls. In addition, AR1254-exposed tissue showed sinusoidal dilation in portal tract and degenerated architectural structure. In AR1254+TET

group, these findings were significantly decreased and normal histological pattern was observed. These findings support that TET exhibits hepatoprotective effect in AR1254–induced hepatotoxicity.

References:

1. S.K. et al., Cell Biochem. Funct. (2005) 167-172.25.

2. J.Z. et al., J. Ethnopharmacol. (2014) 729-732.151.

3. S.S. et al., J. Biochem. Mol. Toxicol. (2012) 522-532.26.

The role of luzindole in the antiinflammatory effect of melatonin in the kidney of the rats with type 2 diabetes mellitus

Hande Yapislar (1), Ebru Haciosmanoglu (2), Turkan Sarioglu (3)

1) Acibadem University Faculty of Medicine Physiolgy Department, Istanbul, Turkey

2) Istanbul Bilim University Faculty of Medicine Physiology Department, Istanbul, Turkey

3) Istanbul University Faculty of Medicine Histology and Embryology Department, Capa, Istanbul, Turkey

Keywords: Type 2 diabetes, melatonin, inflammation

Diabetes is a chronic, metabolic disease with serious complications. The diagnosed diabetes cases are mostly consist of Type 2 diabetes mellitus. Inflammation is one of the main causes of complications observed in Type 2 diabetes mellitus as nephropathy, retinopathy and neuropathy. Inflammation that occurs by different pathways and mechanisms causes a progress in diabetic microvascular complications. Melatonin is a hormone released from pineal gland with circadian rhythm which has antoxidant effects. Melatonin is also related to inflammation. In this study, we investigated the effect of melatonin by suppressing MT2 receptor in diabetes mellitus due to its anti-inflammatory effects. 2,5 months old Sprague Dawley male rats were used for this experiment. Type 2 diabetes was induced with nicotinamide (NA 100mg/kg) and streptozotocin (STZ 50 mg/kg). We had 4 experimental groups consisted of 10 rats each; control group, type 2 diabetes mellitus group, type 2 diabetes mellitus group treated with Melatonin (500 µg/day) and type 2 diabetes mellitus gruop treated with Luzindole (0.25 g/kg) and Melatonin. Xylazine (10mg/kg) and Ketamine 100 mg/kg) were used for anaesthetics. After kidneys were taken, rats were decapitated. We studied inflammation markers, IL-1beta, TNF-alpha, IL-6 and NFkB protein levels with immunohistochemistry in the kidney with immunohistochemistry. Images were analyzed with Image J Programme. All inflammation marker levels were found to be increased significantly in type 2 diabetes group than the control group ($p<0.05$). Our data showed that inflammation markers of melatonin treated groups decreased significantly when compared to type 2 diabetes group ($p<0.05$) in kidney. However, when we applied luzindole, we found that the anti-

inflammatory effect of melatonin was reduced ($p<0.05$). Type 2 diabetes has microvascular complications and inflammation is being blamed for these complications. Kidney are one of the tissues most affected of the disease due to their roles in the body. We observed that melatonin decreased inflammation in kidney of diabetic rats and melatonin has been shown to mediate its antiinflammatory effect through MT2 receptors. Melatonin might be an important agent to prevent microvascular complications by decreasing inflammation in type 2 diabetes mellitus.

References:

1. Peschke E, Frese T, Chankiewitz E, Peschke D, Preiss U, Schneyer U, et al. Diabetic Goto Kakizaki rats as well as type 2 diabetic patients show a decreased diurnal serum melatonin level and an increased pancreatic melatonin-receptor status. J Pineal Res. 2006 Mar;40(2):135-43.

2. Domingueti CP, Dusse LM, Carvalho Md, de Sousa LP, Gomes KB, Fernandes AP. Diabetes mellitus: The linkage between oxidative stress, inflammation, hypercoagulability and vascular complications. J Diabetes Complications. 2016 May-Jun;30(4):738-45.

3. Donath MY. Multiple benefits of targeting inflammation in the treatment of type 2 diabetes. Diabetologia. 2016 Apr;59(4):679-82.

Assembly of interleukin-2 and -15 receptors during trafficking

Julianna Volkó (1), Ádám Kenesei (1), Péter Várnai (2), Felix Bestvater (3), Thomas A. Waldmann (4), Katalin Tóth (3), György Vámosi (1)

1) Department of Biophysics and Cell Biology, University of Debrecen, Egyetem tér 1, H-4032 Debrecen, Hungary

2) Department of Physiology, Semmelweis University, Tűzoltó utca 37-47, H-1094 Budapest, Hungary

3) German Cancer Research Center, Im Neuenheimer Feld 580, 69120 Heidelberg, Germany

4) Lymphoid Malignancies Branch, Center for Cancer Research, National Cancer Institute, Building 10, Room 4N115, Bethesda, MD 20892-1374, USA

Keywords: Interleukin receptors, FRET, ER, Golgi

Interleukin-2 and -15 are important cytokines in the activation and death of T and NK cells. Their membrane receptors exist in the membrane of immune cells as heterodimers or -trimers of their cytokine-specific alpha and shared beta and gamma-c subunits having different ligand binding affinities. Assembly of the subunits has already been characterized at the cell surface, but their formation inside the cell after their synthesis remains to be clarified. Our aim was to investigate the associations of subunits in the ER and Golgi. We created plasmids expressing the different receptor chains tagged with EGFP (as FRET donor) or mCherry (as FRET acceptor). After co-transfecting cells with the receptor chains, their association was characterized by intensity based FRET using confocal microscopy. TagBFP-tagged ER and Golgi markers were used to localize these organelles; FRET data were analyzed in an organelle specific manner. IL-2/15 receptor subunits showed positive FRET efficiency during their trafficking. Our data suggest that the receptor subunits start to assemble prior to reaching the cell membrane, already in the ER. Our data may also imply that in T cells producing IL-2, signaling might take place inside the cell before receptor chains are expressed in the plasma membrane. These results may have clinical importance by helping to understand the inefficacy of interleukin-2 receptor-targeted antibody therapies in certain lymphomas.

Acknowledgements:

This work was supported by grants from the Hungarian Scientific Research Fund K103965 and the German Academic Exchange Service and the Tempus Public Foundation Hungary (#73163) and EFIS-IL Fellowship.

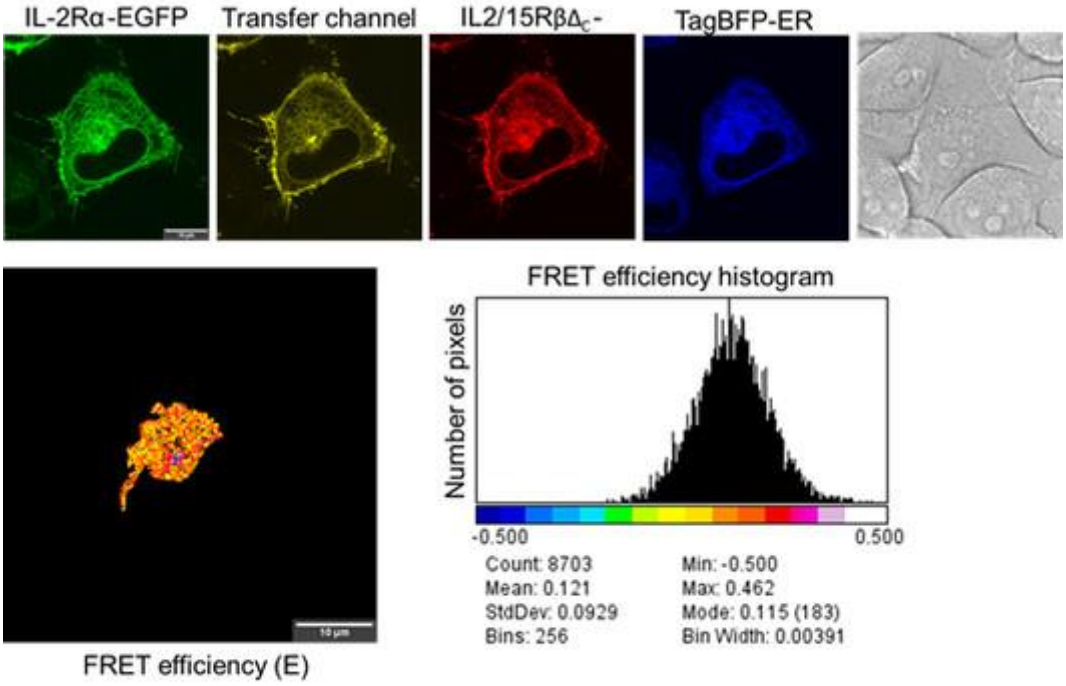

Fig. 1 FRET measured between IL-2Rα and truncated IL-2/15Rβ subunits

L4. Nanobiology and Nanomedicine

INVITED LECTURES L4:

Opportunities and challenges of cancer treatment by SPIONs

Rok Romih (1)

1) Institute of Cell Biology, Faculty of Medicine, Vrazov trg 2, 1000 Ljubljana, Slovenia

Keywords: nanoparticles, SPION, cancer, magnetofection, transmission electron microscopy

Advances in nanoparticle synthesis and functionalization have opened numerous possibilities in the field of nanomedicine. Nanoparticles are used in both therapeutic and diagnostic applications in the clinic, especially in cancer management. In order to improve current cancer treatment strategies, nanoparticles must be optimized to deliver the right therapeutic to the right target and to achieve its localised release and action. The huge benefit of such approach is minimization of systemic toxicity and detrimental side effects. To target cancer cells in the body, nanoparticles must overcome various obstacles, such as phagocytosis by macrophages due to opsonisation, endothelial and epithelial barriers as well as cell barriers (plasma membrane, the membrane of endosomes, cytosol and nuclear envelope). Nanoparticles that may fulfil all these requirements are superparamagnetic iron oxide nanoparticles (SPIONs). SPIONs greatest advantage is that they can be guided to the target cells by applying external magnetic field, yet they do not retain residual magnetism in the absence of the magnetic field. Furthermore, different coatings and functionalization can modify their physicochemical properties, biocompatibility, cellular uptake and intracellular trafficking. In addition, conjugation with therapeutic nucleic acids, such as DNAs, RNAs or siRNAs, makes SPIONs suitable for magnetofection mediated gene therapy. We synthesised SPIONs of different sizes (8 – 14 nm) and coatings (polyacrylic acid (PAA) or silica). Positive and negative surface charge of silica coated SPIONs was obtained by functionalization with amino and carboxyl groups, respectively. PAA coated SPIONs were further functionalised with polyethylenimine (PEI) for binding of nucleic acids. We used plasmid DNA containing reporter gene encoding GFP, plasmid DNA encoding Interleukin 12 (IL-12) and short hairpin RNA against Melanoma Cell Adhesion Molecule (MCAM). We explored the effects of surface charge, functionalization and

external magnetic field on distribution, targeting, cellular uptake and intracellular trafficking of our custom synthesised SPIONs. These effects were determined *in vitro* on normal urothelial cells (PU), MDCK cells, mesothelial cells (MeT-5A), fibroblasts (L929), melanoma cells (B16F1 and SK-MEL-28) and *in vivo* on two tumour mouse models (B16F10 melanoma, TS/A mammary adenocarcinoma). In my talk, I will present the results of our study and discuss the opportunities and challenges of using magnetofection to target cancer cells by intratumorally injected SPIONs. I will focus on the contribution of transmission electron microscopy in investigation, understanding and improvement of cancer management by using SPIONs.

The nano world: strategy for life style improvement

Stefania Meschini (1), Maria Condello (1), Evelin Pellegrini (1), Marina Scarpa (2)

1) National Center for Drug Research and Evaluation, Italian National Institute of Health, Rome, Italy

2) Nanoscience Laboratory, Department of Physics, University of Trento, Povo-Trento, Italy

Keywords: nanomaterials, drug delivery, TEM, cytotoxicity, quantitative analysis

Nanoparticles (NPs) are defined as particles designed and produced to have at least one dimension lower than 100 nm. They have physico-chemical characteristics that are not found in their bulk counterparts and for this reason are used for biological, medical, environmental and industrial applications. The nanomaterials are in the composition of cosmetics, dental cements, electrodes for solar cells, pigments for paints, gas sensors and, not least in the field of environmental remediation, demilitarization of chemical and biological warfare agents and photocatalytic decontamination. Important developments of nanotechnologies in medical diagnostic and photodynamic therapy, food and packaging fields require the benefit-risk assessment. Nanoparticles have also shown to be a great promise in the development of efficient drug delivery systems to reach specific sites such as organs, tissues and cells. Especially in the early diagnosis, for the opportunity of high-resolution imaging in the hard-to-find diseases, such as early-stage malignant cancer and very rare circulating tumor cells. Decreasing particle size, the surface area to volume ratio increases, so small particles can become more responsive to the biological activity. This is matter of concern for the use of nanomaterials in biomedicine and in this regard electronic microscopy analysis provides a platform to evaluate toxicity and interaction of nanostructures with biological systems. At present nanomaterials with different size, shape, chemical composition and surface functional groups are currently produced. Here we show some representative examples. Figure1a is the SEM image of titanate nanotubes that were prepared by the hydrothermal method modified to increase the affinity of this nanomaterial for water (1). The unusual characteristic of this nanomaterial is the reduced length, the high solubility in aqueous environment and the high capacity of exchange small cations, such as sodium ion. These properties suggest that this

nanomaterial has a good biocompatibility and could be useful for biomedical applications, in particular for drug delivery. Figure1b shows the effect of Titaniun dioxide nanoparticles on human epithelial colorectal adenocarcinoma cells (Caco-2). Cell retraction, rounding and microvilli modifications underline cytotoxicity due to the treatment. In *Figure* 1c is clearly visible the toxicological effect of multwall carbon nanotubes (mwCNTs) -OH groups functionalized, on mouse fibroblast cells line (Balb/T3) after 72h of treatment (2). Carcinogenic potential and direct interactions with cell nucleous were observed. Same cells (Balb/T3) treated with gold nanoparticles (AuNPs) for 72h show the nanostructure internalization confined mainly in lipid vescicular bodies (*Figure* 1d) (3). For these reasons, information about the safety, or the potential hazards or benefits of nanostrutured materials using are of high impact in the society.

References:

1. Zennaro L , Scarpa M. et al., ChemPhysChem 14 (2013) 2786 – 2792.

2. Gioria S., Meschini S. et al. Toxicology Letters, 228 (2014) 111-126.

3. Ponti J., Meschini S. et al. Nanotoxicology, 7 (2013) 231-233.

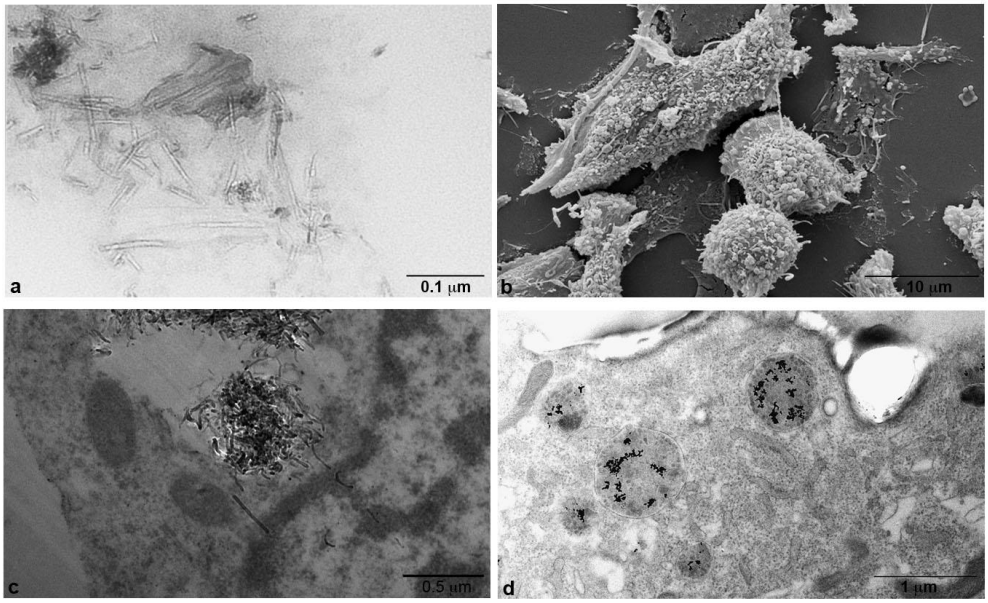

Figure 1. (a) TEM image of Titanate nanotube; (b) SEM image of cells treated withTiO2 NPs (40microng / cm-2 for 72h); (c) TEM image of mwCNTs on Balb/T3 cells (10 microng/ml for 72h); (d) TEM image of AuNPs on Balb/T3 cells (300microM for 72h).

ORAL PRESENTATIONS L4:

Nanoparticles as drug delivery system in skeletal muscle disorders: *in vitro* studies of PLGA nanoparticles as carriers for pentamidine for the treatment of myotonic dystrophy type 1

Valeria Guglielmi (1), Flavia Carton (1), Barbara Stella (2), Silvia Arpicco (2), Gloria Berlier (3), Alessandro Marengo (2), Federico Boschi (4), Rosanna Cardani (5), Laura V. Renna (6), Giovanni Meola (6), Manuela Malatesta (1)

1) Department of Neurosciences, Biomedicine and Movement Sciences, Section of Anatomy and Histology, University of Verona, Italy

2) Department of Drug Science and Technology, University of Turin, Italy

3) Department of Chemistry and NIS Research Centre, University of Turin, Italy

4) Department of Computer Science, University of Verona

5) Laboratory of Muscle Histopathology and Molecular Biology, IRCCS Policlinico San Donato, Milan, Italy

6) Department of Neurology, IRCCS Policlinico San Donato, Milan, Italy

Keywords: myotonic dystrophy, poly(lactic-co-glycolic acid) (PLGA) NPs, pentamidine, nanomedicine, primary human myoblasts

In the recent years, there has been a growing interest in the biomedical applications of nanoparticles (NPs) as drug carriers to control the delivery of therapeutics at the site of action as well as to decrease systemic toxicity. Myotonic dystrophy type 1 (DM1) is a multisystemic disorder that affects 1:8000 individuals worldwide being the most common muscular dystrophy in adults. The genetic basis of DM1 is the expansion of a CTG triplet repeat in the 3' UTR region of the Dystrophia Myotonica Protein Kinase (DMPK) gene. The expanded CTG repeats are transcribed into toxic RNA that accumulate as foci in cell nuclei where retain specific splicing factors such as muscleblind-like protein 1 (MBNL1) leading to the alteration of a subset of developmentally regulated splicing events. Currently, no disease-modifying therapies are

available for DM1 patients. Pentamidine is a FDA-approved compound known to mitigate the pathological hallmarks of DM1 but so far it has had limited therapeutic application due to its high toxicity. In this study, we investigated different types of NPs to identify suitable nanocarriers for pentamidine for the treatment of DM1. Poly(lactic-co-glycolic acid) (PLGA) NPs, mesoporous silica (MSN) NPs and liposomes have been tested on primary human myoblasts obtained from skeletal muscle of healthy subjects to preliminarily evaluate their biocompatibility and biosafety. Treatment with MSN NPs and liposomes resulted in a slight but statistically significant reduction in cell viability at high concentrations and long incubation times. PLGA NPs did not negatively affect myoblasts viability at any of the tested doses and duration of treatment. Based on these results we decided to focus on PLGA NPs. Confocal microscopy imaging of Nile red-labeled PLGA NPs revealed that they are rapidly taken up by most of the myoblasts and persist in the cytoplasm up to 72h where they partially co-localize with fluorescent labeled cell membrane-derived vesicles, suggesting that they enter the cell through the endocytic pathway. Ultrastructural analysis revealed that PLGA NPs are internalized, probably via endocytosis, but they quickly escape endosomes, thus occurring free in the cytoplasm. They re-enter the lytic pathway and, after 72h, many degraded NPs occur within residual bodies. PLGA NPs neither enter the nucleus nor come in close contact with other cellular organelles. We demonstrated that treatment with pentamidine-loaded PLGA NPs results in a statistically significant higher cell viability as compared to cell treated with the free molecule, suggesting that the delivery of pentamidine through PLGA NPs reduces the toxicity of the drug. We are currently using primary human myoblasts obtained from diagnostic muscle biopsies of patients with DM1 as *in vitro* model of the disease to evaluate the ability of pentamidine-loaded PLGA NPs to reduce specific pathological features of DM1 i.e. intranuclear toxic RNA foci and splicing abnormalities.

References:

1. Meola G, Cardani R. Biochim Biophys Acta. 2015. Apr;1852(4):594-606.

2. Warf MB et al. Proc Natl Acad Sci U S A. 2009 Nov 3;106(44):18551-6.

3. Danhier F et al. J Control Release. 2012 Jul 20;161(2):505-22.

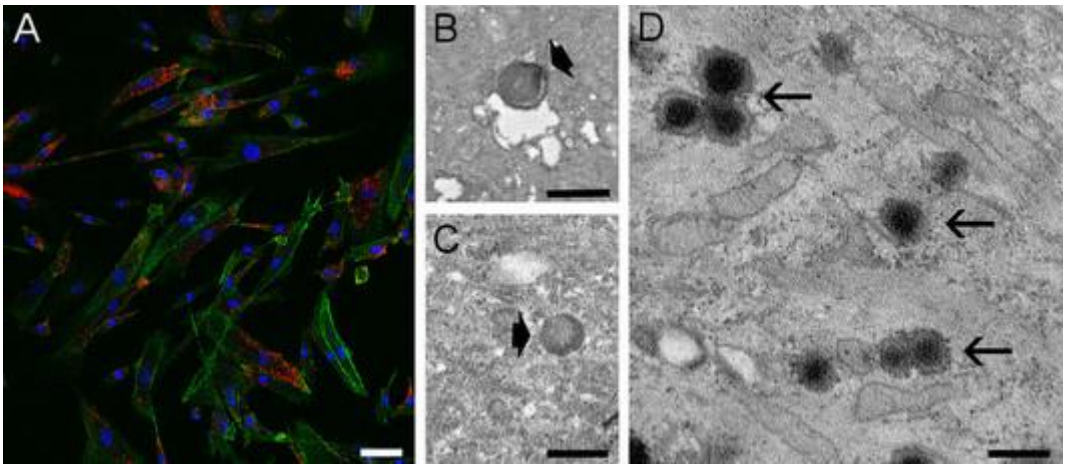

Figure 1. (A) Confocal micrograph: PLGA NPs (red) are internalized into myoblasts. Bar: 50 µm. (B-D) TEM micrographs: PLGA NPs (arrowheads) occur inside endosomes or free in the cytoplasm; residual bodies containing NP remnants (arrows). Bars: 100 nm.

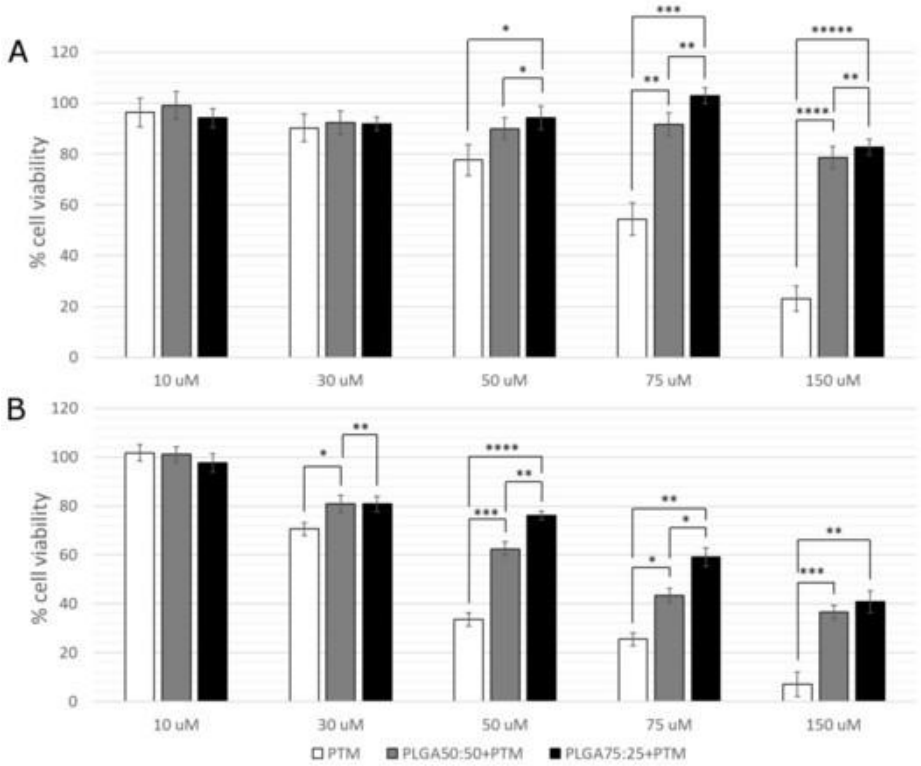

Figure 2. Effect of free PTM and PTM-loaded PLGA NPs on myoblasts viability after 24h (A) and 48h (B) of incubation: NP-mediated drug delivery induces a significant decrease of PTM cytotoxicity. * p<0.05; ** p<0.01; ***p<0.001; ****p<0.0001; *****p<0.0001.

Atomic Resolution Microscopy-EELS/EDS in combination with ultrastructural localization of amphiboles in epithelial cell models: a chance to foresee the biological effect of nano/micro-minerals?

Ruggero Vigliaturo (1), Maja Jamnik (2), Simon Caserman (2), Magda Tušek Žnidarič (3), Marjetka Podobnik (2), Goran Dražić (1)

1) Department for Materials Chemistry, National Institute of Chemistry, Hajdrihova 19, 1000 Ljubljana, Slovenia

2) Department for Molecular Biology and Nanobiotechnology, National Institute of Chemistry, Hajdrihova 19, 1000 Ljubljana, Slovenia

3) Department of Biotechnology and System Biology, National Institute of Biology, Večna pot 111, 1000 Ljubljana, SlovenijaLjubljana, Slovenia

Keywords: asbestos, medical mineralogy, HRTEM, lung cancer, mesothelioma

The aim of this project is to investigate which transmission electron microscopy (TEM) techniques can give a contribution in revealing unclear aspects of the interaction of dangerous and potentially harmful nano/micro-minerals in contact with cells (1). Several natural fibers have the reputation to trigger malignant lung diseases resulting from inhalation (2), this “reverse nanotoxicology” approach may enlighten and allow to foresee the effect of these harmful materials. Our experiment needs a “tunable” amphibole’s structure to be studied in order to evidence those characteristics that can have a role in the disruption of biological equilibrium of model cells that comes after generation of reactive oxygen species (ROS). It has thus been selected a mineral series that belongs to the amphibole family with a simple and representative structure with general formula: $\square$ $(Mg, Fe^{2+}, Mn^{2+}, Li)_7Si_8O_{22}(OH,F,Cl)_2$ (Li < 1.00 apfu). This system allows to select a natural mineral with low content of iron and rich in magnesium that shows a bladed morphology (cummingtonite), a second phase that has higher iron content and similar morphology (grunerite) and the asbestiform correspondent (amosite). On the other side, we tested the interaction with several model cell lines that represent the typical population within the human lungs encountered by the inhaled mineral particles or fibers. All the cell lines were tested for viability, ROS generation and investigated through visual light microscopy and confocal microscopy in order to have a solid analytical feedback to be

compared with the transformation on the mineral characterized by different transmission electron microscopy techniques. The evolution and transformation of minerals at an atomic and nanometric scale are poorly studied and the chance to characterize these transformations will bring to foresee and to better comprehend the carcinogenic mechanism at the very beginning, providing the pharmaceutical industry and biologists with newly expanded margins of intervention. With the application of atomic resolution TEM, dual range electron energy loss spectroscopy (Dual range EELS) and energy-dispersive spectroscopy mapping (EDS mapping) we evidenced the iron fate during the interaction of the mineral with the biological environment drawing a comprehensive scheme of the subsequent ROS cascade within the target cells. Our findings suggest that, just with the observation of the transformed mineral features, could be possible to understand if it has or not been engulfed by the cells which is a fundamental aspect in tracking the carcinogenic response of the human body. Another important aspect in the role of the mineral within a cell is its ultrastructural localization, being this reaction “distance dependent” it is important to understand where in the cell the mineral can get and how this influence is effectiveness in harm the natural ROS equilibrium and the different biological compartment.

Acknowledgements:

This research is supported by a Rotary Global Grant (GG1640842).

References:

1. Vigliaturo et al. 2nd European Mineralogical Conference (2016), Rimini, Italy.

2. Pollastri et al. Chemosphere 164 (2016) 547-557.

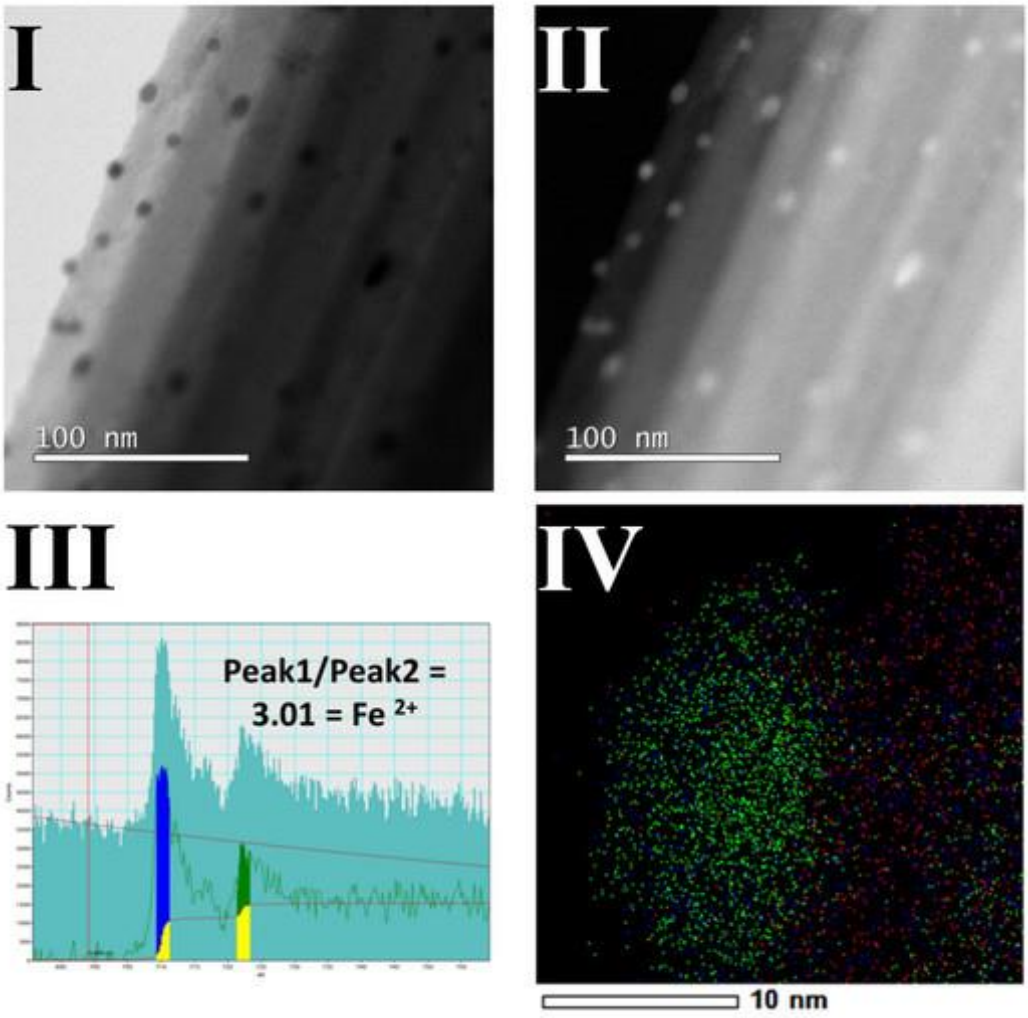

Figure 1. I and II show STEM-BF and MAADF of an asbestos fiber interacted with epithelial cells, nanoparticles are well visible at the surface. EELS spectra (III) of a newly formed iron particle and chemical mapping (IV): Fe (green), Si (Red), O (Blue).

Bacterial growth in the presence of laser produced silver nanoparticles

Lucija Krce (1), Matilda Šprung (1), Ana Maravić (1), Nikša Krstulović (2), Ivica Aviani (3)

1) Faculty of Science, University of Split, Ruđera Boškovića 33, HR-21000 Split, Croatia

2) Institute of Physics, Bijenička cesta 46, HR-10000 Zagreb, Croatia

3) Faculty of Science, University of Split, Ruđera Boškovića 33, HR-21000 Split, Croatia and Institute of Physics, Bijenička cesta 46, HR-10000 Zagreb, Croatia

Keywords: silver nanoparticles, antimicrobial activity, modeling bacterial growth, AFM microscopy

There are numerous reports of antimicrobial activity of the silver nanoparticles (AgNPs) produced by different methods (1-2), but the laser ablation in liquid has been proven to be the most convenient technique for the production of nanoparticles free of chemical byproducts. Here we present the study of AgNPs and the influence these nanoparticles have on the bacteria and their growth kinetics. AgNPs were produced by laser ablation in water and characterized by different experimental methods. Their antibacterial activity was observed by different microscopic techniques. In the present literature, there are only few reports on attempts to model the bacterial growth in the presence of nanoparticles. The reported model (3) is just a modification of the empirical Gompertz model. To explain the obtained growth curves of treated and untreated bacterial cells, we have designed the novel microscopic model described by three differential equations. Our model gives a good description of the experimentally obtained data.

References:

1. I. Sondi and B. Salopek-Sondi, J. Colloid Interface Sci. 275 (2004) 177-182.

2. G. A. Martinez-Castanon et al., J Nanopart Res 10 (2008) 1343–1348.

3. T. Chatterjee, et al., Biochim. Biophys. Acta 1850 (2014) 299–306.

Role of NSCLC exosomes in osteoclast differentiation

Simona Taverna (1), Maria Antonietta Di Bella (1), Marzia Pucci (1), Marco Giallombardo (1), Christian Rolfo (2), Riccardo Alessandro (1)

1) Dept. of Biopathology and Biomedical Methodology (DIBIMED), Biology and Genetic section, University of Palermo, Via Divisi, 83- 90133 Palermo, Italy

2) Phase I-Early Clinical Trials Unit, Oncology Dept, Antwerp University Hospital (UZA) and Center for Oncological research (CORE) Antwerp University, Antwerp, Belgium

Keywords: exosomes, NSCLC, osteoclasts, AREG

Bone metastases represent a frequent cause of morbidity and mortality in patients suffering many types of cancer including breast, kidney, and lung. Non-small cell lung cancer (NSCLC) is one of the most commonly diagnosed neoplasia. About 70% of NSCLC patients develop bone metastasis during the course of disease or at diagnosis. NSCLC frequently induces osteolytic metastases associated to bone lesions or destruction. NSCLC cells induce the release of factors that alter the regulatory networks existing between osteoblast and osteoclasts, modifying the normal balance of the receptor activator of NF-kB ligand (RANKL) and osteoprotegerin (OPG). RANKL is essential during the differentiation stage from the pre-osteoclast to active osteoclast. RANKL activity is counteracted by OPG that blocks the bind of this latter to its receptor RANK, thus preventing the RANK/RANKL signaling. RANK/ RANKL system can be modulated by epidermal growth factor receptor (EGFR) expressed in the pre-osteoclasts. In NSCLC cells EGFR is overexpressed (1), the total effect is an of RANKL upregulation with a induction of osteoclast formation (2). EGFR binds several ligands among which AREG, a molecule overexpressed in several cancers such as colon, breast, and lung. Particularly, high level of AREG has been reported in exosomes released by cancer cells resulting in an increase of the invasiveness. Exosomes, released from cells under both physiological and pathological conditions, have recently been recognized as mediators in the cell-to-cell communication processes as they contain a variety of cargo such as mRNA, microRNA, DNA, and proteins (3). They seem to have a key role in the crosstalk in the tumor microenvironments promoting tumor growth and metastatic dissemination of a primary tumor. Our data report about the effects of NSCLC exosomes in the induction of pre-osteoclast

differentiation to mature osteoclast, focusing on the role of AREG in the EGFR pathway activation and bone metastasis induction. The treatment of murine monocyte cells RAW246.7 with NSCLC exosomes enriched in AREG, modulates the typical phenotype of mature osteoclasts via EGFR pathway that in turn causes an upregulation of RANKL. Exosomes released in CRL-2868 cells conditioned media and in plasma of NSCLC patients, were isolated and morphologically and biochemically characterized. The effect of these exosomes on the RAW246.7 cell was also evidenced by morphological observations. Findings here reported show that RAW246.7 added of exosomes from NSCLC cell line CRL-2868, mature towards the osteoclastic lineage within 7 days from the treatment, resulting in multinucleated cells of various size and configuration. A better understanding of exosomes function can improve the therapeutic strategy to inhibit the attraction between lung cells and bone. In order to take advantage of exosomes as vehicles for delivering therapeutic reagent or drugs in the treatment of malignancies with bone osteolytic lesions.

Acknowledgements:

This research was supported by italian Association of Cancer Research and University of Palermo, FFR.

References:

1. Chan, B. A. et al. Transl Lung Cancer Res 4, 36-54, 2015.

2. Taverna, S. et al. Oncotarget 7, 28748-28760, 2016.

3. Zhu, J. et al. J Biol Chem 282, 26656-26664, 2007.

POSTER PRESENTATIONS L4:

In vivo and *in vitro* biodistribution of solid lipid nanoparticles

Silvia Mannucci (1), Federico Boschi (2), Elisabetta Esposito (3), Rita Cortesi (3), Claudio Nastruzzi (3), Manuela Malatesta (1), Laura Calderan (1)

1) Department of Neurolsciences, Biomedicine and Movement Sciences, University of Verona, 37134 Verona, Italy

2) Department of Computer Sciences, University of Verona, 37134 Verona, Italy

3) Department of Life Sciences and Biotechnology, University of Ferrara, I-44121 Ferrara, Italy

Keywords: solid lipid nanoparticles, transmission electron microscopy, *in vitro* internalization, *in vivo* and *ex vivo* biodistribution

Solid lipid nanoparticles (SLN) are a versatile tool with a high potential of applications. They are constituted by biocompatible and biodegradable matrix with well-established safety profiles. Their matrix can improve the stability and bioavailability of labile molecules, assuring restrained release profile. Moreover, due to the physicochemical properties of lipids (i.e. the low melting temperature), SLN can be easily obtained by direct emulsification of the molten lipids and subsequent recrystallization, thus avoiding the use of potentially toxic solvents that are commonly required for the preparation of polymeric nanoparticles (1). SLN used for this study were produced by a protocol based on emulsification of the molten lipids in water by melt and ultra-sonication method (2), and were functionalized with polysorbate 80 (SLN-P80) for *in vivo* administration. In fact, it has been reported that this surfactant extend the nanoparticle circulation time in the blood, avoiding opsonization with the complement activation and uptake by the reticulo-endothelial system. The influence of nanoparticle composition and functionalization was investigated on morphology, dimension and inner structure by mean of cryogenic transmission electron microscopy (cryo-TEM), X-ray diffraction measurements, photon correlation spectroscopy (PCS) and sedimentation field flow fractionation (SdFFF) (2).

SLN-P80 were labeled with cardiogreen fluorophore to allow their visualization in living organisms, and the *in vivo* biodistribution was evaluated with Fluorescent Luminescent Imaging (FLI) after intraperitoneal (i.p.) administration in a mice model. After the *in vivo* acquisition, mice were perfused and the excised organs (liver, kidney, spleen, brain, lung) were acquired to confirm SLN-P80 accumulation in specific districts (3). Organ tissues were also analyzed at light microscopy (LM) to evaluate SLN-P80 localization. After 4 h from systemic administration, SLN-P80 specifically accumulated in liver (*Figure* 1a). LM revealed that no histological alteration is induced by SLN-P80 administration; however, a marked increase in lipid content (red oil staining) was found in hepatocytes, especially close to the centrilobular venula (*Figure* 1b, c). To clarify this phenomenon, we investigated *in vitro* the uptake and intracellular fate of SLN-P80 in a murine cell line. 3T3 cells were incubated with SLN-P80 for 1, 4 and 24h, and then processed for both LM (red oil staining) and transmission electron microscopy (TEM). SLN-P80 administration induced accumulation of lipid droplets already after 1 h (*Figure* 2a, b). At TEM scarce SLN-P80 were observed inside the cells: they occurred free in the cytoplasm, often in close proximity to lipid droplets showing a peripheral electron dense material (*Figure* 2c). This suggests that SLN-P80 enter the cells by fusion with the plasma membrane, undergo rapid degradation and their components migrate, probably due to chemical affinity, into the lipid deposits.

References:

1. Wolfgang et al. Advanced Drug Delivery Reviews 64 (2012) 83–101.

2. Esposito E et al. Pharm Res. 2008; 25: 1521-1530.

3. Elisabetta et al. J Nanomed Nanotechnol 2015, 6:1, 1-9.

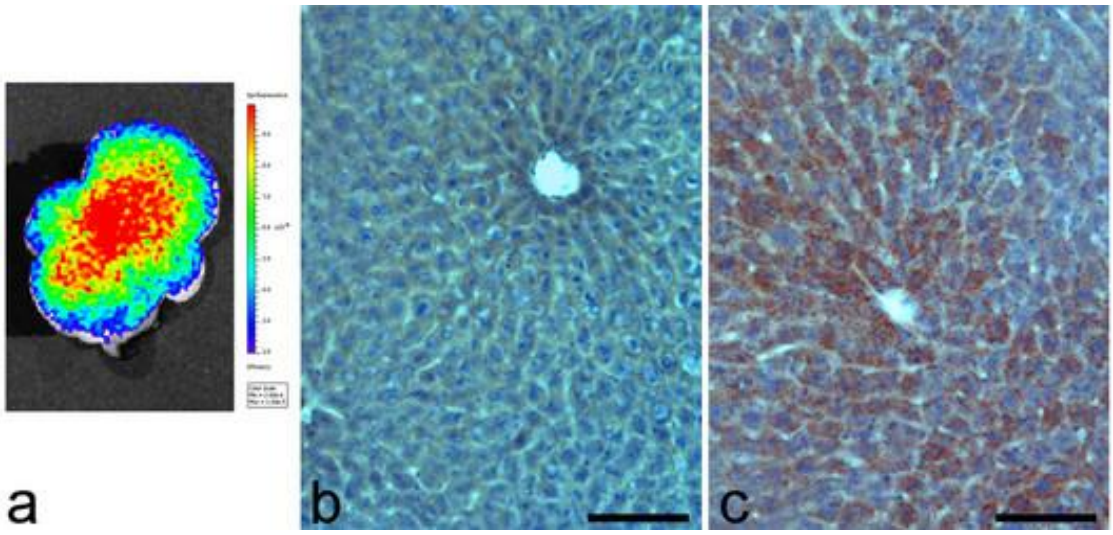

Figure 1. FLI : liver explanted from a mouse 4h after perfusion with SLN-P80 (a). LM: control (b) and SLN-P80-treated (c) liver; note the large amounts of lipid droplets (red oil) in c. Bar, 100 µm.

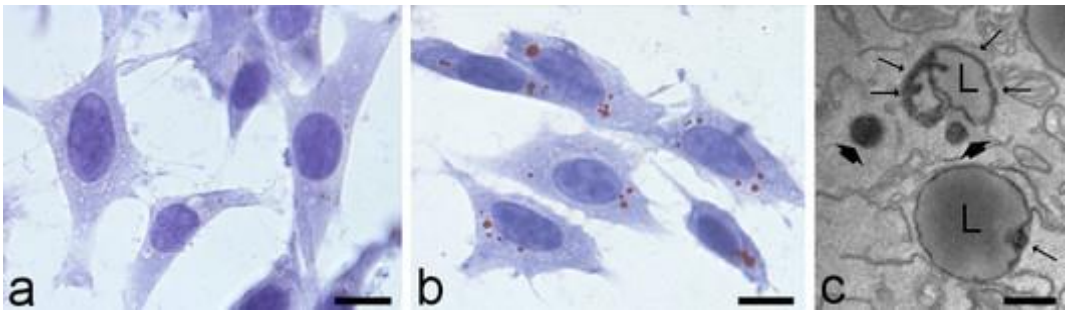

Figure 2. LM: 3T3 cells incubated with SLN-P80 for 1h (b) contain more lipid droplets (red oil) than controls (a). Bars, 20 µm. TEM: SLN-P80 (arrows) occur near to lipid droplets (L) containing electron dense material (thin arrows). Bar, 200 nm.

Biodistribution of different nanocarriers in murine mioblasts

Federica Vurro (1), Manuela Costanzo (1), B. Cisterna (1), F. Boschi (2), Alessandro Marengo (3), Silvia Arpicco (3), B. Stella (3), Gloria Berlier (4), Laura Calderan (1), Manuela Malatesta (1)

1) Dept. of Neurosciences, Biomedicine and Movement Sciences, University of Verona, Str. Le Grazie, 8, 37134, Verona, Italy

2) Dept. of Computer Science University of Verona, Strada le Grazie 15 - 37134 Verona, Italy

3) Dept. of Drug Science and Technology, Via P. Giuria, 9 - 10125, Torino, Italy

4) Dept. of Chemistry, University of Torino, Via P. Giuria, 7 - 10125 Torino, Italy

Keywords: nanoparticles, murine mioblasts, biodistribution, confocal microscopy, transmission electron microscopy

The targeting of drugs or imaging agents to organs, tissues and cells is a main difficulty in the treatment or the diagnosis of different disorders. Nanomaterials are potentially able to solve this problem: thanks to their physico-chemical features, nanocarriers may be efficient tools for drug delivery to the target sites. A wide variety of molecules can be encapsulated in nanoparticles (NPs) and, from a pharmacokinetic point of view, their association has prominent effects, such as delayed drug absorption, metabolism and clearance, restricted drug biodistribution, and the possibility to administer reduced drug amounts (1). Due to this potential, a broad range of drug delivery systems is being designed. In this work we focused on liposomes, mesoporous silica NPs (MSN), and two different formulations of Poly Lactic-co-Glycolic Acid (PLGA) NPs (50% lactic acid and 50% glycolic acid [PLGA 50:50], and 75% lactic acid and 25% glycolic acid [PLGA 75:25]). These nanocarriers were labelled with either fluorescein (liposomes and MSN) or Nile red (PLGA NPs) to make them detectable at fluorescence microscopy. Liposomes, PLGA NPs and MSN were tested on the murine myoblast cell line C2C12 as an *in vitro* cell system. C2C12 cell proliferation and death were evaluated 2h, 24h and 48h after treatment with NPs at different concentrations (Figure 1); the non-toxic ones were used for further investigations. Cell proliferation was also estimated by the BrdU assay 24h and 48h after NPs exposure. Fluorescence and transmission electron

microscopy (TEM) allowed visualising the uptake and intracellular fate of the different NPs, as well as the damages the cellular organelles had possibly undergone. All the NPs were rapidly and efficiently internalised by C2C12 myoblasts (Figure 2). Liposomes enter the cells probably by fusion with the plasma membrane (no overlapping with PKH26, a red fluorescent dye for plasma membrane, was found) and undergo a rapid degradation in the cytosol. PLGA NPs enter the cells via endocytosis as demonstrated by both the cell membrane staining with the green fluorescent dye PKH67 and TEM observation; they are then rapidly degraded by lysosome action. MSN are internalised as small clusters via endocytosis and then follow the lytic pathway. All the NPs exhibited good biocompatibility, since no cell damage was found in C2C12 myoblasts up to 24h incubation. Liposomes, polymeric NPs and MSN had been already tested in HeLa cells (2), with similar but not identical results. In particular, myoblasts showed lower internalisation and degradation efficiency compared to epithelial cells. This confirms and strengthens the notion that the effects induced by NPs may vary depending on the cell type and metabolic rate (3), and this important information should cautiously be taken into account when testing nanocarriers for medical use.

References:

1. F. Re Nanomedicine: Nanotechnology, Biology and Medicine 8 (2012): S51-S58.

2. M. Costanzo et al., Eur. J. Histochem. 60 (2016) 2640.

3. J.S. Chang et al., Environ Sci Technol 41 (2007) 2064-2068.

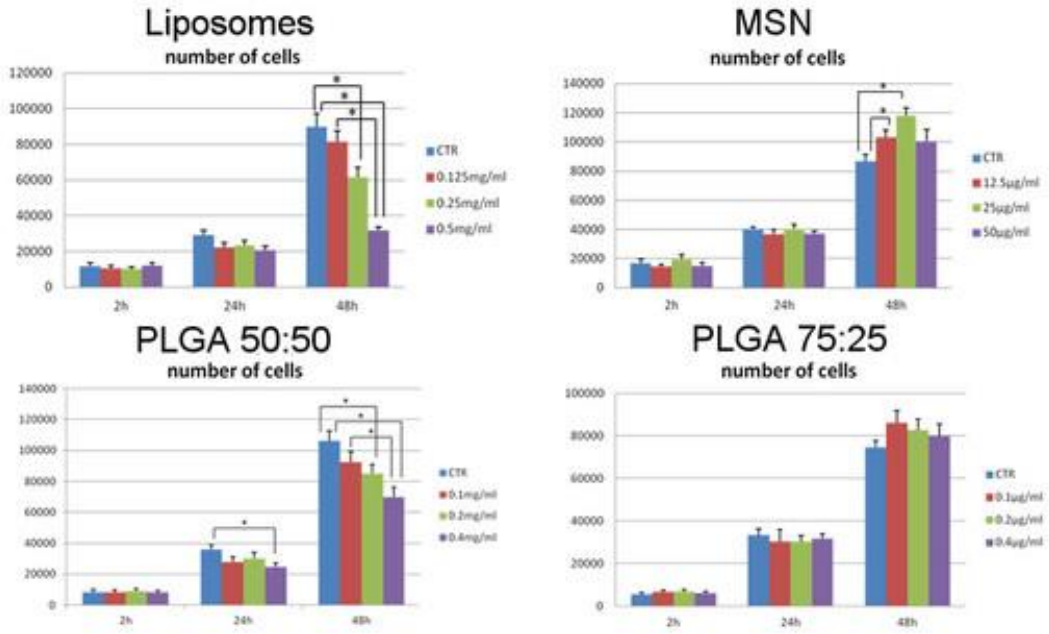

Figure 1. Cell proliferation at different times after treatment with liposomes, MSN, and PLGA NPs. Asterisks indicate statistically significant differences (Mann Whitney test, $p<0.05$).

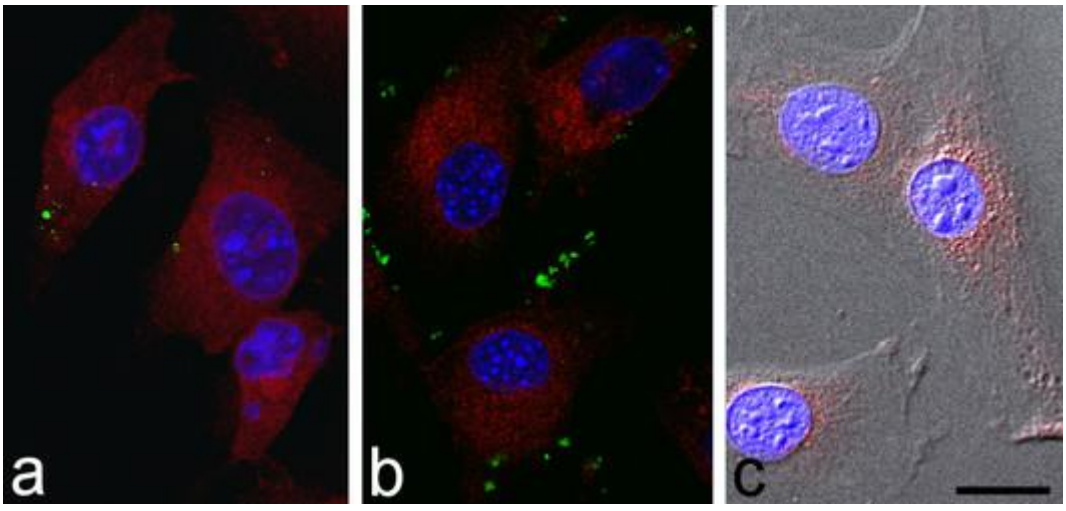

Figure 2. Confocal microscopy: C2C12 myoblasts after 2h incubation with liposomes (a), MSN (b) and PLGA NPs (c). Cytoplasm counterstaining with trypan blue (a, b); DNA staining with Hoechst 33342 (a-c). Bar, 20 µm.

Ultrastructural changes in tobacco cells induced by differently coated silver nanoparticles

Petra Peharec Štefanić (1), Petra Cvjetko (1), Ilse Letofsky-Papst (2), Ivana Vinković Vrček (3), Biljana Balen (1)

1) Division of Molecular Biology, Department of Biology, Faculty of Science, University of Zagreb, Horvatovac 102a, HR-10000 Zagreb, Croatia

2) Institute of Electron Microscopy and Nanoanalysis (FELMI), Graz University of Technology, Graz Centre for Electron Microscopy (ZFE), Austrian Cooperative Research (ACR), Steyrergasse 17, 8010 Graz, Austria

3) Institute for Medical Research and Occupational Health, Ksaverska cesta 2, HR-10000 Zagreb, Croatia

Keywords: silver nanoparticles, tobacco, transmission electron microscopy, ultrastructure, localization

Nanoparticles (NPs) research is currently an area of intense scientific surveys due to a variety of their potential applications. However, the characteristics making NPs attractive for their exploitation in new products have led to concerns that they may pose a risk for environment and human health. Silver NPs (AgNPs) are of particular interest because of their well-known antibacterial and antifungal properties. Therefore, they can be found in various consumer products. Since plants play a significant role in accumulation and biodistribution of many environmentally released substances, they could be influenced by AgNPs, serving as a potential pathway for AgNP-transport and bioaccumulation into food chains[1,2,3]. The aim of the study is to reveal effects of differently coated laboratory-synthesized AgNPs: slightly negatively charged AgNP-PVP, strong negatively charged AgNP-citrate and strong positively charged AgNP-CTAB as well as of silver nitrate ($AgNO_3$) on tobacco cell ultrastructure. Two months-old plants grown *in vitro* on a solid MS medium were exposed to 100 μM AgNPs of each type and to 100 μM $AgNO_3$ in ½ strength MS medium for 7 days. For localization of AgNPs in plant cells and ultrastructural analyses, small pieces of tobacco leaf and root were fixed with 1% glutaraldehyde in 50 mM cacodylate buffer (pH 7.2) for 1 h at +4 °C, washed twice and post-fixed with 1% osmium tetroxide in the same buffer for 1 h at +4 °C followed by 10 min wash in

ice-cold water. After dehydration in a graded series of ethanol, the tissue was embedded in Spurr´s resin. Semi-thin sections of fixed material were stained with mixture of 2% toluidine blue and 2% borax and examined using light microscope. Ultrathin sections were stained with 2% uranyl acetate and 2% lead citrate and examined using the FEI Morgagni 268D electron microscope for ultrastructural study and the monochromated TF20 (FEI Tecnai G2) TEM for confirmation of AgNPs localization in the tobacco cells. Ultrastructural studies revealed changes in root meristematic cells and leaf chloroplasts in both AgNPs- and $AgNO_3$-treated plants. The root meristematic cells became highly vacuolated and due to large vacuoles only nuclei were observed. AgNPs were localized in the root cells and in the intermembrane space. In the leaf cells, the chloroplasts of AgNP-citrate treated plants were swollen and ruptured with no difference in thylakoid system formation compared to control. Leaves of AgNP-PVP treated plants were characterized with thinner and longer chloroplasts with stacked thylakoids compared to control. In AgNP-CTAB treated plants, chloroplasts were well developed with higher content of plastoglobules compared to control. Big chloroplasts with well-developed thylakoid system were characteristic for leaves of $AgNO_3$ treated plants. The obtained results show the impact of AgNPs and silver ions on the ultrastructure of root meristematic cells and leaf chloroplasts, which is also dependent on the applied coating.

Acknowledgements:

This research was supported by the Croatian Science Foundation [grant number IP-2014-09-6488] and TEM analyses have received funding from the European Union Seventh Framework Programme under Grant Agreement 312483 - ESTEEM2 (Integrated Infrastructure Initiative–I3).

References:

1. Rico, C. M. et al. J. Agric. Food Chem 59 (2011) 3485-3498.

2. Vannini, C. et al. J. Plant Physiol. 171(13) (2014) 1142-1148.

3. Qian, H. et al. J. Environ. Sci. (China) 25(9) (2013) 1947-1955.

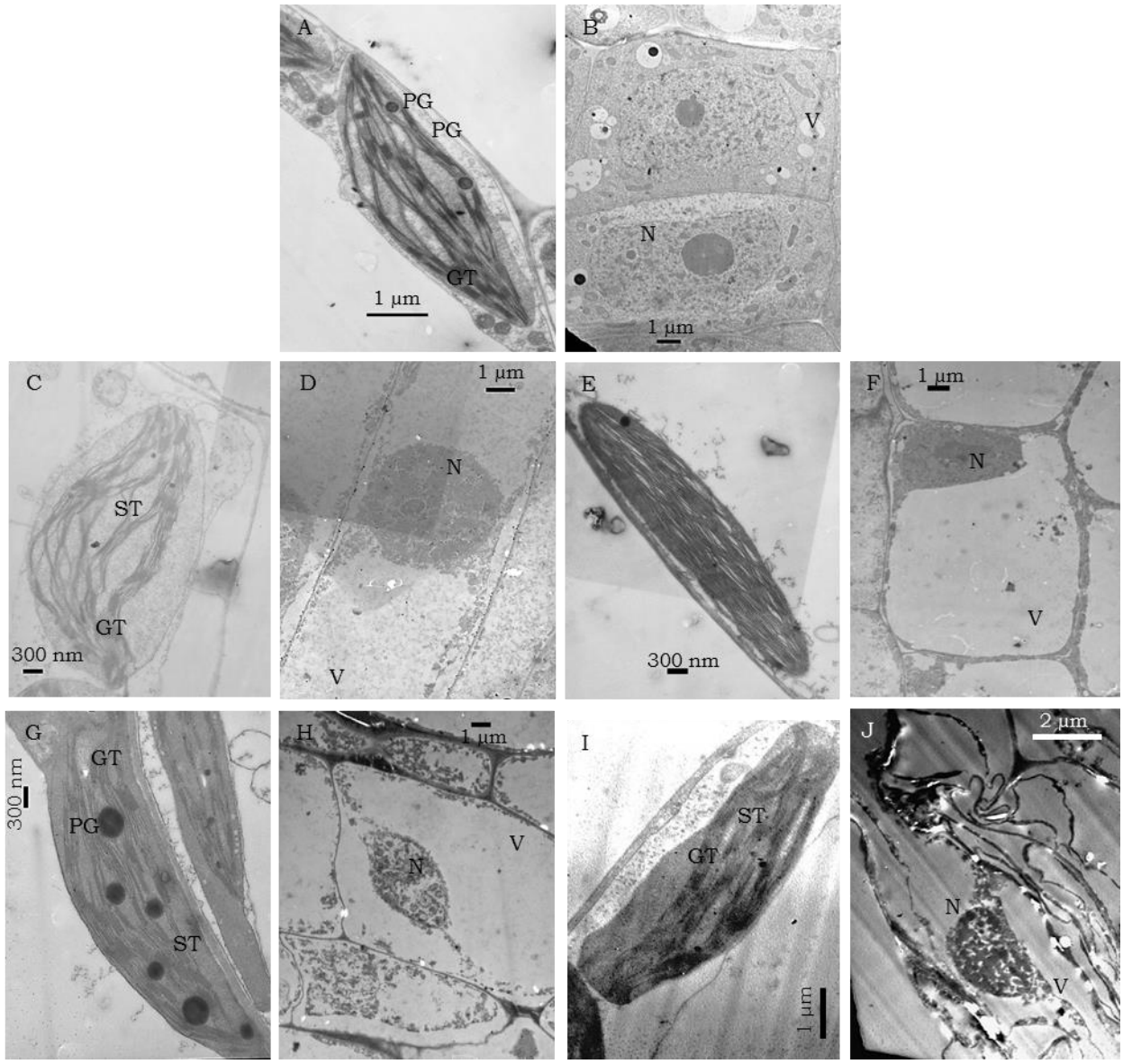

Figure 1. Chloroplast and root cell ultrastructure of control (A, B), AgNP-citrate (C, D), AgNP-PVP (E, F), AgNP-CTAB (G, H) and AgNO3 (I, J) treated plants, GT-grana thylakoids, ST-stroma thylakoids, PG-plastoglobules, N-nucleus, V-vacuole.

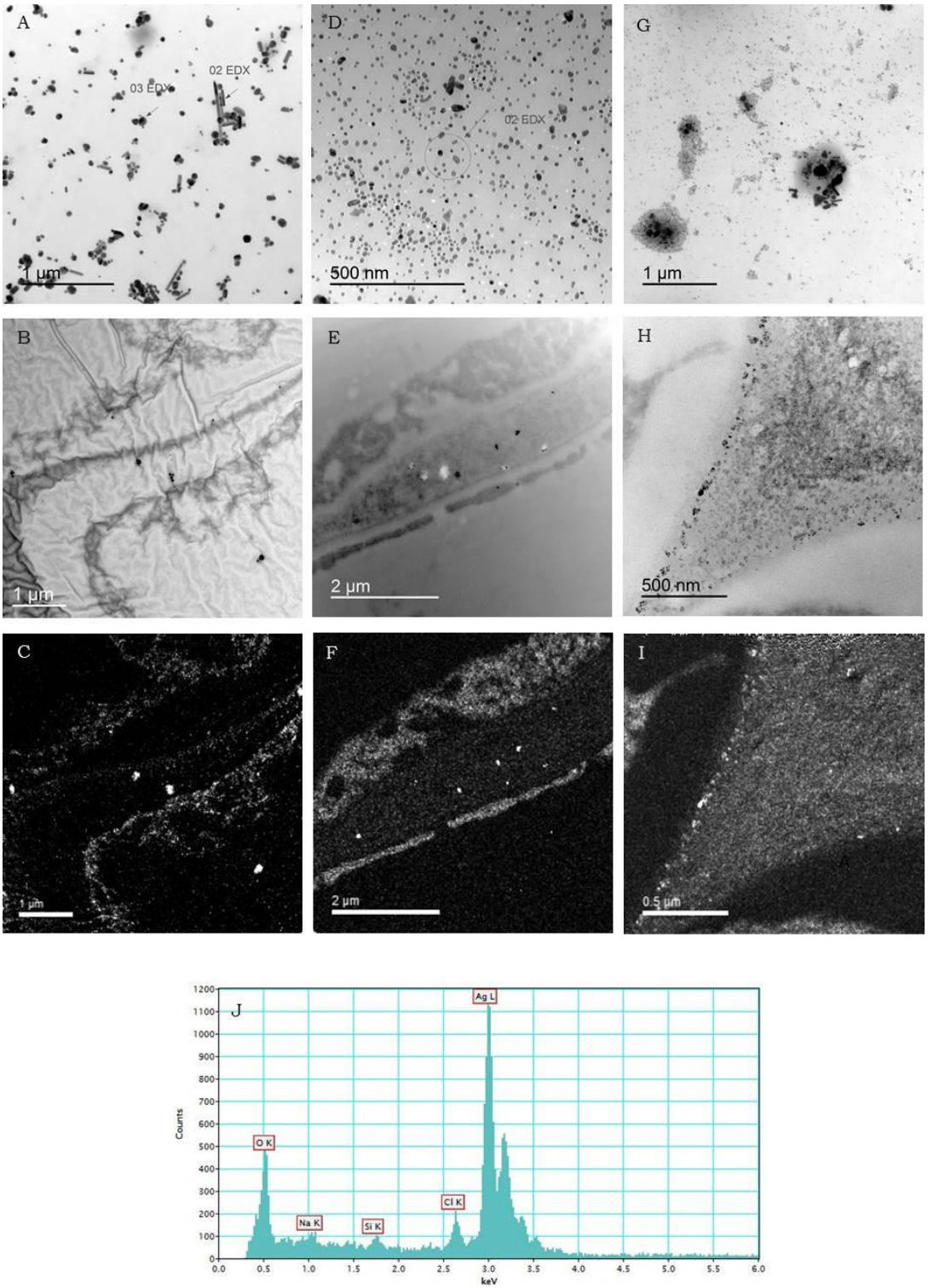

Figure 2. TEM images of differently coated silver nanoparticles (A, D, G) and their localization in tobacco root cells of AgNP-citrate (B), AgNP-PVP (E) and AgNP-CTAB (H) treated plants; bright field image (C, F, I) and energy-dispersive X-ray spectrum (J).

Nanostructured titanium scaffolds as a biocompatible material for bone regeneration

Barbora Kodedova (1,2), Eva Filová (2), Vera Lukášová (1,2,3), Veronika Blahnova (1,3,4), Jaroslav Fojt (5), Ludek Joska (5)

1) Institute of Experimental Medicine of the Czech Academy of Sciences, Videnska 1083, 14220, Prague, Czech Republic

2) Charles University in Prague, Faculty of Science, Albertov 2038/6, 128 00, Prague, Czech Republic

3) University Centre for Energy Efficient Buildings of Technical University in Prague, Trinecka 1024, 273 43, Bustehrad, Czech Republic

4) Second Faculty of Medicine, Charles University in Prague, V Uvalu 84,150 06, Prague, Czech Republic

5) University of Chemistry and Technology, Technicka 5, 166 28, Prague, Czech Republic

Keywords: biocompatibility, nanostructure, osteosarcoma cell, titanium

Titanium is widely used in bone regenerative medicine, moreover there have been problems with implants healing. Titanium surface structure is possible to modify in nanoscale using anodic oxidation. Changed nano topography could help cell adhesion and implants biocompatibility. The aim of our study was to evaluate impact of the nanostructures on the titanium surface on the cell differentiation or viability. Non-modified commercially pure titanium (cpTi) and tree types of nanostructured cpTi scaffolds were tested *in vitro* using osteosarcoma cell line SaoS2. Nanostructures were fabricate using anodic oxidation on 10, 15 or 20 V. Cells were cultivated for 14 days in standard media with addition of ascorbate-2phospate. Cell adhesion were quantitatively and qualitatively verified by immunohistochemical staining using vinculin and talin monoclonal antibody. Proliferation and metabolic activity were evaluated using PicoGreen Assay and MTS test. Additionally, expression of collagen-I and osteocalcin was measured by qRT-PCR and visualised by immunohistochemical staining. We did not observe any difference in cell proliferation among nanostructured or control samples. Nevertheless, metabolic activity was significantly higher after 10 days of culture on nanostructured cpTi (10V,20V). In comparison to control titanium expression of osteocalcin

and collage-I increased on the nanostructured cpTi samples, while the highest synthesis of them were noticed on sample 20V. Nanostructured cpTi supported differentiation of the SaoS2, also influenced adhesion of the cells and vinculin distribution. Therefore, the nanostructured titanium scaffolds, mainly 20V, support SaoS2 cell proliferation and osteogenic differentiation. Thus should serve as a suitable material in bone regeneration.

Acknowledgements:

This project was supported by the Czech Science Foundation No. 16-14758S.

Platelet lysate as a serum replacement for skin cell culture on biomimetic PCL nanofibers

Věra Sovková (1,2,3), Karolína Vocetková (1,2,3), Michala Rampichová (1,3), Andrea Míčková (1,3), Matej Buzgo (3), Věra Lukášová (1,3,4), Eva Filová (1,5), Alois Nečas (6), Evžen Amler (1,2)

1) Laboratory of Tissue Engineering, Institute of Experimental Medicine, Czech Academy of Sciences, Videnska 1083, 142 20 Prague 4, Czech Republic

2) Institute of Biophysics, 2nd Faculty of Medicine, Charles University, V Uvalu 84, 150 06 Prague 5, Czech Republic

3) University Centre of Energy Efficient Buildings, Czech Technical University in Prague, Trinecka 1024, 273 43 Bustehrad, Czech Republic

4) Faculty of Sciences, Charles University, Albertov 2038/6, 128 00 Prague 2, Czech Republic

5) Faculty of Biomedical Engineering, Czech Technical University in Prague, Namesti Sitna 3105, 272 01 Kladno, Czech Republic

6) University of Veterinary and Pharmacuetical Sciences Brno, Palackeho trida 1946/1, 612 42 Brno, Czech Republic

Keywords: platelet lysate, nanofibers, dermal cells

Platelets are a popular source of native growth factors for tissue engineering applications. The aim of the study was to verify the use of platelet lysate as a fetal bovine serum (FBS) replacement for skin cell culture. The cytokine content of the platelet lysate was characterized using the BioPlex system. The cells (fibroblasts, melanocytes, keratinocytes) were cultured on PCL nanofibrous scaffolds to mimic their natural microenvironment. The cytokine content of the platelet lysate was determined, and to the cells a medium containing platelet lysate or platelet lysate in combination with FBS was added. The results showed that 7% (v/v) platelet lysate was sufficient to supplement 10% (v/v) FBS in the culture of fibroblasts and keratinocytes. The combination of platelet lysate and FBS had a rather inhibitory effect on fibroblasts, in contrary to keratinocytes, where the effect was synergic. Platelet lysate did not sufficiently promote proliferation in melanocytes, however the combination of FBS and platelet

lysate yielded a better outcome and resulted in bipolar morphology of the cultured melanocytes. The data indicated, that platelet lysate improved cell proliferation and metabolic activity, and may be used as an additive to the cell culture media.

Acknowledgements:

The study was supported by the Grant Agency of Charles University (Grants Nos. 424213, 1246314, 1262414, 1228214), the Ministry of Education, Youth and Sports of the Czech Republic within National Sustainability Programme I: projects No. LO1605, LO1508, LO1309, Operational Program – Prague Competitiveness CZ.2.16/3.1.00/21528 and The Internal Grant Agency of the Ministry of Health of the Czech Republic (MZ-VES projects nos. 15-33094A and 16-29680A).

Toxicological effects of three differently shaped carbon nanomaterials in *Daphnia magna*: a morphological approach

Renato Bacchetta (1), Paolo Tremolada (1), Irene Valenti (1), Mariangela Longhi (3), Daniela Maggioni (3), Miriam Ascagni (2), Nadia Santo (2)

1) Dipartimento di Scienze e Politiche Ambientali, Università degli Studi di Milano, Via G. Celoria, 26, I-20133 Milan, Italy

2) Dipartimento di Bioscienze, Università degli Studi di Milano, Via G. Celoria, 26, I-20133 Milan, Italy

3) Dipartimento di Chimica, Università degli Studi di Milano, Via C. Golgi, 19, I-20133 Milan, Italy

Keywords: carbon nanomaterials, the shape effect in NP toxicity, acute toxicity, electron microscopy, *Daphnia magna*

Carbon nanomaterials (CNM) are among the most used and promising materials in Nanotechnology, but their environmental compatibility still needs to be evaluated. In this work, we have compared the acute toxicity of three differently shaped CNM (carbon nanopowder, CNP, carbon nanocubes, CNC, and carbon nanotubes, CNT) on the crustacean *Daphnia magna*, to investigate possible concentration-dependent effects and morphological alterations up to an ultrastructural level. The selected concentrations were 1, 2, 5, 10, 20 and 50 mg/L and the morphological approach involved Light, Scanning and Electron Microscopy. CNM were widely characterized. Size distribution and particle morphology were analyzed by TEM, particles composition by SEM/EDS, hydrodynamic diameter and z-potentials by DLS, and PAHs by gas-chromatography and mass-spectrometry (GC-MS-MS). Acute toxicity, measured in terms of immobilization/mortality of individuals, resulted >50mg/L for all the CNM, with the following toxicity order CNC≥CNP>CNT. Despite their low general toxicity, the CNPs and the CNCs presented time- and concentration-dependent toxicity, reaching the maximum of 35% immobilisation in 50 mg/L CNP group and 20% lethality in 50 mg/L CNC group. Differently from CNPs and CNCs, CNTs did not present any significant immobilisation or lethality effects at these concentrations. Stereoscopical observations on exposed daphnids showed an accumulation concentration dependent of CMN inside the digestive system and within the

thoracic appendages, used to filter food particles from water. The CNP and the CNC treated specimens appeared to be the most affected by NPs, their guts being completely full of black masses, while daphnids exposed to the CNTs presented a lower intensity of the NPs inside their guts and within the appendages. SEM observations highlighted the accumulation inside the intestinal lumen, suggesting a mechanical damage due to the pressure and the abrasion by particles on the epithelium. Ultrastuctural analyses were performed mainly focusing onto two possible entry sites: the midgut region, specifically involved in absorption, and gills, associated to thoracic appendages. Histological sections showed integrity of the gut epithelium, except in 50 mg/L CNC treated animals. At TEM analyses they evidenced the most severe effects at both individual (immobilisation and mortality) and cellular levels (thinning of the digestive layer, dissolution of the brush border, detachment of paracellular and basement membranes, appearance of large multi-lamellar body and autophagic vacuoles). All these phenomena, observed also without an evident NP internalisation, led us to hypothesize that the toxicity was primarily caused by mechanical damage to enterocytes, with a sequence of “pressure” of the ingested-CNM-mass coming from the gut lumen, “abrasion” against the peritrofic membrane first and the microvilli later, and finally cellular degeneration.

L5. Microscopy in Microbiology, Plant and Environmental Sciences

INVITED LECTURES L5:

Autophagy and heavy metal induced stress in green algae

Alessio Papini (1), Cristina Gonnelli (1), Corrado Tani (1), Pietro Di Falco (1), Giovanna Wolswijk (1), Giovanni Maretti (1), Raffaello Ballini (1)

(1) Dept. Biology, University of Florence, via Micheli 1-3, Firenze, 50121 Italy

Keywords: autophagy, green algae, heavy metals, stress, ultrastructure

Various genera and species of unicellular green algae proved to be resistant, at different level of effectiveness to heavy metals pollution (Kumar et al. 2015). For instance, species of genera *Chlorella* (Kumar et al. 2015), *Dichtiosphaerium* (Pereira et al. 2015) and *Micrasterias* (Lütz-Meindl 2016) showed different level of resistence depending on the strain and populations. The presence of heavy metals in water can be faced by these organisms in very different ways, with respect to the metal involved and to the strategy carried out by the cell itself. Some cells may arrest the metals at the wall level, by excluding the entrance into the cytoplasm, other may concentrate and precipitate the metal in a vacuole. Besides these methods, some cells appear to increase their turn over by increasing autophagic activity in order to replace organels that get damaged by the heavy metal toxicity. Some preliminary results in *Dictiosphaerium* may even suggest that some members of the populations accumulate faster the heavy metals than the others, eventually dieing subtracting part of the metal from the medium. If confirmed, this activity would represent a Programmed Cell Death case resembling the sacrifice of some cells in multicellular organisms in order to accomplish a specific task of general interest for the entire organisms. Such cases are quite rare or of difficult interpretation in unicellular organisms. The strategy with which such unicellular (or colonial) genera of green algae are able to resist to heavy metals in the environments is object of interest (see, for instance), since the method to reduce the biological effects may provide strains capable of production of industrial products even in polluted cultures and/or suggest methods to remove the heavy metals from polluted

water (phytoremediation). A survey of the ultrastructural morphology of effects of heavy metal-induced stress on cell organelles in unicellular green algae is presented.

References:

1. Lütz-Meindl U. (2016) *Micrasterias* as a Model System in Plant Cell Biology. Front. Plant Sci. 7:999.

2. Pereira M, Bartolomé CM, Sánchez-Fortún S (2014) Photosynthetic activity and protein overexpression found in Cr (III)-tolerant cells of the green algae *Dictyosphaerium chlorelloides*. Chemosphere, 108: 274–280.

3. Kumar KS, Dahms HU, Won EJ, Lee JS, Shina K-H (2015) Microalgae–A promising tool for heavy metal remediation. Ecotoxicology and environmental safety 113: 329-352.

Apoplasmic barriers – sensitive stress-responding structures in plants

Michal Martinka (1), Milan Soukup (1), Monika Bathóová (1), Eliška Mašírová (2), Alexander Lux (1)

1) Department of Plant Physiology, Faculty of Natural Sciences, Comenius University in Bratislava, Mlynska dolina, Ilkovicova 6, 842 15 Bratislava, Slovak Republic

2) Plant Science and Biodiversity Center, Institute of Botany, Dubravska cesta 9, 845 23 Bratislava, Slovak Republic

Keywords: fungi, plant roots, silica phytoliths, suberin lamellae

Apoplasmic barriers are structures mostly based on cell-wall modifications controlling the movement of solvents and solutes via apoplasmic space in plant body. Many plant species need to control the movement of these substances in their cortical tissues – mostly in endodermis and exodermis. We investigated the formation of apoplasmic barriers in the roots of monocotyledonous plants by bright field, fluorescence, scanning and transmission electron microscopy. The cell wall modifications can occur in these tissues in the form of specifically localized deposits of lignin and suberin either in primary or secondary cell walls. Their deposition is under spatiotemporal control and it is ontogenetically-dependent. However, their earlier development can be induced under specific conditions like the stressful environment, e.g. water deficiency or the presence of bioavailable toxic elements or even the presence of biotic stressors. The formation of apoplasmic barriers in plants can be influenced also by the presence of beneficial silicon (Si) in their substrate. The degree of influence depends on the concentration of phyto-available form of Si, the ability of plant to take up and to distribute Si, and the shape and thickness of final silica deposits. The simultaneous presence of Si and apoplasmic barriers can increase the fitness and viability of plants exposed either to the excessive concentrations of essential elements or to the presence of toxic non-essential elements like cadmium or phytopathogenic fungi.

Acknowledgements:

This work was financially supported by Slovak Grant Agency VEGA 1/0755/16.

ORAL PRESENTATIONS L5:

Study of the asbestos bodies and chemical-physical modification of mineral fibres in rat histological tissues using scanning electron microscopy, and high resolution transmission electron microscopy

Nicola Bursi Gandolfi (1), A. F. Gualtieri (1), K. Pollok (2), Ruggero Vigliaturo (3)

1) Department of Chemical and Geological Sciences, University of Modena and Reggio Emilia, Via Università 4, 41121 Modena, Italy

2) Friedrich-Schiller-Universität Jena, Fürstengraben 1, 07737 Jena Germany

3) National Institute of Chemistry, Hajdrihova 19, 1000 Ljubljana, Slovenija

Keywords: SEM-FEG, HR-TEM, asbestos bodies, asbestos, *in vivo* study

Mineral fibres like chrysotile, fibrous amphiboles and erionite are among the most feared minerals worldwide because they may provoke fatal lung diseases, such as mesothelioma, through inhalation. The close relationship between inhaled fibres and respiratory diseases have been demonstrated by many scientific works (1) but the mechanisms of cyto- and geno-toxicity are not completely understood. In fact, it is difficult to draw a conclusive model to explain the biochemical activity of these fibres because a number of parameters act a synergetic role, such as fibre size, crystal habit, morphology, presence of iron and biopersistence (2). Since 2011, a long term Italian Research Project of National Interest (PRIN) entitled "*Interazione fra minerali e biosfera: conseguenze per l'ambiente e la salute umana*" is focused on mineral fibres, with the aim to develop a general model capable to classify each mineral fibre based on its toxicity potential. The attempt to understand the complex biochemical mechanisms between the mineral fibres and the organic matter requires a systematic mineralogical-crystallographic study of the fibres. Hence, eight mineral fibres samples have been selected for the study based on their socio-economic and industrial importance: three chrysotile of different origin (Canada; Balangero and Val Malenco, Italy), four amphibole asbestos species (amosite, anthophyllite, crocidolite and tremolite) and the fibrous zeolite

erionite (from Jersey, Nevada, USA). The systematic characterization has been combined with *in vitro* and *in vivo* tests to assess their toxicity potential. The selected mineral fibres are exactly the same used for a 3 years long *in vivo* testing performed on Sprague–Dawley rats by the Ramazzini Cancer Research Institute of Bologne. The microscopic observation of the fibres and asbestos bodies within the organic tissues, were performed using a FEI *Nova NanoSEM 450 FEG-SEM* (3) located at C.I.G.S. of University of Modena. Each mineral fibre observed in the histological section of rats could be clearly distinguished due to X-EDS analysis. Parts of histological tissue were dissolved, and the mineral fibres recovered were subsequently analysed with a FEI TECNAI G2 200kv TEM located at The Friedrich Schiller University of Jena, and with a JEOL ARM 200F TEM located at National Institute of Chemistry of Ljubljana. The combination of both scanning and high resolution transmission electron microscopy, allowed to study in detail the structural and morpho-chemical changes that occurred in the three mineral fibres that remains in contact with the organic medium for different residence time. On all fibrous samples, dissolution experiments with simulated lung fluid (SLF) solutions are concluding to test *in vitro* their bio-durability. Scanning electron microscopy were used to assess the advancement of the dissolution reaction. The outcome of this study will be described in this contribution.

References:

1. Davis, J.M.G. (1989): Mineral fibre carcinogenesis: experimental data relating to the importance of fiber types, size, deposition, dissolution and migration. In “Non-occupational exposure to mineral fibres”, J. Bignon, J. Peto, R. Saracci, eds., IARC Scientific Publication, Lyon, **90**, 33–45.

2. Donaldson, K., Murphy, F. A., Duffin, R., & Poland, C. A. (2010). Asbestos, carbon nanotubes and the pleural mesothelium: a review of the hypothesis regarding the role of long fibre retention in the parietal pleura, inflammation and mesothelioma. Part. Fibre Toxicol., **7**, 1.

3. Bursi Gandolfi, N., Gualtieri, A. F., Pollastri, S., Tibaldi, E., Belpoggi, F., (2016): Assessment of asbestos body formation by high resolution FEG–SEM after exposure of Sprague–Dawley rats to chrysotile, crocidolite, or erionite. J. Haz. Mat., **306**, 95-104.

FIB-SEM- and TEM-tomography reveal stress induced fusion of mitochondria in different plant cells

Philip Steiner (1), Manja Luckner (2), Gerhard Wanner (2), Ursula Lütz-Meindl (1)

1) University of Salzburg, Cell Biology and Plant Physiology Department, Hellbrunnerstraße 34, A-5020 Salzburg, Austria

2) Ludwig-Maximilians-University Munich, Faculty of Biology, Ultrastructural Research, Großhadernerstr. 2-4, D-82152 Planegg-Martinsried, Germany

Keywords: mitochondria, Micrasterias, FIB/SEM-tomography, TEM-tomography, salt stress

Sub-structural alterations of organelles frequently accompany stress induced physiological and molecular reactions in plant and animal cells. In higher plants and algae, structural stress hallmarks have been reported for example in organelles like chloroplasts or dictyosomes (1). In mitochondria, which are main targets of different stressors and react by either rapid increase or decrease in respiration, ultrastructural changes have been reported as consequence of environmental impact or disease both in plant and animal cells (2,3). Alzheimer's disease for example causes alterations of the inner and outer membrane of mitochondria in transgene mouse brain (3). In many cases advanced electron microscopic techniques, such as electron tomography, have substantially contributed to our understanding of structure related subcellular stress reactions in recent years. In the present study we investigate structural effects of mitochondria in the unicellular freshwater alga *Micrasterias* after exposure to potassium chloride (KCl) by means of FIB/SEM and TEM tomography. The model system *Micrasterias denticulata* is perfectly suited for such investigations as the cells are large and correspondingly contain large, well defined organelles. Moreover, the alga is closely related to higher land plants, which allows drawing conclusions on evolutionary aspects of stress reactions. Whereas mitochondria in untreated control *Micrasterias* cells are single, spherical or slightly elongated organelles, 3-D reconstructions from FIB-SEM series of KCl exposed cells show that they fuse to 3-dimensional aggregates during stress. These mitochondrial clusters all distributed all over the cell during ionic stress. Our reconstructions from TEM tomography series show that the membranous connections, by which the clusters are formed, are

established by protuberance of the outer mitochondrial membrane (*Figure*1). As the mitochondrial respiration potential of KCl stressed cells remained almost the same as in controls (2) and as the sub-structural alterations of mitochondria were reversible during recovery from stress, we assume that mitochondrial aggregation is important for maintaining respiration as essential cellular function during stress. We obtained similar effects in mitochondria in the aquatic higher plant *Lemna* sp. after KCl exposure which we studied for comparison. Together with reports on similar structural mitochondrial changes in the literature, this seems to suggest that mitochondrial cluster formation represents an ubiquitous stress avoidance reaction at least in plant cells.

References:

1. U. Lütz-Meindl et al., J. Microsc. 263 (2015) 129-141.

2. M. J. Affenzeller et al., J. Exp. Bot. 5 (2009) 854-855.

3. K. J. Choi et al., J. Biosci. 39 (2014) 97–105.

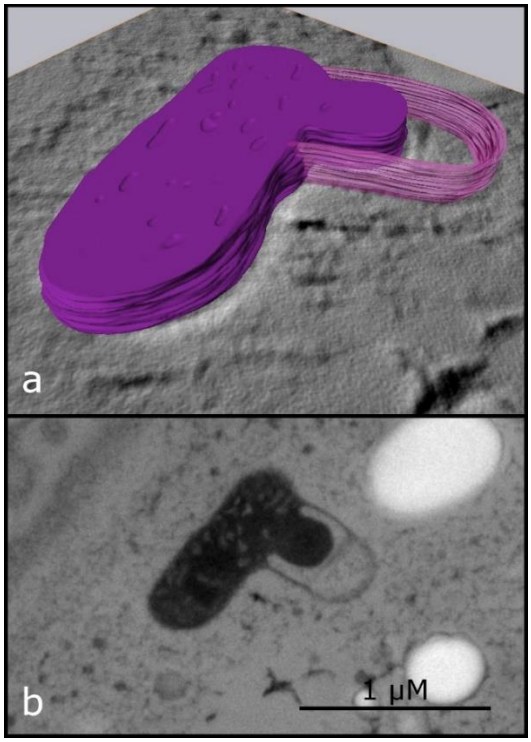

Figure 1. Protuberance of the outer mitochondrial membrane induced by 150 mM KCl in *Micrasterias denticulata*. (a) Reconstruction from TEM tomography series, protrusion in transparent purple. (b) Corresponding TEM micrograph.

Glandular trichomes and essential oil characteristics of *in vitro* propagated *Micromeria croatica* (Pers.) Schott (Lamiaceae)

Svetlana Tošić (1), Dragana Stojičić (1), Violeta Slavkovska (2), Bojan Zlatković (1), Snežana Budimir (3), Branka Uzelac (3)

1) Department of Biology and Ecology, Faculty of Sciences and Mathematics, University of Niš, Višegradska 33, 18000 Niš, Serbia

2) Department of Botany, Faculty of Pharmacy, University of Belgrade, Vojvode Stepe 450, 11000 Belgrade, Serbia

3) Institute for Biological Research "Siniša Stanković", University of Belgrade, Bulevar despota Stefana 142, 11060 Belgrade, Serbia

Keywords: capitate trichomes, micropropagation, peltate trichomes, phytochemical analysis

Morphology and structure of *Micromeria croatica* glandular trichomes in relation to the secretory process were characterized using scanning electron microscopy (SEM) and light microscopy, and their secretion was histochemically analyzed. SEM and histochemical analysis revealed that leaf indumentum of *in vitro* grown *M. croatica* consisted of non-glandular and glandular trichomes (Figure 1a). The main types of glandular trichomes observed in *M. croatica* leaves were peltate and capitate (Figure 1b-d). Peltate trichomes consisted of a broad basal cell embedded in the epidermis, a single-celled stalk, and a large round multicellular head (Figure 1e, h). Two types of capitate trichomes, differing in size and structure, could be distinguished. Type I capitate trichomes were positioned at an angle to the leaf surface and composed of one basal epidermal cell, short cutinized stalk and unicellular ellipsoidal head (Figure 1f). Type II capitate trichomes comprised of one basal cell, unicellular stalk and one apical secretory cell (Figure 1g). Apical cell of mature type II capitate trichomes had well developed round subcuticular space (Figure 1d). Plant extracts secreted from glandular trichomes are a valuable source of biologically active compounds. Phytochemical analysis identified up to 37 compounds in the essential oils (EOs) of wild-growing and micropropagated plants, and revealed differences in both content and the composition of the EOs obtained from different samples. EOs from both native plant material and *in vitro* cultivated plants showed very high percentages of total monoterpenoids, dominated by oxygenated monoterpenes.

Borneol was the main essential oil component detected in wild-growing plants (25.28%) and micropropagated plants grown on plant growth regulator-free medium (20.30%). Micropropagated plants cultivated in the presence of 0.3 μM kinetin had the highest yield of the EO, with geranial (33.53%) and *cis*-*p*-mentha-1(7),8-dien-ol (23.69%) being the main EO components. The percentage of total sesquiterpenoids in micropropagated plant material was considerably lower than in wild-growing plants. Sesquiterpene hydrocarbons accounted for the majority of detected sesquiterpenoids and were dominated by alpha-cadinene and beta-vetivenene. Some of the volatiles were found only in plant material obtained by micropropagation but not in wild-growing plants. Differences in both content and the composition of the essential oils obtained from different samples indicated that *in vitro* culture conditions and plant growth regulators significantly influence the essential oils properties.

Acknowledgements:

This research was financially supported by the Ministry of Education, Science and Technological Development of the Republic of Serbia, Grant № 173015, 173021 and 173030.

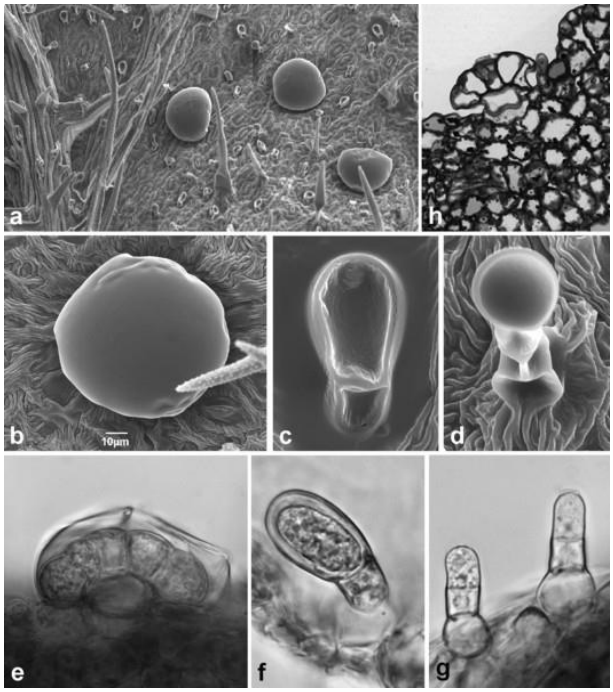

Figure 1. SEM and light micrographs of *in vitro* leaf trichomes of *M. croatica*. (a) Abaxial surface of leaf lamina. (b) Upper view of peltate trichome. Capitate trichome type I (c, f) and type II (d, g). (e,h) Longitudinal sections of immature peltate trichome.

Small-angle neutron scattering provides novel and dynamic insight into thylakoid structure and transmission electron microscopic artefacts

Renáta Ünnep (1), Ottó Zsiros (2), Gergely Nagy (3), Győző Garab (2), Katalin Solymosi (4)

1) Department of Neutron Spectroscopy, Institute for Solid State Physics and Optics, Wigner RCP of the H.A.S., Budapest, Hungary

2) Institute of Plant Biology, Biological Research Centre, Hungarian Academy of Sciences, Szeged, Hungary

3) Laboratory for Neutron Scattering and Imaging, Paul Scherrer Institute, Villigen, Switzerland

4) Department of Plant Anatomy, ELTE Eötvös Loránd University, Budapest, Hungary

Keywords: glutaraldehyde, grana, NaCl, osmotic stress/adjustment, swelling

Photosynthesis is one of the most important metabolic processes for life on Earth. The capture of sunlight happens in pigment-protein complexes located in the thylakoid membrane network present in the chloroplast stroma. In land plants, these membranes consist of solitary membrane sacs (stroma thylakoids) and regular thylakoid stacks (grana). Ultrastructural details of plastid structure emerged by the use of transmission electron microscopy (TEM) and suitable sample preparation protocols. Similarly, biochemical methods were developed to isolate chloroplasts and thylakoid membranes and to preserve them in a 'quasi' *in vivo* state by using osmoprotectants. Isolation procedures and TEM are routinely used to monitor alterations in plastid function and structure under various stress conditions (e.g. salt and osmotic stress). Small-angle neutron scattering (SANS) is a non-destructive method providing information on key structural parameters of multilamellar membrane systems on the mesoscopic scale (1-100 nm) and an insight into their dynamic features. Our aim was to compare SANS and TEM data of chloroplast thylakoids and to identify the strengths and weaknesses of both techniques and sample preparation protocols. SANS is a technique yielding statistically and spatially averaged data on repeat distances (RDs) of granum thylakoid membranes contained in macroscopic sample volumes without fixation, dehydration and

staining. Although it is possible to measure intact leaves by SANS, D_2O infiltration is preferably applied to improve the contrast. Our TEM analyses showed that infiltration may induce swelling of granum end membranes in some species, indicating that SANS sample preparation may need further optimization. On the other hand, the periodicity of grana on TEM micrographs strongly depended on their orientation as revealed by our Fast Fourier Transformation analyses of TEM micrographs. This shows that grana are mechanically compressed during ultrathin sectioning of resin-embedded leaves or cells. Therefore, conventional TEM, while contains a wealth of information on the ultrastructure, per se is not suitable to monitor small (<few nm) alterations in the membrane system. We have also shown that the addition of sorbitol – generally used for osmotic adjustment during thylakoid and chloroplast isolation – results in slight swelling of grana, while NaCl retained better the *in vivo* RDs. This raises further questions about potential isolation and TEM artefacts – because salt/osmotic stress is often associated with thylakoid swelling, while osmoprotectants like sorbitol are thought to prevent it. SANS also clearly showed that the addition of glutaraldehyde (a conventional TEM fixative) or mannitol (used for high pressure freezing during cryo-fixation) induced a decrease in the granum thylakoid RD. It can thus be concluded that simultaneous use of TEM and SANS may complement each other and provide a good basis for the development of sample preparation protocols.

Acknowledgements:

This research was supported by the Bolyai János Research Scholarship (K.S.) and by the Hungarian Scientific Research Fund, OTKA 112688 (G.G.).

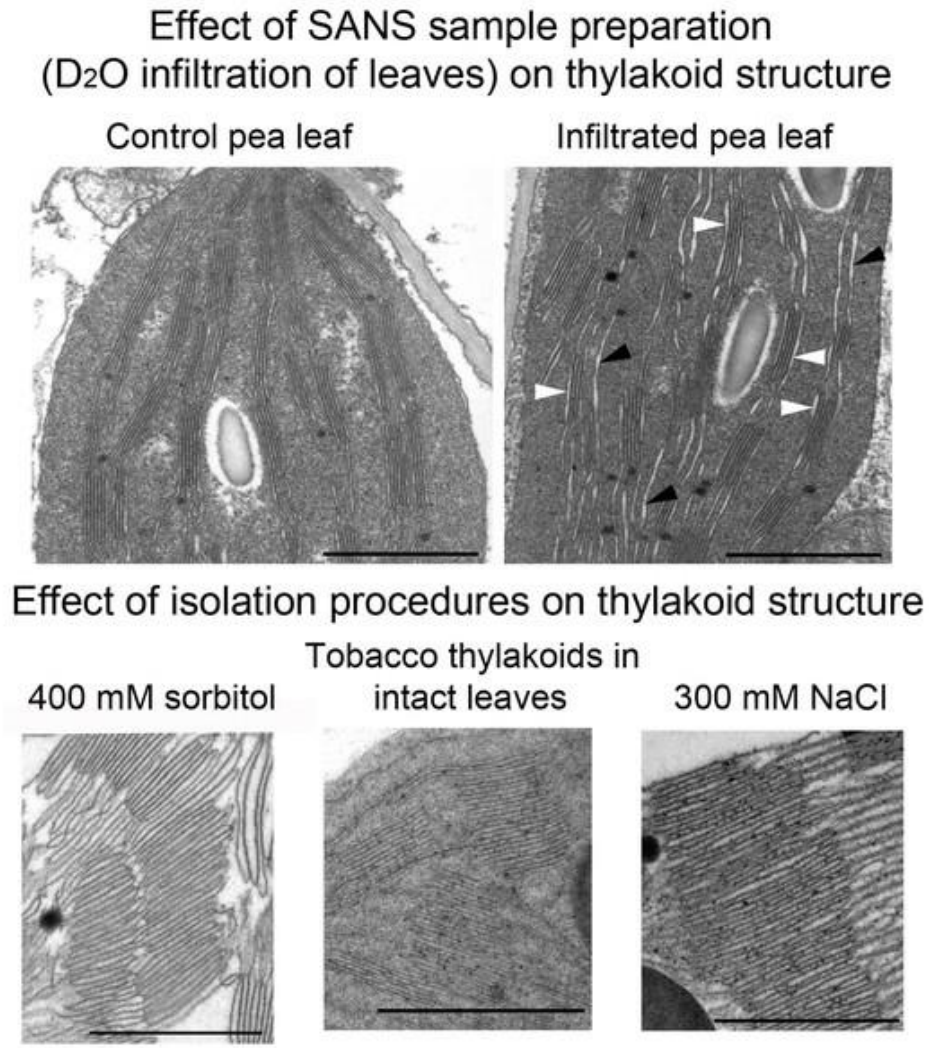

Figure 1. Transmission electron micrographs of pea leaves with or without D_2O infiltration (upper panel). Lower panel: Transmission electron micrographs and SANS profiles of thylakoids in intact tobacco leaves, or after isolation with sorbitol or NaCl.

POSTER PRESENTATIONS L5:

Peculiar tubuloreticular membrane organization in plastids with secretory function

Anna Skribanek (1), Adrienn Dobi (2), Pál Vági (2), Katalin Solymosi (2)

1) ELTE Eötvös Loránd University, Savaria University Center, Department of Biology, Egyetem tér 1–3, 1053 Budapest, Hungary

2) ELTE Eötvös Loránd University, Department of Plant Anatomy, Múzeum krt. 6-8, 1088 Budapest, Hungary

Keywords: Lamiaceae-type peltate glandular hairs, prolamellar bodies, tubular complexes

Several economically important plant species belong to the Lamiaceae family. Their importance is mostly related to the secretory activity of their glandular hairs which produce essential oils and other pharmaceutically active compounds. Several precursors or compounds of the essential oils are synthesized by the secretory plastids of these glandular trichomes. During secretion, the ultrastructure of the plastids is altered in the different cells of the glandular hairs. For instance, prolamellar body (PLB)-like cubic phase membrane structures appear in the stalk cells of the peltate hairs during the secretory stage of development, but similar structures can be observed in secretory plastids of other taxa as well. The highly regular PLBs are typically observed in plastids of dark-grown or low-light grown angiosperm plants impaired in chlorophyll biosynthesis, and are rapidly transformed into chloroplast thylakoids upon high light (1). It should be noted that heterotrophic cells (yeast cells, rat liver cells, tumor cells, amoeba cells) may also contain cubic phase (endoplasmic reticulum) membranes termed tubular complexes, the formation of which is often associated to virus infection or oxidative stress (2). However, it is unclear whether (i) the peculiar inner membrane organization of secretory plastids is structurally more similar to PLBs of dark-grown plants or to the tubular complexes of animal or other cells, and (ii) whether the formation of the cubic phase membranes in secretory plastids is in any ways related to the absence of light or is independent from it, and in the letter case which physiological processes may be related to it. Using

transmission electron microscopy, we studied plastid differentiation in the different cells of capitate and peltate hairs of species belonging to the Lamiaceae family (e.g. *Mentha crispa* and *Mentha piperita*) and have shown that - besides few similarities like the sporadic presence of irregular PLB-like structures - plastid structure shows some differences between the species. Using scanning electron microscopy we have shown that dark growth influenced the development of glandular hairs: less peltate hairs developed on the leaves of dark-grown plants than on those of light-grown ones of the same age, and the diameter of the peltate hairs (head cells) was also reduced in the dark. In the absence of light, plastid differentiation of the secretory tissues was slightly altered. For instance, small and assembling PLB-like membranes appeared in the head cells of the peltate hairs of few species. However, neither the structure nor the size of the PLB-like structures was altered by the absence of light in the stalk cells of the peltate hairs. Our data indicate that these PLB-like membranes are structurally and developmentally not similar to the PLBs of etioplasts, and are probably formed by a special, relatively high lipid/protein/water ratio within the plastids.

References:

1. K. Solymosi, B. Schoefs, Photosynth. Res. 105 (2010) 143–166.

2. Z.A. Almsherqui et al., J. Cell. Biol. 173 (2006) 839-844.

Ecotoxicological effects of sodium metasilicate on green (*Hydra viridissima* Pallas, 1766) and brown (*Hydra oligactis* Pallas, 1766) hydra

Ana Šimičev (1), Goran Kovačević (2), Romana Gračan (2)

1) Ilica 280b, HR-10000 Zagreb, Croatia

2) Faculty of Science, University of Zagreb, Department of Biology, Rooseveltov trg 6, HR-10000 Zagreb, Croatia

Keywords: soluble silicates, toxicology, endosymbiosis, freshwater ecosystems

Hydra is a freshwater invertebrate from the phylum Cnidaria. Due to its widespread distribution, easy cultivation and morphological, behavioural and reproductive traits which are simple to measure, it represents a popular model organism in scientific research. Considering the fact that species of hydra differ in their morphology and physiology, it is possible they have different responses to stressors in the environment. Unlike all other species of hydra, green hydra harbours endosymbiotic algae in its gastrodermal myoepithelial cells. The aim of this research was to determine and compare the effects of sodium metasilicate on green and brown hydra. Sodium metasilicate belongs to the group of synthetic chemicals defined as soluble silicates and was chosen for the experiment because of its widespread use in many human activities such as production of detergents and soaps, cosmetic industry and production of paper. Hydras were treated with four concentrations of sodium metasilicate (0.05 g/L, 0.365 g/L, 0.38 g/L, 0.39 g/L). Morphological, behavioural and reproductive changes on hydras were observed during the following three days using a light microscope. For analysis of cyto-histological changes, standard preparations were made. The results showed that sublethal concentrations of sodium metasilicate caused migration, reduced reactivity to mechanical stimuli, changes in body contraction and damage of tentacles. The observed changes were more pronounced in brown hydra. Higher concentrations caused disintegration of cellular layers. In addition, sodium metasilicate caused changes in distribution of algae inside the body of green hydra. Green hydra showed better adaptability to unfavourable environmental conditions. Higher

concentrations of sodium metasilicate could pose a direct influence on viability of populations of green and brown hydra in nature.

Figure 1. Asexual reproduction in green hydra (*Hydra viridissima* Pallas, 1766).

Figure 2. Asexual reproduction in brown hydra (*Hydra oligactis* Pallas, 1766).

References:

1. Campbell R. D. (1990) Transmission of symbiotic algae through sexual reproduction in Hydra: movement of algae into the oocyte. J. Tissue Cell 22, 137-147.

2. Kovačević G., Matulić A. (2013) Effects of Quercetin on the Green Hydra (Hydra viridissima Pallas). Int. J. Biol. 5, 57-63.

3. Kovačević G., Gregorović G., Matijević A., Kalafatić M. (2015) Toxic effects of iron on green and brown hydra. Curr. Sci. 110, 502-504.

The effect of quercetin on brown hydras, endosymbiotic and free-living algae

Monika Karin (1), Valerija Vujčić (2), Damir Sirovina (2), Goran Kovačević (2)

1) High school “dr. Mate Ujevića” Brune Bušića 59, HR-21260 Imotski, Croatia

2) Faculty of Science, University of Zagreb, Department of Biology, Rooseveltov trg 6, HR-10000 Zagreb, Croatia

Keywords: brown hydra, endosymbiotic alga, free-living alga, quercetin

Quercetin is the most significant flavonoid which is an antioxidant, but sometimes it also performs a prooxidative effect. Brown hydra (*Hydra oligactis* Pallas, 1766) is a freshwater animal belonging to the phylum Cnidaria. It was treated with quercetin (0,2, 0,25, 0,3 gL^{-1}) and compared to the control, as well as endosymbiotic algae isolated from green hydra *Desmodesmus subspicatus* (Chlorophyceae) (Chodat) Hegewald and Schmidt, *Mychonastes homosphaera* (Chlorophyceae) (Skuja) Kalina and Punčochářová and free-living related alga *Chlorella vulgaris* Beij. [K&H, 1992], strain SAG 211-11b. Morphological changes were observed by using a stereo microscope and included migration in the experimental dish, reactions to mechanical stimuli, secretion of mucus from hydra body and mortality. Cytological and histological changes were observed using light microscopy. At higher concentrations of toxicant quercetin caused damages of ectoderm and gastroderm of brown hydra and growth inhibition of endosymbiotic algae. Free-living alga treated with quercetin showed higher viability compared to the isolated endosymbiotic algae.

The effect of naringenin on hydra – alga symbiosis

Valentina Bartol (1), Goran Kovačević (2), Damir Sirovina (2), Valerija Vujčić (2)

1) 6th primary school Varaždin, Dimitrija Demetra 13, HR-42 000 Varaždin, Croatia

2) Faculty of Science, University of Zagreb, Department of Biology, Roosveltov trg 6, HR–10000 Zagreb, Croatia

Keywords: naringenin, hydras, algae, structural changes, microscopy

Flavonoids are plant pigments found in fruit, vegetables, tea, flowers and wine. Naringenin is a flavonoid that belongs to the group of flavanones and its effect was monitored on hyda – alga symbiosis. As test organisms used were: *Hydra viridissima* Pallas, 1766 and *Hydra oligactis* Pallas, 1766, endosymbiotic algae isolated from the hydra host *Mychonastes homosphaera* (Skuja) Kalina and Punčochářová, *Desmodesmus subspicatus* (Chodat) Hegewald and Schmidt and related free – living species *Chlorella vulgaris* Beij. Morphological and cyto – hystological analysis was made using concentrations of 0,2 gL^{-1}, 0,25gL^{-1} and 0,3 gL^{-1} of naringenin. It was determined that the middle concentration does not favor growth of the organisms. Mortality, budding, mucus secretion, migration and contractions of hydra as well as viability of algal cells were monitored by stereo microscopy and changes in structural cell organization were observed by light microscopy.

Monitoring lipid production in yeast using SEM and Raman spectroscopy

Kamila Hrubanova (1), Vladislav Krzyžánek (1), Ota Samek (1), Martin Šiler (1), Pavel Zemánek (1), Andrea Haronikova (2), Ivana Marova (2)

1) Institute of Scientific Instruments of the CAS, v.v.i., Královopolská 147, 612 64 Brno, Czech Republic

2) Faculty of Chemistry, Materials Research Centre, Purkyňova 118, Brno University of Technology, Purkyňova 118, 612 00 Brno, Czech Republic

Keywords: yeast, lipid bodies, SEM, Raman spectroscopy

The main goal of our project is the development of specialized instrumentation and methodology to monitor metabolic states of microorganisms in order to optimize cultivation process for biotechnological applications. Here the attention is given to the oil-producing yeast strain *Metschnikowia pulcherrima.* The influence of different cultivation parameters (such as the effects of temperature regime and medium composition) on cells can be monitored. In our investigations on yeast cells scanning electron microscopy (SEM) and Raman spectroscopy techniques were used. Here, SEM uses electron beam to gain information about morphology of cells which reflects cells response on the different cultivation conditions. Consequently, Raman spectroscopy (1) was used for the determination of lipids/oil present in the biomass. Thus, our study targets some factors which could lead to efficient industrial production of oil in selected biotechnological production. The yeast strains (*Metschnikowia*) were cultivated in medium containing different ratios of C/N (glycerol/yeast extract and/or ammonium sulphate) during a time period of two weeks. On the different days of cultivation, the cells were collected by centrifugation (2000 rpm, 1 min.) and analysed. SEM - the samples of yeast were cultivated as mentioned above and observed by cryo scanning electron microscopy (cryo-SEM). Cells were imaged using a cryo-SEM. For freezing the propane-jet technique was used (JFD030; Bal-Tec, Balzers). After freezing, the samples were mounted onto a double fracture cryo-stage under liquid nitrogen and transferred under inert gas in a cryo-high vacuum shuttle VCT100 (Leica microsystems, Vienna) to a pre-cooled freeze-fracture device ACE600 (Leica microsystems, Vienna) at –140 °C. The samples were then fractured and sublimated at –95

°C for 2 minutes to remove deposited residual water condensation and ice crystals. Finally, they were transferred under high vacuum and low temperature using the shuttle VCT100 to a pre-cooled (–120 °C) cryo-SEM Magellan 400/L (FEI) for the imaging with 1 keV electron beam and beam current 6.3 pA without any metal coating. Raman spectroscopy - cells were analyzed using a Renishaw Invia system (Renishaw inVia Raman Spectrometer, Renishaw plc., Wotton under Edge, UK), with a 785 nm single-mode diode laser as the excitation source on Raman grade CaF substrate (Crystran Ltd., UK). Our experimental results are presented in Figure 1 (SEM) and Figure 2 (Raman spectroscopy). The spectral map (Figure 2) nicely visually monitors (qualitatively) changes in unsaturated oil within the cells at the different collection dates with maximum of unsaturation at the last two days of collections. Based on our results presented here, further systematic studies are required in order to fully monitor mechanisms of lipid accumulation in yeast cells. Such studies are currently under way in our laboratories, exploiting combination of SEM and Raman spectroscopy approaches.

Acknowledgements:

This work was supported by the Czech Science Foundation (GA15-20645S), the infrastructure by the Ministry of Education, Youth and Sports of the Czech Republic (LO1212) and the European Commission (ALISI ED0017/01/01). KH acknowledges the support of FEI/CSMS scholarship.

References:

1. O. Samek et al, Sensors 10 (2010), p. 8635-8651.

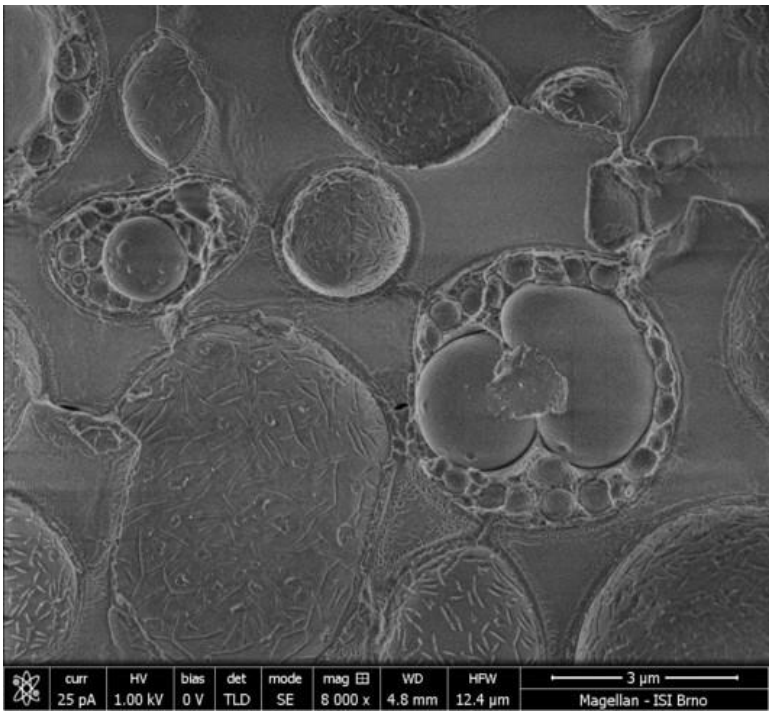

Figure 1. (a) SEM image of *Metschnikowia andauensis*; lipid bodies are clearly visible due to the optimisation of cultivations parameters (sample was collected on day 13).

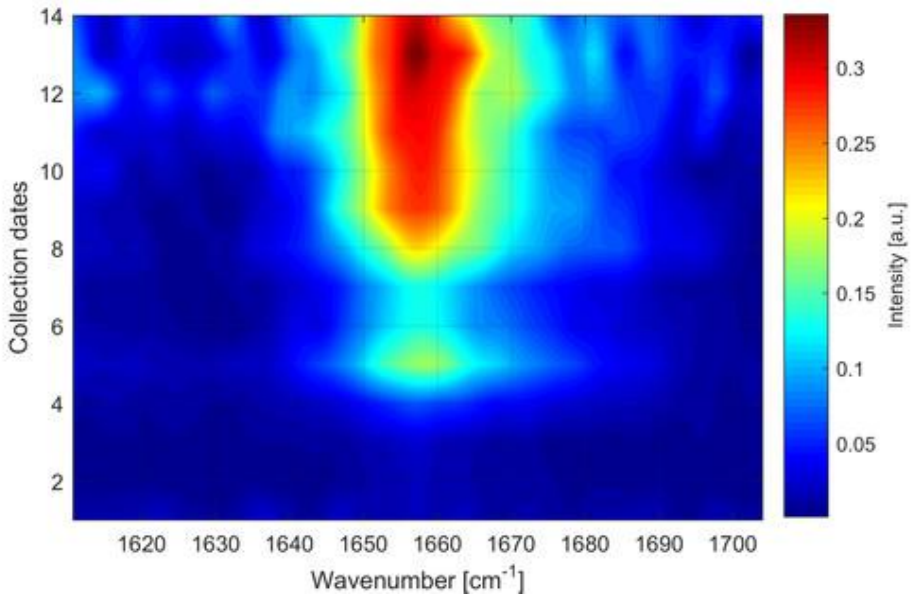

Figure 2. Spectral map plotted using Raman intensities of 1656 cm^{-1} line for monitoring of unsaturated oil. Measurements of oil unsaturation were performed for 14 collection dates (days) in *Metschnikowia andauensis*.

Analysis of pyretrins in extract of *Tanacetum cinerariifolium* using Raman spectroscopy

Ilinka Pećinar (1), Filip Varga (2), Martina Grdiša (2), Ivan Šoštarić (1), Zlatko Šatović (2), Zora Dajić Stevanović (1)

1) University of Belgrade, Faculty of Agriculture, Nemanjina 6, 11080 Belgrade-Zemun, Serbia

2) Department of Seed Science and Technology, Faculty of Agriculture, University of Zagreb, Svetošimunska cesta 25, HR-10000 Zagreb, Croatia

Keywords: Dalmatian pyrethrum, Raman spectroscopy, pyrethrin I, II, cinerin I, II jasmolin I, II

Dalmatian pyrethrum (*Tanacetum cinerariifolium* /Trev./ Schultz Bip (Asteraceae), the species native for East Adriatic coast, is known as the main source of pyrethrin, which is mixture of six active compounds (pyrethrin I and II, cinerin I and II and jasmolin I and II), acting as natural insecticide. Quality of the natural pyrethrin is expresed as pyrethrin I/pyrethrin II ratio (Grdiša et al., 2014). The aim of this paper was to describe possibilities of using Raman spectroscopy, as fast and sensitive method in screening and differentiation of six pyrethrin components of the extract of *T. cinerariifolium* inflorescence. The plant material was collected from ten indigenous populations in Croatia. Ultrasound assisted extraction (UAE) was used for extraction of pyrethrins from samples of dried flowers of Dalmatian pyrethrum. Isolation and purification of six compounds from pyrethrine active substance was performed using liquid chromatography (HPLC-UV/VIS-DAD). Raman spectroscopy of the extracts and pyrethrins was performed in the range 500–1800 cm^{-1} with XploRA Raman spectrometer (Horiba Jobin Yvon). Raman scattering was excited by a frequency-doubled Nd/YAG laser at a wavelength of 532 nm (maximum output power 20-25mW), equipped with a 600 lines mm^{-1} grating. Spectra were analysed using Origine Pro 8.6 software (OrigineLab, USA). Figure 1 represents Raman spectra in the spectral region from 500-1800 cm^{-1} of extracts of *T. cinerariifolium* (Figure 1.1-10), as well as pyrethrines (Figure 2.1-6) which were used as standard chemicals. Due to the high percentage of pyrethrines in the drug extracts, the Raman spectra (Figure 1) actually represent the profile characteristic for this compound. This was evidenced through high similarity of obtained Raman spectra of the extracts and the isolated (standard) pyrethrines

(Figures 1 and 2). The region between 600 and 1710 cm^{-1} of Raman spectra exhibited significant structural information, and therefore informative in distinguishing the variances among extracts originating from different populations (Figure 1). High intensity bands at 1634 and 1437cm^{-1} can be attributed to the six individual pyrethrins, as well as bands at 1703 cm^{-1} (Figure 1.1-10). In addition, the prominent bands at 1646, 1273 and 956 cm^{-1} cm^{-1} indicated the presence of jasmolin and cinerin I (Figure 2b, c), the band at 1259 and 1295 cm^{-1} indicates the presence of pyretrin I (Figure 2a), 1414 cm^{-1} cinerin I, II, (Figure 2c, f). These preliminary results showed that Raman spectroscopy can be used as a screening method for the pyrethrins in extracts but should be combined with HPLC for more precise determination of quality and quantity of extracts.

References:

1. M, Grdiša et al., PLoS ONE 9(8) (2014) e105265.

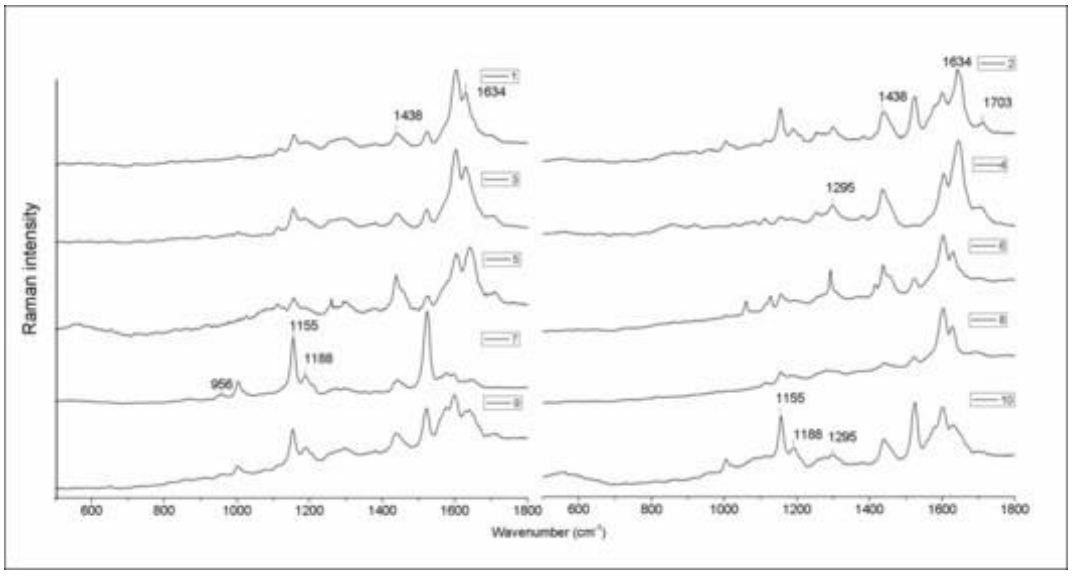

Figure 1. Raman spectra in the spectral region from 500-1800 cm^{-1} of extracts of *T. cinerariifolium* (ten indigenous populations in Croatia, 1-10).

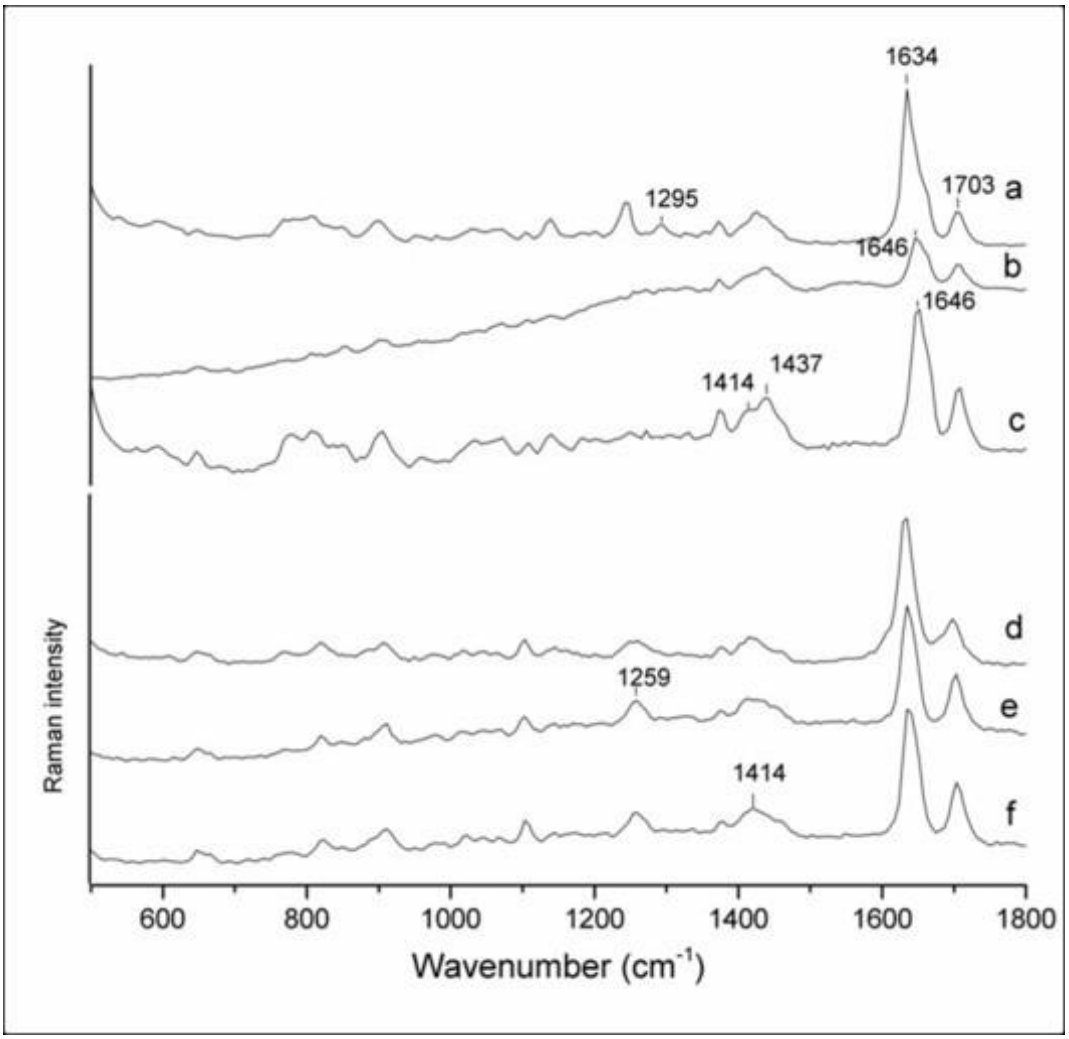

Figure 2. Raman spectra of pyrethrine standards in the region from 500-1800 cm^{-1} (a) pyretrin I, (b) jasmolin I, (c), cinerin I (d) pyretrin II (e), jasmolin II, (f) cinerin II.

Isolated endosymbiotic algae at test: the point of no return?

Goran Kovačević (1), Martina Ivšić (1)

1) Faculty of Science, University of Zagreb, Department of Biology, Rooseveltov trg 6, HR-10000 Zagreb, Croatia

Keywords: endosymbiotic algae, green hydra, Chlorella test, morphometry, iron

It is well known that evolutionary changes in organisms are not limited to the vertical exchange of genes: a transfer of new genetic characteristics from one species to another is possible as a horizontal gene transfer. Symbiosis, denoting close and often long-term interaction between at least two species, is possibly the best way to achieve such a horizontal gene transfer. The aim of this work was to research advantages or disadvantages of releasing from the hydra-alga symbiotic relationship using Chlorella test with iron. The test was performed on endosymbiotic algae *Desmodesmus subspicatus* (Chodat) Hegewald and *Mychonastes homosphaera* (Skuja) Kalina and Punčochářová (*Chlorella zagrebiensis* group Kovac. and Jelen.) isolated from green hydra host (*Hydra viridissima* Pallas, 1766) and on related free-living species *Chlorella kessleri* Fott and Novák. [K&H, 1992] strain LARG/1and *C. vulgaris* Beij. [K&H, 1992] strain SAG 211 - 11b. The results were observed macroscopically and microscopically in relation to various parameters. Isolated endosymbiotic algae showed a higher sensitivity to iron than the free-living relatives. Increasing concentration of iron led to deformations of cells and cell formations. Among others, empty cells, disturbed divisions and reduced intensity of green color in both isolated species were observed. Isolated species were less able to defend against the toxicity of iron possibly due to a transfer of some of their genetic material to the genome of their *Hydra* host. Mutualistic symbiotic lifestyle gives a greater chance of survival in the unfavorable (micro-)environment, but after having lost that advantage the symbiotic partners could become more vulnerable. Mutualistic symbiotic lifestyle gives a greater chance of survival in the unfavorable (micro-)environment, but after having lost that advantage the symbiotic partners could become more vulnerable.

References:

1. Kovačević G., Jelenčić B., Kalafatić M., Ljubešić N. (2008) Chlorella test. Periodicum biologorum 4: 373-374.

The development of Norway spruce somatic embryos visualized with different microscopic tools

Kateřina Eliášová (1), Vilém Neděla (2), Jiří Runštuk (2), Zuzana Vondráková (1)

1) Institute of Experimental Botany CAS, Rozvojová 263, Praha 6 - Lysolaje, 165 02, Czech Republic

2) Institute of Scientific Instruments CAS, Královopolská 147, Brno, 612 64, Czech Republic

Keywords: environmental scanning electron microscopy, confocal laser scanning microscopy, *Picea abies* L. Karst., somatic embryogenesis

Somatic embryogenesis represents useful system for the study of the process of embryogenesis as well as the convenient system for clonal propagation of conifers. It consists in induction of embryogenic culture from somatic cells and the development of early somatic embryos, their maturation, desiccation and emblings development. The detailed characterization of all developmental steps is a prerequisite for optimal regulation of this process. For observation of the structural changes during development of Norway spruce somatic embryos we use light, confocal laser-scanning (CLSM) and environmental scanning electron microscopy (ESEM). Early somatic embryos of Picea abies L. Karst. are composed of densely cytoplasmic small meristematic cells and highly vacuolated elongated suspensor cells. During the process of maturation, embryo proper forms from meristematic cells while suspensor cells undergo degradation in the course of programmed cell death. Embryo proper elongates and polarizes. The basic embryonal structures are gradually established – apical and root meristems on the opposite embryonal poles, protoderm on the embryo surface and the root cap covering the root pole. Mature somatic embryo is completed when the ring of cotyledons is formed around apical meristem above the elongated hypocotyl and radicle. Usage of non-commercial AQUASEM ESEM enables to study the development of surface cell layers that are necessary for protection of inner embryonal tissues against both abiotic and biotic stresses as UV radiation, drought or extreme temperatures and attack of pathogens. We followed the development of protoderm (from tile pattern on the top of the meristematic head of the cylindrical embryo to the elongated protoderm cells of cotyledonary embryo) and root

cap on the surface of somatic embryos during maturation, changes in the arrangement of suspensor cells and establishment of morphological embryonal structures – cotyledons, hypocotyl and radicle. Native samples were observed without chemical fixation and coating under low vacuum conditions (air pressure 520-560 Pa) at a temperature -1°C. Under these conditions we could observe also extracellular matrix covering meristematic heads and/or suspensor cells that have been already shown in somatic embryogenic cultures of conifers (Hřib et al, 2015; Neděla et al, 2016). Histochemically (by staining with Alcian Blue and Toluidine Blue) we proved that this extracellular matrix has, at least partially, mucilaginous character. ESEM observation of Norway spruce somatic embryo structure was compared with the results of viability assay which was done using a double staining with fluorescein diacetate (FDA) and propidium iodide (PI). Fluorescence of these substances in living (green fluorescence of FDA) or dead cells (red fluorescence of PI) was visualized using CLSM. This method permitted us to determine not only the viability of cells but also the arrangement of whole embryo.

Acknowledgements:

This work was supported by Ministry of Education, Youth and Sports, project no. LTC17030.

References:

J. Hřib et al., Open Life Sciences 10 (2015) 285-290 V. Neděla et al., Micron 84 (2016) 67-71.

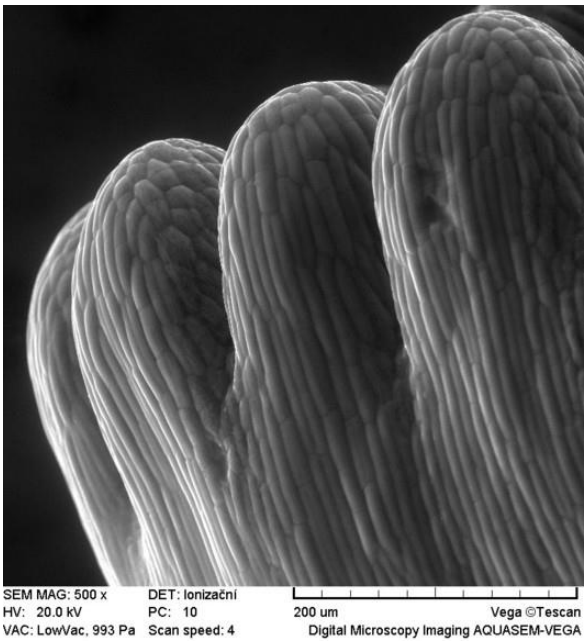

Figure 1. Cotyledons of mature somatic embryo of Norway spruce visualized with ESEM under conditions of low vacuum and temperature -1°C.

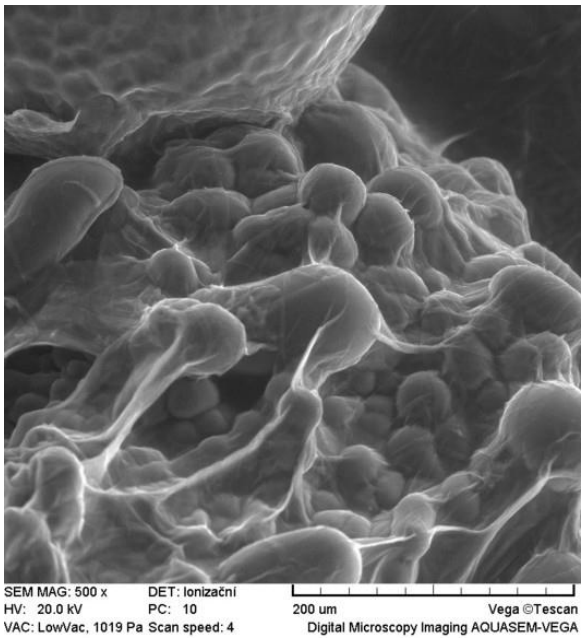

Figure 2. Meristematic head of Norway spruce somatic embryo visualized with ESEM under conditions of low vacuum and temperature -1°C; note the extracellular matrix covering meristematic cells.

L6. Neuroscience and Histopathology

INVITED LECTURES L6:

Fast 3D imaging of neuronal coding in spine, dendritic, and neuronal assemblies in the visual cortex of behaving animals

Gergely Szalay (1*), Linda Judák(1*), Gergely Katona (1,3*), Pál Maák (4), Katalin Ócsai (3), Máté Veress (4), Zoltán Szadai (1,2), Tamás Tompa (1,2), Balázs Chiovini (1,2), Balázs Rózsa (1,2)

1) Laboratory of 3D functional network and dendritic imaging, Institute of Experimental Medicine Hungarian Academy of Sciences, Budapest-1083, Hungary

2) The Faculty of Information Technology, Pázmány Péter Catholic University, Budapest-1083, Hungary.

3) MTA-PPKE ITK-NAP B – 2p measurement technology group, The Faculty of Information Technology, Pázmány Péter Catholic University, Budapest-1083, Hungary.

4) Department of Atomic Physics, Budapest University of Technology and Economics, Budapest-1111, Hungary.*

Keywords: two photon microscopy, neuronal imaging, behaving animals

Our long-term aim is to assess the feasibility of creating an “artificial sense” and, thereby, a possible sensory (visual) prosthetic. While working towards this goal, we will have to address the question of how neural assembly activity relates to subjective perceptions. Finding and understanding these functional assemblies will make it possible to reactivate them in a precise, biologically relevant manner to elicit similar cortical activation as visual stimulation. Recent publications suggest that cortical connectivity can be mapped by two-photon microscopy. Threedimensional (3D) random-access point scanning can simultaneously read out neural activity on both the somatic and dendritic scales which is required to map coding assemblies in the visual cortex. This method can increase measurement speed and signal-to-noise ratio (SNR) by several orders of magnitude, but suffers from one main disadvantage: fluorescence information is lost during brain movement. Therefore we developed a novel 3D microscope technique for highthroughput assembly mapping in behaving animals. The novel 3D DRIFT

acousto-optical scanning microscopy can extend each scanning point to small 3D lines or surface or volume elements, preserving fluorescence information for motion correction. The method effectively eliminates *in vivo* motion artifacts, allowing fast 3D measurement of over 150 dendritic spines with 3D lines, over 100 somata with squares and cubes, or multiple spiny dendritic segments with surface and volume elements in behaving animals. Finally, a four-fold improvement in total excitation efficiency resulted in about 500 µm × 500 µm × 650 µm, scanning volume with GECIs. Using the new microscope we mapped activity of large neuronal assemblies associated with different visual stimulation.

Proximal association of P/Q-type voltage-gated calcium channels and the vesicle fusion sites at cerebellar excitatory synapses

Walter A. Kaufmann (1), Harumi Harada (1), Pradeep Bhandari (1), Ryuichi Shigemoto (1,2)

1) Institute of Science and Technology-Austria, Am Campus 1, 3400 Klosterneuburg, Austria

2) Division of Cerebral Structure, National Institute for Physiological Sciences, Myodaiji, Okazaki 444-8787, Japan

Keywords: voltage-gated calcium channel, synaptic vesicle, immunolabeling, freeze-fracture replica, electron tomography

In neuron synapse, voltage-gated calcium channels in the pre-synaptic active zone trigger vesicle fusion and transmitter release with distinct coupling distance to calcium sensors on vesicles. Still, no direct measurement of spatial distance between calcium channels and vesicle fusion sites has been made. In this study, we investigated ultrastructural localization of P/Q-type voltage-gated calcium channels (Cav2.1) and their distance to docked vesicles and fusion pores in the active zone of cerebellar excitatory synapses, particularly climbing fiber (CF) and parallel fiber (PF) to Purkinje cell synapses. These show striking differences in release probability deduced from paired-pulse ratios. To this end, freeze-fracture replica immunolabeling (FRIL) was applied for Cav2.1 localization at high spatial resolution. Electron tomography of pre-embedding samples was used for concurrent analysis of Cav2.1 distribution and spatial relationship between Cav2.1 and docked vesicles respectively fusion pores. In FRIL, immunogold labeling for Cav2.1 was non-homogeneously distributed in the active zone of both PF and CF synapses forming nanoclusters. Average number of particles in clusters as well as whole active zone compartment was similar in these synapses, and a positive correlation between particle number and active zone area was found. Electron tomography of pre-embedding samples revealed comparable results with similar channel densities in PF and CF synapses although at lower detection efficiency. Yet <30 nm distances of Cav2.1 to docked vesicles and fusion pores were detected in both synapse types. The overall number of docked and fused vesicles appeared the same. These results indicate similar number and distribution pattern of P/Q-type voltage-gated calcium channels in PF and CF to Purkinje cell synapses and comparable coupling distances. Further morphological parameters are going to be dissected as the ratio of docked and fused vesicles closer than 30 nm from calcium channel clusters, which could explain the physiological difference between these synapse types.

ORAL PRESENTATIONS L6:

The Investigation of STAT3 protein expression changes in rat kidney injury model induced by puromycin aminonucleoside application

Halil İbrahim Saygı (1), Zeynep Banu Güngör (2), Fatma Kalay (2), İsmail Seçkin (1)

1) İstanbul University, Cerrahpaşa Medical Faculty, Histology and Embryology Department; Kocamustafapaşa – Fatih/İst., Turkey

2) İstanbul University, Cerrahpaşa Medical Faculty, Biochemistry Department; Kocamustafapaşa – Fatih/İst., Turkey

Keywords: kidney glomerulus, nephrosis, proteinuria, immunohistochemistry, STAT3

Glomerular damages could lead to glomerular losses and ultimately to end stage renal diseases (ESRD). Recent studies showed that JAK/STAT pathway plays role in these damages. The fact that STAT3 could be activated both by extracellular (e.g. growth factors) and intracellular (e.g. oxidative stress) stimulants make STAT3 very important for glomerulus pathology. One of the animal models that depicts glomerular damage is Puromycin Aminonucleoside Nephrosis (PAN) model which is thought to be mediated by oxidative stress. In this study, glomerular STAT3 expression changes are aimed to be analyzed in PAN model. Along with a control group, three PAN groups which were sacrificed on different days are formed by the i.p. injection of Puromycin Aminonucleoside for 5 consecutive days. Throughout the experiment, 24 hour urines are collected on specific days and level of urinary proteins was monitored. At the end of the experiments, tissue specimens were stained with pSTAT and tSTAT antibodies. Moreover they also examined ultrastructurally in electron microscope and stained with Periodic Acid Schiff (PAS) Hemaluan for light microscope. The proteinuria levels did not increase in 5th day of all groups but showed a dramatic increase on 15th day of 15th and 20th day groups. In 25th day group, urinary protein levels decreased and become close to Control group on 25th day. Ultrastructural findings showed glomerular damages such as

significant decrease in SlitPore (SP) number, a significant gradual increase in GBM thickness, podocyte hypertrophy and formation of PAGs on 5th and 15th days; besides significant increase in mesangial matrix. pSTAT and tSTAT immunoreactivities significantly scaled up in this groups but tSTAT immunoreactivity showed its first dramatic increase on 15th days whereas pSTAT on 5th day. These changes come close to Control group levels in 25th day of 25th day group which showed a recovery. Regarding all the groups, it was thought that the increases in the pSTAT and tSTAT immunoreactivity levels correlated with the proteinuria and degenerations of the glomerular structure.

Ultrastructural characterization of chordoma cells

Dagmar Kolb (1), Elisabeth Pritz (2), Bibiane Steinecker-Frohnwieser (3), Birgit Lohberger (4), Alexander Deutsch (5), Thomas Kroneis (6), Amin El-Heliebi (3), Gottfried Dohr (3), Katharina Meditz (3), Karin Wagner (7), Harald Köfeler (7), Gerd Leitinger (7), Andreas Leithner (8), Bernadette Lieg-Atzwanger (5), Dagmar Zweytick (9), Rinner Beate (10)

1) Center for Medical Research, Medical University of Graz, Graz, Austria

2) Institute of Cell Biology, Histology & Embryology, Medical University of Graz, Graz, Austria

3) Institute of Cell Biology, Histology & Embryology, Medical University of Graz, Graz, Austria

4) Ludwig Boltzmann Institute for Rehabilitation of Internal Diseases, Ludwig Boltzmann Cluster for Rheumatology, Balneology and Rehabilitation, Saalfelden, Austria

5) Department of Orthopaedic Surgery, Medical University of Graz, Graz, Austria

6) Division of Hematology, Department of Internal Medicine, Medical University of Graz, Graz, Austria

7) Center for Medical Research, Medical University of Graz, Graz, Austria

8) Institute of Cell Biology, Histology & Embryology, Medical University of Graz, Graz, Austria

9) Institute of Pathology, Medical University of Graz, Graz, Austria

10) Biophysics Division, Institute of Molecular Biosciences, University of Graz, Graz, Austria

Keywords: chordoma, tumor, high pressure freezing, electron tomography, therapeutic approaches

Chordomas are rare bone tumors, largely resistant to chemotherapy. The most impressive about chordomas is their unique phenotype in tumor tissue and especially in cell culture. These tumors are morphologically composed of heterogeneous cells, ranging from smaller non-vacuolated spindly-shaped cells to large cells with prominent vacuoles (1). A detailed ultrastructural investigation of the vacuoles represents an important step towards an improved understanding of their tumor biology. The most efficient way to obtain information on cell interactions, as close as possible to the native state, when using electron microscopy is by combining high pressure freezing (HPF) with electron tomography. The combination of both

techniques enables us to visualize the dynamic process of the cell. These ultrastructural analyses offer valuable information on the biological behavior of chordomas. Furthermore, we show the mitochondria – associated ER complex (MAM complex), a prominante ultrastructural feature in chordoma cells. Within the MAM-complex, rough ER surrounds the mitochondria and is linked to it via proteinaceous tethers. Measurements in 2D on mitochondrial profiles of MUG-Chor1 cells showed that 64.8% of the mitochondrial surface appeared to be completely surrounded with ER. In contrast in U2OS cells none of these profiles were fully covered by ER. The main function of the MAM complex is to enable the transfer of lipids and calcium between the two organelles (2), (3). Our aim was to find a new perspective on the biology of chordoma that would open up the field for completely new therapeutic approaches with regard to lipids and Ca2+ pathways to finally overcome thus far untreatable chordoma tumors.

References:

1. Erlandson RA et al., Cancer Res 28 (1968) 2115–2125.

2. Csordas G et al., J Cell Biol 174 (2006) 915–921.

3. Rizzuto R et al., Science 280 (1998) 1763–1766.

Central exogenous apelin-13 and restraint stress stimulates hypothalamic cholecystokinin via APJ receptor

Gokhan Akkoyunlu (1), Mehmet Bulbul (2), Osman Sinen (2), Melahat Gök (2)

1) Akdeniz University, Faculty of Medicine, Department of Histology and Embryology, Antalya, Turkey

2) Akdeniz University, Faculty of Medicine, Department of Physiology, Antalya, Turkey

Keywords: APJ receptor, apelin, cholecystokinin, paraventricular nucleus, acute restraint stress

Background: Apelin was identified as the endogenous ligand of the G protein-coupled receptor APJ. Apelinergic system is expressed in gastrointestinal (GI) tissues, furthermore, peripherally administered apelin has been shown to increase cholecystokinin (CCK) in plasma and duodenal mucosal cells. Besides the GI tract, both apelin and APJ receptor are widely expressed in numerous brain regions including hypothalamic paraventricular nucleus (PVN) which is also known to harbor CCK-producing cells. In rats, acute restraint stress (ARS) was shown to stimulate the apelin-producing cells in PVN. Although APJ receptors are present in PVN, it is not clear whether ARS-evoked or centrally administered apelin induces hypothalamic CCK release. Methods: In male Wistar rats, artificial cerebrospinal fluid (aCSF) or apelin-13 (30 nmol/100 nL) was injected through a microinjection cannula stereotaxically implanted into PVN. In a separate group, vehicle or APJ receptor antagonist F13A (30 nmol/100 nL) was pre-administered in rats subsequently underwent ARS. Rats were euthanized and brains were dissected. Double labeled immunofluorescence was used for detection of APJ and CCK-positive cells in PVN sections. Results: APJ receptor expression was shown in the neurons of parvocellular and magnocellular regions of PVN. While there were individual labeled APJ or CCK positive cells there were also APJ and CCK double labeled cells present. CCK-positive cell number was increased after apelin-13 administration (Figure 1). The increased pattern is more pronounced with ARS administration (Figure 2). This ARS dependent increase is suppressed after F13A preadministration. Conclusions: Taken together, central apelin appears

to mediate hypothalamic CCK release through APJ receptor. APJ antagonism might be a novel approach for treatment of stress-related disorders.

References:

1. M. Bülbül et al., Neuropeptides. 2017 Jun;63:91-97.

Figure.1

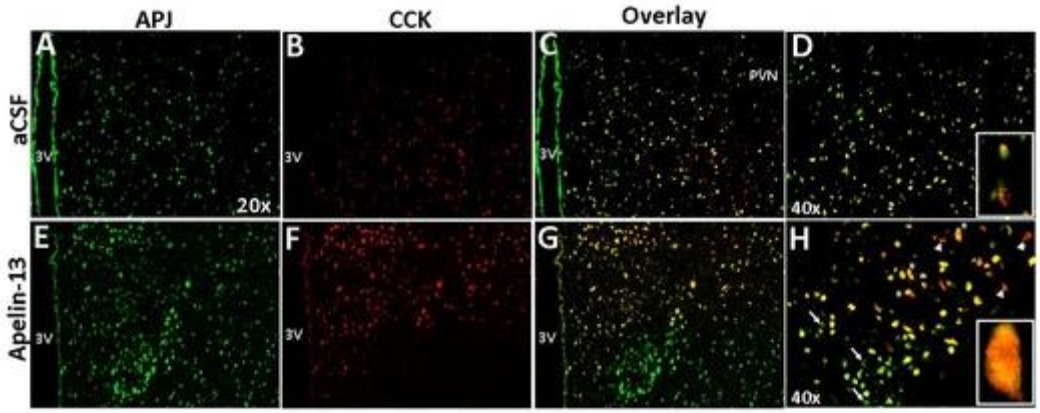

Figure 1. APJ and CCK double stainings in PVN after aCSF (A-D) and Apelin-13 (E-H) administrations.

Figure.2

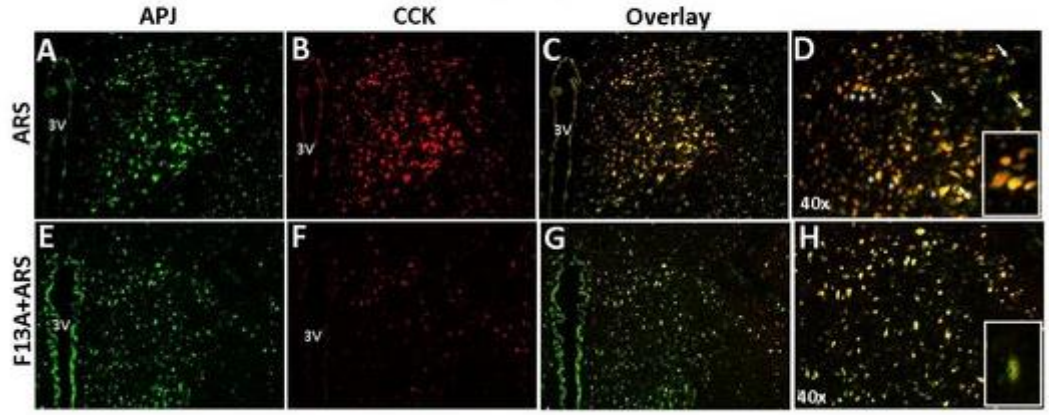

Figure 2. APJ and CCK double stainings in PVN after ARS (A-D) and F13A+ARS (E-H) treatment.

Placental pathology associated with pesticides exposure in female tea garden workers

Shashi N. Kumar (1)*, Banajit Bastia, S. Raisuddin (1), Usha Agrawal*, D Borgohain (2), A. K. Jain* (1)

1) *National Institute of Pathology (ICMR), Safdarjung Hospital Campus, New Delhi, India
1Department of Medical Elementology and Toxicology, Jamia Hamdard, New Delhi, India

2) Assam Medical College, Dibrugarh, Assam, India

Keywords: pesticides, placenta, pathology

The objective of this study was to investigate the pathological changes in placenta from women who were working in tea garden and exposed to pesticides during pregnancy. Sixty term placentas were observed; 30 women working in tea garden, who were at risk of exposure to pesticides during pregnancy, and rest 30 women were living in house, not exposed to pesticides. Placental tissues were analyzed for the quantifications of pesticides by GC/MS. Placental tissues were examined with the microscopes for pathological studies. Pesticides levels were significantly high in placenta of female tea garden workers than those from non female tea garden worker. Placentas of female tea garden workers exposed to pesticides indicated deposition of fibrinoid in villous stroma. Syncytiotrophoblastic lining was more degenerated and a number of syncytial knots found to be increased. In most of the cases of tea garden workers, placenta showed the dynamic changes in syncytialtrophoblasts of nuclei such as increased heterochromatin content and nuclear aggregation (Figs. 1&2). There was increased collagen in the villus stroma and shrunken endothelium in fetal capillaries. Deleterious effect of pesticides on placental barrier of tea garden workers could result in Impairment of placental barrier and restriction of nutrient supply from mother to fetus, finally this could cause the Low birth Weight (LBW). Therefore, it can be concluded that exposure to pesticides during pregnancy is likely to be detrimental to the growth and injure of the fetus in proportion to the level of pesticide exposure.

References:

1. Levario-Carrillo M, Olave ME, Corral DC, Alderete JG, Gagioti SM, Bevilacqua E. Placental morphology of rats prenatally exposed to methyl parathion. Exp Toxicol Pathol. 2004 Jul;55(6):489-96.

2. Levario-Carrillo M, Feria-Velasco A, De Celis R, Ramos-Martínez E, Córdova-Fierro L, Solís FJ. Parathion, a cholinesterase-inhibiting plaguicide induces changes in tertiary villi of placenta of women exposed: a scanningelectron microscopy study. Gynecol Obstet Invest. 2001;52(4):269-75.

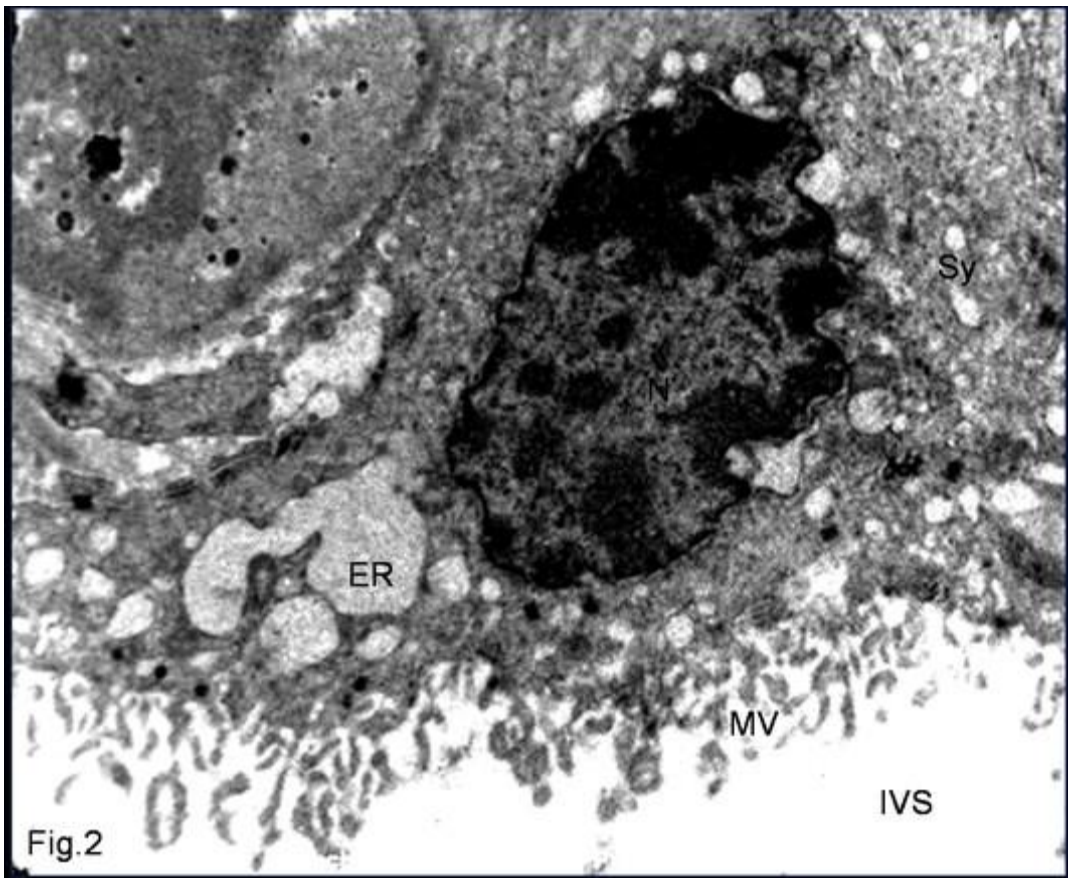

Figure 1. TThe placental villi exposed to pesticides shows syncytiotrophoblast (ST) with regular finger-like microvilli (MV). Syncytial nuclei are swollen and displayed karyolysis with severe loss of the euchromatin. Vacuolation of the syncytiotrophoblast and dilated endoplasmic reticulum (ER).

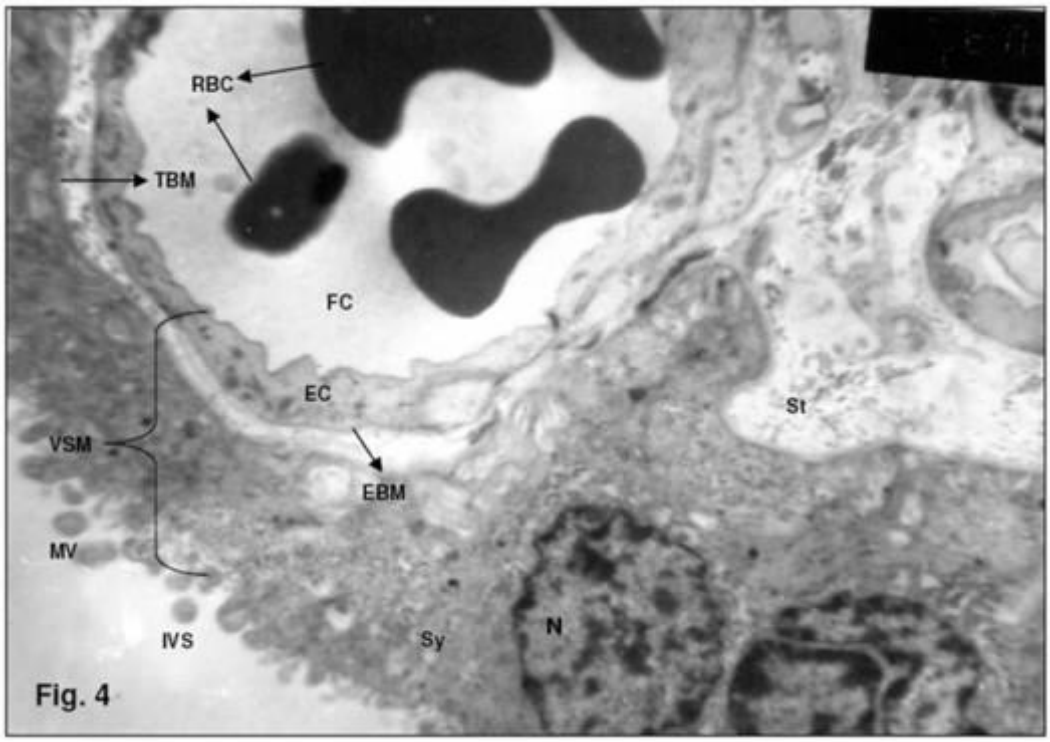

Figure 2. Chromatin condensations are pronounced and the nuclear profiles are frequently small, round and clustered.

POSTER PRESENTATIONS L6:

A histological analysis of glycogen content in hepatocytes of trefoil factor family 2 and trefoil factor family 3 knock-out mice

Edi Rođak (1), Kristina Ivić (2), Tatjana Belovari (1), Ivana Lovrić (1), Nikola Bijelić (1), Mirela Baus Lončar (3)

1) Department of Histology and Embryology, Faculty of Medicine, University of Osijek, J. Huttlera 4, HR-31000 Osijek, Croatia

2) Clinical Hospital Centre Osijek, J. Huttlera 4, HR-31000 Osijek, Croatia

3) Department of Molecular Medicine, Institute Ruđer Bošković, Bijenička cesta 54, HR-10000 Zagreb, Croatia

Keywords: Tff, liver, histology, glycogen

Trefoil factor family (Tff) peptide 2 and Tff peptide 3 are small peptides mostly present in the gastrointestinal mucosa and related to mucosal protection and restitution. Tff3 is included in hepatic glucose metabolism, and both Tff2 and Tff3 peptide stimulate beta-cell proliferation in the pancreatic islets. Tff2 and Tff3 deficient mice including appropriate wild type mice of mixed background (Sv129/C57Bl6) (N=6 per genotype) were kept on standard diet until 6 month old. Glycogen distribution was monitored in PAS stained formalin fixed and paraffin embedded tissue sections (6 μm). Areas of strongest glycogen staining were chosen for analysis and glycogen-positive cells were counted within regions of 100 cells. Using an arbitrary semi-quantitative scale, the signal was classified as weak (0-35 positive cells), medium (36-70 positive cells) and strong (71 or more positive cells). Tff3 deficient mice had the strongest accumulation of glycogen that was statistically increased compared to wild-type mice ($p=0.005$, Mann-Whitney U test). Liver glycogen distribution in Tff2 deficient mice was heterogeneous and overall signal did not differ statistically from that of wild-type mice ($p=0.5$). Our results support the notion that Tff3 peptide is included in the hepatic glucose and glycogen metabolism. Further, metabolism-oriented studies are needed to elucidate the exact metabolic role of Tff3 peptide.

References:

1. Y. Xue et al., Plos One 8 (2013) e75240.

Growth plate and trabecular bone histomorphometry in wild-type and TFF3 knock-out mice

Ivana Lovrić (1), Dunja Stolnik (2), Nikola Bijelić (1), Tatjana Belovari (1), Mirela Baus Lončar (3)

1) Department of Histology and Embryology, Faculty of Medicine, University of Osijek, J.Huttlera 4, HR-31000 Osijek, Croatia

2) Clinical Hospital Centre Osijek, J. Huttlera 4, HR-31000 Osijek, Croatia

3) Department of Molecular Medicine, Institute Ruđer Bošković, Bijenička cesta 54, HR-10000 Zagreb, Croatia

Keywords: TFF3, trabecular bone, primary ossification center, growth plate, histomorphometry

TFF3 peptide is present during intrauterine endochondral ossification in mice. Lack of TFF3 peptide in TFF3 knock-out mice affects histomorphometric parameters describing cancellous bone quality in secondary ossification centers of mouse tibiae, impairing bone formation. The aim of this study was to quantitatively analyze several parameters describing the growth plate and primary ossification centers in tibiae of one month old wild type and TFF3 knock-out mice. For the analysis of primary ossification centers, tibiae of one month old 5 wild type mice and 5 TFF3 knock-out mice were used. Three representative slides were used from each bone, hemalaun-eosine stained and analyzed. Digital photographs of bones were processed by open source computer programs Gimp and FIJI. Histomorphometric parameters describing growth plate were analyzed after staining with Masson's trichrome stain. Growth plate photographs were analysed by QuickPHOTO Pro software. Statistical software Statistica was used to perform Mann-Whitney U test. Morphological analysis of the TFF3 knock-out mice bone showed significantly smaller trabecular number (Tb.N.) and significantly larger trabecular separation (Tb.Sp.), compared to the wild type mice. Trabecular bone volume (BV/TV), trabecular bone surface (BS/TV) and trabecular thickness showed no significant difference between wild type and knock out mice. No significant histomorphological differences between wild-type mice and TFF3 knockout mice were found in epiphyseal plate thickness, in the

thickness of different zones of endochondral ossification, and in the chondrocyte density. There are several histomorphological differences in bone structure between the wild type and the TFF3 knock-out mice. TFF3 probably has an effect on the formation and quality of the cancellous bone in the primary ossification centers. Further research might explain the extent of TFF3 influence on bone development and the function of epiphyseal plate.

Mast cells of the human foetal testis

Viviana Kozina (1), Trpimir Goluža (2), Marina Kos (3), Davor Ježek (1)

1) University of Zagreb, School of Medicine, Department of Histology and Embryology, HR-10000 Zagreb, Croatia

2) University of Zagreb, School of Medicine, Clinical Hospital Centre „Zagreb“, Department for Gynaecology & Obstetrics, HR-10000 Zagreb, Croatia

3) University of Zagreb, School of Medicine, Clinical Hospital Centre „Sisters of Mercy“, "Ljudevit Jurak" Clinical Department of Pathology, HR-10000 Zagreb, Croatia

Keywords: human foetal testis, mast cells, sex cords

Data about the mast cells of human foetal testis are lacking in the literature. The aim of this study is to gain knowledge about the presence of mast cells within the testis during foetal period and how their number is changing with the gestational age. Our hypothesis was that the number of this cells in foetal testis is increasing with the volume of testis ie size of the sex cords and intersititial volume. Specific aims were to visualize the presence of mast cells using histological and immunohistological methods and quantify their number during the intrauterine development of the whole testis. The material was obtained during the routine paedopathological autopsy of 39 spontaneously aborted/stillborn foetuses between 15 and 36 gestational weeks. Qualitative and quantitative analysis was performed. During gestational weeks 15-29, mast cells were exclusively located within the tunica albuginea. After 30th gestational week, besides the tunica albuginea, mast cells populated the loose connective tissue of the tunica vasculosa and the connective tissue of septa/interstitium within the parenchyma. The total number of mast cells increased over the investigated period. Quantitative stereological analysis showed that the development of mast cells coincided with the increase of the volumes of the testis. In contrast to increase of the volume and number of mast cells, diameter of the sex cords remains similar. The development of mast cells in the foetal testis is probably regulated by paracrine factors secreted by cells of the interstitium and sex cords.

References:

1. Sharpe RM., Clin Endocrinol Med (1986) 185-207.

2. Young JC et al.,Semin Cell Dev Biol.(2015) 94-1030.

3. Raz E., Curr Opin Cell Biol (2004) 169-73.

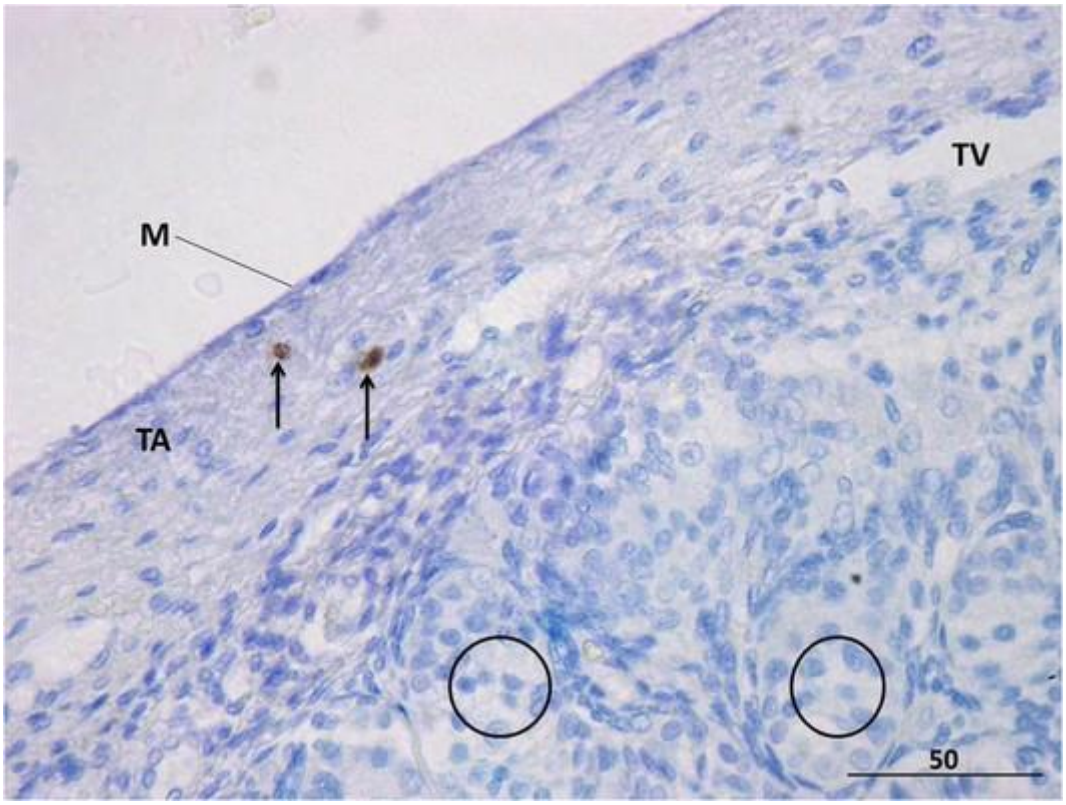

Figure 1. Human foetal testis in the 30th weeek of gestation. Two positive mast cells (□) are visible within the connective tissue of tunica albuginea (M – mesothelium; TV – tunica vasculosa; □ - sex cords). IHC (mast cell tryptase Ab+DAB) counterstained with hemalaun, x 400, scale bar = 50 μm.

Effect of resveratrol and metformin on ovarian reserve and ultrastructure in PCOS

Selenay Furat Rencber (1), Sema Kurnaz Ozbek (1), Ceyla Eraldemir (2), Zehra Sezer (3), Tugba Kum (2), Sureyya Ceylan (1), Elif Guzel Meydanli (3)

1) Kocaeli University Faculty of Medicine, Department of Histology and Embryology, Kocaeli, 41380, TURKEY

2) Kocaeli University Faculty of Medicine, Department of Biochemistry, Kocaeli, 41380, TURKEY

3) Istanbul University Cerrahpasa Faculty of Medicine, Department of Histology and Embryology, Istanbul, 34091, TURKEY

Keywords: PCOS, Resveratrol, Metformin, oxidative stress, inflammation

Polycystic ovary syndrome (PCOS) is a reproductive hormonal abnormality and a metabolic disorder [(1)]. It's frequently associated with insulin resistance (IR), hyperandrogenism, chronic inflammation, and oxidative stress (OS) [(2)]. Resveratrol is a natural polyphenol and may have beneficial effects, including antioxidant, anti-inflammatory and antiapoptotic actions. Metformin is an antihyperglycemic drug widely used for the treatment of type 2 diabetes and can cause reductions in body weight, restore ovulation and increase the rate of pregnancy [(3)]. The aim of this study is to examine the histological, ultrastructural and biochemical effects of Resveratrol and Metformin in PCOS treatment. 63 female Wistar albino rats were initially divided into control (n=9) and experimental (PCOS) groups (n=54). After DHEA administration, PCOS group (n=54) were randomly divided into 6 groups (n=9) as follows. Group 1 (PCOS; no treatment), Group 2 (Resveratrol; 20 mg/kg), Group 3 (Ethanol; resveratrol solvent), Group 4 (Metformin; 300 mg/kg), Group 5 (Salin; metformin solvent) and Group 6 (Metformin+Resveratrol). The daily treatments of both groups lasted for up to 28 days. Estrous cyclicity was monitored by vaginal smears. At the end of the treatment, body and ovary weights were measured. Right and left ovaries were processed for electron and light microscopic examination, respectively. Apoptosis was evaluated by TUNEL assay. Serum FSH, LH and Testosterone levels were analysed with bio-otoanalyzer, while plazma and tissue AMH and

TNF-α were determined by ELISA. Serum MDA levels were also measured. Metformin and combined treatment groups reduced the body and organ weights compared to PCOS group ($p<0.05$). Serum LH levels were significantly higher in PCOS group compared to control groups ($p<0,001$). Because of the excess androgen accumulation, serum testosterone levels were significantly higher in PCOS group, but Resveratrol treatment group reduced this hormone levels ($p<0,001$). Plasma and tissue TNF-α level, as an inflammation marker, were significantly higher in PCOS group than in control group ($p<0,05$) where the same levels were significantly decreased in the all treatment groups when compared to the PCOS group ($p<0,05$). Ovarian sections of the control group exhibited all types of follicles at different stages of maturation whereas PCOS group displayed increased number of secondary, cystic and atretic follicles ($p<0,05$). Increased number of atretic follicles in PCOS group were supported by TUNEL assay findings. In control group, healthy follicles were observed by electron microscopy. In PCOS group apoptotic granulosa cells and hyperplasic theca cells were seen. But all treatment groups ameliorates these findings nearly same as in control group. Resveratrol and metformin improve ovarian follicular cell architecture, hormone profile, oxydative stress, inflammation, and weight gain so might be a good candidate for PCOS treatment.

References:

1. A.E. Joham et al., J. Women's Health. 4 (2015) 299 - 307.

2. M. Murri et al., J. Human Reproduction Update. 3 (2013) 268 - 288.

3. G. Ladson et al., J. Fertility & Sterility. 3 (2011) 1059 - 1066.

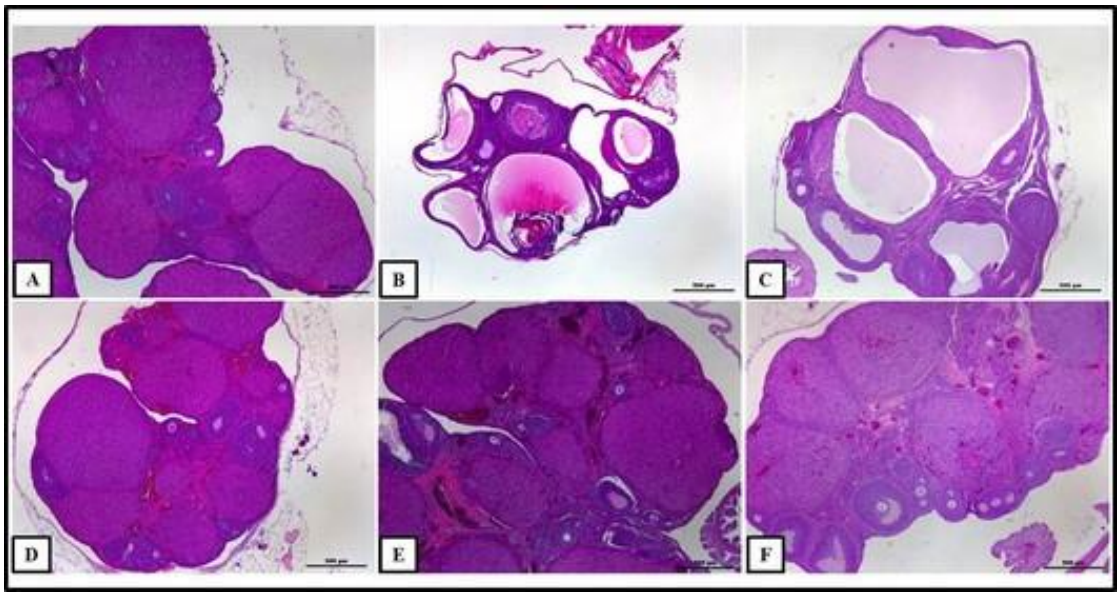

Figure 1. Histologic examination of ovaries in control, PCOS and treatment groups. (A), Control; (B), Group1; (C), Group 2; (D), Group 3; (E), Group 4; (F), Group 6. Note that cystic follicles were seen in Group 1 and 2 (H&E, 4X).

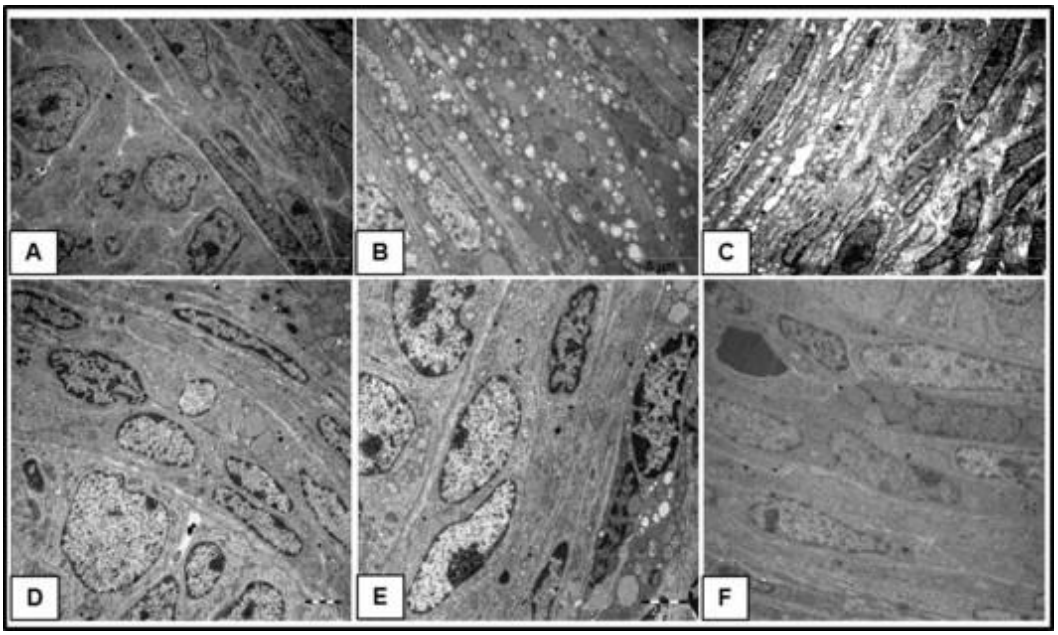

Figure 2. Electron microscopic examination of follicular cells of ovaries in control, PCOS and treatment groups. (A), Control; (B), Group1; (C), Group 2; (D), Group 3; (E), Group 4; (F), Group 6.

Reconstructing a looming sensitive pathway in locusts using serial block-face SEM (SBEM)

Stefan Wernitznig (1), Armin Zankel (2), Claire Rind (3), Susanne Summerauer (1), Manuela Nikolić (1), Mariella Sele (1), Peter Pölt (2), Gerd Leitinger (1)

1) Institute of Cell Biology, Histology and Embryology, Medical University of Graz, Harrachgasse 21, 8010 Graz, Austria

2) Institute for Electron Microscopy and Nanoanalysis, NAWI Graz, Graz University of Technology, Steyrergasse 17, 8010 Graz, Austria

3) Newcastle University, Institute of Neuroscience, Framlington Place, NE2 4HH Newcastle upon Tyne, UK

Keywords: locust, vision, LGMD, SBEM, 3D-reconstruction

The response of animals to different visual stimuli can be investigated behaviourally and physiologically. But to get a real idea of how the detected stimuli are computed in specific neuronal circuits, it is inevitable to investigate the circuits at the ultra-structure level, as only this can provide the exact wiring diagram of the circuit. Therefore describing the structure of neuronal circuits of sensory systems in different organisms throughout the animal kingdom, showing their similarities and variations, is essential to understanding the main principles of stimulus. A special visual pathway in orthopterans such as *Locusta migratoria* detects objects on collision course. This collision sensing pathway and especially its key player, the lobula giant movement detector (LGMD), have been thoroughly studied over the last decades[1–2]. Yet, the exact computation within the circuit is not yet fully understood and the anatomy and connectivity patterns of the afferent neurons presynaptic to the LGMD are still unknown. These afferent neurons connect the second optic ganglion, the medulla, to the LGMD in the third optic ganglion, the lobula complex, and are called trans-medullary afferent (TmA) neurons[3]. For this study on the LGMD and TmA neurons serial block-face SEM (SBEM) was used to trace TmA neurons from their output synapse at the LGMD back to the medulla. We used 4th instar locusts instead of adults to minimise the distance to cover with serial sections. SBEM produces a series of electron micrographs with high resolution that enables us to identify the synapses

and document their location along a 3D reconstruction of the LGMD and TmA neurons. Our findings so far are: first, looking at the connectivity of a 40 µm long LGMD reconstruction we identified over 1100 input synapses at the LGMD. Compared to adult animals with 100% reciprocal synapses, we found 34% for the 4th instar. No clustering of synapses was observed but more synapses (424) were found at the side branches of the LGMD than at the larger branches. Also the vast majority of synapses were located at the LGMD side facing posterior. Second, in two samples, single TmA neurons were traced from the lobula, where they connect with the LGMD, to the medulla, covering a distance of over 300 µm each. Both TmA neurons differ considerable in their morphology and also terminate in different layers of the medulla. Both TmA neurons receive input in the medulla but also form output synapses with other cells; indicating a more complex wiring than initially thought. We also looked at the input neurons of the TmA neuron in the medulla by reconstructing those cells as far as possible. In some cases we can document that these input neurons accompanied the TmA neuron over long distances (40-100 µm), exhibiting several synapses with the TmA neuron along this distance.

Acknowledgements:

The authors gratefully acknowledge the contributions by Elisabeth Bock, Elisabeth Pritz, Gertrud Havlicek and Claudia Mayrhofer. The study was supported by Grant Sponsor: Styrian Provincial Government “das Land Steiermark”, HTI:SMApp Programme 2012.

References:

1. Rind, F. C. A J., Exp. Biol. 149 (1990) 1–19.

2. Jones, P. W. & Gabbiani, F., Curr. Biol. 20 (2010) 2052–2057.

3. Rind, F. C. et al., Sci. Rep. 6 (2016) 35525.

Zika virus interaction with astrocytes

Tomas Bily (1,2), Marie Vancova (1,2), Martin Palus (1,2,3), Daniel Ruzek (1,2,3), Jana Nebesarova (1,2,4)

1) Institute of Parasitology, Biology Centre of the Czech Academy of Sciences, Branisovska 31, CZ-37005, Ceske Budejovice, Czech Republic

2) Faculty of Science, University of South Bohemia, Branisovska 1760, CZ-37005, Ceske Budejovice, Czech Republic

3) Department of Virology, Veterinary Research Institute, Hudcova 70, CZ-62100 Brno, Czech Republic

4) Faculty of Science, Charles University in Prague, Vinicna 7, CZ-12843, Praha, Czech Republic

Keywords: Zika, electron tomography, astrocytes

Zika virus (ZIKV) causes an illness known as Zika fever or Zika virus disease. ZIKV is a positive-sense RNA virus. It is a member of *Flavivirus* genus within the *Flaviviridae* family. ZIKV is transmitted primarily by mosquitoes; however, sexual ZIKV transmission, transmission from mother to child, and transmission through blood transfusion were also reported. Analogously to other flaviviruses (Tick borne encephalitis virus, Denge virus and West Nile virus), ZIKV infects neural cells, where it causes a reorganisation of rough endoplasmic reticulum (rER) into replication factories. We demonstrate extensive remodelling of rER membranes into replication sites in astrocytes infected with ZIKV by means of the transmission electron tomography (ET). We observe a replication sites derived from rER that is highly convoluted. ZIKV-induced replication vesicles are 85.8 ± 8.3 nm (n = 70) in diameter and ZIKV particles are 50.6 ± 1.9 nm (n = 6) in diameter. Infected cells contain numerous neurosecretory vesicles broadly varied in diameter from 38.1 nm to 89.4 nm present in the cytoplasm. Astrocytes were infected with ZIKV for 24 hours. The samples were prepared for ET by using high-pressure freezing and freeze substitution method. Dual axis electron tomography montage 2×2 was done over a tilt from range -60 to 60 degree with 1 degree step (JEOL 2100F equipped with high tilt stage and Gatan camera Orius SC 1000) by means of Serial EM software. Tomogram was aligned, reconstructed and 3D models were generated by manually masking the area of interest using IMOD software package.

Acknowledgements:

The TACR (TE01020118), MEYS Czech Republic (Czech BioImaging LM2015062 and CZ.02.1.01/0.0/0.0/16_013/0001775) supported this work.

Morphometrical evaluation of histopathological alterations in freshwater snail *Holandriana holandrii* exposed to phenol

Maria Špoljar (1), Jasna Lajtner (1), Romana Gračan (1), Martina Ivšić (1), Blaženka Banjad Ostojić (2), Ana Miletić (3), Goran Kovačević (1)

1) Faculty of Science, University of Zagreb, Department of Biology, Rooseveltov trg 6, HR-10000 Zagreb, Croatia

2) Institut IGH, d.d., Water and Environmental Engineering Department, J. Rakuše 1, HR-10000 Zagreb, Croatia

3) Croatian Agency for the Environment and Nature, Radnička cesta 80/7, HR-10000 Zagreb, Croatia

Keywords: hepatopancreas, gills, freshwater molluscs

Morphometrical observations of histopathological changes induced by phenol intoxication were performed and analysed on the freshwater snail *Holandriana holandrii*. We exposed animals to sodium pentachlorophenate (Na-PCP; 0.56, 1.0 mg/L) through the period of acute toxicity, and compared them with the control samples. Morphometrical analysis of target organs were performed on routine paraffine sections using light microscope with a digital camera AxioCam ERc 5s and software Zen 2 Lite (Carl Zeiss Microscopy GmbH, Germany). Measurement was conducted on tubular area, tubular lumen area and vacuoles of digestive tubules and epithelium and lamellar width of the gills. We recorded and compared remarkable histopathological alterations in animals treated with toxicant through the time and between different concentrations, which included shedding and swelling of tubular cells and disorganization of tubules in digestive glands, while lamellar spaces in the gills were distended. Histomorphometry was confirmed as a powerful tool in the quantitative measurements of ecotoxicological impact of xenobiotics upon freshwater organisms.

References:

1. J. Lajtner et al. Period. Biol. 105 (2003) 157-162.

2. D. Žnidaršić et al. Environ. Toxicol. Phar. 13 (2003) 161-174.

Spatial organization of peptidergic axon terminals and myoepithelial cells in salivary glands of tick *Ixodes ricinus*

Marie Vancova (1,2), Ladislac Šimo (3), Tomas Bily (1,2), Jana Nebesarova (1,4)

1) Institute of Parasitology, Biology Centre CAS, Branišovská 31, České Budějovice, Czech Republic

2) Faculty of Science, University of South Bohemia, Branišovská 31, České Budějovice, Czech Republic

3) French National Institute of Agricultural Research, UMR-BIPAR INRA-ANSES-ENVA, Maisons-Alfort, France

4) Faculty of Science, Charles University, Viničná 7, Prague, Czech Republic

Keywords: tick, salivary glands, neurotransmitters, myoepithelial cells

European tick *Ixodes ricinus* is a medicaly important vector of variety of causative disease agents including *Borrelia burgdorferi* causing Lyme borreliosis or tick-borne encephalitis virus. During tick feeding, salivary glands produce a variety of pharmacologically active compounds which significantly compormise the host immune system and thus represent a great route for tick-born pathogens transmission. Recently, it has been shown that activities of salivary glands are controlled by nerves, arrising from tick central nervous system, releasing various peptidergic neurotransmitters such as myoinhibitory peptide (MIP), SIFamide, orcokinin and pigment dispersing hormone (PDF) (1). In presented study, we described for the first time three dimensional morphology of axonal projections, reaching individual acini (alveoly) in the tick salivary gland. Particularly, we focused on the peptidergic axon terminals and their associations with the neighbouring myoepithelial cells that control the contraction of the acini or regulate the activity of acinar valve. Neuropeptides were localized using immunogold labeling on thawed cryosections. We found that myoepithelial cells with their numerous and highly branched protrusions were preferentially stained with hafnium chloride added during the freeze substitution process. This staining facilitated the three dimensional reconstruction of these cells in larger volume by transmission electron microscopy.

Acknowledgements:

This work was supported by the Technology Agency of the CR (TE01020118), MEYS CR (Czech BioImaging LM2015062 and CZ.02.1.01/0.0/0.0/16_013/0001775).

References:

1. Simo et al., J. Comp. Neurol. 522 (2014) 2038–2052.

Histological evaluation of granular dystrophy

Ismail Seçkin (1), Osman Şevki Arslan (2), Başak Işildar (1), Cezmi Doğan (2), Gülşah Tezcan (2), Ümit Yaşar Güleser (2)

1) Cerrahpasa Faculty of Medicine, Department of Histology and Embryology, 34098 Cerrahpaşa-Fatih/İstanbul, Turkey

2) Cerrahpasa Faculty of Medicine, Department of Ophthalmology, 34098 Cerrahpaşa-Fatih/İstanbul, Turkey

Keywords: Granular corneal dystrophy, histology, cornea

Granular corneal dystrophy (GCD) is an autosomal-dominant, bilateral, stromal corneal disorder caused by human transforming growth factor b-induced (TGFBI) gene mutations. Histopathologically, it affects the central and peripheral cornea and eosinophilic material (hyaline) deposition is detected in all the layers of the stroma. Initially the deposits are in the anterior stroma. As the disease progresses, the deep layers of the cornea are also affected The corneal stroma between the deposits is clear (1). In this study, we aimed to light microscopic evaluation of the corneal buttons of 3 patients with granular dystrophy. For light microscopic evaluation, a portion of corneal buttons were embedded into the paraffin blocks after fixation and dehidration steps. Paraffin blocks were cut as 5 µ sections and stained with hematoxylen & eosin. The sections were analyzed and photographed by Olympus: BX61. Semi-quantitative scoring was performed in terms of hyaline deposition, epithelial damage, inflamation and edema. As a result of light microscopic examination, hyaline accumulation was observed in different quantities and locations in the substantia propria cornea (SPC) in every 3 cases. In the case 2 deposits accumulated under the epithelium, while in the cases 1 and 3 hyaline deposits were seen in deep parts of the SPC. The knowledge that the density of hyaline deposits increased and proceeded to the deep parts of the CMB as the disease progressed led us to think that the most severe case was the case 2 (1). While epithelial damage was observed at advanced level in all 3 cases, inflammation and edema were seen at different levels. These data for semi-quantitative scoring are given in Table 1. As in many other corneal dystrophies, the formation mechanisms of granular corneal dystrophy is not fully understood yet. In this context, histologic examination can give an insight about the formation mechanisms

of dystrophies. For example; according to Underhaug et al. the mutations of the TGFBI may cause in reduction of the proteolytic susceptibility of the mutated (Transforming growth factor-beta-induced protein) TGFBIp leading to the abnormal accumulations of the TGFBIp in GCD (2). In conclusion, histopathological evaluation with a systematic approach is important because of the information that can be given about both the diagnosis and the causes of dystrophies.

References:

1. Yagi-Yaguchi, Y., Yamaguchi, T., Okuyama Y., Satake Y., Tsubota, K., Shimazaki J. (2016). Corneal Higher Order Aberrations in Granular, Lattice and Macular Corneal Dystrophies. PLoS One, 11(8):e0161075.

2. Lin, ZN., Chen, J., Cui, HP. (2016). Characteristics of corneal dystrophies: a review from clinical, histological and genetic perspectives. Int J Ophthalmol. 9(6):904-13.

	Hyaline Deposits	Epithelial Damage	Inflammation	Edema
Case 1	+4	+3	+2	-
Case 2	+2	+3	-	+2
Case 3	+2	+2	+1	+2

Figure 1. The data of semi-quantitative scoring.

Therapeutic effect of thymoquinone on amyloid beta-induced neurotoxicity in rats

Birsen Elibol (1), Tuğçe Aydogan (1), Merve Beker (1), Sule Terzioglu-Usak (1), Ulkan Kilic (2)

1) Bezmialem Vakif University, Bezmialem Vakif University, Faculty of Medicine, Department of Medical Biology, 34093, Istanbul, Turkey

2) Istanbul Medipol University, Faculty of Medicine, Department of Medical Biology, 34810, Istanbul, Turkey

Keywords: Thymoquinone, Alzheimer's Disease, immunofluorescence, light microscopy

Alzheimer's disease, characterized by synaptic deficiency, neuronal damage and loss in the brain is the most common neurodegenerative disease in aged population. Due to only symptomatic recovery for treatment of Alzheimer's disease with existing molecules, the investigations of new neuroprotective substances gain importance. One of these candidate molecules is Tymoquinone (TQ), an aromatic hydrocarbon found in *Nigella Sativa*. The aim of the present study was to examine the therapeutic effects of TQ in the hippocampus of rats which have infused with amyloid beta peptide. An infusion canula linked to a micro-osmotic pump including aggregated amyloid beta was placed into the hippocampus of 6 month-old rats. During 15 days, TQ at a dosage of 20 mg/kg/day were intubated intragastrically. At the 16th day, the rats were decapitated and their brains were removed for histological analysis. The rat brain sections were analysed by staining with cresyl-violet for surviving neurons, anti-amyloid beta antibody for amyloid beta toxicity, Fluora Jade for degenerating neurons and Congo red for accumulation of amyloid plaques. According to present results, TQ was effective in the clearance of amyloid beta plaques which was visualized by anti-amyloid beta antibody fluorescently ($p<0.05$). On the other hand, when we perfomed congo red staining to confirm these results, we observed a significant increase in the accumulation of amyloid beta plaques in the amyloid beta infused animals when compared sham animals. However, TQ treatment cannot decrease this fibril deposition, significantly. In addition, the neuronal loss in the CA1 region of hippocampus, but not in the DG region of hippocampus, was ameliorated by TQ. Lastly, the number of degenerating neurons also changed by supplementation this

neuroprotective substance. In conclusion TQ is effective in the clearance of amyloid beta plaques to increase the survival rate of neurons. TQ may be a candidate molecule in the treatment of Alzheimer's disease due to its capacity to recover AD-related neuropathology and to increase the cell survival.

Acknowledgements:

This study is supported by Bezmialem Vakif University Scientific Research Council with grant numbers 12.2014/2 and 9.2015/26.

Beta-Site APP Cleaving Enzyme 1 regulation depends on VDR or PDIA3

Erdinç Dursun (1), Selma Yılmazer (1), İrem L. Atasoy (1), Merve Alaylıoğlu (1), Esin Candaş (1), Duygu Gezen-Ak1 (1)

1) University of Istanbul, Cerrahpasa Faculty of Medicine, Department of Medical Biology, Fatih, 34096, Istanbul, Turkey

Background: Vitamin D regulates more than 1000 genes via its nuclear receptor, vitamin D receptor (VDR). Recent studies suggested that vitamin D has another receptor called PDIA3/1,25-MARRS which is localized in the plasma membrane. The studies demonstrated that it might regulate oxidative stress, intracellular calcium homeostasis, immune response and neurotrophic factor synthesis. Given that vitamin D might be an important molecule in neurodegeneration by regulating the expressions of various proteins. The present study investigated the expression levels of Beta-Site APP Cleaving Enzyme 1 (BACE1) in order to explain whether or not vitamin D has a role in cellular mechanisms that are directly involved in amyloid beta production which is a hallmark of AD pathogenesis. Methods: VDR silencing, PDIA3/1,25-MARRS silencing, VDR and PDIA3/1,25-MARRS double silencing by siRNAs were performed in primary cortical cultures in order to establish cellular model of vitamin D pathway disruption. Silencing efficiency was determined by immunofluorescence labelling of VDR and PDIA3/1,25-MARRS proteins. BACE1 mRNA and protein expression levels were analyzed with qRT-PCR and western blotting. Results: Our results indicated that BACE1 mRNA and protein expressions were significantly induced in response to VDR or PDIA3/1,25-MARRS or double silencing. Conclusion: Consequently, we have determined that vitamin D has an effect on regulating the expressions of key enzyme that have role in amyloid beta production. The results of the present study supply a clue for understanding the molecular mechanisms of Alzheimer’s disease and neurodegeneration via vitamin D perspective.

Comparison of different cryopreservation protocols for human umbilical cord as source of mesenchymal stem cells

Başak Işildar (1), Serbay Özkan (1), Mahmut Öncül (2), Zafer Başlar (3), Semih Kaleli (2), Mustafa Taşyürekli (1), Meral Koyutürk (1)

1) Cerrahpasa Faculty of Medicine, Department of Histology and Embryology, 34098 Cerrahpaşa-Fatih/İstanbul, Turkey

2) Cerrahpasa Faculty of Medicine, Department of Gynaecology and Obstetrics, 34098 Cerrahpaşa-Fatih/İstanbul, Turkey

3) Cerrahpasa Faculty of Medicine, Department of Internal Medicine, 34098 Cerrahpaşa-Fatih/ İstanbul, Turkey

Keywords: Mesenchymal stem cells, umbilical cord, cryopreservation

Mesenchymal stem cells (MSCs) are self-renewal, multipotent cells which have great therapeutic potential and low immunogenicity. They have the ability to differentiate into multiple cell lines. These are plastic adherent cells which show fibroblastic morphology. They show high rates of expression for CD44, CD90, CD105 and negative or low rates expressions for CD34, CD45 (1). MSCs can be isolated from bone marrow, adipose tissue, amniotic membrane and dental pulp. Recently, the researchers have been searching for alternative sources. In this context, they have seen that umbilical cord is an advantageous source for MSCs. Because it does not include invasive procedures during acquisition, it has fewer risks of contamination and fewer bioethics issues (2). In clinics, successful cryopreservation of umbilical cord tissue as autologous stem cell source is important for usage when the necessity arises. It constitutes one of the major objectives of the present stem cell research. In this study, two different cryoprotectants using 10% dimethyl sulfoxide (DMSO) + 0.2 M sucrose and 10% 1,2 propanediol (PrOH) + 0.2 M sucrose, was prepared and used in cryopreservation. The cells which isolated from the cryopreserved tissues are compared with untreated tissue cells in terms of: morphology, immunophenotypes, growth kinetics, adipogenic and osteogenic differentiation and ultrastructural features. Isolation was performed by tissue explant method. Based on the research results, no significant morphological difference observed between

mesenchymal stem cells isolated from cryopreserved tissues and untreated tissues. The isolated cells resulted in high rates of expression for the positive markers of MSCs, CD44 and CD90, and low rates of expression for the negative markers for MSCs, CD34 and CD45. Ultrastructural examination showed that: filopodium and microvillus-like projections, a large quantity of round/elongated mitochondria, enlarged rough endoplasmic reticulum cisternae, endocytotic and autophagic vesicles and abundance of vacuolization when the number of passages increased. Differentiation was observed in all groups. In the growth kinetics analysis; the cells of DMSO group showed similar results in proliferation with untreated tissues however, the cells of PrOH group showed decline. In conclusion, when two different cryopreservation groups are compared, no significant differences observed except for the proliferation rates. Therefore, clarification of their superiority in clinical applications should be supported with further researches.

References:

1. Bourin, P., Gadelorge, M., Peyrafitte, JA., Cappellesso, SF., Gomez, M., Rage C., Sensebe L. (2008). Mesenchymal progenitor cells: Tissue origin, isolation and culture. Transfusion Medicine and Hemotherapy, 35, 160-167.

2. Han, YF., Tao, R., Sun, TJ., Chai, JK., Xu G., Liu J. (2013). Optimization of human umbilical cord mesenchymal stem cell isolation and culture methods. Cytotechnology, s10616-012-9528-0.

The acetamipride, a neonicotinoid insecticide, inhibits cell proliferation and induces apoptosis on rat testis

Yağmur Emre Arican (1), Damla Kayali (2), Feriha Ercan (2), Gül Özhan (1)

1) Istanbul University, Faculty of Pharmacy, Department of Pharmaceutical Toxicology, İstanbul, Turkey

2) Marmara University, Faculty of Medicine, Department of Histology and Embryology, İstanbul, Turkey

Keywords: Acetamipride, cell proliferation, apoptosis, testis

Introduction: The fact about industrialization and advanced technology is that they have cumulative harmful effects on human health and environment while making the life easy, fast and modern. Recently it was reporeted that, many xenobiotics has developmental, reproductive and endocrin system-related toxic effects. Organophosphate and carbamate pesticides were replaced with neonicotinoids, which have sun-light resistance and higher toxicity to pests than mammals. Acetamipride is one of the most preffered and widely used neonicotinoids, act as a selective agonist on acetylcholine receptor. There are some information about effects of acetamipride on male reproductive system in both agriculture laborers and food consumers, however, its antiproliferative and apoptotic effects have not been clarified exactly yet. The aim of the study investigate effects of acetamipride on spermatogenic cell proliferation and cell death in rat testis. Material and methods: Male Sprague-Dawley rats were used in this study. Acetamipride solved in methylselulose were applied to the animals orally, in 12.5, 25 ve 35 mg/kg bw doses for 90 days. In control rats only methylselulose were applied to the animals. Under ether anesthesia testes removed from the animals and prepared for histological observation. Sperm parameters and testis morphology were evaluatated via the routin light microscopy. Spermatogenic cell proliferation was evaluated by PCNA immunohistochemistry and apoptotic cells were evaluated by TUNEL methods. Data were analyzed statistically. Results: The percentage of normal spermatozoa, cell proliferation were decreased, the number of atrophic seminiferous tubules and apoptotic cells were increased in a 35 mg/kg bw dose acetamipride administration comparing to the control rats. Discussion: According to our histopathological results oral administration of acetamipride at 35mg/kg bw dose causes testis damage by decreasing spermatogenic cell line via the induction of apoptotic cell death.

Effects of combined treatment of bisphosphonate and melatonin on stomach tissue in rats with ovariectomy

Esra Bihter Gürler (1), Özlem Tuğçe Kaya (2), Dilek Özbeyli (1), Feriha Ercan (2), Berrak Ç. Yeğen (1)

1) Department of Physiology, Marmara University, School of Medicine, Istanbul, Turkey

2) Department of Histology and Embryology, Marmara University, School of Medicine, Istanbul, Turkey

Keywords: melatonin, alendronate, ovariectomy, osteoporosis

Introduction: Osteoporosis is a postmenopausal disorder characterized by a higher risk of fractures, while the medications aimed to treat osteoporosis, such as bisphosphonates, are known to induce gastric inflammation. In the present study, we aimed to determine the impact of melatonin on the gastric side-effects of bisphosphonates in rats with surgical menopause. Materials and Methods: Sprague Dawley rats (n=56) underwent bilateral ovariectomy (OVX), while control group had sham-surgery (n=8). After the recovery for 4 weeks, OVX rats were treated with saline, alendronate (ALD, 70 um/kg/day, subcutaneously), melatonin (MEL, 25 mg/kg/day, orally), MEL+ALD, MEL+ melatonin receptor antagonist luzindole (LZD, 10 um/kg/day, intraperitoneally) or ALD+MEL+LZD for the following 8 weeks. At the end of 12th week, rats were euthanized. Gastric tissue samples were fixed with 10% neutral formalin and proccessed for routine paraffine embedding for histopathological evaluation. Additional stomach tissue samples were obtained for the measurement myeloperoxidase (MPO) activity, levels of malondialdehyde (MDA) and glutathione (GSH). Statistical analysis was performed using Kruskal-Wallis and ANOVA tests. Results: Compared to control group, in saline- and ALD-treated OVX groups MPO and MDA levels were significantly increased ($p<0.05$), while there was a significant decrease in LZD- and LZD+ALD-treated OVX groups ($p<0.05$-0.001). In ALD-, MEL+ALD-treated OVX and MEL+LUZ+ALD-groups, significant decreases in GSH were observed with respect to saline-treated OVX group. In ALD-treated OVX group, the significant increase in histopathologically determined injury score ($p<0.05$) was abolished by the addition of MEL, but injury was further enhanced in MEL+ALD+LUZ-treated OVX group.

Conclusion: It is observed that melatonin treatment reduced alendronate-induced gastric inflammation. Our results suggest that the choice of combined MEL and ALD therapy should be evaluated in the further clinical studies.

The effects of Trastuzumab and Paclitaxel for metastatic 4T1, MDA-MB231 and MCF-7 breast cancer cell lines

Sevinc Inan (1), Fatma Firat (2), Ibrahim Tuglu (2)

1) Izmir University of Economics, Faculty of Medicine, Turkey

2) Manisa Celal Bayar University, Faculty of Medicine, Turkey

Keywords: Trastuzumab, Paclitaxel, breast cancer cell lines, AKT, ERK

Human epidermal growth factor receptor 2 (HER2) is a transmembrane tyrosine kinase receptor and its signaling stimulates cell proliferation, differentiation and survival. HER2 overexpression is detected in 20–25% of human breast cancers. Trastuzumab (Tmab), a monoclonal antibody is specific to the extracellular domain of HER2. Paclitaxel (PTX) is also among the most active agents in the treatment of metastatic breast cancer, with response rates ranging from 30 to 60% when used as a single agent. The serine/threonine kinase AKT plays a critical role in regulating various cellular functions including growth, proliferation, survival, transcription, protein synthesis and angiogenesis. The AKT signaling cascade is activated by receptor tyrosine kinases, integrins, B - T cell receptors and cytokine receptors. Apoptotic peptidase activating factor (APAF) encodes a cytoplasmic protein that initiates apoptosis. It mediates the cytochrome c-dependent autocatalytic activation of pro-Caspase-9, leading to the activation of Caspase-3 and apoptosis. In this study, the aim was to investigate the combined treatment of Trastuzumab (Tmab) and Paclitaxel (PTX) for metastatic 4T1, MDA-MB231 and MCF-7 breast cancer cell lines and to understand the mechanisms underlying the anti-tumor effects of Trastuzumab. 4T1, MDA-MB-231 and MCF-7 cells were cultured in RPMI-1640 medium containing 10% FBS, 1% L-Glutamine, 1% penicillin-streptomycin. Tmab (10 µg/ml), PTX (5 µg/ml), Tmab+PTX (combined) and no treatment (control) groups were formed. After 36 hours from treatment, the cells were counted and fixed for indirect immunohistochemical staining. Anti-AKT, anti-ERK, anti-COX-2, anti-VEGF, anti-BCL-2 and anti-APAF primary antibodies were applied. Immunohistochemical evaluation was scored as mild, moderate and strong and very strong, according to the intensity of staining. Statistical

evaluation was done by using the ANOVA test. Immunopositivity for all primary antibodies were observed in the cytoplasm of all cancer cells. We observed many prominent apoptotic bodies besides the spindle shaped cells in the combined treatment group. It was observed that there were increased immunoreactivities of AKT, ERK, COX-2, VEGF and BCL-2 in the control groups of 4T1 and MDA-MB231 cells compared to MCF-7 cells. After combined treatment, all of the immunoreactivies were observed as mild to moderate ($p<0.05$). While weak APAF immunoreactivity was detected in the cytoplasm of 4T1 and MDA-MB231 in control groups, the immunorectivity was strong in the combined groups ($p<0.05$). In many biological and clinical aspects of breast tumorigenesis; AKT, ERK, COX-2 and VEGF signals appear to include tumor initiation and progression, metastasis, resistance to chemotherapy and angiogenesis. The results of this study showed that these pathways represent attractive therapeutic targets in breast cancers. In addition, combination of Trastuzumab and Paclitaxel has synergistic effects in metastatic 4T1 and MDA-MB 231 breast cancers.

References:

1. Zhou L, Xu S, et al., Oncotarget. (2017) May 17.

2.Tezuka K, Takashima T., Mol Clin Oncol. (2017) Apr 6(4):534.

3.Toi M, Shao Z., Breast Cancer Res. (2017) Apr 11;19(1):47.

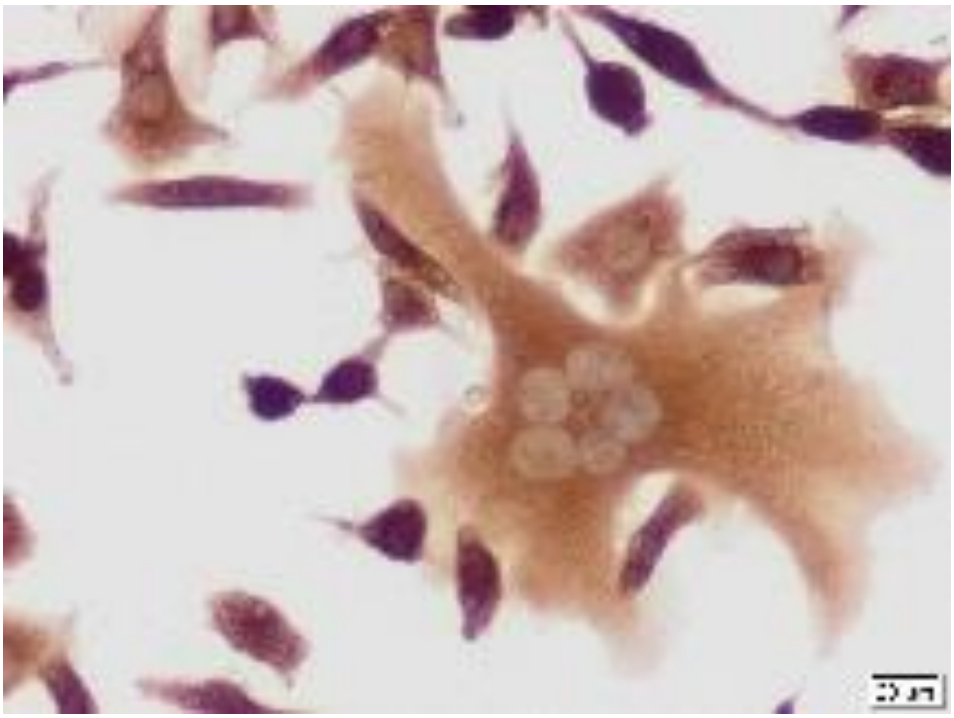

Figure 1. Microphotograph of ERK immunoreactivity from 4T1 cells in control group.

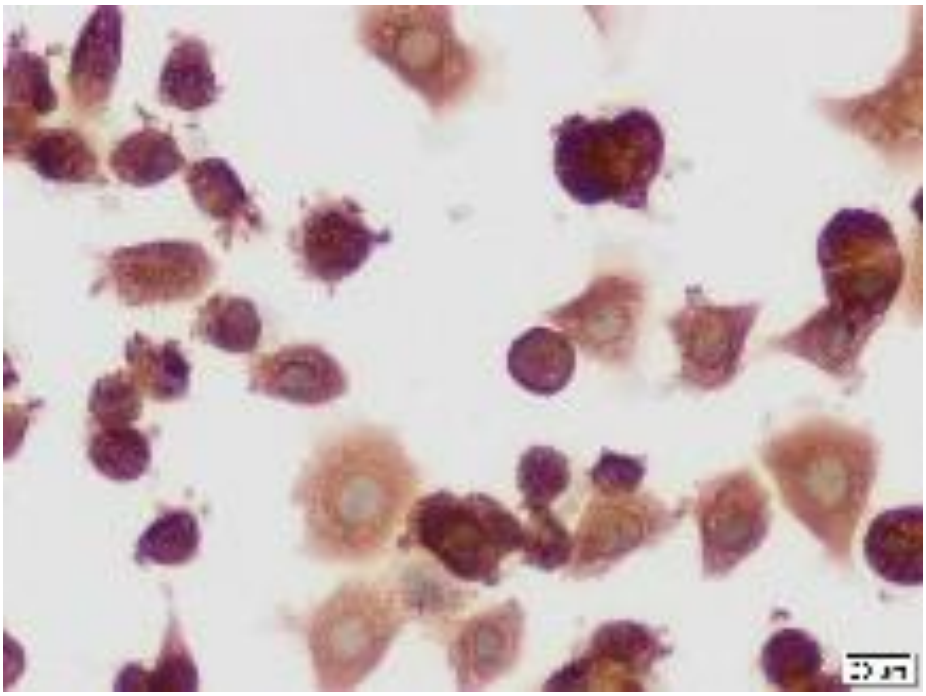

Figure 2. Microphotograph of ERK immunoreactivity from 4T1 cells in Tmab+PTX group.

GABA immunogold labeling in the substansia nigra pars reticulata of kindled genetic absence epilepsy rats

Zehra Nur Turgan (1), Ozlem Tuğçe Kaya (2), Tugba Karamahmutoglu (1), Medine Gülcebi Idrizoglu (1), Cansu Kandemir (2), Dilek Akakın (2), Serap Sirvanci (2), Filiz Onat (1)

1) Department of Pharmacology and Clinical Pharmacology, Marmara University, School of Medicine, Basibuyuk Mah. Maltepe Basibuyuk Yolu Sok. No: 9/1 34854, Maltepe-Istanbul, Turkey

2) Department of Histology and Embryology, Marmara University, School of Medicine, Basibuyuk Mah. Maltepe Basibuyuk Yolu Sok. No: 9/1 34854, Maltepe-Istanbul, Turkey

Keywords: GAERS, kindling, substansia nigra, GABA, immunogold method

Genetic Absence Epilepsy Rats from Strasbourg (GAERS) is a well-known animal model of absence epilepsy and they are resistant to kindling stimulations. The aim of the present study was to examine whether there was a difference in gamma-aminobutyric acid (GABA) levels in the posterior part of substantia nigra pars reticulata (SNR) between GAERS and Wistar rats receiving kindling stimulations. Animals in the kindling group either received only 6 stimulations in the basolateral amygdala region or they were kindled and had grade 5 seizures. Rats were decapitated one hour after the last stimulation. SNR regions were obtained under a stereomicroscope after intracardiac perfusion fixation and vibratome sectioning. GABA immunoreactivity was detected by using ultrastructural postembedding immunogold method. Labeled sections were observed and photographed by JEOL 1200 EXII transmission electron microscope and analyzed quantitatively by Image J program. Quantitative analysis showed that GABA density in fully kindled GAERS group increased significantly compared to that of GAERS group which received only 6 stimulations and therefore did not have grade 5 seizures. GABA density in fully kindled Wistar group showed a tendency to increase compared to that of Wistar group receiving 6 stimulations, however, the results did not reach statistical significance. We concluded that SNR may be an important region in modulating resistance of GAERS to kindling stimulations.

Acknowledgements:

This study was supported by The Scientific and Technological Research Council of Turkey (TUBITAK, project number 111S209).

L7. Multidisciplinary Approaches in Natural and Biomedical Sciences

INVITED LECTURES L7:

Worms under the microscope: how TEM and transcriptomics give us a holistic picture

Ivona Mladineo (1)

1) Institute of Oceanography & Fisheries, Institute of Oceanography and Fisheries, POB 500, HR-21000 Split, Croatia

Keywords: marine helminths, host-parasite interaction, transcriptomics

The immense biodiversity of marine habitats and organisms of the visible size-scale, is nothing compared to the micro word of marine parasites and the myriad of their devious ways of interacting with the hosts. From simple and sacculous exogenous crustaceans with direct life cycle attached to the gills of 200 kg-large tuna swimming 70 km/h and larval hibernating nematodes secluded in the visceral cavity of a sardine dangerous for men, to the gonochoristic digeneans that stay firmly locked their whole adult life embedded in pairs in a tissue cysts, molecular communication between parasite and host remains the most fascinating key to understand their long-lasting evolution. Despite their diversity however, helminths elicit consistent immune responses characterised by hypereosinophilia, considerable plasma cell IgE production, mucous mastocytosis, and goblet cells hyperplasia, accompanied by the production of the cytokines interleukin-4 (IL-4), IL-5, IL-9, IL-10, IL-13, collectively known as T-helper 2 (Th2) immune response (Anthony et al. 2007; Moreau & Chauvin 2010). Interconnected with Th2 response, pro-inflammatory Th1 response is characterised by production of IL-2, IFN-γ, lymphotoxin (LT-α), TNF-α and other chemokines that stimulate phagocytosis, the oxidative burst, intracellular killing of microbes and antigen presentation to T cells. Collateral damage of activated immune response and the mechanical impact of the parasite reflects mostly on epithelial and connective host tissues, therefore its healing potential is important indicator of parasite pathogenicity. For example, while digeneans in tuna gills induced down-regulation of metabolic and signalling groups functionally associated with endocrine, digestive and nervous host system, and an immunity-related pathway consisting of complement and coagulation cascades bideractionally perturbed, anisakid nematodes show versatility in respect to the type of the organism they infect; in fish as a paratenic hosts they

induce fast tissue remodelling after migration, and in rat as a model of accidental host, they induce extreme inflammatory reaction. The possibility of complimenting *in situ* visualisation of the parasite by SEM, TEM and confocal microscopy, with analysis of target genes expressions, microarray and RNA sequencing, enables a deeper understanding of intricate patterns of host-parasite convivence, but still opens more questions than offers clear answers. Herein are presented some of the most interesting and novel cases of marine host-parasite systems where microscopy and transcriptomics helped in building up a more holistic picture.

Acknowledgements:

This research was supported by Croatian Science Fundation HRZZ, project Angel (Anisakis spp: Genomic Epidemiology, grant number 5576).

References:

1. R.M. Anthony et al., Nature Rev. Immunol. 7 (2007) 975–987.

2. E. Moreau, A. Chauvin J. Biomed. Biotechnol. (2010) Article ID 428593.

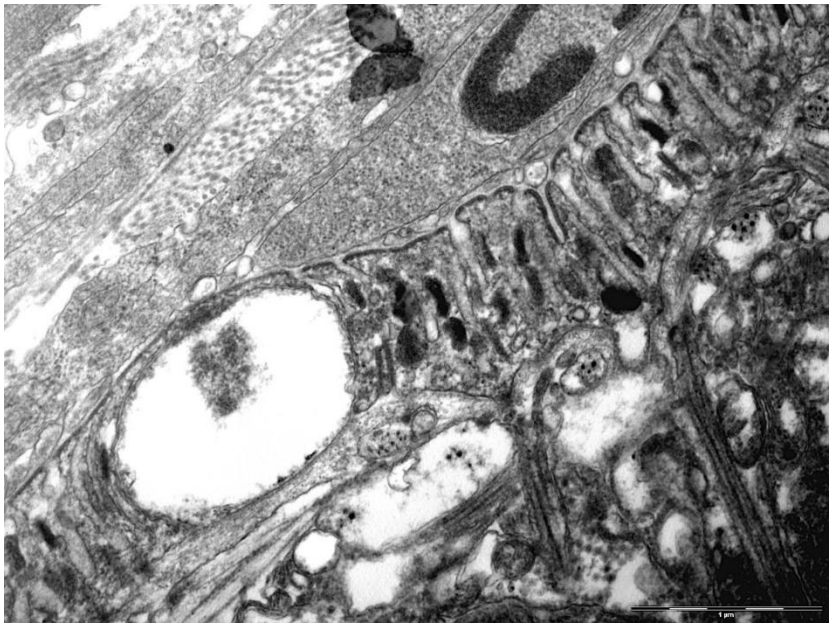

Figure 1. Dermis of the tissue-embedded digenean *Didymosulcus katsuwonicola* showing exchange of vesicles from the surrounding host's connective tissue.

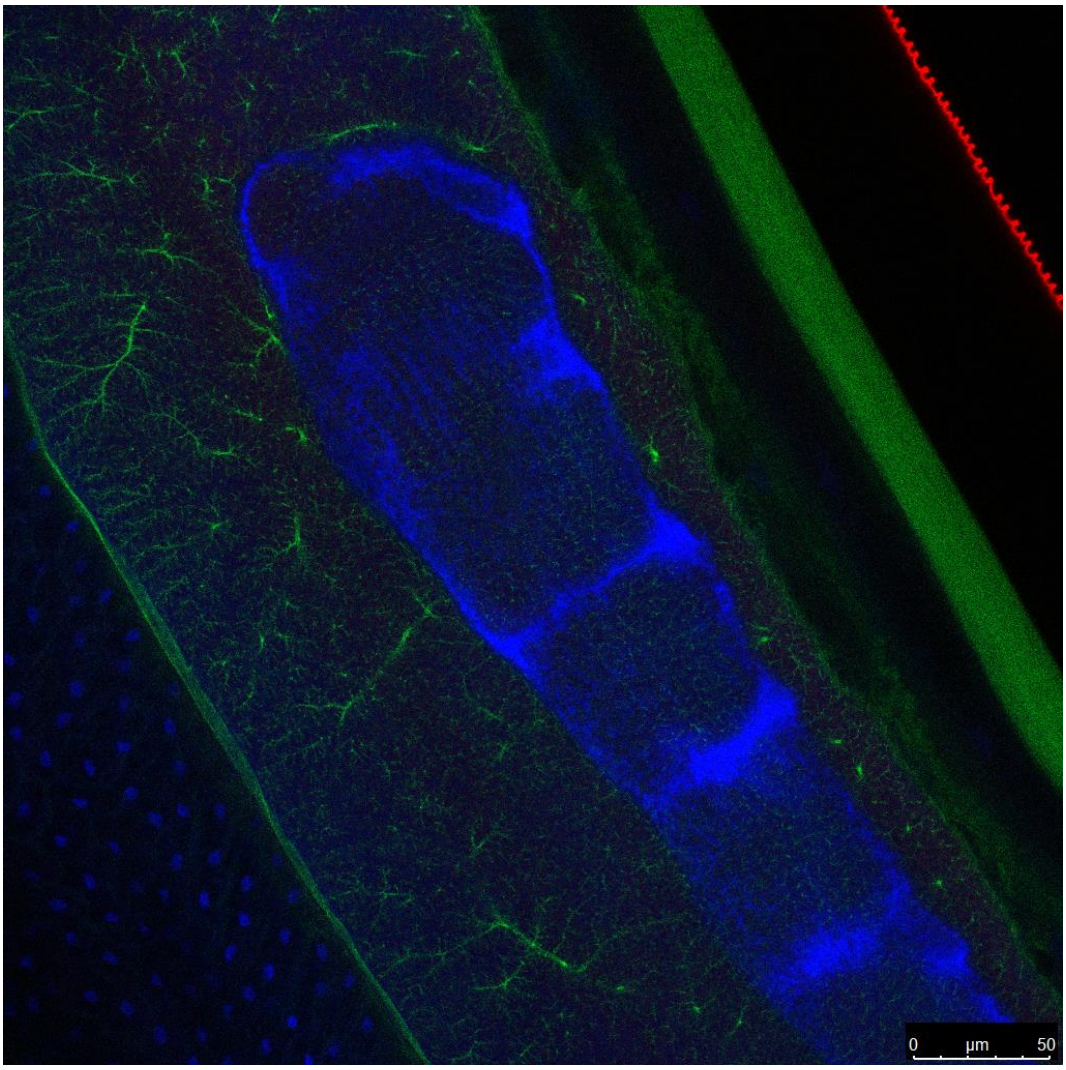

Figure 2. Unidentified structure in the intestine of nematode *Anisakis* pegreffii non-specifically binding DAPI (in blue). In green: positive staining of actin by Alexa fluor phallioidin 488; in red: positive staining of the cuticle by anti-ß tubulin Cy3.

Imaging techniques in connective tissue diseases

Daniela Quaglino (1), D. Taverna (2), F. Boraldi (1)

1) Department of Life sciences, University of Modena and Reggio Emilia, Modena, Italy

2) Department of Chemistry and Chemical Technologies, University of Calabria, Arcavacata di Rende, Italy

Keywords: connective tissue, disease, ultrastructure, imaging mass spectrometry

Almost all organs and tissues of the human body contain some form of connective tissue, namely skin, vessels, lungs, ligaments, tendons, bone, cartilage. Light and electron microscopy have shown that extracellular matrices are organized in many different morphological arrangements also depending on the type of cells and the function of the tissue. In the last decades, histopathological investigations allowed to discover a growing number of ECM components which increased from the originally recognized “collagen, elastin and mucopolysaccharides” to more than 28 different collagen types, a large number of proteoglycans and an increasing number of glycoproteins, including elastin and elastic fibre-related molecules. Approximately 300 molecules have been already recognized, thus forming the core-matrisome. However, there are many more constituents within the ECM, as those resulting from alternative splicings of primary transcripts, cell-membrane receptors mediating cell–matrix interactions and signalling pathways, as well as bioactive fragments that are released from extracellular proteins by limited proteolysis. These matricryptins, having their own biological activities, can regulate numerous physiological and pathological processes such as angiogenesis, wound healing, fibrosis, diabetes and cancer. These findings suggest that the “core-matrisome” and the “matrisome-associated proteins” are key players in connective tissue homeostasis and failure, thus representing new and important diagnostic and therapeutic targets. Since decades, different microscopical techniques (from light to transmission electron microscopy, from histochemistry to immuno-electronmicroscopy) have been applied mainly for diagnostic purposes and for the detailed description of changes occurring on cells and on matrix components. More recently, the development of new structural approaches allowed to improve the knowledge of connective tissue biology and to disclosenew

pathways in the pathogenesis of genetic diseases (collagenopathies, mucopolysaccharidoses, elastinopathies) and of more widespread acquired disorders, partly related to the aging process (i.e. localized or systemic fibrosis, emphysema, rheumatologic diseases, osteoporosis, vascular complications). Furthermore, additional evidence highlighted the importance of matrix components as fundamental regulators of the interactions between cancer cells and stroma. To better dissect the molecular complexity of the matrix network, classical histomorphological methods have been supplemented by new approaches as matrix assisted laser desorption ionization imaging mass spectrometry (MALDI IMS) allowing direct mass spectrometric analysis of tissue sections. Since tissue homogenization is not required, the relative abundance and spatial distribution of proteins, peptides, lipids, metabolites and xenobiotics can be visualized throughout a tissue section and correlated with histology. Moreover, a wide range of proteins can be analysed from affected an unaffected areas within the same tissue specimen, thus avoiding differences due to individual variability. Therefore, the application of IMS represent a promising approach complementary to standard morphological techniques and can be advantageously expanded to the clinic, paving the way for the selection of new molecules to be validated as pathogenic or as potential pharmacological target.

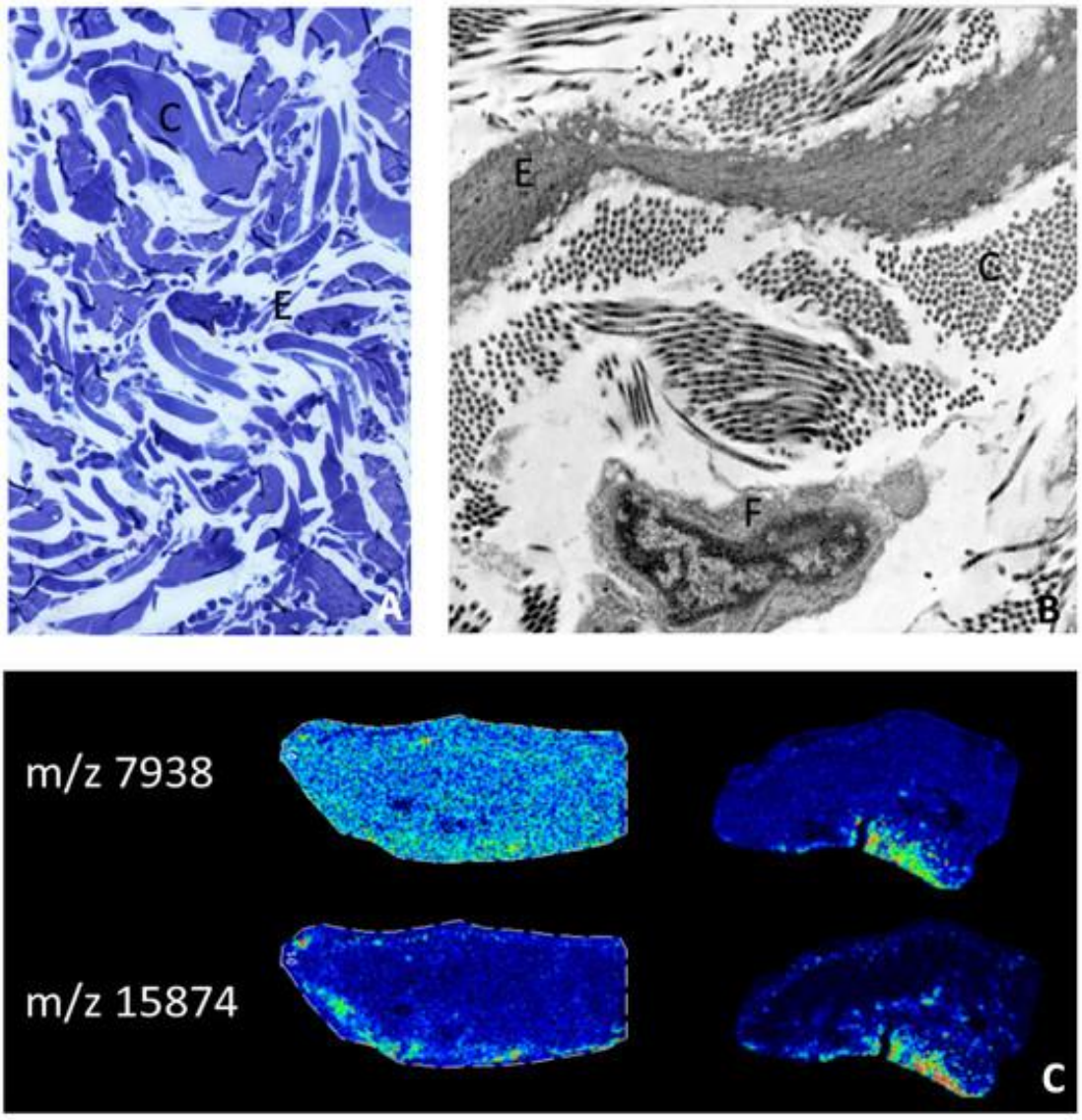

Figure 1. Dermal tissue visualized by light microscopy (A), transmission electron microscopy (B) and Imaging mass spectrometry (C).

ORAL PRESENTATIONS L7:

Overwintering-dependent changes in the epithelial cells of Malpighian tubules in the cave crickets Troglophilus cavicola and T. neglectus (Rhaphidophoridae, Ensifera)

Saška Lipovšek (1,2,3), Tone Novák (2), Franc Janžekovič (2), Barbara Dariš (1), Magdalena Rost-Roszkowska (4), Szymon Gorgoń (4), Karolina Kamińska (4), Gerd Leitinger (5)

1) Faculty of Medicine, University of Maribor, Taborska ulica 8, 2000 Maribor, Slovenia

2) Department of Biology, Faculty of Natural Sciences and Mathematics, University of Maribor, Koroška cesta 160, 2000 Maribor, Slovenia

3) Faculty of Chemistry and Chemical Engineering, Smetanova ulica 17, University of Maribor, 2000 Maribor, Slovenia

4) Department of Animal Histology and Embryology, Faculty of Biology and Environmental Protection, University of Silesia, Bankowa 9, Katowice 40-007, Poland

5) Institute of Cell Biology, Histology and Embryology, Medical University of Graz, Harrachgasse 21, 8010 Graz, Austria

Keywords: cave crickets, epithelial cells, Malpighian tubules, overwintering, ultrastructure

In insects, dormancy is the most usual state of temporarily reduced metabolic activity during unfavorable conditions. This natural starvation period represents stressful conditions for the cave crickets *Troglophilus cavicola* and *T. neglectus* during their overwintering in hypogean habitats. They are among the most numerous invertebrates overwintering in central European caves (1). The larvae of *T.cavicola* hatch in spring and live in epigean habitats until the autumn. Younger larvae enter hypogean habitats and overwinter there. After overwintering, they live outside until the next autumn when they move, as older larvae, for the second time to overwinter in caves. They reach their maturity in caves, mate, lay eggs outside in March, and die by June. *Troglophilus neglectus* larvae enter caves two weeks later and leave them two weeks earlier. Older *T. neglectus* larvae mature, mate and lay eggs in July. During

overwintering, cave crickets do not feed and are therefore convenient for studying the influences of stress conditions caused by natural starvation. The Malpighian tubules (MTs) are the most important excretory and osmoregulatory organs in insects. They transport organic solutes, break down and remove toxic substances, and maintain ionic balance (2). During overwintering, cave crickets do not feed. Changes in the epithelial cells of the MTs are best representative for understanding the *Troglophilus* natural starvation period, because the MTs show the final products of the cell homeostasis processes during their non-nourishing overwintering. In this study, in both species and sexes, ultrastructural characteristics of the MTs were studied using the transmission electron microscopy in three time frames: the beginning, the midle and the end of owerwintering (3). In both species, the general structure of the epithelial cells of the MTs was comparable during overwintering (Figs. 1, 2), while some specific differences appeared in cell characteristics (Figs. 3, 4). During overwintering, spherites were gradually exploited and autophagic structures (phagophores, autophagosomes, autolysosomes and residual bodies) more numerous. The abundance of the autophagosomes increased toward the end of overwintering as shown by both TEM and immunofluorescence microscopy. In both species, the autophagic processes seemed to be more intense in females, as they showed higher rates of cells containing autophagic structures than males.

References:

1.T. Novák et al., Acta Carsolog. 42 (2013), 301−309.

2. K. W. Beyenbach et al., Annu. Rev. Entomol. 55 (2010), 351–374.

3. S. Lipovšek et al., PLOS ONE (2016), https://doi.org/10.1371/journal.pone.0158598.

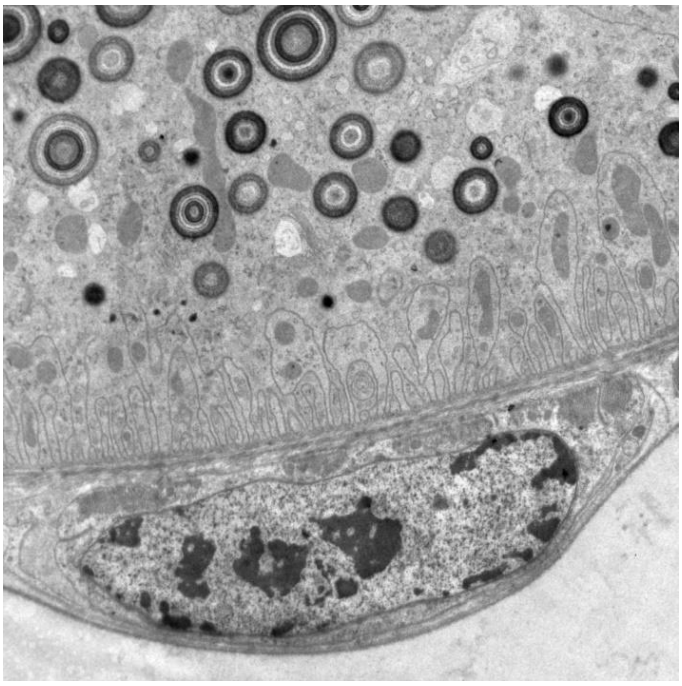

Figure 1. Ultrathin cross-sections of the Malpighian tubules in *T.cavicola* at the beginning of overwintering. Magnification: 3000x.

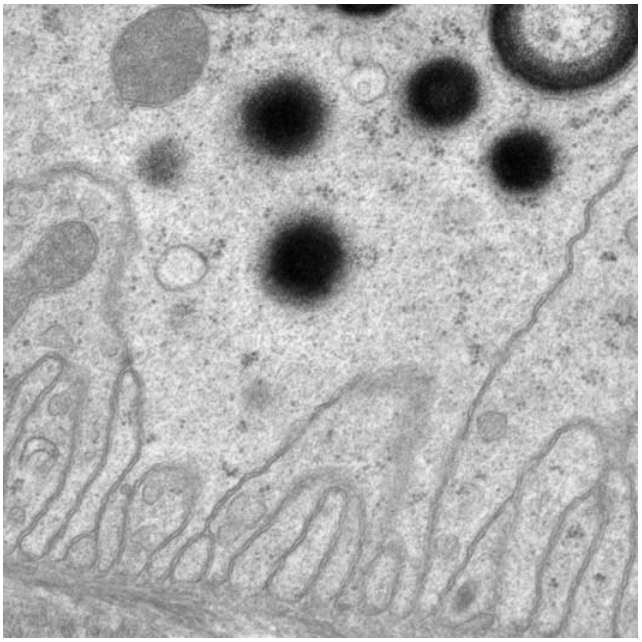

Figure 2. Ultrathin cross-sections of the Malpighian tubules in *T.cavicola* at the beginning of overwintering. Magnification: 7000x.

Characterization of melanosomes involved in production of non-iridescent structural colors in bird plumage (Aves) and their detection in fossil record

Frane Babarovic (1), Jakob Vinther (2)

1) University of Zagreb, Faculty of Science, Department of Biology, Rooseveltov trg 6, HR-10000 Zagreb, Croatia

2) School of Biological Sciences, University of Bristol, Life Sciences Building, 24 Tyndall Avenue, Bristol BS8 1TQ, UK; School of Earth Sciences, University of Bristol, Wills Memorial Building, Queens Road, Bristol BS8 1RJ, UK

Keywords: melanosome fossilization, feather nanostructure, molecular paleontology

The colors in the bird's feather are pigmentary or structural. Pigmentary colors are produced solely by absorption and reflection of light on the molecule of the pigment. Structural colors are produced by the light scattering from nanometer scale arrangements of the molecules that form the feather and are classified as iridescent and non-iridescent colors structural (NISC). Nanostructures that produces NISC is the matrix made of β-keratin and air, below which is a layer of melanosomes that absorbs non-coherently scattered light from the layer above. Despite the fact that a spongy layer is responsible for color production in NISC, a layer of melanosomes placed underneath color-producing structures has been observed. These melanosomes are not directly involved in color production as they absorb incoherently scattered light relative to the coherently scattered light produced by the overlying spongy layer. Without them, i.e. in amelanotic birds, the NISC is found to be washed out. The melanosomes preserve on the surface of the fossil in the shape of elongated or circular granules. The shape of melanosomes is connected to the color of feathers they are involved in the production. Therefore, due to the shape of melanosomes, it is possible to reconstruct the coloration of an extinct organisms. The shape of the melanosomes in the NISC and their detection in the fossil record has not yet been researched. The melanosomes from recent feathers are isolated, their images were taken with scanning electron microscope, and their shape is determined. One-way ANOVA and Tukey's post hoc test of their width and length were used to compare them to other color categories. Results indicate a significant overlap with melanosomes from gray

color, being very large and wide. A sample of unknown melanosomes from the surface of the fossil *Eocoracias brachyptera* from Messel pit in Germany was scanned with Scanning electron microscopy and compared with the other melanosomes categories. (Figure 1.) Reconstruction of the fossils combined with ancestral state reconstruction showed that bird was blue. The importance of self-assembly processes is highlighted during the development of feather. Size and shape of melanosomes are known to affect their movement through keratin matrix and their final location within the feather. To assess the localization of melanosomes within gray feathers and compare it with feathers expressing non-iridescent structural color, the Transmission electron microscopy images of feathers colored with mentioned colors were taken. (Figure 2.) With transmission electron microscopy images of feather cross-sections, the importance of the size of the NISC melanosomes was explained from the aspect of the development of the feather.

Acknowledgements:

This research was supported by ERASMUS+ Internship program.

References:

1. J Vinther, BioEssays (2015) 37 (6), 643-656.

2. MD Shawkey, GE Hill, Journal of Experimental Biology (2006) 209 (7), 1245-1250.

3. R. Maia et al., J R Soc Interface. (2012) 9(69): 734–743.

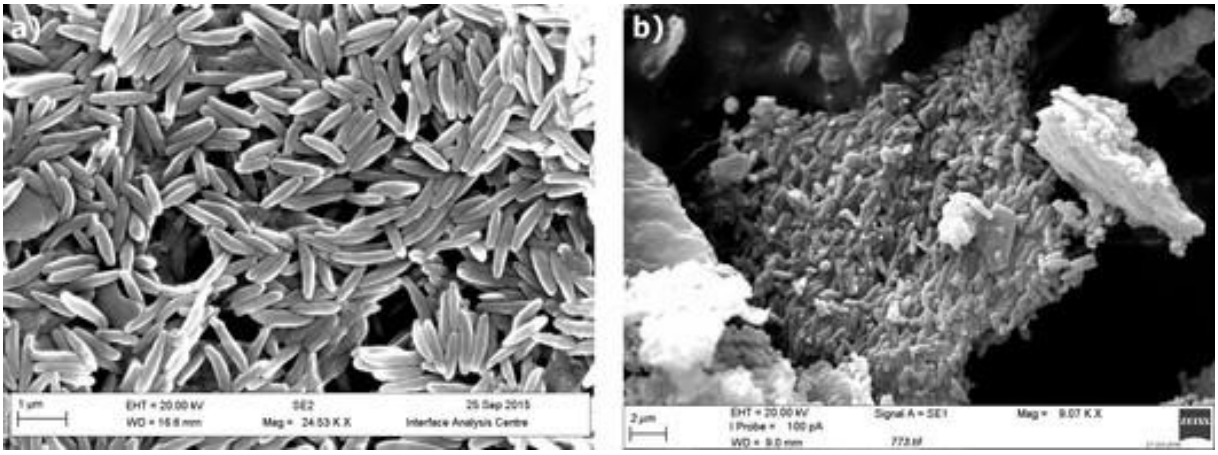

Figure 1. Images of melanosomes taken with scanning electron microscope: (a) melanosomes isolated from fresh feathers, scale bar: 1 μm; (b) melanosomes isolated from fossil sample, scale bar: 2 μm.

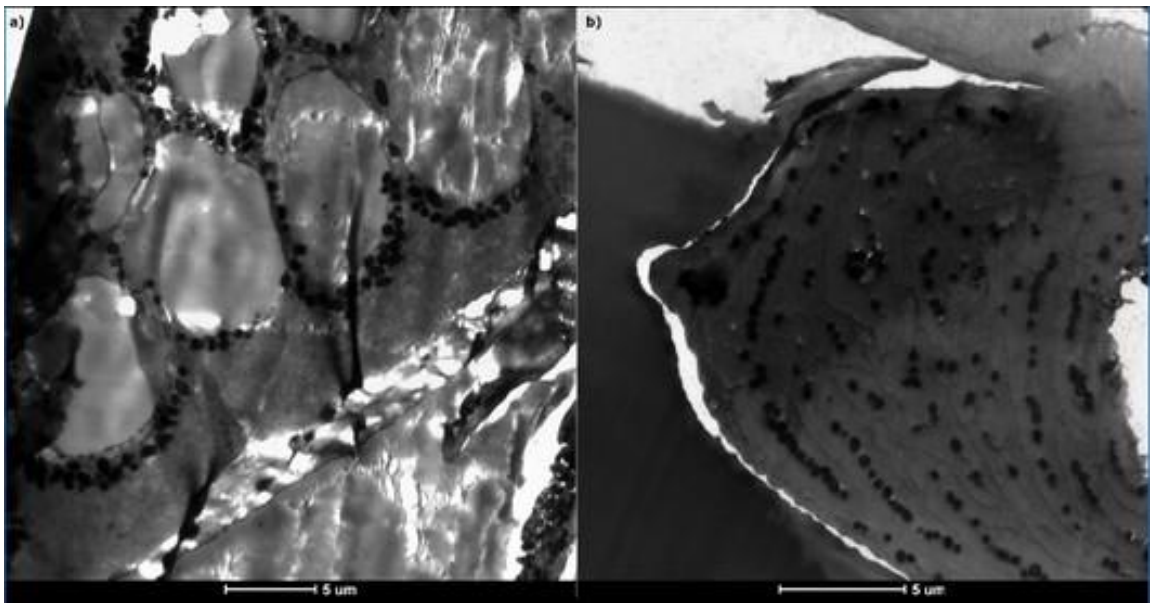

Figure 2. Transmission electron microscopy images of feather nanostructure: (a) *Rupicola peruvianus* grey feather, (b) *Acryllium vultarinum* NISC feather. Scale bar for both images is 5 μm.

Tunneling membrane nanotubes as communication tool between urinary bladder cancer and normal urothelial cells: Insights from combination of microscopic techniques

Mateja Erdani Kreft (1), Nataša Resnik (1), Samo Hudoklin (1), Daša Zupančič (1), Tanja Višnjar (1), Diana Baraga (1), Tim Prezelj (1), Polona Glažar (1), Irenej Kolšek (1), Adolf Ellinger (2), Roman Polishchuk (3), Erik Manders (4), Peter Veranič (1)

1) University of Ljubljana, Faculty of Medicine, Institute of Cell Biology, Ljubljana, Slovenia

2) Medical University of Vienna, Centre for Anatomy and Cell Biology, Department of Cell Biology and Ultrastructure Research, Vienna, Austria

3) Telethon Institute of Genetics and Medicine (TIGEM), Pozzuoli (NA), Italy

4) University of Amsterdam, Swammerdam Institute for Life Sciences, The Netherlands

Keywords: tunneling membrane nanotubes, urinary bladder cancer, super-resolution microscopy, electron microscopy, immunolabeling

Tunneling membrane nanotubes (TnTs) are open-ended channels that mediate intercellular exchange of various components between connected cells (1), and thus represent a novel type of cell-to-cell communication. It is suggested that in animal tissues TnTs are the tools for discrete communication pathways. TnTs balance diverse stress factors caused by pathological changes or fluctuating physiological and environmental conditions, such as oxidative stress or nutrient shortage (2). They are increasingly recognized as central players in a multitude of cellular mechanisms and diseases. However, the possible role of TnTs in urinary bladder cancerogenesis has not been elucidated yet. In our study, we aimed to analyze TnTs between cancer and normal urothelial cells by combining immunofluorescence and super-resolution microscopy, transmission and scanning electron microscopy as well as electron tomography. In addition, we customized a triple labelling of major TnT's cytoskeleton components- actin filaments, intermediate filaments, and microtubules. We showed that TnTs of normal and cancer urothelial cells distinguish in dimensions as well as in the arrangement of cytoskeletal elements and their representative motor proteins. Furthermore, results from co-cultures studies revealed that cells which are in the minority form TnTs toward cells in the majority, which

supports our hypothesis that TnTs are important for the urothelial cell-to-cell communication in stressful conditions. Moreover, this could mimic the situation in human urinary bladder when cancer cells start to communicate with the normal cells to provoke a tumor growth. To sum up, our findings provide new descriptions of TnT's morphological, molecular, ultrastructural, and physiological characteristics, which are prerequisite for use of TnTs as therapeutic targets in translational medicine.

Acknowledgements:

This research was supported by Slovenian Research Agency (J3-7494).

References:

1. Rustom A. et al. Science (2004), 303, 1007–1010.

2. Rustom A. Open Biol (2016), 6, pii: 160057.

Cytotoxic and apoptotic activity of *Prunus spinosa* extract on human cancer cells

Maria Condello (1), E. Pellegrini (1), G. Occhionero (2), S. Delfine (3), F. Mastrodonato (2), Stefania Meschini (1)

1) National Center for Drug Research and Evaluation, Italian National Institute of Health, Viale Regina Elena, 299, 00161, Rome, Italy

2) Italian Society of Biointegrated Medicine, Variante Esterna, 86091, Bagnoli del Trigno (Isernia), Italy

3) Department of Agriculture, Environment and Food Science, University of Molise, Via Francesco De Sanctis, 1, 86100,Campobasso, Italy

Keywords: tumor cells, cytotoxic effect, dietary supplement, morphological alterations

The use of a natural diet supplements to improve chemotherapeutic efficacy and to reduce the side effects of anti-cancer therapy is one of the objectives of the international research. In our studies we investigated the effect of the extract of drupes picked from *Prunus spinosa* Trigno ecotype (PsT®) used in combination with a special blend of aminoacids, vitamins and mineral salts (NAC, Nutraceutical Activator Complex) on human cancer cells (colorectal, uterine cervical, breast and bronchoalveolar carcinoma). MTT and cloning efficacy assays shown that PsT® plus NAC reduced cell vitality; in particular, PsT® 10 plus NAC was the most efficacy combination on all human cancer cell lines. After changing the NAC vehicle with phosphate saline buffer or physiological solution the treatments resulted ineffective, showing the efficacy of PsT® plus NAC treatment. The cytotoxic effect of PsT® plus NAC on colon carcinoma cells (HCT116) has been confirmed by optical (Figure 1) and scanning (Figure 2) microscopic observations, that show evident morphological modifications. Analysis of mitochondrial membrane potential by flow cytometry showed an increase of depolarized mitochondria, proving that this organelle is a target of the combined cytotoxicity. Cell cycle data showed sub G1 peak appearance after treatment, indicating apoptotic cell death induction. Moreover, normal cell (as human fibroblasts and rat intestinal cells) vitality are not altered by PsT® plus

CAN treatment. These data further support the idea that PsT® may be used in combination with antineoplastic drugs to enhance their effectiveness and decrease side effects.

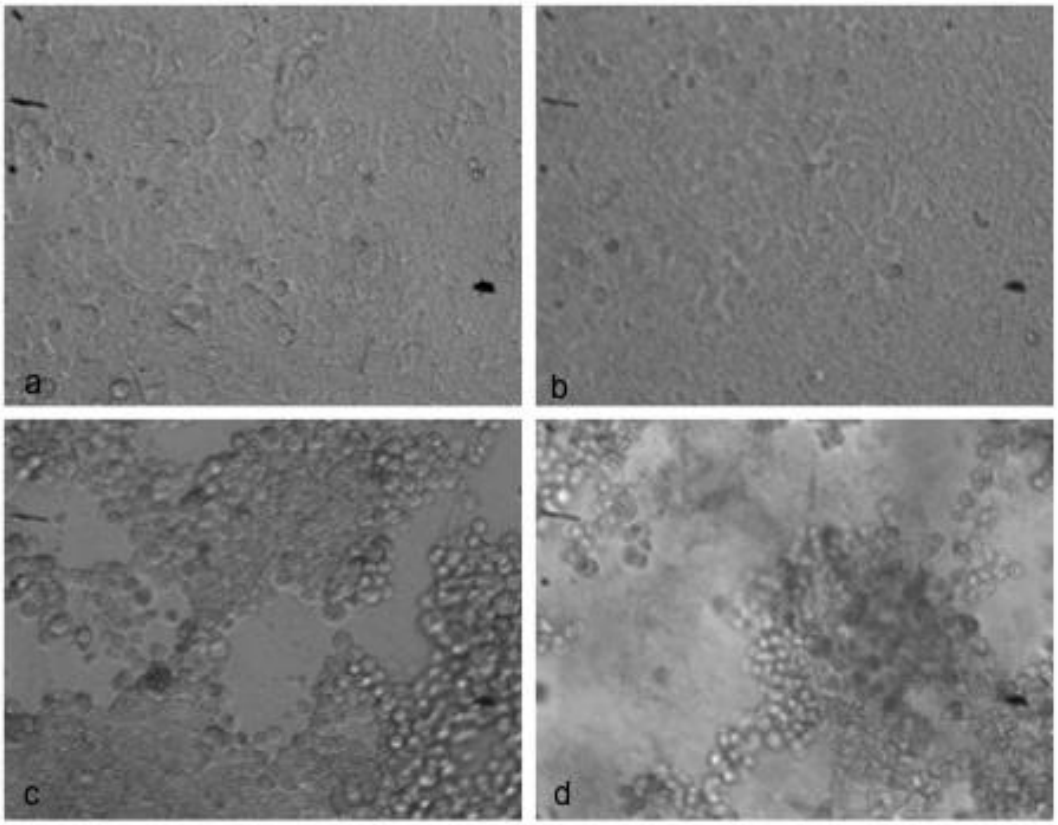

Figure 1. Optical observations of untreated HCT116 cells (a), treated with PsT® 2 mg/ml plus NAC (b), PsT® 4 mg/ml plus NAC (c) or PsT® 10 mg/ml plus NAC (d).

POSTER PRESENTATIONS L7:

A method for measuring area and surface-related parameters on microphotographs by using free and open-source image processing software

Nikola Bijelić (1), Dunja Stolnik (2), Edi Rođak (1), Ivana Lovrić (1), Tatjana Belovari (1)

1) Department of Histology and Embryology, Faculty of Medicine, University of Osijek, J. Huttlera 4, HR-31000 Osijek, Croatia

2) Clinical Hospital Centre Osijek, J. Huttlera 4, HR-31000 Osijek, Croatia

Keywords: histomorphometry, microscopy, software, methods

There are different ways of obtaining area and surface-related parameters for describing the micromorphology of different tissues, including cancellous bone. Histomorphometry and micro computed tomography can be too costly for small laboratories and institutions, especially when proprietary software or expensive equipment is needed. Free and open-source software alternatives are available today. Some of these can be used for histomorphometry. Here we demonstrate how all image processing and morphometry can be done on freely available software. This method was inspired by the paper by Egan et al. (1), however, we further replaced all of the proprietary and expensive software by using free and open-source alternatives. For measurements of the cancellous bone, images were first processed using open-source and free imaging software GIMP (GNU Image Manipulation Program) and measurements were performed by using FIJI software (FIJI is Just ImageJ), a distribution of ImageJ open-source image processing software (2, 3). The measured parameters were: bone area (B.Ar), trabecular tissue total area (T.Ar) and trabecular bone perimeter (B.Pm). Using several mathematical formulas, we calculated the following parameters describing cancellous bone histomorphometry: trabecular bone volume (BV/TV, in %), trabecular bone surface (BS/TV, in /mm), trabecular thickness (Tb.Th, in mm), trabecular number (Tb.N, in/mm) and trabecular separation (Tb.Sp, in mm). These parameters are important in studies of bone development and quality. There are many benefits of using freely available and open-source

software for scientific research, especially the low cost, worldwide availability and transparency, and this work supports that notion.

References:

1. K. P. Egan et al. Histopathology 61 (2012) 1168–1173.

2. J. Schindelin et al. Nat Methods 9 (2012) 676–682.

3. J. Schindelin et al. Mol Reprod Dev 82 (2015) 518–529.

Adipogenic effect of mild ozonisation on human adipose-derived adult stem cells

Manuela Costanzo (1), F. Carton (1), G. Conti (1), E. Solani (1), G. Tabaracci (2), V. Covi (2), Manuela Malatesta (1)

1) Dept. of Neurosciences, Biomedicine and Movement Sciences, University of Verona, Strada Le Grazie 8, 37134, Verona, Italy

2) Poliambulatorio San Rocco, Via Monsignor G. V. Moreni 95, 25018 Montichiari (BS), Italy

Keywords: ozone, stem cells, adipose tissue, light microscopy, transmission electron microscopy

Oxygen-ozone (O_2-O_3) therapy is a modestly invasive procedure based on the regeneration capabilities of low ozone concentrations, and used in medicine as an alternative/adjuvant treatment for different diseases (1). In this work, we investigated the effects of mild ozonisation on human adipose-derived adult stem (hADAS) cells. hADAS are mesenchymal stem cells present in the stromal-vascular fraction of fat tissue, and able to differentiate *in vitro* into meso-, ecto- and endodermal cell lineages (2). For the present study, the cells were grown in a medium with adipogenic factors (IBMX, dexamethasone, rositigliazone, insulin) to obtain differentiation into the adipoblastic lineage. Adipose tissue is largely used in regenerative medicine and tissue engineering and we aimed at exploring the potential of low O_3 concentrations in stimulating hADAS cell differentiation. Based on our previous ozonisation protocols (3), hADAS cells were seeded on glass coverslips and exposed to O_2-O_3 gas mixtures (5 and 10 µg O_3/ml O_2) using an OZO2 FUTURA apparatus (Alnitec); cells exposed to pure O_2 or air served as controls. Cells were treated at early (6 days), intermediate (16 days) and late (20 days) differentiation steps and the effects of O_3 were evaluated 2 and 24 hours after gas exposure. Trypan blue test excluded increased cell mortality following treatment. After gas exposure, cells were fixed with aldehydes and then processed for either light or transmission electron microscopy. For brightfield microscopy, cells were stained with Red oil (to visualize lipid droplets) and hematoxylin (Figure 1a). Quantitative evaluation of the cellular lipid content was performed by measuring cells and lipid droplets area (Image J, NIH).

Statistical comparisons (one-way Anova test) revealed that exposure to 10 µg O_3 significantly increased lipid content after 24 hours at all the differentiation steps considered, whereas 5 µg O_3 exerted a limited effect (Figure 1b). To elucidate the role of the milieu in the adipogenic effect of O_3, cells were grown in a medium devoid of adipogenic factors and treated as described above. Under these conditions, no adipogenic effect was observed. Ultrastructural analysis was carried out in OsO_4-fixed Epon-embedded samples. Notably, no alteration of cell organelles was found in any samples at any treatment times. In all hADAS cells mitochondria were numerous, rough and smooth endoplasmic reticulum were well developed, Golgi complex showed many cisternae and vesicles, while lipid droplets and glycogen progressively increased during differentiation. It is likely that the lipogenic effect observed in hADAS cells is related to the mild oxidative stress caused by low O_3 concentrations. In fact, it is known that an appropriate level of reactive oxygen species is required to stimulate adipogenesis. Our results open interesting perspectives for the application of mild ozonisation to promote differentiation of hADAS and, more generally, stem cells.

Acknowledgements:

This research was supported by University of Verona, Italy (Joint Projects 2015)

References:

1. A.M. Elvis and J.S. Ekta, J. Nat. Sci. Biol. Med. 2 (2011) 66-70.
2. W.K. Ong and S. Sugii, Int. J. Biochem. Cell Biol. 45 (2013) 1083-1086.
3. M. Costanzo et al., Eur. J. Histochem. 59 (2015) 2515.

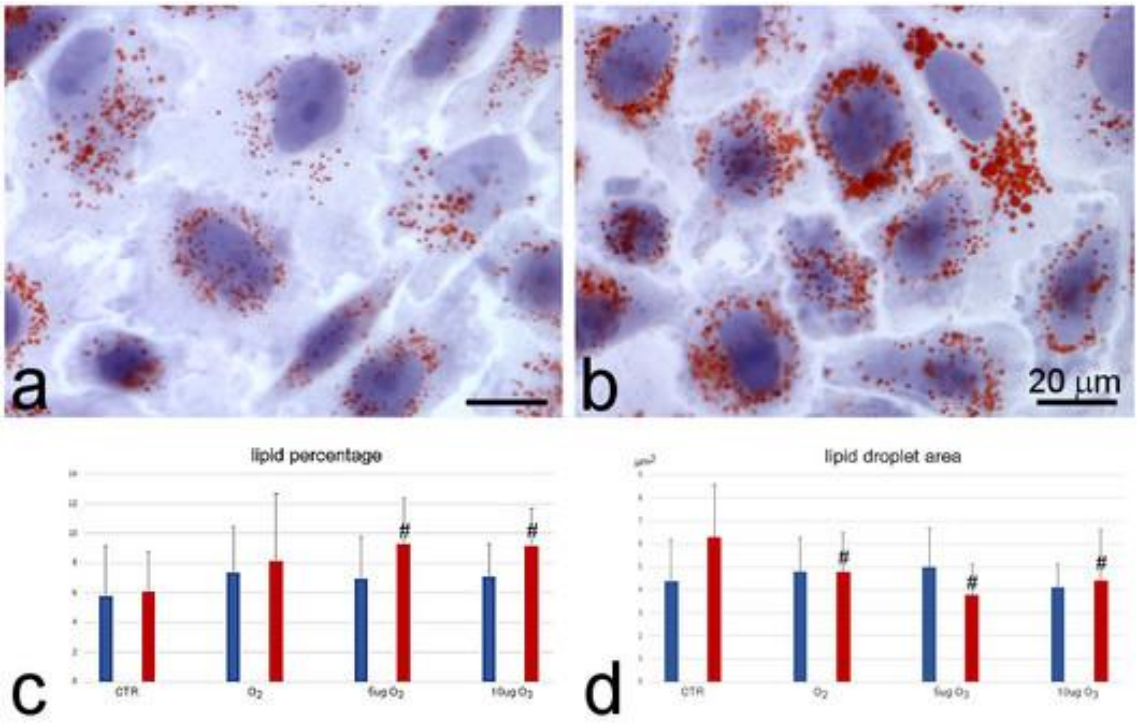

Figure 1. Brightfield microscopy, control (a) and 10 µg O3-treated (b) hADAS cells (16 differentiation days). (c,d) Mean values±SD of variables at 2h (blue) and 24h (red) post-treatment. Symbols indicate values significantly different from control.

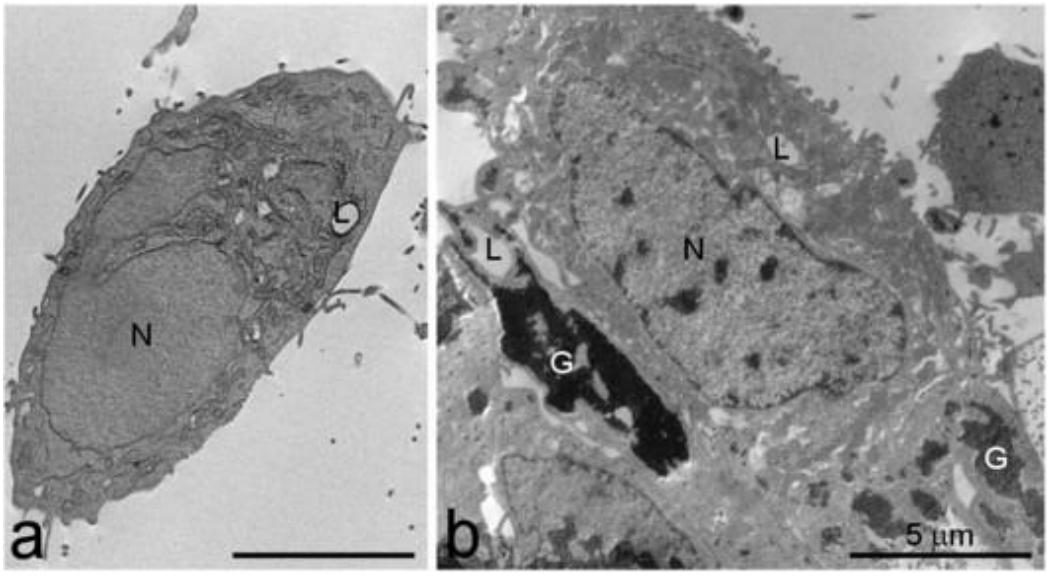

Figure 2. Transmission electron microscopy, 10 µg O3-treated hADAS cells at 16 (a) and 20 (b) differentiation days. Note the increased amount of lipid and glycogen at the late differentiation step. G, glycogen; L, lipid droplet, N, nucleus.

New study on metformin action against testicular injury: prostate cancer, diabetes and diabetes-cancer connection

Pinar Koroglu (1), Omur Karabulut-Bulan (1), Ismet Burcu Turkyilmaz (2), Ilknur Bugan (1), Refiye Yanardag (2)

1) Istanbul University, Faculty of Science, Department of Biology 34134-Vezneciler, Istanbul, Turkey

2) Istanbul University, Faculty of Engineering, Department of Chemistry 34320-Avcılar, Istanbul, Turkey

Keywords: STZ, MAT-Lylu, testes, metformin, oxidative stress.

The prostate cancer is the most common second cancer followed by lung cancer in men (1). Diabetes is a heterogeneous metabolic disease characterized by increase of blood glucose level. The most common consequence of diabetes is generation of reactive oxygen species which can cause oxidative stess and beta cell failure. Diabetes and cancer directly affect male fertility (2, 3). Cancer that is a growing disease with diabetes is a major health concern (4). Metformin is the first choice drug for diabetes treatment and an oral glucose lowering agent (5). Besides, the studies related to reduce the risk of cancer of the metformin have recently drawn attention (6). Aim of this study is to evaluate the role of metformin on testicular injury in prostate cancer, diabetes and prostate cancer+diabetes model via histopathological, immunohistochemical and biochemical methods. In this study, male Copenhagen rats were divided into six groups. 1. Control group: 0.9 % physiological saline was received during 14 days, 2. Diabetic group: 65 mg/kg a single dose of streptozotocin (STZ) was applied with the intraperitoneal injection, 3. Cancer group: $2x10^4$ Mat-LyLu cells were inoculated subcutaneously, 4. Diabetic+cancer group: 2x104 Mat-LyLu cells were received after injection of 65 mg/kg STZ, 5. Diabetic+cancer+metformin group: metformin was received 250 mg/kg by gavage during experimental period, following injection of STZ and inocculation of Mat-LyLu cells, 6. Cancer+metformin group: metformin was received 250 mg/kg during experimental period, following inocculation of Mat-LyLu cells. The experiment was terminated on the 14th day following MAT-LyLu cell injection. Testes tissues were taken and stained with hematoxylin and eosin. Histopathological damage in the seminiferous tubules was evaluated as: normal,

regressive, degenerative and atrophic (7). Apoptotic cells in testes tissue were detected with terminal deoxynucleotidyl transferase dUTP nick end labeling (TUNEL) reaction. Oxidative stress parameters were determined spectrophotometrically such as catalase, superoxide dismutase, glutathione-S-transferase in testicular tissue specimens. In addition to biochemical methods, serum glutathione, malondialdehyde and prostate specific antigen levels were determined by applying Enzyme Linked Immuno Sorbent Assay (ELISA) method. Our results suggest that metformin treatment in cancer and diabetes+cancer group reduced the testicular damage on testes tissue significantly. It was declared that metformin played a role in alleviating the inflammatory responses, which was beneficial in protecting the testes from ischemia-reperfusion injury (5). In conclusion, we can say that metformin has an ameliorative effect on the testes in prostate cancer and diabetes model histopathologically, immunohistochemically and biochemically.

References:

1. Chung SD, Kao LT, Lin HC, Xirasagar S, Huang CC, Lee HC, Patients receiving androgen deprivation therapy for prostate cancer have an increased risk of depressive disorder, PLoS One (2017).

2, 12(3), 0173266- 0173274. 2. Afifi M, Almaghrabi OA, Kadasa NM, Ameliorative effect of zinc oxide nanoparticles on antioxidants and sperm characteristics in streptozotocin-induced diabetic rat testes, Biomed Res Int (2015) 153573-153579.

3.Skakkebaek NE, Rajpert-De Meyts E, Buck Louis GM, Toppari J, Andersson AM, Eisenberg ML, Jensen TK, Jørgensen N, Swan SH, Sapra KJ, Ziebe S, Priskorn L, Juul A, Male reproductive disorders and fertility trends: influences of environment and genetic susceptibility, Physiol Rev (2016)96(1), 55-97.

4. Giovannucci E, Harlan DM, Archer MC, Diabetes and cancer: a consensus report, Diabetes Care (2010) 33, 1674–1685.

5. Asghari A, Akbari G, Meghdadi A, Mortazavi P, Protective effect of metformin on testicular ischemia/reperfusion injury in rats, Acta Cir Bras (2016) 31(6), 411-416.

6. Tao Z, Peng G, Yinan Z, Hui X, Xiao Y, Shan X, Xinyang W, Dalin H, Xunbo J, The antidiabetic drug metformin inhibits the proliferation of bladder cancer cells *in vitro* and *in vivo*, Int J Mol Sci (2013) 14, 24603-24618.

7. Hess RA, Linder RE, Strader LF, Perreault SD, Acute effects and long term sequelae of 1,3-dinitrobenzene on male reproduction in the rat II. quantitative and qualitative histopathology of the testis, J Androl (1988) 9, 327- 342.

The effect of oral administration of shea butter on liver damage caused by lipopolysaccharide-induced sepsis in rats

Nihan Bayindir (1), Mukaddes Esrefoglu (1), Cilem Ercan (2), Fahri Akbas (2), Elif Kilic (3)

1) Bezmialem Vakif University Medical Faculty, Dept. of Histology and Embryology, Istanbul, Turkey

2) Bezmialem Vakif University Medical Faculty, Dept. of Medical Biology, Istanbul, Turkey

3) Bezmialem Vakif University Medical Faculty, Dept. of Medical Biochemistry, Istanbul, Turkey

Keywords: lipopolysaccharide, liver, shea butter

Lipopolysaccharides (LPSs) induce production/release of biochemical mediators and triggers inflammatory cascades, which may result from organ failure and death. During the course of sepsis, the liver plays a crucial role both as an origin of inflammatory mediators as well as a target for these molecules. Shea butter, a natural fat derived from shea tree (*Vitellaria paradoxa*), has antiinflammatory and antioxidant effects. Based on the previous knowledge of low toxicity and anti-inflammatory effect of shea butter, we hypothesized that it should be protective on liver damage caused by LPS. 40 female (4 mount of age) Spraque Dawley rats were divided into the four groups: -Control group (C, n=10), -LPS groups (24LPS, 7LPS, and 7SLPS): Rats received single dose of 6 mg/kg i.p. LPS, dissolved in PBS. In 24 LPS group, at the end of 24th hour, in 7LPS and 7SLPS group at the end of 7th day, livers were removed. In 7SLPS group 1 ml shea butter was administered orally for 7 days following LPS injection. Prior to sacrification, blood samples were obtained from heart. Liver damage was scored by considering sinusoidal dilatation, infiltration, vacuolization, lobular degeneration and necrosis. Each data was scored with a maximum total score of 15. Total oxidant status (TOS) and total antioxidant capacity (TAC) were measured in liver tissue and IL-6, TNF-α, AST, ALT levels in serum by appropriate biochemical methods. Samples from the control group revealed normal histology (Figs. 1A-B). In 24LPS and 7LPS group inflammation, sinusoidal dilatation, vacuolization, lobular degeneration and necrosis were observed (Figs. 1C-F). Hepatic damage

scores of 24LPS and 7LPS groups were higher than that of the control ($p < 0.0001$, $p < 0.05$; respectively). In 7SLPS group histopathological changes were similar to those of 7LPS group. The hepatic TOS level of 24LPS group was higher than that of 7LPS group. TOS level of 7SLPS was similar to that of 7LPS group. The highest hepatic TAS level was detected in 7LPS group. TAS level of 24LPS group was higher than that of the control group. Tissue TAS level was decreased in 7SLPS group versus 7LPS group. The highest serum AST ($p<0,01$ vs control) and ALT levels were detected in 24LPS group. AST and ALT levels of both 7LPS ($p<0,01$) and 7SLPS were lower than those of 24LPS group. No significant differences were detected between therapy groups. The highest level of IL-6 was detected in 7LPS group ($p < 0.01$ vs control). In 7SLPS group IL-6 level was decreased vs 7LPS group ($p < 0.05$). TNF-α level of 7LPS group was higher than those of the control ($p < 0.001$), 24LPS ($p< 0. 0001$) and 7SLPS group. TNF-α was lower in 7SLPS level than 7LPS group. That dose of oral shea butter supplementation seems not to be effective in reducing sepsis induced liver injury. We suggest administering higher doses for demonstrating its antioxidant/anti-inflammatory effects in LPS-induced sepsis model.

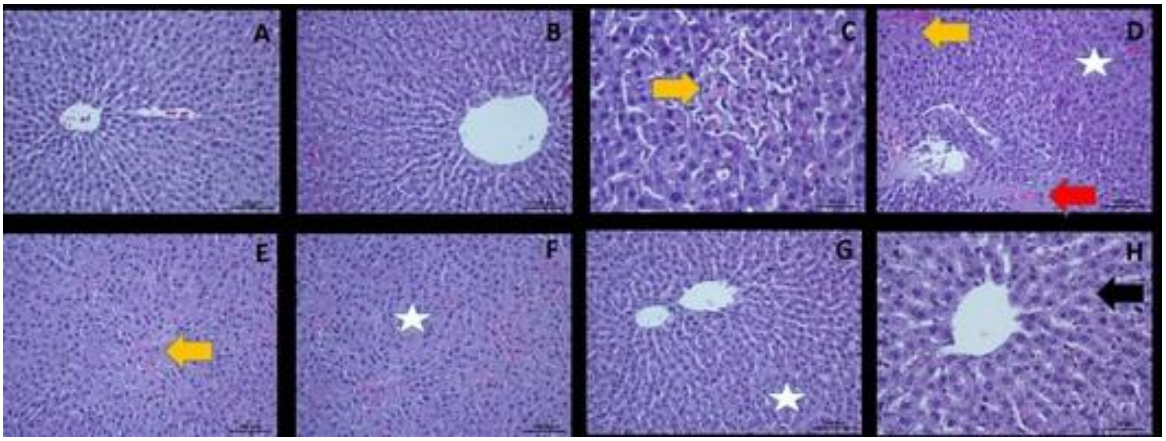

Figure 1. Liver samples of the groups. (A-B) Control; (C-D) 24LPS; (E-F) 7LPS; (G-H) 7SLPS (yellow arrow: necrosis; red arrow: edema; asterisk: lobular degeneration; black arrow: vacuolization). H-E technique.

Effects of UVB radiation and norflurazon on green and brown hydra

Goran Kovačević (1), Petra Korać (2), Katarina Caput Mihalić (2), Ana Matijević (3)

1) Faculty of Science, University of Zagreb, Division of Biology, Department of Zoology, Rooseveltov trg 6, HR-10000 Zagreb, Croatia

2) Faculty of Science, University of Zagreb, Division of Biology, Department of Molecular Biology, Horvatovac 102a, HR-10000 Zagreb, Croatia

3) University Hospital Centre Zagreb, Department of Laboratory Diagnostics, Division of Cytogenetics, Kišpatićeva 12, HR-10000 Zagreb, Croatia

Keywords: Hydra, UVB radiation, norfluorazon, budding, sexual reproduction

The aim of this study was to determine whether exposure to UVB radiation and herbicide norfluorazon had a mutagenic effect on freshwater invertebrate hydra. The experiment was performed in 60 ml volume glass dishes filled with 50 ml of aquarium water for control group and in 60 ml volume glass dishes filled with 50 ml of norfluorazon in concentrations of $2x10^{-6}$ or $2x10^{-7}$ mol/L. Specimens of green and brown hydra were parallely exposed to UVB radiation wavelength *254 nm.* The second part of the experiment was performed in the same way except there was no radiation. In brown hydra, the most visible was the damage to the tentacles, while in green hydra were observed tentacle-like growths on the body of hydra. In some individuals of the experimental animals, there was no visible damage to buds while in others the buds had the form of a damaged polyp. Budding was observed in both species, while sexual reproduction was noticed mainly in samples of green hydra treated with herbicide as well in the control samples. Mortality was low in green hydra samples and radiation proved to be the cause of greater damage than exposure to herbicide. Histology slides of brown hydra showed surface cellular/tissue formations that require further investigation.

Ultrastructural analysis of *in vitro* matured granulosa cell under treatment with the fungicide Mancozeb

Manuel Belli (1), Orlando Donfrancesco (2), Maria Grazia Palmerini (1), Selenia Miglietta (2), Stefania Annarita Nottola (2), Sandra Cecconi (1), Serena Bianchi (1), Sevastiani Antonouli (1), Giuseppe Familiari (2), Guido Macchiarelli (1)

1) Dept. of Life, Health and Environmental Sciences, University of L'Aquila, Piazzale Salvatore Tommasi 1, 67100 Coppito, L'Aquila, Italy

2) Dept. of Anatomy, Histology, Forensic Medicine and Orthopaedics, Laboratory of Electron Microscopy "Pietro M. Motta", University La Sapienza, Via Alfonso Borelli 50, 00161 Rome, Italy

Keywords: Mancozeb, granulosa cells, transmission electron microscopy, scanning electron microscopy, ultrastructure

Mancozeb is an ethylene bis-dithiocarbamate broadly used as fungicide. Reproductive toxicity has been demonstrated *in vivo* and *in vitro* in mouse oocytes, by the alteration of spindle morphology and impairment of the ability to fertilize (1). Mancozeb induced a premalignant status in mouse granulosa cells (GCs) cultured *in vitro*, indicated by decreased p53 expression and tenuous oxidative stress (2). By using this *in vitro* model of reproductive toxicity, made of parietal GCs from mouse antral follicles cultured with increasing concentration of Mancozeb, we aimed to ascertain the *in vitro* cellular toxicity by means of transmission (TEM) and scanning electron microscopies (SEM). Presence and extent of ultrastructural alterations induced *in vitro* by Mancozeb on GCs were not yet studied. GCs were obtained by puncturing antral follicles of PMSG-treated prepubertal CD1 female mice and cultured *in vitro* in DMEM+5%FBS+pen/step without (control) or with increasing concentration of Mancozeb (0.001-to-1 µg/ml) (1) for 36 hrs, 37°C and 5% CO2. At the end of the culture period, cells were aspirated, washed in PBS, centrifuged at 1200 rpm for 5 minutes and immediately fixed in 2.5% glutaraldehyde/PBS. Pellets were maintained at +4° C for 2-5 days, until processing. GCs were then subjected to standard preparative for TEM and SEM observations (3). Results showed a dose-dependent toxicity of Mancozeb on mouse GCs. Ultrastructural data showed intercellular junction alterations, irregular nuclear membrane and chromatin marginalization at

lower concentrations; chromatin condensation, membrane blebbing and cytoplasmic vacuolization at higher concentrations. In conclusion, Mancozeb induced a dose-dependent toxic action against GCs *in vitro*, with ultrastructural signs of cell degeneration probably due to the toxic breakdown product ethylenethiourea. These alterations could be a major cause of reduced/delayed/missed oocyte maturation observed in cases of infertility associated with exposure to pesticides.

References:

1. Rossi G. et al., Mancozeb adversely affects meiotic spindle organization and fertilization in mouse oocytes Reproductive Toxicology. 22 (2006) 51–55.

2. Iorio R. et al., Mancozeb affects mitochondrial activity, redox status and ATP production in mouse granulosa cells. Toxicol *In vitro*. 30 (2015) 438-45.

3. Nottola SA. et al., Ultrastructure of isolated mouse ovarian follicles cultured *in vitro*. Reprod Biol Endocrinol. 9 (2011) 3.

Evaluation of tumorogenic proteins in stanozolol treated rat kidney

Tuğba Kotil (1), Çiğdem Sevim (2), Mehtap Kara (3), Eren Özçağlı (3), Buket Alpertunga (3)

1) İstanbul University, İstanbul Faculty of Medicine, Department of Histology and Embryology, Çapa, İstanbul, Turkey

2) Atatürk University, Faculty of Veterinary Seciences, Department of Pharmaceutical Toxicology, Erzurum, Turkey

3) Department of Pharmaceutical Toxicology, Faculty of Pharmacy, Istanbul University, İstanbul, Turkey

Keywords: anabolic androgenic steroids, stanozolol, kidney, PTEN, PI3K-AKT pathway

Stanozolol, is an anabolic androgenic steroid (AAS) that has widespread usage in bodybuilding, sports and athletics by teenagers and athletes. AAS are synthetic derivatives of testosterone hormone. It was known that AAS caused harmful effects on various systems such as endocrine, cardiovascular, urogenital (1). Some studies reported association between carcinoma and AAS usage (2). Potential effects of stanozolol in kidney functions have not been well defined. In this study we investigated expression of tumor supressor protein PTEN and mRNA levels of PI3K and Akt in kidney treated by stanozolol. We used 34 adult male Spraque Dawley rats. Animals were divided into 5 groups as I-control (n=5), II-solvent control (n=5), III-stanozolol (n=8), IV-solvent control exercise (n=8), V-stanozolol exercise (n=8). Subcutaneous injection of stanozolol (5mg/kg) were applied for 28 days. During the experiments, 20 min/day, 5 days/week swimming exercises were performed by the animals of exercise groups. After 28 days, animals were sacrificed under ether anesthesia and kidneys fixed with 10% buffered formalin. Expression of PTEN were evaluated by immunohistochemistry. The staining intensity were scored as an overall intensity score with 3 levels (+ = weak staining; ++ = moderate staining; and +++ = strong staining). Also relative PTEN, PKI3 and AKT mRNA expressions analysed via RT-PCR. In control, solvent control exercise group strong (+++) PTEN reactivity were detected in cell of the tubules. In steroid group tubule cells have weak (+) PTEN immunoreactivity but showed moderate (++) reactivity in Stanozolol exercise group (Figure 1). mRNA expression of PTEN showed significant decrease, PI3K and Akt mRNA expression

were significantly increased in stanozolol group versus control and the other groups ($p<0.001$). PTEN expression showed increase, PI3K and Akt expression showed decrease with exercise treatment ($p<0.05$) (Graph1). PTEN is a well known tumor supressor gene and showed its effects via inhibition the phosphoinositide 3-kinase (PI3K)- AKT pathway (3). In our study stanozolol treatment caused decrease in PTEN expression level in cells of tubules. PI3K and AKT mRNA expression were also increased in stanozolol group depending on reduced expression of PTEN. Our findings suggested that AAS usage may trigger telomerase activity and kidney tumour generation through PTEN and associated PI3K and AKT pathway.

References:

1. M.S.M. Barbalho et al., International Journal of Sports Science (2015) 5-171-179.

2. C. M. Souza et al., Human and Experimental Toxicology (2017) 36-302-310.

3. N. Chalhoub et a., Annu Rev Pathol. (2009) 4-127–150.

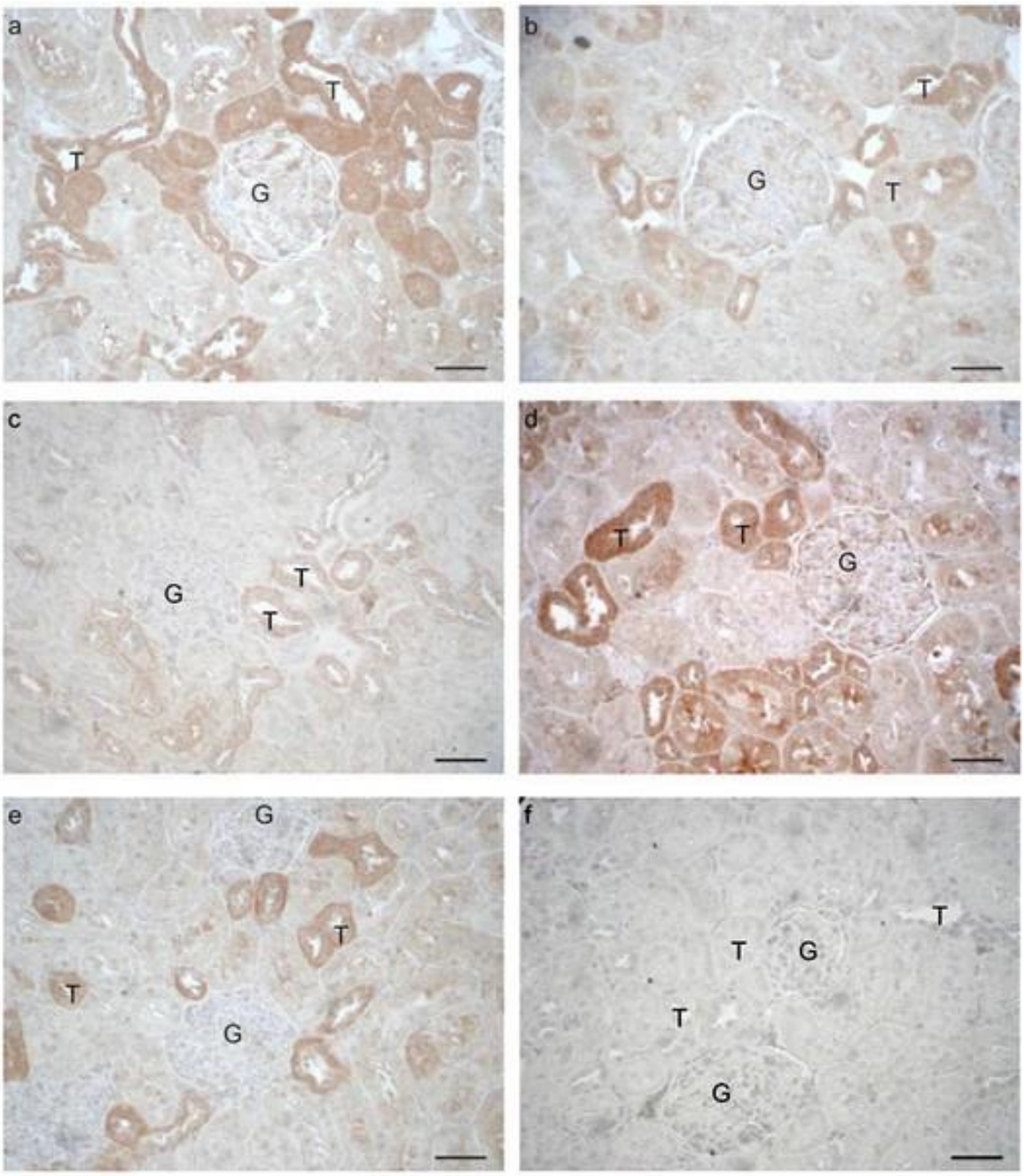

Figure 1. PTEN immunoreactivity, (a) Control group, (b) solvent control group, (c) stanozolol group, (d) solvent control exercise group, (e) stanozolol exercise group. G: Glomerulus, T: tubules.

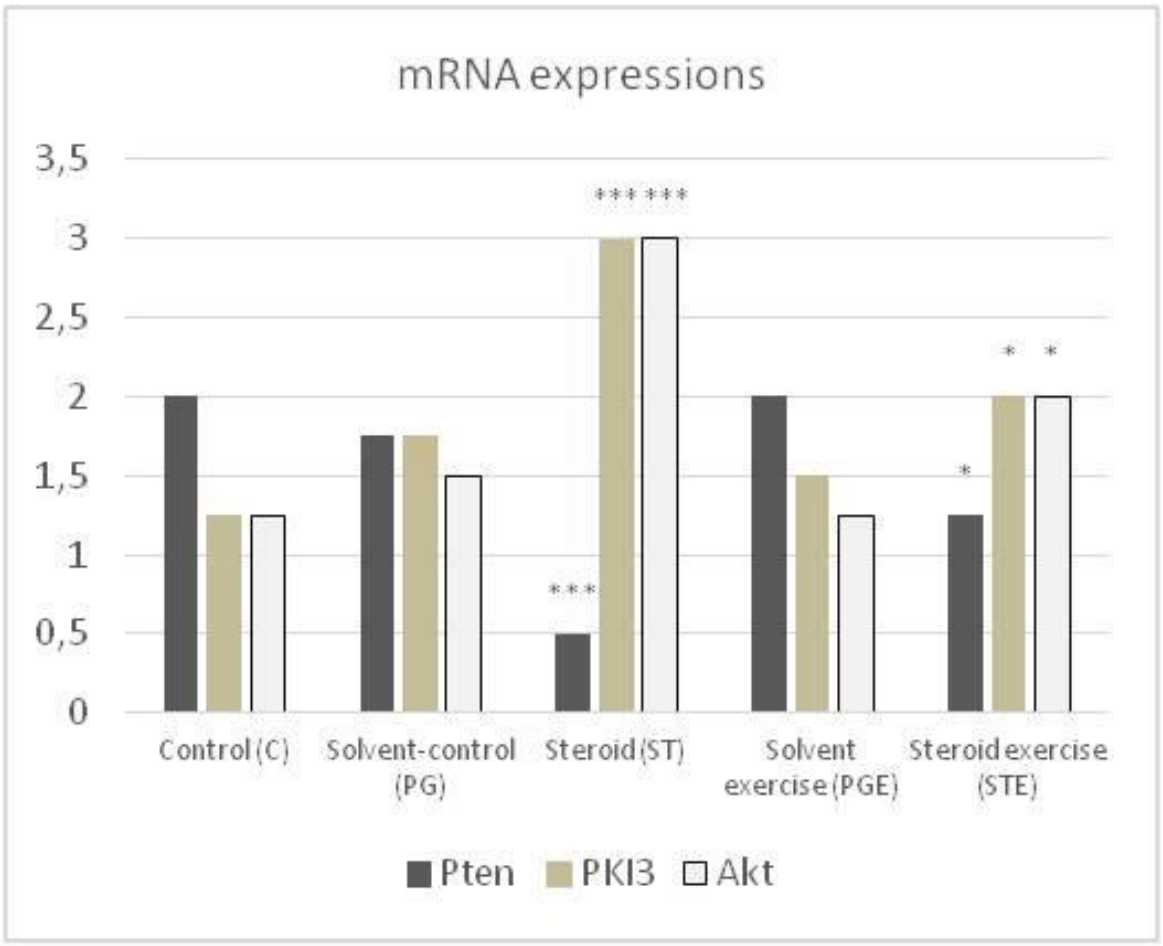

Figure 2. Compares the PTEN, PKI3and Akt expressions between groups. *** p<0.001, * p<0.05.

Spatiotemporal expression pattern of the neuronal markers in the developing human spinal cord

Ivana Restović (1), Ivana Bočina (2), Darko Kero (3), Katarina Vukojević (3), Natalija Filipović (3), Mirna Saraga-Babić (3)

1) Faculty of Philosophy, University of Split, Teslina 12, HR-21000 Split, Croatia

2) Faculty of Science, University of Split, Ruđera Boškovića 33, HR-21000 Split, Croatia

3) Laboratory for Early Human Development, Department of Anatomy, Histology and Embryology, School of Medicine, University of Split, Šoltanska 2, HR-21000 Split, Croatia

Keywords: human spinal cord development, calretinin, NF200, CGRP, VR1

We have investigated the spatiotemporal appearances of the different neuronal markers in the different parts of the developing human spinal cord (SC) in 12 human conceptuses (developmental weeks, DW 5–10) by immunohistochemical and immunofluorescence methods. In the developing SC a dorsoventral (DV) organization can be seen. CV neural wall is consists of three layers, marginal, intermediate and ventricular one. Between roof (placed dorsally) and floor plate (placed ventrally), an abundant of neuroblasts showing a DV organization were found, pointing to anatomically segregated motor and sensory spinal neurons. Dorsal area of the SC is sensory area, while motor neurons and proprioceptors are found in the ventral part. The motoneurons are the first cells that occur, followed by interneurons and finally sensory and autonomic neurons. Intermediate and large neurons are predominantly mechanoreceptors and proprioceptors and could be identified by neurofilament NF200. Small-diameter unmyelinated nociceptive peptidergic neurons can be recognized by expression of neuronal marker calcitonin gene-related peptide (CGRP). The vanilloid receptor (VR1) is expressed by primary afferent nociceptor neurons which are peptidergic small diameter type cells, while calretinin has important role in somatosensory and proprioceptive pathways. In the 5th-6th DW, calretinin first appears in the marginal layer of the developing SC, dorsally, while in the 7th-8th DW it was found in the intermediate layer. In the 9th-10th DW, calretinin was found also in the ventral part. During the 5th-6th DW, NF200 positive cells were found in the intermediate layer ventrally and in the cells lining the marginal layer, while in

the 7th-8th DW NF200 showed moderate expression in the ventricular layer also ventrally, as well as in the intermediate layer dorsally. Co-localisation with DAPI was found only in the ventricular layer. In the 9th-10th DW, NF200 positive cells were predominantly distributed in the marginal layer. CGRP was highly expressed in the intermediate and ventricular layer, as well as in lining cells of the marginal layer during the 5th-6th DW. By the end of the 7th-8th DW, strong expression of the CGRP was seen in the cells lining the central canal, while in the 9th-10th DW it was predominantly expressed in the intermediate layer and strongly co-localised with DAPI dorsally. During the 5th-6th DW, VR1 positive expression was found in the intermediate layer as well in the cells lining the marginal one, while in the 7th-8th DW it was evenly distributed in both, intermediate and ventricular layer. In the 9th-10th DW, strong expression of VR1 was found in intermediate layer and in the cells lining the central canal, also showing strong co-localisation with DAPI within all three layers. Spatial and temporal expression pattern of these neuronal markers with their possible changes during the embryogenesis provide important information for normal spinal cord development.

References:

1. T.M. Jessell, Nat. Rev. Genet. 1 (2000) 20-29.
2. M. Goulding et al., Curr. Opin. Neurobiol. 12 (2002) 508-515.
3. K.W. Dunn, et al. Am J Physiol Cell Physiol. 300 (2011) 723-742.

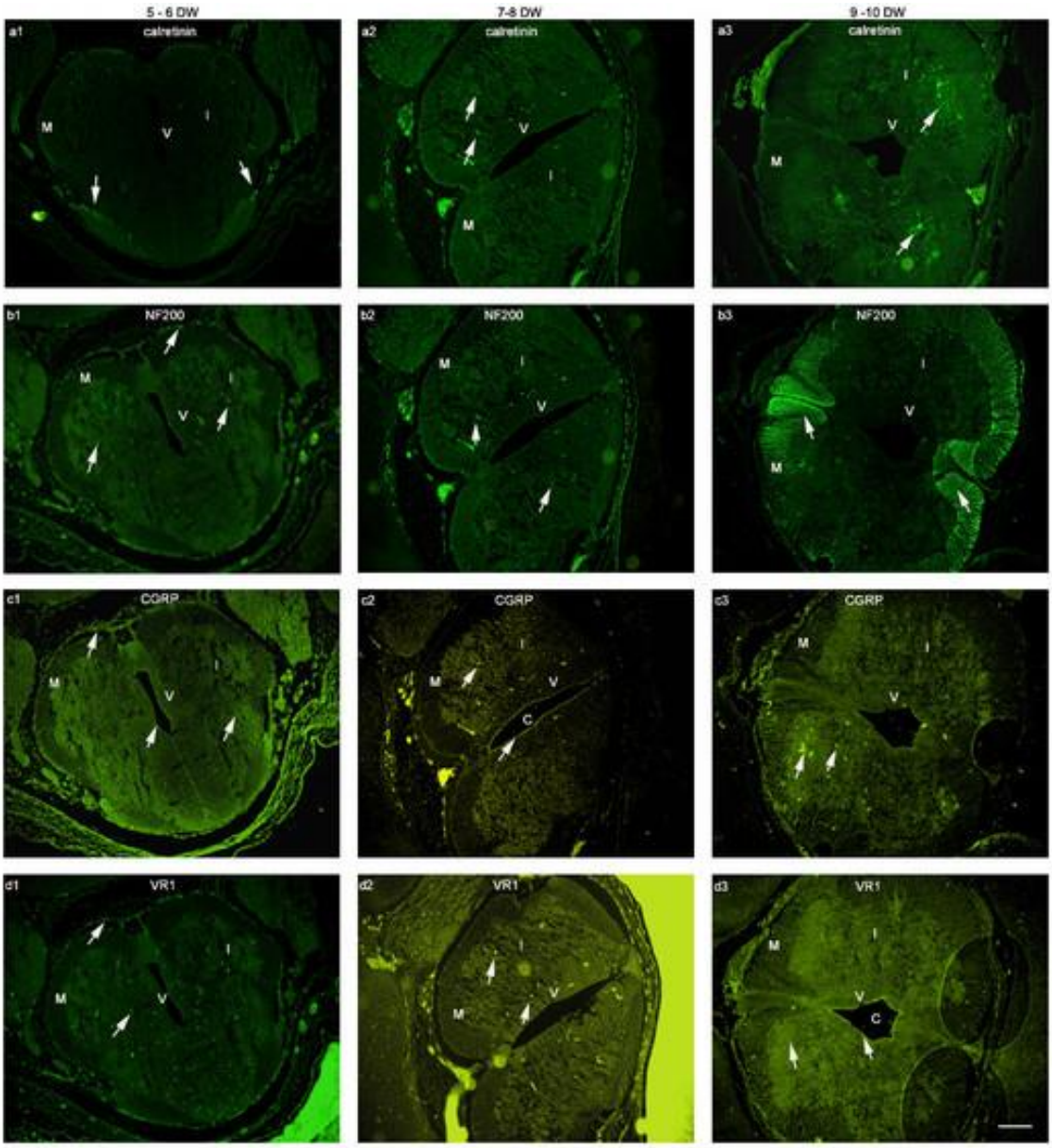

Figure 1. Section through the developing spinal cord of the human embryo at the 5th-10th DW. Investigated neuronal marker positive cells (arrows) in the ventricular (V), intermediate (I), marginal (M) layer and central canal (C). (a1-3) calretinin; (b1-3) NF200; (c1-3) CGRP; (d1-3) VR1. Immunostaining to calretinin, NF200, CGRP and VR1. Magnification 10x, scale bar 100 µm.

The effects of pentoxifylline and caffeic acid phenethyl ester in the treatment of D-galactosamine-induced renal injury in rats

Elif Taslidere (1), Mukaddes Esrefoglu (1), Nigar Vardi (2), Merve Gökşin Karaaslan (3)

1) Department of Histology and Embryology, Faculty of Medicine, Bezmialem Vakif University, İstanbul, Turkey

2) Department of Histology and Embryology, Faculty of Medicine, Inonu University, Malatya,Turkey

3) Department of Chemistry, Faculty of Science, Inonu University, Malatya, Turkey

Keywords: D-GalN, CAPE, PTX , kidney

D-Galactosamine (D-GalN), which is an established experimental toxin, primarily causes liver injury by the generation of free radicals and depletion of UTP nucleotides (1). D-GalN intoxication also induces renal dysfunction thus, renal failure is often associated with the end-stage of the liver damage (2). We have investigated both curative effects of pentoxifylline (PTX) and caffeic acid phenethyl ester (CAPE) in this study. The animals were randomly divided into six groups each consisting of seven rats. Control, D-GAL group: Rats received single i.p. injection of D-GAL (500 mg/kg body weight) dissolved in 0.9% saline on day 0, and at the end of 21st day, they were killed. D-GAL + PTX group: rats received single i.p. injection of D-GAL on day 0 and were treated with PTX dissolved in 0.9% saline at a dose of 50 mg/kg/day for 20 days. D-GAL +CAPE group: rats received single i.p. injection of D-GAL on day 0 and they were treated with CAPE dissolved in 4% ethanol at a dose of 10 mmol/kg body weight for 20 days, CAPE group (10 mmol/kg) and PTX group (50 mg/kg/day). At the end of the experiment, rats were killed by ketamine anesthesia and kidneys were removed. Samples were used for histopathological examination and evaluation of oxidative stress parameters by biochemical methods. Kidney tissue was fixed in 10% formalin and was embedded in paraffin. Tissue sections were cut at 5mm, mounted on slides, stained with hematoxylin– eosin for histopathological examination. In histological evaluations, the kidneys of the control, CAPE and PTX groups showed normal histologic features. However in the GAL group, extensive cortical damage was observed. The affected glomeruli showed shrinkage. Furthermore, interstitial

hemorrhage and inflamatuar cell infiltration were seen in the GAL group. In biochemical analysis, there was an increase in MDA level, while a decrease was observed in GSH activity in group treated to GAL compared to control group ($p<0.05$). On the other hand, there was no statistically significant change in mean GPx activity in GAL group when compared with the other groups ($p>0.05$). However, it was seen that, in the group treated to GAL, histological and biochemical injuries in the kidney were recovered by administration of PTX and CAPE ($p<0.05$). In this study showed that ameliorative effects of PTX and CAPE on GAL induced renal injury.

References:

1. Kmiec Z et al., Acta Biochim Pol (2000) 47:349–353.

2. Javle P. Et al., Gut (1998) 43:272–279.

Serial passaging effects the carcinogenicity, semness and speroid formation of HEPG2 cells, a hepatocellular carcinoma cell line

Olgu Enis Tok (1), R. G. Aktas (2)

1) Bezmialem Vakif University, School of Medicine, Department of Histology and Embryology, Istanbul, Turkey

2) Maltepe University, School of Medicine, Department of Histology and Embryology and Cancer and Stem Cell Research Center, Istanbul, Turkey

Keywords: HepG2, liver cancer stem cell, tumorsphere, OV6, AFP

Introduction: Hepatocellular carcinoma (HCC) is, worldwide, the fifth most common cancers. The liver cancer stem cells (CSCs) have been reported in multiple subtypes of HCC (1). Expressions of some stem cell markers have also been shown in HepG2 cells, a HCC cell line (2). Serial *in vivo* passaging is known to increase the stemness of CSCs (3). Additionaly, it has been shown that CSCs have tendency to aggregate and form spheres known as tumorspheres. We designed this study to examine the relationship between the passage numbers (7th and 14th passages) of HepG2 cells and the formation of spheroids, the carcinogenicity and the stemness. We examined the expression of (i) OV6, as a marker for liver stem/progenitor cell, (ii) alpha fetoprotein (AFP), as an early biomarker for the diagnosis of HCC, (iii) proliferation cell nuclear antigen (PCNA) positivity, as a proliferation marker, and (iv) TUNEL positivity, as an apoptotic index. Materials and methods: HepG2 cells were cultured between 7th and 14th passages. The cells from 7th and 14^{t}h passages were fixed in 4% paraformaldehyde and labeled with OV6, AFP or PCNA, as primary antibodies. Dylight 488 conjugated secondary antibody and Histostain-plus kit were used as secondary antibodies. The number of PCNA and TUNEL positive-stained HepG2 cells were calculated in 10 different fields of each section at 200X magnification. To evaluate the interaction between the staining pattern and the size of spheroids; the spheroids were classified into two groups : The ones containing less than 10 cells (10<) and more than 10 cells (10>). The intensity of OV6 and AFP positive cells and tumorspheres were examined under laser scanning confocal microscope (Carl Zeiss, LSM 780). The data was statistically evaluated. Results: (i) The staining density with OV6 was

significantly higher in 14th passage than 7th passage (p<0,0001). Additionally, statistical difference was detected when compared the size of spheroids (spheroids containing less than 10 cells (10<) (p<0,0001) and more than 10 cells (10>) (p<0,001) and the passage number (7th and 14th passages). There was no significant change at the Ov6 staining intensity when compared the small and big spheroids in 14th passage. The intensity of OV6+ spheres in 14th passage group was higher than the 7th passage. (ii)The intensity of AFP was significantly higher (p<0,0001) in 14th passage when compared with the 7th passage. Statistical difference was also detected during the comparison of the size of spheroids and the passage number (p<0,0001). The intensity of AFP+ spheres in 14th passage was higher than 7th passage. (iii) Proliferation index was significantly higher (p<0,01) in 14th passage than 7th passage. PCNA negative cells were generally seen as single cell in culture. They were rarely observed in spheroids in microscopic analysis. (iv) No significant difference was found between groups for apoptotic index. TUNEL + cells were rarely observed in spheroids. Conclusions: The results of the study support the hypothesis that the stemness, carcinogenity, proliferation capacity and spheroid formation of HepG2 cells increase as the passage number increase. The increase at proliferation capacity is compatible with the changes at carcinogenity and stemness. Apopitotic index has not been effected and is considered as low, as found in many cancer types. This can be used as a useful model for the studies related with liver cancer stem cells and carcinogenic features of hepatocellular carcinoma.

References:

1. S.O. Min et al., Cancer Cell Int (2015) 15:95.

2 Z. Zhu et al., Int J Cancer 2010;126(9):2067–78.

3. J.E. Visvader et al., Nat Rev Cancer 2008; 8: 755–768.

Collagen scaffold for human mesenchymal stem cells osteogenesis induction

Veronika Blahnova (1), Eva Filová (1), Veronika Svachova (2), Martin Trunec (2), Lucy Vojtova (3), Evzen Amler (4)

1) 2. Faculty of Medicine of Charles University, V Úvalu 84, 150 06 Praha 5, Institute of experimental medicine of Czech Academy of Sciences, Vídeňská 1083, Praha 4, Chech Republic

2) CEITEC (Central European Institute of Technology), Purkyňova 648/125, 621 00 Brno-Medlánky, Chech Republic

3) CEITEC(Central European Institute of Technology), Purkyňova 648/125, 621 00 Brno-Medlánky, SCITEG , a.s., U vodárny 2965/2, 616 00 Brno – Královo Pole, Chech Republic

4) Institute of experimental medicine of Czech Academy of Sciences, UCEEB (University Centre for Energy Efficient Buildings), Třinecká 1024, 273 43 Buštěhrad, Chech Republic

Keywords: osteogenesis, collagen, scaffold, hMSCs

Bone fractures and other bone defects caused by an accident or other pathology are one of the most frequently bad healing wounds. Sometimes the size of defect is so called critical. Such a defect has poor ability of regeneration and also a bad prognosis of its function restoration.(1) Implantation of noncellular biocompatible foamed scaffold made of collagen type I and other inorganic substances which naturally occur in bone extracellular matrix could work as a promising alternative therapy of this kind of injuries. We were testing scaffolds with different pore size and made of collagen type I, tricalcium phosphate and calcium phosphate. Porous scaffolds were prepared by lyophilization from the material Lyopor (Sciteg, a.s.). Morphology of each scaffold was determined by scanning electron microscopy. For cellular viability evaluation we used MTS assay based on reduction of substrate by mitochondrial enzymes. We also used rt-PCR to relatively quantify expression of osteogenic transcription factor RunX2 and extracellular protein collagen type I. For staining of another protein osteocalcin the immunohistochemical staining was used. Samples were observed using confocal microscopy. During 21 days lasting cultivation we showed, that no of tested scaffolds had cytotoxic effect on the human mesenchymal stem cells. Scaffold made of collagen and

calcined hydroxyapatite seemed to be the most suitable for ColI and RunX2 mRNA expression stimulation. Proliferation of the cells was also supported for the whole period of cultivation, which means the scaffold provided sufficient mechanical support to the cells. Weak osteocalcin synthesis was observed in some experimental groups. There is therefore need to evaluate samples cultivated longer than 21 days, in order to the cells are confluent for a longer time. In general we can assume that more significant influence on osteogenic differentiation and proliferation of hMSCs had the material of certain scaffold compared to its size of pores.

Acknowledgements:

This research was supported by Ministry of health of the Czech Republic, project no. VES 16-28637A and Ministry of youth education and sports of the Czech Republic, projects no. RP NPU I:LO1309 and LQ1601.

References:

1. Schmitz JP, Hollinger JO, Clin. Orthop. Relat. Res. (1986) (205):299-308.

Cell-free scaffolds functionalized with bioactive compounds for treatment of bone defects

Vera Lukášová (1), Michala Rampichová (2), Matej Buzgo (1), Veronika Blahnova (2), Eva Filová (2), Evzen Amler (1)

1) Laboratory of Tissue Engineering, Institute of Experimental Medicine, Academy of Sciences of the Czech Republic, Videnska 1083, 142 20 Prague 4, Czech Republic

2) University Center for Energy Efficient Buildings, Czech Technical University in Prague, Trinecka 1024, 273 43, Bustehrad, Czech Republic

Keywords: scaffold, osteogenic supplements, osteogenic differentitation, Saos2 cells

A cell-free scaffold for use in bone tissue engineering should serve as a suitable scaffold for cells migrating into the side of the defect and as well should promote cell adhesion. At the same time, scaffold serves as a drug delivery system. The advantage of this system is the gradual release of bioactive substances from the scaffold. The present study focusses on comparison of polycaprolactone (PCL) scaffolds functionalized with enclosed osteogenic supplements (OS), namely β-glycerolphosphate (β-GP), ascorbate-2-phosphate (asc) and dexamethasone (dex), at various concentrations. OS are substances commonly used for induction of osteogenic differentiation *in vitro* (1). Results showed that PCL scaffolds with enclosed OS statistically promoted metabolic activity, proliferation and differentiation of cultured Saos2 cells compared to control groups. PCL scaffolds with enclosed OS at different concentrations were prepared by the method of centrifugal spinning and designated SM1, SM2, SM5 and SM10 (according to increasing concentrations of OS used in the process of centrifugal spinning). The scaffolds were seeded with Saos2 cells and cultured for 21 days in growth medium without OS (SM1, SM2, SM5, SM10). Control groups were seeded on non-modified PCL scaffolds and incubated either in growth medium (CGM) or in medium supplemented with OS (COM). The metabolic activity of cells was determined using the MTS assay, cell proliferation was measured by the PicoGreen assay, adhesion and proliferation was further monitored by confocal microscopy and scanning electron microscopy and cell differentiation was verified by q-PCR. SM1-10 groups, with enclosed OS, promoted cell proliferation statistically more during first two weeks compared to control groups. On day 21,

the lowest cell growth was detected on the COM group. Highest metabolic activities were detected on the SM1-10 groups. Expression of collagen I, a marker of osteogenic differentiation, had an increasing tendency along with the increasing concentration of enclosed OS with the peak reached on the SM5 group. Release of OS enclosed in the PCL scaffold had a positive effect on increased metabolic activity and cell proliferation compared to control groups (CGM and COM). In addition, scaffolds with enclosed OS promoted the expression of collagen I and thus the osteogenic differentiation of Saos2 cells. The results indicate that PCL scaffolds with enclosed OS exhibited suitable biocompatible properties and promoted osteogenic differentiation of Saos2 cells. SM5 is the most suitable scaffold for further testing.

Acknowledgements:

This study has been supported by the Ministry of Education, Youth, and Sports of the Czech Republic (Research Program NPU I:LO1309) and the Czech Science Foundation (Grant No. 15-15697S).

References:

1. Coelho MJ, Fernandes MH. Human bone cell cultures in biocompatibility testing. Part II: effect of ascorbic acid, β-glycerophosphate and dexamethasone on osteoblastic differentiation. Biomaterials. 2000;21(11):1095-102.

Daidzein does not fully reverse changes of pituitary castration cells in rat: immunohistochemical and stereological study

Nestorović Nataša (1), Svetlana Trifunović (1), Milica Manojlović-Stojanoski (1), Ivana Jarić (1), Nataša Ristić (1), Branko Filipović (1), Branka Šošić-Jurjević (1), Verica Milošević (1)

1) University of Belgrade, Institute for Biological Research "Siniša Stanković“, 142 Despot Stephan Blvd, 11000 Belgrade, Serbia.

Keywords: daidzein, soy, castration cells, unbiased stereology

Daidzein is a soybeans-derived isoflavone that has structural and functional similarity to 17 beta-estradiol. It competes with endogenous estrogens for binding to estrogen receptors with preferential binding affinity for estrogen receptor beta over alpha (1). The aim of this study was to examine the potential of daidzein to recover castration cells after long-term orchidectomy (Orx) of adult rats, by quantifying changes in their morphology and intracellular hormone content. To that end we have used design-based stereology that still remains one of the pillars of quantitative biomedical research. Estradiol-dipropionate treatment was used as a positive control. Two weeks post orchidectomy (Orx), adult male rats subcutaneously received 30 mg of daidzein or 0.625 mg of estradiol-dipropionate per kg b.w. for three weeks. Control sham-operated (So) and Orx rats were injected with the solvent. Changes in the volume of pituitary pars distalis, the volumes of individual follicle-stimulating hormone (FSH) and luteinizing hormone (LH) immunoreactive cells, their volume and numerical densities, and number per pars distalis were determined. The FSH and LH intracellular content was estimated by relative intensity of fluorescence. Orchidectomy caused hyperstimulation and hyperplasia of gonadotropes and formation of castration cells that are characterized by prominent vacuolation of cytoplasm. All examined stereological parameters and relative intensity of fluorescence were increased comparing to So controls. After estradiol treatment, gonadotropic cells were smaller in size, polyhedral in shape with homogenous cytoplasm. Volume of gonadotropic cells, their volume and numerical density, as well as intracellular hormone contents, significantly decreased comparing to Orx controls. The parameters that did not return to the level of So controls and in contrast increased, are number of gonadotropic cells and volume of pars distalis. Castration cells in the pituitaries of daidzein-treated rats appeared smaller comparing

to those of Orx males, but vacuolation of cytoplasm was still apparent. Significant decrease of volume of FSH- and LH-labeled cells by 15.4% and 14.4%, respectively, was observed. Additionally, intracellular FSH and LH contents decreased by 50.1% and 41.9%, respectively. Comparing to the values of Orx controls, the number of FSH- and LH-immunoreactive cells per pituitary pars distalis increased by 37.7% and 72.1%, respectively, upon daidzein treatment. The volume density of gonadotropes and the volume of pars distalis remained unchanged. The results of this study suggest that daidzein had an estradiol-like effect by reversing some of examined parameters. However, having in mind that volume and numerical densities of gonadotropic cells remained unchanged or increased, respectively, it can be concluded that dadzein does not have potential to fully recover castration cells in the model of adult Orx rats.

References:

1. C. R. Cederroth et al., Mol. Cell. Endocrinol. 355 (2012) 192-200.

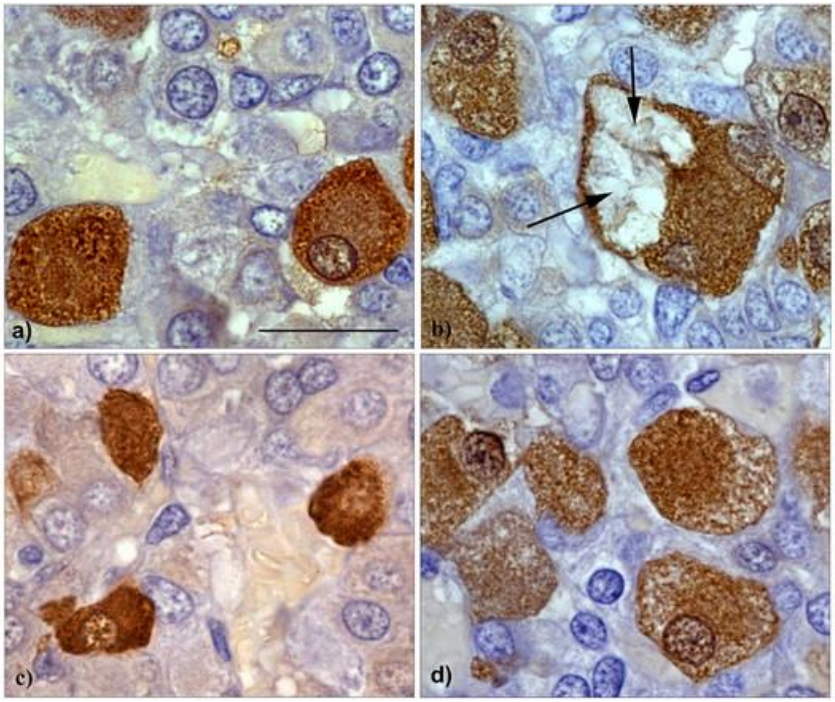

Figure 1. Immunohistochemicaly stained LH cells in the pituitaries of sham-operated (a), orchidectomized (b) estradiol- (c) and daidzein-treated orchidectomized rats. Arrows – vacuolated cytoplasm in the pituitary of orchidectomized rat. Bar- 20 micrometers.

The preparation of biological objects for 3D scanning electron microscopy

Jana Nebesarova (1), Marie Vancova (1), Petra Masarova (1), Jiri Vanecek (1)

1) Biology Centre of CAS, Branisovska 31, 370 05 Ceske Budejovice, Czech Republic

Keywords: SBFSEM, specimen preparation of biological objects, charging, trimming procedure

Serial block face scanning electron microscopy (SBFSEM) is one of current methods which can be used for a 3D reconstruction of large tissue volumes. A small ultramicrotome is placed directly in the SEM chamber and used for cutting of ultrathin sections from the specimen. The new revealed surface of the specimen block is then imaged by detection of backscattered electrons. The sequence of block cutting and sample imaging is repeated and can acquire a thousands of images with perfect alignment in an automated way. Biological sample preparation for this method is based on a procedure that is similar to that used for transmission electron microscopy, starting by aldehyde fixation, staining with heavy metals and embedding in epoxy resins. The improved protocols designed to enhance the signal for backscattered electron imaging were suggested by Denk and Horstman (2004) or Deerinck et al. (2010). They include an increased number of staining steps like ferrocyanide reduced osmium tetroxide post fixation followed by thiocarbohydrazide-osmium liganding and subsequent uranyl acetate and lead aspartate en bloc staining. Regardless of the increased presence of heavy metals, we can observe sometimes heavy charging of the revealed epoxy block surface with an embedded biological sample during the exposition to primary electrons. The aim of this study was to test embedding and trimming parameters and their influence on the charging effect. We measured the electric conductivity and the hardness of different variants of epoxy resins, compared the influence of different trimming tools on the smoothness of the resin block sides and exposed face from which the ultrathin sections were cut (*Figure*1). We tested the way how to stick optimally the trimmed block to a pin and also we tried the choice of other staining procedure.

Acknowledgements:

We thank to Helmut Gnaegi (Diatome) for help with trimming of blocks. This study was supported by the Technology Agency of the Czech Republic (TE01020118).

References:

1. W. Denk, H. Horstmann, S, PLoS Biol. 2 (2004), 1900–1909

2. T.J. Deerinck, E. A. Bushong, V. Lev-Ram, X.Shu, R.Y.Tsien, M.H. Ellisman, Microsc. Microanal., 16 (2010) Suppl.2.

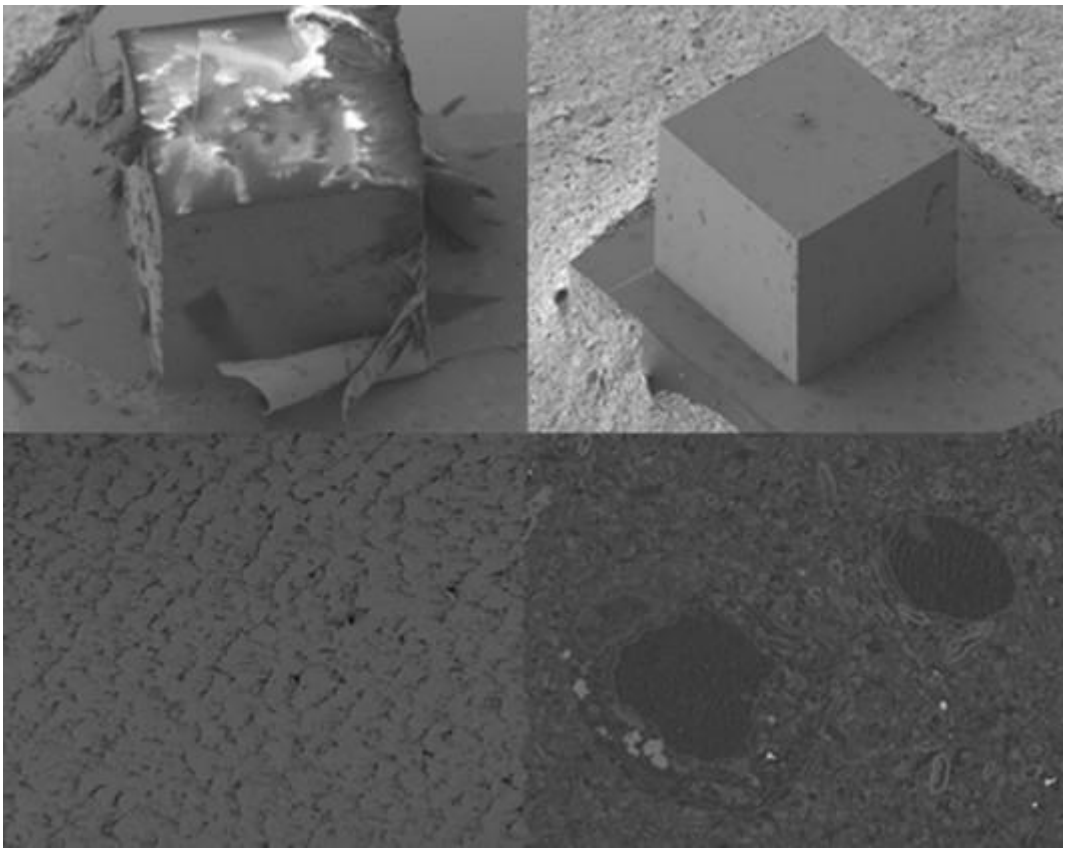

Figure 1. The comparison of blocks with brain tissue in epoxy resin (EMbed 812, hard, EMS) trimmed for SBFSEM using a glass knife (left) and a diamond trimming tool 90° (Diatome) (right). The ultrastructure of the surface of side walls exhibits huge differences, which can influence charging during the observation in SEM.

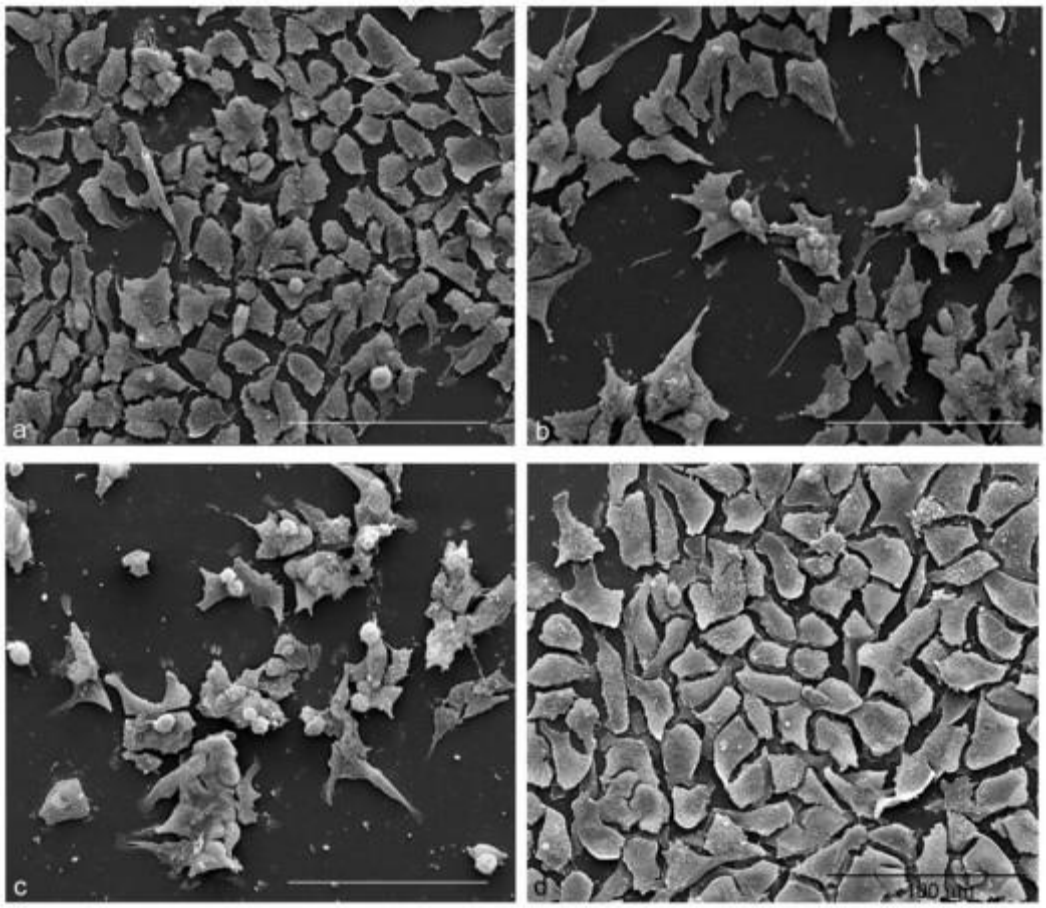

Figure 2. SEM observations of untreated HCT116 cells (a), treated with PsT® 2 mg/ml plus NAC (b), PsT® 4 mg/ml plus NAC (c) or 5-fluorouracil 300 micronMolar, as positive control (d).

Ozone treatment induces antioxidant stress response through Keap1/Nrf2 dependent pathway

Alice Nodari (1), M. Galiè (1), F. Boschi (2), V. Covi (3), G. Tabaracci (3), Manuela Malatesta (1), Manuela Costanzo (1)

1) Dept of Neurosciences, Biomedicine and Movement Sciences, University of Verona, Italy

2) Dept of Computer Science, University of Verona, Italy

3) Poliambulatorio San Rocco, Montichiari (BS), Italy

Keywords: ozone therapy, Nrf2, Keap1, ARE, oxidative stress

Recently ozone therapy has been applied successfully as adjuvant therapy in the treatment of several disorders such as rheumatoid arthrıtis, heart and vascular disease, asthma emphysema and multiple sclerosis (1). Positive effects of ozone therapy have been hypothesized to rely on the capability of mild acute oxidative stress to induce antioxidant response. Nevertheless, molecular mechanisms behind those beneficial effects remain unclear. Some evidence suggests that mild oxidative stress induced by ozone treatments leads to activation of the transcription factor Nrf2 (nuclear factor erythroid-derived-like2) (2). Nrf2 regulates the expression of genes under the control of antioxidant response element (ARE) enhancer. These genes include drug metabolizing enzymes, such as glutathione s-transferases (GSTs) and NAD(P)H-quinone Oxidoreductase 1 (NQO1), and antioxidant genes, such as heme oxygenase-1 (OH-1), the subunit of γ-glutamylcysteine synthetase (γ-GCS) and thioredoxin. Under basal conditions, Nrf2 is sequestered in the cytoplasm by its specific inhibitor Keap1 (Kelch-like ECH associated protein), which promotes Nrf2 ubiquitination and proteasomal degradation within a few minutes after its transcription. Under specific stimuli, Nrf2 dissociates from Keap1 and is preserved from degradation. Then, Nrf2 translocates into the nucleus, heterodimerizes with Maf proteins and trans-activates ARE-mediated genes. The current study was designed to investigate whether ozone therapy might induce ARE activation via Nrf2-dependent mechanisms. First, we established a HeLa cell line engineered to express NanoLuc Luciferase under the control of ARE promoter. We show that the treatment with different concentrations of ozone increased ARE-driven expression of NanoLuc in a dose-

dependent manner (*Figure* 1a). Ultrastructural immunocytochemistry showed Nrf2 to be associated to perichromatin fibrils, which are sites of active transcription (*Figure* 1b). Hela cells were transiently transfected with Nrf2-GFP and/or Keap1-dsRed fusion proteins to enable microscopy visualization of Nfr2 and Keap1 subcellular localization (*Figure* 2a). As expected, in untreated cells Nrf2-GFP disappeared when co-transfected with Keap1-dsRed. In contrast, ozone treatment induced persistence of Nrf2-GFP fluorescence and its massive nuclear translocation, suggesting that ozone might prevent Keap1-mediated Nrf2 degradation. In line with this conclusion we found an increased amount of Nrf2 protein compared to controls over 30 minutes after ozone treatment (*Figure* 2b), likely due to an increased Nrf2 stability. Finally, Keap1 transient overexpression partially reverted ARE-Luc activation in ozone treated cells (*Figure* 2c), thus providing further evidence that ozone treatment is able to induce an antioxidant stress response through a Keap1/Nrf2-dependent pathway.

Acknowledgements:

This research was supported by University of Verona, Italy (Joint Projects 2015).

References:

1. I. Zanardi et al., Curr. Med. Chem. 23 (2016) 304-314.

2. A. Pecorelli et al., Toxicol. Appl. Pharmacol. 267 (2013) 30-40.

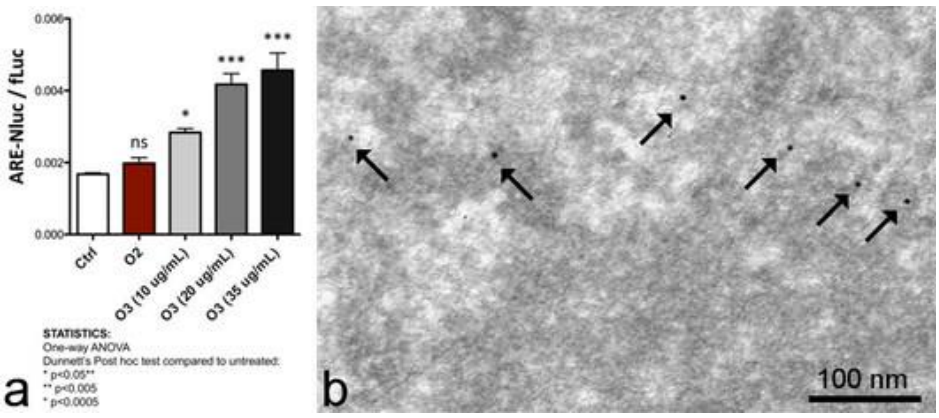

Figure 1. (a) Ozone activates ARE-driven genes expression in a dose-dependent manner. ARE/NLuc was co-transfected and normalized to PGK-driven firefly Luciferase (fLuc). (b) Immunoelectron microscopy: Nrf2 occurs in perichromatin fibrils (arrows).

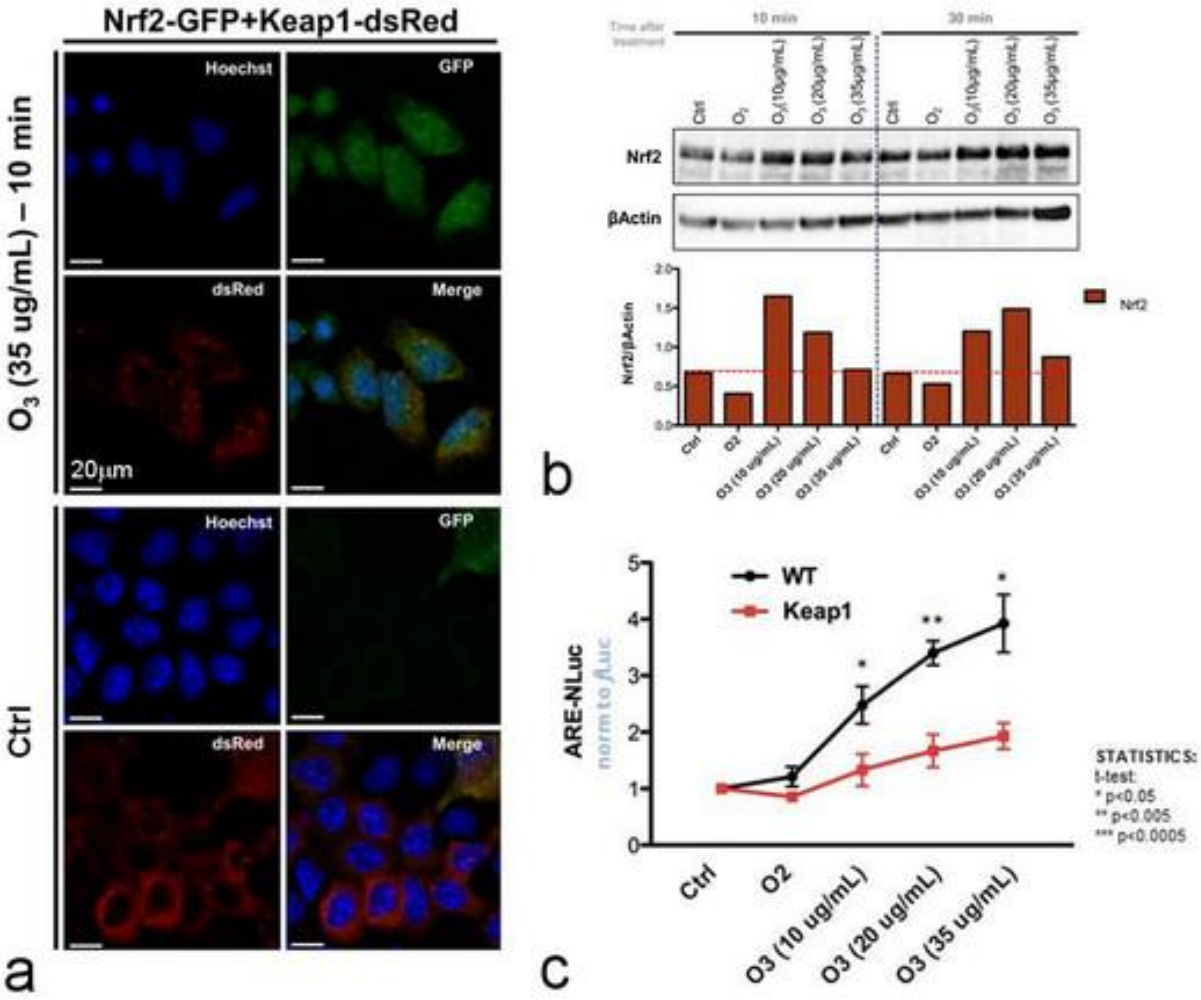

Figure 2. (a) Nuclear translocation of Nrf2 after ozone treatment. (b) Increase of Nrf2 protein due to ozone treatment. (c) Keap-1 suppresses ozone-induced activation of ARE-driven genes. ARE/NLuc was co-transfected and normalized to PGK-driven fLuc.

Hypothyroidism induces maturation arrest of spermatogenesis in adult rat

Isidora Protic (1), Igor Golic (2), Marija Aleksic (2), Vesna Otasevic (3), Aleksandra Korac (2)

1) Department of Reproductive Assistive Technology, Clinic for Gynecology and Obstetrics, Clinical Center of Serbia, Belgrade, Serbia
2) Center for Electron Microscopy, University of Belgrade – Faculty of Biology, Belgrade, Serbia
3) Institute for Biological Research “Sinisa Stankovic”, University of Belgrade, Belgrade, Serbia

Keywords: rat testis, hypothyroidism, spermatogenesis

Thyroid hormones are important for regulation of development, differentiation and metabolism in various mammalian tissues. The thyroid hormones effects on male reproductive system mainly related to proliferation and differentiation of Sertoli and Leydig cells during spermatogenesis. Induced chronic hypothyroidism in rats, from birth to adulthood, may be associated with delayed maturation of the testis, impaired spermatogenesis, germ cells degeneration, and reduced seminiferous tubule diameter. The goal of this study was to investigate the effect of induced hypothyroidism on the Leydig, Sertoli and spermatogenic cell number in seminiferous tubules. Two months old male Wistar rats were divided into two groups and treated for 21 days.Control group received tap drinking water while in hypothyroid group, methimazole was added to drinking water. At the end of experiment, testicles were isolated and fixed in 4% buffered formaldehyde and later routinely dehydrated and embedded in paraffin. 5 μm sections were stained with hematoxylin and observed on Leica DMLB microscope equipped with Leica DFC295 camera. Acquired micrographs were analyzed for total number of Leydig cells, Sertoli cells, spermatogonia, spermatocytes and spermatides per tubule using ImageJ software. The results showed significant decrease in Leydig cell number, while Sertoli cell and spermatogonia number was increased. Number of spermatids and spermatocytes per tubule was not affected. It can be concluded that methimazole-induced hypothyroidism lowers Leydig cells amount in adult rat testicle along with and increases of the pool of spermatogonia and supporting Sertoli cells leading to maturation arrest of spermatogenesis.

Acknowledgements:

This work was supported by Serbian Ministry of Education, Science and Technological Development, Grant #173054.

Microscopy in urolithiasis research

Vesna Babić-Ivančić (1,3*), Maja Dutour Sikirić (1), Anamarija Stanković (2), Silvija Šafranko (2)

1) Ruđer Bošković Institute, Bijenička cesta 54, HR-10000 Zagreb, Croatia

2) Department of Chemistry, J. J. Strossmayer University of Osijek, HR-31000 Osijek, Croatia

3) 3 Faculty of Medicine, J. J. Strossmayer University of Osijek, HR-31000 Osijek, Croatia

*Retired in 01. 01. 2014

Keywords: urolithiasis, microscopy, crystals, calcium oxalate

The crystallization is process of the formation a crystalline phase from a parent phase, e.g. solution. The normal (bone, teeth, shells) and pathological mineralized tissues (stones, caries, gouty arthritis, arteriosclerosis) are biominerals in human body and animals. The formation of biominerals, is the formation of sparingly soluble salts from body fluids (blood, serum, urine) within an organic macromolecular matrix. Processes involved in pathological mineralization are of special interest due to the great medical and social problems that they cause. Urolithiasis, a form of pathologic biomineralization, is a disease which causes the formation of urinary stones in different parts of kidney or bladder (1). The kidney stones formation under biological conditions can be triggered by various metabolic disorders such as: hipercalciuria, hypocitraturia, hiperoxaluria and the change in the urine acidity. The mechanisms and the conditions under which they crystallize are still not completely clarified. In this work, the crystallization from supersaturated solution in model system, calcium oxalates, calcium phosphates, magnesium phosphates, uric acid and/or salts of the uric acid, also in artificial urine were reported. The reactant solutions were mixed under controlled hydrodynamic and thermodynamic conditions; pH, ionic strength, temperature. The influence of aditives, macromolecules on crystal growth morphology and on the composition of the crystallizing phase were determined. The crystalluria from real urine system as one indicator the formation

of calculi were compared with the morphology and composition of crystals which crystalized in model systems. The changes in the composition and morphology of precipitated salts were observed by means of PXRD, light microscopy (Figure 1.), TEM, SEM, IR and TGA.

References:

1. B. Hess, R.L.R., J. Kavanagh, S.R. Khan, D.J. Kok, A.L. Rodgers, H.G Tiselius, *Eur. Urol*. **40** (2001) 220-230.

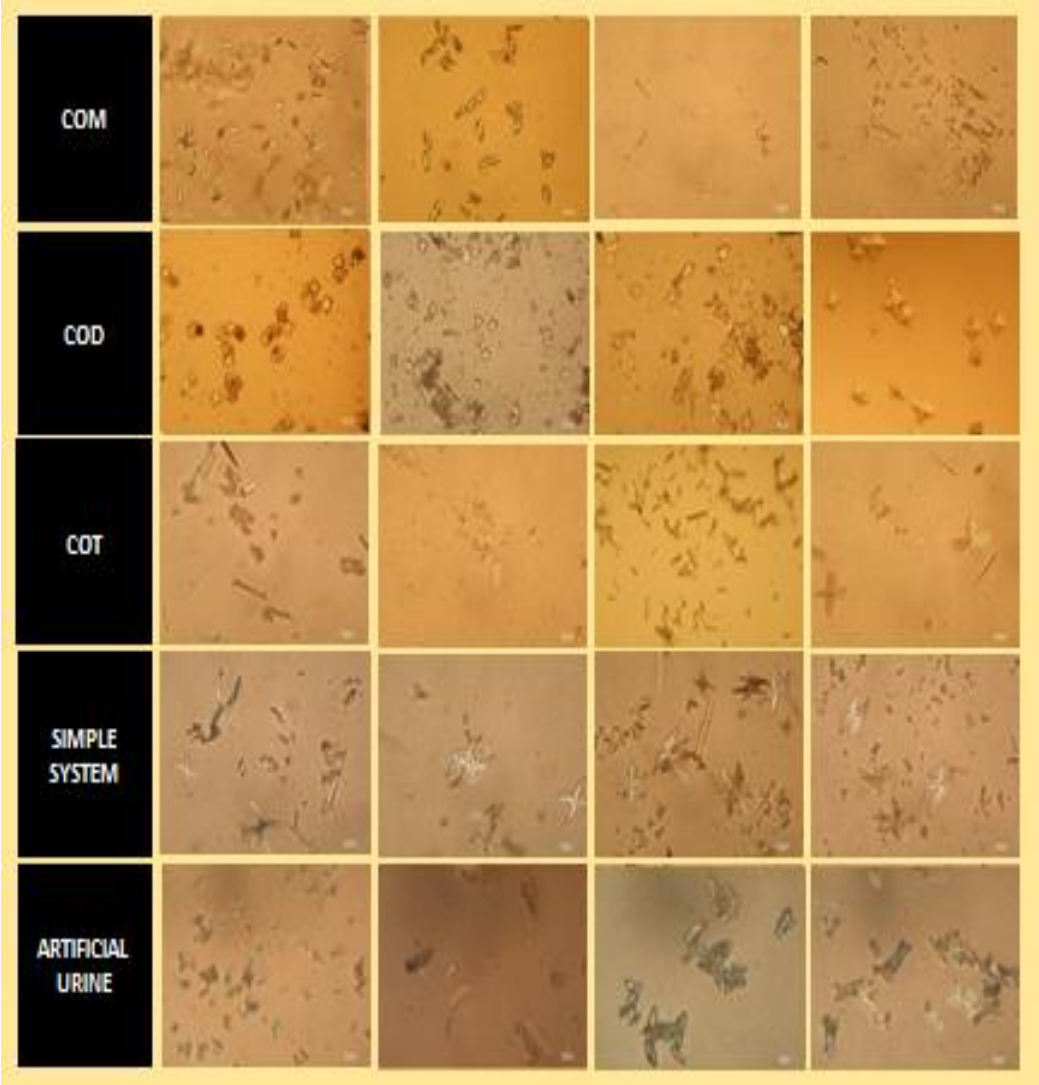

Figure 1. Light microscopy images of calcium oxalate precipitated at differents initial conditions.

The effects of dipeptidyl peptidase-4 inhibitor treatment on liver regeneration in STZ-diabetic rats

Melek Ozturk (1), Fatma Kaya Dagistanli (1), Gamze Argun Kurum (1), A. Seda Akdemir (1), Merve Anapali (1), Gamze Tanriverdi (2)

1) Istanbul University, Cerrahpasa Faculty of Medicine, Medical Biology Department, Turkey

2) Istanbul University, Cerrahpasa Faculty of Medicine, Histology and Embryology Department, Turkey

Keywords: Liver regeneration, Oval cells, neonatal STZ-diabetes, DPP-4 inhibitor

Diabetes mellitus is a severe metabolic disorder. Type-2 diabetes is one of the main causes of diabetic liver diseases. The development of the chronic liver diseases and glucose intolerance are related with dipeptidyl peptidase-4 (DPP-4). Vildagliptin (VG), a DPP-4 inhibitor, regulates insulin secretion and plasma glucose levels. Hepatic oval (Ov) cells as precursors both hepatocytes and bile duct cells are involved the liver regeneration. Streptozotocin (STZ), pancreatic beta cell toxin, induces hyperglycemia and Diabetes Mellitus (1-3). In this study, we aimed to examine the effects of long term VG treatment on liver regeneration in neonatal STZ-diabetic (nSTZ) rats after diabetic liver injury. In this study four groups using Wistar albino rats were performed; (1) control, (2) diabetic (n2STZ) (STZ;100mg/kg, i.p. injected second day after birth), (3) VG-treated diabetic (n2STZ+VG) (VG; 60mg/kg/day, oral during 28 days), and (4) only VG (VG; 60mg/kg/day, oral during 28 days). Body weights and blood glucose levels of all groups were measured. The liver paraffin-embedded tissue sections were stained with hematoxylin and eosin, Masson trichrome and PAS stain, also they were stained immunohistochemically with Ov-6 (for hepatic precursor cells) and PCNA (for proliferation index) antibodies by using the streptavidin-biotin peroxidase technique. All values were analyzed with statistical methods. Blood glucose levels significantly increased in n2STZ groups compared to the other groups. In diabetic group there was lymphocytic infiltration and increased collagen fibers, and also cytoplasmic vacuolization, depleted glycogen and binuclear morphology in most hepatocytes. Oval cells were located predominantly in the periportal region and fibrosis septa on the n2STZ groups. Ov-6 is a marker for newly formed hepatocytes. Ov-

6 staining was seen intensively in the n2STZ+ VG group. Ov-6 immunopositive cell were mainly located in bile ductal cells and peripheral areas of the bile ducts and spreading into the parenchymal areas. Also Ov-6 some hepatocyte like cells which are located far from the portal regions were Ov-6 immunopositive. Additionally, the PCNA index was significantly increased in the n2STZ+ VG and VG groups ($p<0.001$) versus the nSTZ group. Our results indicate that long term VG treatment for diabetic liver injury reduces hyperglycemia, contributes to the improvement of liver histology, enhances liver regeneration which is associated with oval cell expansion, increases hepatocytes proliferation in neonatal STZ diabetic rats. DPP-4 inhibition may be a novel therapeutic approach in the therapy of diabetic liver injury for inducing the regenerative stem cells.

References:

1.K.G. Tolman et al., Diabetes Care. 30 (2007) 734–43.

2.C.K. Chakraborti. J Pharmacol. 40 (2008) 10–14.

3- 4. Y. Wan et al., J. Cell. Mol. Med. 20 (2016). 195-203

Harmful effects of dimethyl sulphoxide on WM-266-4 melanoma cell line

Barbara Dariš (1), Polonca Ferk (2), Željko Knez (3), Saška Lipovšek (1)

1) Department of Cell Biology, Faculty of Medicine, University of Maribor, Taborska 8, SI-2000 Maribor, Slovenia

2) Department of Pharmacology, Faculty of Medicine, University of Maribor, Taborska 8, SI-2000 maribor, Slovenia

3) Faculty of Chemistry and Chemical Engineering, University of Maribor, Smetanova 17, SI-2000 Maribor, Slovenia

Keywords: WM-266-4, dimethyl sulphoxide, phase-contrast microscopy, MTT

WM-266-4 is a metastatic human melanoma cell line with small flat mesenchymal morphology. The key applications of this cell line include various biological assays, drug testing and genetic studies (1). Dimethyl sulphoxide (DMSO), an amphipatic solvent soluble in both water and organic substances, is often used to dissolve hydrophobic substances in biomedical research. However, DMSO was reported to interact with the metabolism and membrane of cells, resulting in cell damage (2, 3). Nevertheless, little si known about the effect of different DMSO concentration on WM-266-4 cells. To address this question, WM 266-4 cells (ATCC®, USA) were treated with 0.1-5% DMSO concentrations for 24h. Changes in cell morphology and proliferation activity were examinated. The cells were seeded in 96-well culture plates and exposed to selected DMSO concentrations for 24h. MTT Colorimetric Cell Viability Kit IV (PromoKine, Germany) was performed to determine proliferation activity of the cells. Morphological analysis was carried out by phase-contrast microscopy, using an inverted microscope (DMI6000B, Leica). Images were taken with Leica camera DFC365 FX at 100x magnification. Significant harmful effects on cells proliferation activity were observed at 0.9% DMSO concentration. After exposure to DMSO, morphological changes of WM-266-4 were observed; cells became round in shape. Less than 25% of cells changed their morphology at 0.1-0.6% DMSO concentrations, 25-50% at 0.7-1.1% DMSO and 50-75% at 1.2-5% DMSO concentrations. Although evident harmful effects of DMSO on WM-266-4 cell line were shown,

DMSO is indispensable solvent in biological assays. However, the solvent should be used at the lowest possible concentration.

References:

1. Dokmeci, D., Testicular torsion, oxidative stress and the role of antioxidant therapy. Folia medica, 2005. 48(3-4): p. 16-21.

2. Al-Maghrebi, M., E.O. Kehinde, and J.T. Anim, Long term testicular ischemia–reperfusion injury-induced apoptosis: Involvement of survivin down-regulation. Biochemical and biophysical research communications, 2010. 395(3): p. 342-347.

3. Karaguzel, E., M. Kadihasanoglu, and O. Kutlu, Mechanisms of testicular torsion and potential protective agents. Nature Reviews Urology, 2014. 11(7): p. 391-399

1. J. Barretina et al., Nature 483 (7391) (2012) 603-607.

2. J. Hebling et al., Dental Materials 31 (2015) 399-405.

3. W. Qi et al., Hearing Research 236 (2008) 52-60.

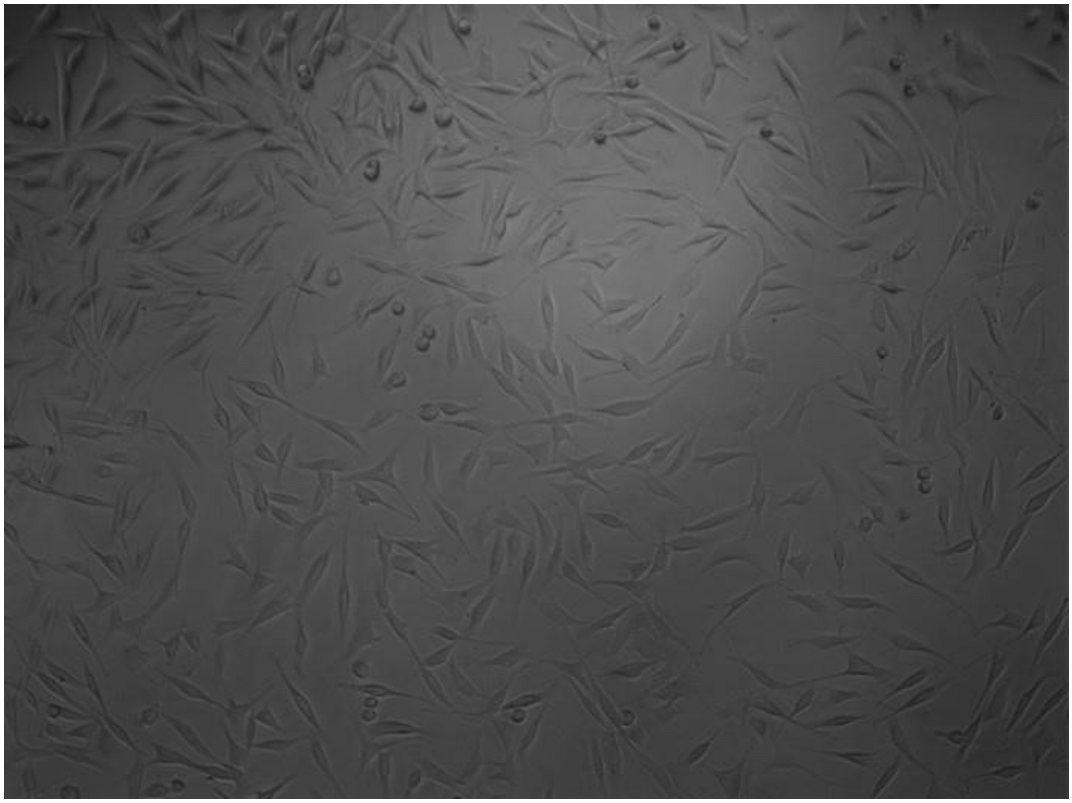

Figure 1. Typical morphological appearance of WM-266-4 cell line (magnification 100X).

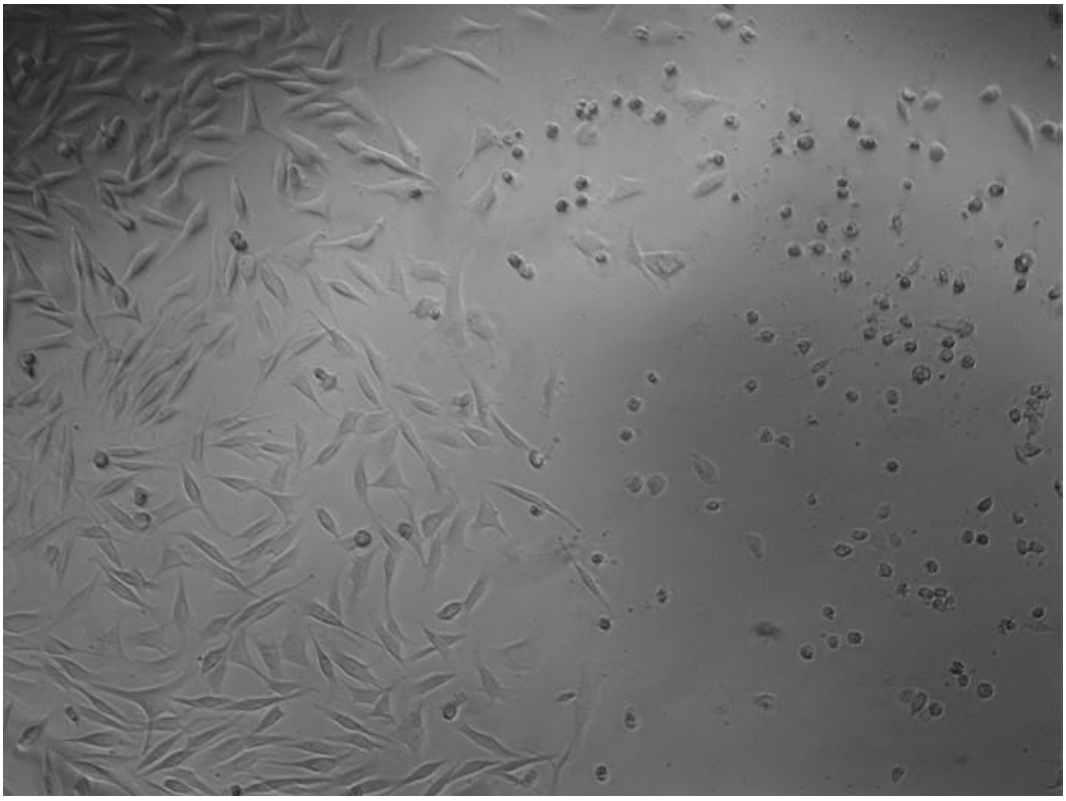

Figure 2. 25-50% of morphologically changed WM-266-4 cells after 24h of exposure to DMSO (magnification 100X).

Comparison of fiber fabrication techniques in tissue engineering

Karolina Vocetková (1), Vera Sovková (1), Matej Buzgo (2), Michala Rampichová (2), Andrea Míčková (2), Vera Lukášová (1), Evzen Amler (2)

1) Istitute of Experimental Medicine CAS, v.v.i., Videnska 1083, 140 00 Prague 4, Czech Republic

2) University Centre of Energy Efficient Buildings CTU, Trinecka 1024, 273 43 Bustehrad, Czech Republic

Keywords: nanofiber, electrospinning, forcespining, skin, SEM

Nano- and microfibrous scaffolds represent a significant area in the field of tissue engineering and regenerative medicine. Depending on the technique employed, fibrous scaffolds of varying structural and functional properties can be fabricated. The aim of the study was to prepare polycaprolactone fibers of core/shell character with encapsulated platelet lyophilizate, using electrospinning and centrifugal spinning (Forcespinning). The prepared scaffolds were characterized using scanning electron microscopy and seeded with keratinocytes and fibroblasts. Metabolic activity was tested on day 1, 7, 10, 14 and 17, as well as cell proliferation. Additionally, the cells were stained and visualized using confocal microscopy. The acquired data showed similar loading efficiency of electrospun and forcespun fibers. Additionally, the differing morphology of the scaffolds influenced the cellular behavior. Keratinocytes strongly preferred the 2D structure of the electrospun scaffolds, whereas fibroblasts showed preferential initial adhesion to the rather 3D structure of the forcespun scaffolds. Simultaneously, the proliferation of fibroblasts exhibited rather dose-dependent increase with increasing platelet lyophilizate concentration. The data suggest suitability of the fibrous scaffolds for tissue engineering applications.

Acknowledgements:

This study was supported by Czech Science Foundation Grant No. 15-15697S, University Center for Energy Efficient Buildings (UCEEB) and research project NPU I:L01508.

Regulation of pancreatic beta cell regeneration by nicotinamide in neonatal streptozotocin diabetic rats

Fatma Kaya Dagistanli (1), Melek Ozturk (1)

1) Istanbul University, Cerrahpasa Faculty of Medicine, Medical Biology Department, Turkey

Keywords: Nicotinamid, neonatal rat, STZ-diabetes, beta cell, regeneration

Streptozotocin (STZ), as an diabetogenic agents, induces DNA strand breaks in pancreatic beta-cell through the formation of free radicals. The breaks induce DNA repair involving the activation of poly (ADP-ribose) polymerase. Nicotinamide (NA), a PARP inhibitor, is a biochemical precursor of nicotinamide adenine dinucleotide that protects beta cells from several toxic agents. Our aim was to observe the effect of Nicotinamide on beta-cell apoptosis and regeneration in newborn diabetic rats. In this study 3 groups, each containing 7 neonatal Wistar albino rats, were established. The first group was the control group. The second and third groups were injected i.p with 100 mg/kg streptozotocin on the second day after birth. Second group was not given any treatment (n2-STZ). The third group received, 500 mg/kg/day NA for 5 days (n2-STZ+NA) by starting from third day. The pancreatic tissue sections were immunostained with insulin, glucagon, somatostatin, pdx-1, ngn3, notch1, jagged1, active caspase-3 and PARP antibodies and also double immunostained with insulin and PCNA antibodies. *In situ* hybridization carried out with insulin probe. TUNEL assay was used for detection of DNA degradation in apoptotic cells. Body weight and blood glucose levels of the animals in all groups were measured. All values were analyzed with statistical methods. The increase of the blood glucose levels in n2-STZ+NA group were significantly decreased by NA treatment($p<0.01$). The number of insulin/PCNA double-positive cells significantly increased in the n2-STZ+NA group compared with the other groups($p<0.001$). n2-STZ group had lower number of insulin and pdx-1 positive cells compared to NA treated diabetic group in islet.The immunopositive insulin, pdx1 and ngn3 cells were located in small cell clusters or scattered in exocrine tissue and close to ducts in n2-STZ+NA. The ngn3 expression was not in any islet. There was significant difference between the numbers of notch1 and jagged1 immunopositive cells when the n2-STZ+NA group were compared with the other groups. PARP1, active caspase-3($p<0,001$) and TUNEL ($p<0,001$) positive cells increased in n2-STZ group compared to other groups. In conclusion, we showed that NA treatment inhibits apoptosis via PARP1

inhibition, and stimulates duct epithelium or acinar cell differentiation into the beta cell via up regulation of ngn3 and pdx1, and down regulation of notch1.

Evaluation of INSL3 in diabetic testicular tissue by admministered JNK inhibition

Onur Ersoy (1), Gulnur Kizilay (1), Sinasi Bayram (1), Yeliz Bozdemir Donmez (2)

1) Trakya University, School of Medicine, Department of Histology and Embryology, 22030 Edirne, Turkey

2) Trakya University, Technology Research and Development Application Research Center, 22030 Edirne, Turkey

Keywords: Diabetes mellitus, testis, SP600125, INSL3

Diabetes mellitus is an important metabolic disease that threatens public health. Diabetic male infertility is a remarkable research topic in recent years. Insulin-like 3 (INSL3) is an important marker of Leydig cell function. c-Jun N-terminal kinases (JNKs), belong to the family mitogen-activated protein kinases, is regulate cell functions including proliferation, gene expression, differentiation, mitosis, cell survival and apoptosis. We aimed to clarify the importance of INSL3 expression of diabetic testis tissue in inhibition of JNK (SP600125). This experimental study was approved by the Ethics Committee of Trakya University. Eighteen Sprague-Dawley male rats, weighing 250–350 g, were divided randomly into three groups; I. group; control animals, received only vehicle; n=6, II. group; Diabetes mellitus (DM), single dose 60 mg/kg streptozotocin (STZ) i.p.,15 days; n=6, III. group; 60 mg/kg STZ + 15mg/kg SP600125, 15 days; n=6. After 4 weeks of the experiment, rats were sacrificed and testis tissue samples were collected. Then, fixation each tissue sample was routinely processed then embedded in paraffin. INSL3 were evaluated by using immunohistochemistry to examine Leydig cell function in the diabetic testis tissues. All data were analyzed using SPSS 20.0 for Windows software. Multiple comparisons were made among the different groups using Mann Whitney U test. P value less than 0.05 was accepted as statistically significant. INSL3 immunpositive cells count was significantly decreased in second and third groups compared with first group (P=0.004, P=0.006 respectively). On the other hand; INSL3 immunpositive cells count was significantly increased in third group compared with second group (P=0.004). We suggested that inhibition of JNK may be effective in protecting Leydig cell functions.

References:

1. A. Bener et al., Int. Urol. Nephrol. 4 (2009) 41-777.84.

2. F. Ermetici et al., Eur. J. Endocrinol. 6 (2009) 161-853.9.

3. C. Li et al., Gene. 2 (2016) 577-275.80.

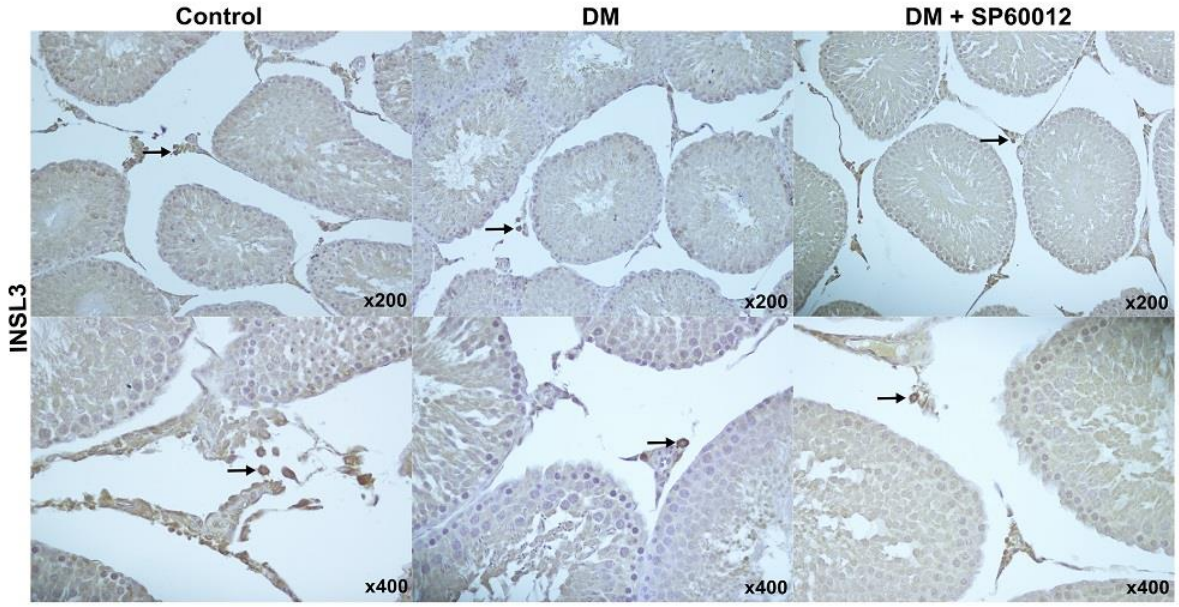

Figure 1. INSL3 immunoreactivity of the Leydig cells (→) in the interstitial area is observed. INSL3 and hematoxylin backround staining.

Effect of royal jelly on apoptosis, proliferation and immunoreactivity of INSL3 in rat diabetic testes tissue

Sirin Yavas (1), Gulnur Kizilay (2), Onur Ersoy (3), Sinasi Bayram (3)

1) Trakya University, School of Medicine, Department of Histology and Embryology, 22030 Edirne, Turkey

2) Trakya University, School of Medicine, Department of Histology and Embryology, 22030 Edirne, Turkey

3) Trakya University, Department of Histology and Embryology, 22030 Edirne, Turkey

Keywords: Diabetes mellitus, testis, INSL3, PCNA, TUNEL, apoptosis

Subfertility or infertility in diabetic male has become a major problem recently. One of the most important histopathological changes in the diabetic testicular tissue are apoptosis. We aimed to contribute the identification of new treatment protocols based on the possible therapeutic effect of royal jelly using insulin-like factor 3 (INSL3) for leydig cell function, proliferating cell nuclear antigen (PCNA) for proliferation and terminal deoxynucleotidyl transferase (tdt)-mediated dutp nick end labeling (TUNEL) for apoptosis in diabetic testicular tissue. Twenty Wistar albino male rats under stable laboratory conditions were divided into three groups. The groups were designated as the control group (n=6), the diabetic group (n=8) was administered a single dose 50 mg/kg of streptozotocin and royal jelly group (n=6) given 400 mg/kg/day royal jelly after a single dose of 50 mg/kg streptozotocin. Testicular weight (P=0.044), testis length (P=0.026) and seminiferous tubule diameter (P<0.001) were significantly higher in royal jelly group compared to the diabetic group. While PCNA immunreactivity (P<0.001) were significantly increased, apoptotic tubule indices (P<0.001) and apoptotic cell indices (P<0.001) were significantly decreased in the royal jelly group compared to the diabetic group. The number of INSL3 immunopositive cells (P=0.026) was significantly increased in royal jelly groups compared to the diabetic group. As a result, we believe that the protective effect of royal jelly may be effective in preventing male infertility caused by diabetes.

References:

1. Y.B. Donmez et al., Acta. Cir. Bras. 29 (2014) 644-50.10.

2. S. Bayram et al., Biotech. Histochem. 91 (2016) 204-11.3.

3. T. Karaca et al., Turk. J. Med. Sci. 45 (2015) 27-32.

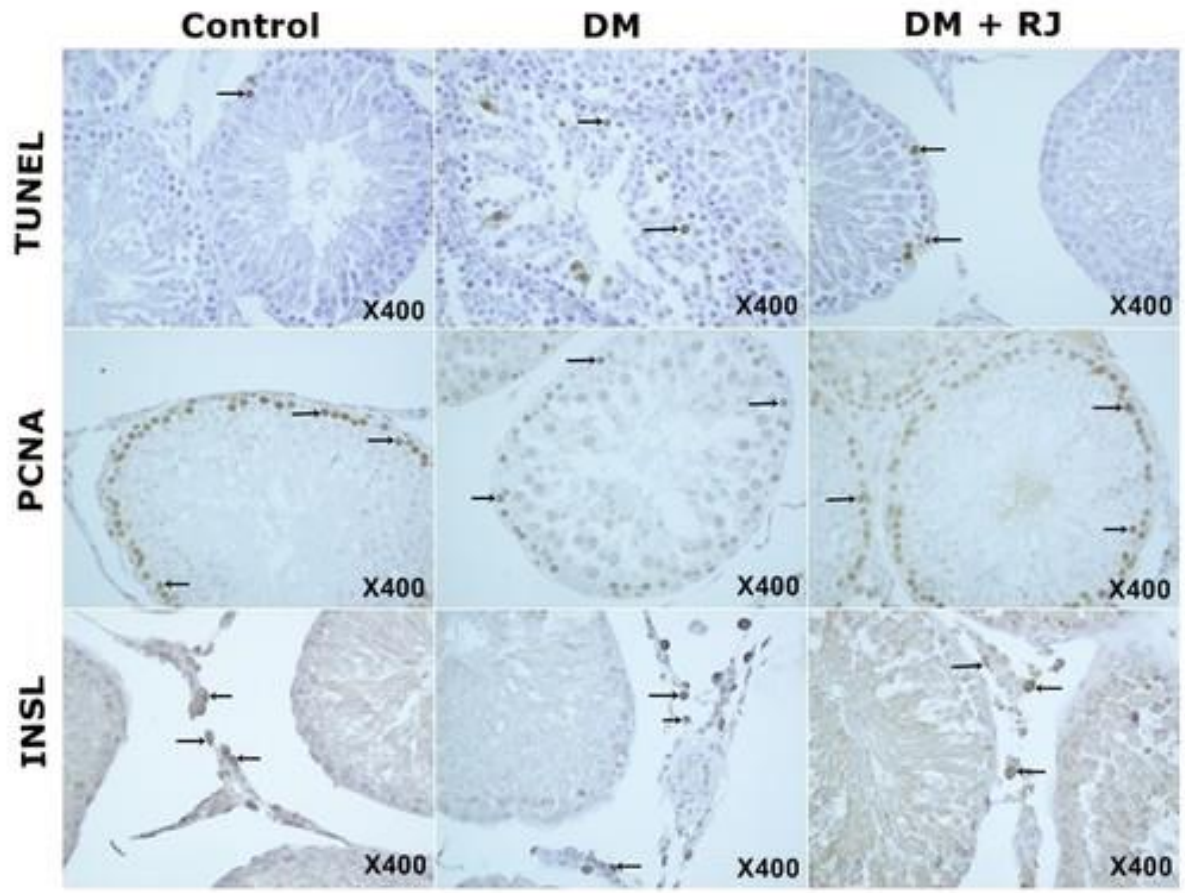

Figure 1. TUNEL, PCNA, INSL3 positive cells (→) is observed.

Fluorescent conjugates of natural products with anticancer potential for imaging and phototherapy applications

Silvie Rimpelová (1), Michal Jurášek (2), Vladimíra Pavlíčková (1), Lucie Peterková (1), Eva Kmoníčková (3), Pavel B. Drašar (2), Tomáš Ruml (1)

1) Department of Biochemistry and Microbiology, University of Chemistry and Technology Prague, Technicka 3, 166 28 Prague 6, Czech Republic

2) Department of Chemistry of Natural Compounds, University of Chemistry and Technology Prague, Technicka 3, 166 28 Prague 6, Czech Republic

3) Institute of Experimental Medicine, Czech Academy of Sciences CR, v.v.i., Vídeňská 1958/9, 140 21 Praha 4, Czech Republic

Keywords: BODIPY dyes, iodo-BODIPY, fluorescence real-time imaging, photodynamic therapy of cancer, sesquiterpene lactone trilobolide

Medicinal plants have proven their value as a source of molecules with high therapeutic potential, and nowadays, they still represent an important pool for identification of novel drug leads. Natural products or their structural relatives comprise of ca. 50% of drugs used for cancer therapy. Since optical imaging, a rapidly developing field of research, has proven to be a valid tool for non-invasive monitoring of disease progression and determining the effects of a drug at a particular target, more advanced, multimodal agents, are being developed. They have the capabilities of both imaging and curing of a disease using the same drug for both. This perspective is of a tremendous importance especially for human burdens such as cancer, since it is one of the high-risk deathful diseases, the mortality of which has been still increasing, thus early detection and more efficient treatment are crucial. On this basis, we have developed four series of multimodal agents based on a natural plant product sesquiterpene lactone trilobolide, which is a structural analogue to thapsigargin, which is currently in clinical trials for solid tumor treatment. Trilobolide, an inhibitor of sarco/endoplasmic reticular Ca^{2+} ATPase, has anticancer, pro-apoptotic and immunomodulatory properties. Using click chemistry, trilobolide was conjugated to newly developed fluorescent BODIPY, (1, 2) iodo-BODIPY, porphyrin, (3) and purpurin 18 derivatives, the last three of which are applicable as multimodal agents in photodynamic therapy (PDT). PDT relies on photoactivation of a photosensitive compound

(PS), which generates toxic, highly reactive O_2 species resulting in cell death. The antiproliferative effect of the trilobolide conjugates was confirmed in various cancer cells line models and the selectivity was compared to primary human fibroblasts. Further biological properties were examined by live-cell fluorescence microscopy, which revealed localization in endoplasmic reticulum (ER). The impact on physiology of mitochondria and ER was studied as well as whole genome gene expression analysis. We are convinced that these newly developed fluorescently labeled trilobolide conjugates could serve as multimodal agents in cancer therapy.

Acknowledgements:

This research was supported by Czech Science Foundation (GAČR) 14-04329S and from Specific university research (MSMT No 20-SVV/2017) by JIGA 2017 UCT grant.

References:

1. M. Jurášek et al., J. Med. Chem. 57 (2014) 7947-7954.

2. L. Škorpilová et al., Beilstein J. Org. Chem. 13 (2017) 1316-1324.

3. P. Tomanová et al. Steroids 97 (2015) 8-12.

Postmortem evaluation of wound healing after Descemet membrane endothelial keratoplasty (DMEK)

Daniele Spinozzi (1), Thomas M. Müller (1), Itay Lavy (1), Robert M. Verdijk (2), Marieke Bruinsma (1), Jack Parker (1), Perry S. Binder (3), Gerrit R.J. Melles (1)

1) NIIOS, Rotterdam, The Netherlands: Netherlands Institute for Innovative Ocular Surgery, Rotterdam, The Netherlands

2) Erasmus MC, Rotterdam, The Netherlands: Department of Pathology, Section Ophthalmic Pathology, Erasmus MC University Medical Center, Rotterdam, The Netherlands

3) Gavin Herbert Eye Institute, Irvine, CA, USA: Gavin Herbert Eye Institute, University of California, Irvine, Irvine, California, USA

Keywords: DMEK, postmortem tissue, histopathology, cornea, keratoplasty

Introduction: Main postoperative complications after Descemet membrane endothelial keratoplasty (DMEK) include incomplete graft adherence, folds and DM-remnants. Histopathology of postmortem DMEK-eyes may elucidate wound healing processes after DMEK. Objectives: To describe the histologic features of postmortem eyes after Descemet membrane endothelial keratoplasty (DMEK) and their potential clinical implications. Methods: Eleven postmortem corneas of eight patients, who underwent DMEK surgery for Fuchs endothelial dystrophy with an average postoperative time of 4 ± 1.9 years were procured after death and processed for light microscopy evaluation. Results: Nine eyes showed a ‘normal’ anatomy in the corneal center. One eye had an anatomically 'normal' periphery, ten showed peripheral abnormalities: in nine, the DMEK-graft overlapped with the host edge of the descemetorhexis; one eye showed a acellular scarring overlying a portion of the DMEK-graft that was detached followed by spontaneously adherence; three eyes showed graft folds with scar-tissue anteriorly; in two eyes (same patient), the anterior banded layer of the host DM was still *in-situ* across the cornea (both required re-bubbling); and two eyes showed host DM-remnants within the corneo-limbal tunnel incision that may have interfered with wound healing. Conclusions: Incomplete host DM removal may relate to postoperative DMEK graft detachment and wound instability. Graft detachments may re-attach with interface scarring. Re-bubbling

procedures may be performed within 4-6 weeks, before scarring of detached graft portions occurs.

Acknowledgements:

Financial Disclosure: Dr. Melles and Dr. Parker are consultants for DORC International BV/Dutch Ophthalmic USA, and Dr. Melles is a consultant for SurgiCube International. The other authors have no conflict of interest to disclose.

The use of microscope in school biology teaching

Mirko Ruščić (1), Antonio Vidović (2), Goran Kovačević (3), Damir Sirovina (3)

1) Department of Biology, Faculty of Science Split, University of Split, HR-21000 Split, Croatia

2) High School Hvar, Island of Hvar, Croatia

3) Department of Biology, Faculty of Science Zagreb, University of Zagreb, Rooseveltov trg 6, HR-10000 Zagreb, Croatia

Keywords: teachers, microscopes, practical work, active learning, microscopy

During the last decade, the Republic of Croatia has been developing a modern educational system focused on a synergy of educational, pedagogic and functional competences in primary and secondary school students and university students. Teaching natural sciences must necessarily include active learning and research, with constant presence of critical thinking. It is essential to teach the students how to observe, generalise, conclude and think, as they are not acquiring mere knowledge, but also the cognitive strategies. Teachers should master the techniques of creating the efficient combinations of teaching methods, in order to guide students to clear and complete concepts which are the basis of quality knowledge. Teaching biology and life sciences in primary and secondary schools involves a lot of material that is not visible to the naked eye and which is valuable for the students' direct insights and discoveries. As these are of key importance for the students' understanding of cell structure, organelle, microorganisms and similar, is it essential to bring this micro-world closer to students and to use microscopes. As a teaching method, microscopy is primarily defined as a visual method, used as a demonstration method and method for practical work. It includes using a microscope as a teaching aid and sample slides as teaching tool. The survey was conducted in 73 primary schools and 30 high schools, mostly with grammar school programme. The results showed that 94% of schools in Split/Dalmatia County have at least one microscope, with monocular light microscopes of primary importance for biology classes. Most common types of microscopes used in teaching are monocular light microscopes (80%), followed by binocular optical microscopes (16%), digital microscopes (3%) and stereomicroscopes (1%). Animal

tissues and plant structure cross-sections are being primarily used in demonstrations, while in conducting a practical work, sample slides most commonly contained plant, protozoan and reproductive cells. In the survey 61% of participants answered to use a microscope only occasionally, whereas 39% of participants often. Average grade awarded to the level of satisfaction with using microscopy in teaching was 3.73. The high number of schools showed to be equipped with microscopes, 97 out of the total number of schools. Only 6 schools did not show to have access to any technical equipment for microscopy. Teachers are sometimes forced to be less engaged in microscopy since, for inexperienced teachers, it represents too much time and effort to create and organise a practical work, with no guarantee that the time and effort will be worthwhile. As main reasons for not using a microscope, the participants stated that this is due to lack of microscopes (53%) and demanding biology and life science syllabus (30%). But, it is evident that among 103 participants in the survey there were no teachers who openly avoid working with a microscope.

Protective effects of curcumin against methotrexate-induced nephrotoxicity in rats: role of nuclear factor-kappa B pathway

Yesim Uz (1), Duygu Uzun (1), Ozlem Delen (1), Leyla Kilinc (2)

1) Department of Histology and Embryology, Trakya University School of Medicine, Edirne, Turkey

2) Department of Histology and Embryology, Akdeniz University School of Medicine, Antalya, Turkey

Keywords: curcumin, methotrexate, nephrotoxicity, nuclear factor-kappa B

Background: Methotrexate (MTX) is a chemotherapeutic agent which is commonly used to treat malignant tumours and inflammatory diseases. However, its clinical use is limited by its nephrotoxicity. One of the most prominent toxicities caused by MTX chemotherapy is nephrotoxicity. Objective: The aim of the present study was to investigate the protective effects of curcumin (CMN) against methotrexate-induced nephrotoxicity in rats. Materials and methods: Eighteen adult *Wistar albino* male rats were equally divided randomly into three groups of six rats each. The control (C) group rats were administered dimethyl sulfoxide (DMSO) intragastrically for 14 days. The rats in the second (MTX) group were administered only a single dose of MTX intraperitoneally (20 mg/kg) on the eleventh day of the experiment. CMN (100 mg/kg/day, dissolved in DMSO) was administered to the third group (MTX+CMN) intragastrically for 14 days and a single dose of MTX (20 mg/kg) was injected intraperitoneally on the eleventh day of the experiment. All rats were sacrificed 24 hours after the last dose of CMN and their kidneys were removed. After routine tissue processing, sections were stained with hematoxylin-eosin and Sirius red for histological examination, or with anti-nuclear factor-kappa B (NF-kB) antibody for immunohistochemical assay. Additionally, blood samples were collected for serum urea and creatinine determination. The data were analyzed statistically. Results: Kidneys of control group animals showed normal histological structure of the glomeruli and renal tubules. However, the kidneys of animals injected with MTX revealed severe histological damage such as tubular dilatation, tubular cell swelling, edema, capsular dilatation, inflammatory cell infiltration, medullary congestion, tubular and glomerular degeneration. In

addition, immunoreactivity of NF-kB was significantly increased in the MTX group compared with the control group. MTX group also showed significantly higher serum urea and creatinine level compared with the control group. Treatment with CMN exhibited significant decreased in levels of serum urea and creatinine as well as histological damage. Furthermore, CMN markedly reduced immunoreactivity of MTX-induced NF-kB. Conclusion: Treatment with CMN may have protective effects against MTX-induced nephrotoxicity, in part, through inhibition of the NF-kB signaling pathway.

References:

1. M. Bozkurt et al., Clin Invest Med. 37 (2014) E19-25.

2. I. Asvadi et al., Eur Rev Med Pharmacol Sci. 15 (2011) 1003-9.

MATERIALS

M1: Thin Films, Coatings, Surfaces and Interfaces

INVITED LECTURES M1:

Void formation during solid state dewetting of thin Al films on single crystalline (0001) oriented Al_2O_3substrates

Stefan Hieke (1), Gerhard Dehm (1), Christina Scheu (1)

1) Max-Planck-Institut für Eisenforschung GmbH, Max-Planck-Straße 1, 40237 Düsseldorf, Germany

Keywords: Al- Al_2O_3 Interface, Dewetting, Voids, STEM, EELS

Al thin films on Al_2O_3 substrates find application in microelectronics, where they are used as connection lines. However, during operation elevated temperature can occur which might lead to a break-up of the thin film into islands. To develop strategies against this failure, the phenomena of solid state dewetting has to be understood in detail. In our work we used a model tetracrystalline Al thin film grown by molecular beam epitaxy on (0001) oriented, single crystalline sapphire substrates and studied the occurring processes during annealing at 600°C, which is slightly lower than the melting point of Al (660°C). The initial film microstructure consisted of two growth variants which are both twinned. The majority of the grains possessed a heteroepitaxial orientation relationship (OR) with the close-packed planes and directions parallel to each other: ± [-110] (111) Al || [10-10] (0001) α-Al_2O_3 (OR I a/b). The minor fraction showed OR II a/b: ± [-211] (111) Al || [10-10] (0001). The film is homogenously covered by a thin, amorphous oxide scale which prevents surface diffusion, such that only interface and grain boundary diffusion can occur. During annealing of the thin film two competing processes were activated. First, texture evolution took place. Grains possessing OR II grew faster than those of OR I and finally dominated as determined by electron back scatter diffraction (EBSD) experiments in the scanning electron microscope (SEM) (Figure 1a). Second, the film locally retracted and facetted voids occurred. The EBSD analysis revealed that high energy grain boundaries and defects were the initial starting points of dewetting. The region of the facetted

voids was analysed in depth using Cs corrected scanning transmission electron microscopy (STEM) performed on a FEI Titan Themis 60-300 X-FEG S/TEM instrument operated at 300 kV. The Titan Themis is equipped with a probe Cs-corrector and a monochromator. Energy-dispersive X-ray spectroscopy (EDS) and electron energy loss spectroscopy (EELS) experiments were done in STEM mode using the attached FEI Super-X windowless EDS system and the post column Gatan GIF Quantum ERS spectrometer. Site-specific cross-sections of Al- void regions were prepared by focused ion beam sectioning using a FEI Helios Nanolab 600 or 600i dual beam SEM/FIB. Two different types of voids were observed. Some of the voids showed a hexagonal shape which can be explained by the inverse Wulff-shape of Al crystals (Figure 1b). High angle annular dark field (HAADF) STEM images revealed that the side walls of the retracting film are partly facetted and that the retracted Al is uniformly redistributed to the surrounding of the void. This is different to the second type of voids which possess an irregular shape (not shown). Pinning of the retracting film leads here to the formation of a rim. Epitaxial ridges were sometimes additionally observed for this void type. The interface between the Al film and the substrate remains atomically abrupt, independent of the OR, as exemplary shown in Figure 1c. Both types of voids are covered by a thin oxide membrane which continues as oxide scale on the remaining Al film as discovered by EDS mappings (Figure 1d). The original amorphous surface oxide layer has transformed during annealing to γ-Al_2O_3 which is confirmed by high resolution HAADF STEM images as well as by EELS (Figure 2). The energy loss near structure features of the continuous oxide film covering the remaining metallic Al as well as the void are different to those of metallic Al and α-Al_2O_3 and are in close agreement to the ones observed in γ-Al_2O_3.

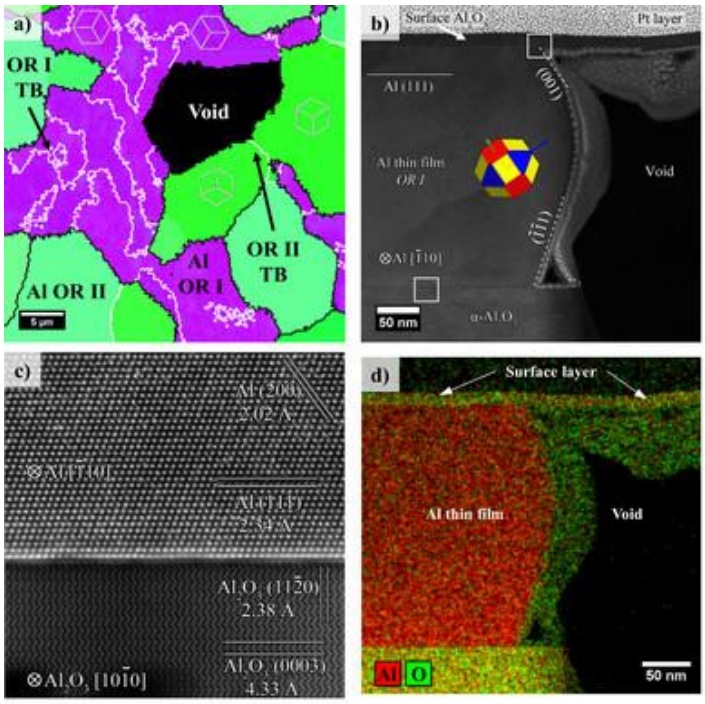

Figure 1. (a) EBSD orientation map showing a facetted void adjacent to grains possessing OR I and OR II. Grain growth and void formation occurred after annealing at 600°C. HAADF image of (b) the film - void – substrate region and (c) film – substrate interface. (d) Al and O EDS map of the region corresponding to (b).

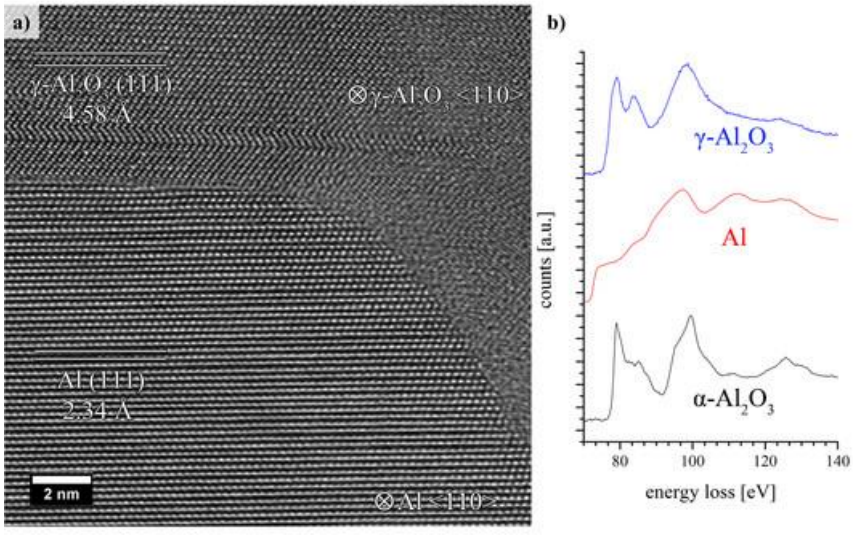

Figure 2. (a) Surface oxide (γ-Al_2O_3) on top of the Al film after annealing at 600°C. (b) shows the EELS data acquired in the surface oxide, the metallic film and the substrate.

Epitaxial strain in oxide thin films and heterostructures

Neven Biškup (1), Maria Varela (1), Juan Salafranca (1), Das Saikat (2), Benjamin P. P. Mallet (2), Virat Mehta (3)

1) Universidad Complutense de Madrid, Avda. de Séneca, 2 Ciudad Universitaria, 28040 Madrid, Spain

2) University of Fribourg, Department of Physics and Fribourg Centre for Nanomaterials, Chemin du Musée 3, CH-1700 Fribourg, Switzerland

3) University of California Berkeley, Berkeley, CA, USA

Keywords: atomic resolution electron microscopy and spectroscopy

Epitaxial strain can change both the structure and the chemical composition of a thin film, resulting in modified, and sometimes even opposite properties when compared to the bulk material. Complex oxides, known for their richness of physical properties (superconductivity, magnetism, ferroelectricity…) are the particularly interesting system to be explored when confined to nanometer dimension. In order to study the material on atomic scale, the atomic resolution microscopy is a necessary tool. The scanning transmission electron microscopy combined with electron energy loss spectroscopy can help us understand the unexpected properties in oxide thin films and heterostructures. We will show how local defects and/or superstructures are able to determine the property of the material. Few examples will be shown including ferroelectrics, ferromagnets and heterostructures of ferromagnetic/superconducting thin films.

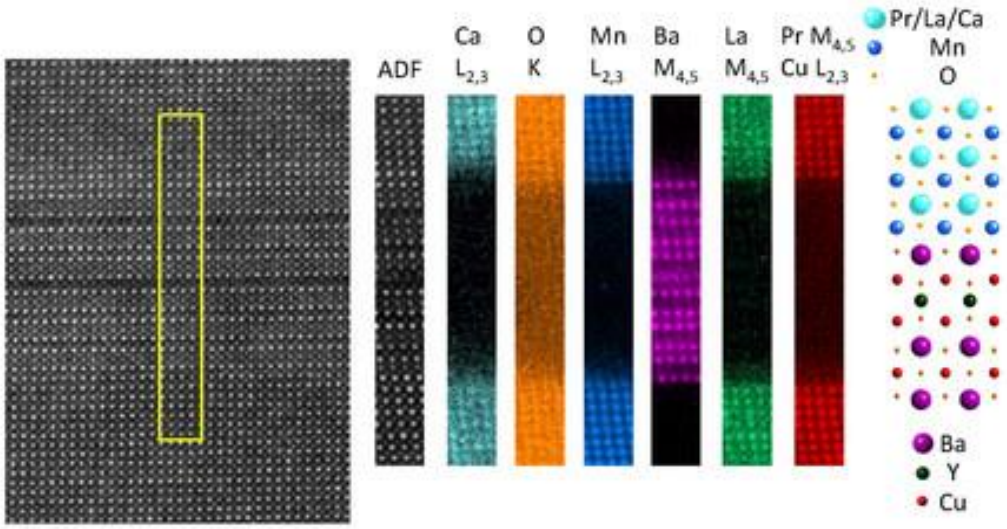

Figure 1. Atomic resolution EELS of PLCMO/YBCO interfaces.

ORAL PRESENTATIONS M1:

In situ observation of electron beam induced nanocrystallization of an ultra thin tungsten foil

Stefan Noisternig (1), Clemens Mangler (1), Christian Ebner (1), Willem Tichelaar (2), Christian Rentenberger (1), Hans-Peter Karnthaler (1)

1) University of Vienna, Physics of Nanostructured Materials, 1090 Vienna, Austria

2) CEOS-GmbH, 69126 Heidelberg, Germany

Keywords: amorphous ultra thin tungsten foil, STEM, beam induced crystallization, surface diffusion

An amorphous ultra thin W foil with a thickness of 2 nm was made by physical vapor deposition of electron beam heated pure W. As support for the W foil an amorphous ultra thin (3 nm) carbon foil was used as supplied by QUANTIFOIL. The beam induced crystallization of the amorphous W foil was carried out in an UltraSTEM 100 Nion instrument operating at a vacuum of about 10^{-10} Pa within the whole instrument. The very stable imaging conditions regarding thermal drift allowed us to image the same specimen area for a long period of time. The data were acquired in form of video files from continuously recordings up to 30 minutes. An acceleration voltage of 60 kV was used. Special care was taken to avoid contamination: The specimen and the holder were heated at 140 °C for several hours in an ultrahigh vacuum and transferred to the microscope. In addition, the method of "beam shower" was used to suppress the contamination of the observed area. Beam shower stands for gathering the contaminants present at the sample surface at an area far off the area of interest by long-time exposure with the electron beam. The experimental results show that during the observation the amorphous structure of W converts to a partially nanocrystalline one (cf. Figure 1.a and Figure 1.b). The time to form the crystalline structure depends on the radiation dose of the electron beam. The radiation dose is controlled by the size of the area selected for the observation using fixed parameters (high voltage, beam current, probe size and acquisition time per pixel). The crystal phase structures are analyzed by Fast Fourier Transformation (FFT) of High Angle Annular

Dark Field (HAADF) images and Medium Angle Annular Dark Field (MAADF) images calculated from selected nanocrystals as shown in Figure 2.a and Figure 2.b. The small pixel counts of the selected nanocrystalline sub areas in the images lead to FFT with low resolution. Therefore, the signal in the FFT is improved by a drift correction for the continuously acquired HAADF and MAADF images followed by the averaging of images which show the same crystalline structures. The FFT analysis reveals that $WC_{0.82}$ and $W_3C_{0.375}$ nanocrystals formed during the radiation of the amorphous W foil under the electron beam. During the continuous acquisitions a movement of bright dots is observed in the HAADF images. We interpret this phenomenon as a surface diffusion of W atoms. The additional W atoms at the sample surface would be visible in HAADF images because of the ultra thin (2 nm) W foil and the dominant Z-contrast of W compared to carbon. We conclude that the electron beam activates surface diffusion at an energy well below the knock-on energy (above 1 MeV for crystalline W). Mean square displacements of bright dots are measured at amorphous areas and at crystalline areas. The calculated diffusion parameters are then compared to literature values as obtained by other methods (1).

Acknowledgements:

We kindly acknowledge financial support by the Austrian Science Fund (FWF): [I1309].

References:

1. Gert Ehrlich and F. G. Hudda, J CHEM PHYS 44 (1966) 1039-1049.

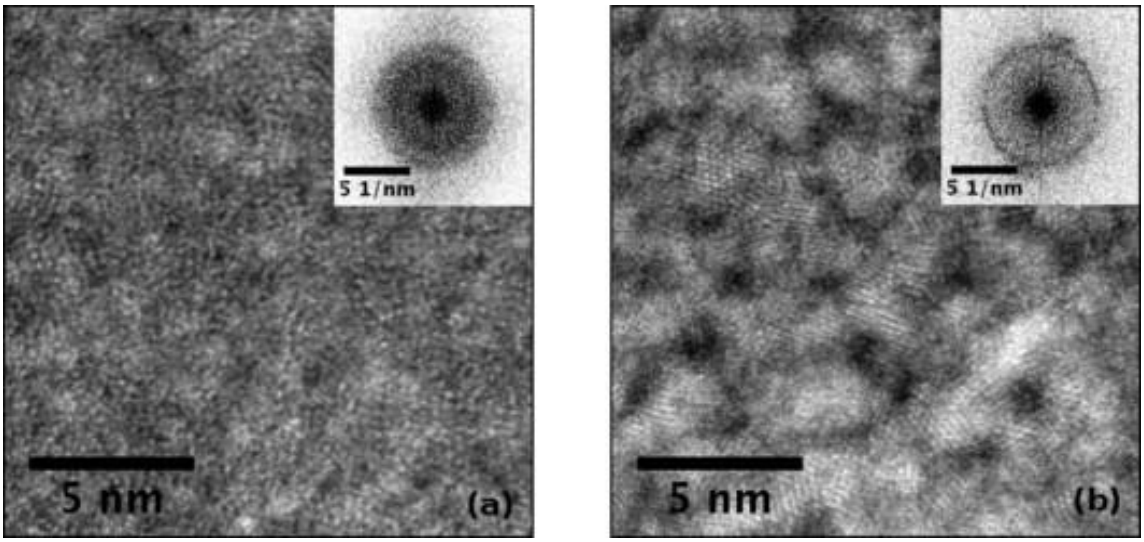

Figure 1. STEM HAADF images of a 16x16 mm² amorphous W area at the start of the image acquisition (Figure 1.a) and after about 10 minutes acquisition time (Figure 1.b).

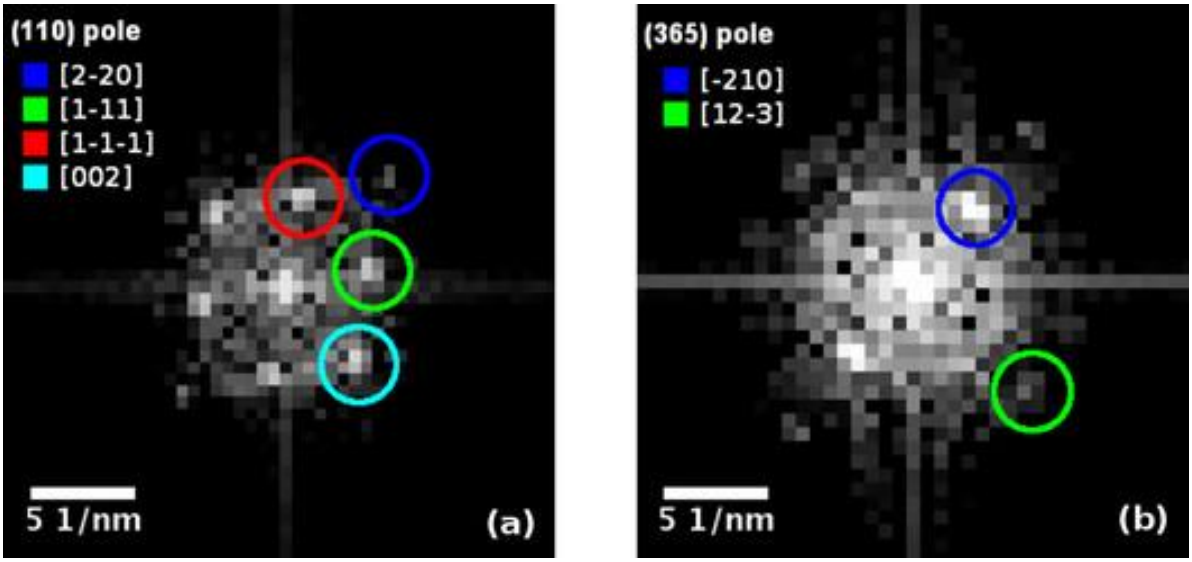

Figure 2. FFT of two different areas in a HAADF image which correspond to a WC0.82 nanocrystal (Figure 2.a) and a W3C0.375 nanocrystal (Figure 2.b). The orientations of the nanocrystals and reciprocal lattice vectors are indicated in the FFT.

Automatic analysis of [110] tilt grain boundaries in III-V zinc-blende semiconductors from aberration-corrected HAADF-STEM images

Roksolana Kozak (1), Fiodar Kurdzesau (2), Ivan Prieto (1), Yadira Arroyo-Rojas Dasilva (3), Oliver Skibitzki (1), Thomas Schroeder (4), Hans von Känel (4), Rolf Erni (5), Marta D. Rossell (1)

1) Electron Microscopy Center, Empa - Swiss Federal Laboratories for Materials Science & Technology, Überlandstrasse 129, CH-8600 Dübendorf, Switzerland

2) MAS “Medical Physics”, ETH Zürich, Gloriastrasse 35, CH-8092 Zürich, Switzerland

3) Laboratory for Solid State Physics, Otto-Stern-Weg 1, ETH Zürich, CH-8093 Zürich, Switzerland

4) IHP, Im Technologiepark 25, 15236 Frankfurt (Oder), Germany

5) Institute of Physics, Brandenburgische Technische Universitaet, Konrad-Zuse Strasse 1, 03046 Cottbus, Germany

Keywords: grain/twin boundary, semiconductor, scanning transmission electron microscopy, image processing

Grain boundaries (GBs) are 2D crystal defects frequently observed in semiconductors (1). Their presence within the material is generally believed to degrade the optical and electrical properties of the devices made therefrom. However, control of the type, orientation, and frequency of occurrence/distribution of GBs in the synthesized structure can greatly enhance the devices’ intrinsic performances (2). Therefore, it is crucial to be able to identify and characterize the local GB structures at the atomic scale in a precise way. Here we present an in-house developed automatic analysis approach and the corresponding processing tool that can be used to recognize [110] tilt grain boundaries in GaAs nanoparticles, which crystallize in the ZnS-type structure (space group *F*-43*m*, Pearson symbol *cF*8) from high-resolution high-angle annular dark-field scanning transmission electron microscopy (HAADF-STEM) images (Figure 1a). Its main processing steps are the following: peak search and refinement, extraction of the misorientation angles and transformation matrices for different twins within the analyzed image by considering the closest atomic (dumbbell) peaks as a single vector following the

polarity given by the direction from the lighter Ga to the heavier As atoms, and finding the common plane(s) by 3D modelling of all possible intersections of the corresponding reciprocal lattices. The structural unit (SU) model (Figure 1b) (3) has also been applied to characterize GB structures and used to validate the data obtained by the developed algorithm. The summary of the results for the symmetric Σ9{221} GB illustrating the performance of the developed script are presented in Figure 1c,d. The developed script can be used to analyze [110] tilt GBs in any *fcc*-based zinc blende material with any degree of complication as long as the dumbbell atomic columns in the HAADF-STEM image are clearly resolved (4).

Acknowledgements:

This work was supported by the Swiss National Science Foundation under Grant 200021L_153558; and by the Deutsche Forschungsgemeinschaft (DFG) under Grant SCHR 1123/10-1 in the framework of the DACH project.

References:

1. D.B. Holt, B.G. Yacobi, Extended Defects in Semiconductors: Electronic Properties, De-vice Effects and Structures, Cambridge University Press, Cambridge (2007).

2. R. Raghunathan et al., Nano Lett. 14 (2014) 4943-4950.

3. J. Thibault et al., J. Mater. Sci. Eng. A 164 (1993) 93-100.

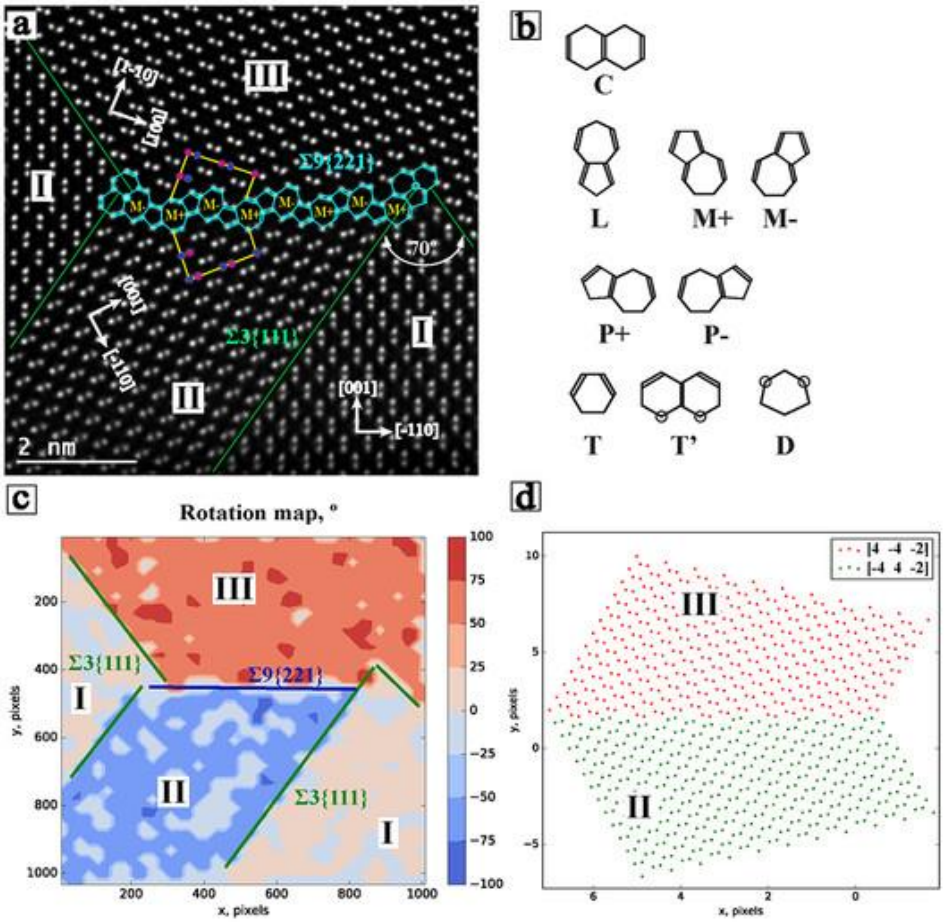

Figure 1. (a) High-resolution HAADF-STEM image presenting a symmetric Σ9{221} (marked in blue) and Σ3{111} (green lines) GBs between twins I, II, and III with overlaid SU analysis. (b) Models of known SUs used for the description of the [110] tilt GBs in zinc blende-type semiconductors (3). (c) Lattice rotation map (in degrees) obtained from the image in panel (a) by using the automatic processing algorithm with the twins colored according to their orientation. (d) Simulation of the incoherent Σ9{221} GB.

Sub-nanometer microanalysis on hematite photoanodes with localized Sn dopants to enhance photocatalytic water splitting

Siyuan Zhang (1), Alexander G. Hufnagel (2), Hamid R. Hajiyani (3), Tong Li (1), Baptiste Gault (1), Dina Fattakhova-Rohlfing (2), Thomas Bein (2), Rossitza Pentcheva (3), Christina Scheu (1)

1) Max-Planck-Institut für Eisenforschung GmbH, Max-Planck-Straße 1, 40237 Düsseldorf, Germany

2) University of Munich (LMU), Geschwister-Scholl-Platz 1, 80539 München, Germany

3) Universität Duisburg-Essen, Forsthausweg 2, 47057 Duisburg, Germany

Keywords: hematite, photoelectrochemical water splitting, aberration-corrected scanning transmission electron microscopy, electron energy loss spectroscopy, atom probe tomography

Photoelectrochemical water splitting is a promising technology for H_2 fuel production. Hematite (α-Fe_2O_3) is a popular materials for the photoanode, owing to its good absorption of solar energy and earth abundance. On the flip side, the low carrier mobility of hematite needs to be overcome, and various strategies including doping (1) and nanostructuring (2) have been investigated. Our study combines the two strategies to demonstrate an optimized performance by doping Sn into different volumes of ultrathin (< 20 nm) hematite photoanodes fabricated by atomic layer deposition (ALD) shown in Figure 1a. In order to correlate the photoelectrochemical performance of the thin films with their microstructure and chemistry, we characterized them by scanning transmission electron microscopy (STEM), electron energy loss spectroscopy (EELS), and atom probe tomography (APT). A probe-corrected FEI Titan Themis microscope was operated at 300 kV and a convergence angle of 24 mrad. EELS spectrum imaging was collected using a Gatan Quantum ERS energy filter operated in the image-coupled mode and using a collection angle of 35 mrad. The APT experiments were conducted on a CAMECA LEAP 5000 XS instrument with a ~80% detection efficiency. Data was acquired in laser pulsing mode at a specimen temperature of 50 K, with a target evaporation rate of 5 ions per 1000 pulses. Although ALD growth allows control of the depth of doping with monolayer precision, a key question is whether Sn atoms diffuse into the nominally undoped volumes upon subsequent calcination to crystallize the hematite films. As shown in Figure 1b, STEM images of the hematite thin film demonstrate a good control of the ALD doping profile to even a monolayer at the surface. Moreover, the coverage of Sn depends on the crystallographic orientation of hematite. We also performed first principles calculations that show a lower overpotential for the water oxidation reaction on the hematite surface with

Sn dopants (3). Microanalysis from energy dispersive X-ray spectroscopy shows a background level of Sn even in the undoped hematite films due to nonlocal contribution from the neighboring SnO_2 substrate. However, the local measurement approaches, EELS and APT, confirm there is negligible Sn diffusion into the undoped volumes. Moreover, there is more signal from the Sn-$M_{4,5}$ edge at grain boundaries (Figure 2a). This is further confirmed by APT (Figure 2b). Segregation of Sn at grain boundaries has an adverse effect on the crystallinity of hematite and is harmful to the charge transport. By imaging and microanalysis at the atomic scale, we are able to examine the local distribution of Sn dopants on the surface, within different volumes, and their segregation at grain boundaries in the hematite photoanodes, thereby explaining the physical mechanisms of their different activity in photocatalytic water splitting.

Acknowledgements:

This research is funded by German Science Foundation (DFG) under the priority programme SPP 1613.

References:

1. K.D. Malviya, et al., J. Mater. Chem. A 4 (2016) 3091.

2. H.K. Dunn, et al., Phys. Chem. Chem. Phys. 16 (2014) 24610.

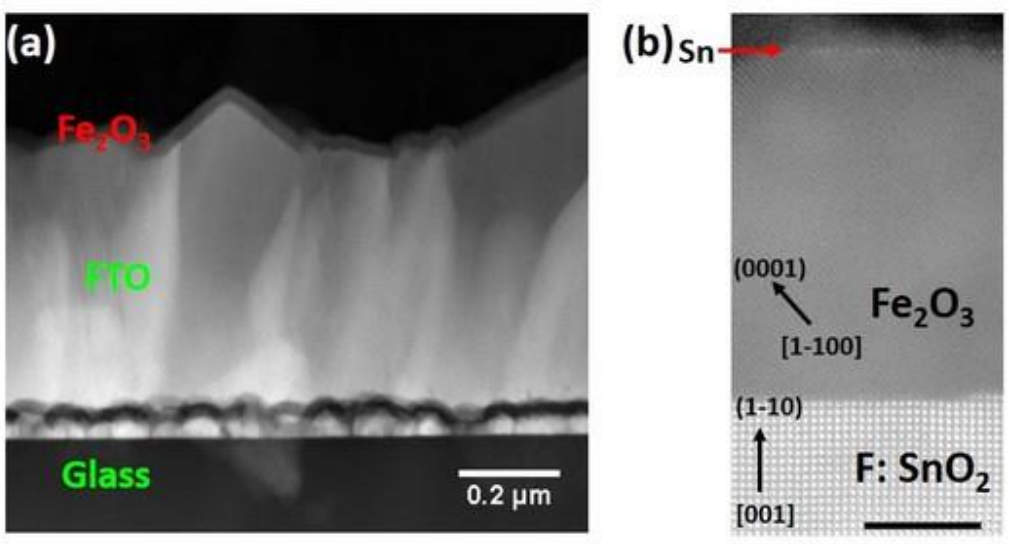

Figure 1. (a) STEM images of ultrathin hematite photoanodes on the FTO substrate; (b) Sn atoms observed at the hematite surface (scale bar is 5 nm).

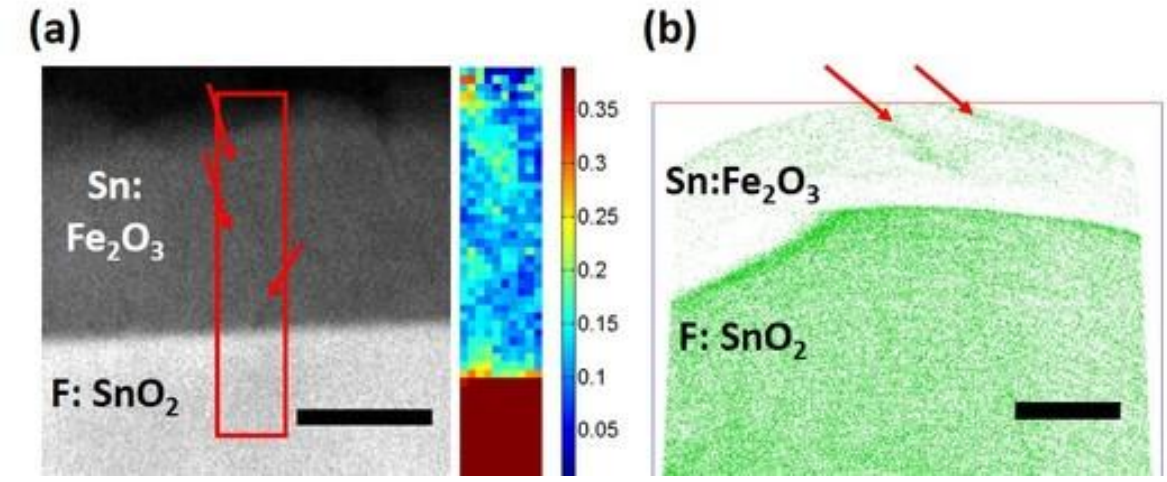

Figure 2. Segregation of Sn at grain boundaries (highlighted by red arrows) as characterized by (a) EELS spectrum imaging of Sn-M4,5 edge and (b) 3D APT reconstruction of Sn atoms (scale bars are 10 nm).

In situ TEM study of micro/nanoscaled amorphous or nanocrystalline freestanding films under stress

Rohit Sarkar (1), Christian Ebner (2), Jagannathan Rajagopalan (1), Christian Rentenberger (2)

1) Department of Materials Science and Engineering, School for Engineering of Matter, Transport and Energy, Arizona State University, Tempe, AZ 85287 , USA

2) Physics of Nanostructured Materials, Faculty of Physics, University of Vienna, Boltzmanngasse 5, 1090 Wien, Austria

Keywords: electron diffraction, nanocrystalline, amorphous, *in situ* TEM

Basic understanding of the mechanical properties of amorphous or nanocrystalline materials is essential for their future potential application. Consequently, various established measurements as well as new developed methods have been used to deepen the knowledge of the deformation behaviour and processes of such materials. In the present work we investigated amorphous or nanocrystalline freestanding thin films using transmission electron microscopic (TEM) methods to study their elastic and plastic behaviour under tensile stress condition. Freestanding microscaled amorphous TiAl and nanocrystalline Al thin films were produced on MEMS devices using DC magnetron sputtering. The MEMS based tensile devices have built-in force and displacement sensing gauges to measure macroscopic stress and strain during *in situ* tensile deformation (cf. Figure 1a). The *in situ* TEM study was performed with a Philips CM200 microscope operating at 80-200kV and a Philips straining holder. Bright-field and diffraction images were acquired with a Gatan Orius^{TM} SC600 at different stress states of the film. Figure 1b shows the stress-strain curves of a nanocrystalline Al sample taken under different imaging conditions. The black curve (first cycle) corresponds to the stress-strain values measured at the gauges without irradiating the samples whereas the red, green and blue curves show the behaviour during imaging using 80, 120 and 200kV, respectively. The analysis of the curves in combination with bright-field imaging of dislocations at different stress states (cf. Figure 1c) indicates a clear electron beam-induced stress relaxation caused by enhanced activation of dislocations (1). The effect is more pronounced at lower accelerating voltages and leads to local sample necking at the irradiated area. Nevertheless, *in situ* TEM can be used to correlate the stress-strain curve with the grain size dependent activity of

dislocations and to understand the deviation from linearity during unloading (Bauschinger effect). Figure 2a shows the diffraction image of sputter deposited TiAl. The broad intense ring is characteristic for an amorphous structure. Under stress the circular ring becomes elliptic as illustrated schematically in Figure 2a. By measuring the position of the intensity maxima (as a function of the azimuthal angle □) and fitting an ellipse the local atomic-level strain can be calculated (cf. Figure 2b). The method, evaluation and calculation using our Digital Micrograph™ script are described in (2). By plotting principal atomic-level elastic strains as a function of stress mechanical properties (Young's modulus, Poisson's ratio) of the thin film can be calculated. The comparison with macroscopic data reveals the presence of anelasticity of the TiAl thin film. In addition, strain maps or time-dependent strain evolution under stress can be obtained by this method [see C. Ebner, this conference].

Acknowledgements:

C.E. and C.R. acknowledge financial support by the Austrian Science Fund (FWF): [I1309].

References:

1. R. Sarkar, C. Rentenberger, J. Rajagopalan, Scientific Reports 5 (2015) 16345.

2. C. Ebner et al., Ultramicroscopy 165 (2016) 51-58.

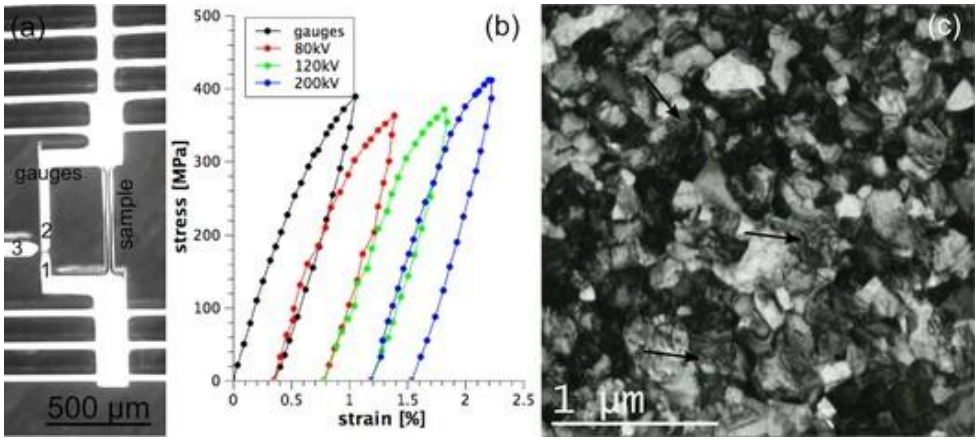

Figure 1. Nanocrystalline Al. (a) Freestanding thin film and stress-strain gauges prepared on a MEMS device. (b) Stress strain-curves measured under different illumination conditions. (c) Bright-field image, sudden contrast changes indicate dislocation activity.

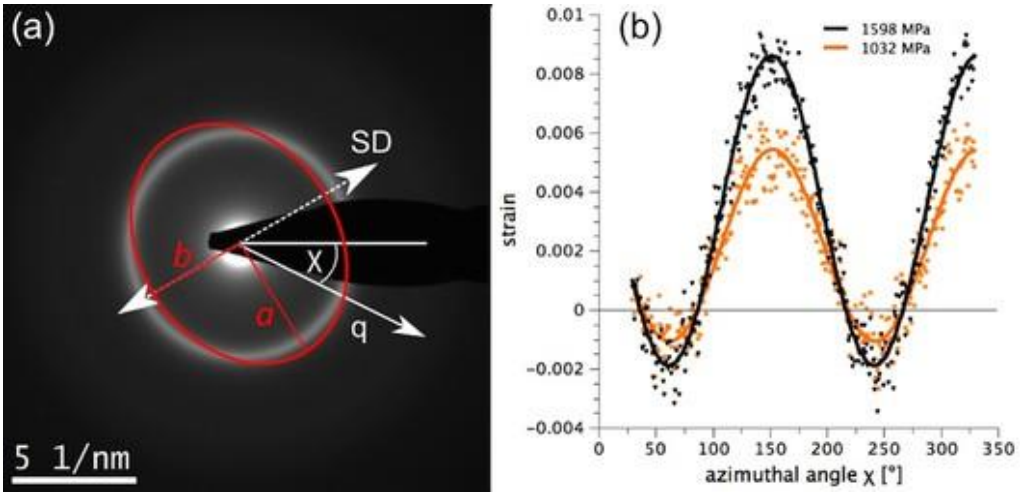

Figure 2. Amorphous TiAl. (a) Diffraction pattern becomes distorted under stress as illustrated by the ellipse (shear direction SD, scattering vector q). (b) Atomic-level elastic strain: maxima and minima correspond to the principal elastic strains parallel and perpendicular to the straining direction, respectively.

POSTER PRESENTATIONS M1:

Microscale characterisation of the next-generation of Nb3Sn superconducting thin films for radio frequency cavity applications

Alexander J. G. Lunt (1), Katsiaryna Ilyina (1), Guillaume J Rosaz (1), Josep Busom-Descarrega (1), Marco Bonura (2), Carmine Senatore (2), Enrico Salvati (3), Alexander M Korsunsky (3), Walter Venturini-Delsolaro (1), Floriane Leaux (1), Mauro Taborelli (1)

1) CERN, CH-1211 Geneva 23, Switzerland

2) Université de Genève, 1205 Geneva, Switzerland

3) University of Oxford, Oxford OX1 2JD, UK

Keywords: Thin films, superconducting radio frequency cavities, residual stress, direct current magnetron sputtering, focused ion beam milling

In recent decades, substantial improvements to the efficiency and magnetic field strength of Superconducting Radio Frequency (SRF) cavities have been achieved through the use of niobium thin films (1). These films are applied to copper cavities to reduce both the manufacturing cost and the likelihood of thermal quenching when compared to conventional bulk niobium designs. For this reason SRF cavities can be operated at higher working temperatures, thereby reducing operating costs. Despite these benefits, a new class of materials with a higher critical temperature than pure niobium is required to significantly improve SRF cavity performance. The low surface resistance of A15 phase materials such as Nb_3Sn makes these intermetallics especially suitable for this application. Direct current magnetron sputtering is a promising deposition method for generating the fully dense Nb_3Sn films required, however the influence of coating pressure, coating temperature, and annealing parameters on the superconducting properties are still unknown. Insight into the influence of these parameters on the microstructure and characteristics of the film is therefore required in order to optimise film manufacture. Following preliminary testing, six Nb_3Sn films were produced using different temperature profiles and coating pressures. After performing critical temperature testing on each of the samples, Focused Ion Beam (FIB) milling was used to

produce cross sections and scanning electron microscopy was performed to image the film topology and microstructure. Energy dispersive X-ray spectroscopy was also used to gain insight into the nanoscale elemental distribution in lamellae extracted from the films. One of the most critical parameters in the reliability of thin films is the magnitude of residual stress which is induced during manufacture, as well as its variation as a function of distance from the film surface. In the case of superconducting films, residual stress magnitude also has an important influence on the critical temperature (2). In order to obtain estimates for residual stress, the ring-core FIB milling and Digital Image Correlation (DIC) approach has been applied to quantify the average in-plane stress in each film at the microscale (3). Insights into the nanoscale residual stress variation with depth has also been obtained using the newly developed multi-ring-core approach. Cross validation of these results was performed using lab-based X-ray diffraction. The results of this analysis indicate that the film microstructure, elemental distribution, residual stress state and critical temperature are sensitive to coating parameters. These insights will be used to optimise film manufacture in order to produce more efficient coatings for the next-generation of SRF cavities. Such improvements will allow these cavities to operate at higher temperatures and with the increased currents required to accelerate particles faster and more efficiently.

References:

1. W. M. Roach et al., Physical Review Special Topics-Accelerators and Beams. 15-6 (2012) 062002.

2. P. Phelan and M. Ghasemi Nejhad, Transactions - American Society of Mechanical Engineers, Journal of Electronic Packaging. 116-4 (1994) 249-257.

3. A. J. G. Lunt et al., Journal of Strain Analysis for Engineering Design. 50-7 (2015) 426-444.

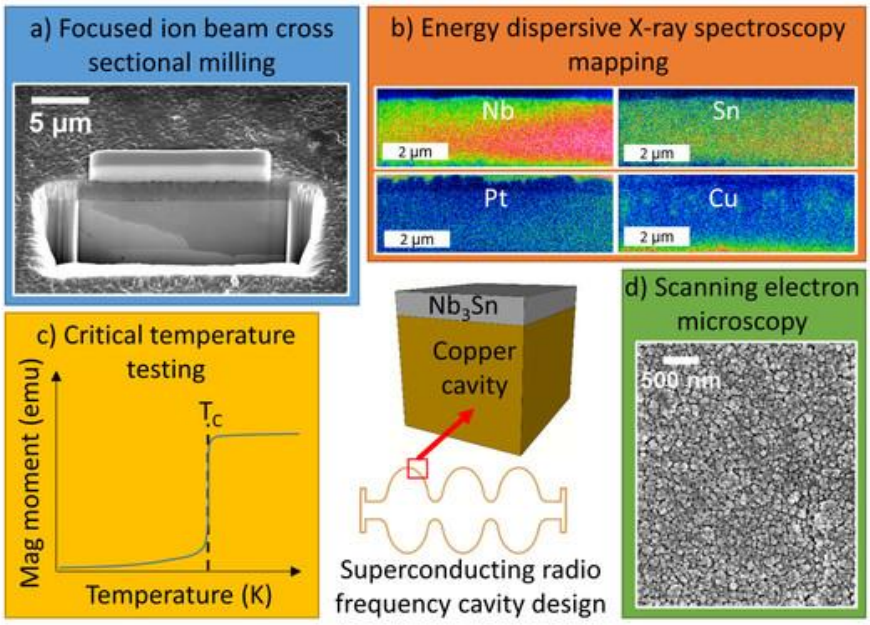

Figure 1. Study overview outlining characterization techniques applied to the thin film. (a) Focused ion beam cross sectional milling. (b) Energy dispersive X-ray spectroscopy mapping. (c) Critical temperature testing. (d) Scanning electron microscopy.

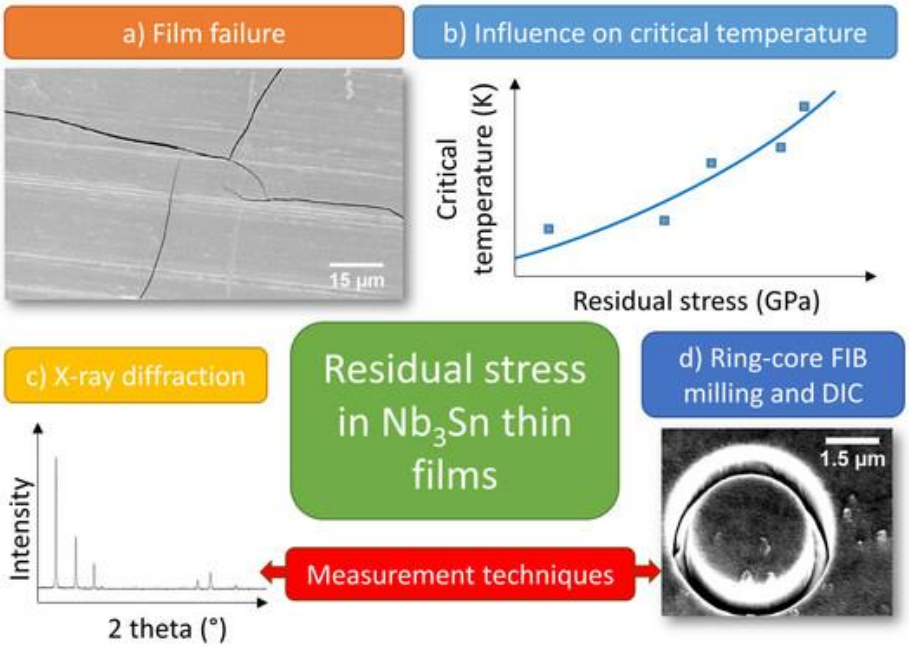

Figure 2. Residual stress analysis of Nb3Sn films. (a) Stress induced film failure. (b) Influence of residual stress on critical temperature. (c) X-ray diffraction. (d) Average and depth resolved residual stress: the ring-core FIB milling and DIC approach (3).

EM analysis to improve the response of tungsten trioxide as gas sensor: SEM, EBSD and TEM analyses versus sensors response.

Alessio Impagnatiello (1), Andrea P.C. Campos (2), Loic Patout (1), Christian Dominici (2), Tomas Fiorido (1), M. Marc Bendahan (1), Kalifa Aguir (1), Claude Alfonso (1), Ahmed Charaï (1)

1) Aix-Marseille Université, CNRS, Université de Toulon, IM2NP - Campus de St Jérôme, 13397 Marseille cedex 20, France

2) Aix-Marseille Université, CP2M - Campus de St Jérôme, 13397 Marseille cedex 20, France

Keywords: tungsten trioxide, films, nanostructured materials, gas sensors

Tungsten trioxide (WO_3) films over oxidized silicon wafer are investigated as sensor for gases (1, 2). An intensive electron microscopy study at different scales is performed in order to determine at different scales the relationship between the microstructure and physical properties. Sensors become more and more present in our daily life because of the increasing demand of the society for more environmental and security requirements. There is research focusing on reducing their size and power consumption in order to create an advanced device for health monitoring wearable as a watch. Our sensors consist of a WO3 film deposited by reactive RF magnetron sputtering on an oxidized silicon wafer with Pt contacts. In order to optimize the sensitivity, several sensors have been prepared and annealed under different conditions. We carried investigations over the samples coupling different complementary microscopy techniques at different scales (SEM, EDS, EBSB, TEM, microdiffraction …) using a Zeiss Gemini500 SEM and a FEI Tecnai 200kV. The efficiency of the sensor is evaluated by its response to 100ppm of ozone, it is defined as the ratio between the electrical resistances under ozone and air. Our results show clearly that the response depends strongly on the conditions of the deposition (sputtering power and pressure, thickness, ratio Ar/O_2) and annealing. The differences are important enough to consider a thorough study of the fine structure of these sensitive materials. A view of the best sample (called a, 93,81% of response) at 15 kV with only secondary electron (HE-SE2) detector reveals the topographical presence

of particular cross-shaped sub-grains (Figure 1a). EBSD analysis (Figure 1b-c) matched as α-WO3 tetragonal (a = 0.525, c = 0.391 nm (3)) the crystal structure of sample a relating these sub-grains as α-WO_3 tetragonal oriented along the [001] direction. In order to confirm this crystal structure and check the existence of any minor phase, TEM foil of sample a has been prepared by mechanical and chemical etching. Micro-diffraction patterns, compared with simulated data, further demonstrate the presence of α-WO_3 tetragonal as P4/nmm. The degree of crystallization influences the response of the film. Figure 2 shows the microstructure of another sample (b) with has equal sputtering conditions of a but lower response (15,67%). Sample b has a lower degree of crystallization, after a lower temperature annealing, and cross-shaped sub-grains are only partly present. These cross-shaped α-WO_3 tetragonal subgrains improves the response of the sensor, probably by increasing the specific surface area of the sensor allowing more gas to be absorbed. Further experimental and simulation studies are underway to investigate the role of these crosses in the large resistance variation and why they improve the properties of the gas sensor.

References:

1. J. Kukkola, J. Mäklin and N. Halonen, Sensor Actuat B-Chem 153 (2011) 293.

2. H. Long, W. Zeng, H. Zhang, J Mater Sci: Mater Electron 26 (2015) 4698.

3. K. K. Zhu et al, Chem Phys Lett 377 (2003) 317.

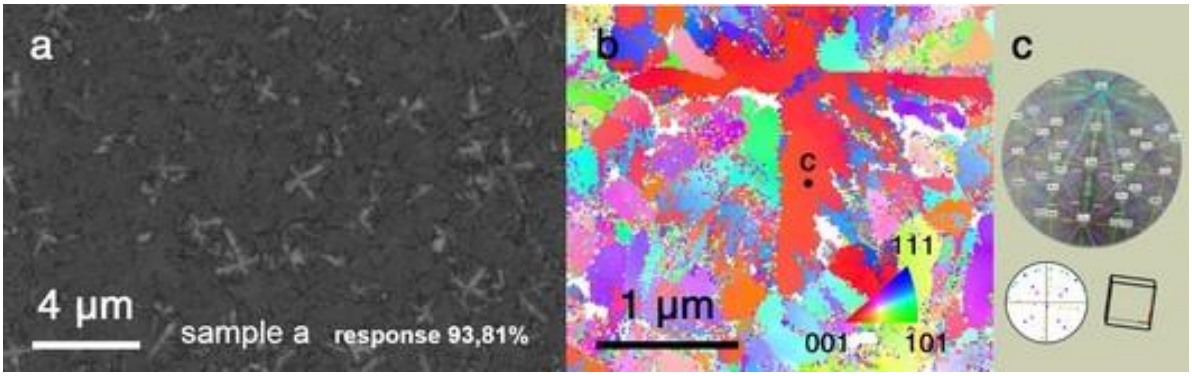

Figure 1. (a) SEM image of the microstructure of sample a characterized by cross shaped subgrains, using a high efficiency secondary electron (HE-SE2) detector at 15 keV. (b) EBSD map of a cross shaped subgrains, from the spot c the measured Kikuchi lines are shown in (c) revealing an orientation close to the [001] direction.

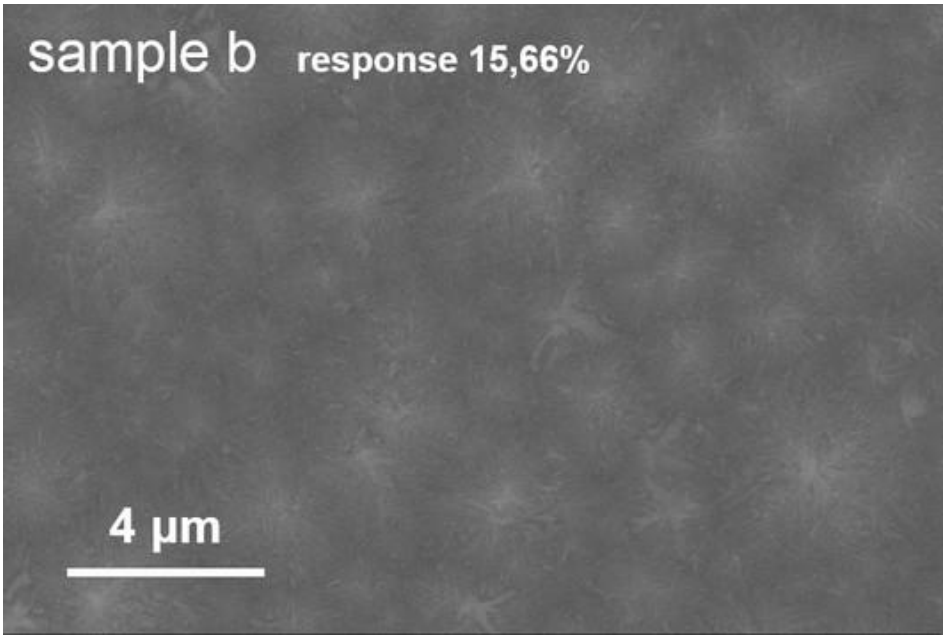

Figure 2. SEM image of the microstructure of sample b partially crystalline, using a high efficiency secondary electron (HE-SE2) detector at 15 keV.

Mechanical properties of magnetron sputtered W-B-C coatings

Vilma Bursikova (1), Jiri Bursik (2), Lukas Zabransky (1), Saeed Mirzaei (1), Mustafa Alishahi (1), Pavel Souček (1), Petr Vasina (1), Ivo Kubena (2)

1) Department of Physical Electronics, Faculty of Science, Masaryk University, Kotlářská 2, 61137 Brno, Czech Republic

2) Institute of Physics of Materials, Academy of Sciences of the Czech Republic, Žižkova 22, 61662 Brno, Czech Republic

Keywords: W-B-C coatings, magnetron sputtering, nanoindentation, AFM, FIB, SEM

Recently, W-B-C thin films appeared among competitive candidates for protective films due to their high hardness, low friction, high melting point and excellent chemical stability (1,2). In this work nanostructured W-B-C coatings were prepared using a custom built sputtering system with four magnetron sputtering heads in balanced magnetic field configuration on single crystalline silicon, high speed steel and tungsten carbide substrates. The coatings were prepared using sputtering of three targets: B_4C, C and W. The B_4C and W targets were DC driven and the carbon target was DC driven or connected to a bipolar pulsed generator working at frequencies up to 350 kHz. The thickness of prepared films was in the range from 1200 to 2000 nm. The mechanical properties of the prepared coatings were studied by means of instrumented nanoindentation technique performed on Hysitron TI950 Triboindenter equipped with a Berkovich indenter. Several testing modes were used in the range of indentation loads from 0.1 to 11 mN, namely quasistatic nanoindentation test, quasistatic nanoindentation with several unloading segments and nanodynamic mechanical analysis (nanoDMA) in the range from 0.1 to 300 Hz. In order to study the fracture resistance of the film as well as the film/substrate system in the load range from 10 to 1000 mN the Fisherscope H100 indentation tester equipped with a Berkovich indenter was used. The scratch resistance of the films was studied using Revetest (Anton Paar) scratch tester equipped with a Rockwell diamond tip (Radius = 200 μm) in linear progressive mode with loading rate of 15 N/min. Thin lamellas were prepared from central part of the indentation print as well as from the nondeformed part of the coating using focused ion beam technique in a scanning electron microscope LYRA 3 XMU FEG/SEM×FIB by Tescan. The details of microstructure for both parts of the coatings

were studied using transmission electron microscopes JEOL 2100F and Philips CM12 STEM. The microstructure of the prepared coatings was studied also using X-ray diffraction analysis performed on Rigaku Smartlab X-ray diffractometer with a fixed angle of incidence. The grazing incidence configuration was used. The surface morphology and roughness were analyzed by an atomic force microscope Ntegra Prima NT-MDT in a semi-contact mode. Figure 1 shows an example of SEM image of an indentation print made with load of 1N in W-B-C film. The C/W ratio of the film was 0.68. This film exhibited high hardness of (27±2) GPa and elastic modulus of (340±5) GPa. On the right hand part of Figure 1 the preparation of thin lamella at the central part of indentation print is illustrated. The 3D AFM image in Figure 2 illustrates the surface structure of the W-B-C film.

Acknowledgements:

The Czech Science Foundation is acknowledged for the financial support of this work (Project 15-17875S).

References:

1. H. Bolvardi, J. Emmerlich, M. to Baben, D. Music, J. von Appen, R. Dronskowski, J.M. Schneider, J. Phys. – Condens. Mat. 25 (2013), 045501 6pp.

2. Y.M. Liu, Z.L. Pei, J. Gongb, C. Sun, Surface and Coatings Technology 291 (2016) 276–285.

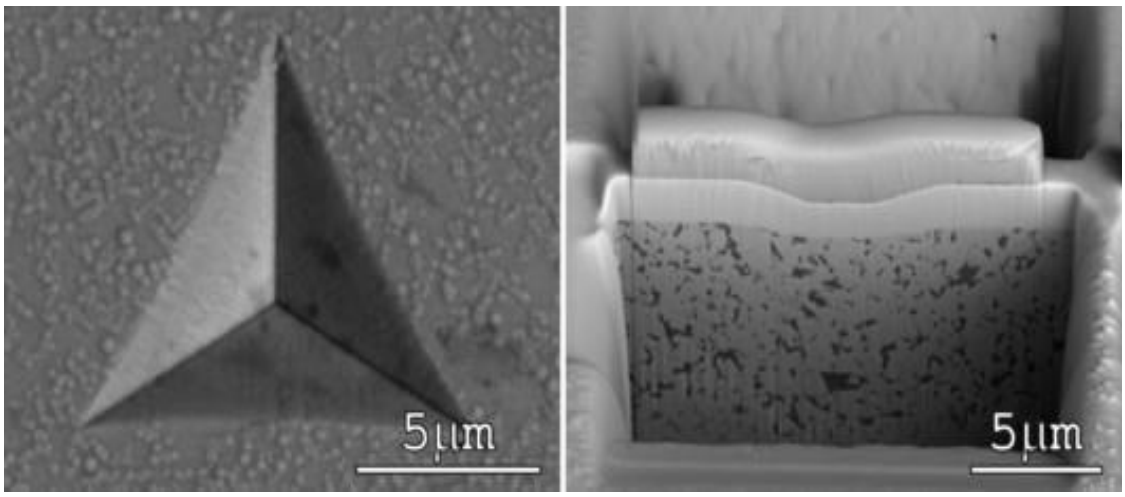

Figure 1. SEM image of an indentation print made with load of 1N in W-B-C film (on the left). Preparation of thin lamella at the central part of indentation print (on the right).

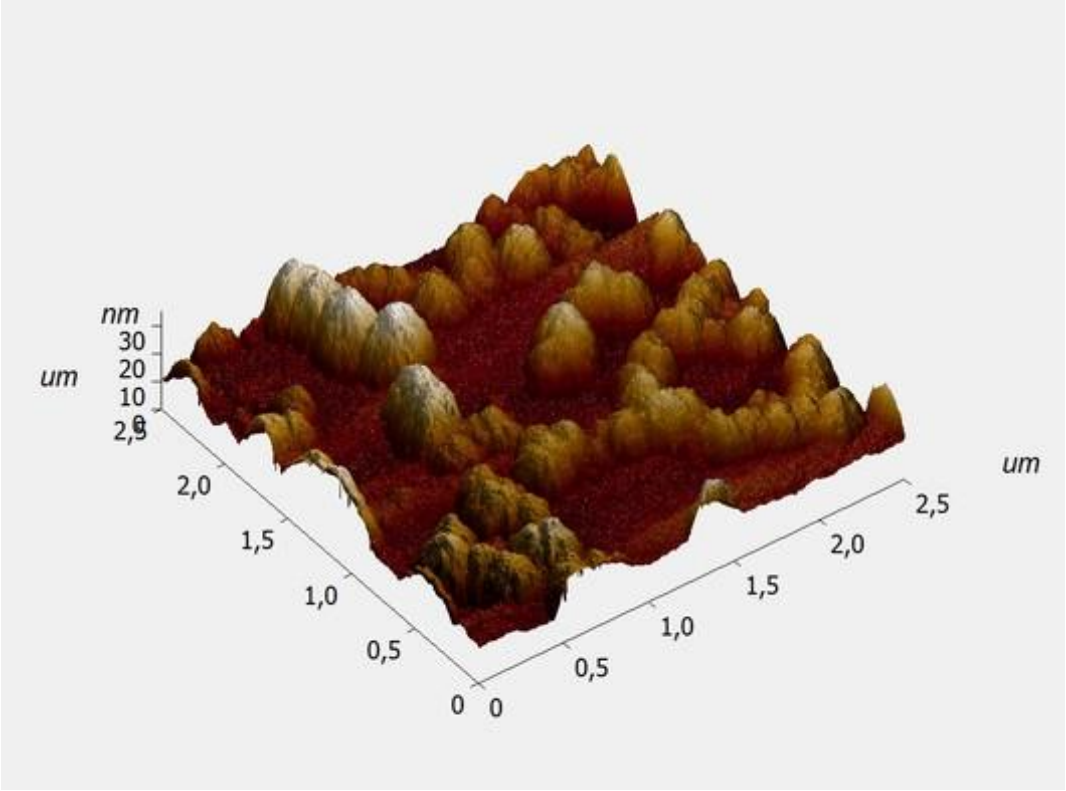

Figure 2. 3D AFM image of the W-B-C film surface.

Microstructural characterization of TaAlN coatings

Mária Čaplovičová (1), Marian Veselý (1), Mário Kotlár (1), Viliam Vretenár (1), Ľubomír Vančo (1), Peter Vogrinčič (1), Milan Mikula (2), Tomáš Roch (2), Leonid Satrapinsky (2)

1) STU Centre for Nanodiagnostics, University Science Park Bratislava Centre, Slovak University of Technology, Vazovova 5, 81243 Bratislava, Slovakia

2) Department of Experimental Physics, Faculty of Mathematics, Physics and Informatics, Comenius University, Mlynska Dolina F2, 84248 Bratislava, Slovakia

Keywords: TaAlN hard coatings, HRTEM, STEM

Ta-Al-N coatings were grown on mirror-polished Al_2O_3 plates (sapphire) at 450°C by means of relative unbalanced magnetron sputtering. As-deposited Ta0.55Al0.45N coatings with thickness 4 μm were annealed in vacuum at temperatures of 900°C, 1000°C, 1100°C, 1200°C, and 1300°C for 3min using a heating rate of 30°Cmin^{-1} and self-limiting cooling rates. Microstructural characterization of Ta-Al-N coatings annealed in vacuum at temperatures of 900°C, 1000°C, and 1200°C for 3 min was performed using JEM ARM 200cF transmission electron microscope(TEM) by cTEM, high resolution (HR) TEM, selected area electron diffraction (SAED), scanning transmission STEM, and energy dispersive spectroscopy (EDS) techniques. Columnar crystals grown in <001> direction of cubic NaCl-type (B1) TaAlN solid solution created the microstructure of the TaAlN coating after annealing at 900°C. Ta0.55Al0.45N coatings retain a columnar grain character also during annealing at 1000°C and 1200°C. STEMHAADF investigations of as-deposited and annealed (at 900°C) coatings revealed the presence of a phase of lower density at column boundaries, appearing as dark lines separating the individual columns. Line scan of STEM-EDS analyses identified relatively high Al content along with Ta very low content in these 2–3 nm thick regions consisting of very tiny nanograins. HRTEM and relevant FFT pattern confirmed that nanocrystals formed at columnar grain boundaries are of wurtzite AlN phase. Therefore, it is supposed that blurred ring in the SAED pattern belonging to wurtzite AlN corresponds to the AlN-rich boundary phase imaged by HAADF and BF STEM. Annealing at 1000°C also promoted the segregation and growth of wurtzite AlN-rich inclusions at column boundaries. Moreover, redistribution of atoms to create coherent cubic TaN- and AlN-rich nanometer-size domains inside the grains was

registered. Formation of coherent cubic TaN- and AlN-rich nanometer-size domains, occurring during the initial stage of thermally induced phase separation within cubic NaCl-type (B1) TaAlN solid solutions, yields a monotonic increase in hardness from 29 GPa (as deposited coatings) up to a maximum of 35 GPa (17%) reached after annealing at 1000°C. Further thermal treatment at T>1000°C leads to the transformation of metastable cubic domains into stable hexagonal TaN and AlN phases, thus resulting in hardness reductions.

Acknowledgements:

This presentation was created with the support of the Ministry of Education, Science, Research and Sport of the Slovak Republic within the Research and Development Operational Programme for the project “University Science Park of STU Bratislava”, ITMS 26240220084, co-funded by the European Regional Development Fund.

Comparison of measuring methods for determination of thickness of the multilayer tin/ticn pacvd coating deposited on cold work tool steel x153crmov12

Darko Landek (1), Suzana Jakovljević (1), Saša Kovačić (1)

1) Faculty of Mechanical Engineering and Naval Architecture, Ivana Lučića Street No.1, 10000 Zagreb, Croatia

Keywords: DC PACVD, TiN/TiCN coating, coating thickness, callotest, SEM, EDS, GDOES

The paper investigates methods for the thickness measurements of the direct current plasma assisted chemical vapor deposition TiN/TiCN coating applied to substrate of hardened and tempered tool steel for cold work grade X153CrMoV12. The developed coating is composed from a TiN sublayer and TiN/TiCN gradient layer with the final TiCN layer. The base coating properties have been characterized by examination of the surface roughness, chemical composition and thickness. The thickness of the sublayer and gradient layer of the same TiN/TiCN coating was determined by the four methods: the ball grinding test (callotest), the scanning electron microscopy (SEM), the electron dispersive spectroscopy (EDS) and by the quantitative depth profile analysis using glow discharge optical emission spectroscopy (GDOES). Results of measurements were statistically analysed in aim to evaluate the accuracy and reliability of tested methods.

TEM investigation of magnetron sputtered TiC, TiC/Ti, Ti(C) thin films

Zsolt Fogarassy (1), Nikolett Oláh (1), Ildikó Cora (1), Horváth Zsolt Endre (1), Tamás Csanádi (2), Katalin Balázsi (1)

1) Thin Film Physics Department, Institute for Technical Physics and Materials Science, Centre for Energy Research, Hungarian Academy of Sciences, KFKI Campus 1121 Budapest, Hungary

2) Institute for Materials Research, Slovak Academy of Sciences, Watsonova 47, 040 01 Košice, Slovak Republic

Keywords: TiC, Sputtering, TEM, Hardness, Nanocomposite

The c-TiC is considered as a promising hard coating material. TiC thin layers are usually produced by magnetron sputtering forming a two-phase layer, in which crystalline c-TiC nano-particles are separated from each other by a 0.5-2 nm thick amorphous carbide matrix (1). The research of these layers is mostly focused on the composition range of around 40 at.% Ti content since the hardness as the function of the Ti content shows maximum at this value. In this work, the c-TiC/h-Ti transition has been investigated, which has been less studied in the literature or was analyzed only by X-ray diffraction (XRD) (2). Our Ti-C layers were prepared by magnetron sputtering at room temperature in ultrahigh vacuum chamber ($3x10^{-8}$ mbar) with varying Ti content from 58 to 95 at.% in the different samples. The composition of each layer was set by the sputtering power. 300 nm thick amorphous SiO_x layers on Si single crystal wafers were used as substrate. Transmission electron microscopic (TEM) investigations were performed on cross sectional samples thinned by Ar^+ ion beam. Shift of the lattice parameters depending on Ti content was determined by XRD in the different samples. The mechanical properties of the samples were studied by nanoindentation. Columnar grains were formed in the deposited layers as it is illustrated on bright-field TEM image (see Figure 1). Diameter of the columns increases with the thickness of the growing layers, this broadening is faster in the layers with higher Ti content. According to both TEM (Fig 2.a) and XRD (Fig 2.b) studies, two phases are present in the samples: c-TiC was formed in layers with Ti-content from 58 to 86

at.%, while in the samples with 86 at.% Ti content the h-Ti is also present. The c-TiC disappears at 90 at.% Ti-content or above, where only h-Ti crystallizes.

With the increase of titanium content, (111) texture of the c-TiC phase dominates, as it can be observed from the cross-sectional selected area electron diffraction (SAED) patterns showed in Figure 2.a. In the sample containing 86 at.% titanium, the c-TIC (111) and the h-Ti (001) peaks in the XRD pattern (Fig 2.b) are overlapping resulting a widely broadened peak. Based on this peak broadening at 2,43 Å and the very weak but clearly visible h-Ti (100) peak at 2,57 Å, the co-existence of the two phases can be supposed. The presence of the two structures was cleared with the HRTEM studies. In the presentation, the structural changes of the Ti-C layers as the function of Ti content will be shown and based on this, the evolution of mechanical properties will be interpreted. Besides, HRTEM studies confirming phase-separation of h-Ti and c-TiC in the sample containing 86 at.% titanium are going to be presented.

References:

1. N. Oláh, Zs. Fogarassy, A. Sulyok, J. Szívós, T. Csanádi, K. Balázsi, Ceramics International 42 (2016) 12215–12220.

2. A. Sato, N. Kikuchi, H. Nanto, A. Kinbara E. Kusano, Surface and Coatings Technology 120-121 (1999) 378-382.

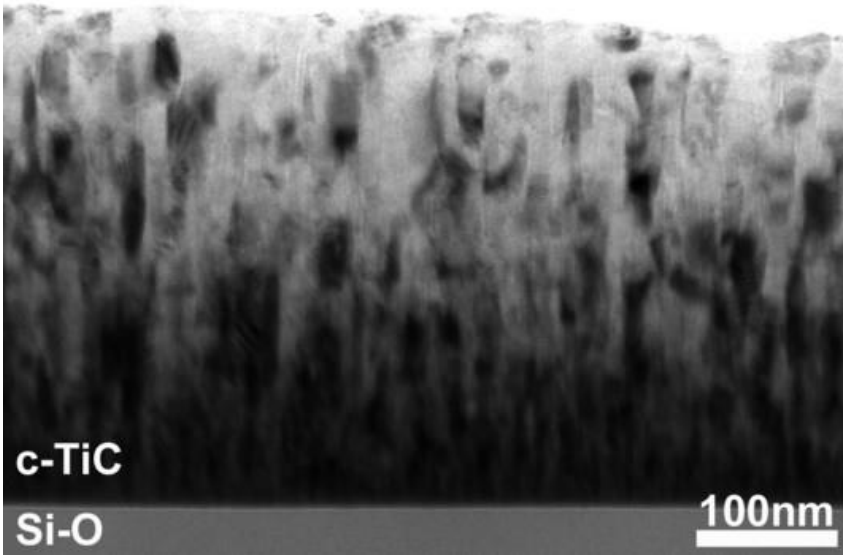

Figure 1. Cross-sectional bright-field TEM image from the c-TiC sample with 58 at.% Ti content.

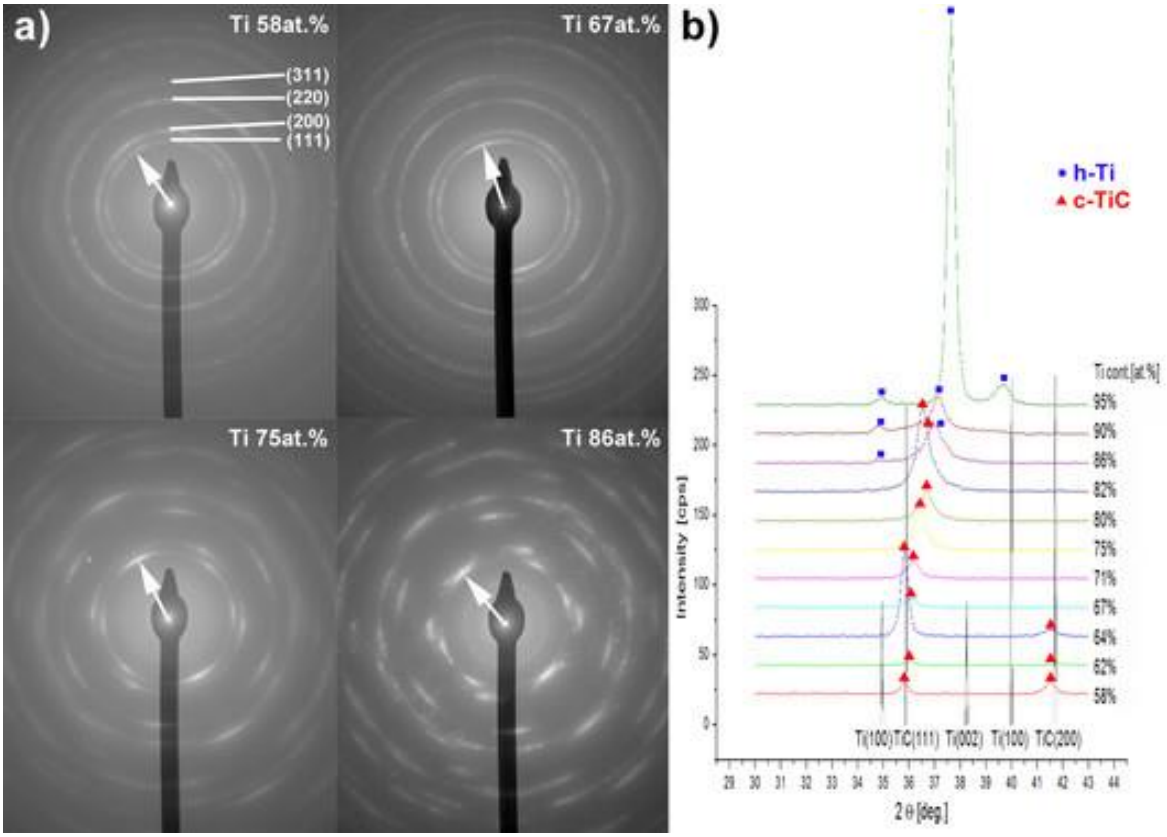

Figure 2. On the left the SAED patterns are shown from the TiC layers containing different amount of Ti. Arrows indicate the direction perpendicular to the surface of the substrate. On the right the XRD patterns of the grown layers.

Barium titanate thin films deposition by spray pyrolysis

Krunoslav Juraić (1), Marco Deluca (2), Robert Wimmer-Teubenbacher (2)

1) Ruđer Bošković Institute, Bijenička cesta 54, 10000 Zagreb, Croatia

2) Materials Center Leoben Forschung GmbH, Roseggerstraße 12, A-8700 Leoben, Austria

Keywords: barium titanate, thin films, spray pyrolysis

Barium titanate ($BaTiO_3$) is emerging as a promising material due to the merits of high dielectric constant, low leakage current and excellent piezoelectric, large electro-optic coefficients and ferroelectric properties. Like in other electronic ceramic materials, the electrical properties of $BaTiO_3$ are closely linked to its microstructural features, such as porosity and grain size. For optimal properties, it is desirable to have a homogeneous microstructure. In principle, $BaTiO_3$ ceramics with a dense structure and fine grains have very good dielectric properties. The $BaTiO_3$ thin films with perovskite structure are of particular interest for electronic device applications due to their useful ferroelectric properties. Perovskite-type $BaTiO_3$ was recently tested as a pure phase porous film electrode in dye-sensitized solar cells (DSSC) and as a TiO_2/$BaTiO_3$ composite electrode and showed better efficiency than a solar cell with the pure TiO_2 electrode. $BaTiO_3$ is an n-type semiconductor, and its band-gap is equal or more than that of TiO_2. Thus, DSSC using these perovskite-type semiconductors may exhibit higher VOC than DSSC using TiO_2, although the band tuning among electrode, dye and electrolyte is necessary. There are various chemical methods for $BaTiO_3$ preparation co-precipitation, alkoxide hydrolysis, metal-organic processing and hydrothermal treatment. In the form of thin films $BaTiO_3$ were also deposited by RF magnetron sputtering, laser ablation, metal-organic chemical vapor deposition (MOCVD), sol–gel processing and spray pyrolysis. Among the listed deposition techniques, the spray pyrolysis method is widely used to grow complex, multi-layered thin films because of its ability to preserve the target stoichiometry to prepare thin films by layer-by-layer growth. In comparison with other deposition techniques, spray pyrolysis has several advantages, such as high purity, excellent control of chemical uniformity and stoichiometry in multi-component systems. The other advantage of the spray pyrolysis method is that it can be adapted easily for the production of large-area thin films. In this work, we will

present results of structural analysis of $BaTiO_3$ thin films by spray pyrolysis. Deposition parameters were optimized to get a very thin homogeneous $BaTiO_3$ layer. Precursor solution based on barium acetate [$(CH_3COO)_2Ba$] and titanium tetraisopropoxide [$C_{12}H_{28}O_4Ti$] were used for spray pyrolysis experiments. Structural properties of obtained layer were examined by XRD, Raman spectroscopy and Scanning Electron Microscopy.

Acknowledgements:

This work has been supported in part by Croatian Science Foundation under the project IP-2014-09-9419 and STSM TO-BE COST action.

References:

[Li2014] 1 Y. Li, C. Wang, Z. Yao, H.-K. Kim, and N.-Y. Kim, Nanoscale Research Letters 9, 530 (2014).

[Kumbhar2015] S.S. Kumbhar, M.A. Mahadik, P.K. Chougule, V.S. Mohite, Y.M. Hunge, K.Y. Rajpure, A.V. Moholkar, and C.H. Bhosale, Materials Science-Poland 33, (2015).

[Okamoto2014] Y. Okamoto and Y. Suzuki, Journal of the Ceramic Society of Japan 122, 728 (2014).

Electron microscopy of Ti/Ni multilayers prepared by magnetron sputtering

Jiri Buršík (1), Vilma Buršíková (2), Pavel Souček (2), Petr Vašina (2)

1) Institute of Physics of Materials, Czech Academy of Sciences, Žižkova 22, CZ-61662 Brno, Czech Republic

2) Department of Physical Electronics, Faculty of Science, Masaryk University, Kotlářská 2, CZ-61137 Brno, Czech Republic

Keywords: multilayer, magnetron sputtering, microstructure, indentation

Nanostructured materials such as nanocomposite thin films, multilayers and nanolaminates are of great scientific and industrial interest. They have often been proven to be superior to conventional protective coatings due to their increased fracture toughness, improved sliding wear resistance and mainly due to the possibility of controlling their toughness and hardness independently (1). Most of the applications require materials which are resistant to deformation, structural changes and failure. However, the nanolayered or nanostructured films may also be designed to exhibit controlled reversible structure changes, which may be prospective for many applications, including information storage, optical communication devices, sensors and actuators, micro-fluidic instruments for drug delivery, and smart tribological surfaces for friction and wear control. One of the main advantages of the magnetron sputtering technique often used for preparation of well-defined coatings is a wide variability of properties of deposited films in dependence on the deposition conditions. One of the most often used diagnostic methods to characterize the local mechanical properties of thin films is based on indentation techniques (2). In the last few decades, an exceeding progress has been achieved due to advances in instrumentation both (i) in the field of micro- and nanoindentation characterization of thin films and (ii) in the subsequent techniques of microstructural study by analytical scanning and transmission electron microscopy (SEM and TEM), namely thanks to routine implementation of focussed ion beam (FIB) in SEM for sample preparation and various sorts of *in situ* testing in both SEM and TEM. In this work we used indentation techniques, SEM with FIB and TEM to study Ti/Ni multilayers deposited on Si substrates. Layered coatings with

alteration of Ni and Ti layers were prepared with different bilayer thickness (here either 2×10 nm or 2×50 nm) and the total coating thickness of 0.4–0.5 μm. A DC (direct current) magnetron sputtering without sample heating was used with Ti and Ni targets, power on each target was 350 W, the deposition pressure was 0.3 Pa, the growth rate was 0.75 nm/s and 1.52 nm/s for Ti and Ni layers, respectively. Figure 1 shows a lamella prepared from 5×(50 nm Ti + 50 nm Ni) multilayer indented with a large load of 1N. Massive pile-ups are shown in the inset and wrinkling of layers is observed in Figure 1 under the white protective Pt layer deposited across the indentation print. The cracks developed in course of lamella preparation as a way to relieve internal stresses. An overview of multilayer 20×(10 nm Ti + 10 nm Ni) is shown on Figure 2. Polycrystalline layers with well-defined planar interfaces are visible near the substrate, with increasing number of layers the planarity subsequently degrades. Mechanical properties obtained from nanoindentation experiments will be discussed in relation to microstructural observations.

Acknowledgements:

The research is supported by the Czech Science Foundation (Project 15-17875S).

References:

1. Nanostructured Materials, G. Wilde (Ed.), Elsevier, 2009.

2. Nanoindentation, A.C. Fischer-Cripps, Springer, 2011.

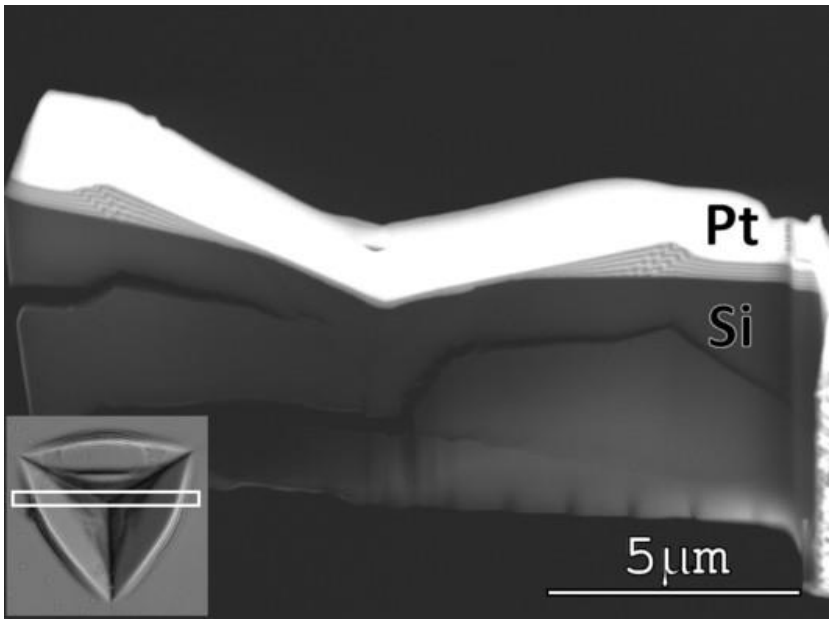

Figure 1. SEM image, cross section of indentation print.

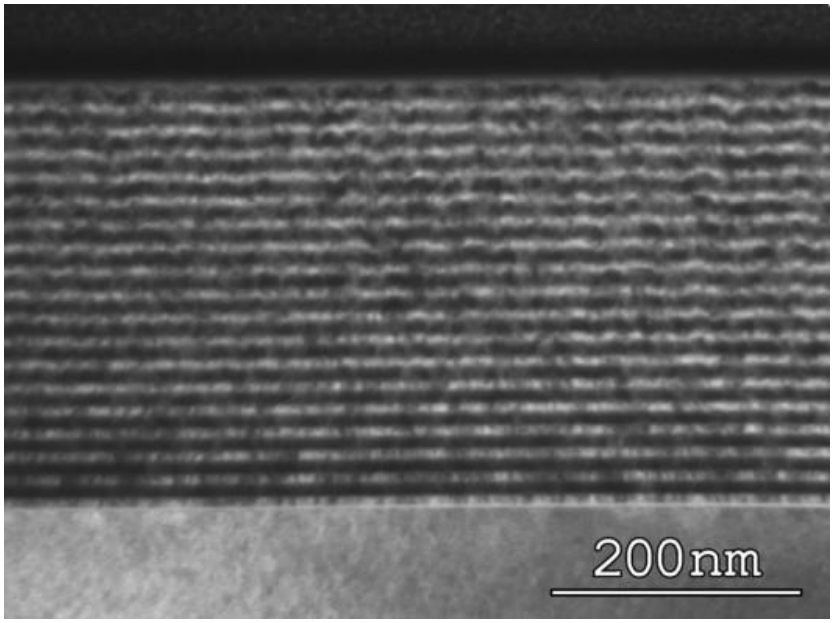

Figure 2. TEM micrograph of a thin lamellar section prepared by FIB.

TEM study of basal-plane inversion boundaries in Sn-Doped ZnO

Vesna Ribic (1), Aleksander Rečnik (2), Goran Dražić (3), Matej Komelj (2), Anton Kokalj (2), Mateja Podlogar (2), Nina Daneu (2), Tina Radosevic (2), Danijela Lukovic-Golic (1), Zorica Brankovic (1), Slavko Bernik (2), Goran Brankovic (1)

1) Institute for Multidisciplinary Research, University of Belgrade, Kneza Višeslava 1, 11030, Belgrade, Serbia

2) Jožef Stefan Institute, Jamova cesta 39, 1000 Ljubljana, Slovenia

3) National Institute of Chemistry, Hajdrihova ulica 19, 1000 Ljubljana, Slovenia

Keywords: ZnO, SnO_2, domain walls, HRTEM, HAADF-STEM

Various dopants are known to produce inversion boundaries (IBs) in ZnO, causing polarity inversion across the interface. These are found either in basal or pyramidal planes and can be of head-to-head or tail-to-tail configuration with respect to the orientation of the polar c-axis. The dopants, known to produce IBs in ZnO are: In_2O_3, Fe_2O_3, Mn_2O_3, Ga_2O_3, SiO_2, SnO_2, TiO_2 and Sb_2O_3. While some of IBs have been studied in detail, many IB structures remain unresolved. In our study we investigated structure and chemistry of basal plane inversion boundaries in SnO_2-doped ZnO. The formation of IBs in this system was first reported by Daneu *et al.* (2000)[1] and using high-resolution transmission electron microscopy the same group attempted to solve structure and chemistry of Sn-rich IBs.[2] Implementing an innovative analytical approach based on acquiring multiple EDS spectra with concentric electron probes they showed that Sn^{4+} ions do not occupy the full IB layer, but rather one half of the layer. This suggested an average oxidation state of III+ for the cations comprising the IB plane. Based on electron micro-diffraction and HRTEM study Daneu *et al*.[1,2] reported that Sn-rich IBs are head-to-head oriented with interfacial cations located in trigonal prismatic sites, however, the exact atomic arrangement of Sn along IB has not been determined. To identify the translation state and atomic arrangement on Sn-rich IBs in ZnO we performed quantitative HRTEM and HAADF-STEM analysis of SnO_2-doped ZnO/Bi_2O_3 ceramics. IBs in ZnO grains were observed for two low-index orientations, [100] and [120], to obtain a 3D information on the translation state of the IB plane. The coordination site of interfacial cations was shown to be octahedral.

Translation obtained from images is compared with three different, so far known, types of the head-to-head IB translations with octahedral coordination of cations at IB-plane: (i) IB with □□□□□□□□□□□□stacking of the cation sublattice, as observed with Sb doping, (ii) IB with□□□□□□□□□□□□, as observed with In and Fe doping and (iii) IB with □□□□□□□□□□□□as observed with Mn doping. For Sn-doped ZnO translations turned out to be (ii) □□□□□□□□□□□□, the same as the one occurring in In- and Fe-doped ZnO. Based on experimental observations of local atomic arrangement, HRTEM and HAADF-STEM image simulations were performed for two different in-plane distributions of Sn and Zn atoms, to better understand experimental image contrast on IBs. The generated models will be further used for ab-initio calculations aimed at determining the electronic structure of IBs. This study was realized within the frame of Serbian-Slovenian bilateral collaboration scheme under the project 'Zero- to Three-Dimensional Nanostructures for Application in Optics, Electronics and Energetics'.

Acknowledgements:

This research was supported by Serbian - Slovenian bilateral project, “Zero- to Three-Dimensional Nanostructures for Application in Optics, Electronics and Energetics”.

References:

1. N. Daneu et al., Microsc. Microanal. (2003) 286–287.9 (S3)

2. N. Daneu et al., J. Am. Ceram. Soc. (2000) 3165–3171.83 (12)

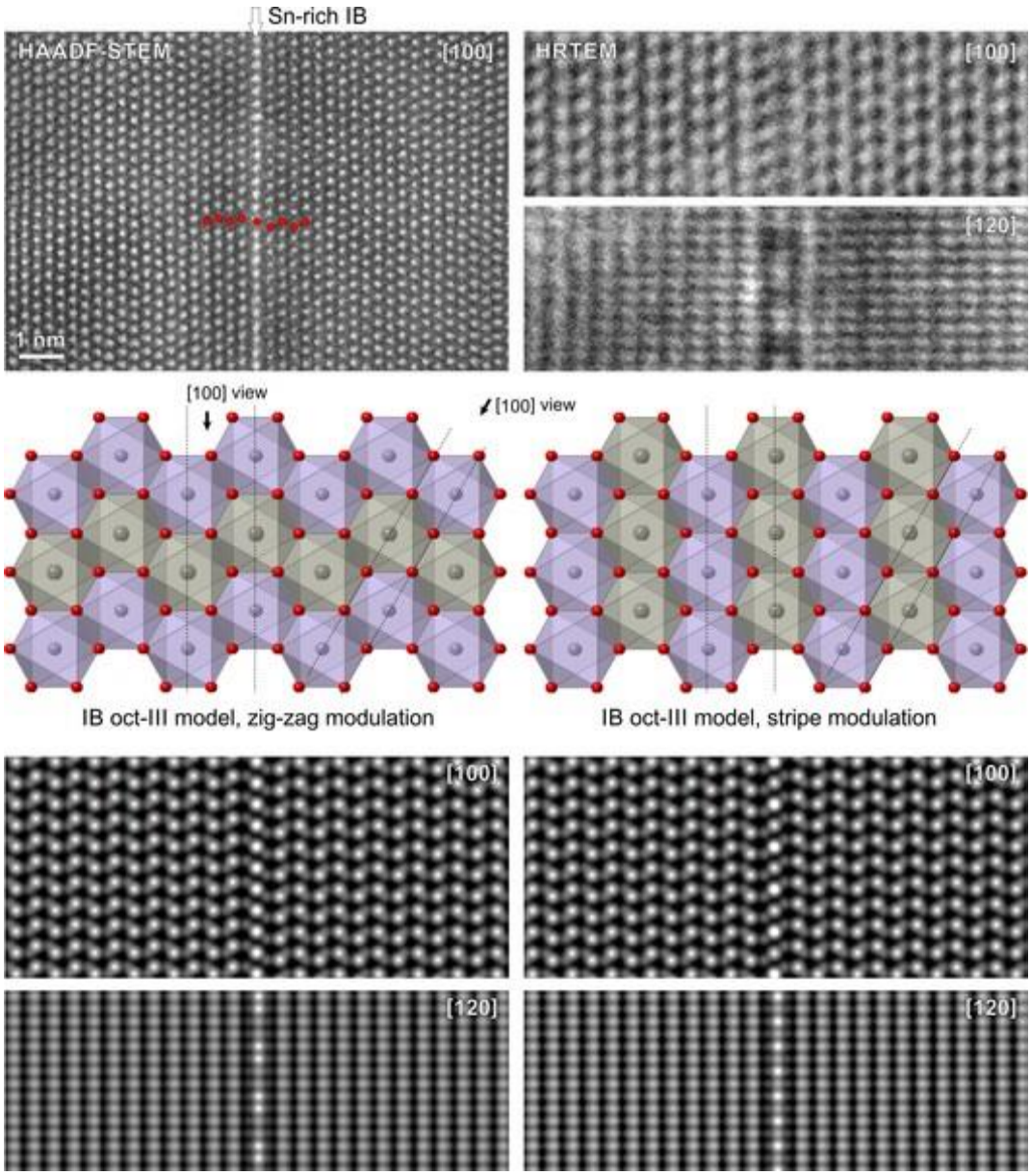

Figure 1. Experimental HAADF-STEM and HRTEM images of Sn-rich IB in ZnO shown in two projections with hypothetical atomic arrangements realizing 1:1 distribution of Sn and Zn atoms at the IB plane. HAADF-STEM image simulations show the image contrast at the IB plane for the two IB modulations.

Measuring buried interface roughness by electron tomography

Georg Haberfehlner (1), Evelin Fisslthaler (1), Wolfgang Jäger (2), Gerald Kothleitner (3)

1) Graz Centre for Electron Microscopy, Steyrergasse 17, 8010 Graz, Austria

2) Institute for Materials Science, University of Kiel, Kaiserstr. 2, 24143 Kiel, Germany

3) Institute of Electron Microscopy and Nanoanalysis, Graz University of Technology, Steyrergasse 17, 8010 Graz, Austria

Keywords: electron tomography, interface roughness, HAADF STEM

The roughness of surfaces and interfaces between different materials at a sub-nanometer scale is an important factor for the functionality of many materials and devices, examples are semiconductor devices or X-ray mirrors. On a local scale, atomic force microscopy (AFM) is usually the method of choice for measuring surface roughness, but AFM is unable to access buried interfaces. For imaging buried interfaces the transmission electron microscope (TEM) is an useful tool, but interface roughness is masked by the projection nature of TEM images. Electron tomography can overcome this limitation by reconstructing a 3D image of a sample for a tilt series of projections, most frequently acquired using high-angles annular dark field (HAADF) scanning TEM (STEM) (1). Thereby, electron tomography shows promises for measuring roughness of buried interfaces. Quantitative measurement of surface roughness by electron tomography is challenging though. Many factors can introduce uncertainties and distortions, such as tilt series alignment, choice of reconstruction algorithm and criterion for interface detection. In this work, we investigate buried interfaces in two materials systems by electron tomography. First, we analyse the interface between SiC and SiO_2, which is a system of utmost importance in the gate stack of SiC power field-effect transistors (Figure 1) and second, we investigate an X-ray mirror consisting of alternating layers of Mo and B_4C with nominal layer thicknesses varying between 1 and 2 nm (Figure 2). On these materials, we will highlight the potential and challenges of measuring roughness through electron tomography, and show routes to quantitative measurements and error estimation.

Acknowledgements:

We kindly acknowledge financial support by the Austrian Research Promotion Agency (FFG) (project 850220/859238)" and by the European Union within the 7th Framework Program (FP7/2007-2013) under Grant Agreement no. 312483 (ESTEEM2). We thank Infin Austria for proving SiC/SiO_2 samples, and U. Heidorn, F. Hertlein, J. Wiesmann from Incoated GmbH, Geesthacht, Germany for multilayer samples.

References:

1. P. Ercius et al., Adv. Mater. 27 (2015) 5638–5663.

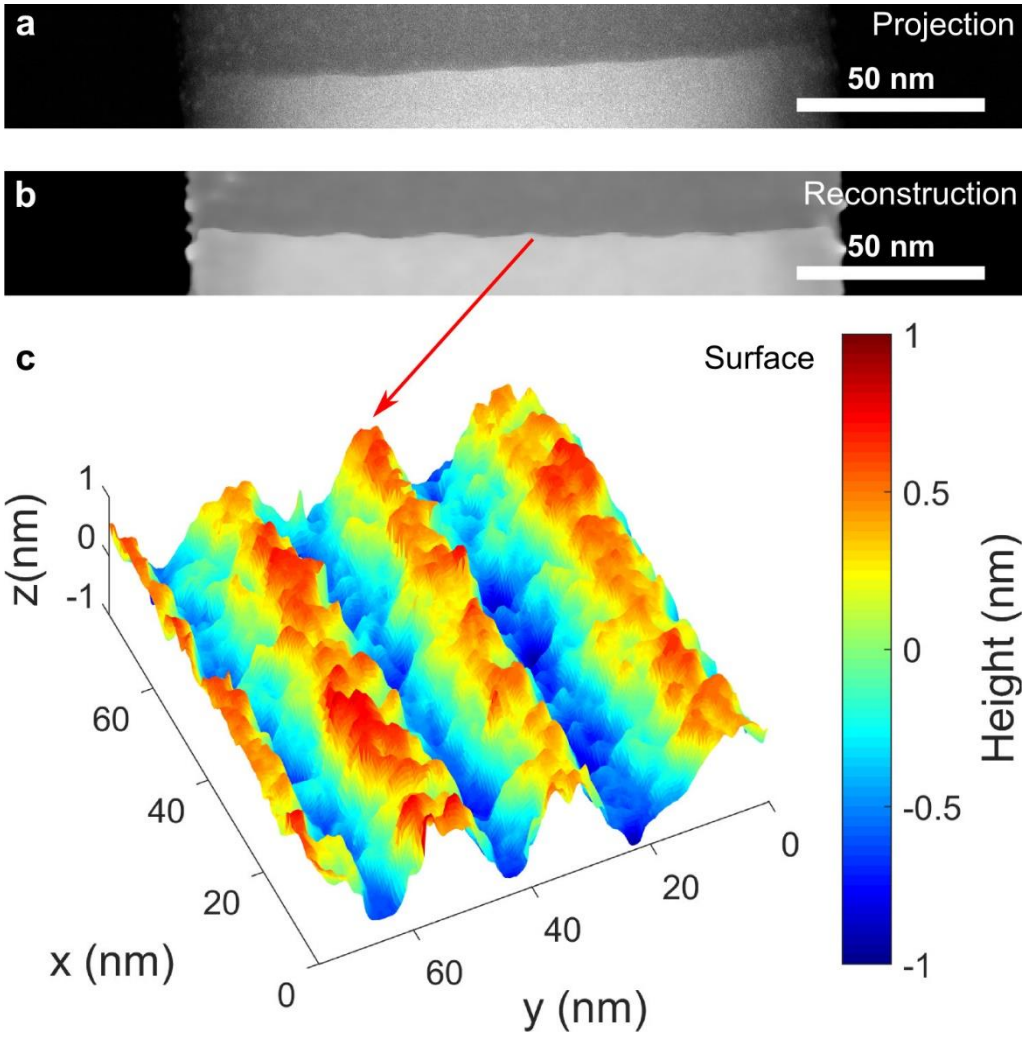

Figure 1. Tomography on SiC/SiO_2 interface. (a) Single HAADF STEM projection from the tilt series. (b) One slice though the reconstruction (c) Surface reconstruction of the interface between SiC and SiO_2. Periodic steps of ~6 atomic layers are well visible in the reconstruction.

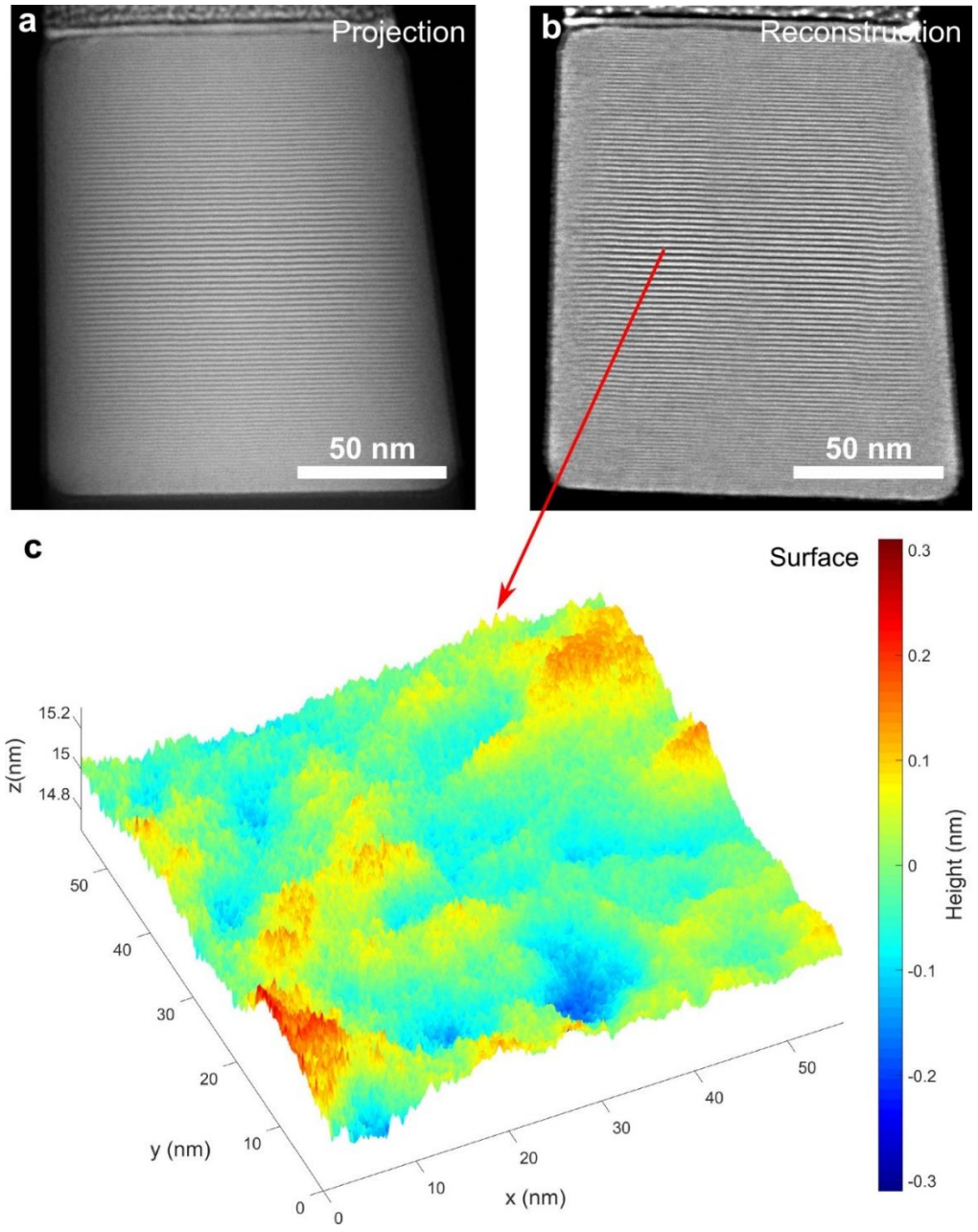

Figure 2. Tomography of a layer system of alternating Mo and B4C layers. (a) Single HAADF STEM projection, (b) Slice through the reconstruction. (c) Surface reconstruction of a single interface from the stack.

Fabrication and characterization of PMN-PT based high-frequency linear ultrasound array

Anton Kabaši (1), Andrijana Ćurković (1), Tonći Čakarić (1), Barbara Malić (2), Mirjam Budimir (3), Ante Bilušić (1)

1) University of Split, Faculty of Science, Ruđera Boškovića 33, Split, Croatia

2) Jožef Stefan Institute, Jamova cesta 39, 1000 Ljubljana, Slovenia

3) Institute for Nuclear Technology – INETEC, Dolenica 28, 10250 Zagreb, Croatia

Keywords: piezoelectric thick films, phased array

We present our initial-phase research with a final goal of development of high-frequency phase-synchronized microarray of ultrasound probes with possible application in ophthalmological diagnostics. Following facts led to the research idea: - a human eye that has been blurred and impermeable to light due to trauma (eg bleeding or disease), is still transparent for ultrasonic waves; - due to small spatial size of microstructures in the eye especially in the front (forehead eyelid, cornea, occipital lens), high-frequency ultrasound devices with central frequency of several tens of MHz have to be used; - classical diagnostic ophthalmic probes use only one piezoelectric element – it is the consequence of the technological limitations of producing micron-scale multi-element probes, although qualitative advantage of millimetre-scale multi-element ultrasound probes over a single-element ones has been proven in industry for decades; - recent technological achievements in the field of piezoelectric thick films (1) have opened up the possibility of producing a phase-harmonized series of independent ultrasonic high-frequency resonators. We will present results of structural and electrical characterization of 30-micrometer thick films of lead magnesium niobate-lead titanate (PMN-PT) produced by sol-gel technique and of their performance as phased-array ultrasound microprobes. Implementation of the research is enabled by the capacities built by the project "*Strengthening the Capacities for Application and Technology Transfer of Microelectromehanical Systems at the University of Split*" (MEMSplit, RC.2.2.08-0052) financed by the European Research and Development Fund.

References:

1. B.P Zhu et al., Ceramics International 39 (2013) 8709–8714.

Zinc oxide for photovoltaic applications

Ivana Panžić (1), Jelena Macan (2), Krunoslav Juraić (1), Krešimir Salamon (3), Andreja Gajović (1)

1) Ruđer Bošković Institute, Bijenička 54, 10000 Zagreb, Croatia

2) Faculty of Chemical Engineering and Technology, University of Zagreb, Marulićev trg 19, 10000 Zagreb, Croatia

3) Institute of Physics, Bijenička cesta 46, 10000, Zagreb

Keywords: zinc oxide, aluminium doped, sol-gel, SEM, GIXRD

Zinc oxide as a wide bandgap II-IV semiconductor is a promising material for many device applications such as solar cells, thin film transistors, chemical and biological sensors. For the application of ZnO as a transparent conducting electrode in solar cells it is important to develop low resistivity films with high transparency in the visible region and high stability against heat. ZnO films have a lot of advantages over widely used indium tin oxide film such as low cost, non-toxicity and high stability in atmosphere with good electrical and optical properties. The influence of preparation procedure and morphology on the electrical properties of the ZnO thin films modified by doping with aluminium were studied. The ZnO and Al doped ZnO (AZO) films were prepared on glass substrates by the sol-gel spin coating method using zinc acetate dihydrate-isopropanol-monoethanolamine sol doped with 1, 2, or 3 at % of Al with respect to Zn. The sol was aged for 24, 48, 72 h and 7 days before the spin coating process. The films were deposited 5,10,15, 20, 25,30 times, with heating for 5 minutes on 150 °C between the layers. When the desired number of layers was deposited, the films were annealed at different temperatures and different heating rates to investigate the influence of the annealing process on the morphological, structural and electrical properties. The morphological, structural, electrical and optical properties of post annealed films were investigated. For the morphological and structural characterization scanning electron microscopy (SEM) techniques, grazing incidence X-ray diffraction (XRD), Raman spectroscopy and FTIR were used. For the optical characterization UV/VIS spectroscopy measurements of transmittance and absorbance were performed.

AZO transparent conductive films with low resistivity and excellent transparency in the visible range were prepared by the sol-gel method. The fabricated films are believed to have great potential in the solar cell applications instead of the commonly used ITO and FTO substrates. Moreover, it was observed that the post annealing temperature and rate of heating influence morphology of the AZO (Figure 1 and Figure 2). Therefore, the sol-gel procedure combined with post-annealing treatment could be also used as the new method for preparation of electron transport layers in solar cells.

Acknowledgements:

This work has been fully supported by Croatian Science Foundation under the project IP-2014-09-9419

References:

1. Y.S.Kim and W.P.Tai, Applied Surface Science, 253 (2007) 4911-4916 2. X.Zhao et al., Thin Solid Films, 605 (2015) 208-214 3.K. E. Lee et al., Current Applied Physics, 9 (2009) 683-687.

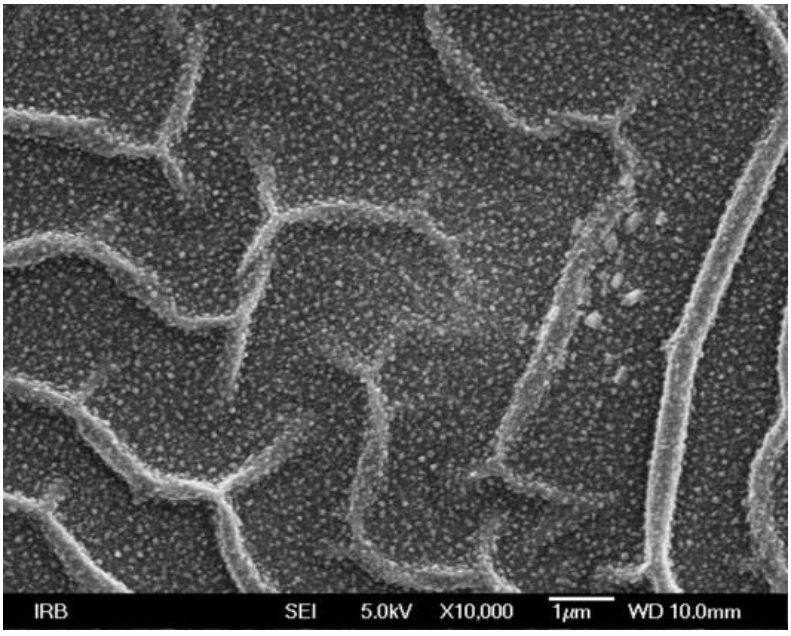

Figure 1. AZO thin film, annealed at 500°C, heating rate 50°C per minute.

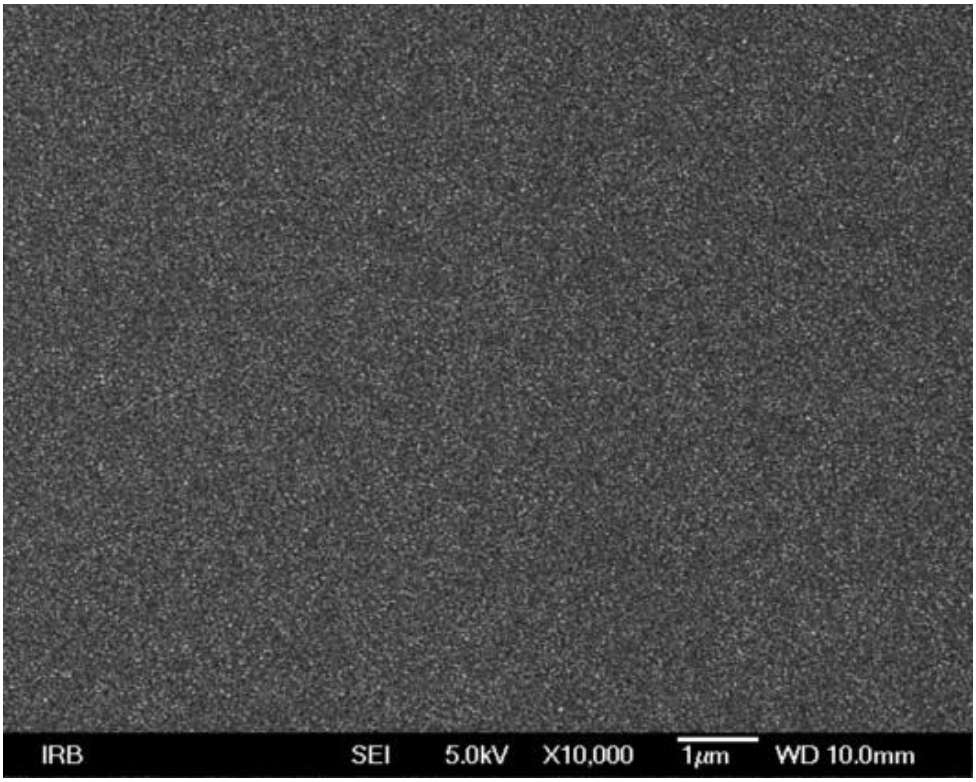

Figure 2. AZO thin film, annealed at 400°C, heating rate 2°C per minute.

Study of crystallization process in gexs1-x glasses by microscopic techniques

Veronika Podzemná (1), Luděk Hromádko (1)

1) University of Pardubice, Center of Materials and Nanotechnologies, nám. Čs. legií 565, 530 02 Pardubice

Keywords: Chalcogenide glasses, Germanium disulfide, Optical microscopy, Scanning electron microscopy

Germanium chalcogenide glasses show several remarkable features. These properties as high refractive index and wide transmission region of light from visible to IR are widely utilized for example in manufacturing optical waveguides of high transparency in the infrared window, as host materials of rare earth ions for photonic applications and others (1-2). Usually the investigation of these materials is focused on indirect monitoring of property changes. Optical and scanning electron microscopy are very useful techniques for direct observation of crystallization process. The crystal growth of GeS2 in Ge-S based glasses was studied. The crystal growth rate as a slope of crystal diameter time dependence is linearly increasing, suggesting interface controlled growth. Kinetics parameters as activation energy of crystal growth, growth mechanism and growth rate maximum versus temperature estimated from measured crystal diameter data will be discussed in this contribution.

Acknowledgements:

This work was supported by the grants P106/11/1152, LM2015082 and CZ.1.05/4.1.00/11.0251 from the Czech Ministry of Education, Youth and Sports of the Czech Republic.

References:

1. S.R. Elliott, Chalcogenide glasses, in: Materials Science and Technology,Wiley-VCH Verlag GmbH & Co. KGaA,Weinheim (2006)

2. V. Krasteva, D. Machewirth, G.H. Sigel Jr., J Non-Cryst Solids, 304 (1997) 213-214

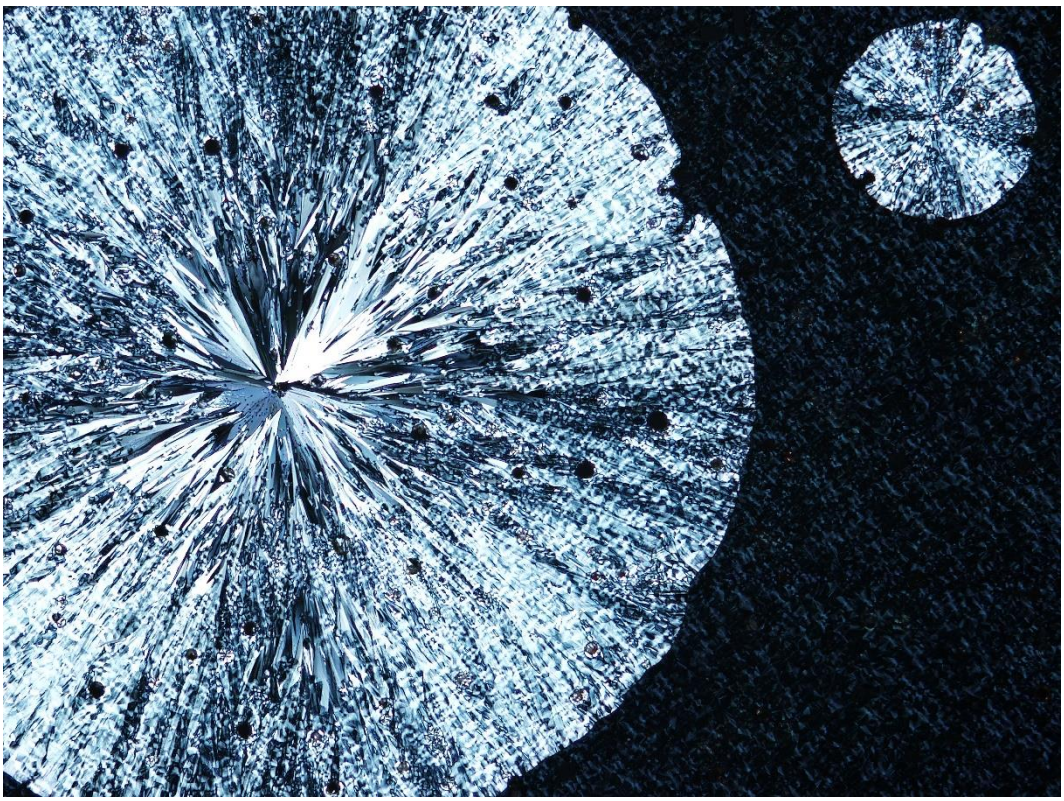

Figure 1. Show of the crystal in Ge32S68 undercooled melt.

M2. Polymers, Organic and Soft Materials

INVITED LECTURES M2:

Supramolecular assembly/reassembly processes at surfaces and interfaces

Artur Ciesielski (1)

1) Universitéde Strasbourg, CNRS, ISIS, 8 allee Gaspard Monge, 67000 Strasbourg, France

Among the many significant advances within the field of supramolecular chemistry over the past decades, the development of the so-called ‘‘dynamers’’ features a direct relevance to materials science. Defined as ‘‘combinatorial dynamic polymers’’, dynamers are constitutional dynamic systems and materials resulting from the application of the principles of supramolecular chemistry to polymer science. Like supramolecular materials in general, dynamers are reversible dynamic multifunctional architectures, capable of modifying their constitution by exchanging, recombining, incorporating components. They may exhibit a variety of novel properties and behave as adaptive materials. In this talk I will focus on the design of responsive switchable monolayers, i.e. monolayers capable to undergo significant changes in their physical or chemical properties as a result of external stimuli. Moreover, I will discuss the dynamic covalent chemistry approaches for tuning the chemical composition and the structure of the monolayers. Scanning tunneling microscopy studies provide direct evidence with a sub-nanometer resolution, on the formation and dynamic response of these self-assembled systems featuring controlled geometries and properties. (1-3)

References:

1. A. Ciesielski et al., Nanoscale 3 (2011) 1397–1410.

2. A. Ciesielski et al., Angew. Chem. Int. Ed. 49 (2010) 1963–1966.

3. A. Ciesielski et al., Nat. Chem. 6 (2014) 1017–1023.

Studying surface-assisted collagen fibrillogenesis by timelapse AFM

Franz M. Clemens (1)

1) Karlsruher Institut für Technologie (KIT), DFG-Center for Functional Nanostructures, Wolfgang-Gaede-Str. 1a, 76131 Karlsruhe, Germany

Fibrillar collagens, such as collagen type I, belong to the most abundant extracellular matrix proteins, but the collagen self-assembly process is still incompletely understood. Visualising the dynamic self-assembly process of collagen I on the molecular scale requires imaging techniques offering high spatiotemporal resolution. High-speed scanning atomic force microscopy (AFM) provides the means to study the assembly kinetics of fibrillar collagen type I nanomatrices on mica surfaces under near-physiological conditions. Furthermore, by modifying the buffer composition and pH value, the kinetics of collagen fibrillogenesis can be adjusted for optimal analysis by fast AFM scanning.

Depending on the particular tissue function, collagen fibril architecture and spacing *in vivo* is further modified by additional regulatory proteins. For instance, lumican and decorin, two members of the small leucine-rich repeat proteoglycan (SLRP) family, are important regulators of collagen I fibril spacing in cornea, which is important for the transparency of this tissue. Both proteoglycans consist of a core protein and a glycosaminoglycan (GAG) chain, but quantitative information regarding the precise role of the protein and GAG moieties in regulating collagen structure is still limited. AFM imaging of aligned collagen I nanofibrils can be used to investigate the role of lumican and decorin on collagen I fibril structure with high resolution. When co-assembled with collagen I, recombinant lumican or decorin proteins lacking the GAG chains decreased collagen fibril width to values below <100 nm and increased interfibrillar spacing in a dose-dependent manner. GAG-containing decorin also increased interfibrillar spacing, decreased fibril width and ultimately inhibited fibrillogenesis, but these effects required lower concentrations compared to recombinant decorin, indicating that the decorin core protein alone cannot compensate for the full regulatory and structural contribution of the GAG chain during collagen I fibrillogenesis. Using a 2D autocorrelation approach to compare the effects of recombinant and glycosylated decorin on collagen ultrastructure provided a quantitative measure for the observed structural differences. AFM analysis of ordered fibrillar collagen

arrays in combination with quantitative autocorrelation image analysis thus provides a useful tool for investigating SLRP-dependent nanoscale effects on collagen fibril structure.

References:

1. D.R. Stamov, E. Stock, C.M. Franz, T. Jähnke, H. Haschke, Imaging collagen type I fibrillogenesis with high spatiotemporal resolution, Ultramicroscopy. 149 (2015)

2. D.R. Stamov, A. Müller, Y. Wegrowski, S. Brezillon, C.M. Franz, Quantitative analysis of type I collagen fibril regulation by lumican and decorin using AFM, J. Struct. Biol. 183 (2013).

3. D.A. Cisneros, C. Hung, C.M. Franz, D.J. Muller, Observing growth steps of collagen self-assembly by time-lapse high-resolution atomic force microscopy, J. Struct. Biol. 154 (2006)

4. T. Gudzenko, C.M. Franz, Studying early stages of fibronectin fibrillogenesis in living cells by atomic force microscopy, Mol. Biol. Cell. 26 (2015)

Use of AFM for mechanical mapping of nanostructured surfaces

Jan Pribyl (1)

1) CEITEC MU, Masaryk University, Kamenice 5, CZ-62500 Brno, Czech Republic

Keywords: Nanoindentation, BioAFM, mica silanization, hydrogels

Atomic force microscopy (AFM) is not only a high-resolution imaging technique but also a sensitive tool able to study mechanical properties of samples (nanostructures, biomolecules, cells). Moreover, such measurements can be performed in laboratory atmosphere (with dry samples) but also under near physiological conditions – i.e. in buffered solutions and elevated temperature (mostly 37 ºC). Micromechanical transducers (cantilevers) are often used to map surface stiffness distribution, adhesion forces and viscoelastic parameters of variety of different surfaces – starting from solid surfaces such as nanostructured surfaces (electrodes, pillars, nanotubes), through the analysis of single molecules and their complexes, the range of sample may finish with the less stiff samples such as hydrogels and living cells. Use of AFM microscopy and spectroscopy will be illustrated on various research projects solved in our laboratory. Synthesis and characterization of new siloxane derivate 1-(3-aminopropyl)silatrane (APS) for binding of DNA molecules to mica surface will be shown. Procedure employing APS derivative brings experimental simplicity combined with lower background roughness of the sample prepared for AFM imaging. APS compound exhibits higher stability in comparison to other silanization compounds. Bioinspired hydrogels are promising materials having many possible applications, materials based on crosslinked serum and structural proteins were investigated. Use of such soft matrix in specific culturing of fibroblasts and effect of the stiffness of supporting material on mechanobiological properties of cells will be shown.

Acknowledgements:

This work was supported by the Ministry of Education, Youth and Sports of the Czech Republic under the projects CEITEC 2020 (LQ1601) and FNUSA-ICRC (LQ1603), as well as grant MSM0021622430, and Grant Agency of the Czech Republic (Grant No. P302/12/G157).

References:

1. G. Nardone et al., Nature Communications, vol. 8, p. ncomms15321, May 2017. 2. M. Pesl et al., Biosensors and Bioelectronics, vol. 85, pp. 751–757, Nov. 2016. 3. V. Horňáková, et al., Monatsh Chem, vol. 147, no. 5, pp. 865–871, May 2016.

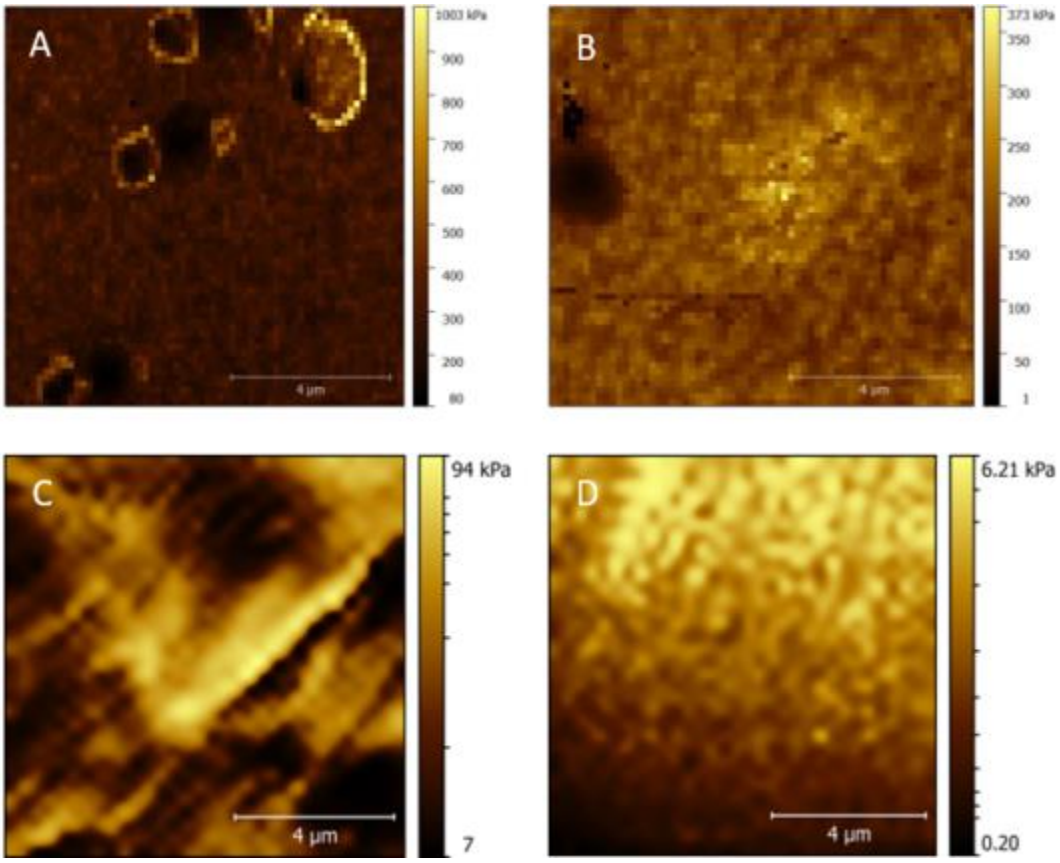

Figure 1. Mechanical properties of bioinspired (A, B) and synthetic (C, D) gels investigated in the region of 10x10 µm^2. Different ratio of crosslinked compounds (either proteins – A, B, or acrylamide – C, D) leads to different stiffness of the surface: 285.4, 169.1, 27.4 and 5.2 kPa for gels A, B, C, and D.

ORAL PRESENTATIONS M2:

Experimental observation, theoretical modelling and quantification of nanoparticle-induced polymer crystallization using *in situ* microscopy

Miroslav Šlouf (1), Sabina Krejcikova (1), Helena Vlkova (1), Antonin Sikora (2), Alexander Zhigunov (1)

1) Institute of Macromolecular Chemistry AS CR, v.v.i., Heyrovského nám. 2, CZ-162 06, Praha 6, Czech Republic,

2) Univerzita Tomáše Bati ve Zlíně, Fakulta technologická, Vavrečkova 275, 760 01 Zlín, Czech Republic

Keywords: semicrystalline polymers, nucleated crystallization, nanoparticles, *in situ* microscopy

Semicrystalline polymers belong among the most important polymer materials. The four most common thermoplastics dominating the market (polyethylene (PE), polypropylene (PP), polyvinylchloride (PVC) and polystyrene (PS)) together represent >80% by volume of world plastics consumption and three of them (PE, PP, and PVC) exhibit semicrystalline character, which strongly impacts on their mechanical performance. The properties of semicrystalline polymers can be further modified by various inorganic additives, which work as nucleating agents (i.e. agents influencing the rate and/or overall extent of the crystallization). In this work, we describe our recently-developed microscopic technique, named sandwich method (1), for direct quantitative comparison of nucleating activity of various nucleating agents in semicrystalline polymers. The samples for sandwich method consist of two thin polymer films (thickness ~100 micrometers) with a thin, homogeneous layer of nucleating agent (thickness < 1 micrometer) between them. The cross-section of the sandwich, containing the central nucleating agent layer, is observed in polarized light microscope (PLM) during crystallization (Figure 1). Control samples without nucleating agent show random growth of the spherulites, while the samples with the central nucleating agent layer display spherulites and/or crystalline

aggregates growing from the central line. The overall crystallization kinetics is closely connected with the nucleating agent activity. The intensity of the polarized light is detected with a digital camera, automatically converted to a qualitative signal and the whole set of micrographs is evaluated in terms of Avrami theory (1, 2). Moreover, the crystallization process in sandwich composites can be modeled, simulated and verified using our program package SCRYST (Figure 2). The output parameters from sandwich method and/or SCRYST, such as Avrami coefficients and crystallization half-times, are used for quantitative evaluation and comparison of nucleating activity of the investigated particles. The sandwich method was recently employed in comparison of the nucleating activity in polyoxymethylene composites with gold nanoparticles (POM/Au), TiO_2-based nanotubes (POM/TiX), talc microparticles (POM/mTalc) and calcium carbonate nanoparticles (POM/nChalk) (1). Moreover, we successfully applied the sandwich method for elucidation and description of somewhat unusual crystallization kinetics in polypropylene and polycaprolactone nanocomposites with TiO_2 micro- and nanoparticles (PP/TiX and PCL/TiX) (2). The results evidenced that the sandwich method is a reliable and reproducible tool for evaluation of nucleating activity of nanoparticles in the microscale. Due to the small size of the sandwich nanocomposites and negligible amounts of the nucleating agents needed, the sandwich method is suitable for evaluation of expensive or difficult-to-prepare polymers and/or nanoparticles.

Acknowledgements:

This research was supported by Czech Science Foundation (project 17-05007S), TA CR (project TE01020118), and MSMT CR (project POLYMAT LO1507).

References:

1. M. Slouf et al., Front. Mater. 2:23 (2015) doi: 10.3389/fmats.2015.00023.

2. T. Vackova et al., Polym. Bull. 74 (2017) 445–464.

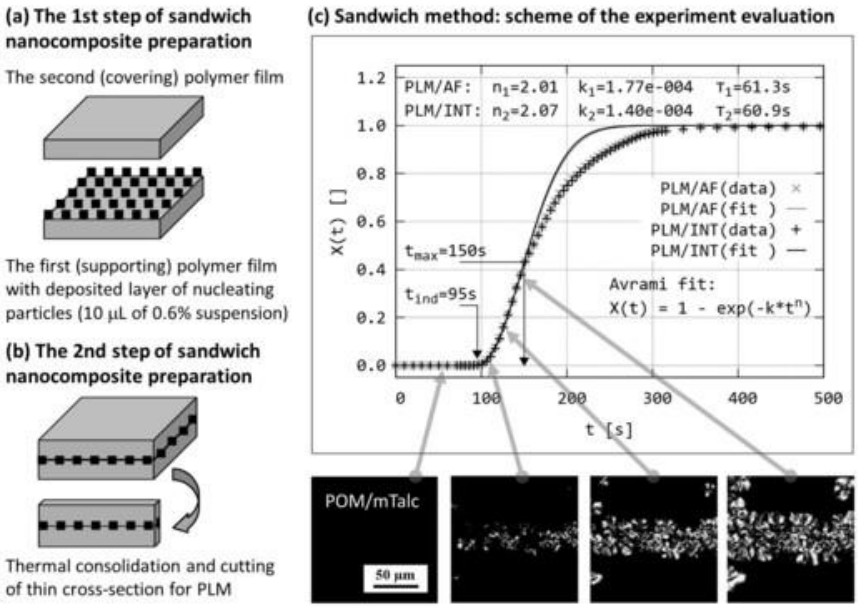

Figure 1. Principle of the sandwich method: (a, b) preparation of the sandwich nanocomposites; (c) evaluation of the results – each PLM micrograph corresponds to one experimental point in crystallization plot, which is interpreted in terms of Avrami theory.

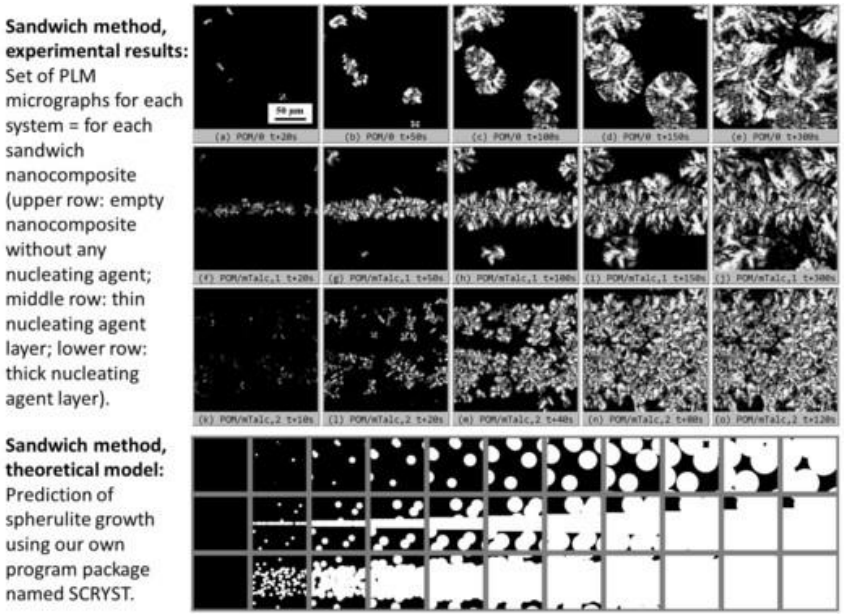

Figure 2. Example of the sandwich method results: (a) experimental PLM micrographs for polyoxymethylene sandwich composites and (b) theoretical simulation of the results using program SCRYST.

Influence of Bismuth oxide nanoparticles on mechanical properties of epoxy resin

Ivana Ropuš (1), Tatjana Haramina (2), Pravin Jagdale (3), Alberto Tagliaferro (3)

1) Energoatest zaštita d.o.o., 10020 Zagreb, Croatia

2) Faculty of Mechanical Engineering and Naval Architecture, Department for Materials, 10002 Zagreb, Croatia

3) Department of applied science and technology (DISAT), Politecnico di Torino, 10129 Torino, Italy

Keywords: nanocomposites, epoxy resin, bismuth oxide, mechanical properties

Bismuth oxide (Bi_2O_3) has very interesting optical and electrical properties (1-2). It is worth then to have a look also at the impact they can have on mechanical properties of composites. In order to investigate mechanical properties of epoxy based composites containing Bi_2O_3 as a filler two composites with 1 wt % and 3 wt % of Bi_2O_3 powder were prepared. Dispersion of the filler in the epoxy matrix was achieved by means of a 3 roll mill calender method. Field Emission Scanning Electron Microscopy (FESEM) was used to analyze nanocomposite cryo-fractured surface morphology in order to investigate powder dispersion. Mechanical properties are tested by means of Vickers microhardness test, three points bending flexural test and dynamic mechanical analysis (DMA). Microhardnesses of the nanocomposites do not change sensibly with respect to the neat epoxy resin. While microhardness of 1 wt % Bi_2O_3 composite is lower than the neat epoxy resin, the microhardness of the nanocomposite with 3 wt % Bi_2O_3 increased with respect to that of the neat epoxy resin. Flexural modulus and strength of both nanocomposites decreased compared to those of the neat epoxy resin. Inclusion of bismuth oxide nanoparticles in the epoxy resin matrices reduced the flexural properties more than 20 %. The effect was more pronounced for the nanocomposite with 1 wt % of filler. Dynamic mechanical analysis (DMA) was performed with tensile stress applied. It shows that 1 wt % of filler has greater impact on properties of the matrix as glass to rubber transition where material turns from stiff to ductile takes place at higher temperatures. However the storage modulus of nanocomposites with 1 wt % of Bi_2O_3 decreases both in glass and rubber conditions compared

to those of the neat epoxy resin and of the nanocomposite with 3 wt % of filler. The damping factor tan δ of the two later materials shows two peaks in the near glass transition region. For the nanocomposite with less nanoparticles the peak at lower temperatures vanishes and the intensity of the peak at higher temperatures increases leading to the conclusion that the polymer structure is more homogeneous. All results lead to the conclusion that for the analyzed systems fewer nanoparticles have higher impact on the material's behavior.

References:

1. Y. Astuti et al., IOP Conf. Series: Mater. Sci. and Engine. 107 (2016) 012006.

2. P. Jagdale et al., App. Surfa. Sci. 303 (2014) 250–254.

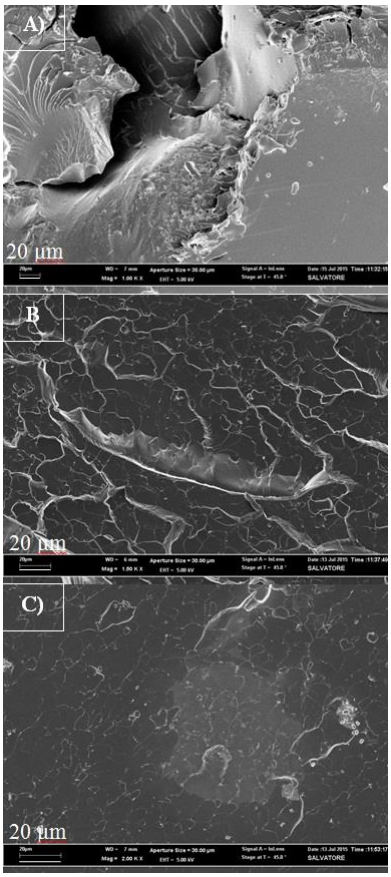

Figure 1. FESEM analysis of neat epoxy resin as well as nanocomposites containing 1 wt% and 3 wt% of filler respectively. (A) Neat epoxy resin. (B) Nanocomposite E/Bi_2O_3 1 % and (C) Nanocomposite E/Bi_2O_3 3 %.

Polymer fracture – Analysis by 3D reconstructions of the fracture region

Manfred Nachtnebel (1), Claudia Mayrhofer (2), Armin Zankel (2), Peter Poelt (1)

1) Institute of Electron Microscopy and Nanoanalysis, NAWI Graz, Graz University of Technology, Steyrerg. 17, 8010 Graz

2) Graz Centre for Electron Microscopy, Steyrerg. 17, 8010 Graz

Keywords: polymer fracture, 3D reconstruction, SBEM, ESEM, *in situ*

As Thermoplastics are a widely used material in nearly every field of application, they are also subjected to various physical tests. By far the majority of these investigations are based, however, upon parameters and characteristics resulting from mechanical tests, e.g. stress–strain diagrams from tensile tests. Additional information can be gained from micrographs recorded from the fracture surfaces by light and electron microscopy. But all these experiments and results provide only limited insight into what is happening in the material during the tests at a microscopic length scale. Performing such experiments in a microscope and observing with high magnification what is happening at the crack tip or at the surface of the specimen might be one possibility to overcome this obstacle (1). Additionally the combination of mechanical tests with other methods like acoustic emission analysis can help to elucidate some of the micromechanical processes (2). But even this does not give information about the structures forming in the bulk of the specimen during the tests. To this aim, the tensile tests were stopped at a predefined force below the yield of the respective material. Subsequently, the specimens were removed from the stage and sectioned by *in situ* ultramicrotomy. Since vital parameters like area of the fracture face or its texture and roughness can help to assess the energy necessary for the formation of the cracks and to gain knowledge about the fracture behaviour at the microscale, 3D reconstructions of the fracture region are imperative. Isotactic polypropylene (iPP) samples modified with either ethylene propylene rubber (EPR) or linear low-density polyethylene (LLDPE) particles of different sizes were subjected to a tensile test, with the test stopped at predefined forces of around 25% or 50 % yield. After removal of the sample from the tensile stage, part of the fracture region was extracted and stained in RuO_4 to

make the different phases visible. Thereafter automated slicing and imaging of the fracture region was performed by use of the *in situ* ultramicrotome 3View® (Gatan, Pleasanton, CA) mounted in an environmental scanning electron microscope Quanta FEG 600 (FEI, Eindhoven, NL). Finally, the resulting stack of images was used for 3D reconstructions. They revealed a different cracking behaviour of the EPR blend compared to that of the LLDPE blend. Figure 1 shows that in the EPR modified iPP widespread cracks were formed inside the matrix. In case of the LLDPE blend the creation of voids, concentrated in a small region perpendicular to the applied force, could be observed (see Figure 2). The size of the cracks or voids was dependent on the maximum applied force. Overall, this technique can be an outstanding method for the investigation of the crack formation at the early stage of the fracture process.

References:

1. P. Poelt et al., Polymer 51 (2010) 3203–3212.

2. M. Schoßig et al., Compos. Sci. Technol. 71 (2011) 257–265.

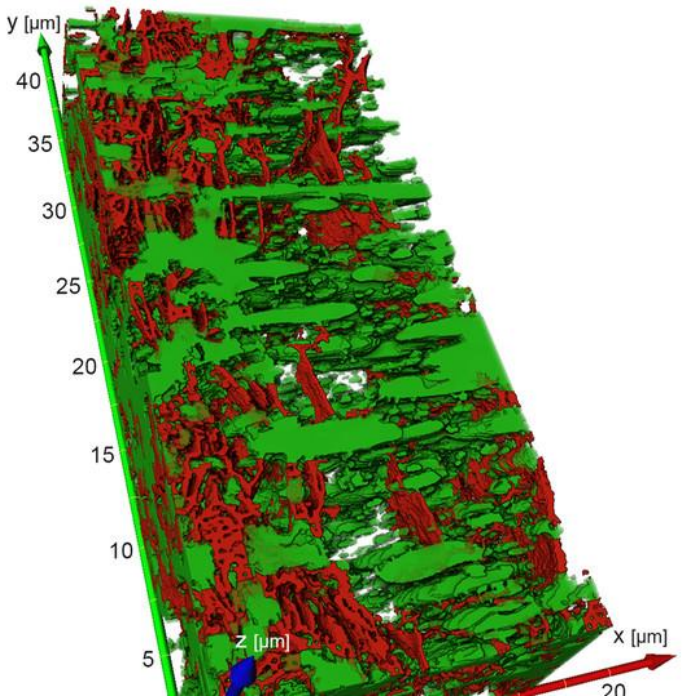

Figure 1. EPR modified iPP – 3D reconstruction of EPR particles (green) and cracks (red) after the carrying out of a tensile test that was stopped at a force of 50 % yield.

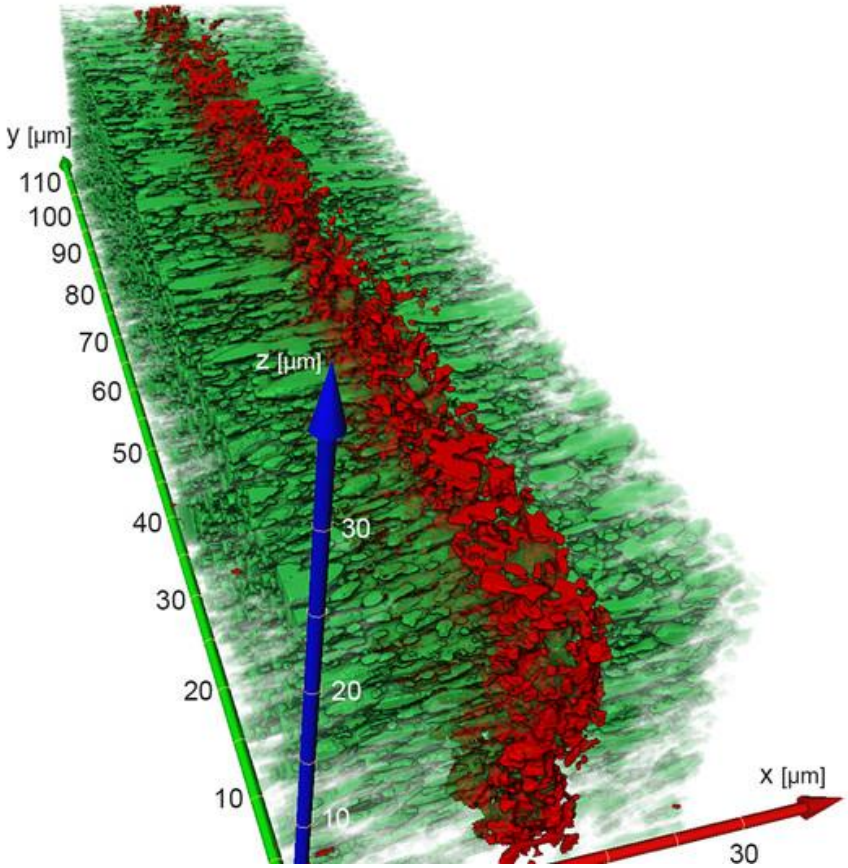

Figure 2. Extraction of the developed voids (red) inside the LLDPE particle (green) modified iPP sample after stopping the tensile test at 50 % yield.

Comparison of EDX and EELS sensibility for resolving the morphology of organic solar cells

Mona Sedighi (2), Pavel Potapov (3), Markus Löffler (1), Petr Formanek (2)

1) Dresden Center for Nano analysis, Technical University of Dresden, 01062 Dresden Germany

2) Leibniz-Institut für Polymerforschung Dresden e.V., Hohe Str. 6, 01069 Dresden, Germany

3) GLOBALFOUNDRIES Dresden Module 1, CCA, Wilschdorfer Landstrasse 101, 01109 Dresden, Germany

Keywords: Organic solar Cell, Morphology, EELS on organic materials, EDX on organic materials

The performance of small molecule organic solar cells strongly depends on the morphology of the blend of donors and acceptors forming the bulk heterojunction. Therefore, resolving the morphology of the blend and visualizing the donor-acceptor phase separation is crucial. Obtaining insights into the morphology of the blend requires high spatial resolution and a contrast mechanism to discriminate two phases with similar average atomic number. Conventional transmission electron microscopy (TEM) usually cannot reveal the morphology and special techniques have to be used. Here we present electron energy loss spectroscopy (EELS) and energy dispersive X-ray spectroscopy (EDX) study of the phase separation in oligothiophene:C60 blends by mapping the local distribution of elements.The specimen is a FIB lamella of pure layers of C60 and dicyanovinyl-dimethyl-pentathiophene ($C_{30}H_{20}N_4S_5$) as well as blends, interleaved with buffer layers, as shown in the Figure 1. Such a specimen design enables calibrating contrast differences as a function of composition. We compare the detection limits and signal to noise ratio of the two techniques under identical conditions, to obtain reliable 2D sulfur, nitrogen, oxygen and carbon maps with minimum radiation damage.

Figure 1. TEM bright field image of the stacks: pure layers of C60 (acceptor) and dicyanovinyl-dimethyl-pentathiophene (donor) as well as blends and buffer interlayers

POSTER PRESENTATIONS M2:

Laser-scanning confocal fluorescence microscopy using elliptically polarized cylindrical vector excitation beam: the visualization of arbitrarily oriented single quantum emitters on planar surfaces

Stepan Boichenko (1)

1) Irkutsk Branch of Institute of Laser Physics of Siberian Branch of Russian Academy of Sciences, 13, Ac. Lavrentieva ave., Novosibirsk, Russia, 630090

Keywords: single molecule visualization, arbitrarily oriented dipole, fluorescence microscopy, cylindrical vector beams, surface enhanced fluorescence

We have demonstrated previously that the task of visualization of arbitrarily oriented single quantum emitters (SQEs) (like single molecules, single quantum dots, single color centers) can be solved efficiently by means of laser-scanning confocal fluorescence microscopy (LSCFM) using an elliptically polarized cylindrical vector excitation beam (EPCVB) for SQEs located in a homogeneous medium and inside a special planar optical antenna providing 99% fluorescence collection efficiency (1). In the present work, we theoretically explore the task of visualization of arbitrarily oriented SQEs located on different planar surfaces by means of EPCVB-based LSCFM. SQEs of two types are considered: linear dipole and 2D dipole (a couple of two incoherent mutually orthogonal dipoles). The efficiency of arbitrarily oriented SQE visualization is described using the approach of comparing the dimmest and the brightest orientations (1). The simulations are performed for the following experiment configurations: SQEs are located on a glass cover slide in air (confifuration I); SQEs are located in air on the top of a polymer film over thin metal film as was suggested by Stefani et al. (2) (configuration II); SQEs are located in a polymer film on the top of layered metal-dielectric structure proposed by Uddin et al. (3) (configuration III). It was demonstrated in (2) and (3) that the layered media of configurations II and III enhance the fluorescence emission pattern of a SQE due to the surface plasmon coupled emission; it makes them attractive for fluorescence microscopy. The results of our present simulations are collected in the table. Here q_i is SQEs' intrinsic quantum

yield, ε is the degree of independence of SQEs' image intensity maxima on SQEs' orientations (ε = 0 indicates strong undesirable orientational dependence, ε = 1 indicates no dependence), η_z and η_{pl} are the collection efficiencies of SQEs perpendicular and parallel to the sample plane, respectively. The data show that the ε-parameter amounts up to about 0.9 when the difference between η_z and η_{pl} is sufficiently small. So, arbitrarily oriented SQEs of some types located on air/glass interface and on the top of the structure of configuration III can be efficiently visualized by means of EPCVB-based LSCFM. For the structure of configuration II this task can be solved, but less efficiently as in this case emitters with transition dipole moments (TDMs) parallel to the sample plane are significantly less observable than emitters with normal TDMs.

	q_i	Linear dipole			2D dipole		
		η_z	η_{pl}	ε	η_z	η_{pl}	ε
conf. I	≈ 0	$1.75 \times q_i$	$0.99 \times q_i$	0.87	$1.98 \times q_i$	$2.74 \times q_i$	0.73
	0.5	0.56	0.45	0.90	0.45	0.51	0.87
	1	0.76	0.71	0.89	0.71	0.74	0.97
conf. II	≈ 0	$2.69 \times q_i$	$0.28 \times q_i$	0.35	$0.54 \times q_i$	$2.97 \times q_i$	0.19
	0.5	0.36	0.10	0.59	0.10	0.28	0.38
	1	0.38	0.16	0.70	0.16	0.34	0.49
conf. III	≈ 0	$1.40 \times q_i$	$0.46 \times q_i$	0.77	$0.92 \times q_i$	$1.86 \times q_i$	0.54
	0.5	0.21	0.13	0.92	0.13	0.18	0.76
	1	0.25	0.18	0.90	0.18	0.23	0.85

References:

1. S. Boichenko & K. König, J. Opt. Soc. Am. B 32 (2015) 601-605.

2. F.D. Stefani et al., Phys. Rev. Lett. 94 (2005) 023005.

3. S.Z. Uddin et al., J. of Appl. Phys. 119 (2016) 204701.

M3. Materials in Geology, Mineralogy and Archaeology, Ceramics and Composites

INVITED LECTURES M3:

Oriented rutile exsolutions from ilmenite under controlled oxidation conditions: electron microscopy study

Nina Daneu (1), Nadežda Stanković (2), Masahiro Kawasaki (3), Goran Dražić (4), Aleksander Rečnik (1)

1) Department for Nanostructured Materials, Jožef Stefan Institute, Jamova cesta 39, Ljubljana, Slovenia

2) Department of Materials Sciences, Institute of Nuclear Sciences Vinča, Mike Petrovića Alasa 12-14, 11001 Belgrade, Serbia

3) JEOL USA Inc., 11 Dearborn Rd, Peabody, MA 01960, USA

4) National Institute for Chemistry, Hajdrihova 019, Ljubljana, Slovenia

Keywords: Keywords: topotaxial recrystallization, diffusion processes, HRTEM, HAADF-STEM

Oxidation of ilmenite is a typical example of a topotaxial recrystallization reaction, where the starting phase, ilmenite ($FeTiO_3$, divalent iron), is transformed to structurally related products, rutile (TiO_2) and hematite (Fe_2O_3, trivalent iron). Such oriented transformation is possible because of the common hexagonally packed (hcp) oxygen sublattice of the starting phase and the products; however, due to the slight tetragonal deformation of the rutile's oxygen sublattice (2.78°), two main orientation relationships (OR) between rutile and ilmenite/hematite can develop: in OR-1, the [001] axis of the exsoluted rutile is parallel to the [210] of ilm/hem and in OR-2, the [101] axis of rutile is parallel to the [210] direction of the ilm/hem matrix.[1] We have studied two types of rutile-hematite intergrowths that formed under different oxidation conditions and resulted in the formation of two different ORs between exsoluted rutile lamellae and the matrix phase. During oxidation of a primary ilmenite single crystal at 800°C in air, oxidation of Fe^{2+} to Fe^{3+} on the surface triggers fast lattice diffusion processes within the ilmenite lattice that progress rapidly from the surface towards the interior.[2] Out-diffusion of Fe^{2+}

triggers rearrangement of the cations within ilmenite and fast exsolution of rutile lamellae according to the OR-1 (Figure 1a). In this case, the rutile lamellae follow six (three unique) directions within the matrix ilmenite, intersecting at 60° or 120°, which are non-crystallographic angles for the rutile-rutile contacts (Figure 1a). The diffusion processes during this process were investigated by HAADF-STEM and EELS. The analyses of the rutile lamellae in two perpendicular directions revealed that they contain exsolutions of secondary ilmenite and hematite, indicating that the rutile lamellae serve as fast diffusion paths (chimneys) for out-diffusion of Fe^{2+} and at the same time in-diffusion of Fe^{3+} form the surface. In natural rutile-hematite intergrowths from Mwinilunga in Zambia[1] we observe the OR-2 between rutile lamellae and hematite matrix (Figure 2b). Due to the small deviation of the rutiles' c-axes from the [210] direction of hematite, the rutile lamellae exsolute in twelve (six unique) directions and these may intersect at different rutile-rutile angles: non-crystallographic contacts at 60°and 120°, low-angle boundaries at 174.44° and 5.56° and also two-types of crystallographic contacts or (101) and (301) twin boundaries at 114.44°and 54.44°. Detailed HRTEM and HAADF-STEM analyses of the rutile-rutile contacts, rutile-hematite interfaces and ilmenite precipitates within the hematite matrix along two perpendicular zone axes revealed that these samples formed from initial hemo-ilmenite crystals during very slow cooling process in low-oxygen environment and these condition enabled the development of the best-matching interfaces between rutile and hematite.

Acknowledgements:

The authors acknowledge financial support of the Slovenian Research Agency (project J1-6742).

References:

1. A. Rečnik et al., Contrib. Mineral. Petrol. 169 (2015) 19/1-22.

2. N. Stanković et al., J. Mater. Sci. 51 (2016) 958-968.

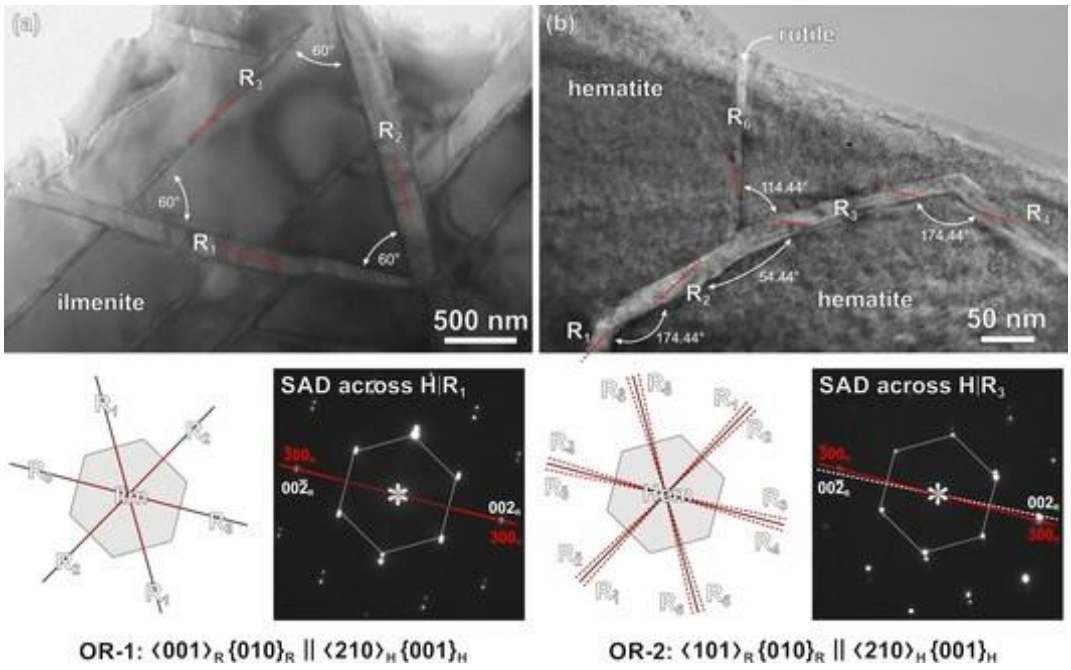

Figure 1. Rutile lamellae in (a) ilmenite heated at 800°in air and (b) natural samples from Mwinilunga, have different OR with the matrix (hematite/ilmenite) due to different oxidation kinetics (fast-slow). Dashed red lines denote c-axes of rutiles.

The applications and contexts of microscopy applied to historic building materials

John Hughes (1)

1) University of the West of Scotland, B121, Richardson Building, Paisley Campus

Keywords: microscopy, cultural heritage, geomaterials

The analysis of historic construction materials encompasses all forms of materials that have been used in the past for building, including the naturally occurring and those processed and manufactured in human activities. This contribution focusses on the reasons, methods and effects of the analysis of what are generally referred to as Geomaterials, i.e. mostly hard, mineral-based composite materials, for example stone, mortar, concrete and ceramics. Analysis of the microstructure of these materials as they occur in historic buildings and in archaeological remains is carried out for various reasons. These include baseline condition diagnosis, to identify the products (and therefore the mechanisms) of decay and characterisation to support the choice of material replacement, and how long term behaviours (e.g. durability) are linked to texture and composition. In archaeology there is a need to understand the materials used historically, not only to aid conservation, but to imply social, economic, technological and environmental processes, choices and impacts of past human activities. The methods used are *mostly* standard light microscopy and electron microscopy but also in a smaller number of studies high resolution transmission electron methods and also, increasingly, three-dimensional tomographic methods such as u-CT. These approaches are applied as static characterisation but also to allow the observation of dynamic processes, both compositional and mechanical, within materials. The contexts for investigations are archaeological, art-historical, conservation and restoration related, and often purely scientific. A significant application is the evaluation of damage, from long term processes of weathering (now influenced by climate change), pollution and acute processes (conflict, fire, climate and seismic disasters). The application of scientific characterisation methods has an impact on the framing of cultural heritage value, which are themselves constrained by the value system that operates across cultural heritage. International charters and western conservation philosophy

privilege the material, and necessitate the application of science to understanding and framing the contexts for conservation. However, the appearance of science in heritage work has also led to the performance of science for its own sake. This moves some to suggest that there is a disconnect between ‘endoscience’ (sense of Munoz-Vinas 2011) and its practical use. Anecdotal, and some semi-quantitative evidence of communication problems between scientists applying microscopy and other stakeholders suggests a need for changes to management of material characterisation in heritage projects.

References:

1. Munoz Vinas, S. (2005) “Contemporary Theory of Conservation”, Routledge, 2011 edition.

ORAL PRESENTATIONS M3:

Formation pathways of alumina particles in supersaturated vapour under micro gravity conditions

Shinnosuke Ishizuka (1), Tomoya Yamazaki (1), Yuki Kimura (1), Sašo Šturm (2)

1) Institute of Low Temperature Science,Hokkaido University, Kita-19, Nishi-8, Kita-ku, Sapporo 060-0819, Japan

2) Department of Nanostructured Materials, Jožef Stefan Institute, Jamova cesta 39, Ljubljana, Slovenia

Keywords: microgravity, nucleation, alumina

Understanding the homogeneous nucleation processes of the first inorganic compounds in the astrophysical environments is vital for understanding the early formation of astronomical dust around dying stars. Due to its highest sublimation temperature among all the major rock-forming minerals, alumina is naturally expected to emerge as the first condensate in the cooling outflows of oxygen rich giants and supergiants (1). In this study homogeneous nucleation and early growth of alumina nanoparticles close to astrophysical conditions was mimicked by thermal evaporation from Al source in the presence of high-purity background gas of Ar (3-38 × 10^3 Pa) and O_2 (2 × 10^3 Pa), under the 20 seconds of microgravity condition (~10^{-1} G), which was achieved during the parabolic flight of the airplane. The resulted alumina particles were studied by means of analytical electron microscopy. Figure 1a shows typical sphere-shaped morphology of alumina dust. Nanoparticles were found to be either perfectly round or they exhibit partial faceting. Atomic-resolution HAADF-STEM images acquired from the individual alumina spheres confirmed the crystalline nature of faceted particles, as shown from the corresponding FFT (Figure 1b). On the other hand, perfectly round particles did not reveal any periodic arrangements (Figure 1c), suggesting that these particles could not exceed the nucleation barrier for crystallization, thus remaining in the amorphous state. In order to unequivocally confirm the crystalline nature of alumina particles an electron energy-loss near

edge structure (ELNES) analysis was applied by using the so-called fingerprint method, where the fine structure of the experimental Al-$L_{2,3}$ ionization edge is compared with the ELNES ionization edges acquired from the well-defined reference materials. Figure 1d shows the resultant ELNES of two representative alumina particles combined with spectra from reference amorphous and crystalline alumina (2), confirming that the perfectly round particles are indeed in the amorphous state. The O/Al ratio of ~3.75 calculated from the corresponding EELS spectra acquired from the amorphous particles indicates significantly higher oxygen concentration when compared with their crystalline counterparts (~1.5). These results confirmed that at least two structurally distinct alumina particle classes can coexist throughout the condensation and solidification process. It is plausible that during the rapid solidification a part of oxygen was not able to completely escape from the molten particle, thus remained trapped inside the heavily distorted structure of amorphous alumina. Consequent crystallization, which proceeds by the continuous breaking and rearrangement of AlO_x (x=4,5,6) clusters enable further release of oxygen, thus lowering the total O/Al ratio. These results could be a motivation for analysing crystalline structure and O/Al ratio of cosmic alumina particles and will give us a better understanding of its formation process.

Acknowledgements:

The Slovenian Research Agency is greatly acknowledged for its financial support.

References:

1. E. E. Salpeter, Formation and Destruction of Dust Grains. Annual Review of Astronomy and Astrophysics, 15, 267-293, 1977

2. D. Bouchet, C. Colliex. Experimental study of ELNES at grain boundaries in alumina: intergranular radiation damage effects on Al-L 23 and OK edges. Ultramicroscopy, 96(2), 139-152, 2003.

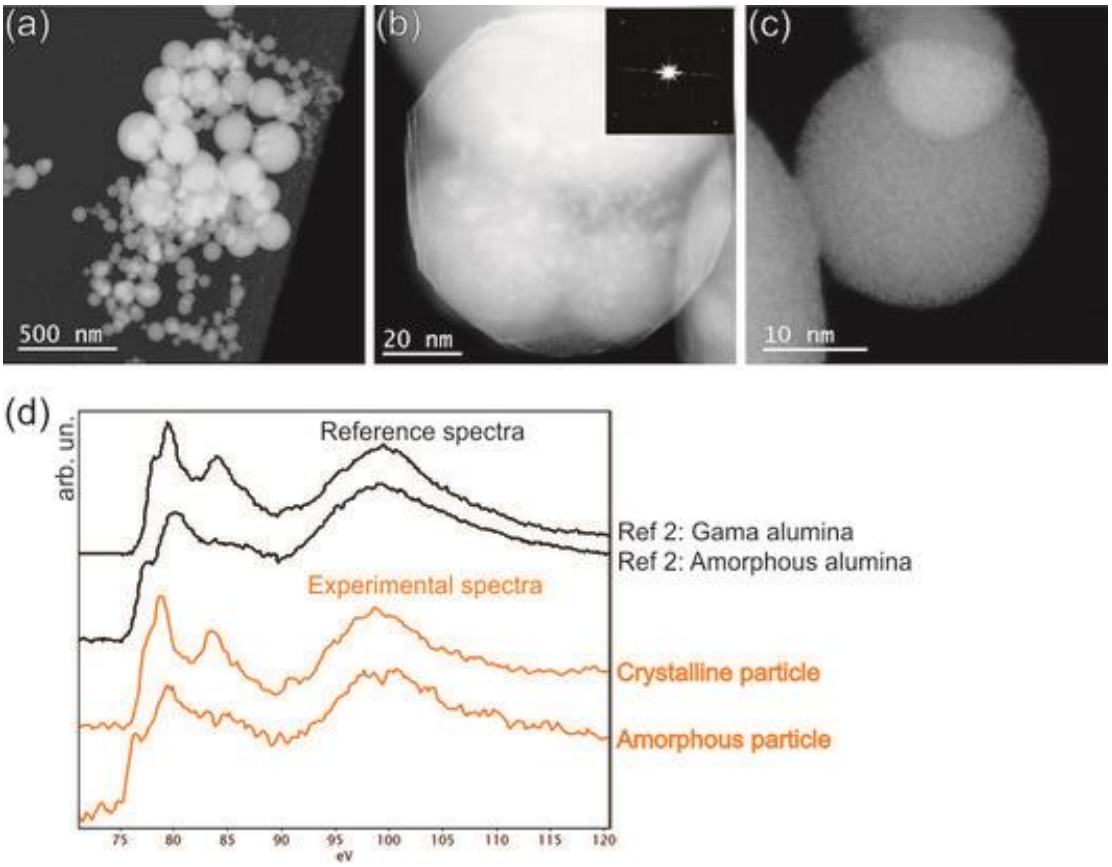

Figure 1. (a) Alumina dust produced from supersaturated vapour under microgravity conditions, revealing (b) faceted, crystalline and (c) spherical, amorphous nanoparticles, (d) with the corresponding experimental ELNES combined with spectra obtained from reference material.

Soil contamination of human dental calculus determined by Energy-dispersive X-ray spectroscopy

Radim Skoupý (1), Dana Fialová (2), Michaela Dörnhöferová (3), Vladislav Krzyžánek (1), Eva Drozdová (2)

1) Department of Electron Microscopy, Institute of Scientific Instruments of the CAS, Královopolská 147, 612 64 Brno, Czech Republic

2) Department of Experimental Biology, Faculty of Science, Masaryk University, Kamenice 5, 625 00 Brno, Czech Republic

3) Department of Anthropology, Faculty of Natural Sciences, Comenius University, Ilkovičova 6, 842 15 Bratislava 4, Slovak Republic

Keywords: soil contamination, human dental calculus, EDX-SEM, element composition, anthropology

Dental calculus (tartar, or calcified dental plaque) is caused by precipitation of minerals from saliva and gingival crevicular fluid in plaque. It is found in all known human populations. Scanning electron microscopy (SEM) gives a lot of information about human diet, oral bacterial flora and the habits of our ancestors. Energy dispersive X-ray spectroscopy (EDX) brings information about the inorganic elemental composition of the calculus. The main elements in dental calculus are calcium, phosphorus, magnesium, fluoride and carbon dioxide. Other special elements are supposed to come from other sources. A study performed by Charlier (Charlier et al. 2010) confirmed various individual elemental compositions of dental calculus from the Etruscan-Celtic necropolis. In this study, we want to distinguish soil contamination from elements which come from calculus (which are special for the individual). We continue in our previous study (Fialova *et. al. 2016)* to recognize elements from external environment which can affect the results of authentic composition of dental calculus. A sample of dental calculus came from a 20-29 year old female from the burial site Kopčany Kačenáreň (from the 9^{th}-10^{th} century, Slovak Republic). For the SEM-EDX analysis, a SEM Magellan 400 (FEI) equipped with an ED APOLLO X Silicon Drift Detector (EDAX) was used. All measurements were taken at an acceleration voltage of 30 kV. Samples were investigated without the use of any surface modifications. The EDX analyses were performed at three places: 1) the side of

calculus which adhered to the tooth (Fig 1a), 2) the outside of the calculus with soil residuals (Fig 1b) and 3) soil (found in a grave) (Fig 1c). As can be seen in spectra and in results in Fig 2, we estimated presence of several elements which are usually not a compound of calculus – silicon, aluminium, manganese and iron. The example of an typical present element is calcium. Our results show the possibility to locate the origins of investigated elements and their permeability, through dental calculus. Si and Al came from the soil and dental calculus was not permeable for these elements, Mn and Ca came from dental calculus because there is only an insufficient amount of it or none in the soil. Fe, however, is more complicated. We assume that the iron is present in the soil and in the calculus as well (because the lowest amount of Fe was outside). As can be seen, the EDX-SEM analysis is a powerful method for a non-destructive estimation of a dental calculus elemental composition. For the elimination of environment contamination we suggest to measure the elemental spectra from three different places – from calculus inside/outside and from the surrounding medium.

Acknowledgements:

This research was supported by the Czech Science Foundation GA17-15451S and the Ministry of Education, Youth and Sports (LO1212). The research infrastructure was funded by Ministry of Education, Youth and Sports of the Czech Republic and European Commission (CZ.1.05/2.1.00/01.0017).

References:

1. P. Charlier et al., Leg. Med. 12(4) (2010) 1344-6223.

2. D. Fialova et al., Microsc. Microanal. 22(3) (2016) 1431-9276.

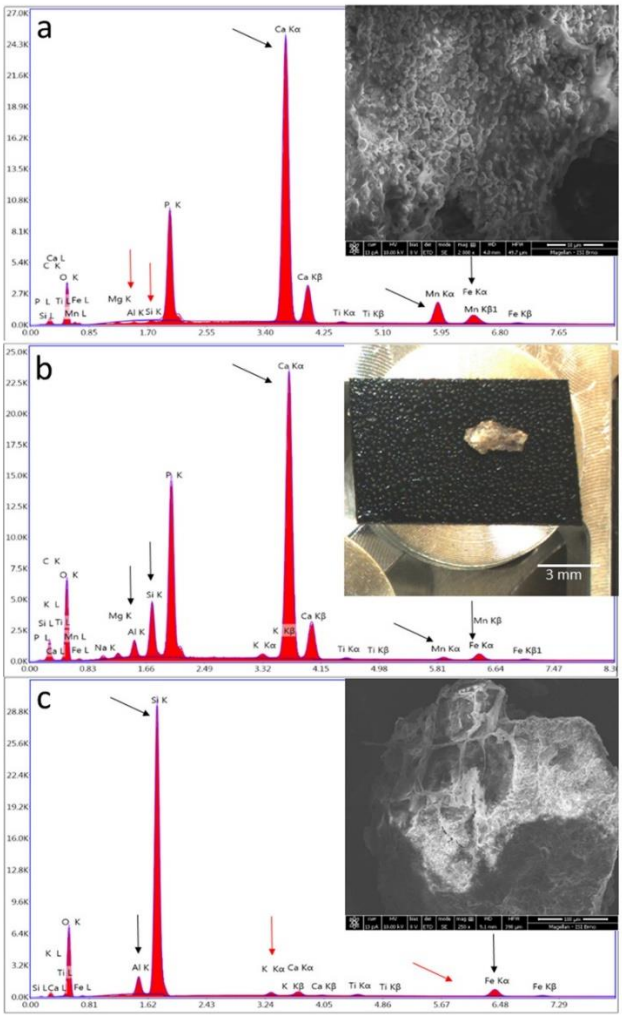

Figure 1. A SEM image and an EDX spectrum of dental calculus inside (a), outside (b) and in soil (c). Black arrows show elements of interest and red arrows show missing peaks.

	Inside			Outside			Soil		
	Wt %	Atomic %	Error %	Wt %	Atomic %	Error %	Wt %	Atomic %	Error %
Si	0,00	0,00	5,21	3,22	2,28	5,53	43,94	32,82	4,45
Al	0,00	0,00	6,66	1,23	0,91	7,98	2,92	2,27	6,99
Mn	5,62	2,38	2,84	0,42	0,15	12,08	0,00	0,00	0,00
Fe	2,26	0,94	4,17	1,10	0,39	5,02	3,24	1,22	3,32
Ca	36,61	21,29	1,42	24,25	12,05	1,51	1,04	0,54	8,02

Figure 2. The amount of elements at three different places (white – no element detected, green – the lowest, yellow – middle and red – the highest).

Low thermal treatment optimisation of sol-gel derived composite-coating for multi-purpose functionality and protection of all-metals

Vilko Mandić (1), Arnaud Tricoteux (1), Christelle Nivot (1)

1) UVHC-LMCPA, Pôle universitaire de Maubeuge Boulevard Charles de Gaulle, 59600 Maubeuge, France

Keywords: Ceramic coatings, Composite, Anticorrosive, Tribological, Sol-gel

Development of protective coatings for the metal surfaces has been continuous demand in wide industrial area and therefore was continuously scientifically researched. Inorganic as well as hybrid organic-inorganic coatings were found to be very favourable solutions. Recently achieved multifunctional layers shown it is possible to exhibit simultaneously both anticorrosion and tribological efficiency. However, discrepancies arise upon consideration of: (a) the up-scale to high area, (b) the price of deposition techniques, (c) the overall stability and (d) the requirements for thermal treatment, all of which prevents real technological applicability. This investigation aims to surpass these discrepancies and yield multifunctional (hard, anticorrosive, tribo-effective) multi-layer coatings (2 or more layers) on behalf of advanced sol-gel-based (cheap, simple) procedure with lower-temperature treatment (applicable, easy scale-up). First of all we withhold from one-pot synthesis and thereof maximise distinctive properties in each of the layers. Sol-gel method was utilised to tailor different but compatible layers. This investigation aims to evaluate the feasibility of a crystalline coating, which was rarely done. As a (metal-contacted) protection-layer, i.e. corrosion barrier (both from environment and chemicals), dense, crystalline (anatase) and thin (50-100nm) was considered. This layer was shown to have low porosity and SS surface, closed pores and good mechanical properties. Next layer was the container-type layer; it was shown to be thicker (300-500nm), consisting of amorphous TiO_2, porous (open mezzo-pores with uniform pore distribution and size 10-50nm) capable of accepting infiltration with another liquid anti-corrosive agent (benzotriazole). This layer show great anti-corrosive behaviour with reasonable mechanical properties. The final layer consists of core-shell particles which somewhat penetrate the pores of the 2nd layer thus closing them (and close the infiltrated anti-

corrosive liquid) and forming additional top layer. The tribo-active core-material was enclosed in outer hybrid shell for stability finally offering reasonable mechanical properties. Materials were extensively characterised using thermal, structural, microstructural and functional methods. Overall, the 3-layer-coating (<1µm) processed below 350°C shows physical, anti-corrosive efficiency and tribo-activity with good mechanical properties.

Acknowledgements:

The support of the INTERREG project TRANSPORT is gratefully acknowledged.

Enhanced photocatalytic properties of the reduced TiO_2 nanotubes arrays decorated with Ag nanoparticles

Milivoj Plodinec (1), Ivana Grcić (2), Xing Huang (3), Adnan Hammud (3), Danail Ivanov (3), Andreja Gajović (4), Marc-Georg Willinger (5)

1) Fritz-Haber-Institute der Max-Planck-Gesellschaft, Faradayweg 4-6, D-14195 Berlin, Germany/Ruđer Bošković Institute, Bijenička 54, HR-10000 Zagreb, Croatia

2) University of Zagreb, Faculty of Chemical Engineering and Technology, Marulićev trg 19, HR-10000 Zagreb

3) Fritz-Haber-Institute der Max-Planck-Gesellschaft, Faradayweg 4-6, D-14195 Berlin, Germany

4) Ruđer Bošković Institute, Bijenička 54, HR-10000 Zagreb, Croatia

5) Fritz-Haber-Institute der Max-Planck-Gesellschaft, Faradayweg 4-6, D-14195 Berlin, Germany/Department of Colloid Chemistry, Max Planck Institute of Colloids and Interfaces, Am Mühlenberg 1, 14476 Potsdam, Germany

Keywords: hydrogenated TiO_2 nanotube arrays, Ag decoration, visible light, surface disorder

Since the black TiO_2 nanostructures show advanced performances in photocatalysis and water splitting reactions, we prepared novel form of black TiO_2-based photocatalyst for waste water purification. The photocatalytic efficiency were studied on the real contaminant from the pharmaceutical company, salicylic acid, listed as a pollutant in precipitation, surface waters and as a constituent of humic material in the fresh waters. The novel photocatalyst was formed by the hydrogenation of TiO_2 nanotube arrays additionally decorated with Ag nanoparticles. Prepared nanotubes arrays synthesized by this procedure are strongly attached on Ti foils. In this way, after catalytic reaction there is no nanoparticles released in purified waste water as in the case of powder catalysts. The results about the influence of nanotube array decoration with silver nanoparticles and susbequently annealed in a hydrogen atmosphere on the photocatalytic activity, using visible and solar simulated radiation, will be presented. TiO_2 nanotube arrays were synthesized by simple, routine, anodization process and decorated by silver nanoparticles using photo-reduction process. Structure and morphology were studied

using Raman spectroscopy, scanning and transmission electron microscopy techniques. Optical characteristic will be investigated by UV-vis spectroscopy and photocatalytic activity in flow cell reactor. HAADF STEM images of cross-section performed on the TiO_2 NT's@Ag sample, that TiO_2 nanotubes have outer diameter (87±10) nm with nanotube wall thickness 14 nm.and length of around 2100 nm. The silver nanoaprticles in average 6 nm and they are uniformly distributed on the nanotubes wall through whole length (Figure 1a and 1b). The preliminary results show the best photocatalytic performances for TiO_2 nanotube arrays decorated with Ag nanoparticles and subsequently annealed in the hydrogen atmosphere (Figure 2a and 2b). The enhancement in the photocatalytic efficiency, particularly under visible light irradiation, can explained by synergetic effects of surface plasmon resonance effect of Ag and creation amorphous layer with Ti^{3+} and oxygen vacancies states at nanotubes surfaces. The evidence of the presence Ti^{3+} in the samples reduced by the annealing in the hydrogen atmosphere were studied by EELS spectroscopy in details. From all the sample were prepared TEM lamella's by focus ion beam with the aim to study the surface disorder at nanotubes wall and to confirm the presence of Ti^{3+} by the EELS profile through the nanotubes wall thickness (Figure 1e-1g). The findings are well supported by the complex kinetic model which allowed a separate study of contribution from salicylic acid photolysis, photocatalysis in UVB, UVA and visible part of applied simulated solar irradiation on overall degradation rate. The synergistic effects were quantified through the factor of synergy, f_{Syn}. The obtained results in this research are promising for large-scale application of these photocatalysts and the development of more efficient photocatalytic reactors, due to novel design that allows easy usage of prepared material.

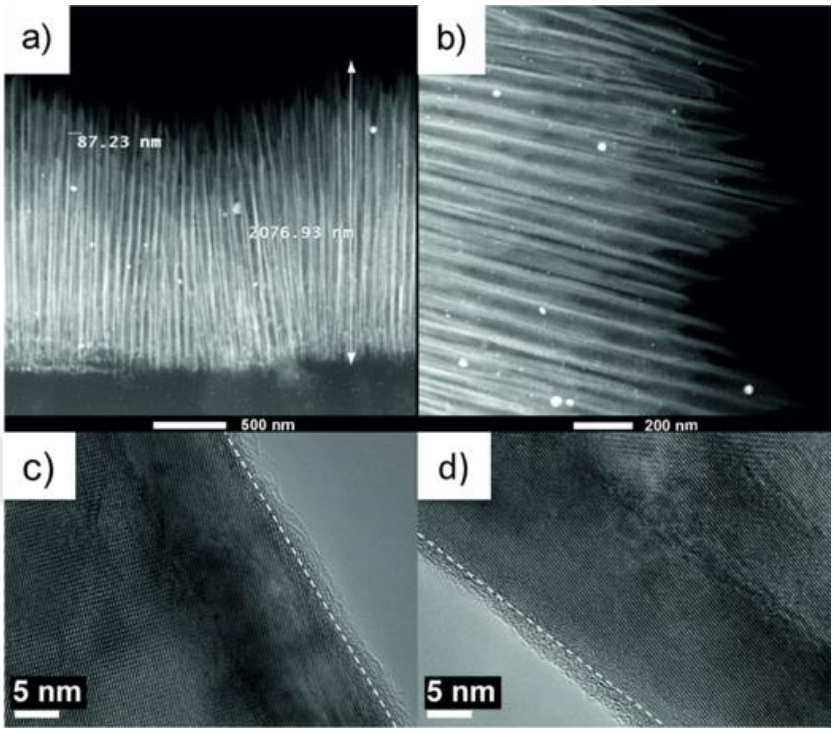

Figure 1. (a) and (b) HAADF image of the TiO_2 NT's@Ag, (c) and (d) HRTEM micrographs of TiO_2 NT's reduced in Ar/H_2 atmosphere at 500 °C, e) – g) HAADF image of EELS line profile of the TiO_2 NT's reduced in Ar/H_2 atmosphere at 500 °C, (f) Ti L2,3 edge of reduced TiO_2 NT's, g) O k-edge of reduced TiO_2 NT's.

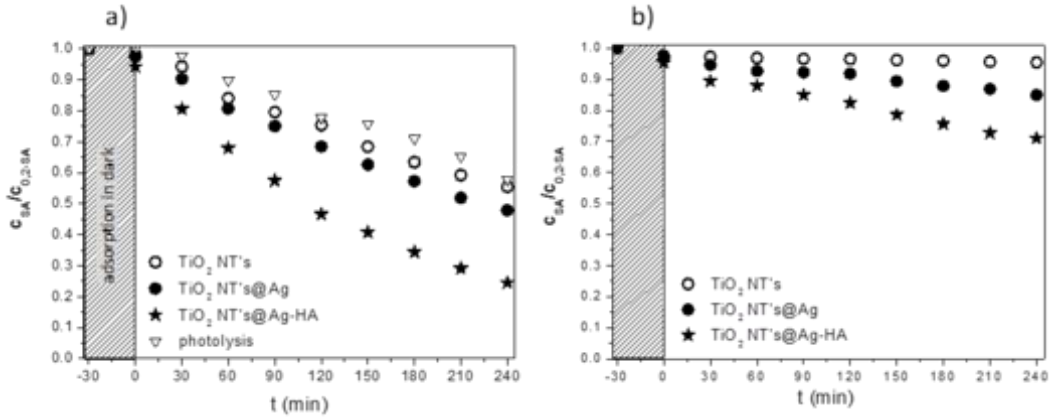

Figure 2. Kinetics of photolysis and photocatalytic degradation of SA under full-spectrum solar irradiation (a) and visible irradiation (photolysis was negligible) (b) using TiO_2 NT's, TiO_2 NT's@Ag and TiO_2 NT's@Ag-HA as photocatalysts (C0, SA = 0.2 mmol dm-3, pH 4).

POSTER PRESENTATIONS M3:

Structural characterization and luminescence properties of Y2MoO6 powders doped with various rare earth elements (Eu^{3+}, Sm^{3+}, Yb^{3+}/Er^{3+})

Nadežda Stanković (1), Marko Nikolić (2), Branislav Jelenković (2), Nina Daneu (3), Branko Matović (1)

1) Vinča Institute of Nuclear Science, Material Science Laboratory, Mike Petrovića 12, Belgrade, Serbia

2) Institute of Physics Belgrade, University of Belgrade, Studentski trg 1, Belgrade, Serbia

3) Jožef Stefan Institute, Department for Nanostructured Materials, Jamova cesta 39, Ljubljana, Slovenia

Keywords: Structural characterization, Phosphors, Y_2MoO_6, Luminescence

Phosphors are emitting radiation known as luminescence when exposed to ultraviolet radiation, X-rays, electron beam, friction or other forms of excitation. They have incorporated activator in the form of rear earth elements (REE) at a proper position in the host lattice. The rear earth ions have a deep-lying 4f shell which is not entirely filled and its electrons are screened by the electrons from the outer shells giving rise to a number of discrete energy levels that leads to their various possible applications depending on the emitting wavelength (1). One of the phosphors extensively studied is Y_2MoO_6 doped with various REE. In this study, we report an experimental investigation of Y2MoO6 powders doped with 5at%Eu^{3+}, 2at%Sm^{3+}, and 2.5at%Yb^{3+}/0.5at%Er^{3+} prepared by means of the self-propagating method and then annealed at different temperatures (600-1400 °C) for 4h. The synthesized powders were examined by X-ray diffraction (XRD), scanning electron microscopy (SEM), transmission electron microscopy (TEM) and luminescence emission and excitation spectra. All samples were single phase Y_2MoO_6 with very low crystallinity at 600 °C, which was confirmed both by XRD and broad emission band in PLE spectra. Already at 800 °C, samples showed ordering of the structure and increase in luminescence intensity and the appearance of narrow emission

lines and sharper peaks in diffraction diagram. Increasing the annealing temperature leads to the ordering of MoO_5 and YO_8:REE units and reducing the defects number. Rietveld refinement showed that rear earth elements take the positions of the yttrium atoms in non-centrosymmetric position in the lattice causing the luminescence due to charge transfer (CT) from MO_6 groups to REE. In the excitation spectrum of Y_2MoO_6 doped with Eu^{3+} broad absorption line in the region from 324 nm to 425 nm The Y_2MoO_6 doped with Sm^{3+} has central emission band at around 652 nm, and Yb^{3+}/Er^{3+} has double emitting luminescence at around 655 and 546 nm. Since Y_2MoO_6 doped with Eu^{3+} and Sm^{3+} emits radiation in red part of the spectra, it can be used as red phosphors in LEDs, while Yb^{3+}/Er^{3+} can be used in lasers and devices for optical communications because of the infrared-to-visible light conversion.

References:

1. Blasse, G. Handbook on the Phys. and Chem. of Rare Earths, (1979). 237-274.

Defects in orthorhombic (Mo,V)Ox mixed oxide – from local to extended

Liudmyla Masliuk (1), Marc Heggen (2), Annette Trunschke (1), Klaus Hermann (1), Marc G. Willinger (1), Robert Schlögl (3), Thomas Lunkenbein (1)

1) Department of Inorganic Chemistry, Fritz-Haber-Institut der Max-Planck-Gesellschaft, Faradayweg 4, Berlin, Germany

2) Ernst-Ruska Centre, Forschungszentrum Jülich GmbH, Jülich, Germany

3) Department of Colloid Chemistry, Max Planck Institute of Colloids and Interfaces, Golm, Germany

4) Department of Heterogeneous Reactions, Max Planck Institute for Chemical Energy Conversion, Mülheim a.d. Ruhr, Germany

Keywords: transmission electron microscopy, intergrowth, motifs, tiling, heterogeneous catalysis

Molybdenum-vanadium mixed oxides are promising catalysts for the partial oxidation of light alkanes. [1] Their activity and selectivity are influenced by a delicate interplay between the real bulk and surface structures. While the dominant ideal crystallographic phases of these catalysts have been investigated in great detail, [2] our work focuses on a local description of the real structure, which includes bulk and surface defects. Corresponding studies are scarce [3] since common averaging techniques, such as X-ray photoelectron spectroscopy (XPS) or X-ray diffraction (XRD) cannot provide insight into the details of local perturbations or distortions. We have applied high resolution transmission electron microscopy (TEM) for atomic-scale investigations of the catalyst surface and a tiling concept for simple and fast identification of local structure details. We have found in total 19 different structures, which can be classified as local and extended defects. The local defects are split further into five linear and two triangular motifs that involve two and three pentagonal structural building blocks, respectively. The extended defects are classified according to their internal motifs and tiling details as well as to the local environment. This classification allows further to investigate the local composition of a given defect and to determine relative local strain highlighting the presence

of inclination or disinclination. Our detailed structure analysis can offer a key for predicting the catalyst activity and stability of the molybdenum-vanadium based mixed oxides.

References:

1. Chieregato, A.; López Nieto, J. M.; Cavani, F. Coordination Chemistry Reviews 2015, 3, 301–302.

2. S. Ishikawa, W. Ueda, Catalysis Science & Technology 2016, 6, 617-629.

3. Lunkenbein, T.; Girgsdies, F.; Wernbacher, A.; Noack, J.; Auffermann, G.; Yasuhara, A.; Klein-Hoffmann, A.; Ueda, W.; Eichelbaum, M.; Trunschke, A.; Schlogl, R.; Willinger, M. G., Angew. Chem., Int. Ed. 2015, 54 (23), 6828-6831.

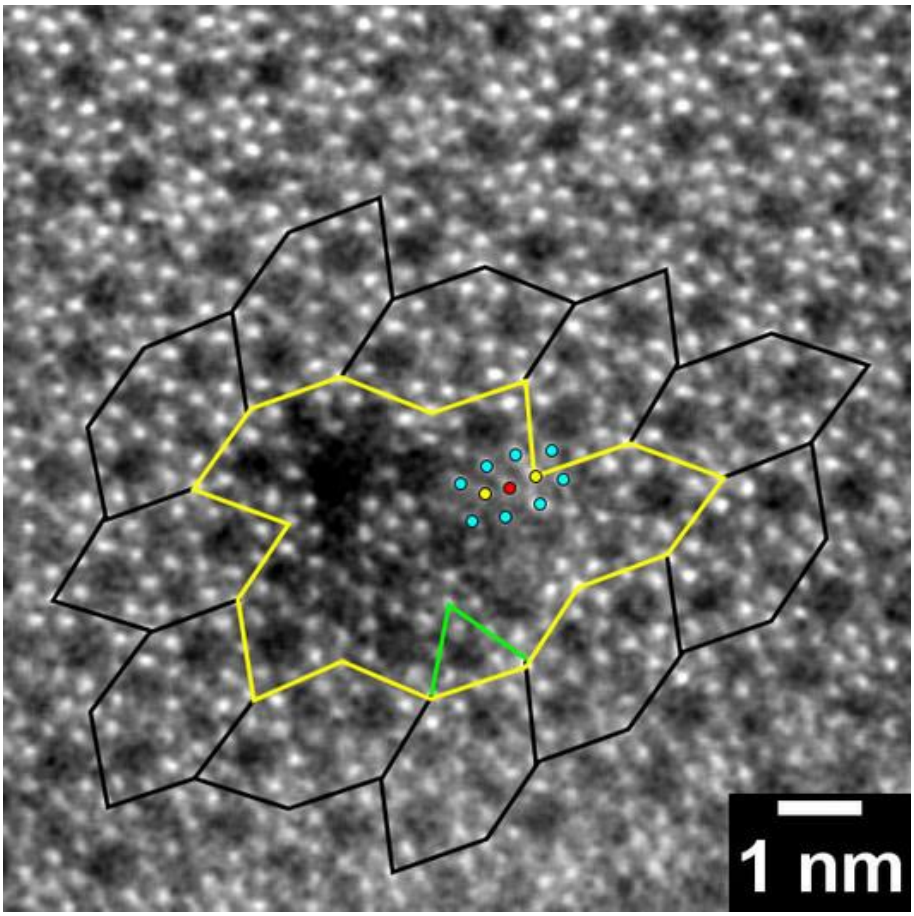

Figure 1. HAADF-STEM image of orthorhombic (Mo,V)Ox mixed oxide viewed along [001] illustrating an extended defect (yellow polygon) surrounded by the orthorhombic bulk (black tiling). Circles indicate the linear shared motif, green triangle – triangular motif.

Microstructural characteristics of staurolite from mica schist of the Drava depression basement (Croatia)

Mario Matošević (1), Sanja Šuica (1)

1) INA – Oil Industry, Exploration & Production, Exploration Sector, Rock & Fluid Analysis Department

Keywords: staurolite, mica schist, dynamic metamorphism, Tisia, Drava Depression

Staurolite, with the chemical formula $(Fe,Mg,Zn)_2Al_9Si_4O_{22}(OH)_2$, is a nesosillicate mineral formed during regional metamorphism in the amphibolite facies (medium grade metamorphism), usually as a porphyroblast. Atypical staurolite has been found in the garnet-staurolite-muscovite-biotite schist of the SW part of the Pannonian Basin System's crystalline basement, in the exploration wells of the Grubišno Polje field, located in the Drava Depression, Croatia. The analyzed rock can be correlated with biotite-muscovite gneisses of the Ravna Gora progressive-metamorphic series (Raffaelli, 1965), a part of the Papuk complex (Jamičić, 1983, 1988) or Hercynian progressive-metamorphic complex of the Slavonian mountains (Pamić & Lanphere, 1991). This is in accordance with Pamić (1999), who claims that the rocks of the surrounding area of Grubišno Polje are connected to the crystalline complex of the Slavonian mountains. Based on modern regional-geological concepts, the Slavonian mountains, along with the area of Grubišno Polje, are a part of the Tisia microplate (e.g. Schmid et al., 2008 and references therein). The rock is characterized by augen structure with mylonitic foliation. The peak metamorphic assemblage includes quartz, biotite, muscovite, staurolite, garnet, K-feldspar and plagioclase. Accessory minerals are apatite and zircon, while tourmaline, carbonate, hematite and chlorite represent retrograde mineral phases. Foliation is defined by the arrangement of quartz and phyllosilicates into distinct elongated and lenticular domains (Q and P domains). Garnet and rare feldspars occur as porphyroclasts, while staurolite appears as an aggregate of finer clasts with sericite-muscovite in intergranular space. The staurolite in the garnet-staurolite-muscovite-biotite schist has been confirmed optically, by using polarizing microscope Olympus BX51, as well as chemically and mineralogically, by the scanning electron microscope (SEM) JEOL JSM-6510 LV with Energy-

dispersive X-ray spectrometry (EDS). The staurolite grains are mainly prismatic, elongated along the *c* axis, with rarely developed twins. Individual grains and fragments (50-400 μm) are formed as a result of cleavage along the *b* axis, along with irregular fracturing. They typically display pleochroism, from colorless to pale yellow. The porphyroblastic schist was developed during regional metamorphism in the amphibolite facies from pelitic protolith enriched with iron and potassium. Later episode of dynamic metamorphism resulted in recrystallization and the occurence of retrograde assemblage. Anastomosing of quartz and phillosilicate domains around staurolite aggregates indicates that the staurolite initially represented porphyroblast as well. The shear stress led to the segmentation and a fracturing of staurolite porhyroblasts, rotation and recrystallization of newly-formed grains and crystallization of sericite-muscovite in fractures between staurolite grains.

References:

1. Jamičić, D. (1988): Strukturni sklop Slavonskih planina (sjeverni Psunj, Papuk, Krndija). – Neobjavljena Disertacija, Rudarsko-geološko naftni fakultet Sveučilišta u Zagrebu, Zagreb, 152 p.

2. Pamić, J. (1999): Kristalina podloga južnih dijelova Panonskog bazena – temeljena na površinskim i bušotinskim podacima. – Nafta, 50 (9) 291-310.

3. Raffaelli, P. (1965): Metamorfizam paleozojskih pelitskih škriljavaca u području Ravne gore. Geološki vjesnik, 18 (1), 61-111

Scanning electron microscopy – original painting or not? Analysis of the 18th century portrait color layers

Snezana Vucetic (1), John Milan van der Bergh (1), Bojan Miljevic (1), Helena Hirsenberger (2), Jonjaua Ranogajec (1)

1) University of Novi Sad, Faculty of Technology, Bulevar cara Lazara 1, 21000 Novi Sad, Serbia

2) University of Novi Sad, Faculty of Technical Science, Trg Dositeja Obradovića 6, 21101 Novi Sad, Serbia

Keywords: multilayered portrait, SEM, EDS, morphology, painting technique

Scanning Electron Microscopy with Energy Dispersive Spectrometry (SEM-EDS) and Polarized Light Microscopy (PM) are commonly used for the characterization of pigments and supportive layers of the historic paintings. Recently the team of the Laboratory for historic materials of the Faculty of Technology was involved in investigation project on 18th century portrait of count Andras Hadik de Futak (work by an author named Jager or Fager from 1764), led by the Provincial Institute for Protection of Cultural Monuments, Petrovaradin, Serbia. During the investigative work on the 18th century portrait a combination of analytical techniques were applied. Five cross sections were selected from damaged parts of the painting in order to mitigate further damage done to the painting. The SEM and PM techniques, and other as XRF and FTIR, showed that all the samples were multilayered and that in fact there were two paintings – original (inner) portrait not visible to the naked eye, and the visible (outer) portrait. Morphologically different layers observed using PM and SEM proved to have characteristic chemical composition, as determined by EDS technique. The analysis of one of the samples unequivocally confirmed the presence of the original inner portrait. The EDS analysis of the cross section identified four different layers. The first (innermost) layer is a red bole support, the second layer contained lead white paint, the next layer was again red bole and, finally, the last layer was the actual visible paint layer. This kind of repeated pairs of support and paint layer (so called “double sample”) was confirmed in another sample by using only SEM and PM techniques which clearly showed morphological differences between present layers. The combination of microscopy techniques (SEM and PM) that provide information about samples

structure, and spectroscopy technique (EDS) which analyses chemical composition of the samples gives invaluable insight in historic materials and remains the first step in conservation and protection of cultural heritage artefacts.

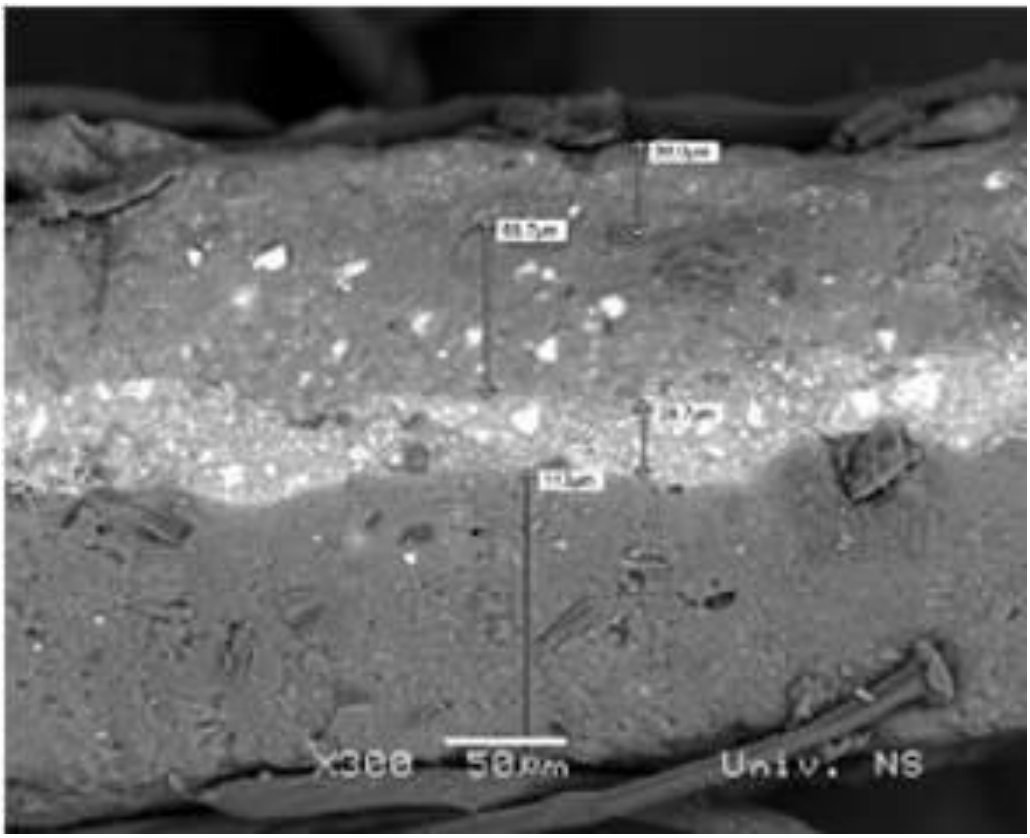

Figure 1. SEM-EDS of the painting layers cross section.

A look into the past: a Focused Ion Beam study of the ultrastructure of fossil plant cuticles

Alessandro Benedetti (1), Jose B Diez (2), Luis M Sender (3), Ignacio Escapa (4), Roberto Cuneo (4)

1) CACTI, Universidade de Vigo, Rúa Fonte das Abelleiras, s/n, 36310 Vigo, Pontevedra, Spain

2) Dept Xeociencias Mariñas, Universidade de Vigo, Marcosende, 36310 Vigo, Pontevedra, Spain

3) Dept Ciencias de La Tierra, Universidad de Zaragoza, Pedro Cerbuna 12, 50009 Zaragoza, Spain

4) Museo Paleont Egidio Feruglio, Trelew, Argentina, and CONICET, Av. Fontana 140, 9100 Trelew, Chubut, Argentina

Keywords: FIB, fossil plants, palaeobotany, ultrastructure

Historically, paleobotany has been severely hindered by the complexity of mechanical slicing and SEM/TEM imaging of fossil material (1). A few years ago, we applied the Focused Ion Beam (FIB) technique to the cross-sectioning and imaging of Cretaceous fossil both spores and pollen grains from several taxonomic species (2), with a spatial resolution unmatched by any conventional technique. Here, we present a study of the inner ultrastructure of fossil plant cuticles of conifers from the Early Jurassic of the Argentinian Patagonia. As every material respond in a different way to the ion beam, we could not directly apply the methodology previously developed. Therefore, we carried out a detailed study to determine the best experimental conditions. In particular, we found out that the use of water vapour-enhanced milling (SCE, Selective Carbon Etching), which would normally speed up the milling process in organic materials, result in the formation of large columnar structures inside the trench. X-ray analysis revealed them to be mostly composed of Ga, which rules out redeposition of milled material as an explanation. Results show (Figs. 1) the presence of cavities and a diversity of nanometer sized structures placed inside them, which had never been seen in the fossil plant record. However, our elemental analysis indicate that great care has to be taken when interpreting the results, as we observed some gallium redeposition on the cavity walls, mostly on the surface of the trench exposed to the milling action of the ion beam; no gallium was found, on the other hand, inside the cavities. These artifacts, which partially alter the local morphology, can be effectively reduced by employing a lower ion acceleration voltage for the final cleaning, which imply a much lower milling rate. Elemental analysis also provided us with

a valuable insight on the internal composition of cavities (Figs. 2 and inset), indicating the presence of elements which may be related to the original atmospheric composition. This insight into the ultrastructure features of fossil plant cuticles provides new data with further applications in taxonomy, climatic and environmental studies concerning both to extinct and extant plants.

References:

1. J. R. Rowley et al, Rev. of Palaeobot. and Palynology 132 (2004) 237 2. U. Villanueva-Amadoz et al, Grana 51 (2012) 1.

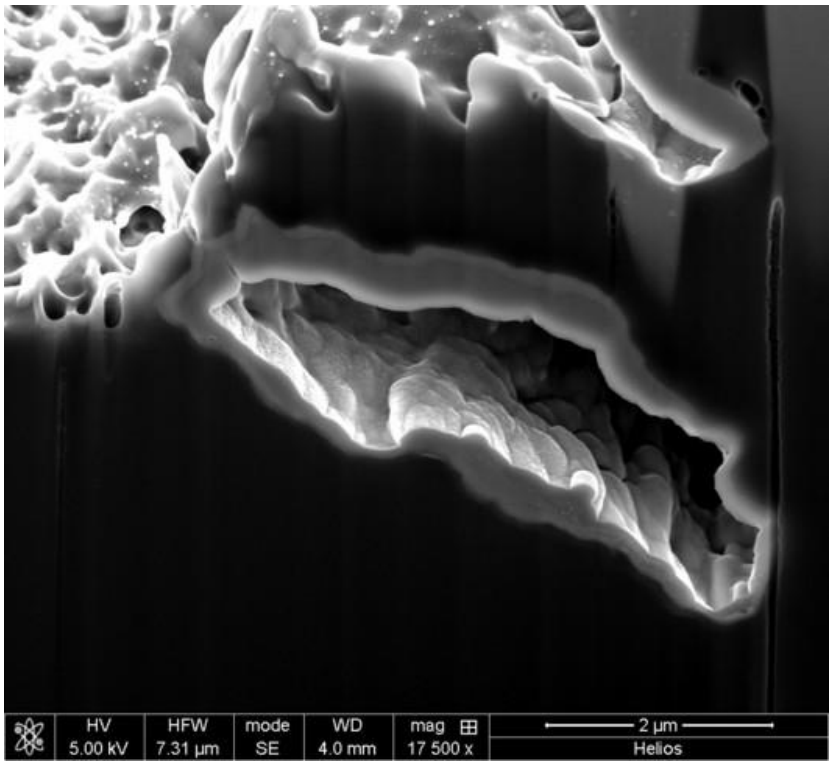

Figure 1. Cavity inside a fossil cuticle.

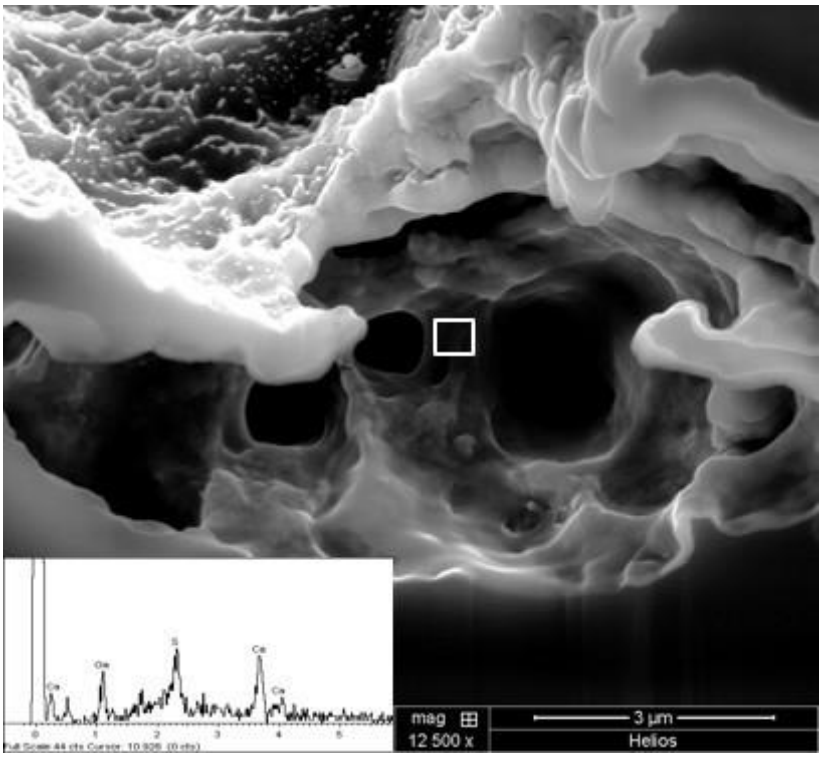

Figure 2. Detail of the same cavity showing ultrastructures; the spectrum from the region framed in white is shown in the inset.

EBSD study of twins in SnO_2-cassiterite

Zoran Samardžija (1), Sara Tominc (1), Nina Daneu (1), Aleksander Rečnik (1)

1) Jožef Stefan Institute, Department for Nanostructured Materials, Jamova cesta 39, Ljubljana, Slovenia

Keywords: EBSD, cassiterite, twins

Crystallographic orientations of the tin dioxide (SnO_2, cassiterite) grains in sintered polycrystalline bulk ceramic material were studied using electron backscatter diffraction (EBSD) technique (Oxford Instruments EBSD system equipped with a Nordlys detector and a HKL CHANNEL 5 software) installed in a FEG-SEM (JEOL JSM-7600F). The SnO_2 sample was prepared for FEGSEM/EBSD analysis by metallographic polishing route with final polishing step done by using colloidal silica of 0.05 □m grade in order to obtain fine, scratch-free, smooth sample surface. The EBSD analyses were performed at SEM operating conditions of 20-kV accelerating voltage, 5-nA beam current, working distance of 18 mm and the specimen tilt of 70 °. The SnO_2 material was sufficiently conductive and no charging was observed under applied analytical conditions. The EBSD patterns were acquired at 50 ms dwell time per point and indexed using the unit cell parameters of tetragonal cassiterite (SnO_2) ICSD 39173. EBSD orientation map was acquired within a rectangular frame of 42 μm x 35 μm with a step of 0.7 μm between the points which gave the total number of 3231 analyzed points. A high indexing efficiency of 93 % was achieved. Non-indexed (7 %) points occurred mainly because of grain boundary effects where local topography, i.e. the curvature of grain edges and gaps between the grains make the pattern acquisition and indexing not possible. All the patterns were indexed with high confidence using 10 characteristic Kikuchi bands with an average mean angular deviation of 0.4 º. The acquired data were subsequently processed to obtain information about crystallographic orientation of SnO_2 crystallites/grains located in the EBSD maps. The inverse pole figure diagram revealed random spatial distribution of the crystallographic orientations of the SnO_2 grains in the ceramic microstructure. Further analysis of local misorientations across the grain boundaries between neighbouring grains showed the presence of numerous twins with characteristic misorientation angle of 67.8 degrees which is

direct confirmation of the *elbow twins* in cassiterite (Figure 1). The misorientation angle distribution histogram given in Figure 2 has distinct maximum at an angle of 67.8 degrees which is due to the increased number of elbow-type cassiterite twins corresponding to {101} type twin boundary.

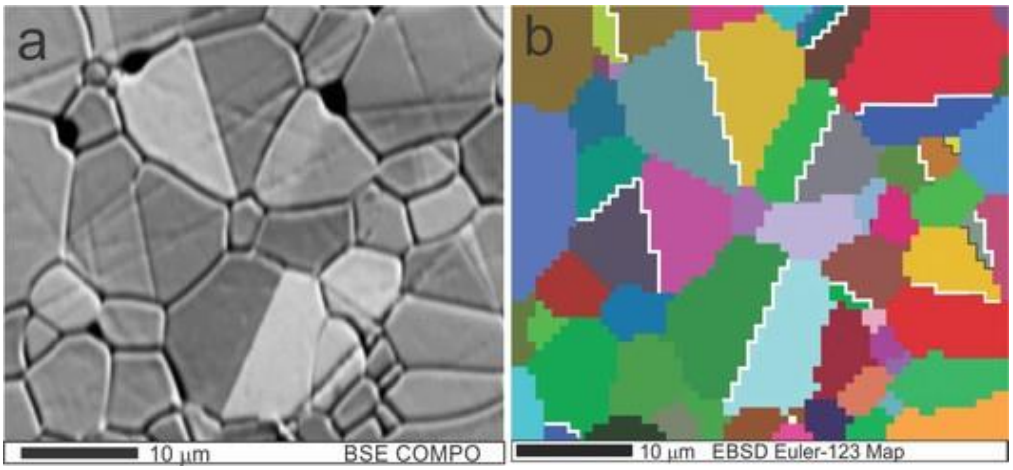

Figure 1. Backscattered electron micrograph (a) and corresponding EBSD orientation map (b) of SnO2 grains with marked twin boundaries in white.

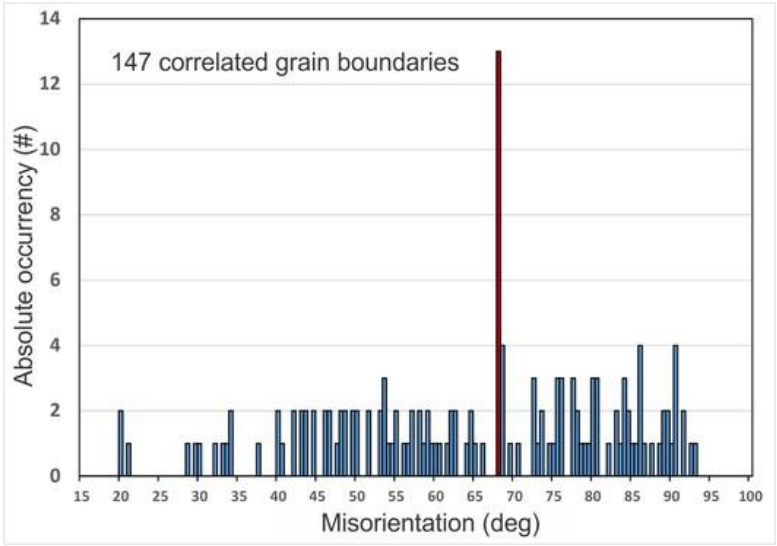

Figure 2. Distribution histogram of the misorientation angles across the 147 correlated grain boundaries (found in the area displayed in Figure 1) shows distinct increase of twin boundaries with 67.8 degrees misorientation which corresponds to elbow-type □101□ twins in cassiterite.

Three-dimensional microstructural evolution during sintering of Ni-SDC cermets for SOFC anode reconstructed by FIB-SEM nanotomography

Gregor Kapun (1), Marjan Marinšek (2), Tina Skalar (2), Endre Majorovits (3), Franci Merzel (1), Sašo Šturm (4), Miran Gaberšček (1)

1) National Institute of Chemistry, Hajdrihova ulica 19, 1000 Ljubljana, Slovenia

2) University of Ljubljana, Faculty of Chemistry and Chemical Technology, Ljubljana, Slovenia Večna pot 113, 1000 Ljubljana, Slovenia

3) Carl Zeiss Microscopy GmbH, ZEISS Gruppe, Carl-Zeiss-Strasse 22, 73447 Oberkochen
4) Jožef Stefan Institute, Jamova cesta 39, 1000 Ljubljana, Slovenia

Keywords: SOFC, Ni-SDC cermet, 3D microstructure, FIB-SEM tomography

A solid oxide fuel cells (SOFC) are one of the most promising energy conversion systems because they can directly convert chemical energy of various fuels into electrical energy with high conversion efficiency in an environmentally friendly manner. To overcome all challenges regarding manufacturing costs and materials long term stability current research efforts are aimed at the development of SOFCs with high power densities operating at temperatures below 700 °C. In contemporary SOFC devices, conventional ion conducting ceramic material, have been typically replaced with samarium-doped ceria (SDC), with superb ionic conductivities, which can be used as an anode when combined with Ni in Ni-SDC cermet. The electro-catalytic activity of cermet anodes towards fuel oxidation is directly related to the length of a triple-phase boundary (TPB) where the fuel, electronic (Ni), and ionic (SDC) conductor meet. High density TPB cermet microstructure is achieved when fine Ni and ion conducting ceramic are mixed. However, in porous cermet fabrication process, sintering of nanometer scale ceramic and metallic powders is one of the most important step to achieve efficient and reliable electrodes. Therefore, in attempt to find an optimal sintering procedure during Ni-SDC anode preparation, it is crucial to establish quantitative relationship between primary microstructural parameters, that can be adjusted during material processing, with the higher order topological features that control the electrochemical performance of the electrode. In

such a cermet composite critical topological features such as connectivity, TPB density and the tortuosity of transport pathways in the pores can only be established based on detailed 3D microstructural information. In this work we present a quantitative characterization of Ni-SDC cermets sintered at 1400°C, 1300°C and 1200°C using FIB-SEM nanotomography. The samples were serial sectioned using a fully automated slicing procedure with advanced drift correction algorithms and auto focusing routine to obtain a series of 2D images with 5 nm slice thickness. Experimental milling and imaging parameters have been optimized in order to obtain a high quality 3D dataset with phase contrast information. Individual phases were identified from analytical images and further segmented using a 3D watershed algorithm. After phase separation, the entire probed volume was reconstructed and 3D quantification algorithms were established. Volume fractions and porosity as well as feature sizes, specific surface areas of individual phases were calculated directly from 3D reconstructed volume. Segmented 3D data cube was used for TPB density calculations and grain connectivity analysis. Quantitative three-dimensional microstructural data related with Ni-SDC cermet microstructure evolution will be used for determination of optimal sintering temperature and optimization of thermal treatment process during Ni-SDC anode material preparation.

References:

1. D.A.Medvedev, J.G. Lyagaeva, E.V. Gorbova, A.K. Demin, P. Tsjakaras, Progress in Materials Science, 2016, 75, 38–79

2. G. Brus, H. Iwai, A. Sciazko, M. Saito, H. Yoshida, Journal of Power Sources, 2015, 288, 199-205.

3. K.P. Mingard, H.G. Jones & M.G. Gee, Journal of Microscopy, 2014, 253, 93–108.

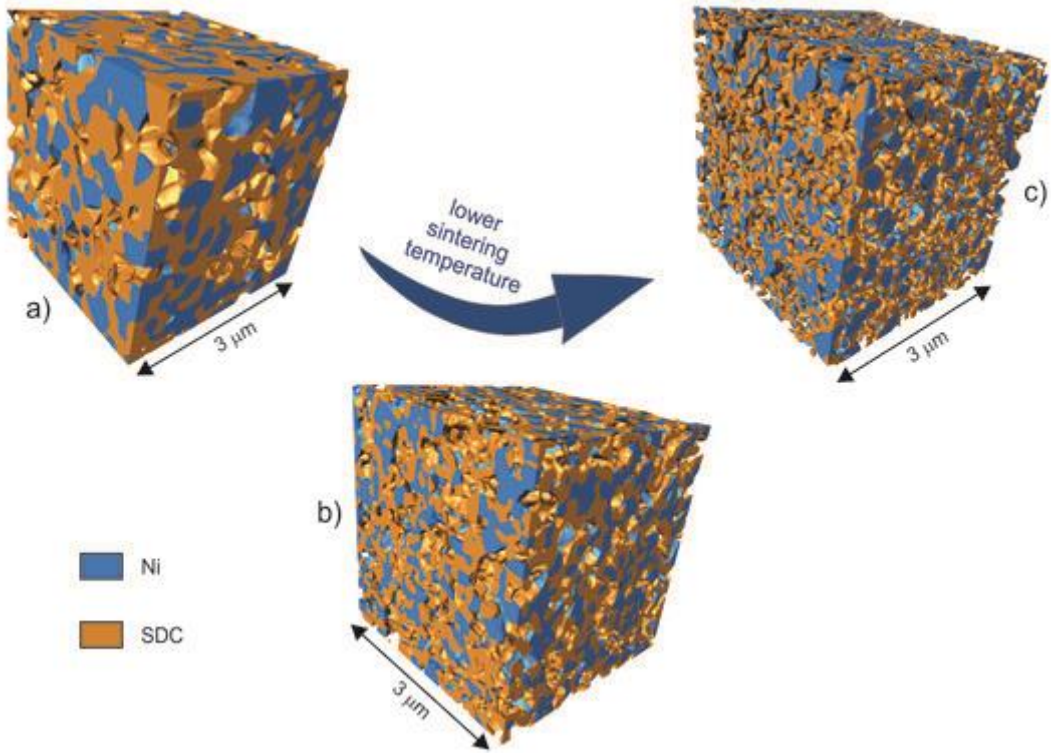

Figure 1. Three-dimensional reconstructions of Ni-SDC cermets sintered at: (a) 1400 °C, (b) 1300°C and (c) 1200°C.

Occurrence of clinozoisite-epidote minerals in the metamorphic suite and granitic intrusions of the Dunje area, South Macedonia

Nenad Tomašić (1), Sabina Strmić Palinkaš (2), Andrea Čobić (1), Blažo Boev (3), Ivan Boev (3), Vladimir Bermanec (1)

1) University of Zagreb, Faculty of Science, Department of Geology, Division of Mineralogy and Petrology, Horvatovac 95, HR-10 000 Zagreb, Croatia

2) UiT The Arctic University of Norway, P.O. 6050 Langnes, NO-9037, Tromsø, Norway

3) University "Goce Delčev"- Štip, Faculty of Natural and Technical Sciences, Blvd.Krste Misirkov, 10-A, P.O.Box 210. 2000 Stip Republic of Macedonia

Keywords: clinozoisite-epidote mineral series, metamorphic suite South Macedonia, polarizing light microscopy, SEM-EDS

Epidote group minerals occur in various geological settings reflecting local lithology and geological history. From petrogenetic point of view these minerals are quite unspecific because of wide temperature and pressure stability fields (Franz & Liebscher, 2004).The Dunje area is situated in the Pelagonian Massif of southern Macedonia comprising a Precambrian metamorphic suite composed of gneisses, amphibolites and schists. Granitic intrusions and concomitant pegmatitic veins in the metamorphic host rocks are quite common (Temovski, 2016). The studied area is located 3 km in SSW direction from village of Dunje. Occurrence of the clinozoisite-epidote series minerals in the granitic intrusions and host gneisses in contact with pegmatite veins is investigated in this study. The studied granitic rocks outcrop roughly 100 m in NNE direction from the investigated gneiss-pegmatite contact. Plane-polarized light microscopy (Zeiss, Axiolab) and scanning electron microscopy (SEM) with EDS system (Bruker, Quantax 70) were used to study micro-features of the rock samples with special interest into the co-existence of clinozoisite-epidote minerals and Ti-rich phases, which both seem to be quite abundant in the investigated rock suite. The host gneiss is coarsely foliated and composed of clinozoisite-epidote, amphibole, quartz, plagioclase, titanite and sparse but large grains of opaque minerals. The intruding granite is composed of quartz, orthoclase with occasional perthitic lamellae, biotite, small elongated or irregular grains of clinozoisite-epidote,

titanite, and sparse garnet. The occurrence of clinozoisite and epidote in both host gneiss and granite represents a mineral chemistry change at small scale, and even in polarizing light epidote and clinozoisite are readily distinguished by a clear distinction in interference color. Both minerals appear mutually in a very close contact (Figure 1A and 1B; Ep – epidote, Czo – clinozoisite, Amp – amphibole, Ttn – titanite, Pl – plagioclase). SEM-EDS analysis (Figure 1C and 1D) indicates an inhomogeneous distribution of iron throughout the clinozoisite-epidote grains, thus giving rise to a simultaneous occurrence of both phases. Amphibole is of Mg-Fe series containing some Ca (intergrowths?), and a frequent occurrence of titanite indicates a significant availability of titanium in both metamorphic suite and granite. Besides, in the host gneiss rutile grains are also identified. A detailed micro-chemical characterization of the mineral phases in the rocks of the studied metamorphic suite is in progress especially focusing to a possible relationship between occurrence of clinozoisite-epidote minerals in host rocks and granitic/pegmatitic intrusions.

References:

1. G. Franz et al.,Phys. Reviews in Mineralogy and Geochemistry (2004), 56, 1-82

2. M. Temovski, Evol. of Karst in Lower Part of Crna Reka Riv. Bas. (2016) Springer p. 265

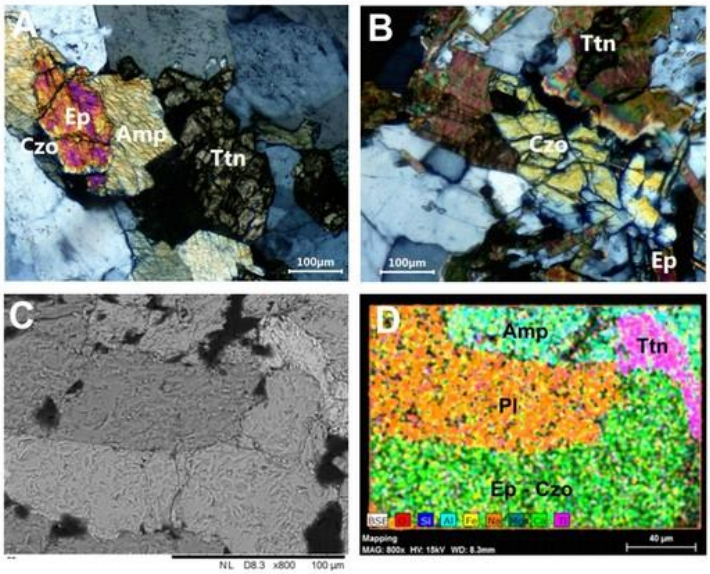

Figure 1. Plane-polarized light images (with crossed polars) of gneiss close to a pegmatite contact (A) and of granite (B). BSE (C) and mapping (D) images of the gneiss showing clinozoisite-epidote in contact with other major phases.

The mineralogy and texture of shales from palaeozoic baltic basin (Northern Poland) - data from SEM/EDS analysis

Arkadiusz Gąsiński (1),

1) Institute of Geochemistry, Mineralogy and Petrology, Faculty of Geology, University of Warsaw, Poland

Keywords: shale, hyper-mapping, preferred orientation

The mineral composition of fine grained rocks is one of the main factor that influence the geomechanical properties of shales. Thus the proportion of different minerals and texture features of grains are of primary importance for planning the hydraulic fracturing. The thin sections made from drill cores of Ordovician and Silurian rocks from the Palaeozoic Baltic Basin in northern Poland were the objects of the research. These rocks represent a wide range of siliceous and argillaceous rocks. Due to very small grains, the optical microscopy is not adequate to get all necessary data. Much better results is obtained with scanning electron microscopy, especially in BSE mode. However it is still not enough, due to similar gray values for different minerals (e.g. chlorite and calcite). The BSE imaging and the elemental hyper-mappings were performed using Sigma VP (Zeiss) scanning electron microscope equipped with two Bruker's XFlash 6/10 EDS detectors and Esprit 1.9 software. The mappings were performed on the relatively large area of thin sections, some scans were done using low vacuum mode. About 500 to 1000 of BSE pictures and hyper-maps were taken from each of thin sections. The stitching of images and mappings was done using plug-in written by Preibisch et al. (2009) and an automatic macro wrtitten in ImageJ macro-language. The analysis of elemental x-ray hyper-mappings were performed in order to visual qualification of each pixel to chemical phases. All samples show a rather complex mineralogical composition with illite, micas, quartz, calcite, dolomite and chlorites as major minerals. It was possible to detect microzones that contain higher amount of brittle minerals and therefore should be especially prone to cracking.

Anisotropy in clay-rich sedimentary rocks is receiving increasing importance. This feature is very useful for the prospecting for hydrocarbon deposits and for hydraulic fracturing. Anisotropy of diffusion has become relevant for environmental contaminants, including nuclear

waste. In both cases, the orientation of component minerals is a critical ingredient. In this study I also show the orientation of different mineral components in shales with image analysis methods that allow me to characterize the shape of grains and its preferred orientation with respect to their elongation quantitatively. It is clear that not only clay minerals but also brittle minerals (quartz, carbonates, feldspars) contribute to anisotropy of shales.

Acknowledgements:

The research was supported by ShaleMech project, funded by the Polish National Centre for Research and Development (NCBiR), grant no. BG2/SHALEMECH/14.

References:

1. S. Preibisch et al., Bioinformatics 25 (2009), 1463-1465.

M4. Metals, Alloys and Intermetallics

INVITED LECTURES M4:

TEM analysis of core-shell and hollow nanospheres

Sašo Šturm (1), Kristina Žužek Rožman (1), Boštjan Markoli (2), Evangelia Sarantopoulou (3), Cefalas Alciviadis-Constantinos (3), Kollia Zoe (3), Spomenka Kobe (1)

1) Department for Nanostructured Materials, Jozef Stefan Institute, 1000 Ljubljana, Slovenia

2) Department of Materials and Metallurgy, Faculty of Natural Sciences and Engineering, University of Ljubljana, 1000 Ljubljana, Slovenia

3) National Hellenic Research Foundation, 11635 Athens, Greece

Keywords: nanotechnology, TEM/HRTEM, pulsed-laser, nanoparticles

Some predict, that nanotechnology is likely to have a profound impact on our economy and society in the early 21st century, comparable to that of semiconductor technology, information technology, or cellular and molecular biology. Science and technology research on the nano-level promises breakthroughs in areas such as materials and manufacturing, nanoelectronics, medicine and healthcare, energy, biotechnology, information technology, and national security. Nanotechnology is any technology on a nanoscale that actually has applications in real world. This technology literally encompasses the production and application of physical, chemical, and biological systems at scales ranging from individual atoms or molecules to submicron dimensions, as well as the integration of the resulting nanostructures into larger systems. We have focused our attention on analysis of core-shell and nano-spheres produced via pulsed laser ablation-PLA, in three different systems, i.e. Al-O, Sm-Fe(Ta)-N, and Co–Pt. These are very promising system in areas of magnetism, and catalysis, with the possibility to fine tune the physical properties by adjusting both the composition and the morphology of nanoparticles. By means of various techniques of transmission electron microscopy we aimed to characterize both structure and composition of synthesised nanoparticles as well as to determine the nitrogen pressure inside the individual voids in the case of hollow nanospheres. Experimental data were used for the reconstruction of the formation mechanism of nanospheres, and

suggestions were made towards the general formation mechanism for gas-filled nanospheres in other metallic systems.

References:

1. Bhushan B 2010 *Springer Handbook of Nanotechnology* (Springer-Verlag Berlin Heidelberg).

2. Šturm S., Žužek Rožman K., Markoli B., Sarantopoulou E., Kollia Z., Cefalas A. C. and Kobe S. *Nanotechnology* (2010) **21** 485603.

3. Šturm S, Rožman K Ž, Markoli B, Antonakakis B E, Sarantopoulou E, Kollia Z, Cefalas A C, Kobe S. *Acta Materialia (*2013) **61** 7924.

FIB/SEM in metallography

Tonica Bončina (1), Franc Zupanič (1)

1) University of Maribor, Faculty of Mechanical Engineering, Smetanova ulica 17, 2000 Maribor, Slovenia

Keywords: Metals, Metallography, Focused Ion Beam (FIB), Scanning Electron Microscopy (SEM)

Metallography is a science dealing with the analysis and determination of the microstructure constituents in metals, alloys and other materials. It comprises a number of research methods, techniques and practices of sample preparation. Recently, the Focused Ion Beam (with the liquid metal Ga source) combined with Scanning Electron Microscopy has been increasingly used for the characterization in metallography, mainly as a complementary method to other metallographic techniques. Dual-beam microscopes are additionally equipped with different detectors (ET, BSD ICE…) to acquire ions and various types of electrons. The dual-beam system allows not only the imaging with electrons and ions but also the processing of the sample at precisely selected places on the surface. By using FIB, one can reveal the microstructure with physical etching by ions without any metallographic preparation. By making cross-section the microstructure under the surface is revealed, and after the serial cutting of the slices, a 3D-reconstruction of the microstructure can be obtained. Interactions of ions with the matter can produce different types of contrast: topographic, phase and channelling (Figure1 and 2). The ion beam can produce images with enhanced crystallographic orientation contrast using secondary electrons (SE) generated from the ions (channelling). The ion beam induced secondary electron yield strongly depends on the crystallographic orientation of the specimen. In crystalline materials, ions can penetrate several times deeper along directions with low Miller indices as in other directions or amorphous targets. FIB/SEM method allows a unique preparation of samples for HRTEM (thickness below 50 nm) and Atom Probe Tomography (APT), where materials are shaped into sharp needles (tip radius 50–100 nm). Dual-beam FIB microscopes equipped with EDS and EBSD can provide information about subsurface chemistry and crystallographic orientation. In the presentation, we will present

several cases of use FIB/SEM methods in metallography, advantages and disadvantages of the method.

References:

1. Giannuzzi, L. A., Stev ie, F. A. (2005): Introduction to Focused Ion Beams; Instrumentation, Theory, Techniquesand Practice. Springer-Science + Business Media LLC.

2. Lojen G., Bončina T., Zupanič F. Materiali in tehnologije, 46 (2012), 329-333.

3. Zupanič F., Bončina T., Pipić D., Henč-Bartolič Višnja. Journal of alloys and compounds, 465 (2008), 197-204.

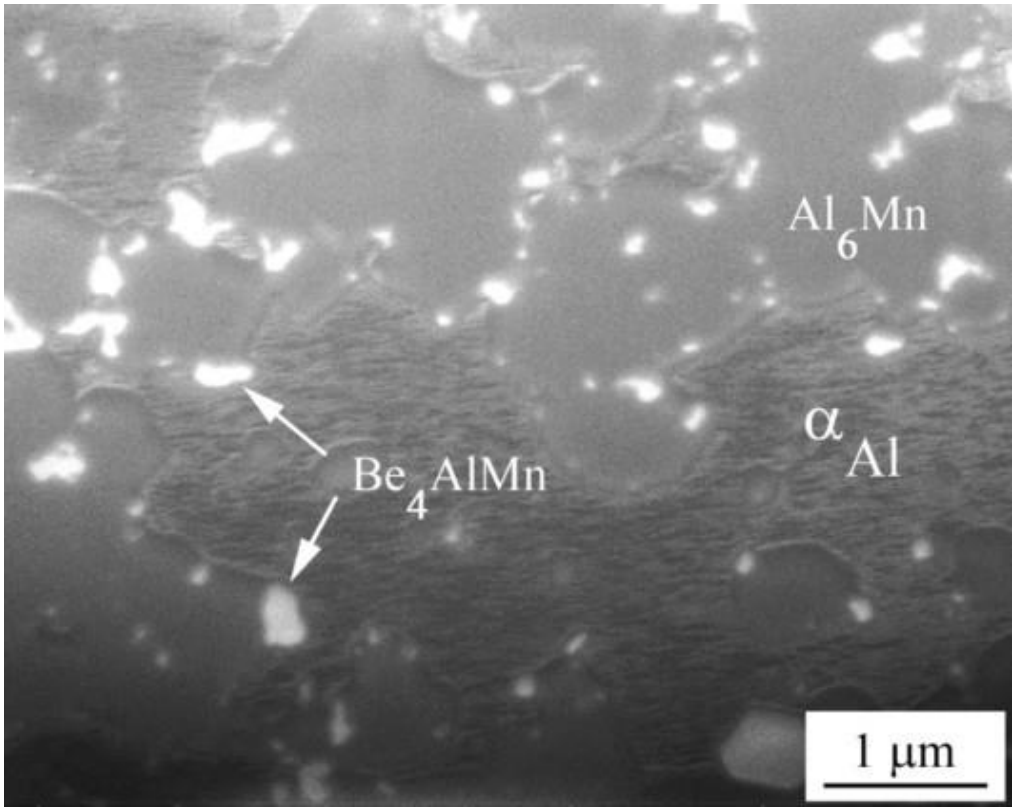

Figure 1. Ion induced secondary-electron image of an *in situ* FIB prepared cross-section of the alloy Al-Mn-Be. Strong phase contrast revealed Be4AlMn phase that contained a light element Be.

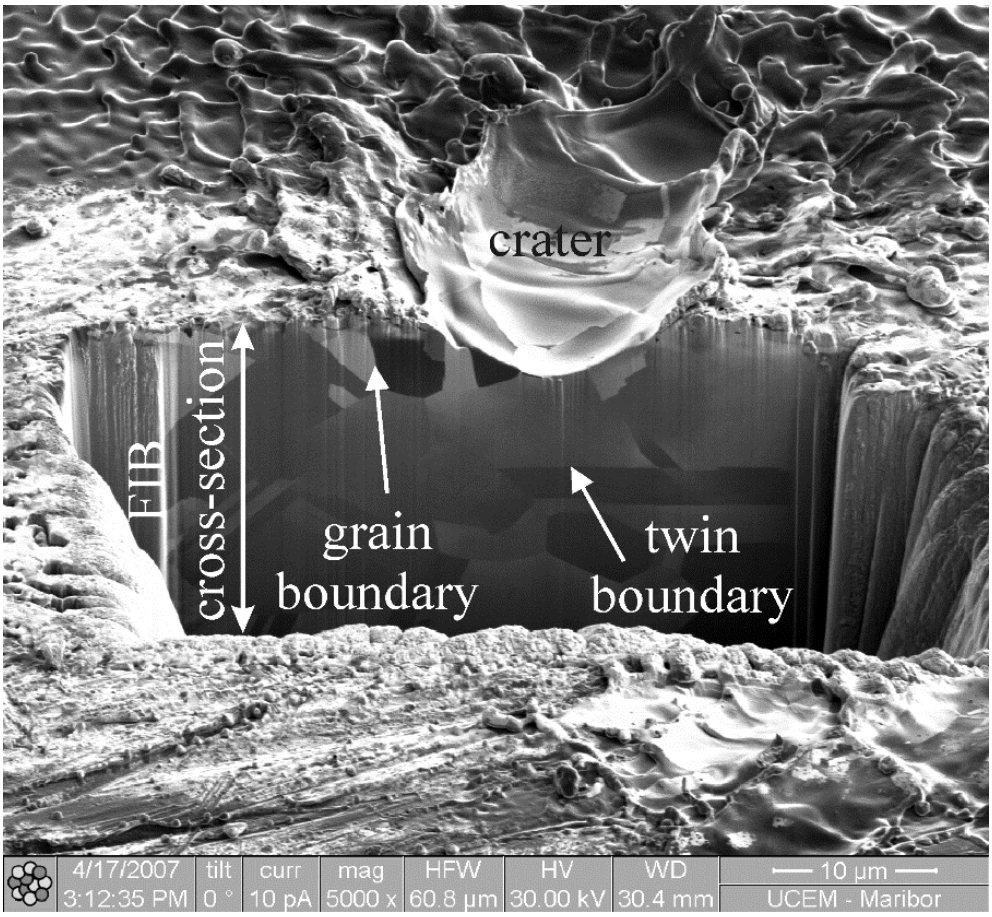

Figure 2. Ion induced secondary-electron image of an *in situ* FIB prepared cross-section through the deepest point of a crater formed after 10 pulses in pure copper. Note equiaxed grains beneath the crater, with straight grain and twin boundaries (topological and channelling contrast).

ORAL PRESENTATIONS M4:

Using organic additives to form the defect structure of electrodeposited nanocrystalline Ni

Tamás Kolonits (1), Péter Jenei (2), Péter László (3), Imre Bakonyi (3), Jenő Gubicza (2), Zsolt Czigány (1)

1) Institute of Technical Physics and Materials Science, Centre for Energy Research, Hungarian Academy of Sciences, Konkoly Thege M. út 29-33, H-1121 Budapest, Hungary

2) Eötvös Loránd University Faculty of Natural Sciences, Department of Materials Physics, 117 Budapest, Pázmány Péter sétány 1/a, Hungary

3) Institute for Solid State Physics and Optics, Wigner Research Centre for Physics, Hungarian Academy of Sciences, Konkoly-Thege Miklós út 29-33, 1121 Budapest, Hungary

Keywords: electrodeposition, crystal defects, nanocrystalline, X-ray diffraction, TEM

The effect of various organic additives on the defect structure of electrodeposited Ni films was investigated by X-ray diffraction (XRD) line profile analysis (eCMWP model) and transmission electron microscopy (TEM). The main task of the project is the synthesis of chemically homogenous nickel layers with various nanostructure i.e. carefully controlled crystal and defect structure and texture. These various layers are able to be basics of some current fundamental research and industrial applications. The aim of the present lecture is a sub-topic of the main task: namely, to investigate the effect of the additives on the grain structure and defect (dislocation and twin) density which influence the macroscopic properties and application of the layers. The electrodeposited layers were deposited at room temperature with low current density (6.25 mA/cm^2) onto various substrates (Al_2O_3, Cu, Si). The basic electrolyte mainly contained nickel sulphate ($NiSO_4 \cdot 7\ H_2O$) and boric acid (H_3BO_3). Formic acid, saccharin and trisodium citrate were used as orgainc additives. Using complementary features of XRD and TEM, a detailed grain size, defect density and phase analysis was carried out to determine the microstructure. In addition to the detailed mapping of the various microstructures, we underlined the importance of understanding how the refinement of the particle size, the

formation of the texture, the formation of dislocations and twin boundaries were induced by the different types of electrolytic solutions, their additives and contaminants. To support these arguments, we also made a composition analysis with EDS. Based on our measurements, the incorporated metallic (e.g. Na) and non-metallic components (such as S) are responsible for the refinement of the particle size which components are clearly incorporated form the organic additive or by its effect. Similarly, the built-in sulfur is responsible for the development of twin boundaries (and thus for a significantly increased dislocation density).

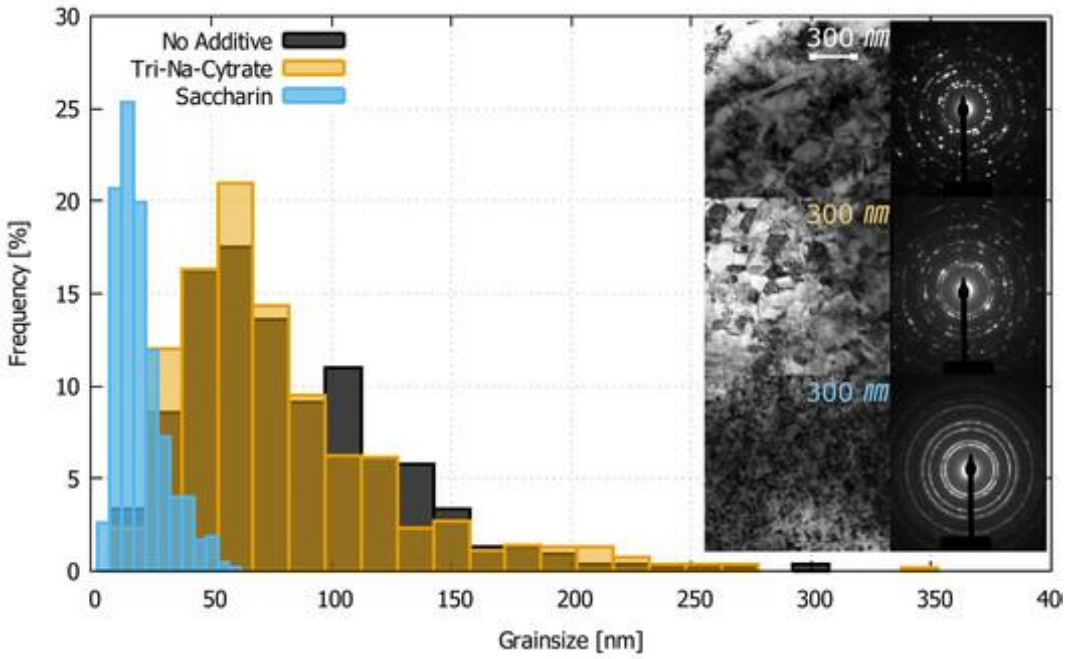

Figure 1. grain size distribution and the corresponding TEM/SAED patterns of samples deposited with no organic additive, trisodium citrate additive and saccharin additive.

Structure determination of a new phase Ni_8Ti_5 by PEDT

Mariana Klementova (1), Miroslav Karlik (2), Pavel Novák (3), Lukas Palatinus (1)

1) Institute of Physics, Na Slovance 1999/2, 182 00 Prague 8, Czech Republic

2) Czech Technical University, Faculty of Nuclear Sciences and Physical Engineering, Department of Materials, Trojanova 13, Praha 2, 120 01Prague, Czech Republic

3) University of Chemistry and Technology, Prague, Department of Metals and Corrosion Engineering, Technická 5, 166 28 Prague 6 – Dejvice, Czech Republic

Keywords: electron diffraction tomography, dynamical refinement, shape-memory alloys

NiTi alloys with approximately equimolar composition are well known functional materials exhibiting shape memory effect and pseudoelasticity, which make them attractive for various applications in robotics and automotive, aerospace and biomedical industries. The new phase Ni_8Ti_5 was studied in the Ni-48 at.%Ti alloy prepared from elemental powders by self-propagating hightemperature synthesis and subsequent annealing at 1000 °C for 12 h, followed by slow cooling to room temperature. The phase forms micrometer-sized precipitates within NiTi matrix. It was also observed in the alloy of the same composition prepared by conventional vacuum induction melting from bulk Ni and Ti metals. So its existence is not related only to the powder metallurgy preparation route. For the structure determination of the unknown phase, thin foils prepared by mechanical thinning and ion milling using Gatan PIPS were studied by Transmission Electron Microscopy (TEM) performed on a Philips CM 120 (LaB_6, 120 kV) equipped with a NanoMEGAS precession unit DigiStar. The diffraction data were collected by means of precession electron diffraction tomography (PEDT). Data were recorded from several precipitates/crystals. Each crystal was sequentially tilted by the step of 1 deg. From -55 to +55 deg. (depending on the crystal position on the grid the tilt range was slightly different for every crystal), and at every tilt step a precession diffraction pattern was acquired using a precession angle of 1 or 1.5 deg. The data processing was carried out in the PETS software (1). Structure solution and refinement were performed in the computing system Jana2006 (2). The structure was solved by the charge flipping algorithm using the program Superflip (3). The structure of Ni_8Ti_5 was solved and refined from precession electron diffraction

tomography data using dynamical refinement approach. It has trigonal symmetry *R*-3*m* (*a* = 12.24(5) Å, *c* = 15.33(5) Å) with a structure related to the structure of Ni_4Ti_3. The greatest challenge of the structure determination was the assignment of atomic types due to the proximity of scattering powers of Ti and Ni. Several approaches to determination of atom type distribution over atomic positions were used; (1) analysis of the Wyckoff position multiplicities, (2) refinement of displacement parameters, and (3) geometrical analysis of the structure and comparison with known structures. These approaches consistently pointed to one distribution, which was confirmed by a significant improvement of the refinement figures of merit.

References:

1. L. Palatinus, PETS - Program for Analysis of Electron Diffraction Data, Institute of Physics of the AS CR, Prague, 2011. http://pets.fzu.cz/.

2. V. Petricek, M. Dusek, L. Palatinus, Crystallographic computing system JANA2006: general features, Z. Krist. 229-5 (2014) 345e352.

3. L. Palatinus, G. Chapuis, SUPERFLIP - a computer program for the solution of crystal structures by charge flipping in arbitrary dimensions, J. Appl. Cryst. 40 (2007) 786e790.

4. The research was conducted using instruments of the ASTRA lab established within the Operation program Prague Competitiveness - project CZ.2.16/3.1.00/24510.

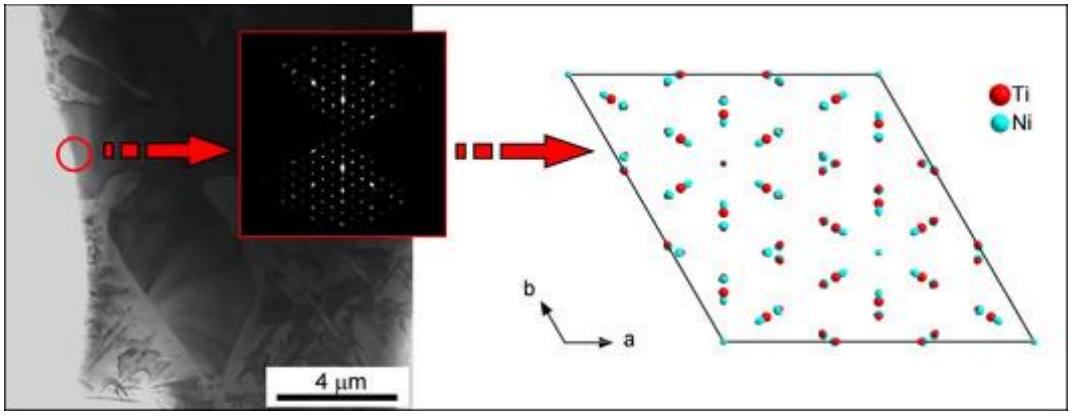

Figure 1. Bright-field TEM image with electron diffraction pattern, and resulting atomic structure of Ni8Ti5 viewed along [001].

Observation of the structural transformation of multinary nanoparticles by *in situ* transmission electron microscopy

Alba Garzón-Manjón (1), Gesa Zahn (2), Christina Kuchshaus (2), Alfred Ludwig (2), Christina Scheu (1)

1) Max-Planck-Institut für Eisenforschung GmbH, Max-Planck-Straße 1, 40237 Düsseldorf, Germany

2) Ruhr-Universität Bochum, Werkstoffe der Mikrotechnik, Universitätsstr.150, D-44801 Bochum, Germany

Keywords: Nanoparticles, Multinary-Alloy, Sputtering, HRTEM, EDS

Combinatorial sputtering was used to synthetize alloy nanoparticles (NPs), of interest for different applications ranging from catalysis and energy to medicine, cosmetics, among other. Ionic liquids[1] (salts with a melting point <100°C) are used as liquid substrates, due to their low vapor pressure they are able to provide outstanding possibilities as media for the sputter synthesis of NPs. The ionic liquid itself can act as an electronic as well as a steric stabilizer preventing particle growth and particle aggregation leading to the formation of extremely small sizes with a strong effect on the morphology of the formed NPs. In addition, this methodology can demonstrate a high efficiency to produce the desired NPs. Our research is based on the preparation and in-depth atomic-scale characterization of noble-metal based NPs systems, such as binary, ternary and multinary alloys. The main focus is set on the investigation of these multinary alloy NPs by using various microscopy techniques, such as high-resolution (scanning) transmission electron microscopy ((S)TEM), energy dispersive X-ray spectroscopy (EDS) and electron energy loss spectroscopy (EELS). With these techniques the final size, shape, microstructure, chemical composition and electronic properties are studied. Some of the fabricated multinary NPs appear amorphous after the synthesis as can be seen in the high resolution TEM image and the corresponding Fast Fourier Transformation (FFT) (figure 1). During illumination with a 200 kV electron beam structural changes occur. Up to 40 min the NP remain in the amorphous state. Above 40 min the illumination of the NP leads to a structural transformation to a crystalline state as visible in the lattice fringes observed in the HRTEM

image and the corresponding reflection in the FFT (figure 2). Similar observation have been reported by *Uematsu et al.* for Au NPs[2]. Further *in situ* studies will be performed to study Ostwald ripending on the atomic scale and to investigate how the different diffusion constants of the various atomic species will affect the growth.

Acknowledgements:

This work was funded by German Science Foundation (DFG) via the project SCHE 634/21-1.

References:

1. König, D. et al. Adv. Funct. Mater. 24, 2049–2056 (2014).

2. Uematsu, T. et al. J. Am. Chem. Soc. 136, 13789-13797 (2014).

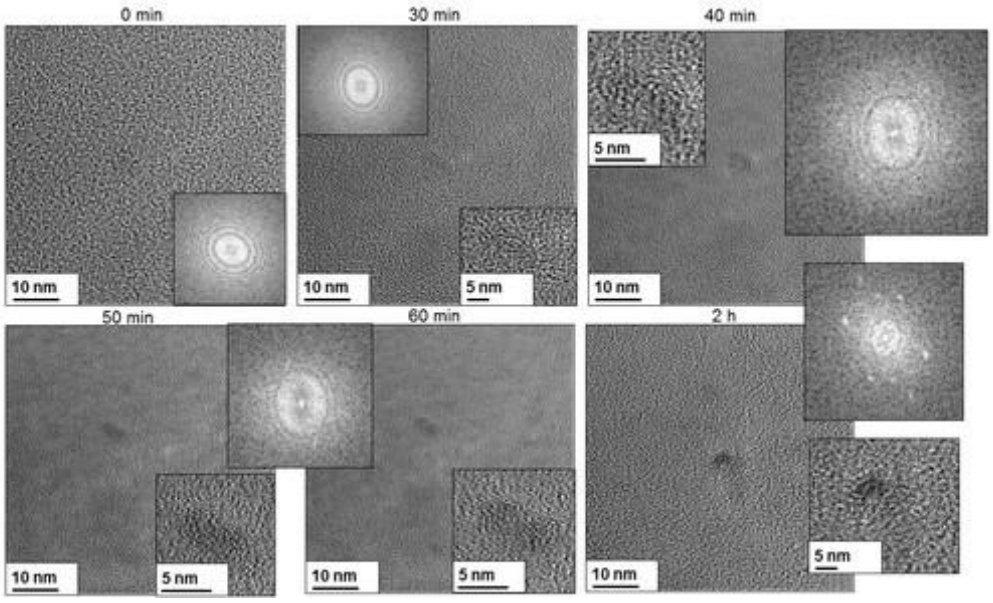

Figure 1. Time sequence of high resolution TEM images of multinary nanoparticles during the observation with a 200 keV electron beam.

The role of Mo on formation and stability of the ordered omega phase in multi-phase TiAl alloys: experimental and theoretical aspects

Boryana Rashkova (1), Thomas Klein (1), David Holec (1), Helmut Clemens (1), Svea Mayer (1)

1) Department of Physical Metallurgy and Materials Testing, Montanuniversität Leoben, Roseggerstr. 12, 8700 Leoben, Austria

Keywords: intermetallic TiAl alloys, HRTEM. APT, ab initio calculation

Advanced intermetallic TiAl alloys are designed for high temperature application as lightweight materials which can withstand temperatures up to 750°C, while maintaining attractive functional and structural properties. Particularly, the so-called TNM alloy has been recently implemented as a structural material in the aerospace and automotive industry. TNM alloys, exhibiting a nominal composition of Ti-43.5Al-4Nb-1Mo-0.1B (in at.%), are multi-phase β-solidifying γ-TiAl-based alloys, where the microstructure is determined by the manufacturing process as well as subsequent heat treatments. At room temperature, the TNM alloy consists predominantly of γ-TiAl, α_2-Ti_3Al and β_o-TiAl phases, which are present in different morphologies. The alloying with Mo leads to a formation of additional phases such as the ω_o-Ti_4Al_3Nb phase (1, 2 and Refs. Therein). In this work we present detailed investigations on the effect of Mo on the formation mechanism and evolution of the ω_o-phase. The microstructure of the constituent phases in differently heat-treated specimens was examined by conventional and high resolution transmission electron microscopy (HRTEM). The chemical composition of β_o and ω_o was determined by means of energy dispersive X-ray spectroscopy, whereas the local elemental composition of the phases was quantified by atom probe tomography (APT). In particular, the impact of Mo on the growth of the ω_o-grains within the β_o-matrix was investigated. Additionally, the thermodynamic stability of the β_o and ω_o phases by Mo was calculated by *ab initio* simulations using the Vienna Ab initio Simulation Package. The experimental results reveal that the ω_o-phase nucleates in the β_o-matrix without significant diffusional alloying element redistribution (Figure 1a), while the subsequent growth is controlled

by the diffusion of Mo, i.e. its rejection from the ω_o-phase and its subsequent accumulation in the β_o-phase (Figs.1b-c). Detailed HRTEM studies show the fine ω_o precipitates within the β_o-matrix after a heat treatment (Figure 2a) and a dislocation-free segment of the atomically abrupt and coherent β_o/ω_o interface after the creep test (Figure 2b). *Ab initio* calculations of the energies of formation confirm the experimentally observed phenomena: a strong destabilization of the ω_o-phase after incorporation of Mo, while the β_o-phase is stabilized by Mo. More details about the experimental conditions and the obtained results are given in the original full-length papers, i.e. (1, 2).

References:

1. M. Schloffer et al., Acta Materialia 64 (2014) 241-252.

2. T. Klein et al., Intermetallics 85 (2017) 26-33.

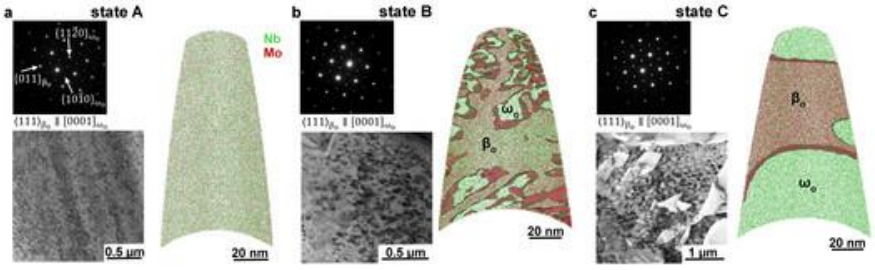

Figure 1. TEM images with selected area diffraction analysis and APT reconstructions of regions containing the beta and omega phase in differently heat-treated TNM specimens (2).

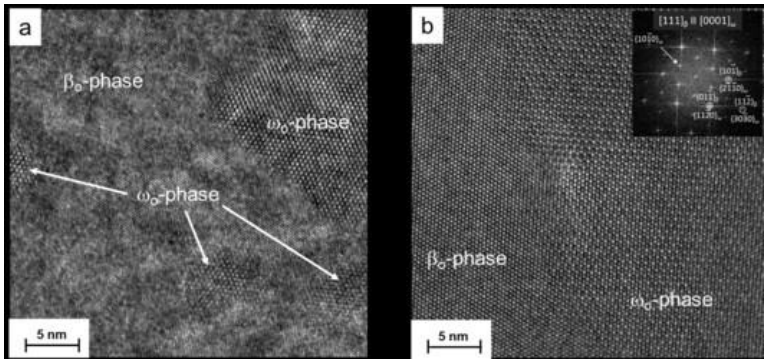

Figure 2. HRTEM images showing the omega precipitates within the beta phase: (a) after furnace cooling and (b) after creep testing (1).

POSTER PRESENTATIONS M4:

Microstructure development in as cast Al-Mg-Li alloy

Franjo Kozina (1), Zdenka Zovko Brodarac (1), Mitja Petrič (2)

1) University of Zagreb, Faculty of Metallurgy, Aleja narodnih heroja 3, 44000 Sisak, Croatia

2) University of Ljubljana, Faculty of Natural Sciences and Engineering, Aškerčevacesta 12, 1000 Ljubljana, Slovenia

Keywords: Al-Mg-Li alloy, lithium, magnesium, phase precipitation, microstructure

Since the beginning of economical crisis, weight reduction and temperature stability, as well as high strength and stiffness, have become the key driving forces for new material development and utilization in aerospace and space industry. One of the more promising materials to be utilized is aluminium-magnesium-lithium alloy due to combination of high strength and light weight as well as the god weldability, and corrosion resistance. While, every 1% of lithium added to aluminium increases elastic modulus roughly for 3 GPa and decreases density by approximately 80 kg/m^3, the exact influence of magnesium on the phase precipitation and strengthening of Aluminium-Magnesium-Lithium ternary system is not fully understood. The aim of this investigation is to identify the Mg influence on microstructure development of Aluminium-Magnesium-Lithium alloy in as cast condition. The results of preliminary metallographic testing conducted on Al-2,5wt.%Mg-0,72wt.%Li produced under laboratory conditions have shown existence of two different secondary phases, T(Al_2LIMg) and Al_3Mg_2 in $\alpha_{al.}$ While optical microscopy shows existence of phases precipitated in interdendritic areas and grain boundaries, electron microscopy allows for them to be localised based on differences in magnesium and aluminium content. Ultimately, T has been identified to precipitate in interdendritic areas, whilst Al_3Mg_2 will precipitate at drain boundaries of last solidifying areas.

References:

1. S. Betsofen et al., Quantitative Phase Analysis of Al-Mg-Li and Al-Cu-Li Alloys, Aluminium Alloys 2014, 794-796 (2014) 915-920

2. A. Deschamps et al., Experimental and modelling assessment of precipitation kinetics in an Al-Li-Mg alloy, Acta Materialia 60(5) (2012) 1917-1928.

3. N. Prasad et al., Aluminium–Lithium Alloys, Aerospace Materials and Material Technologies 2017

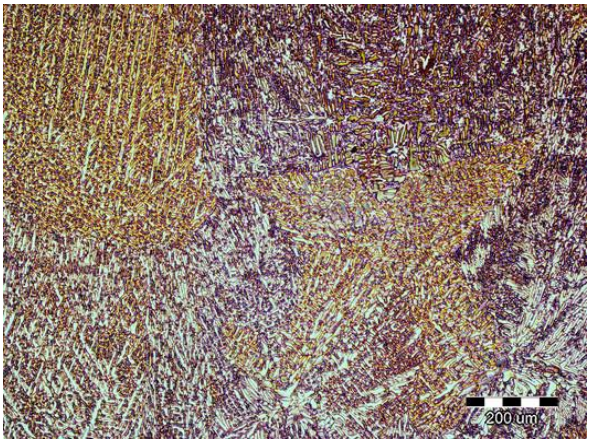

Figure 1. Dendritic cell growth and orientation, 100 X.

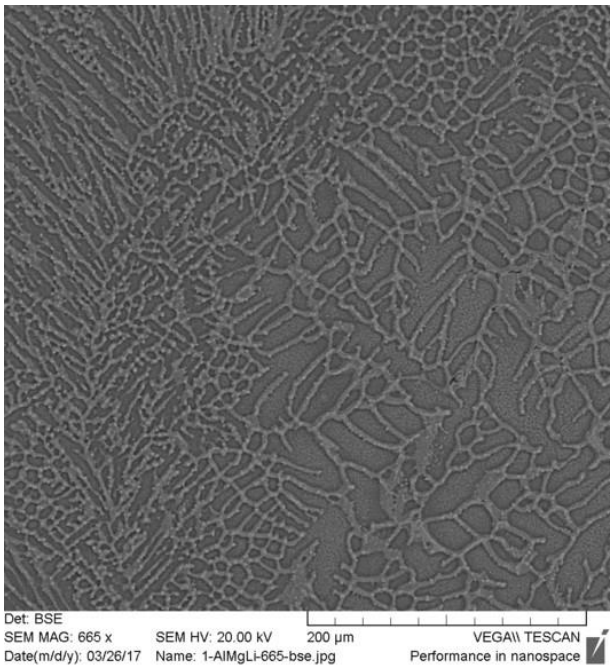

Figure 2. SEI showing phase precipitation at interdendritic areas as well as grain boundaries represented as interfaces between differently oriented dendrites.

Influence of neutron irradiation on the microstructure and magnetic properties of Nb3Sn superconductors

Stephan Pfeiffer (1), Johannes Bernardi (1), Michael Stöger-Pollach (1), Thomas Baumgartner (1), Michael Eisterer (1), Johannes Hecher (1), Amalia Ballarino (2), Luca Bottura (2), Christian Scheuerlein (2)

1) TU Wien, Wiedner Hauptstrasse 8-10/057B, A-1040 Wien, Austria

2) CERN, CH-1211 Geneva 23, Switzerland

Keywords: superconductivity, magnets, Nb3Sn, neutron irradiation

An increase of the high field critical currents in commercial Nb_3Sn wires by about 50 % is required for the design of Future Circular Collider (FCC) superconducting magnets. Creating additional flux pinning centers by means of fast neutron irradiation that induces defects in the crystal structure is one promising approach for reaching this target. In this study, the underlying mechanisms are investigated through combined microstructural and magnetic analyses. This knowledge is a requirement for manufacturing such high-performance superconductors in an industrial process. The nuclear research reactor of TU Wien was used to irradiate various Nb_3Sn wires produced by different manufacturing techniques as well as transmission electron microscopy (TEM) specimens. Micro- and nanostructural examinations of grain geometry, grain boundary morphology, compositional gradients, local texture and defect structure were performed before and after irradiation by transmission electron microscopic methods such as high-resolution TEM (HRTEM), energy-dispersive X-ray spectroscopy (EDX), electron energy loss spectroscopy (EELS) and selected area diffraction. The results thereof are correlated with measurements of the superconducting properties, in particular scanning Hall probe experiments and SQUID magnetometry to determine the global critical current as well as the local critical current density within the superconducting subelements. The established correlation *contributes to a better understanding of the influence of irradiation damage and the resulting microstructure on local superconducting properties and ultimately on the macroscopic performance of the superconductor.*

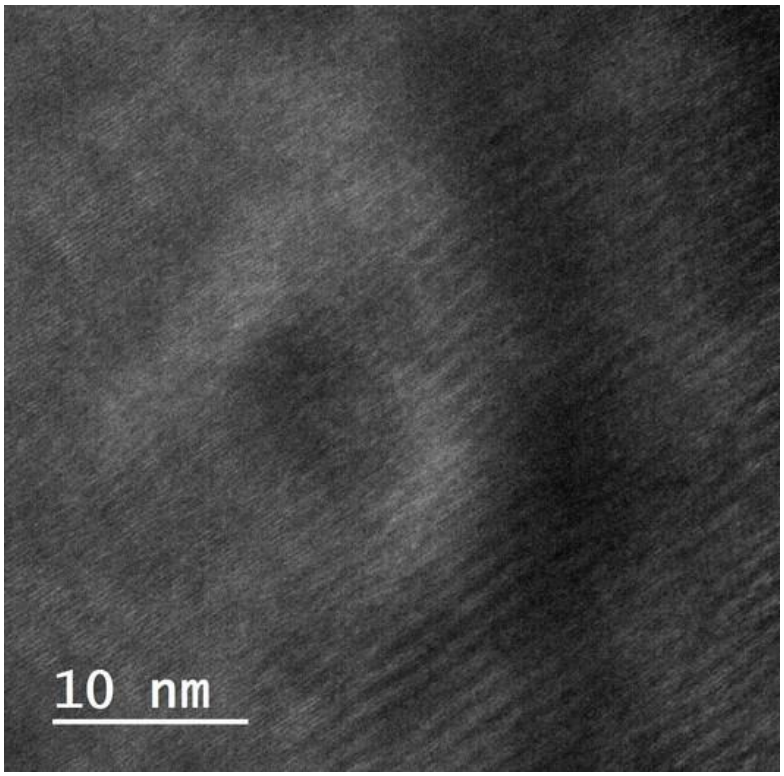

Figure 1. High-resolution TEM image of a neutron impact site.

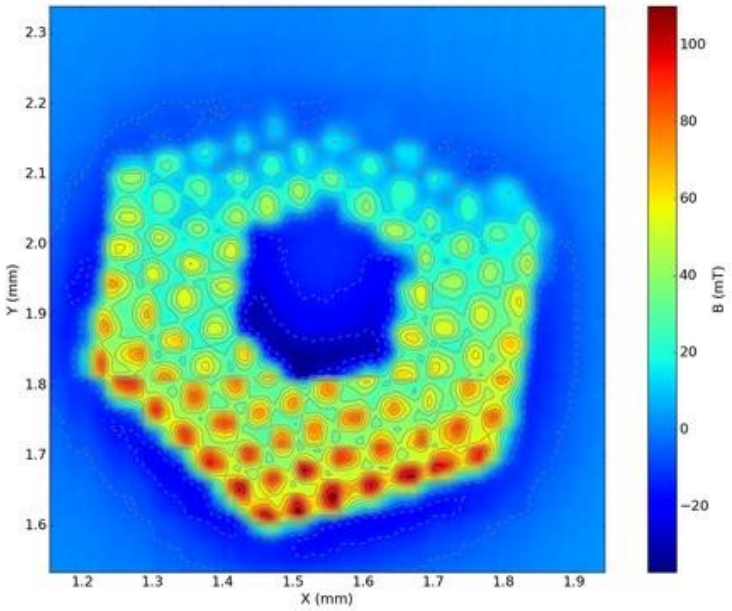

Figure 2. Remanent field Hall scan of the cross section of a Nb3Sn wire at 4 K.

Electron microscopy analysis of flash-annealed CuZr based bulk metallic glass

Christoffer Müller (1), Christoph Gammer (2), Konrad Kosiba (3), Simon Pauly (3), Christian Rentenberger (1)

1) Physics of Nanostructured Materials, Faculty of Physics, University of Vienna, Universitätsring 1, 1010 Vienna, Austria

2) Erich Schmid Institute of Materials Science, Österreichische Akademie der Wissenschaften, Erich Schmid Institute of Materials Science, Jahnstrasse 12, 8700 Leoben, Austria

3) Institute for Complex Materials, IFW Dresden, Helmholtzstraße 20, 01069 Dresden, Germany

Keywords: fluctuation electron microscopy, amorphous structure, bulk metallic glass, flash-annealing

Bulk metallic glasses (BMGs) are amorphous materials showing attractive mechanical properties due to their unique atomic structures. Despite the lack of long-range order, still topological and chemical short-range and medium-range order are expected to occur. Although being amongst the strongest engineering materials known, they exhibit a disappointingly low plastic deformability. To circumvent this limited ductility the concept of heterogeneous microstructure by the formation of composites has recently been used (1). One way to achieve such a structure is thermal treatment of the BMG. This work deals with flash-annealed CuZr based BMGs. During the flash-annealing process the atomic structure of the $Cu_{44}Zr_{44}Al_8Hf_2Co_2$ BMG is modified by rapid heating to different target temperatures above glass transition temperature (712 K) and the subsequent cooling in a water bath. The samples were heated to 817 K, 898 K and 916 K with a mean rate of 67 K/s. Using back-scattered electrons the SEM observation of the sample heated to 916 K reveals both an amorphous and a crystalline part each taking up about half of the sample with spherical crystallites of different size in between. The diffraction pattern (DP) of the crystallites contains superlattice reflections indicating the presence of the B2 ordered structure. This is interesting as in crystalline CuZr based materials, devitrified from the amorphous structure, $Cu_{10}Zr_7$ and $CuZr_2$ structures are expected to occur.

In order to analyse and compare the structures of the fully amorphous samples flash-annealed to 817 K and 898 K as well as the amorphous part of the sample heated to 916 K, variable resolution dark field (DF) fluctuation electron microscopy (FEM) was applied. Fluctuations of DF image intensity (cf. Figure 1a) reveal structural ordering at the medium range. Acquiring a series of DF images at different vectors k and azimuthal angles φ provides the mean intensity and normalized variance as a function of k. Figure 1b illustrates the mean intensity and variance curves of the differently treated samples for a given spatial resolution defined by the aperture size. It is interesting to compare the profile of the normalized variance to the 4 most intense peaks in the X-ray spectrum of B2 structured CuZr, as they show remarkable similarities. By changing the aperture size and thus varying the spatial resolution the correlation length (a length scale for medium-range order) can be derived from the pair persistence model (3). Figure 2 compares the correlation lengths of the flash annealed amorphous samples to the as-cast state showing an increase in medium-range order with increasing target temperatures. In a nutshell, depending on the target temperature flash-annealing of CuZr based BMGs facilitates an increase of the medium-range order length scale in the amorphous phase or the formation of B2 ordered crystalline structure.

References:

1. J. Eckert, J. Das, S. Pauly, C. Duhamel, Journal of Materials Research 22, 285 (2007).

2. C. Gammer, C. Mangler, C. Rentenberger, H. P. Karnthaler, Scr Mater 63, 312 (2010).

3. J.M. Gibson, M.M.J. Treacy, P.M. Voyles, Ultramicroscopy 83, 169 (2000). We kindly acknowledge financial support by the Austrian Science Fund (FWF): [I1309, J3397].

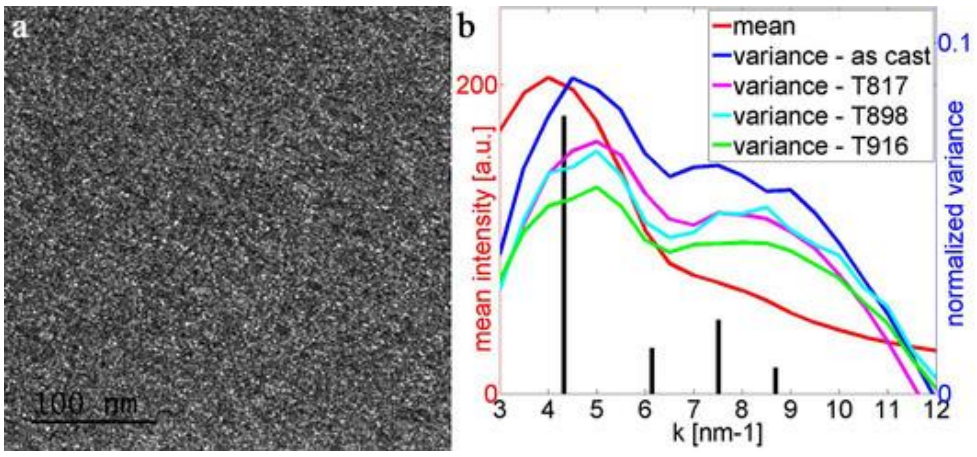

Figure 1. (a) Tilted DF image showing intensity variations due to local structural correlations. (b) Intensity and variance curves, each derived from a series containing 320 DF images, and the 4 most intense peaks of the X-ray spectrum of B2 ordered CuZr.

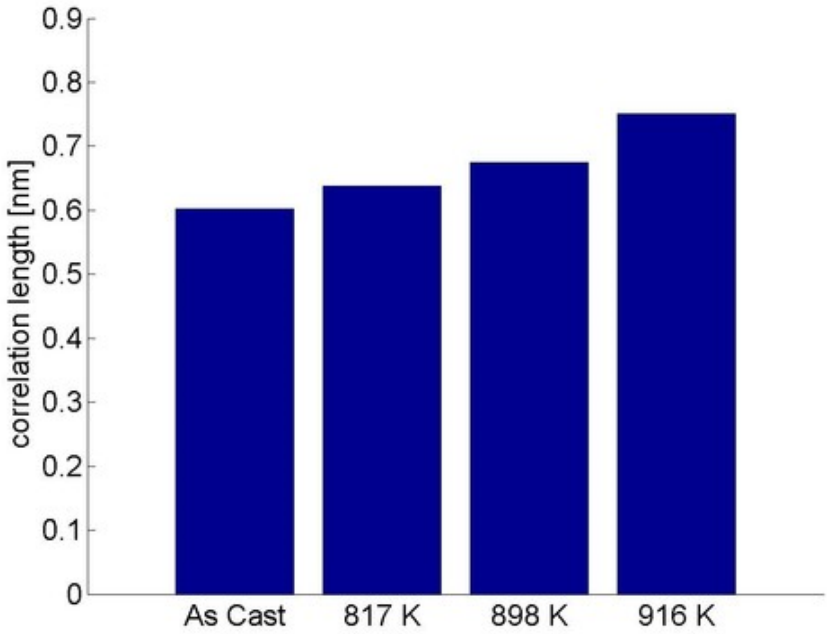

Figure 2. Comparison of the correlation lengths of the flash-annealed amorphous samples to the as-cast state showing an increase in medium-range order with increasing target temperatures.

Systematic study of structural changes in the vicinity of indentation marks with HR-EBSD

Zoltán Dankházi (1), Szilvia Kalácska (1), Péter Dusán Ispánovity (1), István Groma (1)

1) Eötvös Loránd University (ELTE) Department of Materials Science, H-1117, Pázmány Péter sétány 1/a., Budapest, Hungary

Keywords: indentation, HR-EBSD, 3D reconstruction, FIB

In crystalline materials a deeper understanding of the effects of external deformation is essential to develop new materials. The mechanical properties are highly influenced by the lattice defects (mainly dislocations) and their dynamics in the crystal structure, since the dislocation movement is most often responsible for the plastic deformation. The primary task of the research is to gain more experimental knowledge on the dislocations forming in the metals' crystal structure as a result of external deformation. During these experiments an indentation head was pressed into the sample to a depth of a few micrometers. After the removal of the head high resolution electron backscatter diffraction (HR-EBSD) measurements were carried out in the vicinity of mark, from which we are expecting a better understanding of the whole deformation process. It is also important to investigate the depth distribution of stain values. In order to achieve this we have removed thin layers of the matter along the cross-section of an indentation mark using focused ion beam (FIB). On each of newly formed surface a HR-EBSD measurement could be done. Combining the images of these slices a 3 dimensional map is forming. The method (so called "slice and view") is a novel approach in HR-EBSD measurements, which will be also introduced during the presentation.

Investigation of domains in $Pr_2NiO_{4+delta}$ by transmission electron microscopy

Christian Gspan (1), Edith Bucher (2), Andreas Egger (2), Nina Schrödl (2), Christian Berger (2), Martina Dienstleder (1), Stefan Mitsche (3), Werner Sitte (2), Werner Grogger (3)

1) Graz Centre for Electron Microscopy, Steyrergasse 17/III, 8010 Graz, Austria

2) Chair of Physical Chemistry, Montanuniversitaet Leoben, Franz-Josef-Straße 18, 8700 Leoben, Austria

3) Institute of Electron Microscopy and Nanoanalysis, Graz University of Technology, Steyrergasse 17/III, 8010 Graz, Austria

Keywords: LACBED, domains, phase transition

Praseodymium nickelate is a very promising candidate for high temperature solid oxide fuel cell cathodes. However, the synthesis of the pure material is not straightforward and therefore the characterization of the microstructure in a transmission electron microscope (TEM) is essential for the correlation with the materials properties. The crystal structure and the physical properties of $Pr_2NiO_{4+delta}$ are well known (1) and also two structural phase transitions. The high-temperature phase transition from the orthorhombic to the tetragonal crystal system occurs in the temperature range between 650 and 700 K, depending on the oxygen partial pressure. This phase transition can be observed by electron diffraction in the TEM. In this study we will show the formation of domains and how they change at temperatures in the range of this phase transition. TEM investigations reveal the existence of different types of domains, especially micro twin domains along certain crystallographic directions (Figure 1). The domains are clearly visible in some regions of the crystal while in other regions there are no domains present. In order to understand the crystallographic nature of the domains and their boundaries, electron diffraction measurements were performed in combination with high resolution images. In particular, large angle convergent beam electron diffraction (LACBED) patterns show a clear difference between areas with and without domains (Figure 2). In addition, Kikuchi lines corresponding to certain lattice planes may provide an even deeper insight into the structural changes. In order to obtain a better understanding of the formation

mechanism of the domains, TEM measurements were performed at elevated temperatures. The appearance and the shape of these domains change with the temperature and strongly depend on the heating/cooling rate.

Acknowledgements:

Financial support by the Klima- und Energiefonds within the program "Energieforschung (e!MISSION)" is gratefully acknowledged.

References:

1. E. Niwa, et al., Thermochimica Acta 575 (2014) 129-134.

2. This research was supported by the Austrian Research Promotion Agency FFG (No. 853538).

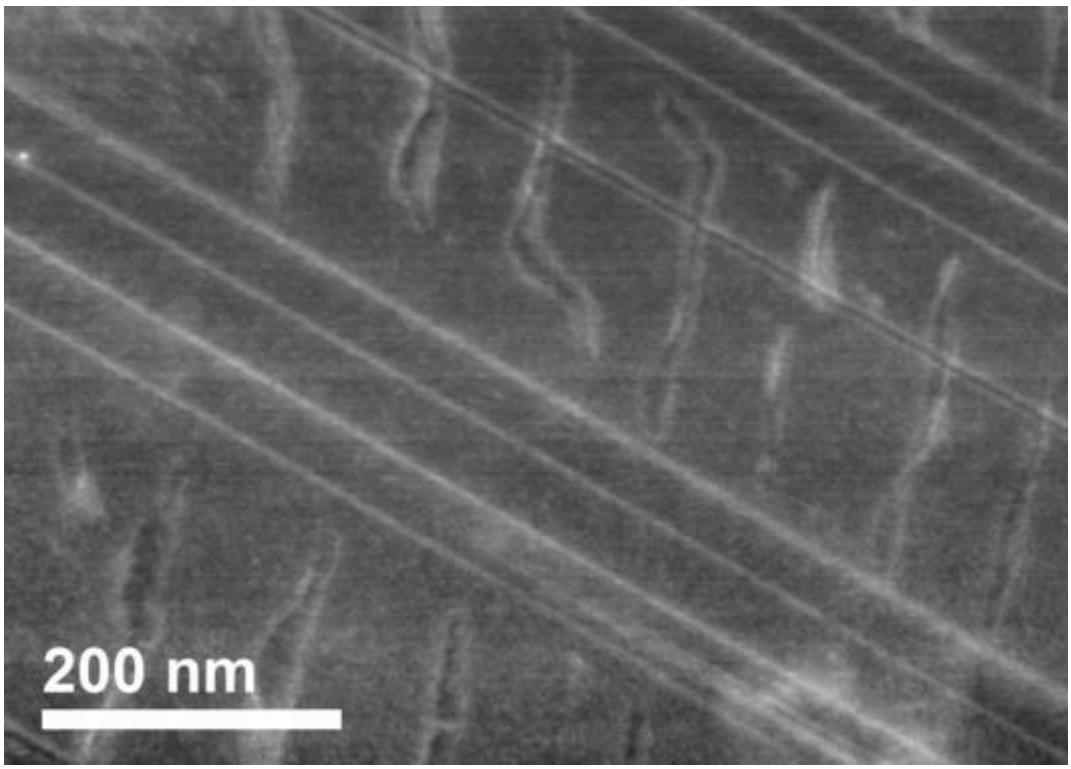

Figure 1. Annular dark field image of a $Pr_2NiO_{4+delta}$ crystal in [0 0 1] orientation.

Microstructure of rapidly solidified aluminium powder alloys compacted by Spark Plasma Sintering

Anna Knaislová (1), Alena Michalcová (1), Ivo Marek (1)

1) Department of Metals and Corrosion Engineering, University of Chemistry and Technology in Prague, Technická 5, Prague 6, 166 28, Czech Republic

Keywords: Microstructure, Rapid solidification, Aluminium alloys, Spark Plasma Sintering

Aluminium alloys are used in the manufacturing of highly stressed components for aerospace and automotive industry. Their main advantages are low density and relatively high strength. Conventional cast aluminium alloys are characterised by good mechanical properties, but their main disadvantage is low thermal stability, which significantly limits their use to only low temperature (up to 200 °C). Dispersed aluminium alloys, formed by aluminium and one or more transition metals (eg. Ni, Fe, Zr, Ti), are used for temperature range around 400 °C today. Rapidly decrease of strength at higher temperature (above 200 °C) is result of relatively high diffusion coefficients of alloying elements in Al matrix. Alloying elements suppress recrystallization of material. However, proportion of transition metals in alloy is considerably limited by creation of hard and brittle intermetallic phases, which decrease plasticity, ductility and strength of material. Aluminium alloys with new metastable nonequilibrium phases (amorphous, quasicrystalline and crystalline), fine-grained structures and fine- and uniformly-distributed intermetallic phases can be prepared by rapid solidification method, which enable increasing of transition metals concentration above their limits of solubility. Several technologies of rapid solidification exist: melt atomization by pressure medium, surface melting by laser or electron beam, or melt spinning. High cooling rates suppress crystallization and support formations of amorphous alloys, but are achieved only in small bulk of melt. After rapid solidification, obtained powders are consolidated by hot extrusion (400 - 600 °C). Tensile strength is increased by consolidation (up to 1000 MPa), also elongation and thermal stability. In this work, microstructure of AlFeCrSiTi alloy prepared gas atomization will be characterized. Rapidly solidified powder was sifted into different granulometric fractions (under 63 μm, 63 - 125 μm, above 125 μm). Powder contains two types of particles: type 1 contains almost

spherical intermetallic phase, evenly distributed in solid aluminium matrix and dominates in fraction under 63 μm. Type 2 is formed by irregularly oblong intermetallic phase and predominates in the coarse fraction. Quasicrystalline decagonall phases were also found in the powder alloy. Rapidly solidified powders were then consolidated by Spark Plasma Sintering method and influence of temperature on microstructure of compacted material was described (1, 2, 3).

Acknowledgements:

This research was supported by Czech Science Foundation, project No. GJ17-25618Y.

References:

1. B. Bártová et al., Journal of Alloys and Compounds 387 (2005) 193–200

2. A. Michalcová et al., Micron 45 (2013) 55–58

3. D. Vojtěch et al., Journal of Alloys and Compounds 475 (2009) 151–156

On-line monitoring of steel microsturcture changes within tensile testing

Martin Bystriansky (1), Ludmila Kucerova (1), Jan Prochazka (1)

1) University of West bohemia, Regional Technological Institute, Univerzitní 8, Pilsen, Czech Republic

Keywords: tensile testing, *In situ* testing, steel microstructure

Scanning electron microscope (SEM) equipped with *in situ* tensile testing stage was used for experiments aimed at both crack development and microstructure changes during tensile testing of steel specimen. Mostly TRIP (transformation induced plasticity) steels were used. Imaging using secondary electrons detection or by electron backscattered diffraction was applied. The microstructure affects the mechanical properties of the material and influences the results mechanical testing. Equally the microstructure of the material can be affected as mechanical testing is proceeded.

Acknowledgements:

The present contribution has been prepared under project LO1502 ‘Development of the Regional Technological Institute‘under the auspices of the National Sustainability Programme I of the Ministry of Education of the Czech Republic aimed to support research, experimental development and innovation.

References:

1. J. Prochazka et al., IOP Conference Series: Materials Science and Engineering 179 (2016)

2. L. Kucerova, M. Bystriansky, Journal of Achievements of Materials and Manufacturing Engineering (2016)

Study on the kinetics of the intermediary phase formation in Ni-Al system

Andrea Školáková (1), Pavel Novák (1)

1) Department of Metals and Corrosion Engineering, University of Chemistry and Technology, A, Technická 5, 166 28, Prague 6 - Dejvice, Czech Republic

Keywords: kinetics, microstructure, Ni-Al alloys

NiAl alloys are perspective materials for gas turbine applications due to their high melting temperature, low density, high thermal conductivity and oxidation resistance up to 1300 °C. This alloy belongs to the group of new generation materials which could replace nickel-base superalloys. The problem lies in theirs low ductility and toughness. Moreover, this alloy has been produced by induction melting under argon atmosphere which influences microstructure negatively. For this reason, reactive sintering is very promising and easy method for preparing intermetallic phases only from powders. Intermetallic phases form during this process and on the basis of observation of their formation, kinetics could be estimated. In this work, kinetics of the formation of intermetallic compounds in the Ni-Al system was studied. Kinetics was determined by an experimental model consisting of bulk nickel submerged into molten aluminium. Layers of intermetallics form on the interface between nickel and aluminium and grow gradually. Based on the thickness of layers depending on the process duration, the controlling process of the formation of intermetallics could be determined.

Ackowledgements:

The research was supported by Czech Science Foundation, project No. P108/12/G043

Microstructure evolution of AlFe7Mn4 alloy during its preparation by powder metallurgy

Alena. Michalcová (1), Ivo Marek (1), Anna Knaislová (1)

1) Department of Metals and Corrosion Engineering, University of Chemistry and Technology in Prague, Technická 5, Prague 6, 166 28, Czech Republic

Keywords: Microstructure, Rapid solidification, Aluminium alloys, Spark Plasma Sintering

Rapidly solidified Al-TM (TM = Transition metal) alloys are well known for their ability to form metastable phases such as quasicrystals (1). These phases often decompose at elevated temperatures, which is accompanied by change of morphology of the intermetalic particles (2). The aim of our research is to prove if this effect can give to the material so-called “self-healing“ properties. The main question is if the phase transformation is able to close initial cracks in material. The crucial point to study this phenomenon is to prepared material with high amount of quasicrystals. Rapidly solidified alloy usually have the form of powders or thin ribbons. Powder metallurgy processes that are used for subsequent consolidation require thermal exposure of material. It can lead to decomposition of quasicrystals during the compaction process. Because of this, the SPS process was chosen while it needs only several minutes for compaction of the material. Ribbons of AlFe7Mn4 alloy were compacted by SPS process in three ways: 1) ordered perpendicularly to the uniaxial pressing while SPS process, 2) randomly ordered 3) after short milling in ball mill. Microstructure of compact materials were studied by light, scanning electron and transmission electron microscopy.

References:

1. A. Michalcová et al., Micron 45 (2013) 55–58

2. M. Galano et al. Acta Materialia 57; (2009) 5107 –5119

Influence of low temperature on the microstructure and fracture mode of unalloyed ADI material

Dragan Rajnovic (1), Olivera Eric Cekic (2), Leposava Sidjanin (1), Sebastian Balos (1), Danka Labus Zlatanovic (1), Miroslav Dramićanin (1), Petar Janjatovic (1)

1) University of Novi Sad, Faculty of Technical Sciences, Trg D. Obradovica 6, 21000 Novi Sad, Serbia

2) University of Belgrade, Faculty of Mechanical Engineering, Innovation Centre, Kraljice Marije 16, 11000 Belgrade, Serbia

Keywords: ADI material, low temperatures, microstructure, hot tinting

Austempered Ductile Iron (ADI) is an advanced engineering material produced from ductile iron by austempering heat treatment. Through this process, a unique microstructure of ausferrite - a mixture of ausferritic ferrite (AF) and carbon enriched retained austenite (RA), is obtained. Due to the microstructure obtained, the ADI have a wide range of mechanical properties: a remarkable combination of high strength, ductility, and toughness, combined with good wear and fatigue resistance. The ADI materials are used increasingly in many wear resistant and critical components of machinery that work in all weather conditions. However, at low temperatures retained austenite might transform to a mixture of ferrite and carbides (bainite) or to martensite, resulting in loss of ductility (1, 2). In this paper microstructure and fracture mode at low temperatures of unalloyed austempered ductile iron have been studied. Two different ADI materials were produced by austenitization at 900°C for 2h followed by austempering at 300°C (ADI-300) or 400°C (ADI-400) for 1h. To study microstructure and fracture mode at low temperatures the Charpy impact tests in range of -196 to +24°C were used. The microstructure has been examined by a “Leitz-Orthoplan” light microscope using a special heat tinting procedure (3) which produces the following colors: purple (the higher the carbon content, the darker the purple color) - reacted, carbon enriched RA; light blue - metastable austenite (MA); beige - AF; white to cream - carbides; and light to dark blue - martensite (M). The fracture mode was studied by the scanning electron microscope JEOL JSM 6460LV, at 20kV. The ADI microstructure, after heat tinting, is presented in Figure 1ab

and 2ab. The ADI-300 and ADI-400 microstructure was fully ausferritic consisting of a mixture of ausferritic ferrite and retained austenite, with 16 and 31.4% of RA, respectively (Fig 1a and 2a). However, the carbon content in RA, which influences stability of austenite has an opposite trend. The ADI-300 with lower RA is more stable due to carbon content of 2.08%C, while the ADI-400 with higher RA and 1.64%C is less stable. After the ADI-300 is cooled to -196°C, the stable, high carbon enriched RA content decreases to 10.6%, while the light blue color area of low carbon enriched MA increases, Figure 1b. Moreover, finely dispersed carbides appear, as carbon content decreases to 1.61%C. In the case of the ADI-400, after cooling, the less stable RA transforms into MA, bainite (B) and lenticular martensite (M), Figure 2b. Namely, the RA decreases to 16.7% and carbon content to 1.5%C. In addition, the microstructure transformation influence the change of fracture mode from ductile (ADI-400) or quasi-cleavage (ADI-300) to fully brittle (Figure 1cd and Figure 2cd). Finally, to conclude, after cooling the stable retained austenite becomes thermally unstable and trough diffusionless decomposition transform to MA, bainite or even martensite, hence causing brittleness of ADI.

Acknowledgements:

This research was supported by The Ministry of Education, Science and Technological Development of the Republic of Serbia through the Project TR34015.

References:

1. L. Sidjanin et al., Mater Sci Tech-Lond, 26 (5) (2010) 567-71;

2. D. Rajnovic et al., J. Microsc. – Oxford, 232 (2008) 605-10;

3. B.V. Kovacs, Modern Casting, 41 (1987) 34-5;

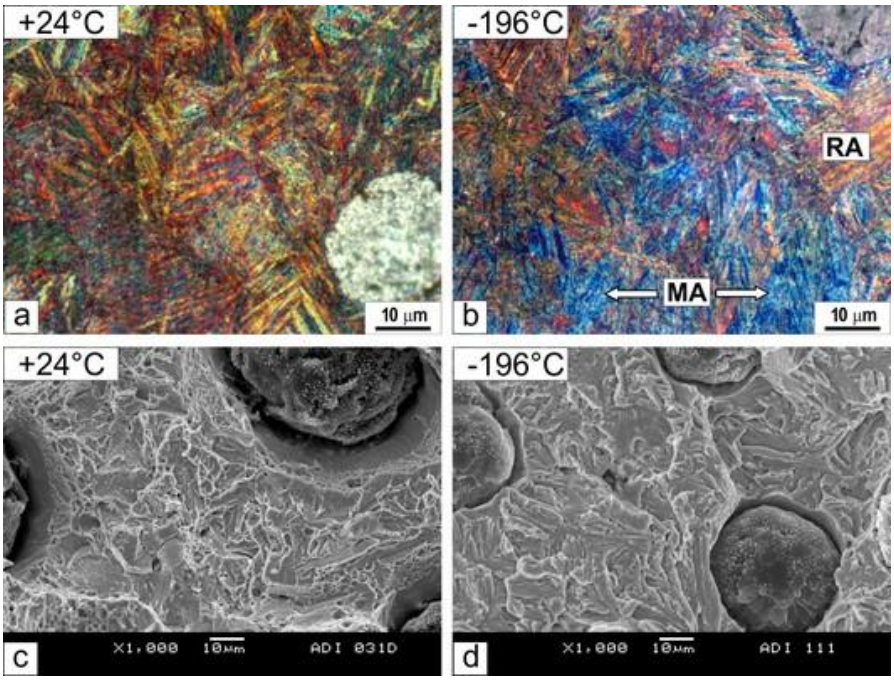

Figure 1. The ADI 300: a,b) Microstructure revealed by heat tinting (LM); c,d) Fracture mode (SEM).

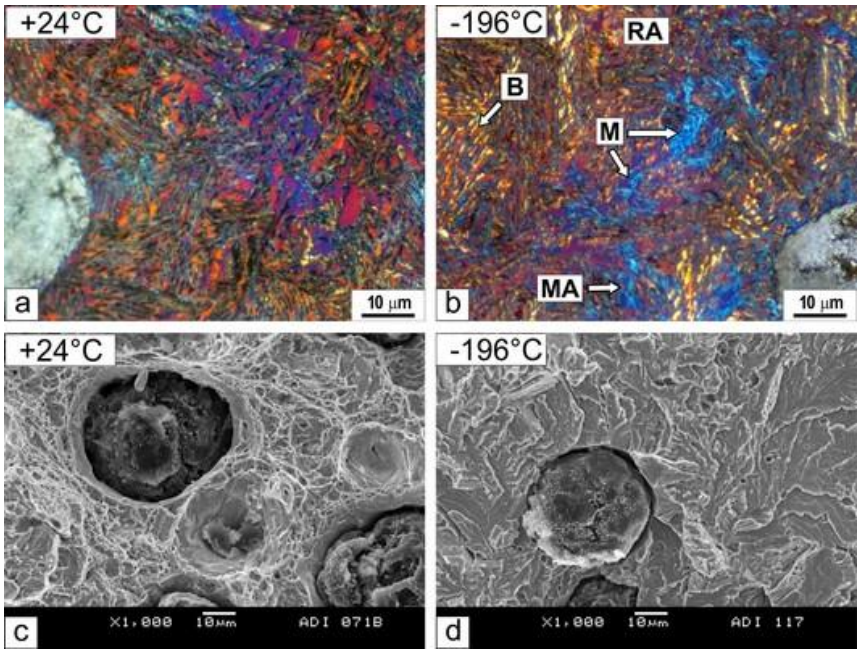

Figure 2. The ADI 400: a,b) Microstructure revealed by heat tinting (LM); c,d) Fracture mode (SEM).

Deformation and fracture of copper and silicon during indentation. acoustic emission measurements.

Vladislav Perfilyev (1), Alexey Moshkovich (1), Igor Lapsker (1), Lev Rapoport (1)

1) Holon Institute of Technology, Golomb St 52, Holon, 5810201, Israel

Keywords: Indentation, Acoustic emission, Plastic deformation

The acoustic emission (AE) signals during different phases in indentation (loading, dwell, and unloading times) of ductile Cu and brittle Si were studied. The effect of load and time of loading on the AE parameters were studied. The waveforms and dominant frequency ranges were analyzed. In order to clarify the effect of friction during indentation on the AE signals, the indentation was performed through lubricant film. It was shown that the main AE signals were observed just in the loading phase in indentation of Cu. The low-amplitude wide band noise-like high-frequency-range AE signals, observed during indentation of Cu, can be associated with breakaway and jump in the motion of dislocations. Much larger duration of the AE signals in indentation of Cu indicates a substantially larger dislocation glide in annealed Cu in comparison with limited deformation in Si. The waveform during the indentation of brittle Si presents strong burst-type AE signals. Indentation of Si is accompanied by high-energy and low frequency AE signals characterizing development of the dominant damage and limiting level of plastic deformation. Indentation through the lubricant film leads to the formation of flaky cleavage and swelling around the impression.

Novel stem-edx analysis of radiation-induced precipitates in a self-ion irradiated cold-worked 316 austenitic stainless steel used for pwr baffle-bolts

Jan Michalička (1), Zhijie Jiao (2), Gary Was (2)

1) Brno University of Technology, CEITEC Nano Research Infrastructure, Purkynova 123, Brno, 612 00, Czech Republic

2) University of Michigan, Department of Nuclear Engineering and Radiological Sciences, 1921 Cooley Bld., Ann Arbor, MI 48109 USA

Keywords: Radiation-induced damage, self-ion irradiation, austenitic stainless steels, PWR, STEM-EDX

High neutron irradiation doses exceeding 100 dpa (displacement per atom) are estimated for reactor vessel internal components such as baffle-bolts (1), when the pressurized water reactor (PWR) life extension beyond 60 years will take place. At doses above 100 dpa, there are no literature data of the general radiation-induced microstructure of a cold-worked 316 austenitic stainless steel (CW 316SS). Furthermore, the information about radiation-induced precipitates evolution is still limited even from intermediate doses and mechanisms of their evolution is still not well understood. The missing experience about the radiation damage at the high doses and temperatures can be achieved with use of self-ion experimental irradiations. In comparison with neutrons, the self-ion irradiations with high dose rates on the order of 10^{-3} dpa/s shorten the irradiation times of 100 dpa from decades to days, these experiments are low cost and do not produce activated samples. Therefore, 5 MeV Ni^{++} and Fe^{++} ion irradiations were performed to investigate radiation-induced precipitates evolution in a cold-worked 316 austenitic stainless steel at high doses and temperatures. The irradiation conditions were 23 dpa at 380°C, 130 dpa at 380°C, 23 dpa at 500°C, and 15 dpa at 600°C. Complementary techniques, TEM selected electron diffraction (SAED), TEM dark-field imaging, STEM energy dispersive X-ray (EDX) spectroscopy mapping and atom probe tomography (APT) determined crystallography, morphology and chemical composition of fine radiation-induced precipitates in nano-scale. The precipitates were predominantly in form of the Ni_3Si rich γ' phase at all irradiation conditions. The EDX analysis further determined Ni-Si-Mo-P and Ni-Si-Mn rich

precipitates after irradiation at 380°C and 600°C, respectively. The precipitates were found close to saturated state between 23 and 130 dpa at 380°C irradiation conditions. A different effect of higher irradiation temperatures was found between 500°C and 600°C. In case of the irradiation to 23 dpa at 500°C, the average size of precipitates was similar to irradiations at 380°C, but the density was lower. However, the precipitates revealed substantially larger size and very low density following the irradiation to 15 dpa at 600°C. The original dislocation network introduced by cold-working was found by STEM-EDX and APT as dominant sink for intra-granular solute radiation-induced segregation (RIS) and possibly took place as primary nucleation site of radiation-induced precipitates at irradiation temperatures 380°C and 500°C. At the temperature 600°C, the RIS at dislocation network almost vanished and the main nucleation sites became twin boundaries as more energetically favorable intra-granular sinks. An example of the fine/scale precipitates studied by all TEM techniques is shown in Figure 1.

Acknowledgements:

The research could be performed thanks to support of facilities provided by the Michigan Ion Beam Laboratory and the Electron Microbeam Analysis Laboratory at University of Michigan, the CEITEC Nano Research Infrastructure at Brno University of Technology (MEYS CR (ID LM2015041)), the Tescan Orsay Holding in Brno (MIT CR (4.2 PT03/586)), and the Institute of Materials of Czech Academy of Science in Brno (MEYS CR (No. LM2015069)). Financial support was provided by DOE under contract DE-FG07-07ID14894.

References:

1. S.J. Zinkle, G.S. Was, Acta Materialia, 61 (2013) 735–758.

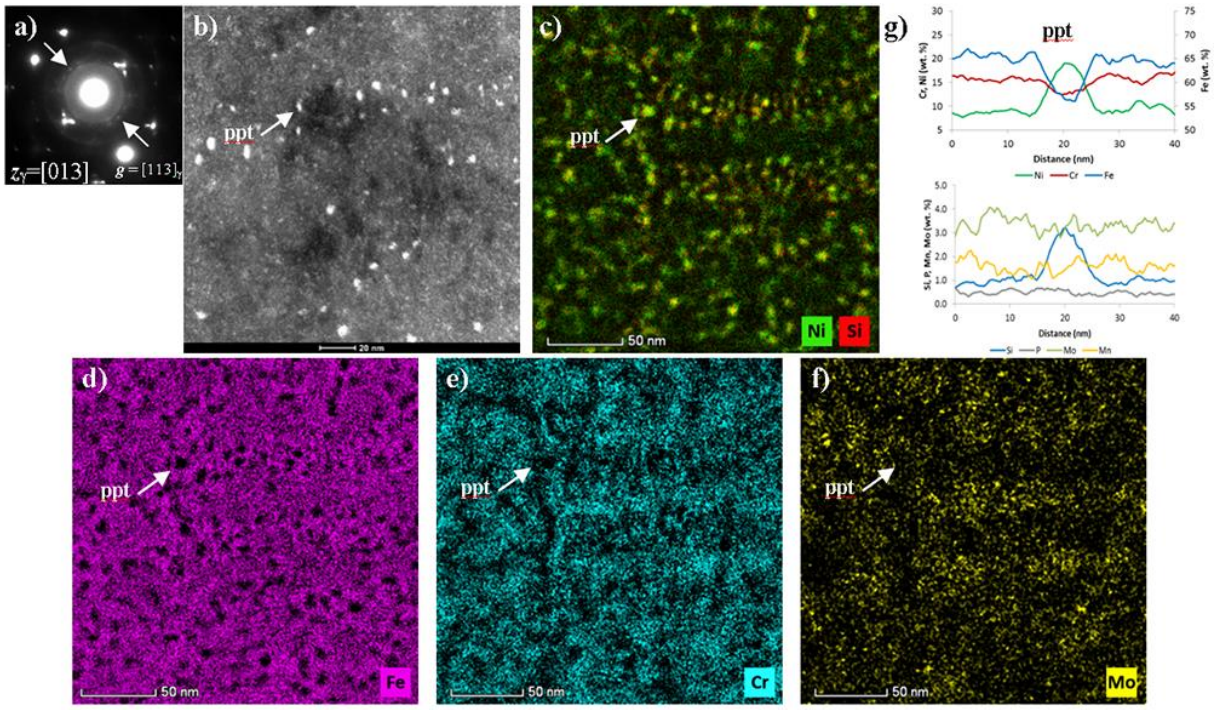

Figure 1. Radiation-induced precipitates of Ni_3Si gamma´ phase in CW 316SS irradiated to 130 dpa at 380°C. The SAED, TEM-DF image (a,b) and STEM-EDX maps (c-f) are from the same area. Chemical composition of one precipitate (ppt) is shown in a line profile (g.

M5. Nanostructures and Materials for Nanotechnology

INVITED LECTURES M5:

Multi-Scale observation of red-ox dynamics by *in situ* scanning and transmission electron microscopy

Marc Willinger (1), Ramzi Farra (1), Jing Cao (1), Zhu-Jun Wang (1), Elena Willinger (1), Xing Huang (1)

1) Department of Inorganic Chemistry, Fritz Haber Institute of the Max Planck Society, Faradayweg 4, 14195 Berlin, Germany

Keywords: *in situ* SEM/TEM, catalyst dynamics

In order to observe working catalysts in their active state, we have recently implemented commercially available sample holders for *in situ* studies under controlled atmosphere and temperature inside a transmission electron microscope. Since we need to relate local processes that occur on the nanometre scale with collective processes that involve fast movement of large numbers of atoms, we have furthermore adapted an environmental scanning electron microscope (ESEM) for the investigation of catalytically active surfaces (1). Using these two instruments, we are now able to cover a pressure range from 10^{-4} to 10^{3} mbar and a spatial resolution ranging from the mm to the sub-nm scale. Both setups are equipped with mass spectrometers (MS) for analysis of the gas-phase composition and detection of catalytic conversion. I will present structural dynamics that are observed during oscillatory red-ox reactions on different metal catalysts (see Figure s 1 and 2).The ability to directly image the active catalyst and associated morphological changes at high spatial resolution enables us to refine the interpretation of spatially averaged spectroscopic data that was obtained under otherwise similar reaction conditions, for example, during near-ambient-pressure *in situ* XPS measurements (2). It will be shown that the ability of observing the adaption of an active surface to changes in the chemical potential of the surrounding gas phase in real-time potentially offers new and direct ways of optimizing catalysts and applied reaction conditions.

References:

1. Z.-J. Wang et al., Nature Communications 7, Article number: 13256 (2016).

2. M. T. Greiner et al., Phys.Chem.Chem.Phys. 17 (2015), p. 25073

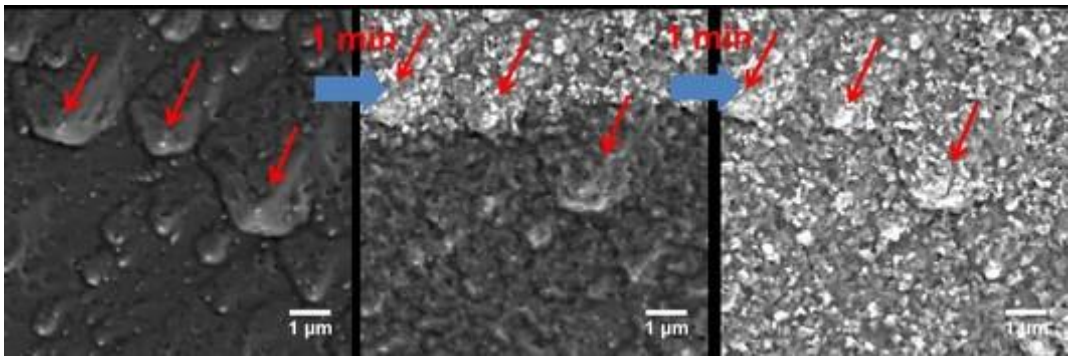

Figure 1. *In situ* ESEM observations of thermo-kinetic oscillations during hydrogen oxidation on a Ni foil. The surface shows rich dynamics and periodic changes from an oxide (bright) to a metallic state (dark).

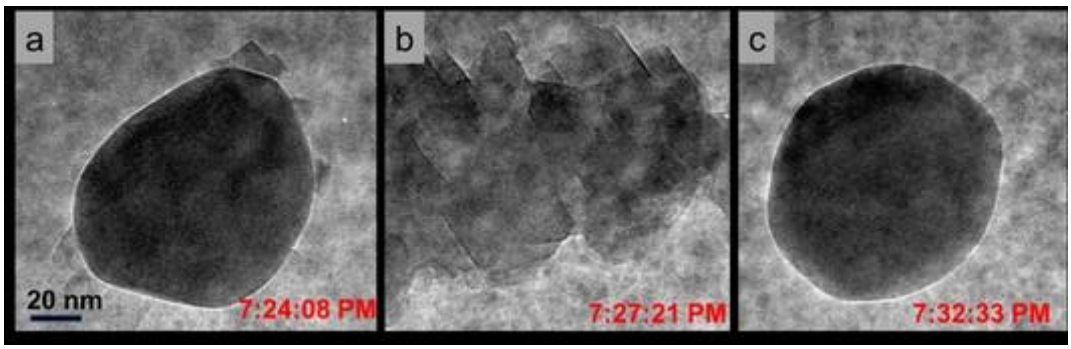

Figure 2. Corresponding *in situ* TEM observations showing a Ni particle oscillating between metallic (a and c) and oxide state (b) during hydrogen oxidation at 700 °C.

Multipurpose cantilever sensors

Vuk V. Radmilović (1), Thomas Duden (2), Velimir R. Radmilović (3)

1) University of Belgrade, Innovation Center of the Faculty of Technology and Metallurgy, Karnegijeva 4, 11120, Belgrade, Serbia

2) Ernest Rusca-Centre and Peter Grünberg Institute, Forschungszentrum Jülich, Wilhelm-Johnen-Straße, 52428 Jülich, Germany

3) Serbian Academy of Sciences and Arts, Knez Mihailova 35, 11000, Belgrade, Serbia

Keywords: Cantilever Sensors, Transmission electron microscopy (TEM), atomic force microscopy (AFM), Fabry–Perot interferometry, Energy dispersive spectroscopy (EDS)

Transmission electron microscopy (TEM), atomic force microscopy (AFM) and fiber optic interferometry (optical feedback) in the focused ion dual beam DB225 instrument (DB-FIB), which possesses field emission electron gun scanning electron microscopy (SEM-FEG) capabilities for imaging, have been used to characterize multipurpose cantilever sensors fabricated using aluminum-32 at.% molybdenum (Al-32at.%Mo) metallic thin films. High resolution TEM demonstrates the presence of nanocrystallites with a body-centered cubic (BCC) crystal structure, densely dispersed throughout the amorphous matrix. The presence of an oxide layer was observed, which coats the surface of the film as well as the space between the grain columns, with a maximum thickness of 3 nm. Local stoichiometry of the columns and boundaries were captured by jump ratio EFTEM images for the molybdenum $M_{4,5}$-edge and the oxygen *K*-edge. Elastic properties of freestanding single-clamped cantilever sensors were obtained using resonant frequency (RF) measurements in the dual beam FIB system where the optical fiber tip was modified *in situ*, in order to obtain a clean and optically transparent face without breaking vacuum. High sensitivity to specimen vibrations is achieved by the combination of optical Fabry–Pérot interferometry and narrow band RF detection. The Al-32at.%Mo cantilever sensor performance is limited by energy dissipation caused by the surface oxide and internal friction (1).

Acknowledgements:

VVR and VRR acknowledge support from the Ministry of Education, Science and Technological Development of the Republic of Serbia, under the projects III45019 and 172054, respectively. VRR acknowledges support from Serbian Academy of Sciences and Arts, under the project F-141.

ORAL PRESENTATIONS M5:

$PtCu_3$ fuel cell catalyst nanoparticles studied from growth to degradation using transmission electron microscopy

Francisco Ruiz-Zepeda (1), Matija Gatalo (1), Primož Jovanović (2), Nejc Hodnik (3), Marijan Bele (1), Miran Gaberšček (1)

1) Department of Material Chemistry, National Institute of Chemistry, Hajdrihova Ulica 19, 1000 Ljubljana, Slovenia

2) Department of Analytical Chemistry, National Institute of Chemistry, Hajdrihova Ulica 19, 1000 Ljubljana, Slovenia

3) Department of Catalysis and Reactor Engineering, National Institute of Chemistry, Hajdrihova Ulica 19, 1000 Ljubljana, Slovenia

Keywords: Nanostructure, TEM, Nanoparticles, Pt-based electrocatalyst,

Currently, big efforts are being made to search for a cathode catalyst to increase the kinetics of the slow oxygen reduction reaction (ORR) in proton exchange membrane fuel cells (PEM-FC) (1). Some of the catalytic materials are typically comprise of Pt based alloys, usually with high activity but that rapidly drops due to the harsh electrochemical environment and detrimental effects occurring in fuel cells (2). Bimetallic core-shell or skin type structures have been reported to possess high activity, and are the subject of an active field of study (3). The catalytic properties of metal nanoparticles depend on size, shape and crystal structure, and several approaches have addressed the material composition as well to find an affordable, active and stable catalyst. In the present work, we study the growth and later the effects of activation of a gram-scale $PtCu_3$ catalyst. This study is divided in two parts. First we observed the formation process of electrocatalyst nanoparticles $PtCu_3$ on HSAC by annealing precursors on *in situ* heating TEM. The composite, obtained from a partial galvanic displacement of copper on carbon support with a platinum precursor salt, is then further annealed in order to obtain $PtCu_3$ nanoparticles (Figure 1). This view provided insight and feedback into the annealing part of the synthesis. Afterwards, we studied *ex situ* the nanoparticles at different stages (Figure

2): right after annealing, subsequent electrochemical activation (200 cycles) and further degradation (10 000 cycles). The morphology and composition of the nanoparticles is imaged and analyzed in order to understand the catalytic activity and stability of the catalyst.

References:

1. M. Shao et al., Chem. Rev. 116 (2016) 3594−3657. 2. I. Katsounaros et al., Angew. Chem., Int. Ed. 53 (2014) 102-121. 3. Y.-J. Wang et al., Chem. Rev. 115 (2015) 3433−3467.

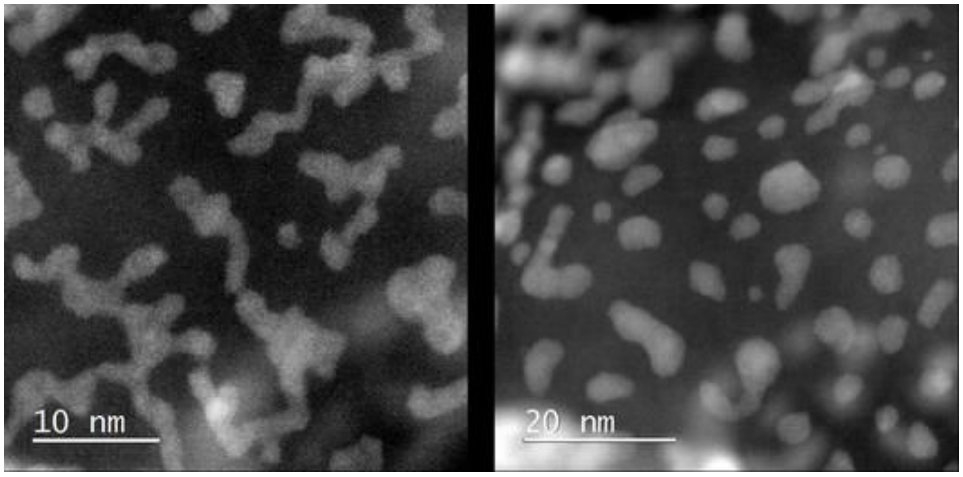

Figure 1. STEM-HAADF images of *in situ* heating experiment. Left, CuPt nanoparticles at room temperature. In the right, CuPt nanoparticles after annealing at 500 °C.

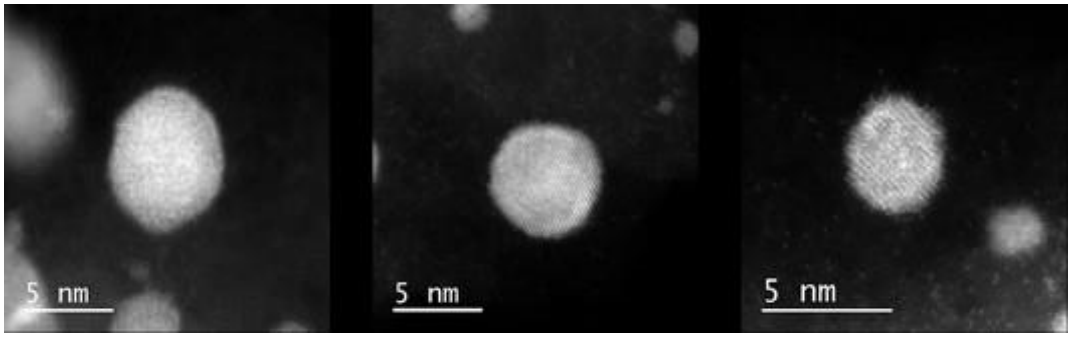

Figure 2. STEM-HAADF images of representative Cu3Pt nanoparticles at three different stages: left, after annealing, center, electrochemical activation (200 cycles) and right, further degradation (10 000 cycles).

Advanced electron microscopy characterization of silver nanowires for transparent electrode applications

Vuk V. Radmilović (1), Peter Ercius (2), Colin Ophus (2), Erdmann Spiecker (3), Velimir R. Radmilović (4)

1) Innovation Center, University of Belgrade, Faculty of Technology and Metallurgy, Karnegijeva 4, 11120 Belgrade, Serbia

2) National Center for Electron Microscopy, Molecular Foundry, Lawrence Berkeley National Laboratory, Berkeley, CA 94720, USA

3) Center for Nanoanalysis and Electron Microscopy, Friedrich-Alexander University Erlangen-Nürnberg, Cauerstrasse 6, 91058 Erlangen, Germany

4) Serbian Academy of Sciences and Arts, Knez Mihailova 35, 11000 Belgrade, Serbia

Keywords: Silver Nanowires (AgNWs), Aluminum-Doped Zinc Oxide (AZO), Nanoweld formation, Solid-State Wetting, Nanowire Sintering

For their ease and cost-effectiveness of synthesis and processing, silver nanowires (AgNWs) have been extensively studied as a transparent electrode alternative to conventional solutions like indium tin oxide (ITO) for the application in optoelectronic devices like solar cells. In this study, AgNWs were synthesized by a simple polyol reduction process. The main focus of this research was elucidating the solid-state wetting and welding mechanisms that occur during annealing of AgNWs before a layer of aluminum doped zinc oxide (AZO) is deposited on them, for the enhancement of properties essential for an electrode in a solar cell (1). Microstructural characterization using scanning electron microscopy (SEM) and scanning transmission electron microscopy (STEM) revealed that solid-state wetting and subsequent welding occurred only between nanowires whose contact geometry is characterized by an enormous difference in radii of curvature. Results also indicated that, during annealing, the AgNW in contact through a smaller radius of curvature dissolves, Ag atoms diffuse and are incorporated in a welded zone between the AgNWs whose crystallographic orientation is inherent from the AgNW in contact through a large radius of curvature. Wetting angle between two welded AgNWs was measured to be below 4.8°, indicating almost complete wetting (Figure 1).

Tomography, based on 3D reconstruction of STEM imaging, was employed to better understand the morphology of the welded zone and geometric relationship between the AgNWs (Figure 2). Electron diffraction orientation and strain mapping were performed in order to elucidate possible strain fluctuation across the AgNWs. Crystal lattice distortion, directly measured by atomic column displacements in drift corrected cross-sectional atomic resolution STEM images of an AgNW, prepared by focused ion beam (FIB), demonstrated non-uniform distribution of strain in five twin segments of the AgNW. It has been demonstrated that welding of AgNWs significantly reduces electrical resistivity while preserving high optical transparency, properties essential for transparent electrodes utilized in solar cells (2).

References:

(1) M. Göbelt et al., Nano Energy 16 (2015) 196-206.

Acknowledgements:

This research was supported by the Ministry of Education, Science and Technological Development of the Republic of Serbia, contract No. III45019. The aid of M. Göbelt and prof. dr Christiansen is gratefully acknowledged.

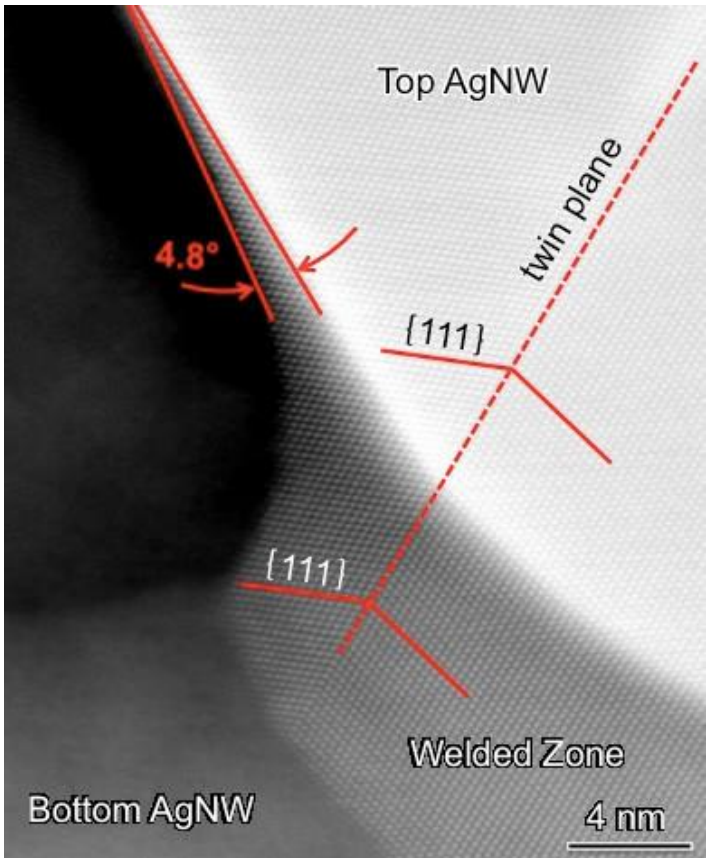

Figure 1. High resolution ADF STEM cross-sectional image of welded zone between two AgNWs.

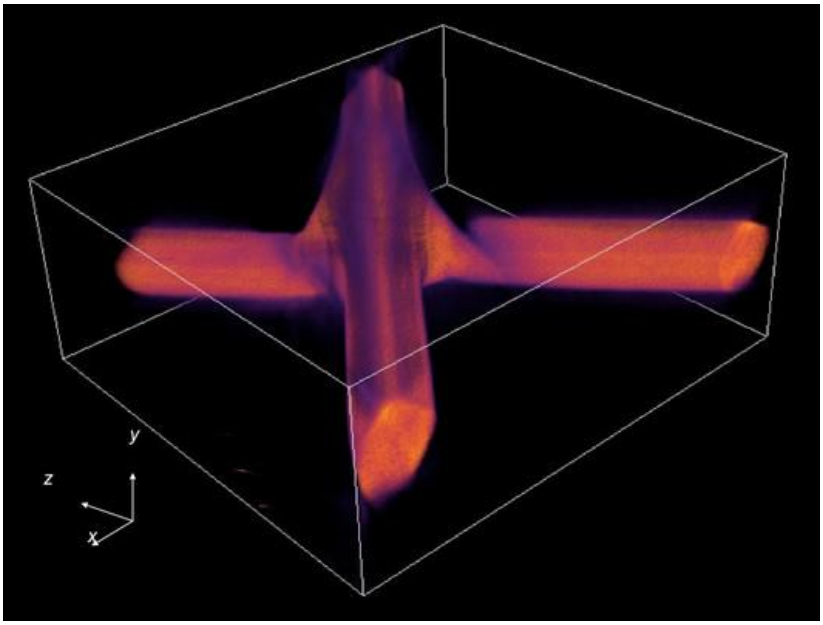

Figure 2. 3D volume rendering of welded AgNWs.

Manganese oxide based materials as insertion cathodes for Mg-ion batteries

Elena Tchernychova (1), Ana Robba (1), Anna Randon-Vitanova (2), Miran Gaberšček (1), Robert Dominko (1)

1) National Institute of Chemistry, Hajdrihova ulica 19, 1000 Ljubljana, Slovenia

2) Honda Europe R&D, Carl-Legien-Straße 30, 63073 Offenbach am Main, Germany

Keywords: Mg-ion batteries, EELS, EDX, spinel, birnessite

One of the strategies to increase the energy density of a battery in comparison to the current Li-ion technology is to apply a multivalent intercalation cathode material pared with metal electrode. Among the promising candidates, Mg with its 2 valence electrons possesses high volumetric specific capacity of 3833 mAh cm^{-3}, absence of the dendrite growth, safe handling in an ambient atmosphere and large availability throughout the planet has gained increased attention. Chevrel phase Mo_6S_6, layered V_2O_5, graphitic fluoride, etc. showed the initial promise for multivalent intercalation. However, the limited mobility of Mg ions and possible concurrent insertion of water and/or protons lowers the cycling stability of these host materials. Therefore, we have chosen the manganese oxide variants, which were shown to exhibit higher voltages than the Chevrel phases. The $MgMn_2O_4$ spinel and $(Mg_xNa_y)Mn_2O_4$ birnessite phases were investigated in this study. The crystal structures of the former and the latter materials employ different mechanisms for keeping the stability upon cycling and allow for Mg de/insertion. The aim of the study was to investigate the Mg insertion mechanisms in both materials by correlating the cyclic voltammetry (CV) results with the structural and compositional changes of these cathode materials assessed by S/TEM at the atomic level upon increasing number of cycles in magnesium nitrite aqueous electrolyte. The STEM-EDX of birnessite confirmed a partial exchange of Na over Mg with the Mg occupying fully the smaller particles and only the outer shells of the larger particles, with Na still present in the inner cores. Same behaviour was observed in the spinel material, where the small particles had a higher Mg content than the large particles (above 200 nm). Both materials in charged state, i.e. demagnesiated, exhibited etched microstructure, where the initially single-crystalline particle structure had changed into

the patchwork of small regions with variously orientated crystallites, which was observed by HAADF and ABF imaging. Evaluation of the ELNES data in line profiles of the crystallites aggregates showed changes of the Mn valence towards Mn^{2+} and Mn^{3+}, indicating the presence of Mn_3O_4 spinel phase in both materials. Upon galvanostatic magnesiation (battery discharge) both spinel and birnessite phases resembled their initial crystalline structures, however, leaving voids and defects behind with damage being more prominent in the birnessite. The degradation of both materials through the permanent change of the crystal structure led to the battery failure.

Acknowledgements:

The authors gratefully acknowledge the financial support of Honda Initiation Grant Europe and the Ministry of Education, Science and Sport of the Republic of Slovenia through the Research program P2-0393.

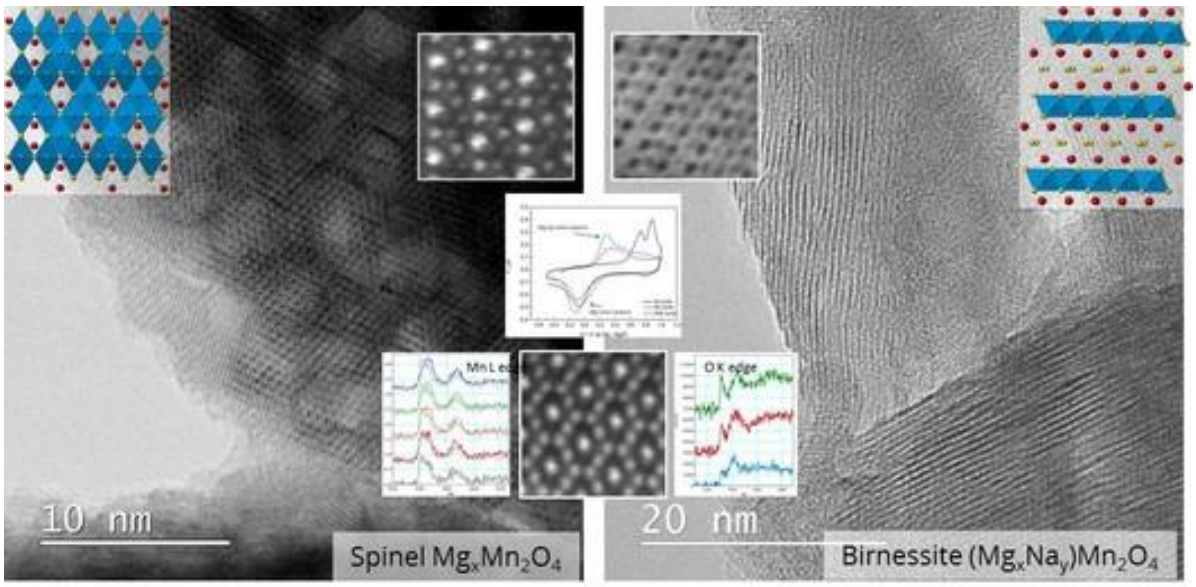

Figure 1. STEM-BF images of the spinel and birnessite. On the insets, the atomic structure, its evolution upon cycling, example of cyclic voltammetry curve for spinel, and EELS spectra of Mg-L and O-K edges showing changes in electronic structure are shown.

Transmission Kikuchi diffraction in SEM; application in various materials system

Hossein Alimadadi (1), Alice Bastos Fanta (1), Andrew Burrows (1)

1) Technical University of Denmark, Center for Electron Nanoscopy, Fysikvej 307, DK 2800 Lyngby, Denmark

Keywords: Transmission Kikuchi Diffraction, Orientation Microscopy, SEM

Electron Backscatter Diffraction (EBSD) is a well stablished technique and routinely applied for obtaining automated microstructure related crystallographic information in a scanning electron microscope (SEM). However, the spatial resolution of the technique is a limiting factor for investigating nano-scale crystals. To overcome this shortcoming, it has been proposed to study electron transparent specimens positioned perpendicular to the standard EBSD sample position (1). This new technique has been termed “transmission electron forescatter diffraction (t-EFSD)” or “transmission Kikuchi diffraction in the SEM (SEM-TKD)” and is emerging as a very promising technique to characterize materials in the nano-scale. Of particular interest, a recent development has shown the effective resolution of the technique is comparable with the available orientation microscopy techniques in the transmission electron microscope (2). In this presentation the application of TKD on material systems that are beyond the resolution limit of conventional EBSD, such as nanowires, nanoplasmonic disc are shown. Additionally, the benefits and challenges of utilizing the SEM-TKD to characterize fine microstructural features in metallic materials such as functionally graded electrodeposits, heavily deformed material and hierarchical structure in the steels are outlined. The importance of sample thickness in standard TEM sample preparation and focused ion beam lift out technique is addressed. And finally, very recent *in situ* TKD annealing experiments carried out in our lab and the potentials that is opened up using such experimental set-up is discussed.

References:

1. R.Geiss, et. al. Microscopy and Microanalysis 17 (2011) 386–387.

2. P. W. Trimby, Ultramicroscopy 120 (2012) 16–24.

Structural characterization of carbon-supported bimetallic aucu nanoparticles derived from metal vapors

Marcello Marelli (1), Andrea Jouve (2), Alberto Villa (2), Laura Prati (2), Vladimiro Dal Santo (1), Antonella Balerna (3), Claudio Evangelisti (1)

1) The Institute of Molecular Science and Technologies (ISTM-CNR), Via C.Golgi 19, 20133 Milano, Italy

2) Department of Chemistry, Università degli Studi di Milano, via C.Golgi 19, 20133 Milano, Italy - Istituto di Scienze e Tecnologie Molecolari (ISTM-CNR), Via C.Golgi 19, 20133 Milano, Italy

3) Laboratori Nazionali di Frascati, INFN, Frascati, E. Fermi 40, Roma, Italy

Keywords: AuCu Bimetallic, Metal Vapor Synthesis, HRTEM, XAFS, Catalysis

Bimetallic nanoparticles have caught great interest in catalysis over the past decade. The electronic or structural modifications of the active sites arising from interactions among metals at the nanoscale can result in a material with enhanced catalytic properties. Recently, bimetallic catalysts composed of Au and Cu have been widely studied in heterogeneous catalysis; the addition of Cu is an attractive way to promote activity and selectivity of Au-based catalysts in different catalytic reactions (1,2). We report here the synthesis of AuCu bimetallic nanoparticles by the simultaneous co-condensation of Au and Cu vapors with acetone, according to the solvated metal atom (SMA) technique (Figure 1) (3). The AuCu nanoparticles where then supported on carbon by direct impregnation. Samples containing three different metal ratios (i.e. Au:Cu 1:10; 4:1 and 17:1), as well as the corresponding monometallic systems, were prepared. The fine structure and the analytical local composition of the unsupported AuCu nanoparticles were investigated by corrected TEM and STEM analysis combined with energy filtered maps and EDX measurements. The structural features of the corresponding carbon-supported systems having a total metal loading (Au+Cu) of 1 wt.% were then characterized by HRTEM and X-ray absorption fine structure (XAFS) spectroscopy. Interestingly, nor nanoparticles aggregation nor structural modifications occurred during the deposition step. The catalytic performances of the 1%wt AuCu/C catalysts with different Au:Cu ratio were evaluated

in both oxidation and hydrogenation of glycerol, highlighting the different role of Cu in modifying the activity/selectivity with respect to the monometallic counterparts.

Acknowledgements:

Authors kindly acknowledge the ESTEEM2 European Network and Project iZEB from ACCORDO QUADRO REGIONE LOMBARDIA - CNR

References:

1. C.L.Bracey P. R. Ellis, G.J. Hutchings Chem. Soc. Rev. 38 (2009) 2231-2243.

2. L. Delannoy, G. Thrimurthulu, P.S. Reddy, et Alt. Phys. Chem. Chem Phys. 16 (2014) 26514-26527

3. C. Evangelisti, et Alt. ChemPhysChem (2017), in press, doi:10.1002/cphc.201700215.

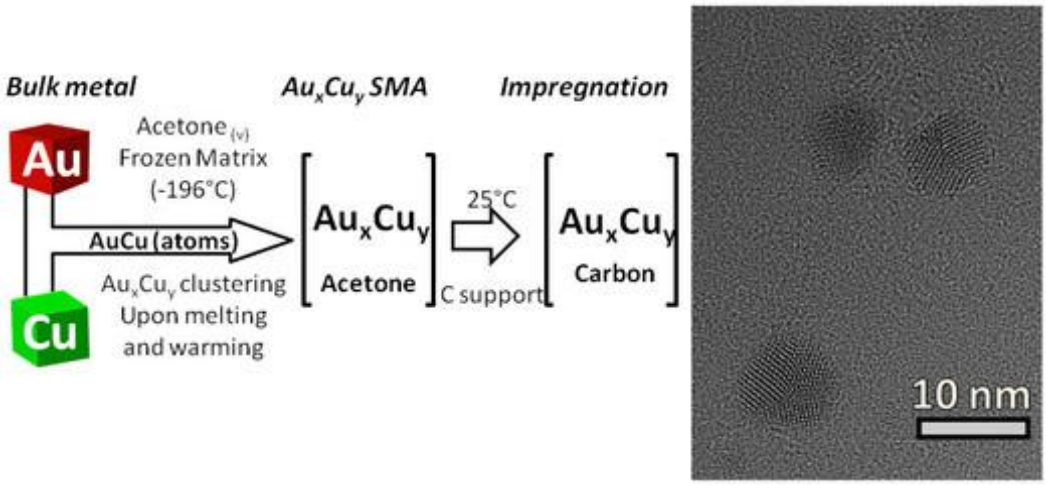

Figure 1. On the left side, schematic of SMA synthesis and catalyst preparation. On the right side, representative HRTEM micrograph.

POSTER PRESENTATIONS M5:

Microscopic study on carbon fibre surface modification for tuning the plasma treatment parameters

Pravin Jagdale (1), Aamer Abbas Khan (1), Dimitrios Dragatogiannis (2), Stavros Anagnou (2), Mauro Raimondo (1), Kostas Mpalias (2), Zhenxue Zhang (3), Iryna Husarova (4), Yevheniia Tishchenko (4), Pietro Mandracci (1), Hanshan Dong (3), Alberto Tagliaferro (1), Costas Charitidis (2)

1) Department of applied science and technology (DISAT), Politecnico di Torino, Torino-Italy-10129

2) RNanolab, National Technical University of Athens, School of Chemical Engineering, Athens-Greece-15780

3) Department of Metallurgy, and Materials, University of Birmingham, Edgbaston, Birmingham-UK-B15 2TT

4) Yuzhnoye State Design Office, Dnipro, Ukraine

Keywords: FESEM,Carbon fibre,surface, plasma, EDS

Globalization and infrastructural growth on the planet are in growing stage. The rising awareness about benefits of carbon fibre over metals is encouraging carbon fibre use in various applications. Carbon fibre reinforced plastics are lightweight and have excellent mechanical properties. Carbon fibre surface, however, is chemically inert and leading to the potential problem of inadequate adhesion and hence weaker composite than the expected one. It indicates the better bonding between the matrix and the reinforcement materials must be acquired. Therefore, it becomes important to study the structural change on carbon fibre before and after surface modification. There are many known techniques to study this structural modification. This study is presenting the microscopic analysis on carbon surface modification. Microscopic analysis is one of the fastest way to extract the structural information. It helps to tune the online process parameters at commercial scale. Field emission scanning electron microscope coupled with Energy-dispersive X-ray spectroscopy was employed to study the carbon surface modification. The analysis technique was mainly focused on topographical and elemental information at higher magnifications, with a virtually unlimited depth of field. In-house

made and commercial carbon fibres are considered for this comparative study. Commercial Toray carbon fibres are used as a standard source of carbon fibre. Carbon fibres were coated with chromium layer (5 nm) to avoid charging effect from the bombardment of the secondary electrons. Field emission scanning electron microscope confirms the physical modification on carbon fibre surface. Energy-dispersive X-ray spectroscopy collects the elemental information on the carbon fibre surface. The information extracted in this study is important in assistance the tuning of the process parameters for plasma treatment.

Acknowledgements:

This work has received funding from EU FP7 Project “Functionalized Innovative Carbon Fibres Developed from Novel Precursors with Cost Efficiency and Tailored Properties” (FIBRALSPEC) under Grant Agreement No. 604248.

Babinet principle for plasmonic antennas: complementarity and differences

Michal Horák (1), Vlastmil Křápek (2), Martin Hrtoň (1), Ondřej Metelka (3), Tomáš Šamořil (2), Michael Stöger-Pollach (4), Aleš Paták (5), Tomáš Šikola (2)

1) CEITEC—Central European Institute of Technology, Brno University of Technology, Technická 3058/10, 616 00 Brno, Czech Republic

2) CEITEC—Central European Institute of Technology, Brno University of Technology, Technická 3058/10, 616 00 Brno, Czech Republic

3) Institute of Physical Engineering, Brno University of Technology, Brno, Czech Republic

4) University Service Center for Transmission Electron Microscopy, Vienna University of Technology, Vienna, Austria

5) Institute of Scientific Instruments, The Czech Academy of Sciences, Brno, Czech Republic

Keywords: Babinet principle, complementarity, plasmonic antennas, cathodoluminescence, EELS

Plasmonics deals mainly with surface plasmon polaritons (SPP), which are collective oscillations of free electrons at metal-dielectric interfaces connected with the local electromagnetic field. When SPP are spatially restricted to a metallic nanoparticle, we talk about localized surface plasmons (LSP). LSP resonances can be characterized with an excellent spectral and spatial resolution by electron energy loss spectroscopy (EELS) and cathodoluminescence. Both techniques utilize an electron beam that interacts with the metallic nanoparticle and excites the LSP resonances. EELS measures the energy transferred from electrons to the LSP and cathodoluminescence deals with the light which the LSP emit during their decay. Babinet principle, originating in the wave theory of light and analysis of diffraction, relates the optical response of apertures in thin films and their complementary particle analogues. According to the Babinet principle, LSP in complementary particles and apertures have identical resonance energies and their near fields are closely linked: the electric field distribution of a specific in-plane polarization for an aperture corresponds to the magnetic field distribution of a perpendicular polarization for a particle[1]. On the other hand, additional

differences can be related to different fabrication processes and experimental techniques involved in the characterization of real structures. To assess the theoretically predicted Babinet complementarity, we have studied a set of gold disc-shaped plasmonic antennas with various diameters, both particles and apertures. The plasmonic antennas were fabricated by focused-ion-beam lithography of a thin gold layer on a silicon nitride membrane. LSP resonances were characterized by both the cathodoluminescence and EELS. Babinet complementarity was confirmed for main plasmon properties such as the LSP resonance energy, but differences were found, for example, for the excitation efficiency. Figure 1 shows measured cathodoluminescence spectra followed by the plasmon dispersion relation: The energy of LSP resonance is plotted as a function of inverted antenna diameter (i.e. effective wave number). The excitation electron beam was focused on the edge of the structure to maximize the excitation efficiency. Note the generally stronger response of the apertures. In the lower row, dark-field micrographs of a gold disc and an aperture (a hole in the thin gold layer) with the diameter of 100 nm followed by electron energy loss intensity maps at the energy loss range of measured LSP resonances by EELS are shown (yellow color corresponds to the maximal intensity).

Acknowledgements:

This research has been supported by Czech Science Foundation (17-25799S), CEITEC Nano RI (MEYS CR, LM2015041), and Brno University of Technology (FSI/STI-J-17-4623).

References:

1. M. Hentschel et al., Nano Lett. 13 (2013) 4428–4433.

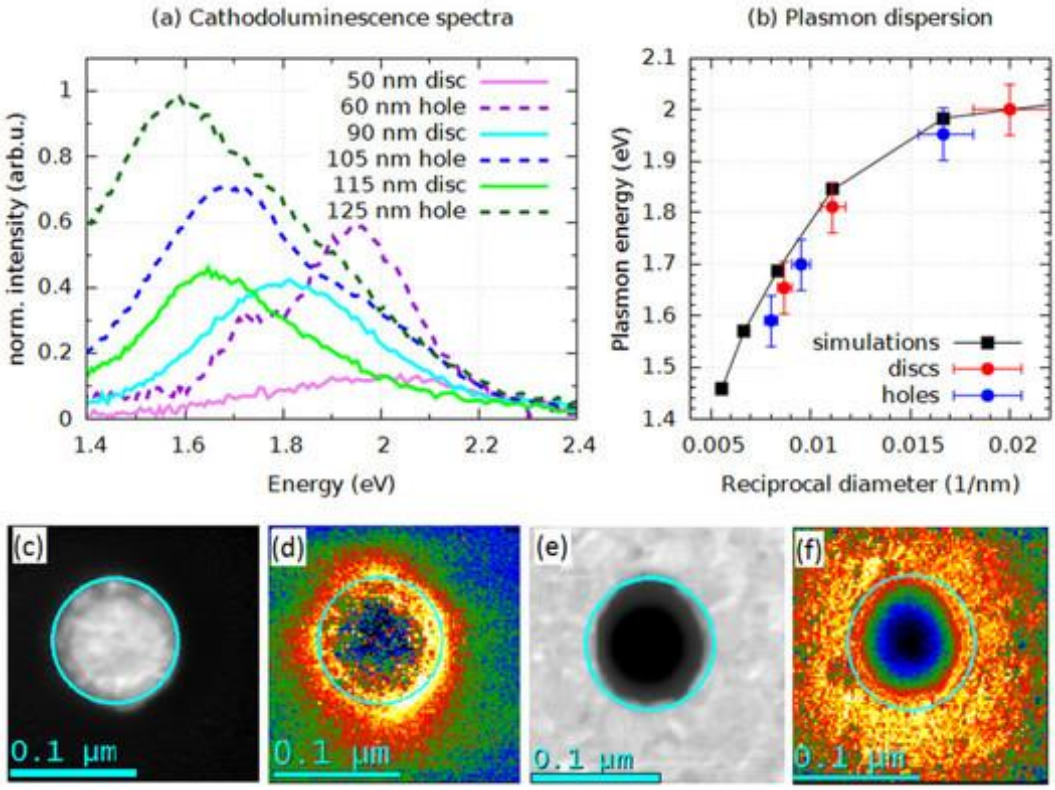

Figure 1. Cathodoluminescence spectra of gold disc antennas and apertures (a) and dispersion relation of the LSP resonance (b). Dark field micrographs of 100 nm gold disc (c) and aperture (e) with intensity maps (d,f) of the LSP resonance measured by EELS.

Electron beam effect on the mechanical properties of alumina and silica coated metal nanowires.

Mikk Vahtrus (1), Boris Polyakov (2), Magnus Mets (1), Mikk Antsov (1), Sven Oras (1), Aivar Tarre (1), Jaan Aarik (1), Rünno Lõhmus (1), Sergei Vlassov (1)

1) Institute of Physics, University of Tartu, W. Ostwaldi 1, 50412, Tartu, Estonia

2) Institute of Solid State Physics, University of Latvia, Kengaraga 8, LV-1063, Riga, Latvia

Keywords: Core/shell nanowires, mechanical properties, electron beam

Metallic (e.g. Au and Ag) nanowires (NWs) are promising materials for nanoscale systems due to their excellent electrical and thermal conductivity, perfect structure and ease of synthesis. Properties of these NWs can be further enhanced by coating them with a thin layer of another material resulting in formation of a 1D core/shell type heterostructure. In the present work, effect of the oxide coating on the mechanical properties of metallic NWs were studied for SiO_2 (1) and Al_2O_3 coatings. Ag NWs were coated by SiO_2 using sol-gel method, atomic layer deposition (ALD) was employed to cover Ag and Au NWs with Al_2O_3. Morphology and structure of the uncoated and the coated NWs were characterized by a high resolution scanning electron microscopy (HR-SEM) and a transmission electron microscopy (TEM). The mechanical characterization of the NWs was mainly carried out by an *in situ* HR-SEM cantilevered beam bending scheme. The NWs were deposited on TEM grids and the half-suspended NWs were bent in-plane using an atomic force microscope tip attached to a micromanipulator. Ag/SiO_2 core/shell NWs demonstrated high fracture resistance and withstood severe deformation without visible fracture. More importantly, the bending test revealed a novel electron beam (e-beam) induced shape restoration effect. The NWs were bent close to the plastic yield point of the core and the external force was removed, the NWs first rabidly and then slowly (within several minutes) restored to their initial straight profile (Fig 1a-d). When the e-beam was switched off, the shape restoration ceased and the NW profile was “frozen”. As soon as the beam was switched on again, the shape restoration resumed. Similar behavior was shown for Al_2O_3 coated Au and Ag NWs. The bending experiments on the uncoated NWs revealed that the NWs behave purely elastically at moderate deformations. Furthermore, the bending test in

AFM revealed brittle nature for SiO_2 and Al_2O_3 shells. Dynamics of the shape restoration under e-beam resembled the behavior of viscoelastic materials (Fig 1e). Overall response of the core/shell system to bending deformation is determent by an interplay between the elasticity of the core and the e-beam induced viscosity of the shell. Observed phenomena can be explained by the nonthermal e-beam induced structural relaxation in elastically deformed oxide via creation and increased mobility of defects. The viscosity of the shells was estimated quantitatively by finite element method simulations by fitting experimental data. The viscoelastic behavior and ability to “freeze” arbitrary profiles of the core-shell NWs under e-beam irradiation demonstrated in the present study can be considered as a new approach to manipulation of nanostructures and their properties.

References:

1. S. Vlassov et al., Nano Lett. 14 (2014) 5201-5205.

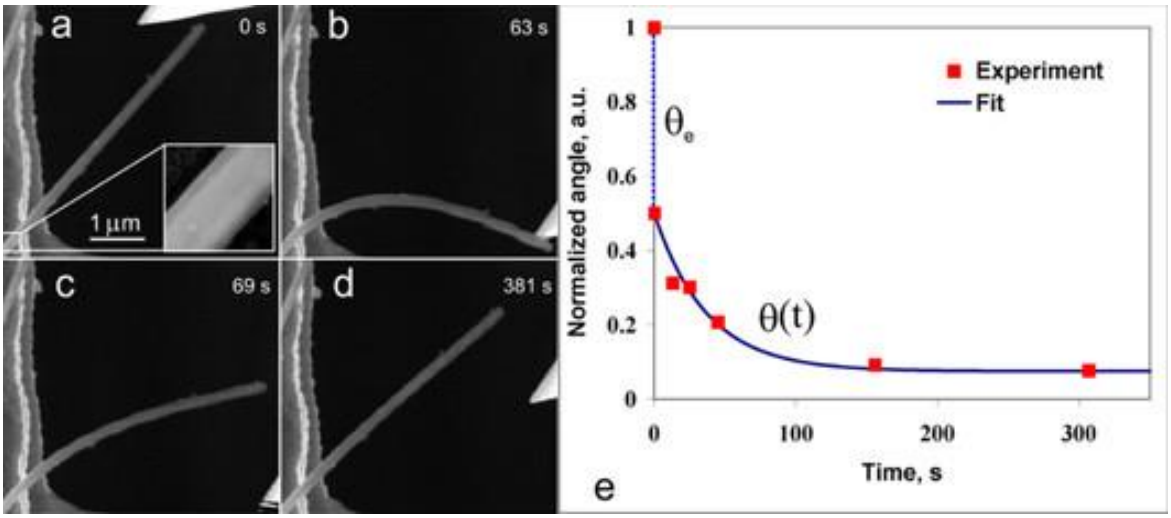

Figure 1. Bending and gradual shape restoration of Ag/SiO2 core/shell NW (a-d). Corresponding plot of the normalized restoration angle versus time (e).

The comparative XRD and SEM analysis of electrochemically produced silver nanostructures

Nebojša D. Nikolić (1), Ljiljana Avramović (2), Miroslav M. Pavlović (1), Vesna M. Maksimović (3), Marina Vuković (4), Jasmina S. Stevanović (1), Mile Bugarin (2)

1) ICTM-Department of Electrochemistry, University of Belgrade, Njegoševa 12, Belgrade, Serbia

2) Mining and Metallurgy Institute, Zeleni bulevar 35, Bor, Serbia

3) Vinča Institute of Nuclear Sciences, University of Belgrade, P.O.Box 522, 11000 Belgrade, Serbia

4) Institute for Multidisciplinary Research, University of Belgrade, Kneza Višeslava 1a, Belgrade, Serbia

Keywords: electrodeposition, silver, powder particles, SEM, XRD

Electrodeposition technique is very suitable way to obtain nanostructures of the desired shapes and dimensions. It is attained by the choice of regimes and parameters of electrolysis, such as the type and composition of electrolyte, temperature of electrolysis, the type of working electrode, the time of electrolysis, the addition of additives, application of periodically changing regimes of electrolysis, etc. (1). Thanking its unique electrical, chemical and optical characteristics, silver nanostructures found wide applications in electronics, optics, catalysis, sensors, etc (2). In this study, we produce silver nanostructures via electrochemical route from the two various types of electrolytes: basic (nitrate) and complex (ammonium) ones. Ag particles were produced by the potentiostatic regime of electrolysis at the room temperature using Pt as the working electrode. Electrodepositions were performed at overpotentials which corresponded to the plateaus of the limiting diffusion current density, i.e. at 90 mV (for the nitrate electrolyte) and 625 mV (for the ammonium electrolyte). Morphologies of the obtained particles were characterized by the technique of scanning electron microscopy (SEM), while the preferred orientation of the particles was evaluated by X-ray diffraction (XRD) analysis by calculation of the „Texture Coefficient“, *TC*(*hkl*) and the „Relative Texture Coefficient“, *RTC*(*hkl*) (3). The needle-like dendrites, as that shown in Figure 1a, were formed from the

nitrate electrolyte at 90 mV. The X-ray diffraction (XRD) analysis of the needle-like dendrites (Figure 2) showed their strong (111) preferred orientation. On the other hand, very branchy 3D (three dimensional) pine-like dendrites (Figure 1b) were formed by electrodeposition at 625 mV from the ammonium electrolyte. Analysis of the pine-like dendrites showed that they are constructed from corncob-like forms with spherical grains as the basic element. The X-ray diffraction analysis of the pine-like dendrites (Figure 2) showed the considerably smaller degree of Ag crystallites oriented in the (111) plane indicating almost random orientation of crystallites in these particles. The strong difference in morphology of the obtained particles is explained by different affiliation of Ag electrodeposition processes from these two electrolytes. Namely, Ag electrodeposition from the nitrate electrolyte belongs to the fast electrochemical processes (the high exchange current density values), and then, Ag is classified into the group of the normal metal (1). On the other hand, when Ag is electrodeposited from the ammonium electrolyte, then Ag is classified into the group of the intermediate metals which the basic characteristics are considerably lower exchange current density values than the normal metals. Simultaneously, the different preferred orientation of the obtained particles can be ascribed to different growth rate on these crystal faces caused by different surface energy values.

References:

1. K.I. Popov et al., Springer: New York, USA, 2016; pp. 1–368.

2. L. Fu et al., Chem. Pap. 68 (2014) 1283–1297.

3 L.Ph. Berube et al., J. Electrochem. Soc. 136 (1989) 2314–2315.

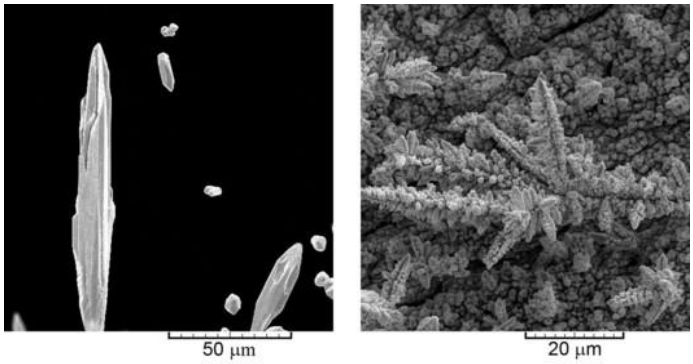

Figure 1. (a) The needle-like dendrite electrodeposited at an overpotential of 90 mV from 0.10 M $AgNO_3$ in 2.0 M $NaNO_3$, and (b) The pine-like dendrites electrodeposited at an overpotential of 625 mV from 0.10 M $AgNO_3$ in 0.50 M $(NH_4)_2SO_4$ with the addition of NH_3 in excess to dissolve silver sulfate precipitate.

Role of hydrogen in creating morphology of nanostructured NiCo alloy powder particles

Vesna M. Maksimović (1), Vladan B. Kusigerski (1), Milovan M. Stoiljković (1), Jelena R. Maletaškić (1), Nebojša D. Nikolić (2)

1) Vinča, Institute of Nuclear Sciences, University of Belgrade, P.O. Box 522, Belgrade, Serbia

2) ICTM-Department of Electrochemistry, University of Belgrade, Njegoševa 12, Belgrade, Serbia

Keywords: Electrodeposition, Ni-Co powder particles, morphology, magnetic parameters

Electrodeposition processes in the hydrogen co-deposition range are very promising ways to obtain metals in the desired form at the micro and nano scale which are suitable for applications in various technologies (1). Electrodeposition of alloys is more difficult to study in compare to pure metals, due to the co-deposition of at least two metals, and the various possible crystallographic structures arising from the phase diagram. Electrodeposition of the binary Ni-Co system has been studied comprehensively, mainly because of its importance in the field of soft magnetism. However, another reason is that the deposition of Ni-Co alloys demonstrates the phenomenon of anomalous co-deposition. Based on the binary *Ni-Co phase diagram,* nickel and cobalt build series of solid solutions in the whole range of concentrations. The aim of this work has been to study the role of hydrogen in creating of the final morphology of binary NiCo powder particles deposited from electrolytes with different Ni^{2+}/Co^{2+} ions ratios (Ni^{2+}/Co^{2+} = 4; 1.5; 0.67 and 0.25) and their magnetic properties, phase and chemical composition. The morphology, phase and chemical composition of these powders were investigated using XRD, SEM, and AES analysis. Magnetic measurements were performed at room temperature using a commercial SQUID-based magnetometer. Depending on Ni^{2+}/Co^{2+} ratio, the three main types of surface morphology were observed: dendrites, the coral-like and spongy-like particles. With increasing the Ni^{2+}/Co^{2+} ratio morphology of powder particles changed from dendrites to the spongy-like particles. At the first sight, it is clear that the shape of observed particles is determined by hydrogen evolution as a parallel reaction to alloy electrodeposition, with a tendency of increasing quantity of evolved hydrogen with the increasing Ni^{2+}/Co^{2+} ratio.

Hydrogen generated during an electrodeposition process causes a stirring of the electrolyte in the near-electrode layer, leading to a decrease in the thickness of the diffusion layer, an increase in the limiting diffusion current density and a decrease in the degree of diffusion control of the electrodeposition process. The increase of Ni^{2+}/Co^{2+} ratio caused a complete inhibition of dendritic growth. For example, the particles deposited from electrolytes with Ni^{2+}/Co^{2+} = 1.5 shown in Figs. 1a-c have the open structure which is a result of hydrogen evolution reaction, and these small holes are consequence of detached hydrogen bubbles. These particles can be denoted as coral-like, and it is noteworthy that this type of particle has been observed in this investigation for the first time. The XRD patterns of Ni/Co powder particles with the characteristic peaks of nickel-rich solid solution with fcc lattice (□) and hcp cobalt phase (□) are shown in Figure 2a and magnetic parameters obtained from *M*(H) curves recorded at room temperature are given in Figure 2b where M_S and H_C denote saturation magnetization and coercive field, respectively.

Acknowledgements:

This work was financially supported by the Ministry of Education, Science and Technology Development of the Republic of Serbia through the Project No. III-45012

References:

1. K.I. Popov et al., Springer, New York, (2016).

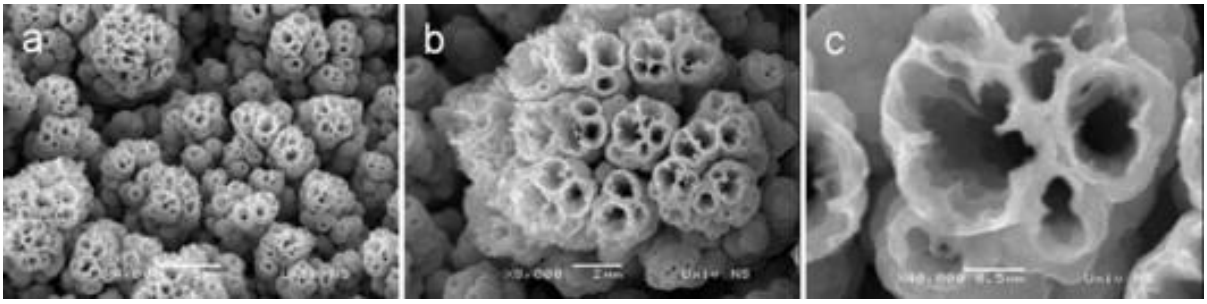

Figure 1. Morphology of NiCo powder particles obtained at a current density of 100 mA cm^{-2} with the Ni^{2+}/Co^{2+} = 1.5: (a) the agglomerates constructing coral-like structure, and (b, c) the holes formed at the top of coral-like particle.

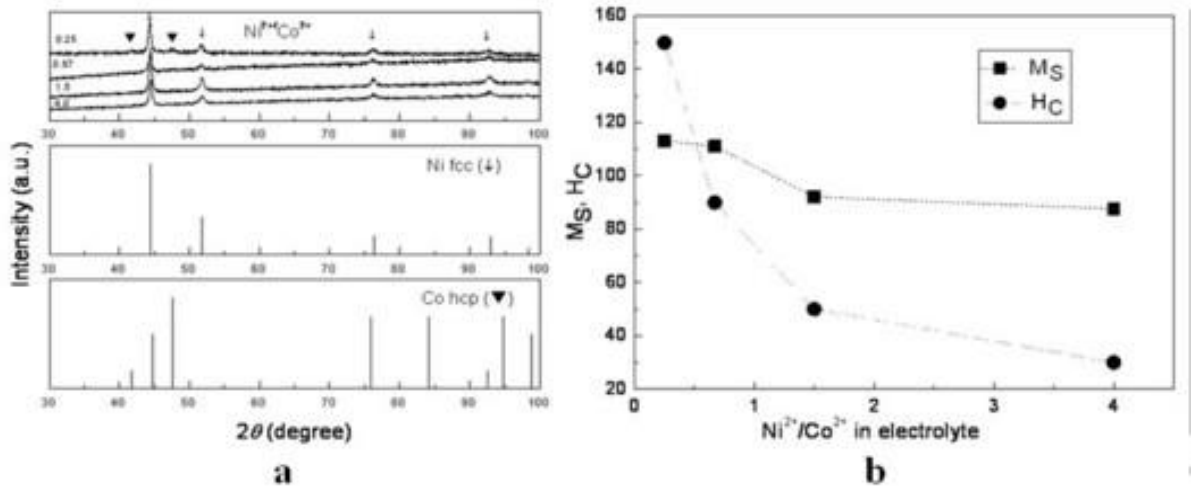

Figure 2. (a) XRD patterns and (b) magnetic parameters of Ni/Co powder particles deposited from electrolytes with different Ni^{2+}/Co^{2+} ions ratios (Ni^{2+}/Co^{2+} = 4; 1.5; 0.67 and 0.25).

Synthesis of magnetic α-Fe_2O_3 -carbon allotropes nanocomposites

Paloma Almodovar (1), Carlos Díaz-Guerra Viejo (1), Julio Ramirez-Castellanos (1), Javier Piqueras (1), Jose M. González-Calbet (1)

1) Complutense University of Madrid, Av. Séneca, 2, 28040 Madrid, Spain

Keywords: α-FeO, carbon allotropes, nanocomposites

Transition metal oxide composites based on carbon allotropes have received much recent attention, owing to their potential applications in diverse fields. For example, these composites stand out in many promising applications such as energy conversion devices, water purification, sensors or catalysts (1-3). In the particular case of iron oxides, most of the studies have been about magnetite (Fe_3O_4) based composites, as promising anode material for rechargeable lithium-ion batteries (LIBs), owning to its high specific capacity. For example, in the last few years the charge-discharge cycles of Fe_3O_4/graphene nanocomposites have been evaluated (4), as well as in Fe_3O_4/graphite nanocomposites (5). In contrast, the study of hematite (α-Fe_2O_3) in this kind of composites, and the reduction to graphene oxide based composited for water purification (6) and as anode material for lithium batteries (7). Hematite is an abundant, low cost, and nontoxic material and is therefore a promising candidate for the study of such applications and in other fields. α-Fe_2O_3 nanoparticles and the respective composites with graphene, graphene oxide (GO) and graphite, were obtained by means of a sol-gel method. The structure and composition of the materials were studied in detail by X-ray diffraction (XRD), micro-Raman spectroscopy and high-resolution transmission electron microscopy (HRTEM). They reveal the formation of the hematite nanoparticles, with a high crystallinity and an average particle size of 4nm, as well as, a homogeneous distribution on the graphene/GO/graphite sheets. It was also confirmed by compositional maps realized by energy dispersive X-ray microanalysis (EDX) by using aa scanning electron microscope (SEM). A super paramagnetic behavior with strong interactions between the hematite particles was observed, in all cases. Memory effect in the thermal variation of ZFC magnetization (8) allowed us to confirm this behavior and affirm, for the first time, the presence of hematite nanoparticles with a super spin-glass behavior.

References:

1. Zhong-Shua Wu et al., Nano Energ. 1, 107 (2012).

2. T.S. Sreeprasad et al., J. Hazard. Mater. 186, 921 (2011).

3. Yun Xu et al., J. Phys. Chem. Lett. 3, 309 (2012).

4. Xiaodan Huang et al., J. Alloy. Comp. 514, 76 (2012).

5. Weidong Zhang et al., J. Power Sources 223, 119 (2013).

6. Rajendra C. Pawar et al., Int. J. Hydrogen Energ. 40, 767 (2015).

7 . Xianjun Zhu et al., ACS Nano 5, 3333 (2011).

8. M Sasaki et al., Phys. Rev. B 71, 104405 (2005)

Analytical electron microscopy of submicrocrystalline skutterudite with addition of metallic borides

Jiří Buršík (1), Gerda Rogl (2), Peter Franz Rogl (2)

1) Institute of Physics of Materials, Czech Academy of Sciences, Žižkova 22, CZ-61662 Brno, Czech Republic

2) Institute of Materials Chemistry and Research, University of Vienna, Währingerstr. 42, A-1090 Wien, Austria

Keywords: skutterudite, boride, thermoelectrics, microstructure

Skutterudites are known as excellent thermoelectric (TE) materials and have already achieved good efficiencies for the conversion of heat to electricity. They can be produced easily and fast from relatively cheap starting materials, they can be used in a wide temperature range and besides an excellent TE quality they also show a long-term stability. Researchers try to further enhance the figure of merit, ZT. For maximum TE efficiency not only a high maximum ZT at a certain temperature is compulsory, but also high ZT values over the entire temperature range are involved. TE properties can be enhanced e.g. by doping, (multi)filling, by dispersing nanoparticles or by nanostructuring. In the recent works of Vienna group (1,2) various additives were tested with the aim of shortening phonon free path and thus reducing thermal conductivity without changing electrical resistivity and Seebeck coefficient. It was shown that small additions of metallic borides to $(Mm,Sm)_yCo_4Sb_{12}$ skutterudite enhanced the maximum ZT from 1.2 to 1.3 and increased the thermal-electrical conversion efficiency in the whole temperature range from 300 to 823 K. At the same time the boride additives enhanced the hardness, elastic moduli and fracture resistance. In this work we studied the microstructure of composite material prepared by mixing of industrial n-type $(Mm,Sm)_yCo_4Sb_{12}$ skutterudite with 1 wt.% $Ta_{0.8}Zr_{0.2}B$ (Mm stands for the Mischmetal, a rare earth alloy, which typical composition includes approximately 50% Ce and 25% La, with small amounts of Nd, Pr and other trace rare earths). After sieving the skutterudite and boride powders and blending them manually, they were high energy ball milled and then uniaxially hot pressed. In order to prevent oxidation all work with powders was performed in a glove box. The processing resulted in well compacted material

with fine equiaxial polyhedral grains (200–400 nm, see Figure 1). Thin cross sectional lamellas were prepared using a focused ion beam (FIB) in a scanning electron microscope (SEM). Analytical transmission electron microscopy (TEM) was used on lamellas to study details of microstructure (see Figure 2). It turns out that grain boundaries are decorated by particles (20–50 nm) of Sm-rich phase. Another type of smaller precipitates (sized down to several nm) is homogeneously distributed in the grain interiors. These observations explain enhanced phonon scattering of the tested material.

Acknowledgements:

The research was supported by the Czech Science Foundation (Project 17-12844S).

References:

1. G. Rogl and P. Rogl, Curr. Opin. Green Sus. Chem. 4 (2017) 50–57.

2. G. Rogl, A. Grytsiv, F. Failamani et al., J. Alloys Compd. 695 (2017) 682–696.

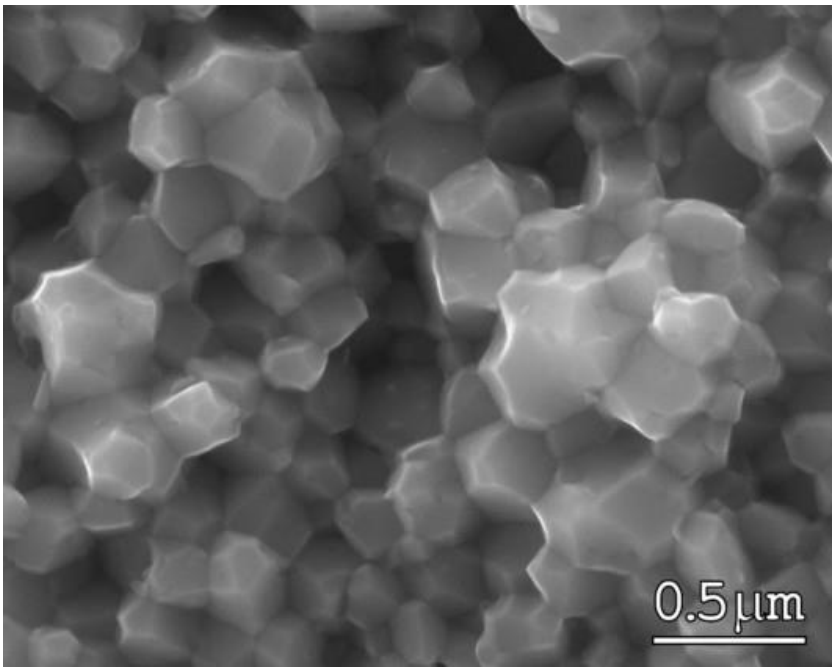

Figure 1. SEM of fracture surface, signal of secondary electrons.

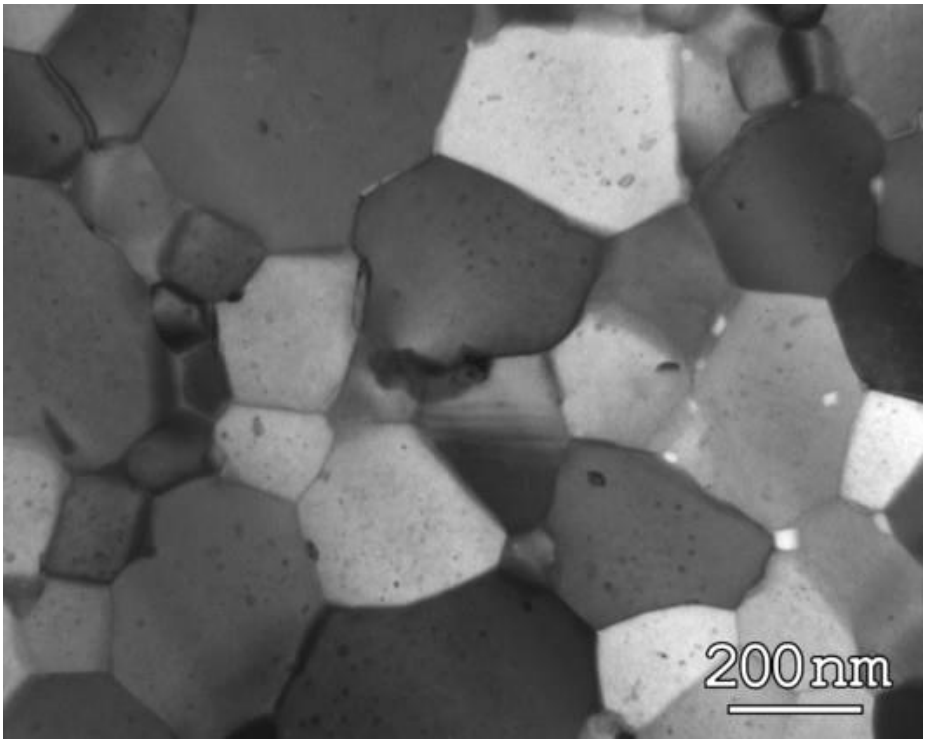

Figure 2. TEM micrograph of a thin lamellar section prepared by FIB.

The role of oxygen non stoichiometry in the CO oxidation activity of $BaFeO_{3-\delta}$

Marina Parras (1), Aúrea Varela (1), Jose M. González-Calbet (1), María J. Hernando (1), R. Cortés (1), Achraf el Hadri (1), Eloy del Río (2), Juan C. Hernández (2), Juan J. Delgado (2), Jose J. Calvino (2), Javier García-García (1)

1) Universidad Complutense Madrid, Av. Séneca, 2, 28040 Madrid, Spain

2) Universidad de Cádiz, C/ Ancha, nº 16, 11001 Cádiz, Spain

Keywords: $BaFeO_3$ nano-particles microstructural study catalytic behavior

The substitution of so-called critical elements, among which Noble Metals (NM) and some Rare Earths (RE) are included, has become a question of major concern to reach the goal of sustainable development. In the particular context of Heterogeneous Catalysis, the substitution of NM by Transition, mostly 3d, Metals, is an issue that has already received attention. In connection with this target, ABO_3 perovskite related oxides have been essayed as catalysts in a number of reactions, most of them redox processes. Lanthanide based Fe, Mn and Co perovskites, LnBO3 (Ln=lanthanide, B=Fe, Co, Mn), have been extensively studied systems, particularly as catalysts in the CO oxidation reaction. Substitution of La by an alkaline earth element (Sr^{2+} being the most widely studied case) has been reported to significantly modify the catalytic activity of $LnBO_3$ perovskites, the modification depending on the B element, the amount of the alkaline addition and, of course, the particular reaction. Total substitution of La by Ba fits perfectly with the actual demands to replace critical RE. $LnFeO_3$ (Ln=La, Sm, Nd). $BaFeO_{3-\delta}$ ($0.2 < \delta < 0.4$) depicts a 6H perovskite hexagonal structural type with Fe both in III and IV oxidation states and oxygen nonstoichiometry accommodated by random distribution of anionic vacancies. The perovskite with the highest oxygen content, $BaFeO_{2.78}$, proved to be more active than its lanthanide-based counterparts, $LnFeO_3$ (Ln=La, Sm, Nd). Removal of the lattice oxygen detected in both TPO and TPR diagrams at around 500 K, and which leads to the complete reduction of Fe^{4+} to Fe^{3+}, i.e. to a $BeFeO_{2.50}$ perovskite, decreases significantly the catalytic activity, especially in the low temperature range. The analysis of thermo-gravimetric experiments performed under oxygen and of TPR studies run under CO clearly support the involvement of oxygen lattice in the CO oxidation on these Ba-Fe perovskites, even at the lowest temperatures. Atomically-resolved images and chemical maps obtained using different Aberration-Corrected Scanning Transmission Electron Microscopy techniques, have provided a clear picture of the accommodation of oxygen- non-stoichiometry in these materials. Besides, the temperature dependence of the redox process has been followed by *in situ* X-ray and selected area electron diffraction. From the whole results obtained it has been possible to propose the role of the oxygen deficiency responsible for the CO oxidation activity of $BaFeO_{3-\delta}$.

Micro and nanosized 4H-$SrMnO_3$: structural and physical properties

Aúrea Varela (1), Marina Parras (1), Jose M. González-Calbet (1), Almudena Torres-Pardo (1), Irma N. González-Jiménez (1), María del Mar García-Hernández (2), Alicia de Andrés (2), E. Clement (2)

1) Universidad Complutense Madrid, Av. Séneca, 2, 28040 Madrid, Spain

2) Instituto de Ciencia de Materiales, CSIC, Campus de Cantoblanco, Calle Sor Juana Inés de la Cruz, 3, 28049 Madrid, Spain

Keywords: $SrMnO_3$ nanoparticles, Microstructural study, thermocromic behaviour

The great progress of technology during the last decade requires the continuous stabilization of new compounds at the nanometer scale for the development of advanced devices. Mn perovskite related mixed nano-oxides constitute a promising set of materials in the field of nanoscience and nanotechnology as a result in part of the high oxidation state's number in which Mn can be stabilized providing a structural variety and a wide range of electrical and magnetic properties. In this work, we report the synthesis as well as the structural characterization of 4H-$SrMnO_3$ particles obtained by two synthetic routes: i) from the thermal decomposition at low temperatures of the heterometallic precursor $[SrMn(edta)(H_2O)_5]\cdot{}^3/_2H_2O$ ii) and an hydrothermal method from metallic salts in KOH medium. Only the former method leads to SrMn-oxide particles with nanometric size (average particle size 70 nm). Local structural information, provided by atomically-resolved electron microscopy techniques, shows that $SrMnO_3$ nanoparticles exhibit the structural features corresponding to a 4H phase, although structural disorder due to edge-dislocations is observed. On the contrary, hydrothermal method gives rise to faceted microcrystals which morphology depends on the nature of the metallic precursor. The influence of particle sized in the thermocromic properties of 4H- $SrMnO_3$ have been explored by means of different diffractometric (X-Ray, Neutron and Electron Diffraction) and spectroscopic (Raman) techniques, working in the temperature range between 40 and 450 K. From these results we have shown the existence of a phase transition from a hexagonal (hchc)-4H ($P6_3/mmc$) to an orthorhombic ($C222_1$) phase at temperature close to 340 K in the bulk sample. This structural change would involve a slight tilting of the corner-sharing octahedra. When temperature decreases, non-trivial structural distortions take place at temperatures close to 280 and 170 K. Finally, at 120 K the maximal orthorhombic distortion seems to be achieved. These structural changes promote the modification of the electronic structure of this oxide originating the observed color change from black to violet. These structural features are not clearly apparent when decreasing particle size down to the nanoscale and, in this case, only a very small orthorhombic distortion is detected below 170 K. A decrease in the orthorhombic distortion degree may be the reason why a color change is not observed in nano particles of 4H-$SrMnO_3$.

EELS simulations of IrOx catalysts for water splitting

Walid Hetaba (1), Elena Willinger (1), Marc-Georg Willinger (2), Robert Schlögl (2)

1) Max-Planck-Institute for Chemical Energy Conversion, Stiftstraße 34-36, 45470 Mülheim an der Ruhr, Germany

2) Fritz Haber Institute of the Max Planck Society, Faradayweg 4, 14195 Berlin, Germany

Keywords: EELS, ELNES, DFT, IrOx, Catalyst

Iridium oxides and hydroxides are promising catalysts for water splitting due to their high stability and activity. (1) In order to gain greater insight into their functionality and (electronic) structure, a number of microscopical and analytical techniques were applied to iridium oxide and potassium iridium oxide as well as IrO_x-hydroxides. (2) Previous work suggests that the amorphous IrO_x-hydroxides can consist of IrO_2-rutile and $K_{0.25}IrO_2$-hollandite structural motifs. With the purpose to improve understanding of the electronic structure, EELS analysis was performed. In this work, DFT based simulations of the O-K edge ELNES for different iridium oxides were performed, analysed and compared to experimental spectra. We used the FP-LAPW code WIEN2k and the TELNES subroutine (3) to carry out the calculations for different materials: rutile-structured IrO_2, several hollandite structures and a todorokite-like structure. The simulated hollandite structures contain Li, Na and K, respectively and show different octahedral distortions. The results were analysed with respect to the contribution of the different oxygen atoms to the total spectrum. Figure 1 shows the total O-K edge ELNES of the calculated structures. The relative intensities of the first and second peak differ for the investigated materials. Furthermore, the intensity maxima are shifted to different energy losses. However, the ELNES of the three hollandite structures are rather similar. In Figure 2, the symmetry-projected Ir d-DOS and O p-DOS of rutile-structured IrO_2 is shown. From these plots the different contributions to the EELS signal as well as the bonding between the atoms in the structure can be analysed. The same analysis was performed for the other calculated structures. In addition, for these structures the contributions of atoms of the same element but at different crystallographic positions was investigated. Comparison of the calculated and experimental spectra (not shown) leads to a good agreement. Furthermore, the simulations confirm the results of experimental EELS measurements and pair distribution function analysis of previous work (2). This suggests that the amorphous IrO_x-hydroxide synthesized at FHI is best described by hollandite structural motifs. Additionally, the calculated spectra allow to distinguish the contributions of each atom at different crystallographic positions to the total spectrum. Furthermore, the bonding between the atoms in the structures can be investigated. This improves the understanding of the structure-property relationship of these highly promising catalyst materials.

References:

Massue et al., ChemSusChem, DOI: 10.1002/cssc.201601817 Willinger et al., in preparation Blaha et al., WIEN2k, TU Wien (2001), ISBN 3-9501031-1-2

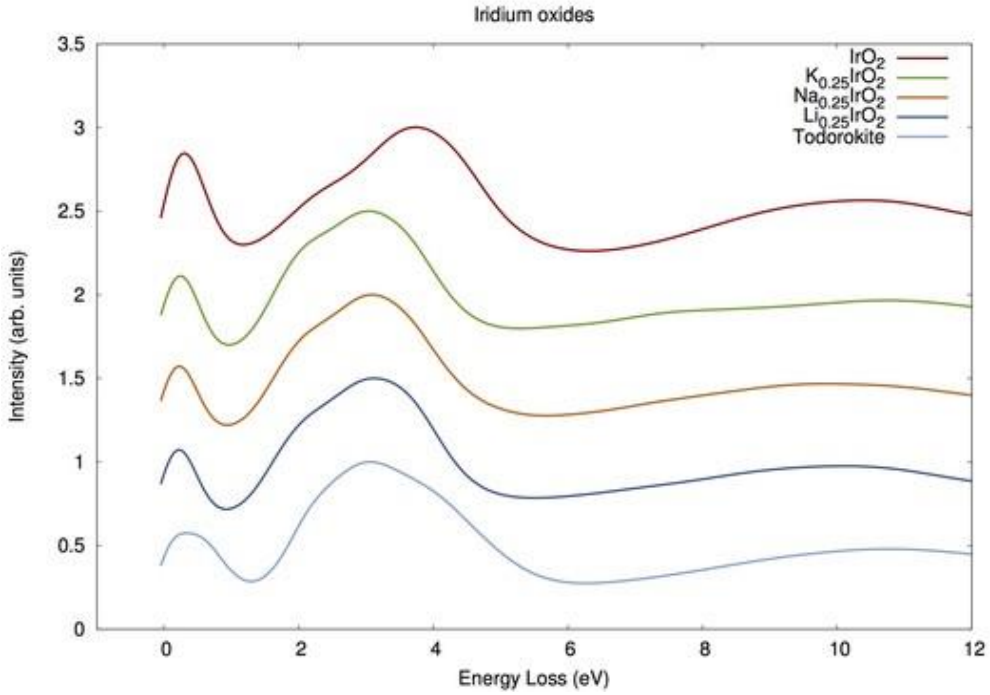

Figure 1. Oxygen K-edge ELNES calculation for different iridium oxide structures.

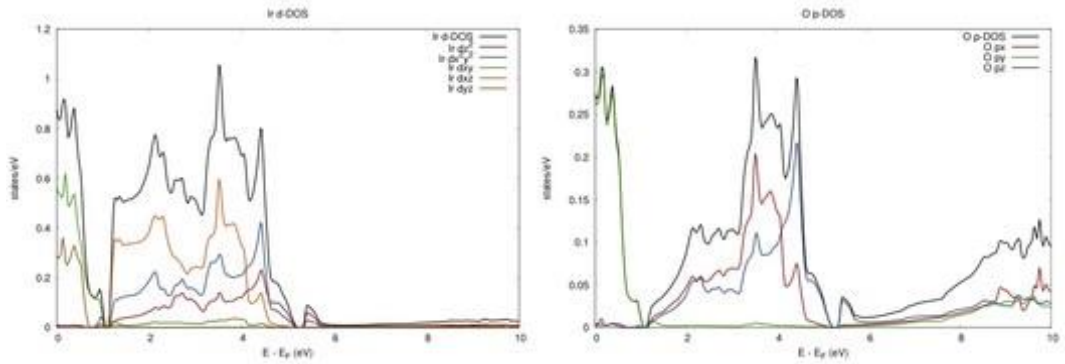

Figure 2. Symmetry-projected Ir d-DOS and O p-DOS of rutile-structured IrO_2.

EM investigation of DC jet plasma grown Cu-oxide nanowires for amine detection

Janez Zavašnik (1), Harinarayanan Puliyalil (2), Johannes Gruenwald (3), Gregor Filipič (4)

1) CEMM, Jožef Stefan Institute, Jamova 39, 1000 Ljubljana, Slovenia

2) Department of catalysis and chemical reaction engineering, National institute of Chemistry, Hajdrihova 19, Ljubljana 1000, Slovenia

3) Independent researcher, Nová 167, 252 42 Zlatniky-Hodkovice, Czech Republic

4) Jožef Stefan Institute, Jamova 39, 1000 Ljubljana, Slovenia

Keywords: Cu-oxide nanowires, DC jet plasma, electron microscopy, amine detection

Copper oxide nanowires (NWs) can be synthesised in many ways: thermal oxidation, hydrothermal methods, electrospinning, etc. (1) However, not many can grow NWs directly on a temperature sensitive and non-conductive substrate. In this work we present NWs that have been deposited on polymer substrates by means of atmospheric non-thermal DC Ar plasma with a sacrificial electrode as copper source (2). Plasma induced growth of nanostructures at atmospheric pressure offers a promising alternative as there is no vacuum systems involved, resulting in lower costs, and faster process time (3). Copper oxide nanostructures have already found many applications: for supercapacitors (4), optoelectronic devices (5) and photo-electrochemical applications (6). As they have antimicrobial properties there is growing interest for their use in medical and food applications (7) and to their sensor response also in bio- and gas sensors (8,9) .Thus, the proper identification and characterisation of such obtained nanostructures is of major importance for their practical use. Copper-oxide nanostructures that were synthesized by Atmospheric Pressure Plasma Source (APPS) were tested for amine detection at elevated temperatures (373 K) and investigated by various electron microscopy (EM) techniques before and after amine exposure: chemistry and morphology were investigated by scanning electron microscopy (SEM), while their structure and phase composition were investigated by transmission electron microscopy (TEM) techniques. Two sets of samples, before and after the amine treatment, were observed under SEM and then

directly transferred to TEM without any further alterations to commercially available Ni-supported amorphous carbon grids and investigated using analytical beryllium double-tilt holder. SEM and CTEM observations revealed up to 1 μm sharp Cu-oxide monocrystals growing atom bulk polycrystalline Cu matrix. Phase composition was determined in TEM by selected area electron diffraction (SAED) as Cu_2O – cuprite. Phase composition of nanostructures after amine treatment was preserved, while the surface of cuprite monocrystals was additionally covered by up to 20 nm thick amorphous C-N-O layer. Since the sensor would be exposed to higher temperature for longer times their structure was observed at elevated temperatures by *in situ* TEM heating experiment. Initial Cu_2O crystals undergo rapid transformation to pure Cu monocrystals at 373 K. Further temperature increase only speed-up the growth of Cu, eventually resulting in large, bulky, heavily twinned Cu monocrystals. The result is somehow unexpected since even just the melting point of copper oxide is much higher (1505 K) that the heating experiment.

References:

1. G. Filipič et al. Nanotechnology 23 (2012): 194001001-194001016

2. J. Gruenwald et al. Plasma Process. Polym 13 (2016): 766–774

3. J. Gruenwald et al. Plasma Process. Polym. 13 (2016) 946–954

4. B. Vidyadharan et al. J. Alloys Compd. 633 (2015) 22–30

5. V. Binh Nam et al. Nanomaterials 6 (2016) 47-63

6. L. Chen et al. J. Mater. Chem. 20 (2010) 6962–6967

7. Y. Abboud et al. Appl. Nanosci. 4 (2014) 571–576

8. Y. Zhang et al. Sens. Actuators A 191 (2014) 86–93 (9) O. Lupan et al. Phys. Status Solidi RRL 10 3 (2016) 260–266

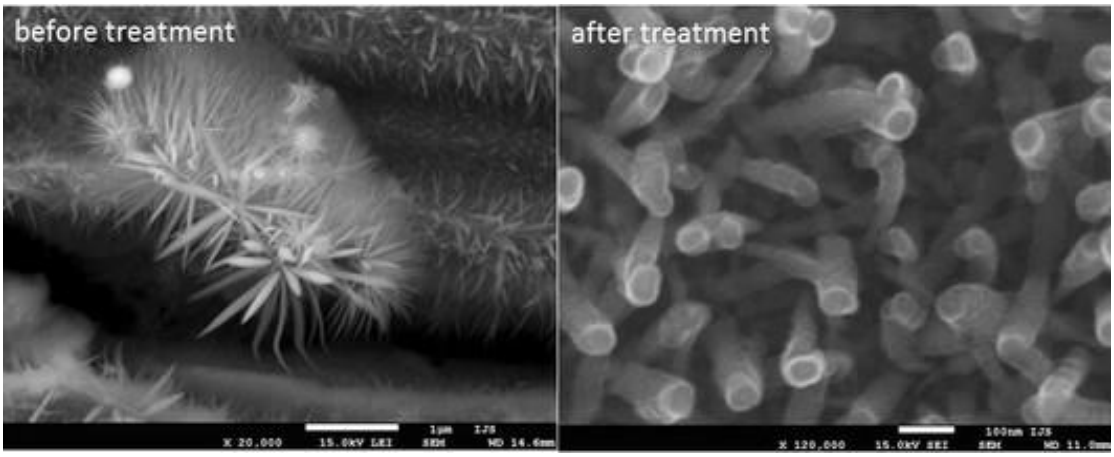

Figure 1. Cu-oxide nanostructures before and after amine treatment; while general size and elongated shape of the individual crystal is preserved, their morphology is changed.

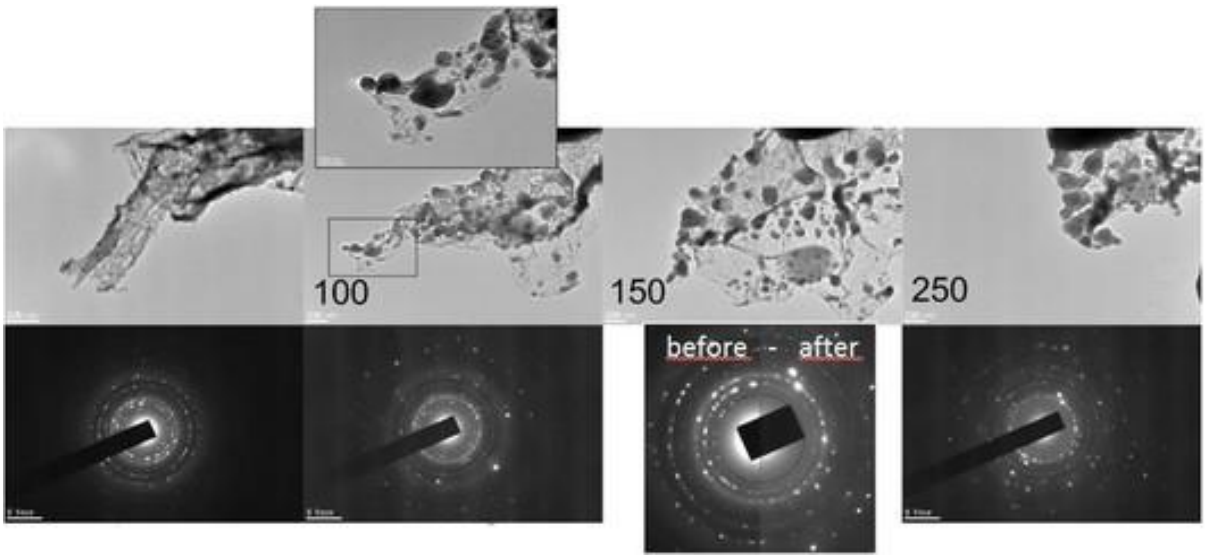

Figure 2. *In situ* heating experiment of Cu-oxide nanostructures, starting at room temperature. SAED patterns confirmed that initial Cu_2O (cuprite) transforms to pure Cu at 200 °C.

Assemblies of Sub-10 nm nanoparticles - imaged by SEM in impeding conditions

Kristina Kučanda (1), Rafal Klajn (1)

1) Weizmann Institute of Science, Herzl St 234, Rehovot, 76100, Israel

Keywords: scanning electron microscopy (SEM), nanoparticles, nanostructures, self-assembly, crystallization

Self-assembly of nanoscale components is a widely studied bottom-up approach to formation of nano- and microdevices and structured materials. The structure and function of the resulting assemblies are governed by interactions between the nanoscale and molecular ingredients, and in some cases can be tuned by stimuli such as magnetic field (Ref. 1) or light (Ref. 2). Among the research topics of our group are chemical, solution-based synthesis of small inorganic nanoparticles (mainly noble metal or metal oxide nanoparticles with diameters around 10 nm or less) covered with a monolayer of organic ligands; and their self-assembly, especially reversible, responsive to multiple stimuli. That research has provided fundamental insights about concepts such as interplay of interactions, symmetry breaking (Ref. 1), and chemical reactivity in nanoconfined environments (Ref. 2), as well as applications for catalysis (Ref. 2) and magnetic transport. In order to see our assemblies, besides transmission electron microscopy and optical microscopy, we have developed expertise in scanning electron microscopy at sub-10 nm resolution. We routinely image supracrystalline and disordered assemblies in which nanoparticles of diameters 5–10 nm are clearly observed, including within strongly magnetic wires hundreds of micrometers long (Figure 1) or nearly equal volume of organic (carbonaceous) material (Figure 2). The assemblies of gold and magnetite nanoparticles as shown in the figures in this abstract were obtained by precipitation via non-solvent vapor diffusion crystallization method (Ref. 3). The long magnetite assemblies (wires) formed in permanent magnetic field ("neodymium magnet"). SEM samples were prepared by drop-casting on a silicon wafer, blotting with a paper tissue, and washing with methanol. The micrographs were acquired with SEM Ultra 55 FEG (Zeiss), at 8 kV, aperture 30 μm and working distance 2–4 mm, with in-lens detector. To our knowledge we are the first to report 3D

supracrystalline assemblies of quasi-spherical magnetite nanoparticles, and the dependence of the shape (crystal habit) and crystalline order of gold and magnetite nanoparticle assemblies on simple, small-molecule, commercially available chemicals.

Acknowledgements:

This research was supported by the European Research Council. KK thanks Dr. Ifat Kaplan-Ashiri for the basic training and allowing 24/7 access to the SEM, and Michał Sawczyk for help with finding optimal imaging settings.

References:

1. G. Singh et al., Science 345 (2014) 1149-1153.

2. H. Zhao et al., Nature Nanotech. 11 (2016) 82-88.

3. D. Haubold et al., Adv. Funct. Mater. 26 (2016) 4890-4895.

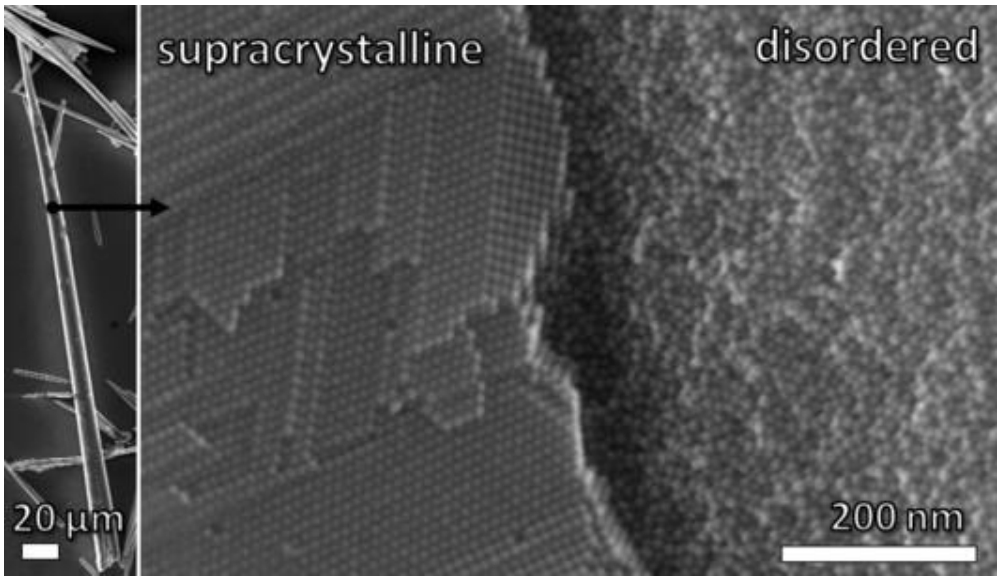

Figure 1. Wire-like assemblies of magnetite nanoparticles (average diameter 9 nm).

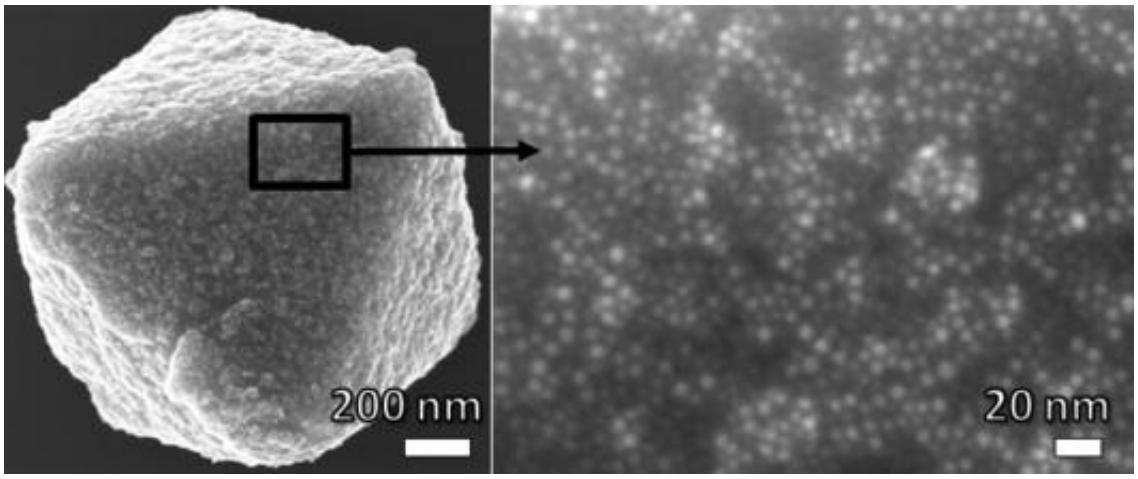

Figure 2. Octahedral assembly of gold nanoparticles (average diameter 6 nm) with a large amount of triphenylphosphine.

Colloidal synthesis of metastable AuCuS phase nanocrystals and *in situ* TEM heating study of their transformation

Muhammad Imran (1), Liberato Manna (1), Rosaria Brescia (1)

1) Istituto Italiano di Tecnologia, via Morego 30, 16163 Genova, Italy

Keywords: Colloidal synthesis, *in situ* heating TEM, metastable phases, Cu_2S

In this contribution the authors report on a novel, metastable ternary phase, with composition AuCuS, resulting from a colloidal synthesis protocol. Au^+ ions from solution diffuse into stoichiometric Cu_2S (high chalcocite) disk-shaped nanocrystals obtained by formerly reported procedures (Figure 1a) (1). Inward diffusion of Au^+ ions is accompanied by outward migration of an equal number of Cu^+ ions, resulting in a sort of cation exchange reaction (2). Independent of the Au concentration in solution, the resulting particles are preferentially Janus-type structures, with the novel phase domain and the remaining Cu_2S one separated by sharp interfaces (Figure 1b). Only in few cases, the nanocrystals evolve entirely into the ternary phase, in which case the energetically favored structure is composed by multiple domains. In addition, the thermal stability of the AuCuS phase has been examined by *in situ* heating TEM experiments, during which outwards diffusion of Au and metallic Au domain formation was observed at about 150°C. This is due to the high diffusivity of Au through the Cu_2S template structure, eventually leading to Au-decorated $Cu_{2-x}S$ nanocrystals (Figure 1c). The initial ternary phase, the mechanisms leading to it starting from the parent high chalcocite phase and its thermal stability will be discussed in detail in this contribution.

Acknowledgements:

We acknowledge funding from the European Union under grant agreement n. 614897 (ERC Grant TRANS-NANO).

References:

1. F. Wang et al., J. Am. Chem. Soc. 137 (2015) 12006−12012.

2. D. H. Son et al., Science 306 (2004) 1009-1012.

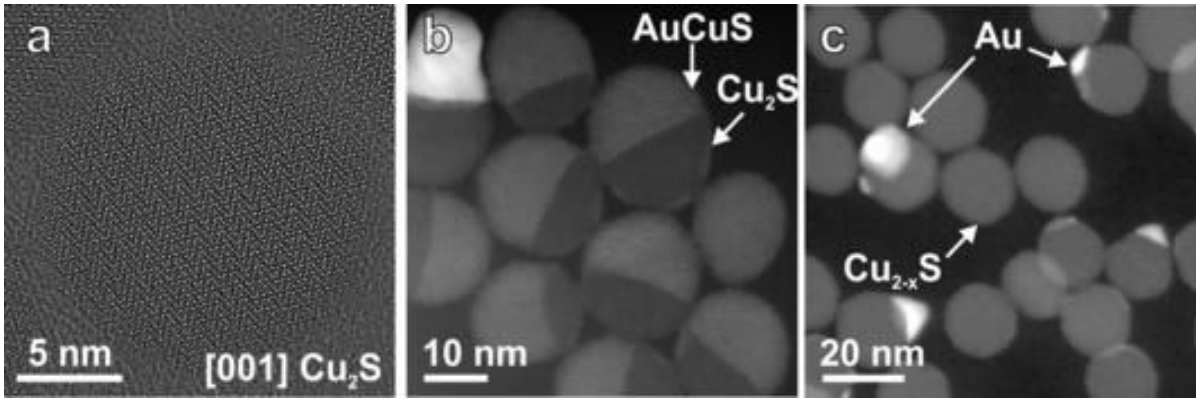

Figure 1. (a) HRTEM image of a pristine Cu2S (high chalcocite) nanodisk. (b) HAADF-STEM image of AuCuS-Cu_2S Janus-type nanoparticles. (c) Outcome of *in situ* heating-up of the heterostructures up to 150°C, with formation of few Au-decorated Cu_2-xS nanodisks.

Imaging zeolite NaA

Gerardo Algara-Siller (1), Thomas Lunkenbein (1), Robert Schlögl (1), Marc G. Willinger (1)

1) Fritz Haber Institute of the Max Planck Society, Faradayweg 4, 14195 Berlin, Germany

Keywords: HRTEM, Zeolite A

Zeolites have been studied thoroughly using different TEM techniques, but until now the mechanisms for radiation damage in zeolites are not fully understood due to the complexity of their structure. Some works have given a general indication on the origin of the radiation damage. From these works, it can be derived that the main factors for the stability of a zeolite under the electron beam are: Si/Al ratio i.e. the lower the ratio the more sensitive to electron irradiation; the type of the cations; and the water content. In this work we present the synthesis and TEM characterisation of zeolite NaA (LTA framework). This type of zeolite has a Si/Al ratio of 1 and exhibits sodium cations in the channels. Zeolite NaA was synthesized based on the synthetic protocol of Wenqing et al.(1) In order to know the sample purity we characterised the sample, previous to TEM, by XRD and XRF. The results show that the sample is NaA zeolite with a 1.10(5) Si/Al ratio. HRTEM characterisation was performed in an aberration-corrected TITAN 80-300. We found that using electron dose rates up to 10^3 e/nm^2 s the atomic structure of such material can be obtained over a timespan that is necessary for imaging. In addition, we did not observe any significant influence of the electron energy (80 keV, 200 keV and 300 keV) used for characterization. The latter result suggests that by using an electron energy above 80 keV, the damage due to electronic excitations (e.g. radiolysis) and knock-on are simultaneously taking place. These results are in agreement with previous findings reported by Urgulu et al. Although the structure of zeolite could be obtained, invariable damage occurred during recording, however, at a slow rate. In conclusion, these results are one step forward for the understanding of radiation damage mechanisms in molecular sieves, and a step towards imaging the cation positions.

References:

1. Wenqing et al., Proceedings of the 7th International Zeolite Conference, Elsevier (1986)

In situ characterization of M@Co_3O_4 (M = $NiFe_2O_4$, $ZnFe_2O_4$) core-shell nanoparticles for the Fischer-Trospch Synthesis

Ezra J. Olivier (1), Alisa Govender (2), Werner Barnard (2), Roy P. Forbes (3), Eric Van Steen (4), Johannes H. Neethling (1)

1) Center for HRTEM, Nelson Mandela University, Nelson Mandela University, University Way, Summerstrand, Port Elizabeth, 6001 South Africa

2) Group technology R & T Analytics, Sasol South Africa, , PO Box 1, Sasolburg 1947, South Africa

3) School of Chemistry, University of the Witwatersrand, 1 Jan Smuts Avenue, Braamfontein 2000, Johannesburg, South Africa

4) Catalysis Research Unit, Department of Chemical Engineering, University of Cape Town, Private Bag X3, Rondebosch, 7701 Cape Town

Keywords: *In situ*, TEM, Catalyst

Recently Co_3O_4 based catalysts have found application in a variety of catalytic reactions. This is due to the relatively high catalytic activity of Co. Some important processes include oxidation reactions for environmental applications[1] as well as hydrogenation reactions (after reduction)[2], such as the Fischer-Tropsch synthesis[3]. Unfortunately, the use of cobalt leads to a significant increase in the cost of these catalysts. Consequently, routes to synthesize a lower cost catalyst containing cobalt oxide as the active material are constantly being sought. One such option is the design of a core-shell catalyst, in which the shell of cobalt oxide is combined with a core of a less expensive material. Calderone and co-workers[3] proposed that a cheap, simple scalable method is needed to produce a particular cobalt shell thickness for a certain crystallite size whilst maintaining an overall cost saving and achieving a high performance material. In this present work, the characteristics of $NiFe_2O_4$@Co_3O_4 and $ZnFe_2O_4$@Co_3O_4 core-shell nanoparticles, before and after reduction, was studied and compared to Co_3O_4 using various techniques. Additionally, the influence of a reducing environment at particular temperatures, on the make-up of each core-shell nanoparticle system was studied using *in situ* TEM. Moreover, these core-shell nanoparticles were tested for its performance in the Fischer-

Tropsch Synthesis. Importantly, correlations between the characterization results and catalytic performance were made. Whilst the observed catalytic behaviour of core-shell nanoparticles may be explained by the adsorption properties of the active metal, the observed characteristics will be largely dependent on the structure of the active phase surface after activation. The atomic level structure of nanoparticles, particularly those comprised of multiple metals, may evolve into different surface arrangements when exposed to a reactive environment such as hydrogen and increasing temperature. Although the nanoparticle can undergo a re-structuring due to various factors, the primary purpose of the atomic movement is to reduce the surface free energy of the nanoparticle. As a result, the reduction process done on the core-shell nanoparticles prepared in this work could induce changes to the atomic ordering and/or surface composition of the nanoparticle. This means that establishing the structure of these nanoparticles, particularly after activation, is essential to understand the relationship between the surface structure of the material and the mechanisms at play during the reaction

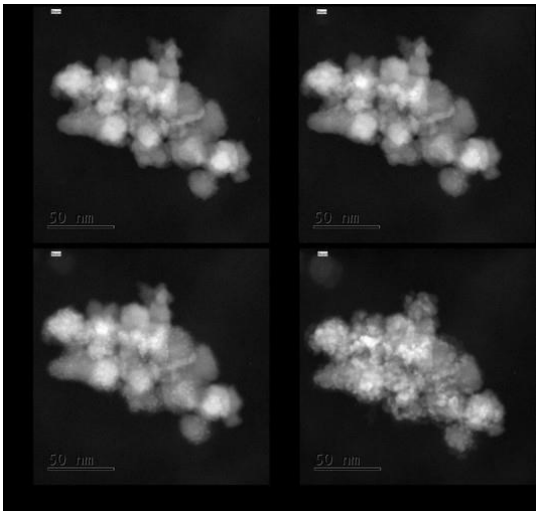

Figure 1. HAADF-STEM images of NiFe2O4@Co3O4 obtained (a) ex-situ and during the *in situ* TEM reduction at (b) 230 °C, one atm, one hour hold time; (c) 230 °C, one atm, two hour hold time and (d) 280 °C, one atm, one hour hold time.

References:

1. Choudhary, T.V., Banerjee, S. and Choudhary, V.R. (2002) Appl. Catal. A: Gen. 234, 259.

2. Sewell, G.S., O'Connor, C.T. and van Steen, E. (1995) Appl. Catal. A: Gen. 125, 97. 3. Chalderone, V.R. et al. (2013) Angew. Chem. Int. Ed. 52, 4397.

Examination of 2D crystals in a low voltage SEM/STEM

Eliška Mikmeková (1), Luděk Frank (2), Josef Polčák (3), Aleš Paták (1), Michael Lejeune (4)

1) Institute of Scientific Instruments of the CAS, v.v.i., Královopolská 147, Brno 612 64, Czech Republic

2) Institute of Scientific Instruments of the CAS, v.v.i., Královopolská 147, Brno 612 64, Czech Republic

3) CEITEC—Central European Institute of Technology, Brno University of Technology, Technická 3058/10, 616 00 Brno, Czech Republic

4) Laboratoire de Physique de la Matière Condensée, Universite Picardie Jules Verne, 33 rue Saint Leu, 80028 Amiens, France

Keywords: Low voltage SEM/STEM, 2D crystals, contamination

Development of new types of materials such as 2D crystals (graphene, MoS_2, WS_2, h-BN, etc.) requires emergence of new surface-sensitive techniques for their characterization. As regards the “surface” sensitivity, the (ultra) low energy electron microscopy can become a very powerful tool for true examination of these atom-thick materials, capable of confirming physical phenomena predicted to occur on their surfaces. Modern commercial scanning electron microscopes enable imaging and analyses by low energy electrons even at very high magnification. In the case of the SEM, resolution even below 1 nm can be achieved at low landing energy of electrons (1). Since specimen contamination increases with increasing electron dose and decreasing landing energy, specimen cleanness is a critical factor in obtaining meaningful data. A range of various specimen cleaning methods can be applied to selected samples. Typical cleaning methods, such as solvent rinsing, heating, bombarding with ions and plasma etching have their limitations. Electron-induced *in situ* cleaning procedure can be gentle, experimentally convenient and very effective for wide range of specimens. Even a small amount of hydrocarbon contamination can severely impact on the results obtained with low energy electrons, as illustrated in Figure 1A. During the scanning of surfaces by electrons, the image usually darkens because of a carbonaceous layer gradually deposited on the top from adsorbed hydrocarbon precursors (2). This effect can be described as the electron

stimulated deposition. The surface diffusion of hydrocarbon molecules around the irradiated area serves as a source of additional precursors, responsible for even darker frame of the contaminated field of view. On the other hand, the effect of electron stimulated desorption occurs at the same time, especially at low energies, so fundamental question arises what process, deposition or desorption, will dominate – see Figure 1B. Examination of phenomena taking place on surfaces bombarded with very slow electrons may open the door to the performance of many surface studies outside an ultrahigh vacuum. Our unique equipment enabling measurement of both the transmissivity and reflectivity of 2D crystals for electrons of arbitrary energy, presented in Figure 2 – WS_2 crystals prepared by CVD.

Acknowledgements:

The work was financially supported from the Technology Agency of the Czech Republic: Competence center Electron microscopy, no: TE01020118. 1. D. Phifer, L. Tuma, T. Vystavel, P. Wandrol, R. J. Young, Microscopy Today (July 2009) 2. R. F. Egerton, P. Li, M. Malac, Micron 35 (2004), 399-409.

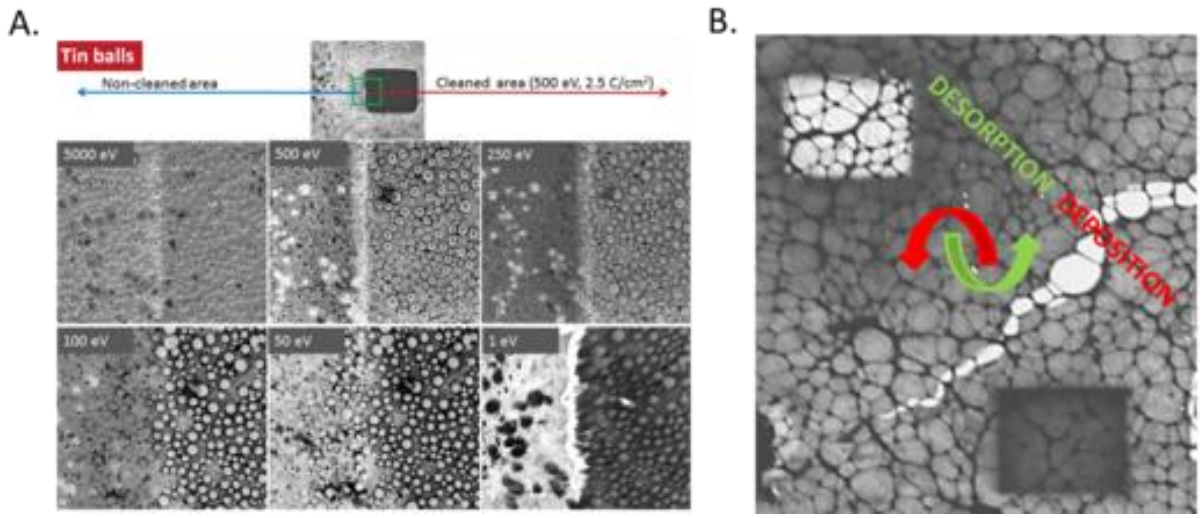

Figure 1. (A) Tin balls observed with 5000 eV, 500 eV, 250 eV, 100 eV, 50 eV and 1 eV electrons; (B) Low voltage STEM observation at 100 eV of graphene after irradiation by electrons causing deposition at 5 keV and desorption at 500 eV.

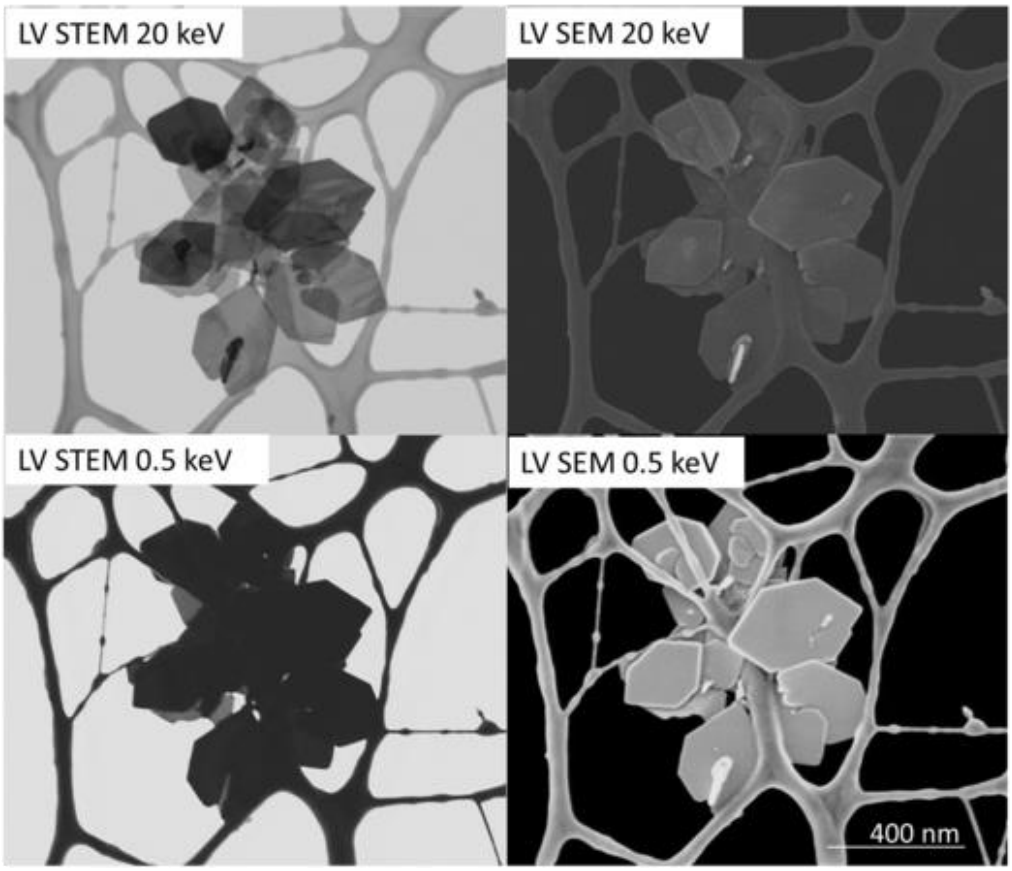

Figure 2. Low voltage STEM and SEM observation of CVD prepared WS2 crystals.

Structure, morphology and kinetic analysis of $Gd_2Ti_2O_7$ nanopowders

Milena Marinović-Cincović (1), Bojan Janković (2), Bojana Milićević (1), Slavica J. Porobić (1), Miroslav D. Dramićanin (1)

1) Institute of Nuclear Sciences “Vinča”, University of Belgrade, P.O.Box 522, 11000 Belgrade, Serbia

2) Faculty of Physical Chemistry, University of Belgrade, Studentski trg 12-16, P.O.Box 137, 11001 Belgrade, Serbia

Keywords: $Gd_2Ti_2O_7$ nanopowders, Pechini method, kinetic analysis, structure and morphology

Particularly for nanosized materials, grain size is important factor that affects their structural stability and crystallization properties. The SEM and TEM analysis were conducted to investigate morphology of gadolinium pyrochlore-phase dititanate nanopowders ($Gd_2Ti_2O_7$), prepared by a Pechini method. The results from these measurements show that increasing the heat-treatment temperature resulted in rapid transformation of the porous sponge-like structure into a dense structure composed of regular polyhedron-like nanocrystals, which were uniformly dispersed and weekly aggregated and the average particle size is in the range of 20–50 nm. Structural and crystallization properties of $Gd_2Ti_2O_7$ nanopowders were studied using X-ray diffraction analysis and differential thermal analysis, respectively. The average values of activation energy in the case of non-isothermal crystallization process of powder precursors sample was estimated by various isoconversional (“model-free”) methods, including the Ozawa, Kissinger-Akahira-Sunose and Friedman. Based on the results of DTA analysis and calculated values of Avrami exponent determined through Ozawa and Matusita-Sakka method it was concluded that the crystallization may be characterized as heterogeneous, where the major portion of nucleation started from the surface. In addition, utilizing the Matusita-Sakka equation and the value of E_a (calculated from isoconversional methods), the calculated parameter m is close to 1. These values suggest a three-dimensional crystal growth with polyhedron-like morphology. The presented results of the morphology for the final product were

in good agreement with kinetic analysis, in the case of crystallization process under considered experimental conditions.

Acknowledgements:

This work has been completed and presented at MCM2017 thanks to the on-going Serbia-Croatia bilateral project (2016-2017) ”Radiolytic degradation of some drugs in dilute aqueous solution”. B.Mihaljević and M.Marinović-Cincović thank the Ministry of Science and Education of the Republic of Croatia and the Ministry of Education, Science and Technological Development of the Republic of Serbia for their financial support of this bilateral project.

Characterization of Nd_{3+}-doped TiO_2 nanopowders synthesized by hydrolytic sol-gel method: structural, morphological and optical properties

Bojana Milićević (1), Radenka Krsmanović Whiffen (1), Vesna Đorđević (1), Andreja Gajović (2), Barbora Bartova (3), Damien Bregiroux (4), Miroslav D. Dramićanin (1)

1) Vinča Institute of Nuclear Sciences,University of Belgrade, P.O.Box 522, 11000 Belgrade, Serbia

2) Ruđer Bošković Institute, Bijenička cesta 54, 10000 Zagreb, Croatia

3) École Polytechnique Fédérale de Lausanne EPFL, CH-1015 Lausanne, Switzerland

4) Université Pierre et Marie Curie, Tour 44-54, 4 place Jussieu - 75252 Paris cedex 05, France

Keywords: TiO_2, rare earth doped anatase, application in photovoltaic cells

Titanium dioxide and nanostructures based on TiO_2 have for many years attracted the attention of the scientific community, primarily due to their superior photocatalytic activity, chemical stability, low cost and nontoxicity. However, the practical application of TiO_2 as a photocatalyst is limited as TiO_2 is active only for UV radiation due to its wide band gap and so less than 5% of sunlight can be used for photoexcitation. Numerous studies have attempted to modify the optical properties of TiO_2 mainly by doping it with other elements or by sensitization with various inorganic or organic compounds (1-3). In our project we are searching options to modify. the optical properties of TiO_2 by adjusting its nanostructure and activating both its surface and volume. The properties are optimized primarily for use in photovoltaic devices, but are also applicable to other optoelectronic devices, sensors and photocatalysts. For these applications the ability of the prepared material to absorb light in the widest possible range of the solar spectrum is crucial. In order to increase the efficiency of the absorption of solar radiation and the stability of the material we created an anatase nanopowder of appropriate geometry and changed the chemical structure of TiO_2 by adding atoms of the rare earth metal neodymium. The next step will be to perform the surface modification of TiO_2 with different ligands such as salicylic acid and create thin films from the obtained nanostructures. Anatase TiO_2

nanocrystalline powders were synthesized by a highly practical hydrolytic sol-gel method. The effect of Nd^{3+} doping was studied by X-ray powder diffraction, transmission electron microscopy, Raman, UV-vis and PL spectroscopy. The introduction of 1 at.% Nd^{3+} ions into the TiO_2 matrix was reflected in the reduction of the crystallite size from 14.9 nm to 6.8 nm, and an increase in the specific surface area from 9.7 m^2/g to an astounding 101.5 m^2/g. In this study, an X-ray EDS system (Esprit/Quantax Bruker) in STEM mode in a FEI Tecnai Osiris microscope (200 kV X-FEG field emission gun, X-ray detector Super-X with 4 × 30 mm^2 windowless SDD diodes and a 0.9 sr collection angle) was used. The results from these measurements show that there was no precipitation or enrichment present; all the elements (Ti, O and Nd) were equally distributed. The elemental concentrations in atomic % (within a 95% confidence level) confirmed the presence of 0.98 at.% of introduced neodymium. Diffuse-reflectance spectral analysis revealed a large number of absorption bands in the spectral region of 450–950 nm, originating from the dopant Nd^{3+} ions. A radiative emission was observed in a near-IR region, and the emission bands were assigned to the following Nd^{3+} *f-f* transitions: $^4F_{3/2} \rightarrow {}^4I_{9/2}$ (916 nm), $^4F_{3/2} \rightarrow {}^4I_{11/2}$ (1095 nm) and $^4F_{3/2} \rightarrow {}^4I_{13/2}$ (1385 nm).

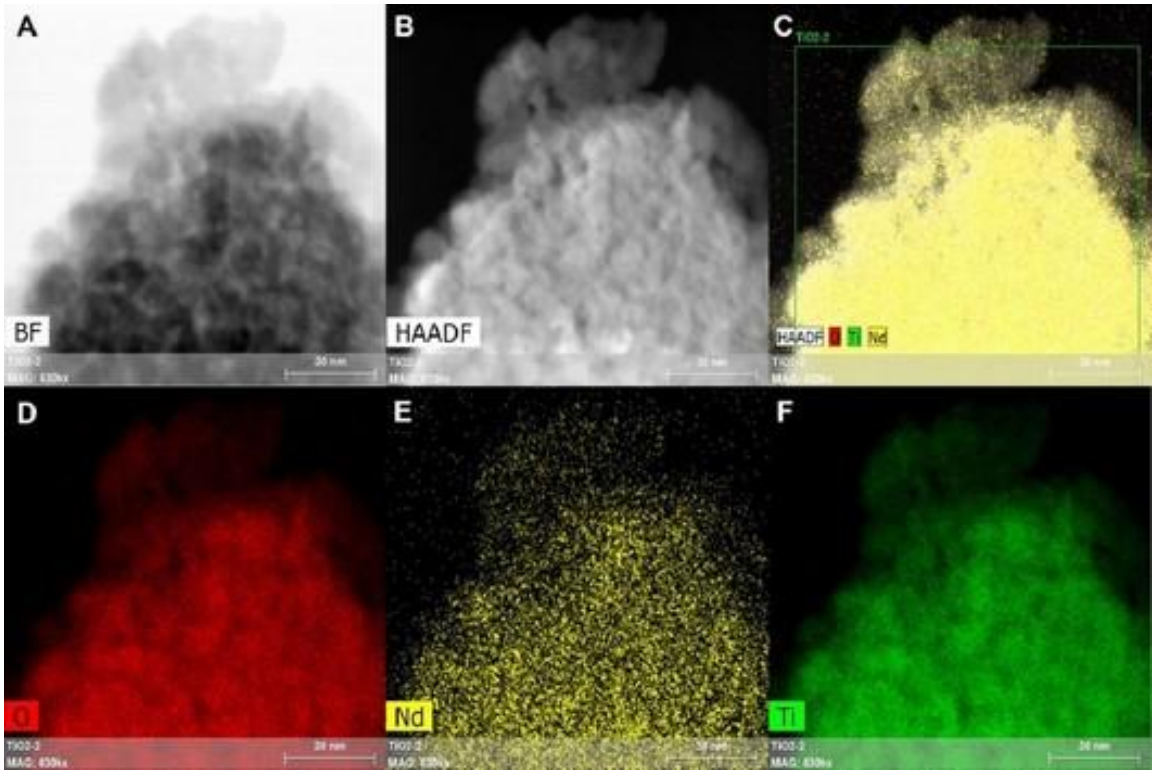

Figure 1. Bright field image, HAADF image and elemental maps of Ti, O and Nd taken from Nd-doped TiO_2 sample.

Acknowledgements:

This work has been completed and presented at MCM2017 thanks to the on-going Serbia-Croatia bilateral project (2016-2017) ”Preparation and characterization of thin films from modified TiO_2 nanostructures for application in photovoltaic cells”. A. Gajević and R. Krsmanović Whiffen thank the Ministry of Science and Education of the Republic of Croatia and the Ministry of Education, Science and Technological Development of the Republic of Serbia for their financial support of this bilateral project.

References:

1. M. Grätzel, Accounts Of Chemical Research 42 (2009) 1788¬-1798.

2. H. Wang et al.,Thin Solid Films 558 (2014) 1–19.

3. M. Plodinec et al., Journal of Alloys and Compounds 591 (2014) 147–155.

TiO_2 modified by Sm and catechol for photovoltaic use

Wiebke Frandsen (1), Marc-Georg Willinger (1), Bojana Milićević (1), Miroslav D. Dramićanin (2), Ivana Panžić (3), Milivoj Plodinec (1,3), Andreja Gajović (3)

1) Fritz Haber Institute of Max Planck Society, Faradayweg 4, 14195 Berlin, Germany

2) Vinča Institute of Nuclear Sciences, University of Belgrade, P.O.Box 522, 11000 Belgrade, Serbia

3) Rudjer Boskovic Institute, Bijenička 54, 10000 Zagreb, Croatia

Nanostructured titanium dioxide is known as a material with excellent physical and chemical properties, such as high specific surface area, high photo-activity and environmental stability as well as low cost synthesis. TiO_2 exists in three different crystalline phases: anatase, rutile and brookite, but it was found that anatase (Eg ~ 3.2 eV) is more photo-active than other modifications. It has gathered much research for its application in solar energy, primarily as electron transporting layer in perovskite and dye sensitized solar cells. Furthermore, numerous studies were done with the aim to furthered improve optical properties of TiO_2 e.g. by doping with other elements and by modification with different organic and inorganic substances. In this work we studied the influence of doping with samarium and furthered modification with organic catechol to improve TiO_2 morphology, structure, optical properties and photovoltaic performance. TiO_2 samples doped with samarium were prepared by sol-gel syntheses, while further modification by catechol was obtained by immersing overnight in solution of different concentration. The structure and morphology of nanostructured TiO_2 doped with Sm and modified by catechol was studied using FEG-TEM Philips CM200-F. HAADF-DF and BF were used with the aim to study doping of the TiO_2 and were performed using JEOL-ARM300. The thin layers of porous doped and modified TiO_2 for photovoltaic application are prepared by sintering of the materials applied at the conducting glass substrates by blade casting. The morphology of the obtained layers was studied by HR-SEM Hitachi. Electron microscopy results were related to Raman spectroscopy measurements, while the optical properties are studied by UV-vis spectroscopy. The dye sensitized solar cells solar cells were prepared using different types of doped and modified TiO_2 as electron conductive layers. TEM measurements of doped as well as doped and additionally modified TiO_2 samples indicated crystallite sizes smaller than 10 nm and strong agglomeration of the particles (Figure 1), which influenced

preparation of the thin layers. HAADF-DF measurements show successful doping of the TiO_2 nanoparticles by Sm that are inbuilt substitutionary in the crystal lattice of TiO_2 (Figure 2). The Raman spectroscopy measurements clearly indicated anatase structure of TiO_2, but also bands characteristic for luminescence due to the Sm in crystal lattice were observed. The solar cell performances will be discussed in the view of structure and crystallite sizes of the starting TiO_2 powder with different doping and modification as well as in the view of the morphology of the obtained electron conducting layers.

Acknowledgements:

This work has been supported in part by Croatian Science Foundation under the project IP-2014-09-9419, by Croatian-Germany bilateral project and by Croatian-Serbian bilateral project.

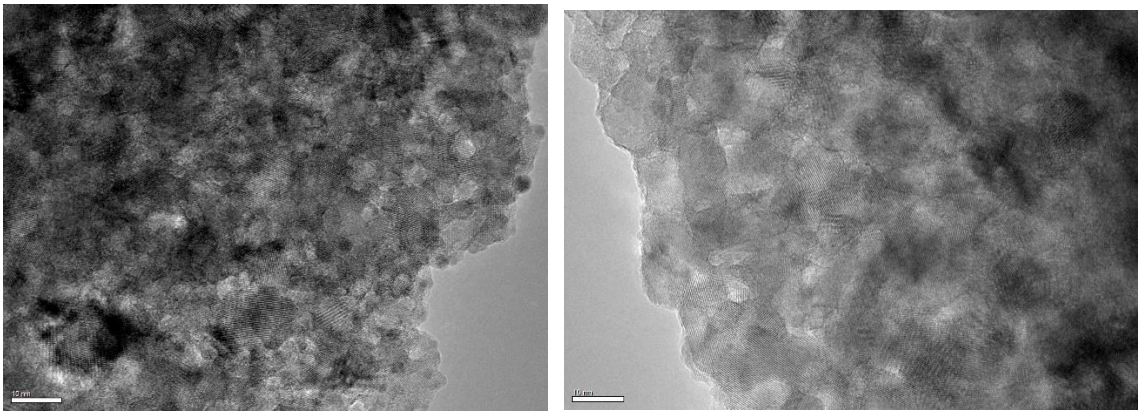

Figure 1. TEM images of (a) TiO_2 samples doped with samarium, (b) TiO_2 samples doped with samarium and further modified by catechol. Scale bars are 10 nm.

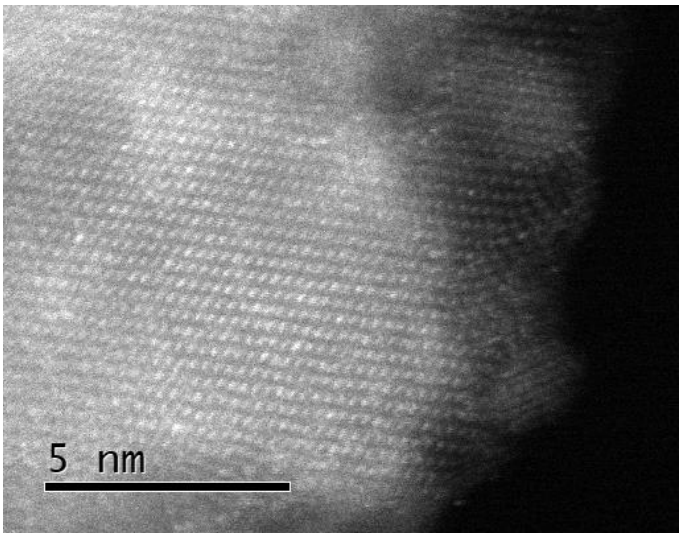

Figure 2. HAADF-DF of TiO_2 doped with samarium.

M6. Semiconductor Materials and Devices

INVITED LECTURES M6:

Advanced STEM-EELS characterisation of semiconductor materials beyond the nanoscale

Giuseppe Nicotra (1), Ioannis Deretzis (1), Quentin Ramasse (2), Fiorenza Patrick (1), Filippo Giannazzo (1), Enzo Rotunno (3), Paolo Longo (4), Maria Caporali (5), Maurizio Perruzini (5), Laura Lazzarini (3), Giancarlo Salviati (3), Antonio Politano (6), Corrado Bongiorno (1), Fabrizio Roccaforte (1), Antonino La Magna (1), Corrado Spinella (1)

1) IMM-CNR Institute, Zona industriale Strada VIII, 5, 95121 Catania, Italy

2) SuperSTEM Laboratory, STFC Daresbury Campus, Daresbury WA4 4AD, United Kingdom

3) IMEM-CNR Institute, Parco Area delle Scienze 37/A, 43124 Parma, Italy

4) Gatan Inc., 5794 W. Las Positas Blvd., Pleasanton, CA 94588, USA

5) CNR-ICCOM, Via Madonna del Piano 10, 50019 Sesto Fiorentino, Italy.

6) Dipartimento di Fisica, Universit a della Calabria, via ponte Bucci, cubo 31/C, 87036 Rende (CS), Italy

Keywords: STEM, HAADF, EELS, semiconductors, 2D materials

Nowadays Cs-corrected scanning transmission electron microscopes (STEM) have reached such a high performances and versatility to allow simultaneous acquisition of both structural and chemical informations at atomic scale. Direct atomic resolution images may be acquired by STEM-HAADF configuration and the electron properties may be probed simultaneously by EELS or EDS spectroscopy. EELS spectroscopy combined with ColdFEG electron source equipped microscopes gives information comparable with that of a synchrotron light source with the plus of much higher spatial resolution. An extensive study of semiconductor materials, performed through the "sub-Ångstrom microscope lab" located at CNR-IMM laboratories in Catania, will be presented by coupling high spatial and high energy resolution. A series of recents results, such us the study of few layers of exfoliated MoS2 for application in the field

of opto- and microelectronics will be presented. Among the 2D materials, the Phosphorene is particularly important and a study, both in plan and cross view, together with its electronic properties will reported. Combined STEM and EELS datasets acquired at the interfaces of systems made by Graphene based specimens growth on different kind of substrates, together with system made by SiO_2 grown on SiC, for application in the field of power semiconductor devices, will be also presented together with density functional theory (DFT) simulations, obtained by using WIEN2K and FEFF, for the interpretation of experimental EELS data.

Acknowledgements:

This work was performed at Beyondnano CNR-IMM, which is supported by the Italian Ministry of Education and Research (MIUR) under project Beyond-Nano (PON a3_00363).

References:

1. Rotunno et. al., Nat Commun et al 2016; 7: 13044.

2. G Nicotra et. al., Physical Review B, Volume: 91 Issue: 15 Pages: 155411 3. G Nicotra et. al., ACS nano, Volume: 7 Issue: 4 Pages: 3045-3052 g on si-sic .

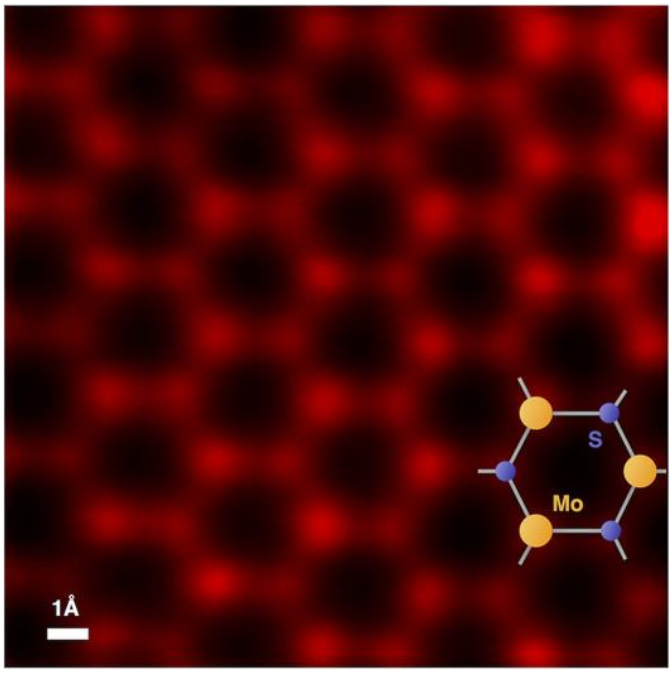

Figure 1. Atomic resolution STEM-HAADF image of few layers of MoS_2 flakes.

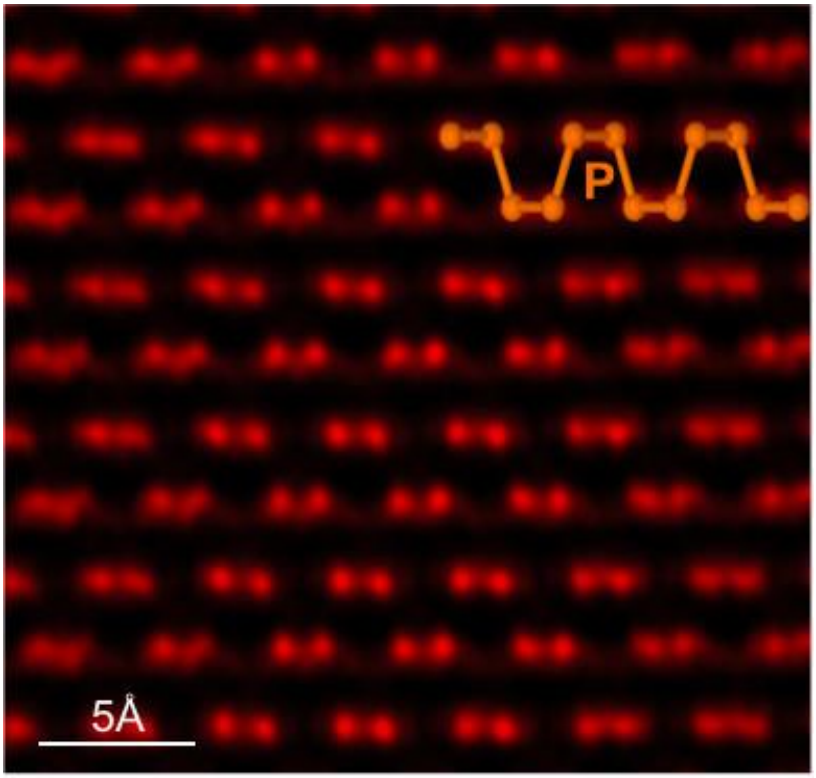

Figure 2. Atomic resolution STEM HAADF image of AB stacked Black Phosphorus in cross view.

Atomic-scale characterisation of accumulated charged defects at domain walls in $BiFeO_3$

Goran Dražić (1), Andreja Benčan (2), Hana Uršič (2), Boštjan Jančar (2), Gašper Tavčar (2), Maja Makarovič (2), Julian Walker (2), Barbara Malič (2), Naonori Sakamoto (3), Dragan Damjanović (4), Tadej Rojac (2)

1) National Institute of Chemistry, Hajdrihova ulica 19, 1001 Ljubljana, Slovenia

2) Jožef Stefan Institute, Jamova cesta 39, 1000 Ljubljana, Slovenia,

3) Shizuoka University, 3-5-1 Johoku, Naka-ku, Hamamatsu City, Japan

4) Swiss Federal Institute of Technology – EPFL, CH-1015 Lausanne, Switzerland

Keywords: $BiFeO_3$, ferroelectrics, domain walls, STEM, EELS

Multiferroic bismuth ferrite ($BiFeO_3$) with Neel and Curie temperatures well above room temperature is a promising material for high-temperature piezoelectric devices. A serious drawback is its high electrical conductivity, which has been recently found to be localized at domain walls (DW) (1, 2). Origin of this local conductivity was theoretically explained with the accumulation of charged defects at domain walls, but no experimental evidence of these defects has been yet obtained. Recently, we have reported that in contrast to the usually assumed oxygen vacancies, the dominant defects in $BiFeO_3$ are bismuth vacancies along with compensating electron holes, associated with the presence of Fe^{4+} (3). We proposed that in addition to electrostatic forces, the lattice strain at DWs may also drive the defects towards the DW region (Figure 1). In this work two analytical techniques (electron-energy loss spectroscopy, and quantitative high-angle annular dark-field, imaging) which lead to the identification of iron (IV) ions and bismuth vacancies, accumulated at the domain walls will be explained and discussed. We will further show the results of the domain wall dynamics studied by ex-situ poling experiments. It will be demonstrated that the local domain-wall conductivity can be tailored by material processing. The structure of domain walls in the BFO ceramics was analyzed by atomically resolved Cs-probe corrected JEM-ARM 200CF STEM microscope, operated at 200 kV. Atomic column positions were determined using 2D Gaussian fit and normalized Bi-column intensities were measured from background subtracted HAADF images.

A systematic lowering of the intensity of Bi columns at the domain wall was observed. Using quantitative analysis we found that all types of domain walls (71°, 109°and 180°) exhibit around 20% lowering of the column intensity. To correlate the Bi column intensities with the amount of Bi vacancies we performed HAADF image simulations with QSTEM code. Calculations were done on a R3c $BiFeO_3$ structural model (ICSD #97591) in which the concentration of Bi vacancies was varied in selected columns. By comparing the results obtained from simulated images with those obtained experimentally we estimated a concentration of 30% of Bi vacancies at DWs. These vacancies are likely compensated with the presence of Fe^{4+} determined from EELS analysis (Figure 2) (3). Experimental details, estimations of errors of the various techniques used during this study, ex-situ poling experiments and the influence of the preparation conditions on the presence and concentration of Bi vacancies and Fe^{4+} ions will be explained and discussed.

Acknowledgements:

This work was financed by the Slovenian Research Agency (programmes P2-0105 and P2-0393; projects J2-5483 and J2-6754).

References:

1. J. Seidel et al., Nature Materials 8 (2009), p. 229.

2. T. Rojac, et al., Adv. Funct. Mater. 25 (2015), p. 2099.

3. T. Rojac, et al., Nature Materials (2017), 16, p. 322.

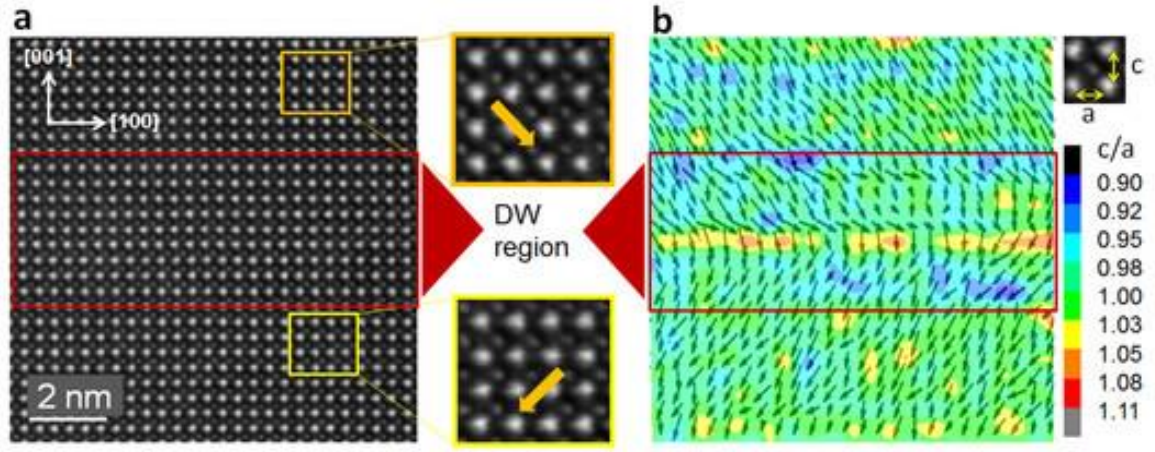

Figure 1. HAADF-STEM image of (a) 109° DW with indicated DW region (red box) and Fe displacements (see arrows in the insets). (b) vector map of Fe displacements from the center of the Bi sublattice (arrows) superimposed on the c/a lattice-strain map.

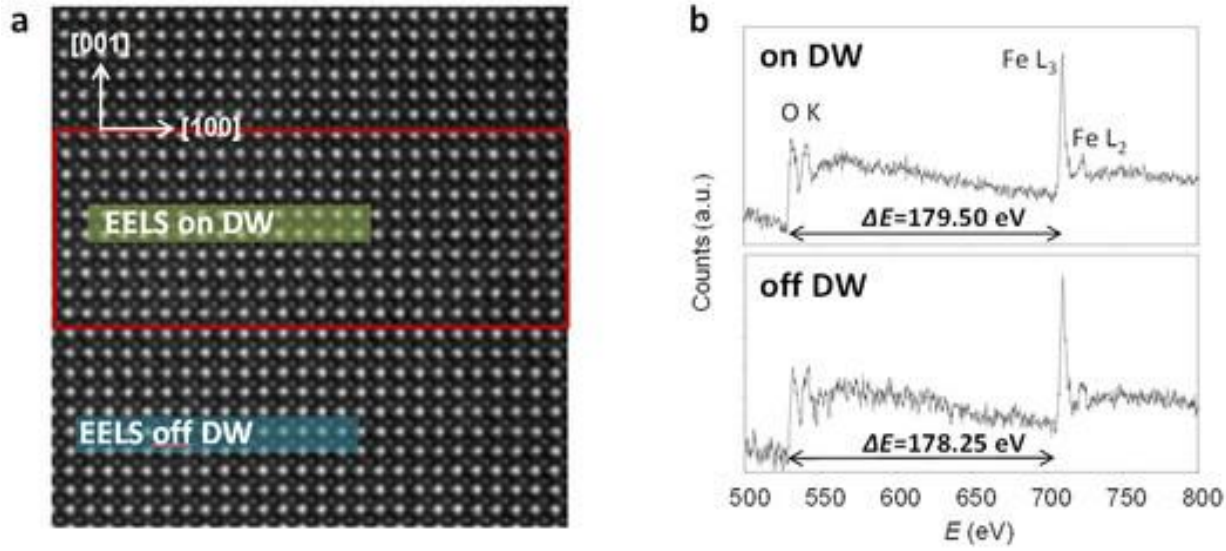

Figure 2. (a) HAADF-STEM image of a 109° DW indicating on and off DW areas where EELS spectra were collected. (b) EELS spectra from indicated areas showing different O K – Fe L3 onset energy difference.

ORAL PRESENTATION M6:

Structural analysis of InAs/InP nanowires at atomic scale

Antonietta Taurino (1), Massimo Catalano (1), Antonio Della Torre (1), Rosaria Rinaldi (2), Stefano Roddaro (3), Francesco Rossella (3), Lucia Sorba (3), Daniele Ercolani (3), Stefano Masiero (4)

1) Institute for Microelectronics and Microsystems IMM-CNR, via Monteroni 73100 Lecce, Italy

2) Dipartimento di Matematica e Fisica 'Ennio de Giorgi', Università del Salento, I-73100 Lecce, Italy

3) NEST, Scuola Normale Superiore e Istituto Nanoscienze-CNR, Pisa, Italy

4) Dipartimento di Chimica "Giacomo Ciamician", Università di Bologna, Via S.Giacomo 11, Bologna, Italy

Keywords: nanowires, InAs/InP heterostructure, Au-catalyst epitaxy, polytypism

Self-assembled semiconductor nanowires (NWs) are nanostructured materials very promising for application in nanoelectronics. Homogeneous, as well as radially or axially heterostructured nanosystems can be obtained by different growth methods and can be used as a whole in the pristine assembly, or as single nanostructures isolated on substrates for the realization of nanodevices (1). In this work, InAs/InP heterostructured NWs have been grown by Au-catalyst epitaxy; the heterostructure nominally consists of a 2 μm long InAs NW containing two 5 nm-thick InP barriers, separated by a 20 nm long InAs island. These nanostructures have been recently used to fabricate highly-confined single-electron transistors (SETs) (2). The evolution of the crystalline structure of InAs NWs may be affected by polytypism, i.e. by the occurrence of hexagonal Wurtzite and cubic Zinc-Blende structure in the same NW (3). Polytypism is naturally observed in NWs grown in the preferential ⟨111⟩ B direction and is favoured by the fact that the cubic and hexagonal structures exhibit the same crystalline arrangement in the (111) and (001) planes, respectively. Zinc blende (111) differs from wurtzite (001) only by virtue of the stacking sequence of atomic layers, being ABCABC for zinc blende and ABAB for wurtzite.

Polytypism strongly affects transport phenomena occurring in NW-based electronic devices. Thus considerable effort is made in order to understand and finally control polytypism in NWs.Here InAs/InP NWs, preserving the same crystalline arrangement along the whole growth axis, were obtained by a chemical beam epitaxy. Growth was performed at 420°C using trimethylindium, tertiarybutylarsine and tributylphosphine as precursors. No growth interruption but a switch of the group V precursors was used at the heterointerface. Scanning Transmission Electron Microscopy (STEM) investigations were carried out by using a JEM-ARM200F instrument, operating at 200 kV, with a resolution of 78 pm. Figure 1 reports the high angle annular dark field (HAADF) STEM images of InAs/InP NWs: the low magnification image (a) shows few isolated NWs (the bright contrast particle on the tip is the catalyst) and the high resolution image (b) evidences the sequence of the InAs and InP semiconductor materials and the relevant interfaces. The stacking sequence of the atomic layers is compatible with the wurtzite structure, as evidenced by the high resolution image (c), obtained from the InAs region, and showing the In-As dumbbell in the 010 zone axis orientation. Stacking faults are observed only at the InAs/InP interface, where the transition from the ABAB to the ABCABC sequence is evident but confined to few atomic MLs. Analytical investigations were carried out in order to study the chemical sharpness of the interfaces and to obtain information about the functionalization of the NW surface with metallo-porphyrin molecules, for possible applications in molecular nanoelectronics.

References:

1. M.S. Gudiksen et al., Nature 415 (2012) 617-620.

2. L. Romeo, et al., Nano Lett. 12 (2012) 4490−4494.

3. D. Kriegner et al., Nano Lett. 11 (2011) 1483–1489.

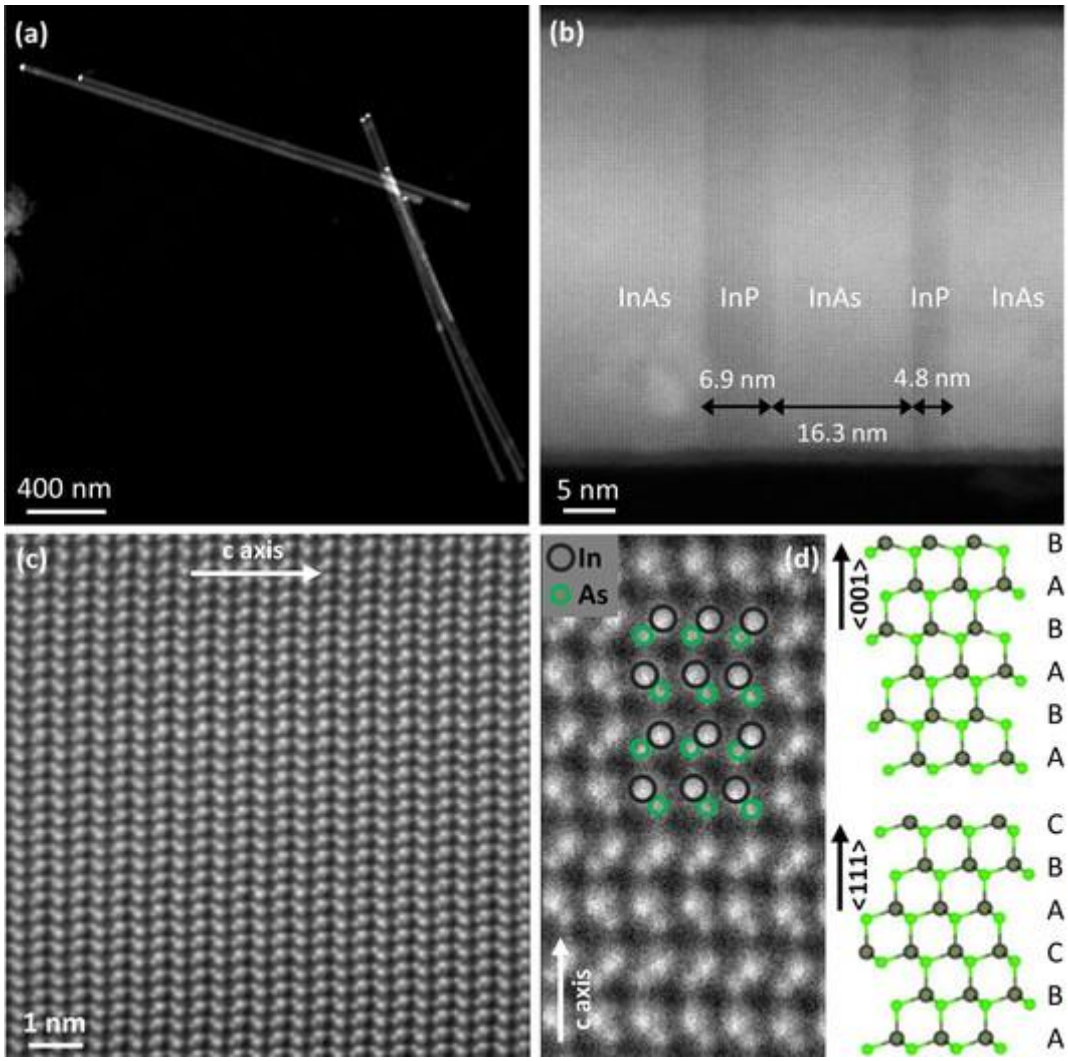

Figure 1. (a) low mag HAADF image of a group of NWRs and the relevant high resolution STEM images (b, c, d) showing the InAs/InP heterostructure (b) and the InAs region (c). In (d), the hexagonal stacking sequence of atomic layers is highlighted.

Ferromagnetic manganese germanide thin films characterization by correlation of scanning electron microscopy, transmission electron microscopy and laser assisted atom probe tomography

Hannes Zschiesche (1), Elie Assaf (1), Andrea Campos (2), Marion Descoins (1), Martiane Cabié (2), Thomas Neisius (2), Maxime Bertoglio (1), Christian Dominici (2), Khalid Hoummada (1), Sylvain Bertaina (1), Alain Portavoce (1), Ahmed Charaï (1), Dominique Mangelinck (1), Claude Alfonso (1)

1) IM2NP - CNRS, Aix-Marseille University, Faculté des Sciences de Saint-Jérôme, F-13397 Marseille, France

2) CP2M, Aix-Marseille University, Faculté des Sciences de Saint-Jérôme, F-13397 Marseille, France

Keywords: Manganese Germanide thin films; Structure and composition; Electron microscopy; Atom probe tomography; Ferromagnetism/energy harvesting

Manganese Germanides are of interest for their magnetic properties. In particular Mn_5Ge_3 is ferromagnetic with a Curie temperature close to room temperature (T_C=297 K (1)). Such thin films are thus promising for applications as spintronic devices. However, in order to reach spin current injections at temperatures higher than room temperature, tuning of the Curie temperature is crucial. A precise engineering of the Curie temperature requires an even better understanding of the mechanisms involved during the formation of these thin films. Therefore, to get complementary characterization about the structure and the composition at the atomic scale, a correlative investigation using SEM (Zeiss GeminiSEM 500), TEM (FEI Titan 80 Cs-corrected) and atom probe tomography (APT, LEAP 3000XHR) was performed on Mn-Ge thin films. There are different possibilities to effect a change of the magnetic properties of a thin film. For example, it was recently proposed that a significant increase of the Curie temperature in Mn_5Ge_3 thin films can be performed by adding C into Mn_5Ge_3 (1). Additionally, molecular beam epitaxy allows to grow Mn_5Ge_3 in epitaxy on Ge(111) substrate with high purity and a Mn_5Ge_3/Ge interface with a very good crystallinity and no defects (1). In this work, Mn_5Ge_3 thin films were grown on SiO_2 using magnetron sputtering at room temperature followed by an annealing in a furnace at 400°C. Successive or simultaneous deposition was done in order to

compare two kinds of reaction: reactive diffusion (RD) and non-diffusive reaction (NDR), respectively. An increase of the Curie temperature of NDR has been found (2) (Figure 1) while the RD exhibit similar magnetic properties as MBE-grown monocrystalline Mn_5Ge_3 thin films (1,2). SEM and TEM EDS show that films are not homogeneous with grains whose stoichiometry is compatible with the one of Mn_5Ge_3 and others with higher concentration of Ge. To achieve a better precision on composition, APT analysis has been performed and points out significant differences: In the RD films, the composition is in the expected stoichiometry of Mn_5Ge_3 (3) with slightly less Ge (~ 0.4 at. %) and a small amount of C. In contrast, in the NDR films the concentration of Ge is unexpectedly lower (~ 5.3 at. %) than the range of stoichiometry for Mn_5Ge_3 (3). Instead, an important concentration of O, a higher C concentration and a low concentration of N were found. TEM cross-section images show the NDR films are polycrystalline with a thickness of about 45 nm (Figure 2b). In addition, a non-expected multilayer-type contrast is visible with a period of about 6 nm. The APT analysis exhibits similar layers containing Manganese oxides (Figure 2c) which can be correlated to the contrast in TEM. Furthermore, to check the influence of a single crystal substrate, Mn_5Ge_3 was grown on Ge(111) under same conditions.

References:

1. M. Petit et al., Thin Solid Films 589 (2015) 10.1016/j.tsf.2015.05.068.

2. E. Assaf et al., Appl. Phys. Lett. 110 (2017) 10.1063/1.4976576.

3. A.B.Gokhale et al. Bulletin of Alloy Phase Diagrams 11, 5 (1990) 10.1007/BF0302929.

Acknowledgements:

This work was supported by the French government through the program “Investissement d’Avenir A*MIDEX” (Project APODISE, No. ANR-11-IDEX-0001-02) managed by the National Agency for Research (ANR).

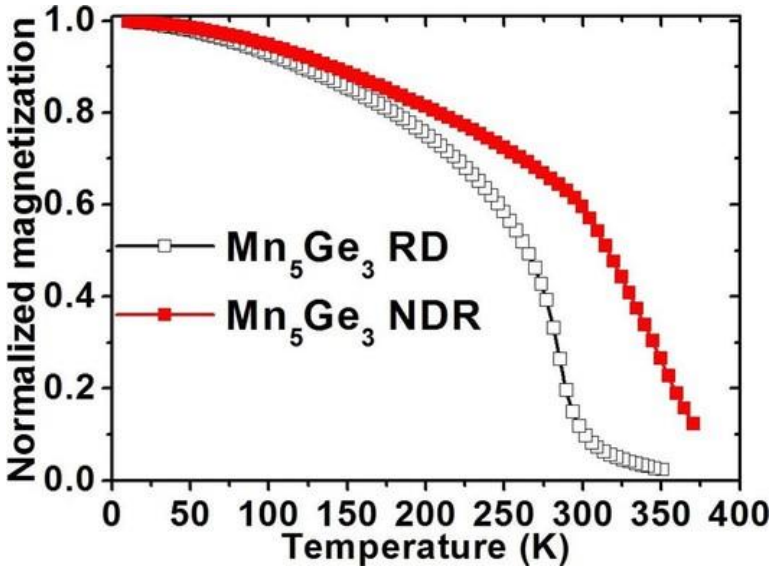

Figure 1. Evolution of the magnetization for rising temperature with a magnetic field of 0.01 T applied in-plane: The Curie temperature of Mn_5Ge_3 RD is ~300K, for Mn_5Ge_3 NDR the Curie temperature is ~385 K. From (2).

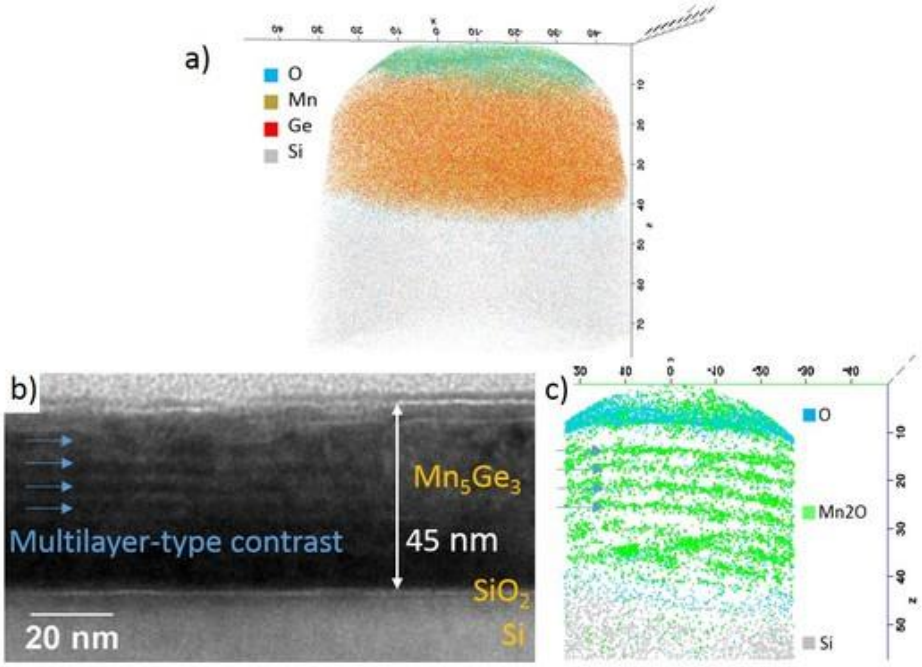

Figure 2. (a) Exemplary 3d-APT reconstruction of a NDR Mn_5Ge_3 tip; (b) Bright-field TEM image of NDR Mn_5Ge_3 film grown on SiO_2. A multilayer-type contrast inside the film is visible; (c) Slice of APT reconstruction of (a) exhibits the presence of layers of Mn_2O.

Microscopy of nitride layers with integrated graphene

Bella Pécz (1), Andras Kovács (2), Martial Duchamp (2), Anelia Kakanakova (3), Rositza Yakimova (3)

1) Institute for Technical Physics and Materials Science, Centre for Energy Research, Hungarian Academy of Sciences, Konkoly-Thege 29-33, Budapest, Hungary

2) Ernst Ruska-Centre for Microscopy and Spectroscopy with Electrons and Peter Grünberg Institute, Forschungszentrum Jülich, 52425 Jülich, Germany

3) Department of Physics, Chemistry and Biology, Linköping University, S-581 83 Linköping, Sweden

Keywords: GaN, graphene

Due to its excellent physical properties graphene has been the subject of several scientific papers in the last years. The integration of graphene into GaN devices is also a hot topic. Graphene contacts to III-nitride devices are studied in several laboratories and even new device concepts like hot electron transistor were published (1). Graphene was also integrated into GaN power devices in order to decrease the self-heating in an efficient way. On the other hand there are experiments in order to form 2D layers of nitrides with intercalation growth between SiC and graphene.The present work focuses on the microscopy of nitride layers grown on patterned graphene/SiC, which is a promising heat management solution in high pwer GaN transistors. The nitride layers were grown on patterned graphene/6H-SiC by Metalorganic Chemical Vapour Deposition (MOCVD). The growth is similar to the well-known Epitaxial Lateral Overgrowth method in which the graphene buried stripes are overgrown laterally from the window regions, where AlN could grow on bare SiC with epitaxy. An AlN buffer layer was first deposited on patterned graphene/6H-SiC surface followed by a deposition of ~ 300 nm thick $Al_{0.2}Ga_{0.8}N$ and ~ 1.5 µm thick GaN layer (2). The top surface of the layer is flat. The AlN buffer deposited onto the graphene stripe was grown in a 3D way (Figure 1a). A peculiar detail of this study is the appearance of the AlN/GaN superlattices, which were formed in a self-organised way over the buffer layer. Instead the ternary AlGaN we have superlattice (Figure 1.b and c) in which the thickness of the AlN/GaN is determined by the available

elements from the $Al_{0.2}Ga_{0.8}N$ which we wanted to grow. The control sample (without graphene) showed a much more flat AlN buffer and a ternary $Al_{0.2}Ga_{0.8}N$ on that without any phase separation. EDX mapping and also superlattice reflections show however, clearly the complete phase separation in the case the nitride layers are grown on graphene. We suppose, that some excess carbon induced the phase separation. Figure 2 shows the edge of graphene and how that was overgrown laterally by AlN. The high resolution image in Figure 2 shows three layers of graphene. Below them the last SiC layer shows a brighter contrast, this is known as buffer layer for the graphene. EELS spectroscopy gave further details on the graphene layers with a layer by layer resolution. The HAADF image in Figure 2.c is shown with the Si and Al maps. The results show that we can grow high quality GaN layer over graphene/SiC, which can serve as templates for high power GaN devices.

Acknowledgements:

Authors thank the support of the Hungarian National Scientific Foundation (OTKA) through Grant No. NN118914 (GRIFONE FLAG-ERA).

References:

1. F. Gianazzo et al., Phys. Status Solidi A, 1-16 (2016) DOI 10.1002/pssa.201600460.

2. A. Kovács et al., Advanced Materials Interfaces, published online: 22 DEC 2014 | DOI: 10.1002/admi.201400230, Vol. 2, Iss. 2, January 21 201597.

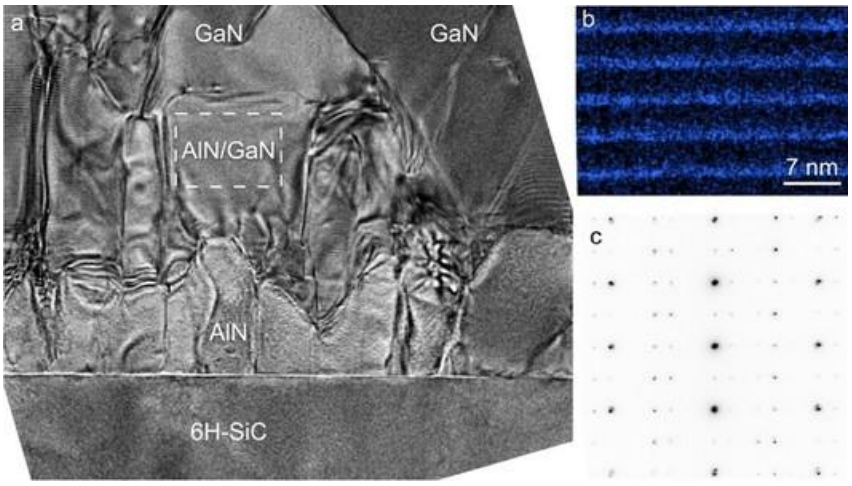

Figure 1. (a) Cross section of the interface region with AlN buffer, AlN/GaN superlattices and GaN layer, (b) EDXS map of Al in the region marked by dashed box in Figure 1a. (c) diffraction pattern taken in the superlattice region.

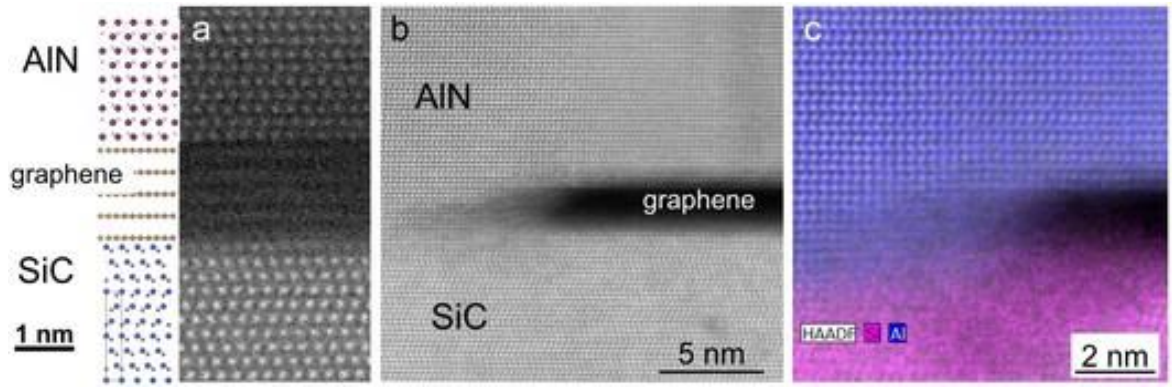

Figure 2. (a) graphene overgrown by AlN together with the atomic arrangements (b) high resolution HAADF STEM image (c) HAADF image with Si and Al maps.

Influence of microstructure of $Ag_{16.7}Sb_{30}Te_{53.3}$ bulk thermoelectrics on their performance

Lamya Abdellaoui (1), Siyuan Zhang (2), Oana Cojocaru-Mirédin (3), Yaron Amouyal (4), Dierk Raabe (2), Christina Scheu (5)

1) Phd Student in Max-Planck Institut für Eisenforschung GmbH, Max-Planck Straße 1, 40237 Düsseldorf, Germany

2) Max-Planck Institut für Eisenforschung GmbH, Max-Planck Straße 1, 40237 Düsseldorf, Germany

3) University of RWTH Aachen, I. Institute of Physics, Sommerfeldstraße 14, 52056 Aachen, Germany.

4) Department of Materials Science and Engineering, Technion-Israel Institute of Technology, Haifa, 3200003, Israel.

5) Christina Scheu, Max-Planck-Straße 1, 40237 Düsseldorf, Germany

Keywords: Thermoelectric materials, Silver-antimony-telluride compounds, Thermal conductivity, Electron microscopy, Microstructure evolution.

The challenge of waste heat recovery ranging from transportation vehicles to oil refineries and multiple industrial infrastructures motivates research on thermoelectric materials (TE). TE compounds can directly convert heat into electricity through the Seebeck effect. The conversion efficiency is determined by the dimensionless *figure of merit*, ZT, which depends on the thermal and electrical conductivity, the Seebeck coefficient and the temperature. Attempts to optimize ZT require reducing lattice thermal conductivity, while maintaining relatively high values of electrical conductivity. In our study, we synthesized and characterized the ternary Ag–Sb–Te system which is a subsystem of the very promising quaternary compounds Pb-Ag-Sb-Te (LAST) and $(AgSbTe_2)_{1-x}(GeTe)_x$ (TAGS), alloys which can be achieved via doping of $AgSbTe_2$. The samples having the nominal composition of $Ag_{16.7}Sb_{30}Te_{53.3}$ were investigated after quenching and subsequent heat treatments for 8h and 192h at 380°C by several probing methods such as electron backscatter diffraction (EBSD), scanning electron microscopy (SEM), Cs-probe corrected scanning transmission electron

microscopy (STEM), focused ion beam (FIB) sectioning, energy dispersive X-ray spectroscopy (EDS) and atom probe tomography (APT). This allowed us to obtain information on chemistry and crystal structure of the various microstructural features, which form during the heat treatment, and which are important for the TE performance.For example, the sample annealed at 380 °C for 8h exhibits a relatively good TE performance with ZT=0.5 at 300°C. This is related to the various microstructural features such as the large precipitates (3µm width) observed with EBSD which are shown in Figure 1 (a). The large precipitates contain 1 to 8% Ag and assume Sb_2Te_3 crystal structure. We prepared a site specific TEM lamella by FIB of the interface region between the metastable lamellar Sb-Te rich precipitates and the cubic matrix, Figure 1 (c). High angle annular dark field STEM images of this region confirmed the 5 atomic layer stacking sequence typical for the Sb_2Te_3 crystal structure and revealed an abrupt interface (Figure 1 d-f). EDX conducted in the STEM showed that we have up to 10% Ag embedded in the Sb_2Te_3 precipitates and no enrichment of any of the elements at the interface, which is in accord to the APT results. We find correlation between the measured thermal and electrical conductivities and the applied heat treatments, we attribute these findings to the delicate interplay between formation of precipitates and the corresponding gradual decay in the degree of quenched-in solute supersaturation. Thus, in our opinion, these structural and chemical informations are essential for understanding the mechanisms acting on the efficiency improvement and thus to further design better TE materials.

References:

1. Oana Cojocaru-Mirédin, Lamya Abdellaoui, Michael Nagli,Siyuan Zhang,Yuan Yu,Christina Scheu, Dierk Raabe, Matthias Wuttig, and Yaron Amouyal, "Role of Nanostructuring and Microstructuring in Silver Antimony Telluride Compounds for Thermoelectric Applications". ACS Appl. Mater. Interfaces.2017.

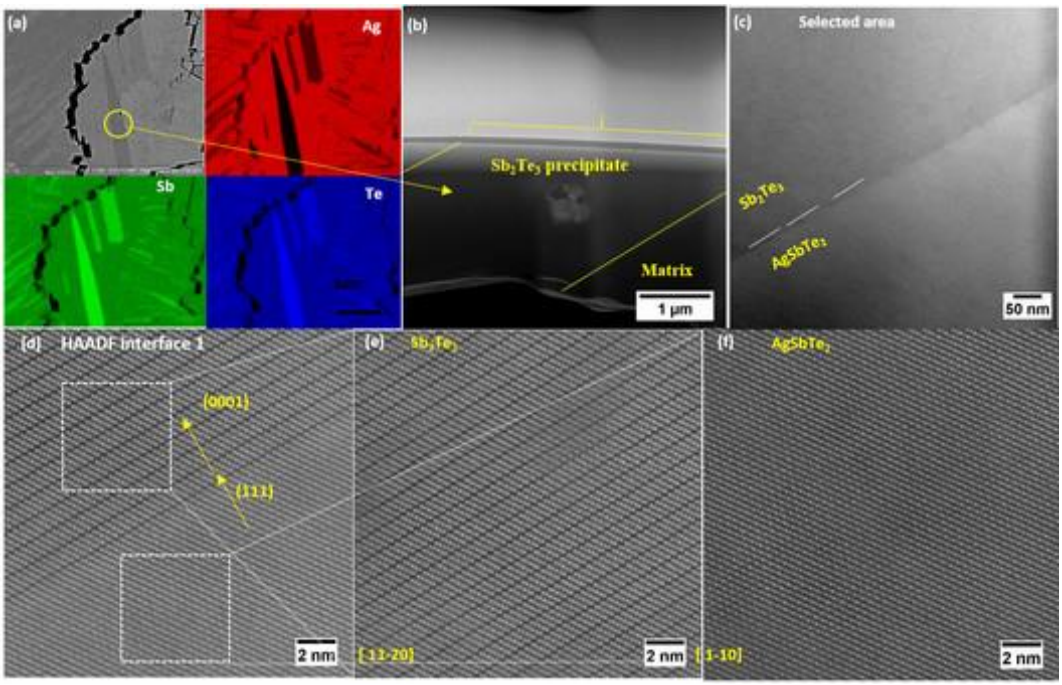

Figure 1. (a) SEM image and corresponding elemental maps showing the presences of large precipitates, (b) image of the area investigated by STEM, (c) overview of the region between the matrix and precipitate,(d)HAADF image of the $(Ag,Sb)_2Te_3$ precipitate/$AgSbTe_2$ matrix interface. Atomic structure of (b) $(Ag,Sb)_2Te_3$ precipitate and (c) $AgSbTe_2$ matrix.

POSTER PRESENTATIONS M6:

In situ formation of crystallographically-oriented semiconductor nanowire arrays via selective vaporization for high-performance optoelectronic applications

Xing Huang (1), Yongqiang Yu (2), Travis Jones (1), Hua Fan (1), Lei Wang (3), Jing Xia (3), Zhujun Wang (1), Lidong Shao (4), Xiangmin Meng (3), Marc Willinger (4)

1) Fritz-Haber Institute of Max-Planck Society, Faradayweg 4-6, 14195, Berlin, Germany

2) Hefei University of Technology, Hefei, 230009, P. R. China

3) Technical Institute of Physics and Chemistry, Chinese Academy of Sciences, 100190, Beijing, P. R. China

4) Shanghai University of Electric power, No.2588 Changyang Road, Yangpu District, 200090 Shanghai, P. R. China

Keywords: Semiconducting nanowire arrays, wurtzite, selective vaporization, *in situ* observation, photodetectors

Mass production of high-quality semiconductor nanowire arrays (SNAs) with precisely controlled orientation and structure is essential for their application in nanoelectronics and optoelectronics. Herein, we report a facile and efficient method for large-scale fabrication of [0001]-oriented CdS and CdSe SNAs *via* direct heating of their bulk components in a H_2/Ar atmosphere. *In situ* environmental SEM experiments clearly demonstrate that the SNAs form through selective vaporization with respect to the crystallography of wurtzite crystals. Together with DFT calculations we propose that the selective vaporization relies on the low symmetry of the wurtzite structure with large differences between surface energies of low-index planes. Further, we demonstrate that the approach can be extended to zinc-blende type structures through a cation exchange process. Specifically, we show that wurtzite-structured ZnS nanowire arrays are achieved by heating powder mixture of wurtzite CdS and zinc-blende ZnS. In this process, the CdS crystal serves as a WZ structural template for the formation of nanowire arrays. Finally, the high-quality of the SNAs is demonstrated by fabrication of

photodetector. The device presents excellent performances, including large on/off ratio (~10^7), high detectivity (~1.86×10^{13} Jones), high linear dynamic range (~140 dB), and fast photo-response speed. We believe that our method represents a transformative new fabrication platform for large-scale fabrication of orientated SNAs with novel functionalities.

References:

1. X. Huang, Y. Q. Yu, T. Jones, H. Fan; L. Wang, J. Xia, Z. J. Wang, L. D. Shao, X. M. Meng, M. G. Willinger, Adv. Mater. 28 (2016) 7603-7612.

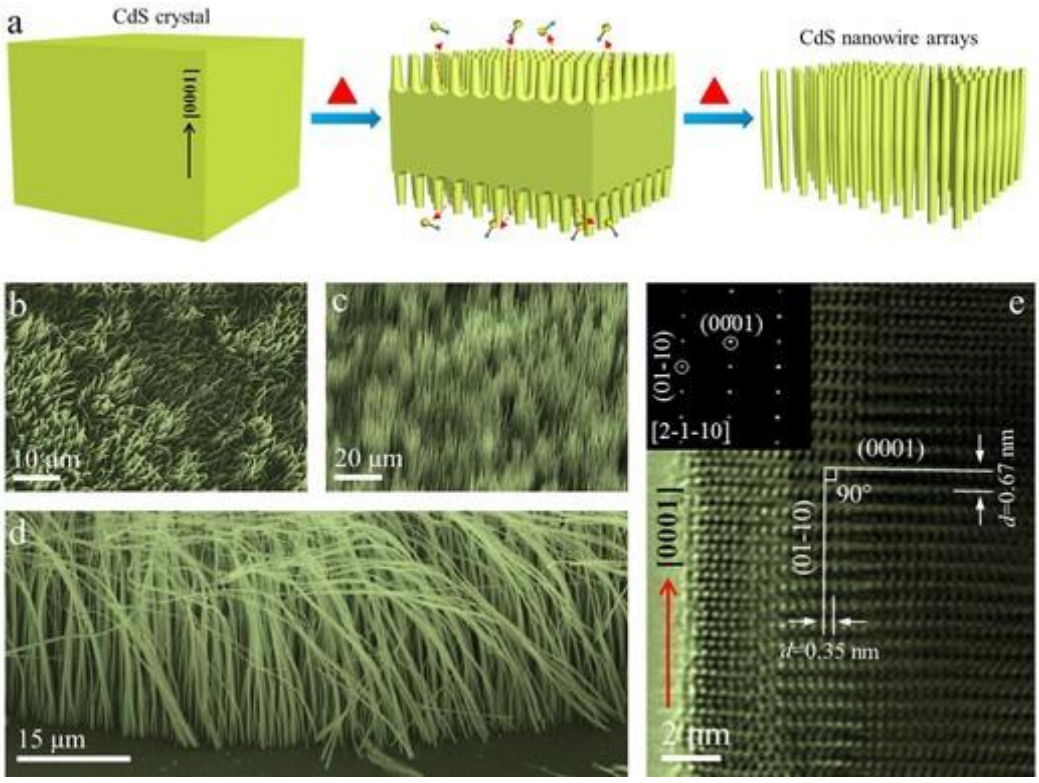

Figure 1. (a) Schematic drawing of *in situ* formation of semiconducting nanowire arrays; (b-d) SEM images of formed CdS nanowire arrays; (e) HRTEM image and corresponding SAED pattern of a CdS nanowire.

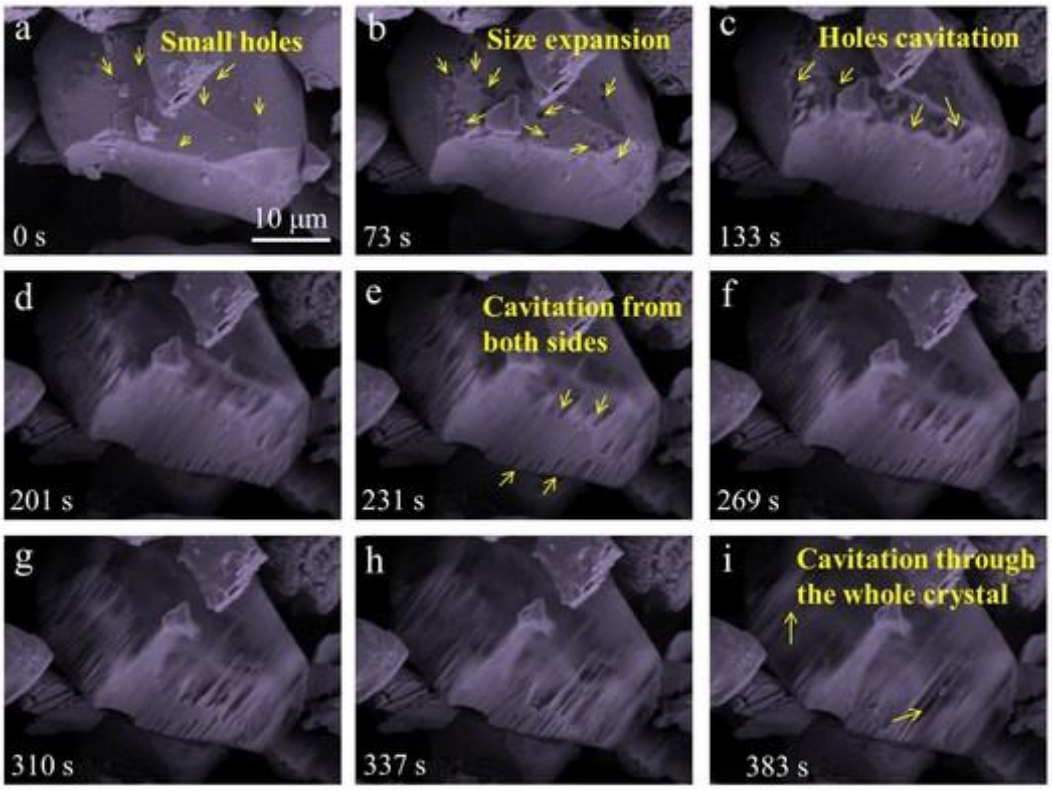

Figure 2. A series of SEM images recorded during real-time observation of formation of CdS nanowire arrays upon heating.

TEM study of the as-deposited and annealed Ga_2O_3 films grown by vapor phase epitaxy

Ildikó Cora (1), Francesco Mezzadri (2), Francesco Boschi (3), Matteo Bosi (4), Maria Čaplovičová (5), Gianluca Calestani (2), István Dódony (6), Béla Pécz (1), Roberto Fornari (3)

1) Institute for Technical Physics and Materials Science, Centre for Energy Research, Hungarian Academy of Sciences, Konkoly Thege M. út 29-33, H-1121 Budapest, Hungary

2) Department of Chemistry, University of Parma, via Università, 12 - I 43121 Parma, Italy

3) Dept. of Mathematical, Physical and Computer Sciences, University of Parma and IMEM-CNR, Parco Area delle Scienze 7/A, 43124 Parma, Italy

4) IMEM-CNR Institute, Parco Area delle Scienze 37/A, 43124 Parma, Italy

5) Slovak University of Technology, Vazovova 5, 812 43 Bratislava 1, Slovak Republic

6) Department of Mineralogy, Eötvös Loránd University, Pázmány Péter sétány 1/a, 1117 Budapest, Hungary

Keywords: epitaxial Ga_2O_3, HRTEM, ED, XRD, MOVPE

Ga_2O_3 is a wide bandgap semiconducting oxide (~4.7 eV), promising for UV optoelectronics and power electronics. Several Ga_2O_3 layers were grown onto (001) surface of α-Al_2O_3 by vapor phase epitaxy at 650 °C and 100 mbar for 15 min. and some of them were annealed up to 1000 °C for different time (2 and 6 hours). The as-deposited layers and two annealed samples were studied by high resolution transmission electron microscopy and X-ray diffraction. Previous XRD studies on the *as-deposited film* carried out by some of the authors (1) showed that these films are single crystal epitaxial layers and exhibit hexagonal $P6_3mc$ space group symmetry, characterized by partial occupation of the Ga sites. Such a phase is normally referred to as ε phase, -with disordered Ga atoms in the structure in the current literature. In the present work, detailed TEM studies allowed to investigate the real structure of this phase at the nanoscale (2). It was found that the Ga distribution is not random, but it exhibits a short-range order, giving rise to 5-10 nm large (110)-twinned domains. Each domain actually has an orthorhombic structure with $Pna2_1$ space group symmetry, called κ-Ga_2O_3 (following the nomenclature previously used for the similar Al_2O_3 polymorph). Parallel XRD analysis carried out on thicker samples (9-10 μm) confirmed the same results, and refined

structural parameters are provided. The crystal structure of these Ga_2O_3 layers consists of an ABAC oxygen close-packed stacking, where Ga atoms in between occupy octahedral and tetrahedral sites forming two types of polyhedral layers parallel to (001). The edge-sharing octahedra and the corner-sharing tetrahedra form zig-zag ribbons along the [100] direction. Anti-phase boundaries are common inside the domains. The polar character of the structure is confirmed, in agreement with the characteristics of the *Pna2₁* space group and our previous observations. Phase conversion to β-Ga_2O_3 starts at about 700 °C. The duration of the thermal treatment at 1000 °C strongly influenced the crystallinity of the samples: while for a 2 hour annealing the sample was found to be polycrystalline and strongly textured, the sample annealed for 10 hours was almost single crystalline. The crystallographic relationships between the substrate and the annealed layer corresponding to the two treatments were also determined by TEM.

References:

1. F. Mezzadri, G. Calestani, F. Boschi, D. Delmonte, M. Bosi and R. Fornari, Inorg. Chem. 55 (2016) 12079

2. I. Cora, F. Mezzadri, F. Boschi, M. Bosi, M. Čaplovičová, G. Calestani, I. Dódony, B. Pécz, and R. Fornari, Cryst. Eng. Comm. 19 (2017) 1509–1516.

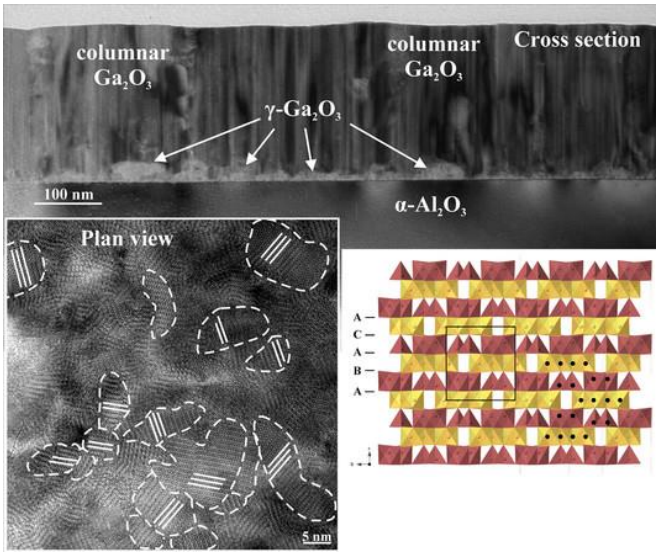

Figure 1. TEM images of the cross section and the plan view TEM specimens of the as-deposited layers with the corresponding crystal structure of κ-Ga_2O_3. The structure is textured consisting of 5-10 nm large (110)-twinned orthorhombic domains.

STEM study of $NiSi_2$/Si interface at inclusion boundaries

György Z. Radnóczi (1), Daniel Knez (2), Ferdinand Hofer (2), Nikolaos Frangis (3), Nikolaos Vouroutzis (3), John Stoemenos (3), Béla Pécz (1)

1) Centre for Energy Research, Institute for Technical Physics and Material Science, Hungarian Academy of Sciences, MTA EK MFA, Konkoly-Thege M. u. 29-33, 1121 Budapest, Hungary

2) Institute for Electron Microscopy and Nanoanalysis and Graz Centre for Electron Microscopy, TU Graz, Steyrergasse 17, 8010 Graz, Austria

3) Department of Physics, Aristotle University of Thessaloniki, GR-54124 Thessaloniki, Greece

Keywords: interface, $NiSi_2$, MILC, STEM

Crystalline Si whiskers obtained by Ni induced lateral crystallization of amorphous Si at low temperature (413°C for 11days + 420°C for 11days) were characterized by STEM with special regard to tetrahedral $NiSi_2$ inclusions found in the whiskers earlier. A detailed investigation of the $NiSi_2$/Si interface at the boundary of tetrahedral inclusions was carried out to determine the atomic configuration at the interface. High resolution high angle annular dark field (HAADF) images were recorded on inclusions accurately aligned to the <110> zone axis of the face centred cubic lattice. Nickel containing atomic columns were located based on comparison of the scattering intensity maxima corresponding to the atomic columns. The results were then compared to geometrical models of tetrahedrons with various interface configurations and image simulation results. The Ia type interface was identified which is characterized by 7-fold coordination of the Ni atoms at the interface. The orientation of the inclusions is uniform within one whisker despite the geometrical constrains allowing two equivalent orientations inside the Si crystal. A whisker grown in the [111] direction exhibits only tetrahedral inclusions with one vertex pointing in the direction of growth whereas the tetrahedrons having a different orientation would point to the opposite direction. The formation process is selective for the two different orientations due to different relations of the inclusions to the whisker lead edge during growth.

References:

This research was financially supported in the frame of a Hungarian-Greek bilateral scientific collaboration (Project Codes TET-10-1-2011-0570 for Hungary and HUN92 for Greece) and also by OTKA K108869. The research leading to these results has received funding from the European Union Seventh Framework Programme under Grant Agreement No. 312483 ESTEEM2 (Integrated Infrastructure Initiative–I3).

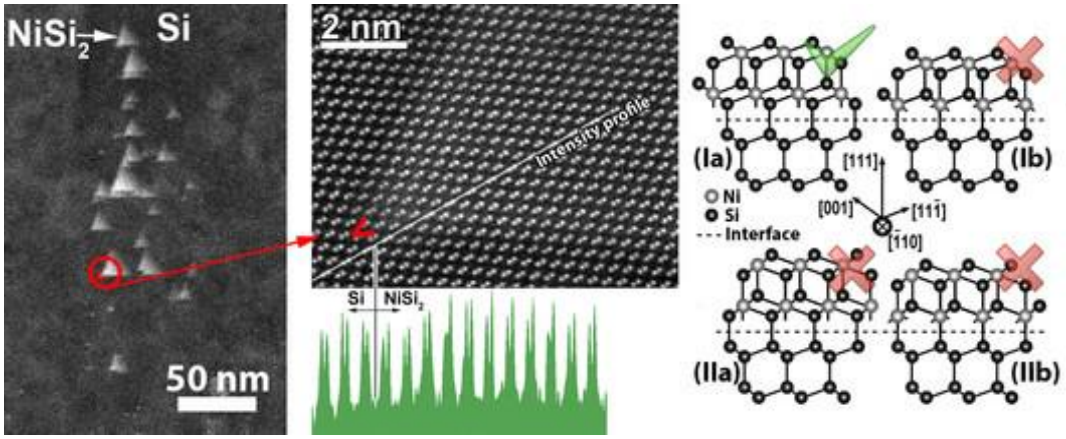

Figure 1. STEM HAADF images of $NiSi_2$ tetrahedrons in a Si whisker showing uniform orientation (left) and lattice resolution image with the line profile measured (middle) to determine the atomic configuration of the structure (right).

Structural investigation of nanocrystalline ZnO:Al thin films deposited by PLD in RF excited oxygen atmosphere

Daniel Meljanac (1), Krunoslav Juraić (1), Davor Gracin (1), Milivoj Plodinec (1), Nikša Krstulović (2), Krešimir Salamon (2), Hrvoje Skenderović (2), Iva Šrut Rakić (2), Sigrid Bernstorff (3)

1) Ruđer Bošković Institute, Bijenička 54, 10000 Zagreb, Croatia

2) Institute of Physics, Bijenička 46, 10000 Zagreb, Croatia

3) Elettra-Sincrotrone Trieste, SS 14, Km 163.5, I-34049Basovizza (TS), Italy

Nanocrystalline Al-doped ZnO thin films were deposited in vacuum and in oxygen atmosphere with and without RF excitation by pulsed laser deposition (PLD). The gas pressures during deposition were varied between 10 and 70 Pa in order to investigate the influence on structural properties and point defect dynamics. The surface structures were monitored by atomic force microscopy (AFM) and field-emission-gun scanning electron microscope (FEG-SEM), while the obtained nanostructural changes were analyzed by x-ray scattering at grazing incidence angles. The imaged surfaces, obtained from AFM, are not homogenous and flat, but show a granular structure. The surface roughness mostly follows the trend, where the roughness increases with the oxygen pressure, and also by applying RF excitation. Grazing incidence small angle x-ray scattering (GISAXS) and grazing incidence x-ray diffraction (GIXRD) showed also the trend, that the roughness of film surfaces increases with increasing gas pressure, and the density decreases due to the formation of nanovoids. The nanocrystals sizes estimated from GIXRD were around 20 nm, while the sizes of the nanovoids increased from 1 to 2 nm with the oxygen pressure. Furthermore, as seen from the SEM micrographs, various larger particles are present on the surface, possibly as a consequence of droplet formation in the laser plume. The samples deposited under vacuum condition and at lower pressures, contain on the surface nanostructures with cylindrical shape, hollow at lower pressures, while solid at higher pressures. At 70Pa, the cylindrical shapes turned to spherical. The addition of excited oxygen particles from a RF plasma improves the structural ordering by lowering the defect level, which is evident from GISAXS and photoluminescence (PL) measurements. The PL consisted of 3 well defined peaks, UV emission that corresponds to a band-to-band transition,

blue emission that appeared due to Zn vacancies, V_{Zn}, and red emission that is probably due to oxygen interstitials, O_i. For all pressures the RF excitation lowered the defect level related to blue emission and resulted in a narrower UV luminescence peak, indicating better structural ordering. The red emission peak is only seen using a RF excited oxygen atmosphere at 70Pa. The observed influence of the pressure and RF excitation on the films properties is a consequence of two main effects: the variation of the energy transfer from the laser plume to the growing film due to a different collision rate in the gaseous phase and changes of the growth chemistry due to various concentrations of active oxygen species.

Acknowledgements:

This work has been fully supported by Croatian Science Foundation under the project IP-2014-09-9419.

References:

1. D. Meljanac et al., J. Vac. Sci. Technol. A 34 (2016) 021514.

2. This work has been supported in part by the Croatian Science Foundation under the projects IP-2014-09-9419 and IP-11-2013-2753.

Structural study of Mg- and Ga-doped ZnO thin films grown by atomic layer deposition

Ildikó Cora (1), Zsófia Baji (1), Zoltán Szabó (1), Aleksander Rečnik (2), Zsolt Fogarassy (1), Csaba Dücső (1), Béla Pécz (3), Zsolt Endre Horváth (1)

1) Institute of Technical Physics and Materials Science, Centre for Energy Research, Hungarian Academy of Sciences, Konkoly Thege M. út 29-33, H-1121 Budapest, Hungary

2) Jožef Stefan Institute, Department for Nanostructured Materials K7, Jamova cesta 39, 1000 Slovenia

3) Institute of Technical Physics and Materials Science, Centre for Energy Research, Hungarian Academy of Sciences, Konkoly Thege M. út 29-33, H-1121 Budapest, HUNGARY

Keywords: SAED, HRTEM, ALD, GZO, MZO

ZnO is a transparent conductive oxide and it is widely used in photovoltaics, thin film transistors and light emitting devices. The highly n-type doped zinc oxide is one of the most promising replacements of In-doped Sn-oxide (ITO), due to its excellent transparency in the visible range and similar electrical conductivity (1-2). Mg and Ga-doped ZnO (MZO and GZO) thin films are observed to possess advantageous features such as a tunable, wide and direct band gap, large exciton binding energy, and low growth temperature (3). For example, Mg doping can increase and enlarge the band gap and the absorption coefficient. Mg and Ga doped layers were deposited by atomic layer deposition with different dopant element concentrations (1, 10 and 100 at% Mg and 3 at.% Ga). Samples were grown at different ambient temperatures (250°C and 300°C) and some of them were further *ex-situ* annealed at 500, 700 and 800°C. We used 4 different substrates: (001) sapphire, (001) GaN, (110) Si and (001) diamond. Samples were studied by XRD, transmission electron microscopy (SAED, HRTEM), UV-VIS spectroscopy and their band gaps were calculated. The electronic structure of the films was examined with Hall measurements. Dopant induced defects in the ZnO crystal structure were studied in detail. In the case of the pure MgO layer the crystal growth started at the interface with epitaxy, however, due to the large misfit between the substrate and the MgO dislocations and stacking faults are common parallel to (100). After 10-20 nm random orientation was

formed (**Figure**). In the doped samples (1% and 10 %) Mg always appears form of cubic MgO buffer layers at the interface with ZnO growing epitaxially onto them: (001)GaN, (001)Al_2O_3 and (110)Si are || to (111) MgO. In the samples doped with Ga grown at low temperature (250°C) the layer is polycrystalline but strongly textured. While in the samples grown at an elevated temperature (300°C), the film is single crystalline showing strong mosaicity. In the samples which were grown at lower temperature (110)-type dislocations dominates while in samples grown at 300°C defects parallel to (001) are typical (stacking faults, polarity changing inversion boundaries). Further annealing of the doped layer increases the crystal quality and the layer is almost single crystalline with low defect density. All films are highly transparent with sharp absorption edges. The incorporation of the Ga atoms into the films can be seen from the shift of their absorption edges toward the blue regime due to the Burstein-Moss effect. The band-gaps were also calculated, and the addition of the dopant atoms increases the gap of the ZnO materials. The Hall measurements also supported this result.

Acknowledgements:

The research was funded by the National Research, Development and Innovation Fund (NKFIA) via the TÉT_16-1-2016-0025 project and by ARRS, Slovenia (project no. BI-HU/17-18-003). Zs. Baji thanks to the support of the Hungarian National Science Fund OTKA (Grant No. PD 116579).

References:

1. Z.H. Li et al., Appl. Surf. Sci., 314 (2014) 97.

2. Z.G. Ju et al., Appl. Phys. Lett. 93 (2008) 173505.

3. S. Choopun et al., Appl. Phys. Lett. 80 (2002) 1529.

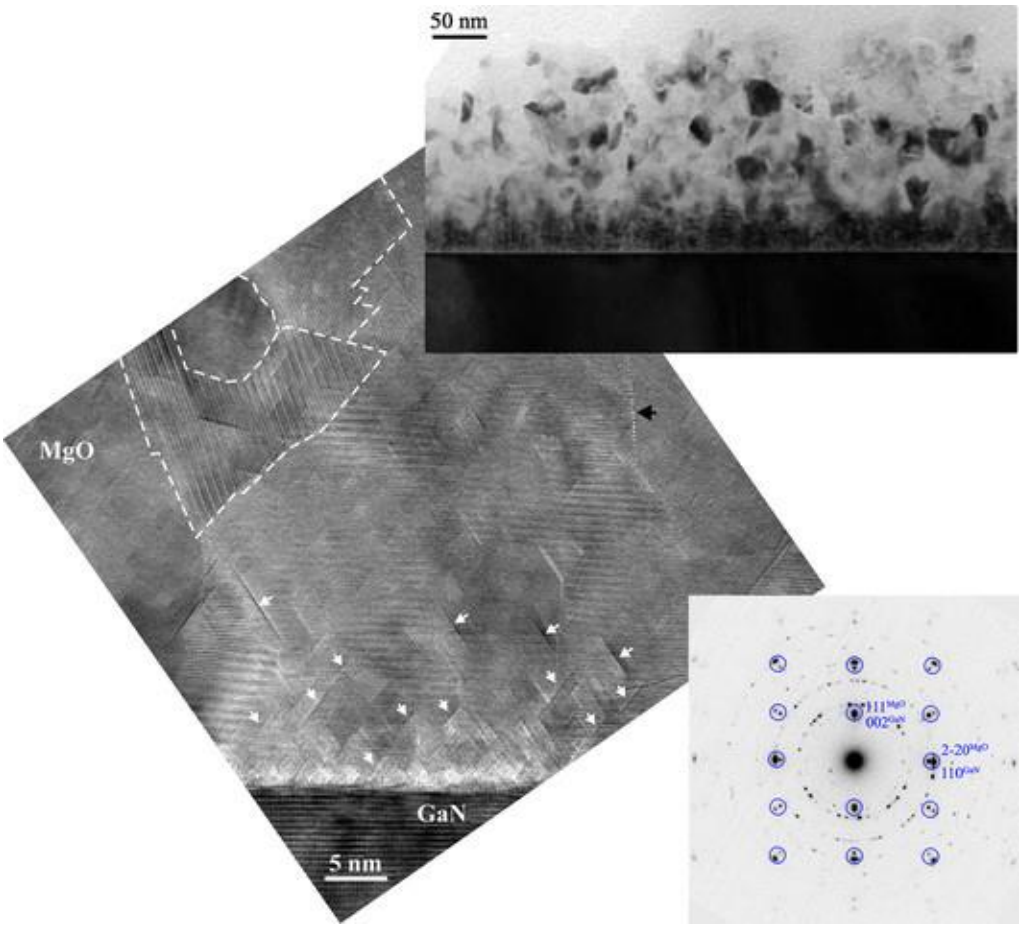

Figure 1. Bright field image, high resolution TEM image and SAED pattern of MgO film grown by ALD onto GaN (001). Lower part of the film grows epitaxially onto the GaN substrate, while the upper part of the layer is polycrystalline with strong texture.

TEM study of heterostructures of AlN on epitaxial graphene

Ildikó Cora (1), Anelia Kakanakova-Georgieva (2), Béla Pécz (1), Rositsa Yakimova (2), Filippo Giannazzo (3)

1) Institute for Technical Physics and Materials Science, Centre for Energy Research, Hungarian Academy of Sciences, P.O.Box 49, H-1525 Budapest, Hungary

2) Department of Physics Chemistry and Biology (IFM), Linköping University, Sweden

3) CNR-IMM, Strada VIII, 5, Zona Industriale, 95123 Catania, Italy

Keywords: TEM, AlN, MOCVD

A widespread interest is currently emerging in integrating group III nitrides with epitaxial graphene (1) with applications in, e.g., high frequency electronics and flexible electronics. The heteroepitaxy of mostly wurtzite (wz) GaN (2) but also wz-AlN on epitaxial graphene (2) has been approached by some research groups. Here, we employ conventional transmission electron microscopy (SAED and HRTEM) to understand the microstructure of epitaxial layers of AlN grown directly on epitaxial graphene. The epitaxial graphene was obtained by thermal desorption of Si from SiC. The epitaxial graphene is of predominantly one or two monolayers, whereby a buffer layer exists at the interface with the SiC substrate. The MOCVD of AlN was performed at various temperatures, 1100-1410 ^{o}C, which are typical for the growth of epitaxial layers of AlN of high-crystal quality on SiC substrates (3). In some of the growth runs ammonia precursor was introduced at the end of the temperature ramping step and ahead of the introduction of the precursor trimethylaluminum, giving opportunity to explore the impact of the high-temperature ammonia surface treatment of epitaxial graphene and subsequent AlN deposition. With the present TEM study we could demonstrate how the deposition temperature influences the the stability of the graphene and quality of the AlN layers. At 1410°C the top surface of the SiC substrate shows stacking disorder, and the AlN grows epitaxially onto it, while the graphene layer diminishes. Voids between the SiC and the AlN are common if the substrate is pre-treated by H_2/NH_3. At 1240°C the AlN grows onto SiC with epitaxial orientation. The AlN crystals grow in islands and at their coalescence threading dislocations are common. Graphene diminishes again. At 1100°C graphene is still stable, but the layer is polycrystalline.

Acknowledgements:

Support for this work by the FLAG-ERA JTC 2015 project GRIFONE is acknowledged.

References:

1. F. Gianazzo et al., Phys. Status Solidi A 214 (2017) 1600460.

2. Z.Y. Al Balushi et al., Surf. Sci. 634 (2015) 81.

3. D. Nilsson et al., J. Phys. D: Appl. Phys. 49 (2016) 175108.

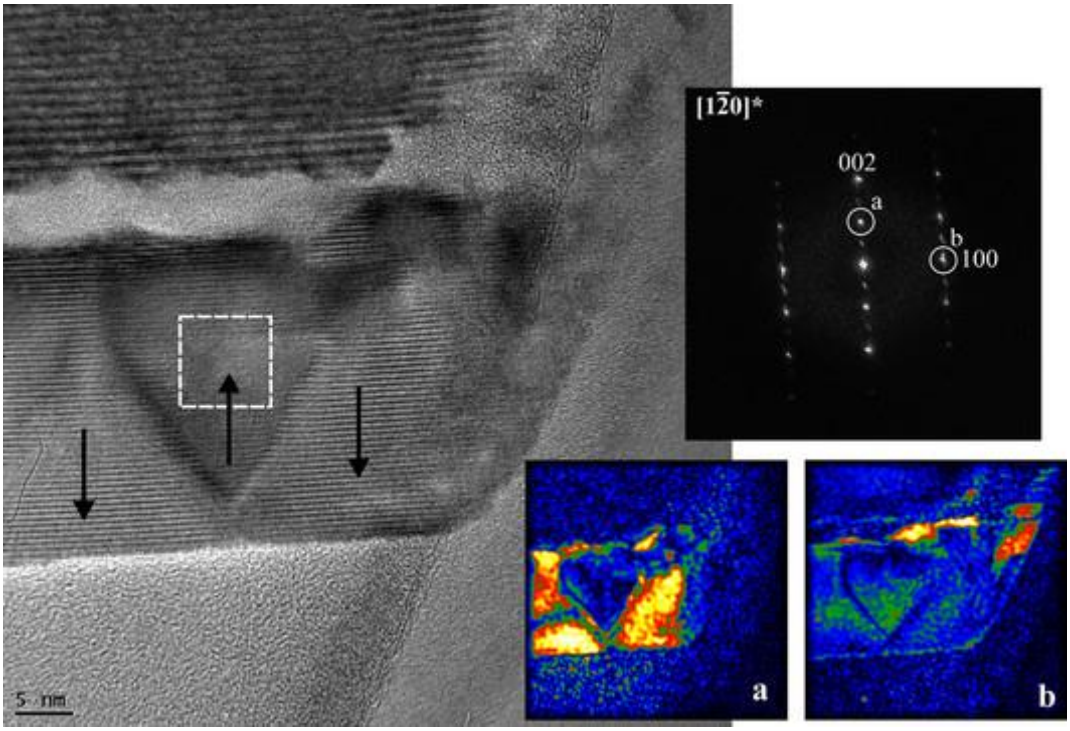

Figure 1. HRTEM and FFT images show that AlN grows onto the substrate epitaxially at 1410°C and voids between them are common. Geometric phase maps calculated by the two reflections show that the layer is inhomogeneous and it grows in 3D.

Effects of Li^+ co-doping on Eu^{3+} activated TiO_2 anatase nanoparticles

Vesna Đorđević (1), Bojana Milićević (1), Jelena Papan (1), Goran Dražić (2), Miroslav D. Dramićanin (1)

1) Vinča Institute of Nuclear Sciences,University of Belgrade, P.O.Box 522, 11000 Belgrade, Serbia

2) Laboratory for Materials Chemistry, National Institute of Chemistry, Hajdrihova 19, 1000 Ljubljana

Keywords: TiO_2 anatase, nanoparticles, europium, doping

Anatase TiO_2 nanocrystalline powders were synthesized by hydrolytic sol-gel method. In order to achieve photoluminescent nanoparticles, the powders were doped with trivalent europium ions. Introducing of 3 at.% of Eu^{3+} ions in the TiO_2 matrix significantly disturbs the structure by lowering crystallite size from 11 nm to 4 nm, while forming substantial amount of amorphous phase. The doped samples were co-doped with Li^+ ions in the concentrations from 0 up to 12at.%. The effect of Li^+ co-dopant was studied by X-ray powder diffraction (XRD), transmission electron microscopy (TEM), and photoluminescence emission and lifetime spectroscopy. XRD patters showed that the samples of TiO_2:Eu,Li crystallize as pure TiO_2 anatase in addition of 3at.% Eu^{3+} and addition of Li^+ ions up to 9at.%. Addition of Li^+ co-dopant partially compensated the disturbance between Eu^{3+} and Ti^{4+} ions, ordering the structure and improving the crystallinity. With the increase of the of the Li^+ ions content reduction of unit cell volume was observed, mainly due reduction of the c unit cell parameter. Also, with the increase of Li^+ content the enhancement of the Eu^{3+} emission intensity and the increase of the lifetime of $^5D_0$ excited state was observed, leading to the increase of the internal quantum efficiency of Eu^{3+} emission of 37.5%.

Quantitative analysis of internal interfaces - structural and quantitative analysis via high resolution STEM

Evelin Fisslthaler (1), Christian Gspan (1), Georg Haberfehlner (1), Werner Grogger (2)

1) Graz Centre for Electron Microscopy, Steyrergasse 17, 8010 Graz

2) Institute of Electron Microscopy and Nanoanalysis, Graz University of Technology, Steyrergasse 17, 8010 Graz

Keywords: HR STEM, ELNES, EELS, quantitative analysis

The scope of the research project “Quantitative analysis of internal interfaces” is the high resolution analysis of internal interfaces in multilayer materials for electronic devices via aberration corrected STEM combined with HR EELS and EDX. For this purpose, a variety of different approaches for both data acquisition and data analysis is consequently refined to provide reliable and reproducible datasets with high accuracy in both spatial and energetic resolution as well as in terms of quantitative reliability. Concomitantly, TEM sample preparation methods were sufficiently enhanced and modified to provide specimens with adequate quality. One of the key topics of the project is the detection and analysis of interfacial layers with few- or even sub-monolayer dimension in silicon based materials. The transition area between Si and SiO_2 is of major interest, since the properties as well as the extent of this region can be crucial for device performance. Therefore, the ELNES signals of both silicon and oxygen are traced with high spatial and energetic resolution to yield detailed information about the chemical composition of the few atomic layers that form the interface between the two materials. In order to obtain the contributions of individual silicon oxidation states from the ELNES signal, various signal optimization and fit procedures are used. In dependence of the material system that is examined, these measurements are combined with low level EELS measurements for the detection of trace elements that are adsorbed at or close to the interface between the semiconductor and the oxide, and that affect the device characteristics – presumably via their influence on the nature of the transition area. These procedures are then applied for several silicon based material systems to determine the exact composition of the

transition region in order to advance material fabrication procedures for silicon based electronic devices.

Acknowledgements:

We kindly acknowledge financial support by the Austrian Research Promotion Agency (FFG) (project 850220/859238).

References:

1. Oh et al., PhysRevB 63 (2001) 205310 2. Batson, Nature 366 (1993) 727

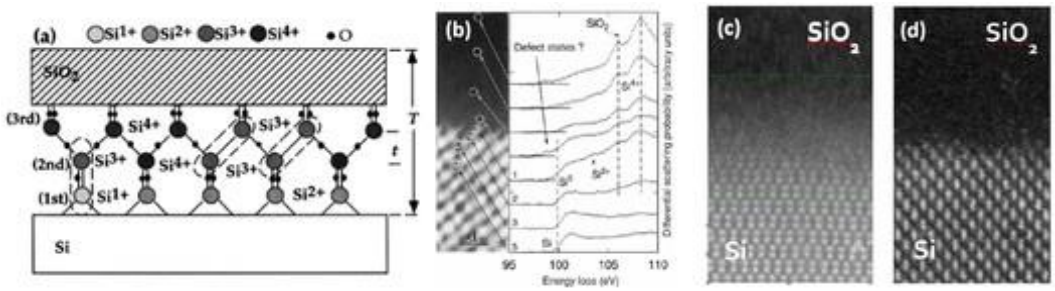

Figure 1. Schematic of transition area between Si and SiO_2 (a) (1), HR-EELS of SiL-edge during transition (b) (2), HR STEM HAADF images of the interface Si/SiO_2 (optimized for spatial resolution (c), and for both spatial and energetic resolution (d)).

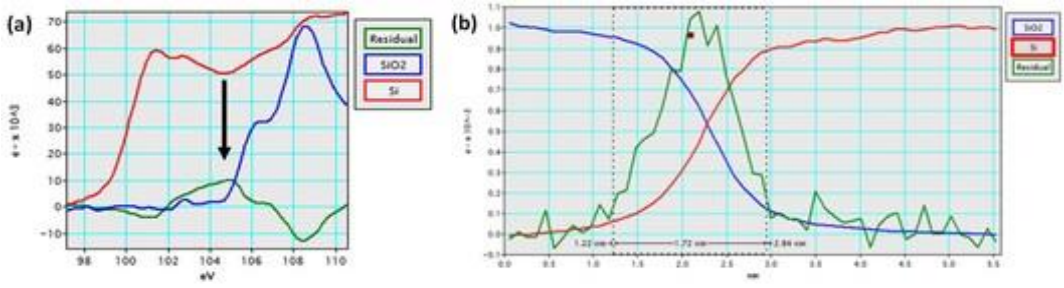

Figure 2. ELNES signal of SiL-edge for Si (red), SiO_2 (blue) and residual signal in transition area showing a peak in the area characteristic for the Si^{2+} state (a), line profile of the signals across the transition area (b).

Atomically resolved structure of luminescent $ZnkIn_2O_{3+k}$

Javier García-Fernández (1), Almudena Torres-Pardo (1), Julio Ramirez-Castellanos (1), A. Cremades (1), Javier Piqueras (1), Jose M. González-Calbet (1)

1) Universidad Complutense de Madrid, Av. Complutense, s/n, 28040 Madrid, Spain

Keywords: $ZnkIn_2O_{3+k}$, electron microscopy, luminescence

Indium zinc oxides (IZOs) have attracted the interest due to their physical properties and high chemical stability. These materials constitute a large field of research due to its applications as transparent electrodes in transistors, flat panel displays, solar cells, sensors and photocatalysis properties. In this work, several terms of the homologous series $Zn_kIn_2O_{3+k}$ with $3 \leq k \leq 13$ materials were prepared by the ceramic method. The microstructure of the materials has been elucidated by means of X-ray Diffraction (XRD), high-resolution transmission electron microscopy (HRTEM and STEM) and Raman spectroscopy. Additionally, luminescence properties were measured by cathodoluminescence in a scanning electron microscope. The structure can described based on a hexagonal symmetry, with *R-3m* space group for those terms with odd *k*, and *P6$_3$/mmc* for *k* even, although overlap of the diffraction maxima occurs for higher members of the series. HRTEM images show these materials are formed by the ordered intergrowth of layers of InO_2^- octahedral sharing edges with $InZn_kO_{k+1}^+$ blocks stacked perpendicularly to the c-axis of the crystal, where zinc and indium occupy tetrahedral and trigonal bipyramid sites. The existence of extended defects such as twins, dislocations and disordered intergrowths were also observed (Figure 1). (S)TEM in High Angle Annular Dark Field (HAADF) and Annular Bright Field (ABF) modes show the indium and zinc distribution along [1-10] and [010] zones axes. The characteristic modulation of this homologous series (a zigzag pattern) is also visualized. Cathodoluminescence (CL) measurements show the existence of a main emission band centered at 1.75 eV (Figure 2), associated to Zn vacancies. The variation of the intensity and width of the band depends on the chemical composition of the material. These results suggest that physical properties can be tailored for technological applications depending on the material composition.

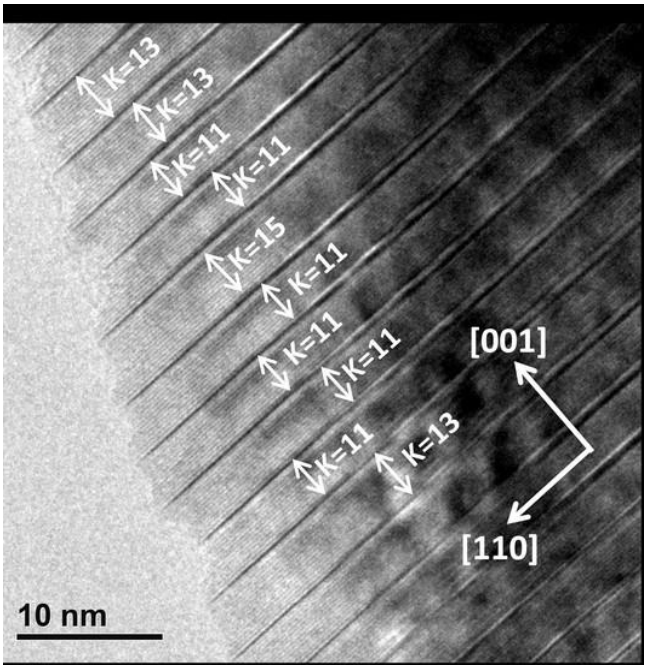

Figure 1. HRTEM image showing the presence of structural defects.

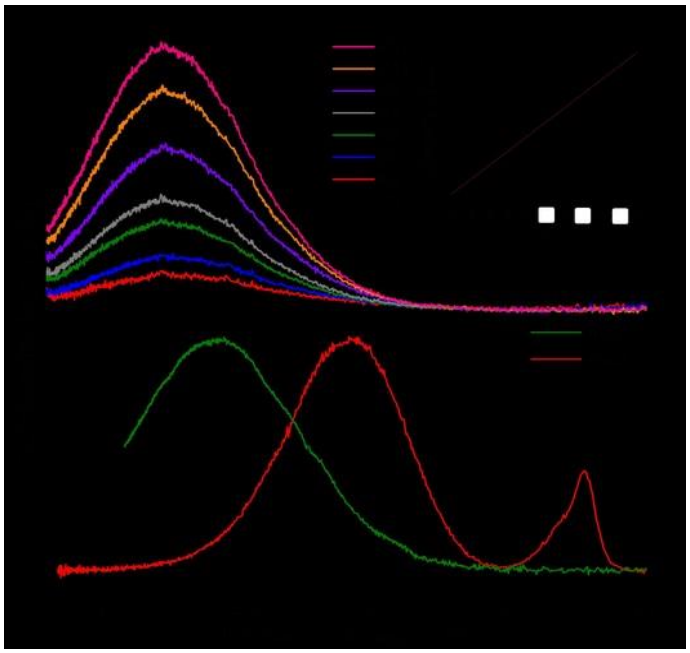

Figure 2. Cathodoluminescence (CL) measurements.

Wide bandgap AlGaN semiconductors: doping and polarity”

Lucia Spasevski (1), Robert Martin (1), Paul Edwards (1), Gunnar Kusch (1), Pietro Pampili (2), Vitaly Zubialevich (2), Peter Parbrook (2), Dinh Van Duc (3)

1) Department of Physics, SUPA, University of Strathclyde, 107 Rottenrow, Glasgow G4 0NG, UK

2) Tyndall National Institute, University College Cork, Lee Maltings, Dyke Parade, Cork, Ireland

3) The University of Sheffield, Western Bank, Sheffield S10 2TN, UK

Keywords: Wide bandgap, semiconductors, WDX, hyperspectral CL, SEM

Two sets of wide bandgap $Al_xGa_{1-x}N$:Si samples with AlN content ranging from 60% up to 85%, grown in a polar and semipolar direction were examined in this study. The samples were produced at the Tyndall Institute by metalorganic vapour phase epitaxy. Different scanning electron microscope techniques were employed to investigate the doping, and the impact of polarity. Wavelength dispersive X-ray spectroscopy (WDX) and cathodoluminescence (CL) hyperspectral imaging are used to correlate the composition and optical properties. Changes introduced by the Si doping will be considered and challenges for doping of high AlN-content AlGaN will be discussed.

M7. Biomaterials and Biosensors

INVITED LECTURES M7:

Biomolecules and living cells monitored by label-free optical waveguide sensors

Robert Horvath (1)

1) MTA EK MFA Nanobiosensorics Lab, Konkoly Thege Miklós út 29-33, H-1121 Budapest, Hungary

Keywords: label-free, optical biosensor, waveguide, biomolecules, living cells

The present talk highlights the most recent optical waveguide based biosensors to monitor biomolecules and living cells. Our group is developing and applying such sensors for highly sensitive analyzis of surface processes in real time, without the need for any labels. These biosensors offer the possibility to monitor the binding of small molecules, the adhesion kinetics of cells, and molecular movement inside living cells; highly relevant for the development of biomedical surfaces and drug discovery. Label-free biosensors are especially promising candidates to measure the kinetics of surface processes. From the kinetic measurement of protein adsorption we are able to measure nanoscale parameters of biomolecules, like the footprint of adsorbed species, in aqueous solution, in an *in situ* manner. Optical waveguide employing more modes are also applicable to measure molecular scale ordering in the adsorbed layer, using optical anisotropy analyzis. When living cells are monitored, multimode reverse symmetry waveguides can be employed to optically slice the living cells and measure refractive index variations in cellular sublayers. Moreover, the most advanced waveguide configurations have a high lateral resolution to resolve the label-free signals of living cells making them ideal to combine them with singe cell manipulation techniques, such as computer controlled micropipette or FluidFM.

Acknowledgments:

This work was supported by the Lendület Program of the Hungarian Academy of Sciences and by the ERC_HU Project of NKFIH.

References:

1. www.nanobiosensorics.com

2. https://www.researchgate.net/profile/Robert_Horvath5/publications

ORAL PRESENTATIONS M7:

Biologically templated synthesis of magnetic filaments

Éva Bereczk-Tompa (1), Ferenc Vonderviszt (2), Balázs Tóth (2), Barnabás Horváth (3), István Szalai (3), Mihály Pósfai (1)

1) Department of Earth and Environmental Sciences, University of Pannonia, Egyetem u. 10., Veszprém, Hungary

2) Bio-Nanosystems Laboratory, Research Institute of Biomolecular and Chemical Engineering, University of Pannonia, Veszprém, Hungary

3) Institute of Physics and Mechatronics, University of Pannonia, Veszprém, Hungary

Keywords: flagellin, magnetite, bio-nanotechnology, magnetic nanofibers

We aimed at creating one-dimensional biological templates that either trigger the nucleation of magnetite (a magnetic iron oxide, Fe_3O_4) from solution or bind magnetite nanoparticles from their aqueous suspension, with oth processes leading to the formation of filamentous magnetic nanostructures (Figure 1). Bacterial flagellar filaments are built of thousands of copies of the flagellin protein. The central domain (D3) of flagellin is displayed and periodically repeated on the surface of the flagellum, and can be replaced by protein fragments having specific functionalities. We engineered mutant bacteria with flagellin in which D3 was substituted with the functional parts of two proteins known from the magnetosome membrane of magnetotactic bacteria. These proteins (Mms6 and MamI) are thought to play important roles in the biomineralization of magnetite within the cells of the bacteria. In addition, we created four mutants by using oligopeptides that were known to either bind iron ions from solution, or to have strong affinity to adhere to magnetite particles. All six mutant bacteria were able to grow flagella (Figure 2a). The mutant flagella were then used as scaffolds onto which premade magnetite nanoparticles were attached. From the six different mutants the filaments displaying the MamI fragment proved to be bound most strongly to magnetite (Figure 2b), as shown by a magnetic selection procedure. In contrast, the mutants carrying the functional part of Mms6 and the two iron-binding sequences did not attach to magnetite nanoparticles at all. On the

other hand, all six mutant filaments were able to nucleate magnetite on their surfaces, when they were incubated in a solution containing iron ions. Both experimental approaches resulted in filamentous structures covered by randomly oriented magnetite nanoparticles (Figure 2c). The magnetic filaments can be aligned in an external magnetic field, resulting in a twofold increase in viscosity relative to the control sample. The produced magnetic nanofibers can be potentially used in various applications in the future, including magnetic nanoparticle imaging and for the preparation of new soft intelligent materials.

Acknowledgments:

This research was supported by grants ERA-CHEMISTRY NN117642 and BIONANO_GINOP-2.3.2-15-2016-00017.

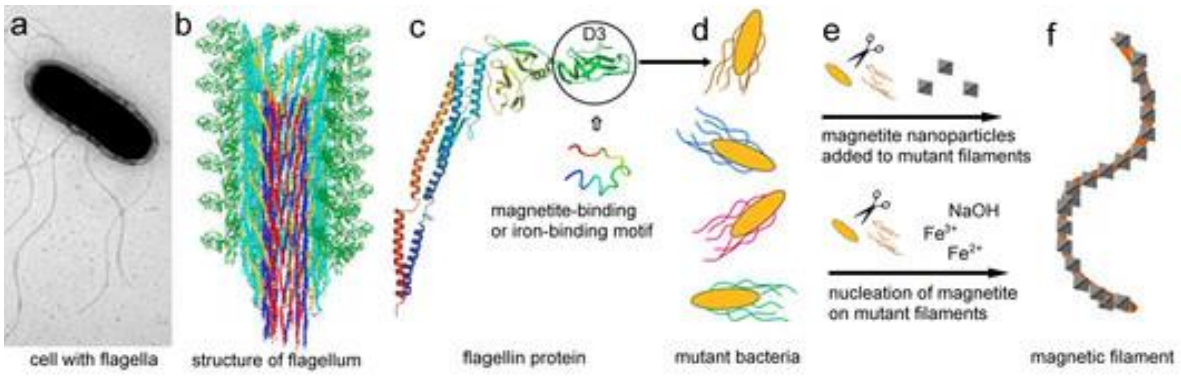

Figure 1. Graphic illustration of the concept of our study. Flagellar filaments (a) are made of flagellin (b), the D3 domain of which is replaced by specific motifs (c); bacteria with mutant flagella (d) are used in two ways (e) to make magnetic filaments (f).

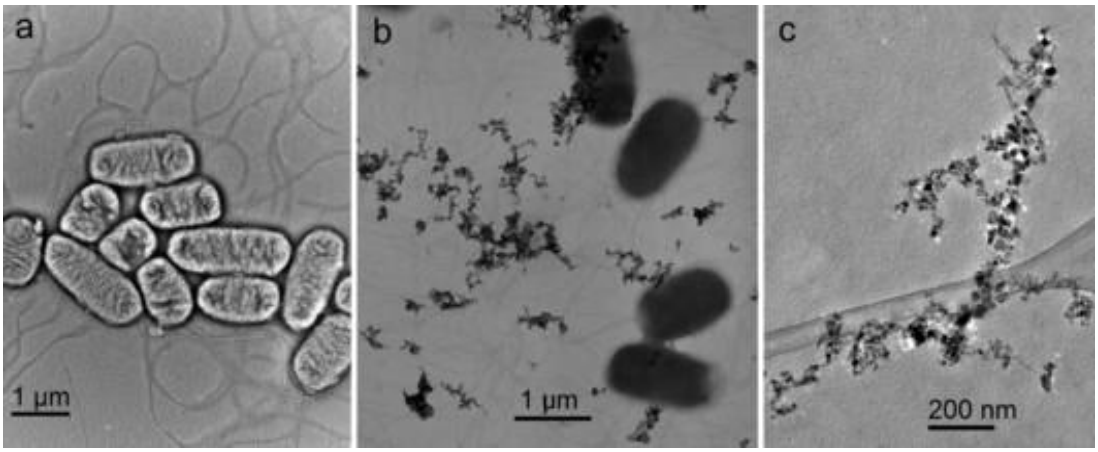

Figure 2. (a) Cells of genetically engineered bacteria with long flagella; (b) cells with mutant flagella, partly covered by magnetite nanoparticles; (c) magnetic, filamentous structure, formed by the attachment of magnetite particles to mutant flagella.

The role of chitin in the biomineralization of mollusks and its integration in a PVP-CMC hydrogel scaffolds as a bone tissue regeneration biomaterial

Vida Čadež (1), Maja Dutour Sikirić (1), Suzana Šegota (1), Darija Domazet Jurašin (1), Galja Pletikapić (1), Srečo D. Škapin (2), Ivan Sondi (3), Nabanita Saha (4), Petr Saha (4)

1) Ruđer Bošković Institute, Bijenička cesta 54, 10000 Zagreb, Croatia

2) Jožef Stefan Institute, Jamova cesta 39, 1000 Ljubljana, Slovenia

3) Faculty of Mining, Geology and Petroleum Engineering, Pierottijeva 6, 10000 Zagreb, Croatia

4) Centre of Polymer Systems, University Institute, Tomas Bata University in Zlin, tř. Tomáše Bati 5678, 760 01 Zlín, Czechia

Keywords: biomaterials, bone tissue engineering, hydrogels, biomineralization, chitin

Functionalized hydrogels have a great potential as biomaterials for bone tissue reparation. They can be used as matrices for bone tissue ingrowth, as therapeutics (by increasing disk hydrations) or/and as drug delivery systems. The challenge is to develop hydrogel scaffolds that are highly porous, but strong enough to withstand diverse mechanical strains, while mimicking the natural extracellular matrix (ECM) structure. Integration of ECM as a part of a biomaterial provides simple and efficient way to obtain scaffolds with enhanced framework structure. In this sense, marine organisms attract special attention as ECM sources (1). Their extracellular organic matrix is rich with diverse proteins and chitinous fibers. Potential of chitin is already known in the biomimetics (1,2), but most research is conducted on the chitin isolated from arthropods, i.e. on α-chitin. In comparison, β-chitin is more suitable to serve as a biomaterial since it has better water retention possibilities, but it is also more difficult to extract from highly mineralized mollusk shells (3). Therefore, the incorporation feasibility of chitin, a bioactive, antibacterial and biodegradable material (1,2), was examined in order to test its ability to enhance properties of the perspective mineralized PVP-CMC hydrogel scaffold (4,5). Chitin based PVP-CMC hydrogels were prepared and characterized both as non-mineralized and mineralized form of hydrogel scaffolds. Both α-chitin (commercially bought) and β-chitin

(isolated from the *Sepia officinalis* cuttlebone) were individually tested. Structure – function relationships of organic matrix and hydrogel scaffold structures were examined from morphological and structural perspective with the use of Fourier transmission spectroscopy (FTIR), atomic force microscopy (AFM), field emission scanning electron microscopy (FESEM) and rheometry. It was observed that at 1% strain all hydrogel scaffolds have linear trend, with highly pronounced elastic properties in comparison to viscous ones. Incorporation of β-chitin increased storage modulus of all mineralized samples, making it interesting biomaterial for further research on its utilization as a scaffold for bone tissue reparation.

Acknowledgements:

This research was partially supported by the Croatian Science Foundation under the projects 2504 (NanoMin) and 5055 (Bio-Mat-Form) and Ministry of Education, Youth and Sports of the Czech Republic, Program NPU I (LO1504). The work was performed according to the work plan of COST Action MP1301, New Generation Biomimetic and Customized Implants for Bone Engineering "NEWGEN". The first author is thankful to COST Action MP1301 for providing financial support of 5th call of STSM 2016.

References:

1. Čadež et al. JCIS 508 (2017) 95-104.

2. R. Jayakumar, et al., Int. J. Mol. Sci. 12 (2011) 1876–1887.

3. I. Younes, M. Rinaudo., Mar. Drugs 13 (2015) 1133–1174.

4. R. Shah et al., Int. J. Polym. Mater. Polym. Biomater. 65 (2016) 619–628.

5. Čadež et al. AIP Conf. Proc. 1843 (2017), 050009/1-050009/7.

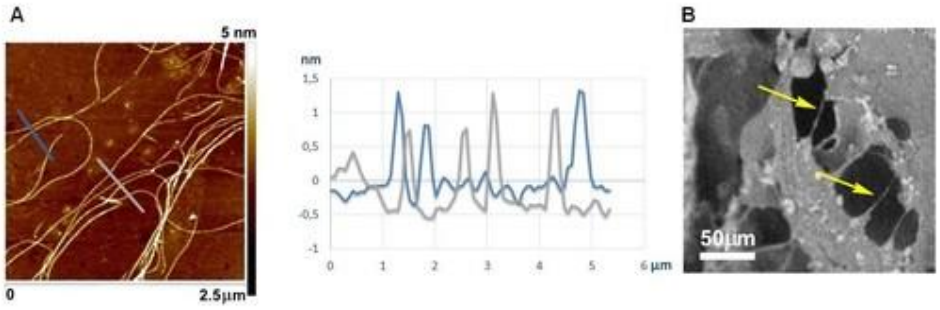

Figure 1. AFM and FESEM images of biomaterials: (a) AFM image of β-chitin isolated from the *Sepia officinalis* cuttlebone with cross section of β-chitin fibers, marked as blue and grey lines, (b) FESEM of biomineralized hydrogel scaffold, fibers marked with yellow arrows.

Surface characterization of porous calcium phosphate architectures and their effect on cell colonization and metabolic activity

Jean - Christophe Hornez (1), Shaan Chamary (1), Edwige Meurice (1), Dominique Hautcoeur (2), Anne Leriche (1), Maria H. Fernandes (3), Fernando Jorge Mendes Monteiro (4), Andreja Gajović (5), Franck Bouchart (1)

1) Laboratoire des Matériaux Céramiques et Procédés Associés - Université de Valenciennes, 59313 Valenciennes Cedex 9, France

2) Belgian Ceramic Research Center, Avenue Gouverneur Cornez 4, B-7000 Mons, Belgium

3) Faculdade de Medicina Dentara da Universidade do Porto, Rua Dr. Manuel Pereira da Silva, 4200-393 Porto, Portugal

4) Instituto de Engenharia Biomédica, Rua Alfredo Allen, 208, 4200-135 Porto, Portugal

5) Ruder Boskovic Institute, Bijenička 54, 10000 Zagreb, Croatia

Keywords: Bioceramic, calcium phosphates, bone substitute

Bioceramics, such as calcium phosphates, have been used for decades in orthopedic and dental reconstruction protocols of bone defects. The quality of the bone substitute integration relies on many parameters. For instance, pore size, shape, volume and the presence of interconnections are key factors in osteogenesis. By developing new processing techniques, these parameters can be controlled in order to generate novel architectures and properties. The latter will influence cell invasion and activity. This study sets out to explore the links between cell invasion (Osteoblasts (MG63) and Human Mesenchymal Stem Cells (HMSC)) and the porous architecture of a bone substitutes made out of β Tricalcium Phosphate (β-TCP). Three processing methods were chosen for their ability to generate interesting porous network. Freeze casting or ice templating generates structure exhibiting interconnected and oriented elliptical tubular pores. This peculiar morphology could guide and enhance vascularization thus improving cell invasion. Comparison will be made with other structures achieved by techniques such as slip casting (Slurry impregnation of an organic scaffold) and stereolithography. Samples were used as cell culture supports. Colonization, cell morphology, extracellular matrix production, mineralization and surface topography were observed through electron, optical and confocal microscopy whereas metabolic activity, vitality were assessed

through MTT and Resazurin assays and trough Raman spectroscopy phase composition was assessed. Phosphatase alkaline activity was also measured. The preliminary results that came from the MG63 cultures showed that β-TCP's bioactivity was not altered by the shaping processes. We were also able to select the optimal fabrication parameters for ice templating. The HMSC revealed ice templating obtained samples' osteogenic potential. Even if they exhibited low density population compared to samples fabricated by slip casting or stereolithography, ALP activity was significantly higher. Furthermore, cell colonization and migration into the porous network was better compared to the other types of sample. Slip casting and stereolithography yielded good cell culture supports but the latter poorly influenced HMSC's differentiation. It seems that the porous network generated by ice templating enhances and improves differentiation process of the osteoblastic lineage *in vitro*.

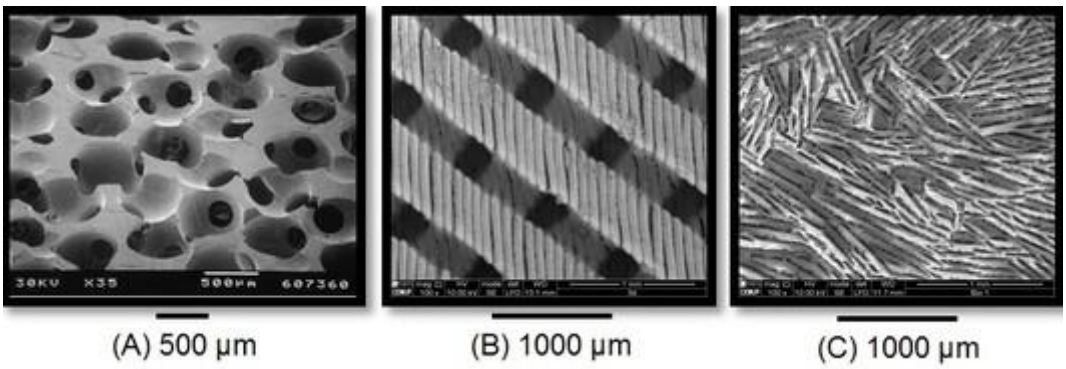

Figure 1. SEM images of (A) slip casting, (B) stereolithography and (C) ice templating

Microscopic analysis of micro-patterning of calcium phosphate bioceramics promoting bone cells adhesion and proliferation

Marie Lasgorceix (1) Cédric Ott (1) Laurent Boilet (1) Stéphane Hocquet (1) Anne Leriche (2) Maria Helena Fernandes (3) Fernando Jorge Mendes Monteiro (4) Véronique Lardot (1) Francis Cambier (1)

1) Belgian Ceramic Research Centre, member of EMRA, Avenue Gouverneur Cornez, 4, B-7000 Mons, Belgium
2) LMCPA-UVHC, Pôle Universitaire de Maubeuge, Boulevard Charles de Gaulle, 59600 Maubeuge, France
3) Faculdade de Medicina Dentária, Rua Dr. Manuel Pereira da Silva, 4200-393 Porto, Portugal
4) Laboratorio de Biomateriais, INEB - Instituto de Engenharia Biomedica, Rua do Campo Alegre 823, 4150-180, Porto, Portugal

Keywords: CaP ceramics; laser patterning; physico-chemical surface characterization; biological assessmen

The bioactivity of synthetic bone implants is highly impacted by their surface topography, especially by the presence of micro-patterns likely to influence cell behaviour. In this study, laser machining technology was employed in order to produce controlled regular micro-patterns on dense calcium phosphate surfaces, without any contamination. Beta tricalcium phosphate substrates with perfectly controlled micro-patterning and without any secondary phase were obtained by controlling the process parameters (laser power, scanning speed, pulse frequency). An accurate optimization of the process parameters allowed obtaining micropatterns with several complex designs. The microstructural characteristics were investigated by means of 3D confocal microscopy and 3D rugosimeter. Surface analyses are completed with the phase identification performed by X-Ray Diffraction and micro-Raman spectroscopy. The effect of the process parameters on the patterning are highlighted in this work. The influence of surface micro-patterning on osteoblast cells behaviour was determined by *in vitro* assays. In particular, an elongation of the cells shape was observed along linear grooves, whereas cells appeared more spread on smooth surfaces with same chemical composition. These results show that linear patterning should promote cell migration. The effects of the micro-patterning design and particularly the presence of angular shapes, on stem cell adhesion, proliferation and differentiation are currently being evaluated.

Acknowledgements:

The authors are grateful to the Walloon Region for financial support, within the “BEWARE” program (convention n°1510392) co-funded by Wallonia and European Union (FP7 – Marie Curie Actions). All the authors also thank the JECS Trust Action "Frontiers of Research" for the financial support facilitating the collaborative work between laboratories.

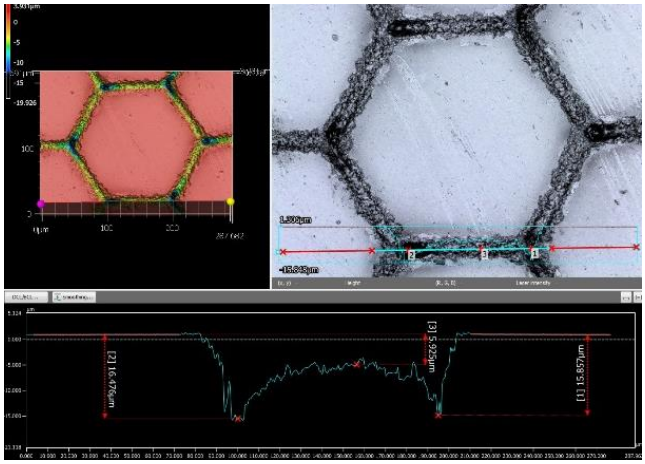

Figure 1. Beta-TCP substrate textured by femtosecond laser - profile analysis with 3D rugosimeter.

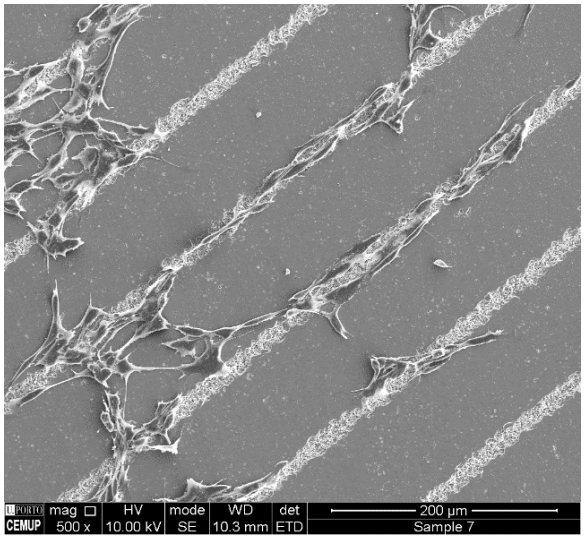

Figure 2. MG63 cells adhesion on Beta-TCP substrates linearly textured by femtosecond laser - day 1 after seeding.

Bio-inspired design: beyond materials and structures

Dusan Chorvat (1), Alzbeta Marcek Chorvatova (2)

1) International Laser Centre, Ilkovicova 3, 841 04 Bratislava 4, Slovakia

2) University of Ss. Cyril and Methodius, Faculty of Natural Sciences, Námestie J. Herdu 2 917 01Trnava, Slovakia

Keywords: functional, design, cells, sensors

Despite significant advancements in understanding cell biology, we still lack a clear insight into precise mechanisms that are responsible for the cell functionality. It is becoming increasingly apparent that this information does not reside neither in the genome, nor in individual proteins, as no real biological functionality is expressed at these levels (1). Deeper knowledge of principles guiding living cell function, based on recent advances of optical and electron microscopy methods, can be translated into the conceptual progress in design of emerging sensing and manipulation devices. In our contribution we present a new approach for creation of bio-inspired devices, that will be based not only on structural analogies to organic materials, but rather on knowledge derived from understanding of functional principles that control the behaviour of the living cells. From our viewpoint, new designs should be based on understanding of the non-linear integrative physiological behavior of the complex molecular interactions in their natural environment and precise spatio-temporal topology. Such approach emphasize investigation of cell structure and its communication system from the "engineering" perspective. In our case we are referring to our previous work (2,3), describing living cells as an analog to biological “quantum resonators”, paving the new road for conceptually new class of biosensors.

References:

1. Noble D, The music of life. Biology beyond the genome, Oxford University Press (2006).

2. Chorvat D. Jr. and Chorvatova A., BioSystems 92/1 (2008): 49-60.

3. Chorvatova A. Chorvat D., Jr., Chapter 2: 25-44, Cardiac Pacemakers - Biological Aspects, Clinical Applications and Possible Complication, Mart Min (Ed.), InTech (2011).

Atomic force microscopy in conjunction with super-resolution optical microscopy and optical tweezers

Jan Vavra (1), Philipp Rauch (1), Heiko Haschke (1), Torsten Jähnke (1)

1) JPK Instruments AG, Colditzstr. 34-36, Haus 13, Eingang B,12099 Berlin, Germany

Keywords: optical tweezers, atomic force microscope, STED, QI, OT-AFM

The latest NanoWizard family developments extend the seamless integration of atomic force microscopy (AFM) into advanced super-resolution STED microscopy and even optical tweezers making it an indispensable tool for high-resolution studies under native conditions. Here, we introduce the novel “Easy-to-Use” software module for the latest “Quantitative Imaging” (QI™) mode in the JPK NanoWizard® 4 in order to simultaneously acquire topographic, nano-mechanical, and adhesive sample properties with only a few clicks from setting up to having images acquired. This is achieved by setting most parameters automatically which makes it convenient to use and allows non-expert users to acquire data of highest standards. With automated batch processes even more complex data, such as, contact point images, Young´s moduli images, or even recognition events can be achieved. Here, we present data showing the major-minor groove of DNA resolved in buffer environment. Further research towards automated AFM has been put into the feature “Experiment Control” which gives the opportunity to control all main parameters of the AFM remotely conveniently on any device, such as, a tablet, PC or mobile phone without interfering with the setup. With recent tip-scanning AFM developments we extended our capability of performing fully simultaneous measurements with AFM and STED on a living cell – to our knowledge the first time with a fully commercial system. We will show AFM QI elastic moduli data of individual living skin fibroblast cells and actin super-resolution STED images of the same cell acquired in one experiment. In addition, we will present data on the stimulation of individual SiR-labelled microtubules in live skin fibroblasts observed simultaneously with STED microscopy. Thus, conclusions can be drawn on the mechanics of microtubules in live cells. The novel OT-AFM Combi-System pairs the exceptional surface force measurement and imaging capabilities of AFM with the ability of optical tweezers to apply and measure smallest forces in the femto-newton range in 3D. We will present AFM adhesion experiments between dendritic cells (DC) and conventional T-cells

(Tconv) while regulatory T-cells (Treg) are attached to and removed from the DC with optical tweezers to test its influence on the binding strength. It is found that Treg attachments reduce DC-Tconv interactions. After the Treg is removed, the adhesion level is almost restored (Yan Shi et al – submitted).

POSTER PRESENTATIONS M7:

Fractographic analysis of biomedical Ti-based alloys with acicular microstructures

Ivana Cvijović-Alagić (1), Zorica Cvijović (2), Nenad Gubeljak (3), Marko Rakin (2)

1) Institute of Nuclear Sciences „Vinča“, University of Belgrade, Mike Petrovića Alasa 12-14, 11001 Belgrade, Serbia

2) Faculty of Technology and Metallurgy, University of Belgrade, Karnegijeva 4, 11120 Belgrade, Serbia

3) Faculty of Mechanical Engineering, University of Maribor, Smetanova 17, Maribor, Slovenia

Keywords: Biomedical Ti-based alloys, thermo-mechanical processing, fracture resistance, SEM observation, fractographic analysis

The mechanical biocompatibility is essential for biomedical Ti-based alloys used for orthopedic implants. Therefore, many studies are focused on decreasing the elastic modulus closely associated with the microstructural features. Recently, it is established that acicular microstructure, such as fully martensitic microstructure, results in a significant enhancement of the biomechanical compatibility. The obtained improvement depends on alloy chemical composition and geometrical parameters of acicular phase. Thus, a newly developed Ti-13Nb-13Zr (mass %) alloy has lower elastic modulus than standard Ti-6Al-4V (mass %) alloy in the same microstructural condition. On the other hand, a martensitic microstructure shows inferior fracture properties. The crack nucleation and propagation resistance of these implant materials is possible to optimize by the proper martensitic characteristics. A most critical parameter can be determined by the fracture surface morphology evaluation. In this study, the relationship between acicular microstructure, induced by different processing conditions, attaining the required biomechanical compatibility and fracture mode of Ti-13Nb-13Zr and Ti-6Al-4V ELI (extra-low impurity) alloys was established. Two microstructures with different untransformed β phase amount and martensite plates aspect ratio were developed by water quenching after

solution treatment above the *β* transus temperature. The scanning electron microscopy (SEM) observations of the broken tensile test specimen surfaces were correlated with their quantitatively determined geometric characteristics. The fractographic analysis reveals that presence of thin martensitic needles elongated to a higher extent than in Ti-13Nb-13Zr alloy microstructure, resulting in higher yield and ultimate tensile strength of the Ti-6Al-4V ELI alloy, experiences very limited plastic deformation before fracture. The fracture surface displays predominantly intragranular quasi-cleavage fracture mode. A so-called basket weave microstructure with coarser martensitic plates of smaller aspect ratio in Ti-13Nb-13Zr alloy hot rolled in the (*α*+*β*) phase field before quenching is beneficial to minimize the amount of cleavage facets. The larger amount of intragranular dimples mixed with those on the ridge walls, suggesting the change of dominant fracture mode, corresponds to one order of magnitude higher elongation at fracture. This indicates that martensitic microstructure produced through the applied thermo-mechanical processing of Ti-13Nb-13Zr alloy contributes to a superior tensile-fracture properties balance.

Acknowledgements:

This research was supported by the Ministry of Education, Science and Technological Development of the Republic of Serbia through the Project No. ON174004.

Structural investigation of waste biomass-derived carbon for bioelectrocatalytic applications

Egon Rešetar (1), Milivoj Plodinec (2), Stanislav Kurajica (3), Damir Iveković (1)

1) Faculty of Food Technology and Biotechnology, University of Zagreb, Pierottijeva 6, HR-10000 Zagreb, Croatia

2) Ruđer Bošković Institute, Bijenička c. 54, HR-10000 Zagreb, Croatia and Fritz Haber Institute of the Max Planck Society, Inorganic Chemistry Department, Faradayweg 4-6, 14159 Berlin, Germany

3) Faculty of Chemical Engineering and Technology, University of Zagreb, Marulićev trg 20, HR-10000 Zagreb, Croatia

Keywords: Pyrolytic carbon, bioelectrocatalysis, direct electron transfer, HRTEM, STEM-HAADF

Biomass-derived carbon (BDC) is environmentally friendly and cost competitive material produced by pyrolysis of plant (lignocellulosic) biomass. Due to its electric conductivity combined with high porosity and tunable surface properties, BDC has recently attracted considerable interest in the field of electrochemistry, primarily as an electrode material for electrochemical supercapacitors and high-performance metal-ion batteries or as an electrocatalyst for oxygen reduction and hydrogen evolution reactions (1,2). In this work, we studied the suitability of BDC as a substrate for enzyme immobilization and its applicability as electrode material in bioelectrocatalysis. Conductive carbon samples were prepared by rapid pyrolysis (at a heating rate of 100 °C/min) of spent coffee grounds in the temperature range between 600 and 900 °C in an inert (N_2) atmosphere, with the addition of iron salt as a graphitization catalyst. The obtained pyrolytic carbon was employed as a substrate for immobilization of horseradish peroxidase (HRP), a model redox enzyme that catalyzes the reduction of hydrogen peroxide in the presence of a suitable organic electron donor or, in the special case of HRP adsorbed on electrode, through the process of direct electron transfer between the enzyme redox-center and conductive substrate, usually referred as a 'bioelectrocatalysis'. It was observed that both the bioelectrocatalytic activity and the stability of immobilized enzyme were significantly better for HRP immobilized on pyrolytic carbon

samples prepared in this work, than for HRP immobilized on graphite, a commonly employed electrode material in bioelectrocatalysis. Observed enhancement of the bioelectrocatalytic properties of HRP will be discussed in terms of the structural characteristics of prepared pyrolytic carbon samples (porosity, phase composition, density of surface groups, relative abundance of sp^2- and sp^3-hybridized domains, disorder and deformation of the carbon layers within the graphitic domains), as determined by scanning electron microscopy (SEM), X-ray diffraction (XRD), infrared and Raman spectroscopy, high-resolution transmission electron microscopy (HRTEM), and high angle annular dark field scanning transmission electron microscopy (STEM-HAADF).

References:

1. J. Deng et al., Green Chemistry, 18 (2016) 4824-4854.

2. L. Yan et al., Green Energy Environ. 2 (2017) 84-99.

Electron and neutron diffraction based PDF analysis of bioactive glasses

Viktoria K. Kis (1), Margit Fábián (1), János L. Lábár (1), Zsolt Kovács (2)

1) Centre for Energy Research, Hungarian Academy of Sciences, H-1121 Budapest, Konkoly-Thege Miklós út 29-33.

2) Department of Material Physics, Eötvös Loránd University, H-1117 Budapest, Pázmány Péter sétány 1/C

Keywords: electron diffraction, neutron diffraction, pair distribution function, Reverse Monte Carlo simulation, bioactive glass

Structure of the amorphous and nanocrystalline materials are generally characterized by pair distribution functions (PDFs) based on neutron or synchrotron X-ray powder diffraction data. These diffraction techniques require large quantity of material which is supposed to be homogeneous. Conversely, electron diffraction based PDF analysis (e-PDF) using conventional microscopy technique suits to small, miligramm quantities (e.g. for pharmaceuticals), thin film coatings and inhomogeneous materials as well (1). It has been shown that the e-PDF and X-ray based PDF are in good agreement for homogeneous nanocrystalline samples (2), but similar investigation has not been published yet on amorphous materials. In this study we present e-PDF and neutron diffraction based PDF (n-PDF) analysis of bioactive Si-Na-Ca-P glasses in the 0-5 mol % P_2O_5 phosphate content range. For e-PDF analysis, bulk silica glass and a-SiO_x film with nominal thickness of 40 nm were used to test the effect of sample thickness and the applied scattering angle (Q_{max}). Standardized and calibrated electron diffraction measurements were evaluated with the ProcessDiffraction software (3). Neutron diffraction (ND) measurements were carried out at the LLB Orphée research reactor using the 7C2 diffractometer (4). For the analysis of the ND measurements, besides n-PDF calculation (based on Fourier transformation) Reverse Monte Carlo (RMC) simulation (5) has been applied as well. For e-PDF of a-SiO_x, it was found that the Si-O and O-O distances are in good agreement with literature data (1.6 Å and 2.59 Å, respectively) and independent of sample thickness and the applied Q-range. However, sample thickness has strong influence on the initial slope of the G(r), and thus on the derived value of density

(G(r)=−4πrρ). By the addition of alkali elements, the first nearest neighbour distance increases (1.62 Å) and a separate peak appears at 2.3 Å, which can be assigned to the Na/Ca-O distance. Small phosphate addition to the Si-Na-Ca glass decreases the first nearest neighbour distance in the e-PDF. In case of 5mol% phosphate content, which implies that the P constitutes the 18% of the network former cations, the first peak shifts down to 1.57 Å. For ND measurements, RMC simulation was applied to generate a 3-dimensional atomic configuration, which is consistent with the experimental data. The results of RMC and n-PDF show well-defined first neighbour distances for the Si-O at 1.6 Å, P-O at 1.55 and 1.9 Å, Ca-O at 2.2(5) Å and Na-O at 2.2 Å. The intensity of the second P-O peak at 1.9 Å increases with the P content. Significant intermediate-range correlations have been revealed for the second neighbor distances, indicating a stable and well-defined network. Similarities and differences between the two methods, namely n-PDF and RMC, and the reliability of e-PDF analysis in case of amorphous materials are discussed.

References:

1 T.E. Gorelik, M. U. Schmidt, U. Kolb, S. J. L. Billinge (2014) Microsc. Microanal. doi:10.1017/S1431927614014561

2. J.L. Lábár (2009) Microsc Microanal 15, 20–29

3. O. Gereben, P. Jóvári, L. Temleitner, L. Pusztai (2007) J. Optoelectron. Adv. Mater 9, 3021

Novel method of drug delivery system

Mislav Mustapić (1), Suzana Šegota (2), Shahriar Al Hossain (3), Boris Martinac (4)

1) Josip Juraj Strossmayer University of Osijek, Department of Physics, Trg Ljudevita Gaja 6, 31000 Osijek

2) Laboratory for Biocolloids and Surface Chemistry, Division of Physical Chemistry, Ruđer Bošković Institute, 10000 Zagreb, Croatia

3) Institute for Superconducting and Electronic Material (ISEM), University of Wollongong, Squires Way, North Wollongong, NSW 2522, Australia

4) Molecular Cardiology and Biophysics Division, Victor Chang Cardiac Research Institute, NSW 2010, Australia

Keywords: Drug delivery system, porous Fe_3O_4, magnetic fields

Design and construction of a complete drug delivery system, from a drug nano-carrier to an efficient system for drug activation in a localized volume of the human body requires a multidisciplinary approach and substantial investment. Porous materials possess a large surface area and thus have the capability to store different molecules (drugs) within their structure making them potential drug carriers. As an ideal canditate porous Fe_3O_4 structures can be used as a vehicle for the transport of drugs adsorbed onto their surface. This material enables controlled release of the chemical payload via activation by a magnetic field. Porous structures made up of Fe_3O_4 nanoparticles were used to adsorb methyl blue in water. Controlled release of the methyl blue to water was then achieved by application of a magnetic field. Application of a pure DC field did not result in any release. Application of a pure AC field caused released of the methyl blue. However, a combination of both DC and AC fields resulted in much faster release. The mechanism by which this operated is believed to result from viscous friction. Nanoparticles are strongly aligned in the DC field and oscillate under the influence of the AC field. This study demonstrates a concept for controlled drug delivery, where pharmaceutical molecules, similar to methyl blue, would be adsorbed onto porous Fe_3O_4 structure and the released at a target by application of appropriately localised magnetic fields. In an expanded research, we developed superparamagnetic nanoparticles for activation of the

MscL (Large Conductance Mechanosensitive Channel) nanovalves by magnetic field. Synthesised $CoFe_2O_4$ nanoparticles with the radius less than 10 nm were labelled by -SH groups for attachment to MscL. Activation of MscL by magnetic field with the nanoparticles attached was examined by the patch clamp technique showing that the number of activated channels under ramp pressure increased upon application of the magnetic field. Finally, in this research we present two promising concepts of precise drug delivery system in very early stages.

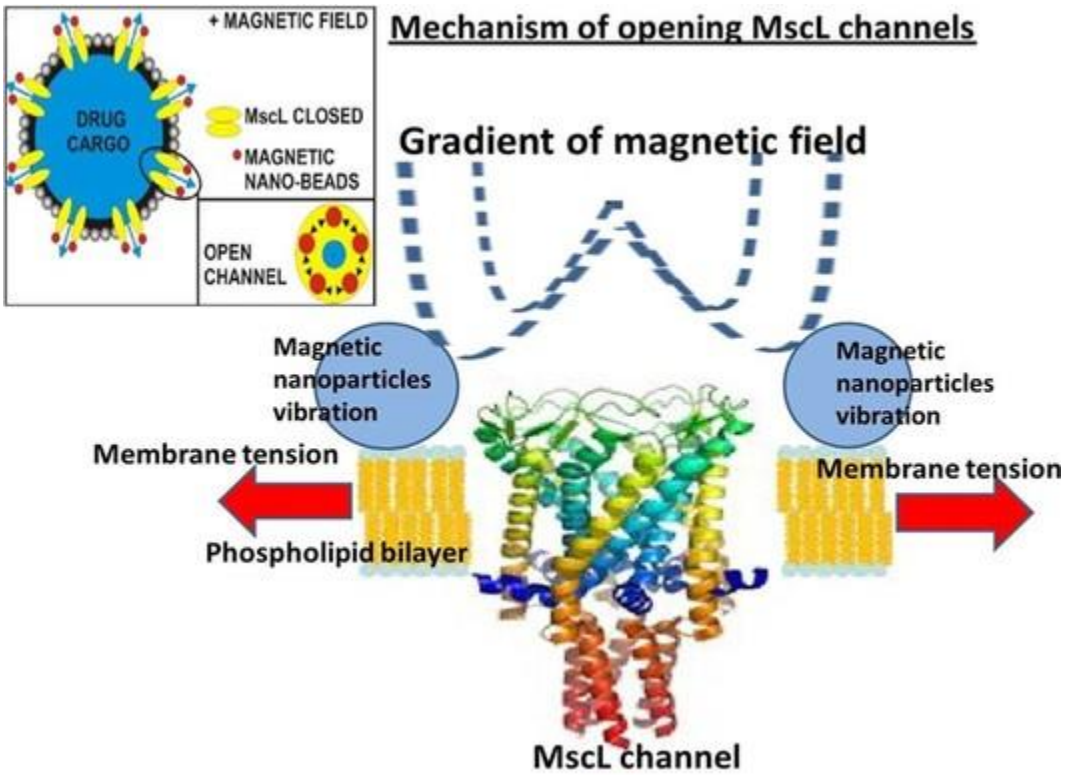

Figure 1. Illustration of drug delivery concept with nanoparticles attached to MscL channels incorporated in liposomes bilayer.

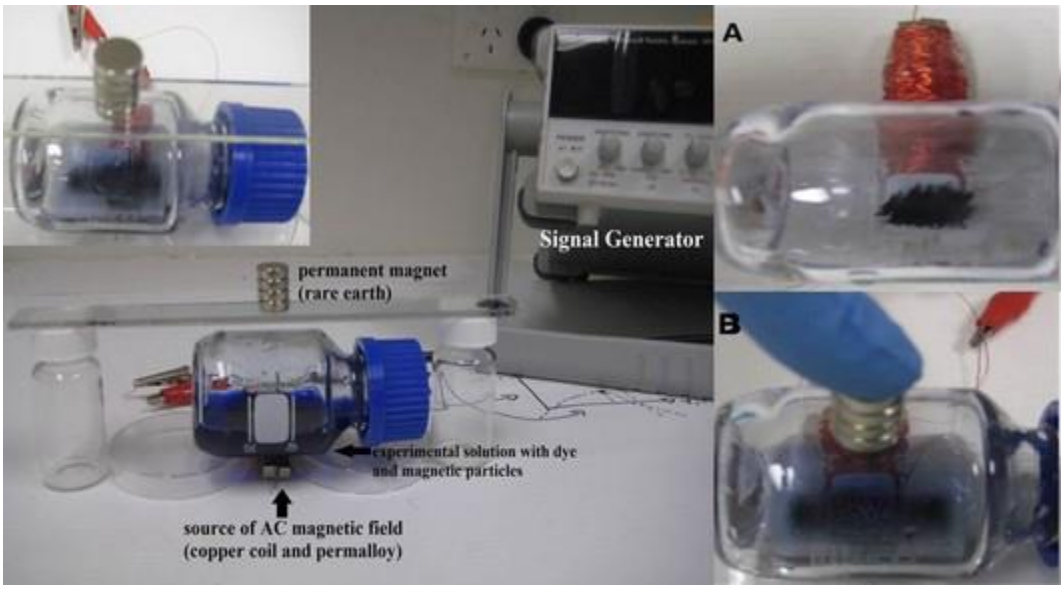

Figure 2. Experimental apparatus of simple and highly efficient set up showing how AC and DC magnetic fields were applied.

Acknowledgements:

This work was also supported by the Australian Research Council (Grant no. DE130101247). The help of Prof Shi Xue Dou at ISEM is gratefully acknowledged.

References:

1. C. Sun, et al., Adv Drug Deliv Rev 60:1252–1265. Y. Nakayama, et al.,, Eur. Biophys. J. 44 (2015) 647e654.

2. M. Mustapić, et al., Micropor. Mesopor. Mater. 2016, 226 243-250.

Microstructure of plasma sprayed bioactive coatings

Annamária Dobrádi, Kristóf Kovács (1)

1) University of Pannonia, Institute of Materials Engineering

Keywords: bioactive glass ceramics, plasma spraying

Natural bone derived glass-ceramics are promising biomaterials for implants. Due to their price and mechanical properties however they are preferably applied as coatings on load bearing implants. The presentation will describe result obtained by plasma spraying of bioactive glass ceramics containing natural bone onto selected implant materials such as stainless steel, alumina, and titanium alloy. Basic frit and raw mixtures as described elsewhere (1, 2) were used for plasma spraying. The plasma sprayer operated with a moderate feed rate for the powder, and argon carrier gas. The microstructure of coatings as well as the interface between the substrates and coatings were tested by SEM of cross sections. The results show a defect free interface between the support and the coating. No cracks or gaps are observed in the substrate to coating interface. SBF treatment of plasma sprayed coating is not influencing the boundary between the support and the coating. Dissolution rate in SBF is readily controlled by the bone additives (phase composition), as well as microstructure. As a result of the above described plasma spraying of the protein free and the sintered protein free bovine bone containing glass-ceramics a crack free, nearly dense, low porosity coatings was obtained. The plasma spraying modifies the phase composition, and new calcium phosphate phases e.g. α-whitlockite, tetracalcium phosphate, etc. are formed at the high temperature of the plasma. Adherence of the coating is excellent, and the process itself is beneficial to the dissolution properties, because the dissolution rate is slower as compared to the bulk material. The plasma spraying of glass-ceramics containing different natural calcium phosphates provides a method of controlling the incorporation, hence the ossification. Moreover, the improvement of dissolution rate/ossification is easily controlled by the appropriate selection of animal bone treatment. A simulated body fluid as described by Kokubo and Takadama (3) was used to test bioactivity as well as body fluid induced surface changes of bioglass ceramics. The surface of all substrates is fully covered by these plasma sprayed coatings. Although the coatings do not

show a fully dense, pore free microstructure, they perfectly cover the substrates and have low porosity. Pre-treated protein free bovine bone containing coatings (GC-PTB) have smaller porosity, higher Vickers microhardness in bulk, and higher compressive strength. Such microstructure will easily dissipate mechanical stresses and will not deteriorate even after the subsequent SBF-treatment (during the formation of a new Ca-phosphate layer), they will neither crack nor scale. This way the specific surface is higher and therefore it will provide a better contact with the body fluid which in turn promotes the formation of a new layer and enhances the binding of implants.

References:

1. A. Dobrádi et al., Ceram Int, 41 (2015) 4874-81.

2. A. Dobrádi et al., Ceram Int, 42 (2016) 3706-3714 3. T. Kokubo et al., Biomaterials 27 (2006) 2907-2915.

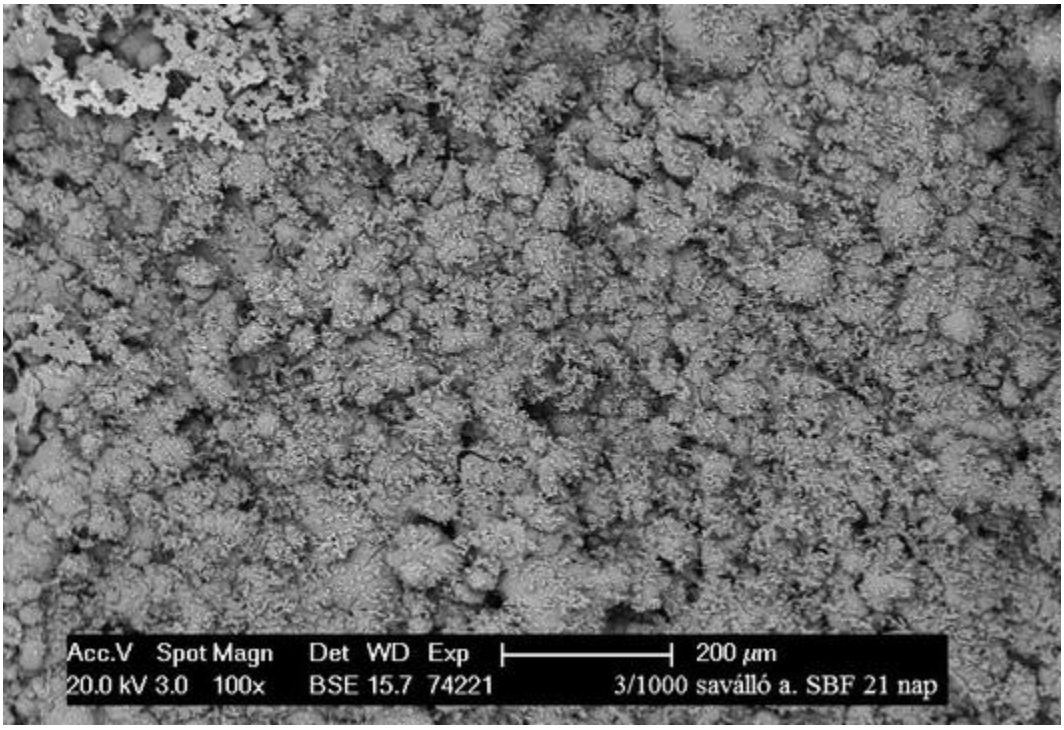

Figure 1. Surface of plasma sprayed coating on a stainless steel substrate after 21 days of SBF treatment.

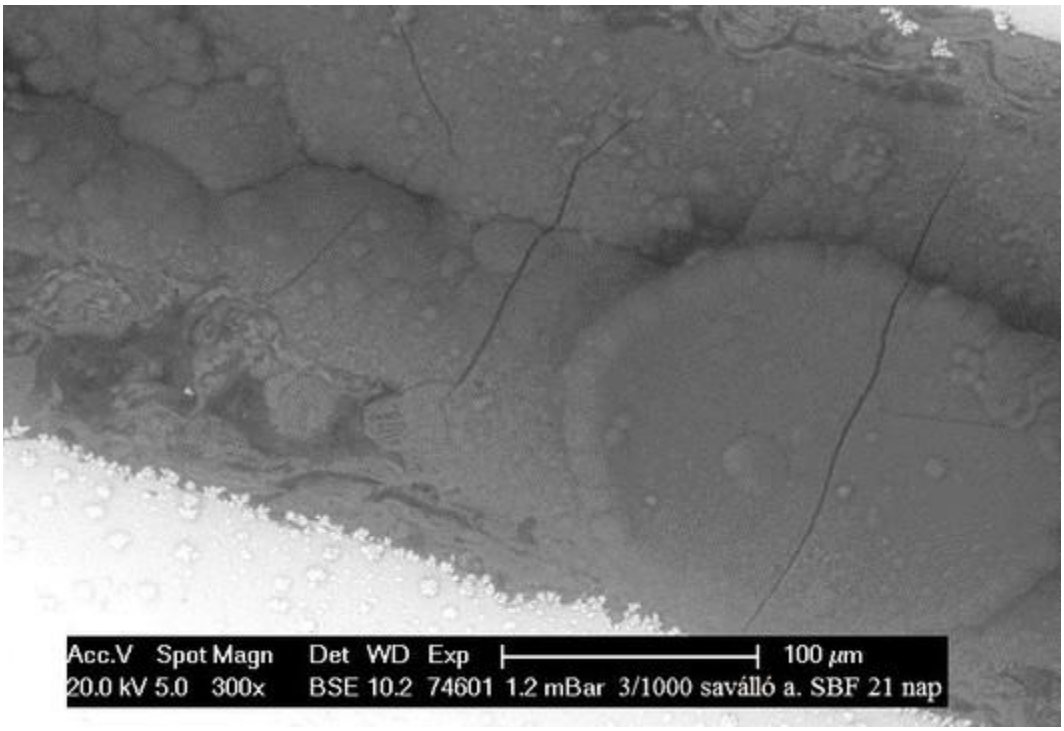

Figure 2. Cross section of plasma sprayed coating on a stainless steel substrate after 21 days of SBF treatment.

APPENDIX

Immunolabelling of nuclear PIP2 islets on replicas

Zuzana Lubovská (1), Margarita Sobol (2), Vlada Philimonenko (3), Pavel Hozák (3), Toyoshi Fujimoto (4)

1) Institute of Molecular Genetics ASCR v.v.i., Microscopy Center, Electron Microscopy Core Facility, Prague, Czech Republic

2) Institute of Molecular Genetics ASCR v.v.i., Department of Biology of the Cell Nucleus, Prague, Czech Republic

3) Institute of Molecular Genetics ASCR v.v.i., Microscopy Center, Electron Microscopy Core Facility, Prague, Czech Republic, Institute of Molecular Genetics ASCR v.v.i., Department of Biology of the Cell Nucleus, Prague, Czech Republic

4) Department of Molecular Cell Biology, Nagoya University Graduate School of Medicine, Nagoya, Japan

Keywords: nucleus, PIP2, quick-freezing – freeze fracture replica labelling

During the last decade, the importance of phosphoinositides in the cell nucleus was uncovered. We defined previously unknown nuclear structures which occupy nearly 2% of nuclear volume and contain almost 30% of the nuclear pool of phosphatidylinositol 4,5-bisphosphate (PIP2). These non-membranous structures of 40 – 100 nm in diameter are decorated by PIP2, so we name them “PIP2 islets”. PIP2 islets are surrounded by nucleic acid- and protein-rich structures, while the interior carbon-rich compounds are presumably lipids. We showed that PIP2 is associated with Pol II transcription complex, chromatin, and nascent RNA transcripts on the periphery of the islets, and that PIP2 islets contribute to efficient DNA transcription. We studied the ultrastructure and precise composition of the islets to clarify their role in the nuclear architecture. For *in situ* studies of PIP2 islets by electron microscopy, we have previously compared different sample preparation techniques, including on-section immunolabelling of resin-embedded cells, pre-embedding immunolabelling, and Tokuyasu method. While all these methods produced comparable results in visualization of PIP2 islets, all of them use certain steps that might cause lipid translocation or/and extraction. As lipids are not chemically fixed by aldehydes, we employed quick-freezing – freeze-fracture replica labelling (QF-FRL). Using this method, the biological material is fixed physically – by high-pressure freezing, and

subsequently mechanically – by coating with carbon/platinum layer. Due to it, QF-FRL fixes also lipids, furthermore the samples are considered to be closer to the native state as compared to resin embedding or Tokuyasu protocols. We were able to immunolabel PIP2 present in membranes as well as PIP2 which is localized in non-membranous compartments. We mapped PIP2-containing intranuclear structures, such as nucleoli, nuclear speckles and PIP2 islets. PIP2 islets in the nucleoplasm were of the same size and shape as revealed by other techniques. The results demonstrate that PIP2 islets are stable structures resistant to aldehyde fixation and extraction, which is possibly ensured by interactions of lipidic components with proteins. This work was supported by JSPS (15K21738), GACR (15-08738S, 16-03346S), TACR (TE01020118), HFSP (RGP0017/2013), IMG grant (RVO: 68378050), MEYS CR (LM2015062), OPVVV (CZ.02.1.01/0.0/16_013/0001775). We gratefully acknowledge lending ACE900 from Leica Microsystems. The microscopy work was performed in the IMG Microscopy Centre – Electron Microscopy Core Facility.

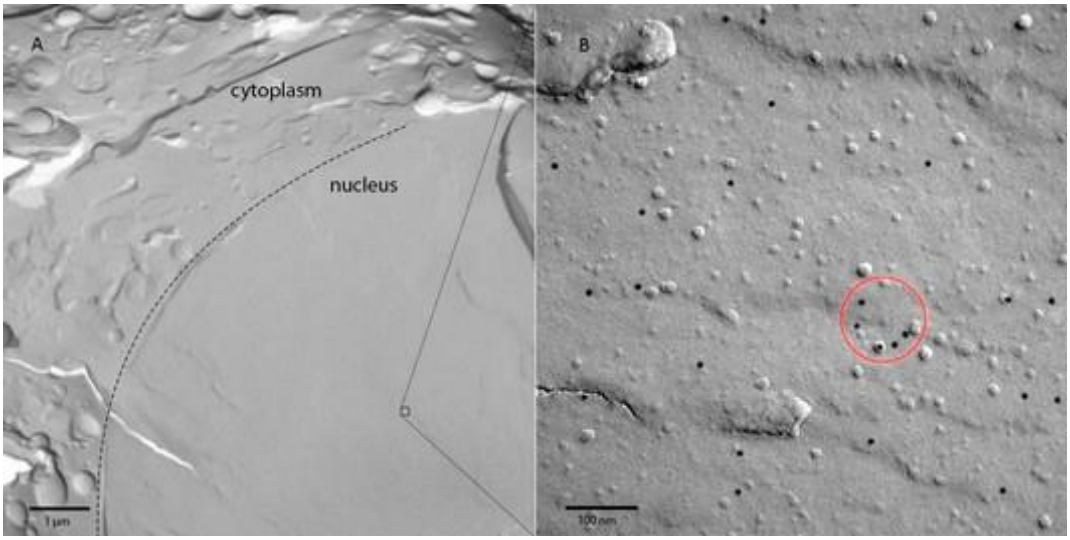

Figure 1. Nuclear PIP2 islets on replicas. A: Replica of HeLa cell with cross section through nucleus. B: Magnified region of interest from picture A. PIP2 molecules are detected by anti-PIP2 antibody, nucleoplasmic PIP2 islet is highlighted by a red circle.

AUTHOR INDEX